# Shear band induced damage development during the bending of ultra-high strength steels

**Mr Robert Dowding**

A thesis submitted in partial fulfilment of the requirements for the degree of
Doctor of Philosophy

The University of Sheffield
Faculty of Engineering
Department of Mechanical Engineering

Submission Date

14/08/2021

*I, the author, confirm that the Thesis is my own work. I am aware of the University's Guidance on the Use of Unfair Means (www.sheffield.ac.uk/ssid/unfair-means). This work has not been previously been presented for an award at this, or any other, university.*

Please ensure that any publications arising from the thesis are acknowledged in this section.

# Acknowledgements

I would like to thank my family and friends for helping me through the project. Mum for providing advice as always. My supervisor, Christophe has always been very helpful and assisted with the work immeasurably enabling this project to flourish. Didier also provided great assistance in the project and without his insight, this project would have been significantly less fruitful. I would also like to thank colleagues for their inputs throughout the work, particularly; Abraham, Alejandro, Kenneth, Jundi and Syeda. While working at home the visits from the neighbour's cat, Nel provided great relief from the stress of writing by always wanting attention.

# Abstract

The bending of ultra high strength steel removes the need to perform welding with its associated environmental damage from gases or power usage and can cause adverse health conditions for welders. Bending is also known to be stronger than a welded component and offer financial benefits with lower-skilled operators and lower costs. The ultra high strength steel market is currently growing 7% year on year primarily within the automotive sector and reducing the need for welding using the Tata steel ultra high strength steel products will bring environmental, economic, quality of life for manufacturers and health and safety benefits.

To facilitate this, this study analyses the bendability of Ultra high strength steel. This currently has limited manufacturing processes due to poor bendability and shear bands have been identified as the failure mode. The project identifies the mechanisms promoting shear bands and how these develop into damage.

Using a rigorously developed new tooling in an insitu bend test module with scanning electron microscope imaging, a new methodology for micro strain analysis in bending has been developed. This has been enhanced by implementing new specimen design and preparation methods to leverage the application of new tooling. Using interrupted tensile and bend tests with digital image correlation, DIC found that shear bands are detected at the onset of plasticity. Shear bands in bending are promoted with mode 2 loading, shearing at around 45° to the top surface. The harder surface promoted sharp cracks that act as stress raisers and propagate through the depth. While the softer surface in bending deformed plastically at microstructural interfaces, shearing resulted in no damage propagation into the subsurface. The hardness has an inverse correlation with the number of shear bands, promoting localisation of strain and damage initiation. Angled bend test specimens showed a change from plastic tearing to crack formation at soft and hard areas respectively.

Using finite element modelling of 3-point bending with both flat and waviness on the top surface of the sample showed increasing strain hardenability. This resisted the formation of micro shear bands and strongly correlates with formability equations found in the literature. While surface waviness acts as stress raisers and changes the failure mode from shear bands to a singular location of strain at the trough of each wave.

This demonstrated that shear bands are formed in bending and priority should be promoting numerous shear bands visible at a microscopic level of detail. These resist the microscopic strain localising at the macroscale that promotes bending failure.

# Contents

# Nomenclature

| | |
|---|---|
| $r_i$ | The radius of bend test former (mm) |
| $T$ | The thickness of the bend test specimen (mm) |
| $F$ | Force (N) |
| $d$ | Mean diagonal of the micro indentation (µm) |
| $A_r$ | Area of the residual impression (µm$^2$) |
| $H_n$ | Nanoindentation hardness (unit) |
| $H_m$ | Micro indentation hardness (unit) |
| $n$ | Hardenability |
| $m$ | Strain rate hardenability |
| $\eta$ | Triaxiality |
| $\bar{\theta}$ | Lode angle |
| $\theta$ | Angle (°) |
| $\theta_B$ | Bending angle (°) |
| $\alpha_\theta$ | Half bending angle (°) |
| $F_y$ | Bending force (N) |
| $L_0$ | The initial horizontal distance from the centre of the former to the centre of support in 3 point bending (mm) |
| $M_0$ | Initial bending moment (Nmm) |
| $R_f$ | The radius of bending former (mm) |
| $R_s$ | The radius of bending support (mm) |
| $S$ | Punch displacement (mm) |
| $M_B$ | Bending moment for $\theta_B$ (N.mm) |
| $L_B$ | The horizontal distance between the 2 contact points during 3 point bending (mm) |
| $Q$ | Sum of the former, support and thickness of the plate in bending. (mm) |
| $R_T$ | Sum of the radius of the former, support and thickness of the plate in bending (mm) |
| $P_1$ | Part 1 of the true bending calculation formula |
| $P_2$ | Part 2 of the true bending calculation formula |

| | |
|---|---|
| $\alpha$ | Flow localisation factor |
| $\sigma$ | Stress (MPa) |
| $\varepsilon$ | Engineering strain |
| $\varepsilon_T$ | True strain |
| $\dot{\varepsilon}$ | Strain rate (dimensionless/s) |
| $\gamma'$ | Strain-rate strain-hardening rate (dimensionless/s) |
| $\varepsilon_p$ | Plastic strain |
| $K$ | Strength coefficient (MPa) |
| $\eta$ | Triaxiality, the stress state of a region under stress |
| $\sigma_m$ | Mean stress (MPa) |
| $\sigma_{eq}$ | Equivalent stress (MPa) |
| $L$ | Lode angle parameter |
| $HV$ | Vickers hardness |
| $A_c$ | Berkovich indentation area ($nm^2$) |
| $h_{max}$ | Maximum indentation depth of a Berkovich in nanoindentation (nm) |
| $C$ | The area of indentation fitting parameter for nanoindentation |
| $m_i$ | The second fitting parameter for nanoindentation |
| $h$ | Nano indentation depth (nm) |
| $h_f$ | Residual depth in nano indentation (nm) |
| $h_c$ | Contact depth in nano indentation (nm) |
| $S_h$ | Nano indentation stiffness (nm) |
| $F_{max}$ | Maximum force when performing nano indentation (N) |
| $\varepsilon_h$ | Indentation geometry correction factor |
| $H_n$ | Nano indentation hardness (GPa) |
| $A_s$ | Fracture area ($mm^2$) |
| $w_s$ | Width prior testing (mm) |
| $w_s'$ | Necked width post-test (mm) |
| $t_s$ | Thickness before testing (mm) |
| $t_s'$ | Necked thickness post-test (mm) |
| $k_m$ | Module stiffness (N/mm) |

| | |
|---|---|
| $k'_m$ | Stiffness of the module and specimen outside of the gauge length (N/mm) |
| $k_s$ | Sample stiffness (N/mm) |
| $u_m$ | Module elastic extension (mm) |
| $u_s$ | Sample elastic extension (mm) |
| $u_T$ | Total of the module and sample elastic extension (mm) |
| $u_s^{OGL}$ | Sample elastic extension outside gauge length (mm) |
| $u_s^{GL}$ | Sample elastic extension within gauge length (mm) |
| $u'_m$ | Total of the extension from the module and sample excluding the gauge length (mm) |
| $l_s$ | Gauge length (mm) |
| $\theta_l$ | Left side bending angle (°) |
| $\theta_r$ | Right side bending angle (°) |
| $S_s$ | Shear band spacing (µm) |
| $W_{xx}$ | Width of the field of view (µm) |
| $N_s$ | Number of shear bands in the field of view |
| $F_T$ | Bending force in tons (tons) |
| $w$ | Width of the specimen (mm) |
| $T$ | The thickness of specimen (mm) |
| $\sigma_{UTS}$ | Ultimate tensile strength of the material (MPa) |
| $W_{cc}$ | Width from the centre of one support to the centre of the other support (mm) |
| $\varepsilon_{cp}$ | Critical plastic strain |

# Acronyms

| **Acronyms** | **Meaning** |
|---|---|
| UHSS | Ultra high-strength steel |
| AHSS | Advanced high-strength steel |
| SEM | Scanning electron microscope |
| FEM | Finite element modelling |
| FCC | Face centred cubic |
| EBSD | Electron backscatter diffraction |
| BCC | Body centred cubic |
| RD | Rolling direction |
| TD | Transverse direction |
| ND | Normal direction |
| $R_{tot}$ | Hot rolling reduction |
| ASTM | American Society for Testing and Materials |
| BSI | British Standards Institution |
| SB | Shear band |
| MSB | Macroscale shear band |
| µSB | Microscale shear band |
| ECAP | Equal channel angular pressing |
| FZ | Fracture zone |
| BZ | Burnish zone |
| MnS | Manganese sulfide |
| GTN | Gurson–Tvergaard–Needleman |
| DP | Dual phase |
| GB | Grain boundary |
| DIC | Digital image correlation |
| DSCM | Digital speckle correlation method |
| EDM | Electro discharge machining |
| UTS | Ultimate tensile strength |
| EDS | Energy-dispersive X-ray spectroscopy |
| SD | Standard deviation |

# 1 Introduction

## 1.1 Engineering applications

The bending of materials is a common procedure in manufacturing. A flat part undergoes localised plastic deformation that deforms the specimen into a new profile. This is often performed with a press brake, these function by using top and bottom tooling to impart bending force on the bending specimen. Powerful hydraulic rams impart a force onto the specimen via the tooling and bend the specimen into the users desired form. There is a significant enough market that several companies produce press brakes and tooling of various forms, sizes and functionalities [1]–[3]. Bending has become a popular manufacturing method due to its speed, low cost, limited use of consumables, reduced number of piece parts and low expertise needed. Using bending as a standard manufacturing procedure the manufacturers expect specimens to be possible be bent with consistent quality and no visible damage or defects [4], [5].


*Figure 0-1: An example of a modern press brake* [6].

The market for UHSS is worth $590.92 million [7] and is forecast to grow at 7.18% per year until 2026 [8]. In this market, Tata Steel is a major manufacturer. The market growth is due to the increase in the adoption of use in the automotive, defence and aeronautical industry [9]. In the automotive sector, this is due to it allowing lighter structures in cars which is particularly important with our transition to battery electric vehicles. In this market, any weight saving is critical to reducing the

weight of the vehicle overall. This is because “a reduction in 10% vehicle mass reduces fuel usage 6-8%” [10] thus driving significant environmental benefits from the introduction of lighter UHSS parts. The UHSS market is due to grow and Tata Steel will aim to provide an innovative steel grade that adds value to the end-user by allowing the adoption of bending in the production. This offers 2 benefits to the user. One is that bending produces a stronger final part than a welded part [11]. The other major benefit is to the health of the operators who no longer get exposed to welding fumes [12]. One of the common health problems is respiratory disease but the fumes are also known to be carcinogenic [13]. To limit the exposure users have to these fumes guidelines have been provided to give standards that fume extraction systems should meet [13]. Minimising the use of welding with other operations such as bending will improve the quality of life for these operators.

To form these structural elements 3-point bending can be used. This forming method uses a single former and two supports. Force can be applied from either the former, supports or both. When bending force is applied the specimen deforms and the ductility of the material allows it to plastically deform until the desired bend test angle is achieved $\theta_B$. The force can then be removed, as the plasticity retains the profile of the bend and the final bend angle of the specimen is the bend test angle minus the spring back due to elasticity.

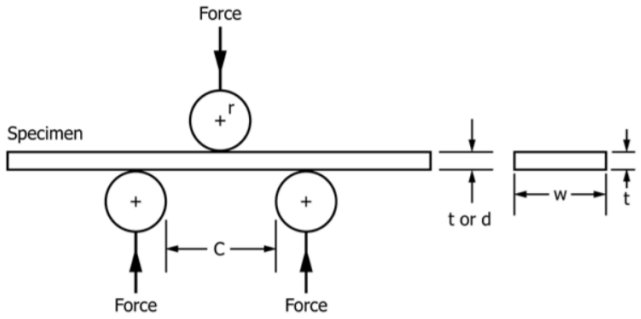


*Figure 0-2: ASTM standard diagram for 3-point bend testing [1].*

While 3-point bending has many benefits, the bending process strains the material in a non-uniform manner through the thickness. This adds some unique requirements of the materials used in bending where highly localised plasticity is imparted on the top and bottom of the specimen in tension and compression.

The ease with which the material can be bent is defined as the bendability of the material [14]. This is a quantifiable limit used in industry. It has been found that ultra-high-strength steels (UHSS) have limited bendability even though it has a good elongation to failure of 8% or more [15]. When bent at progressively smaller radii, shear bands, surface waviness and failure at the tensile surface have been observed [14]. These are not suitable for manufacturers; this has prompted Tata Steel Europe to

research the properties of the bendability and define the factors limiting UHSS to produce an improved product. In these trials, 3 point bending was chosen as it is more challenging than 4 point bending for the material to withstand. For smaller bending radiuses only 3 point being or v bending is viable. This makes 3 point bending the worst-case scenario for the 3 point bend

Current published studies show a lack of understanding of the formation of shear bands which limit the bendability of UHSS. A new approach is therefore needed to develop new insight into the conditions leading to the formation of shear bands.

## 1.2 Research aims

The research aims were to understand at a microscopic level of detail the features controlling the onset of shear bands leading to crack initiation and ultimately failure in UHSS steels in 3-point bending.

## 1.3 Objectives

1. Characterize the S960 steel.
    a. Overall and sub size tests through the thickness of the material to obtain material properties such as elastic limit, tensile stress, maximum strain at different regions through the thickness.
    b. Analyse overall tensile properties for full-thickness samples
    c. Perform micro and nano hardness indentation testing analysis.
2. Understand the limit of bendability
    a. Perform initial bend test analysis
    b. Design and develop tooling to promote shear bands and damage in specimens.
    c. Design compatible specimens to observe the shear bands and analyse their initiation and transition to damage.
        i. Test varied material properties in bending tests to understand the effects of changing material properties for bendability.
    d. Optimise sample preparation to prepare specimens for bend testing
    e. Perform bend tests analysing the localised deformation in bending
    f. Quantify the density of shear bands and perform a statistical analysis of strain localisation.
3. Create models in Abaqus to model stress, strain and damage using information gathered from the material characterisation.

a. Use 3D models to develop enhance the modelling of specimens and optimise both tooling and specimens
b. Simulate 2D simulations to study the effect of surface layer properties.

4. Use these results to inform the development of improved bendability.

## 1.4 Structure of the thesis

To develop a means to fulfil the research aims the project is broken into the following 6 sections:
The Literature review looks at the current literature and seeks to find the current state of art, what can be understood and what the gaps in the knowledge were. This was used to identify where to focus the work.
The experimental & finite element modelling methodology set out to identify what techniques and technologies to use and the methodologies to make best use of them. This informed the testing procedure and was adapted during lockdown to be compatible with the new working environment.
The Tooling and specimen design and methodology were dedicated to the development of the bend test tooling used in the Results section. These were changed to increase the strain on the specimens and produce repeatable bend test results with little tool deflection and highly localised strain in 3 point bending.
In Results, the new methodologies were used to produce results. This shows in detail how the approached evolved as the project matured, particularly in the Bend testing section with 3 different tooling designs used and 3 different specimen geometries. The tooling improved with each generation and the specimens helped identify different features limiting bendability. These provided in microscopic detail the development of strain localisation in shear bands and damage initialisation in bending. While the Modelling results highlighted that shear bands can be formed in 2D continuum models.
These results are analysed and compared to those found in the literature in the Analysis and discussion section. The modelling was found to be a useful tool to explore the impact of varying material properties and geometry. These were used to study the initiation of shear bands and study how these differ to those found experimentally.
This is drawn to an end in the Conclusion with actions for Tata Steel and Further work both covered to maximise the impact of this work.

# 2 Literature Review

## 2.1 Steel manufacturing process

Steel has been a popular material to manufacture with since it was mass-produced due to several factors:

- Steel consists of mostly iron, which is one the most abundant material by mass on the earth's mantle [16]. Making the material cheap to mine with reduced environmental effects.
- Easy to process, no energy-intensive production routes compared to other metals such as aluminium or composites.
- Low cost.
- Good machinability.
- Simple to use in production.
- Good toughness.
- Has a wide range of properties depending on its production methods. This can be varied depending on the customers' needs.
- Offers high strength with good ductility in many variants.
- Can be recycled infinitely.

Iron products became obsolete with the introduction of steel into mass production two centuries ago. This was driven by new technology, manufacturing processes and ideas that developed a means of removing the impurities of cast iron and adding alloys to produce steel. This resulted in a greatly improved material over the previous iron which was significantly cheaper than the small scale production of steel. Since then, those drivers have continued to develop improved steels, enhancing them to become a stronger, more diverse, and more economical material. This has allowed steel to remain a viable material in a huge number of applications in the modern world with frequent new developments being made to improve its properties and diversify its applications.

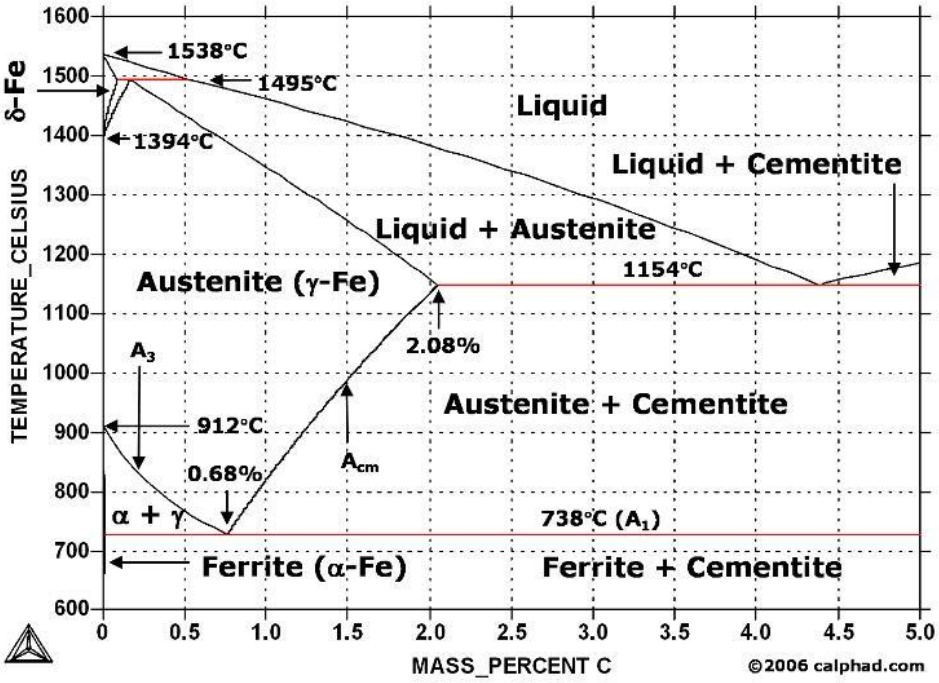


*Figure 2-1: Steel metastable phase diagram for iron and carbon* [17]

Modern steels are carefully designed to suit their product roles. The UHSS is used in cranes requiring a high strength but also high toughness to avoid brittle failure. The carbon content is below 0.1% to improve its welding properties [18]. One method of obtaining higher strength steels is to add additional carbon and this affects the microstructures produced as shown in Figure 2-1. A more complicated phase diagram would be required considering several alloys elements used in modern steel.

### 2.1.1 Microstructures

When at temperatures above 1000K steel is a soft ductile phase known as austenite. As this cools the austenite is no longer stable and transforms into a different microstructure. The alloys, cooling rate and thermomechanical treatment can all be used to develop different microstructures each with different properties. The cooling rate changes the transformation kinetics this allows different microstructures to be developed as shown in Figure 2-2.

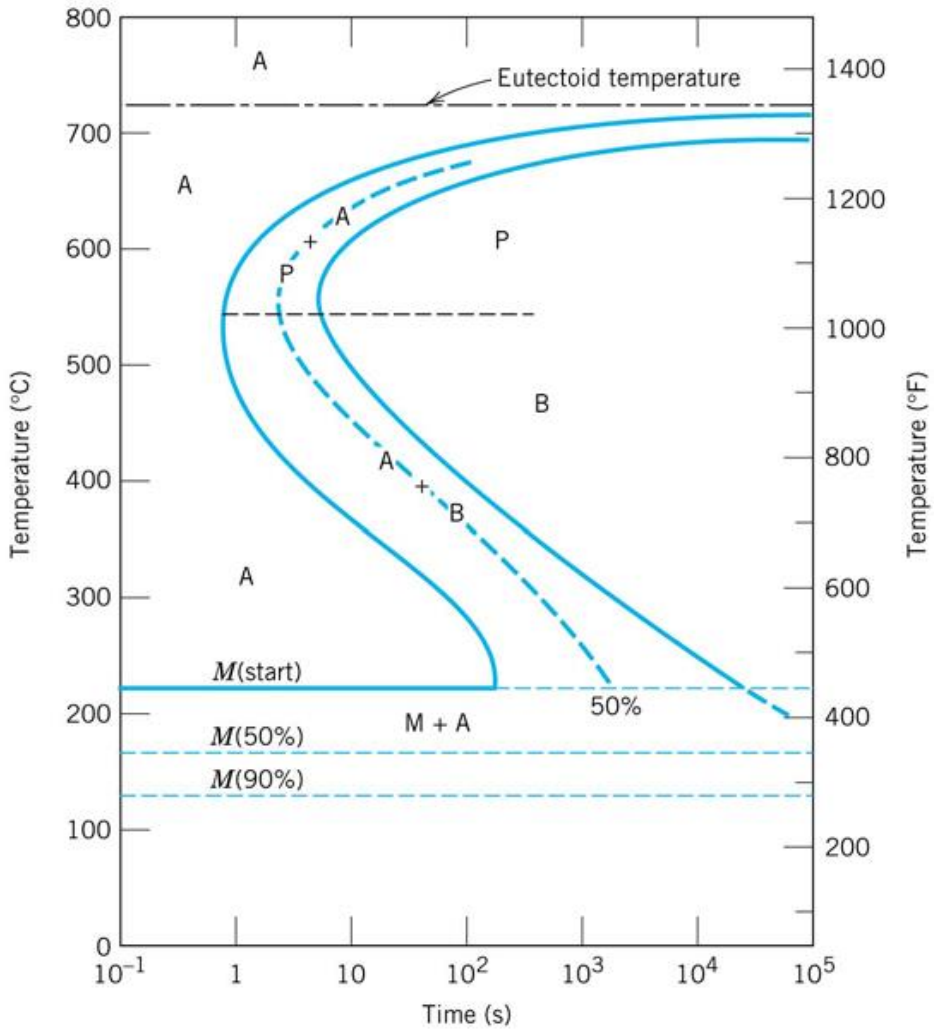


Figure 2-2: TTT diagram for 1080 steel, 0.8% carbon, A for austenite, M for Martensite, P for pearl

Using a rapid means of cooling the steel can produce martensite which is used in stronger less ductile steels including S1100 and S960. Slower cooling promotes bainite and ferrite, these softer microstructures are also found in S960 and S700.

#### *2.1.1.1 Austenite*

At temperatures above 1000K steel is in a soft phase known as austenite. This microstructure has a face-centred cubic (FCC) atomic structure, this structure allows for the absorption of a lot of carbon and alloys. During cooling, this structure becomes unstable and changes to other microstructures. While austenite can be difficult to observe with SEM imaging if electron backscatter diffraction (EBSD) is used the FCC structure that differentiates it from other phases can be identified.

#### *2.1.1.2 Martensite*

When austenitic steel is rapidly cooled martensite is formed. This transformation is described as a "military transformation" by Christian et al [19] Here the face centred cubic structure of austenite transforms into a deformed body-centred tetragonal or body centred cubic of martensite. Due to the speed of the transformation, the alloys cannot diffuse out of the austenite this results in the

martensite being supersaturated by alloys. This can then receive further heat treatment to allow the alloys to diffuse onto the grain boundaries to improve toughness with limited reduction in the strength of the steel. These result in precipitates at the boundaries of the microstructures. These can be observed with high magnification SEMs

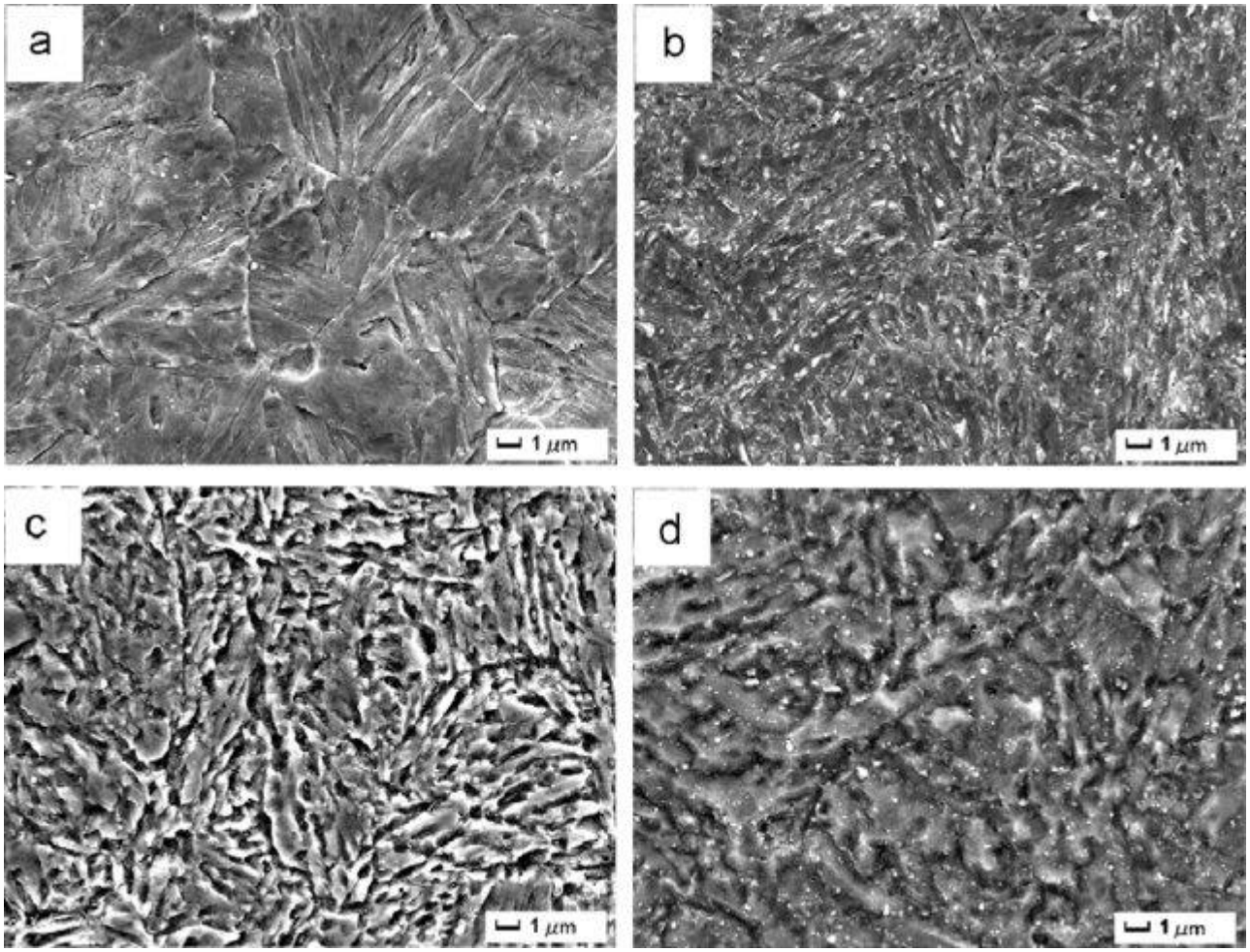


*Figure 2-3: SEM micrographs martensite with different manufacturing processes, a, quenched, b, tempered at 200°C, c, 650°C and d, 700°C* [20].

### *2.1.1.3 Bainite*

Bainite is generated when steel is cooled at a rate between martensite and ferrite and consists of ferrite and austenite in lathes. This can be further refined to being upper and lower bainite where the upper bainite is stronger due to the austenite retaining the alloying elements as shown in the left micrograph in Figure 2-4. While lower bainite is softer as cementite nucleates on the interface between the ferrite and austenite. When bainite is formed in non-isothermal, continuously cooled conditions this generates granular bainite, this is generated in a random granular pattern rather than lathes as shown in the right micrograph in Figure 2-4. Bainite is more ductile than martensite, but properties vary between upper and lower bainite with the lower bainite having the better ductility.

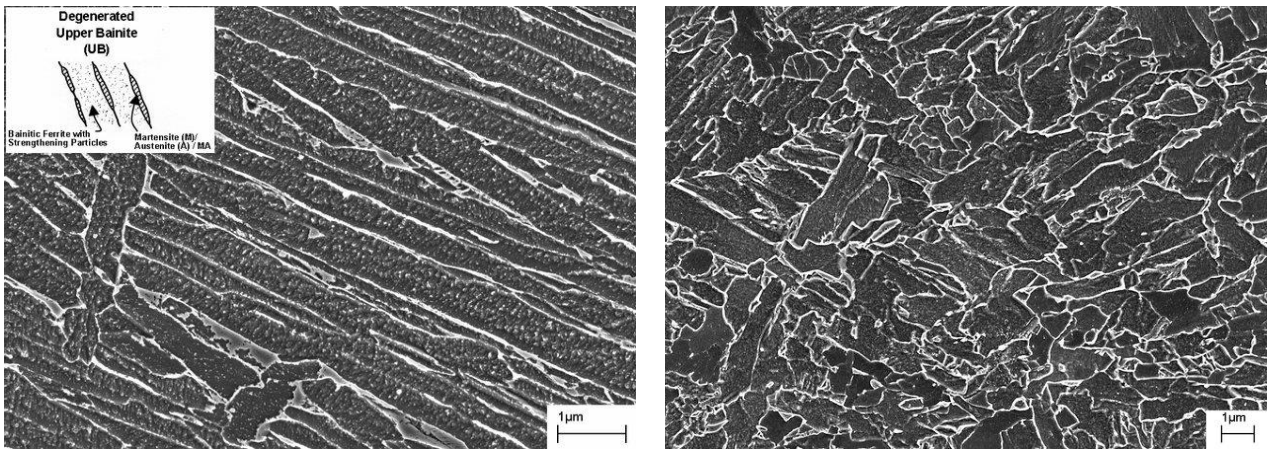


*Figure 2-4: Micrographs of bainite, left, SEM micrograph of upper bainite with the bainitic ferrite and austenite visible and right, SEM micrograph of granular bainite* [21]

### *2.1.1.4 Ferrite*

The slowest cooling rates promote ferrite this is the softest and most ductile of the phases other than austenite. This allows significant diffusion of carbides out of the microstructure producing the soft phase. This can be distinguished from martensite by its darker colour in SEM micrographs particularly with backscatter electron micrographs. This allows easy identification of DP steels consisting of martensite and ferrite with SEM imaging as shown in micrographs b and c in Figure 2-5. Ferrite is known to have excellent formability due to its low hardness and is often used with martensite in car body panels for its combined mechanical strength and formability [22].

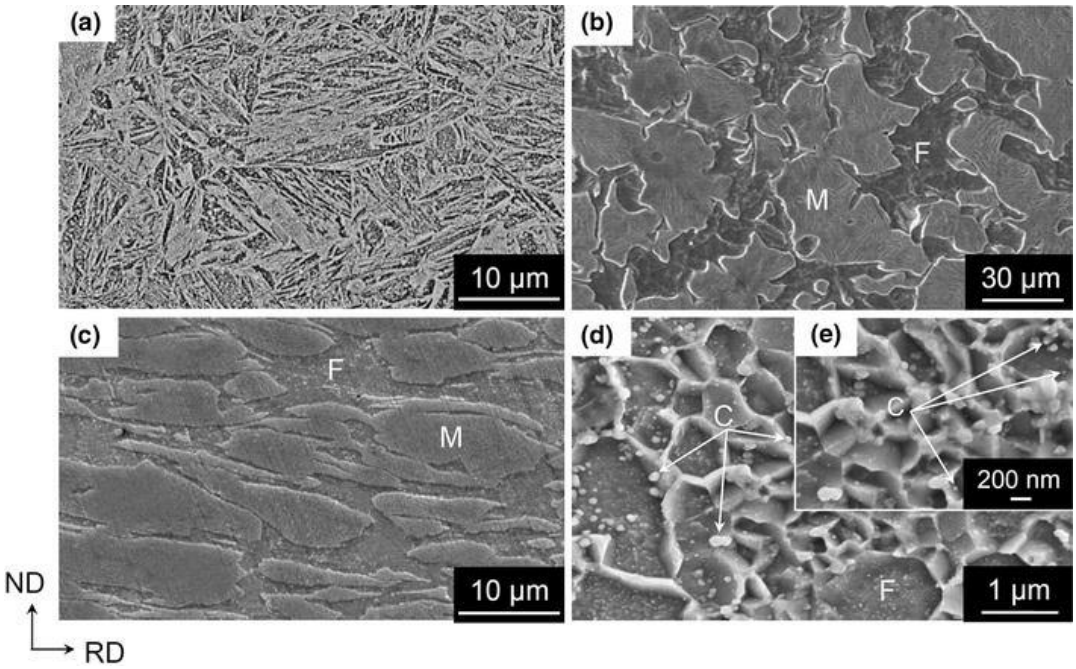


*Figure 2-5: SEM microstructures with them marked as F, ferrite, M, martensite, C, carbide, with the manufacturing processes a, quenched, b, intercritical annealed, c 80% cold-rolled, d, e annealed at 600°C* [23]

### 2.1.2 Hot Rolling, thermomechanical processing.

The process of hot rolling is an economically viable production method of thermo-mechanically processing steel. This changes the properties of the steel while being of low cost due to there being less time spent cooling for cold rolling processes. This process is normally done above the recrystallisation temperature allowing the austenite to transform into new phases after the rolling operation. Although if the hot rolling is done under the recrystallization temperature this can result in a pancaking effect on the microstructure and the austenite can transform into polygonal ferrite at the surface [24]. This can be driven by adjusting the finish rolling temperature and so grain boundaries are developed that are then subjected to strain changing the diffusion [25]–[27] as shown in Figure 2-6.

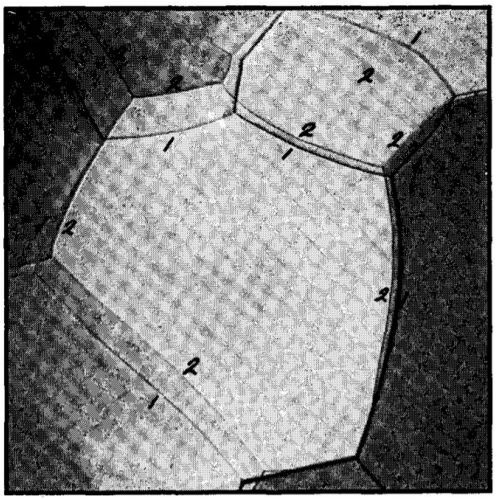

*Figure 2-6: micrograph of boundary movement in grain in aluminium* [28]

Performing this while adjusting the alloying content has been attempted to change the material properties and develop a soft top surface region. The texture of the material at the surface region becomes impacted and intensifies {111} textures [29], [30] and {112}<111>$_\alpha$ at the subsurface as shown in Figure 2-7 [27], [31], [32]. The novel steels have niobium and calcium added that changes their transformation mechanisms while hot rolling with lower final rolling temperatures used. This promotes a refined microstructure at the surface and a softer top surface.

It is reported that this anisotropic behaviour is due to the {112}<111>$_\alpha$ texture of the steel having a geometric softness in one direction[26]. This texture has been promoted by increasing $R_{tot}$ [31], but this, in turn, promotes softer microstructures that are linked to improving bendability [32].

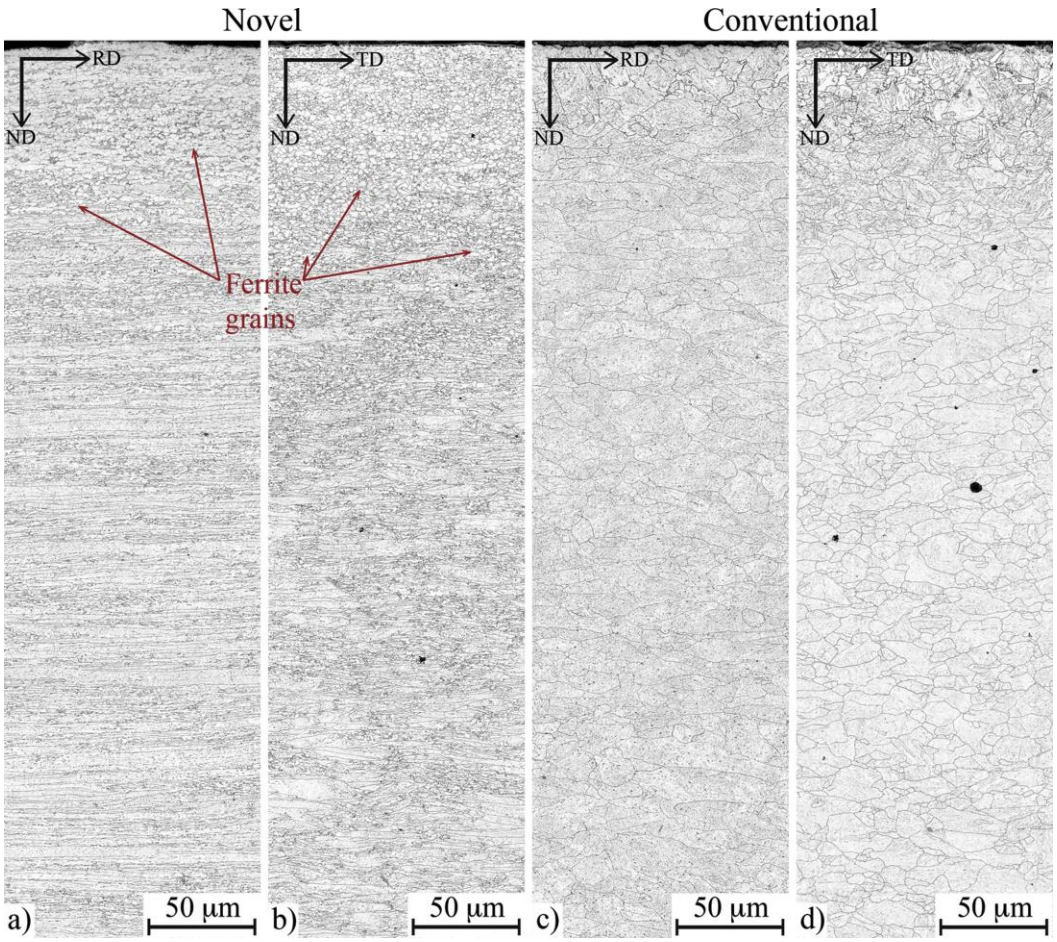


*Figure 2-7: Laser scanning confocal microscope micrograph of a novel and conventional steels* [27]

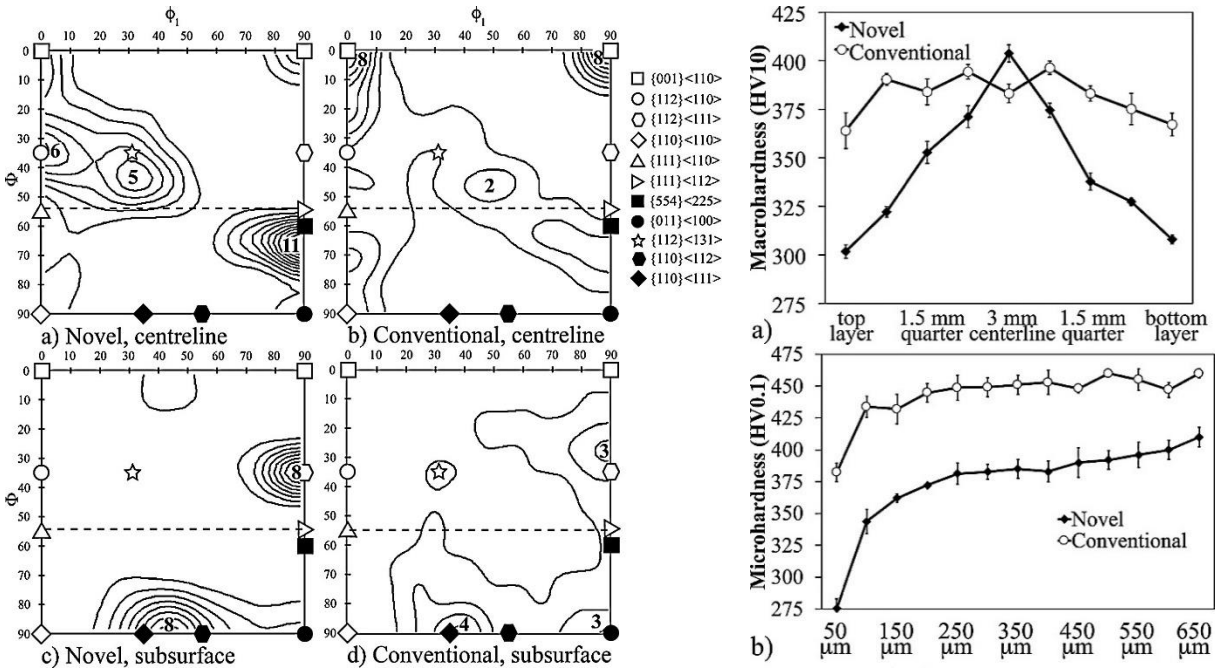


*Figure 2-8: left; $\phi 2 = 45°$ ODF sections showing the textural components at the centreline and subsurface of the novel and conventional steel, right; microhardness from the surface depth of the novel and conventional steel* [27].

### 2.1.3 Decoiling & levelling

To produce the strip steel, it is coiled then tempered. This then requires decoiling and levelling to produce the final steel product. The process involves the material being thermally and mechanically reprofiled with rolling mills to flatten the steel. Tata Steel has state of the art recoiling facilities in the UK suitable for UHSS [33]. This is reported to add minimal amounts of plastic deformation.

## 2.2 Bendability

In industry, the common method of assessing the bendability of a material is to find the materials former radius to thickness ratio $r_i/T$, where a lower ratio has the greater bendability. The bendability ratio is shown in Equation 1 and the internal radius, $r_i$ and thickness, $T$ are shown in Figure 2-9.

$$\frac{1}{Bendability} = \frac{r_i}{T}$$ *Equation 1*

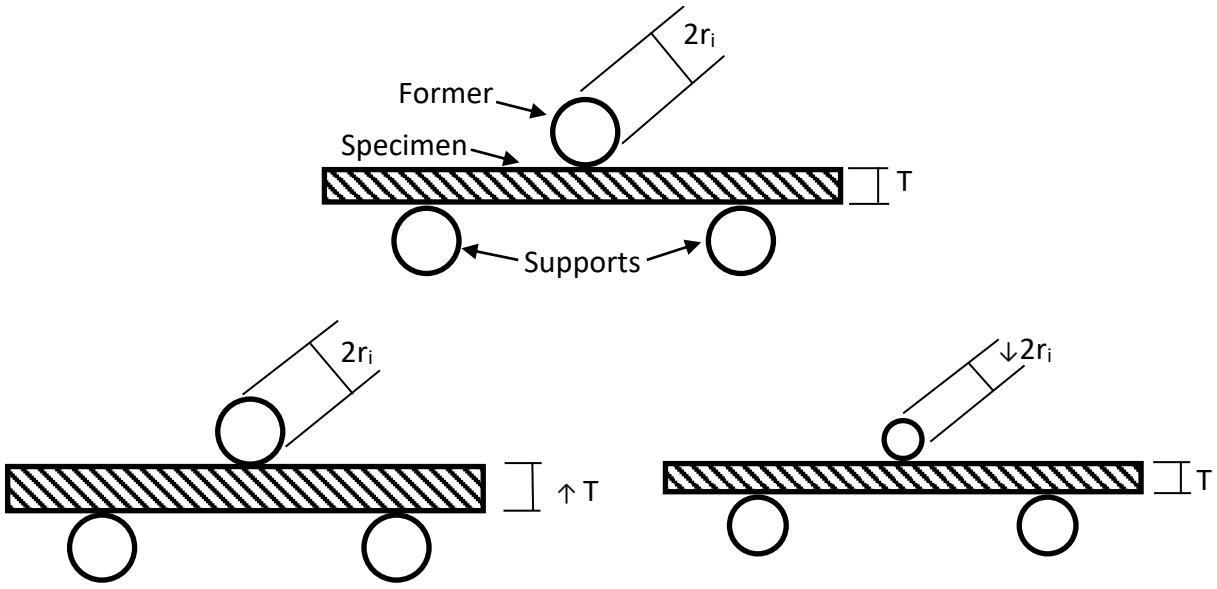


*Figure 2-9: diagrams for evaluating bendability, top, diagram of the variables, bottom left, increase the bendability by increasing thickness, bottom right, increase bendability by reducing radius.*

This is a convenient means of following the correct bending procedure by selecting the appropriate radius former for the materials given thickness. If a bend is performed at a $r_i/T$ ratio and the resulting bend has no imperfections it is considered to have been a success as defined by the ASTM and BSI standards [4], [5]. As shown in Figure 2-9 the $r_i/T$ ratio can be reduced, increasing the demands on the material to pass this test. This can be done by an increase in thickness, reduction in former radius or both. The ASTM and BSI standards define a failure to have occurred if a defect or crack occurs in the central region of the bend one thickness of the specimen from the edge, to be considered a failure this must be observed by eye with no visual aids [4], [5].

While this is acceptable in industry, this knowledge is empirically derived, qualitative and provide any detail on the formation of shear bands in the material. With this being considered other literature on

the bending of plate and strip was investigated to develop a better understanding of how further information can be extracted from bending of materials through other methodologies.

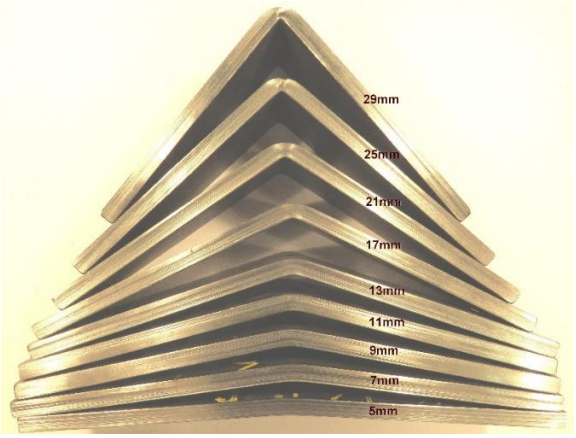


*Figure 2-10: S960 test strip bent via a series of stroke lengths specified in the image* [14].

To standardise the bending geometry the ASTM and BSI standards have defined the following equations with the dimensions as defined in Figure 2-11. These equations are effectively identical and show the standard tooling design.

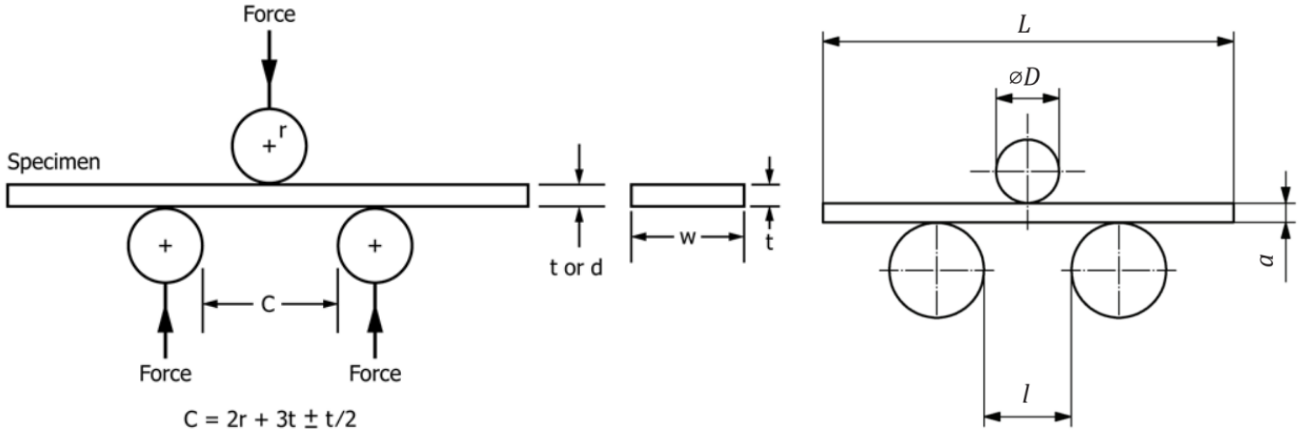


C = 2r + 3t ± t/2

NOTE 1—*C* = distance between lower supports,
*r* = radius of the end of the mandrel or plunger,
*t* = sheet specimen thickness,
*d* = round specimen diameter, and
*w* = sheet specimen width.

$$l = (D + 3a) \pm \frac{a}{2}$$

*Figure 2-11: Bend test tooling geometry as defined by on the left, ASTM* [4] *and right, BSI* [5].

### 2.2.1 The mechanics of bending

The bending of metallic materials stresses the material into the plastic region in the inner and outer faces of the bend which then propagates through the thickness of the material. When the required bending angle is achieved this plastic deformation then freezes the bend in place after some spring back when the bending forces are removed. There are regions through the thickness of the bend, these are:

1. The tensile stressed region on the outer surface.
2. The neutral axis is typically found near the middle where stresses are zero.
3. The compressive stress region in the inner surface.

Typically bend testing is studied by performing a bend test in different orientations with the bend line running either parallel or transverse to the rolling direction. This was to study the effect of specimen orientation and then bent swapping the top and bottom surfaces to check for anisotropy. This provides force-displacement curves that allow the study of force drops indicating the initiation of damage. These when combined with observation of the specimens have been used to study the initiation of damage in specimens.

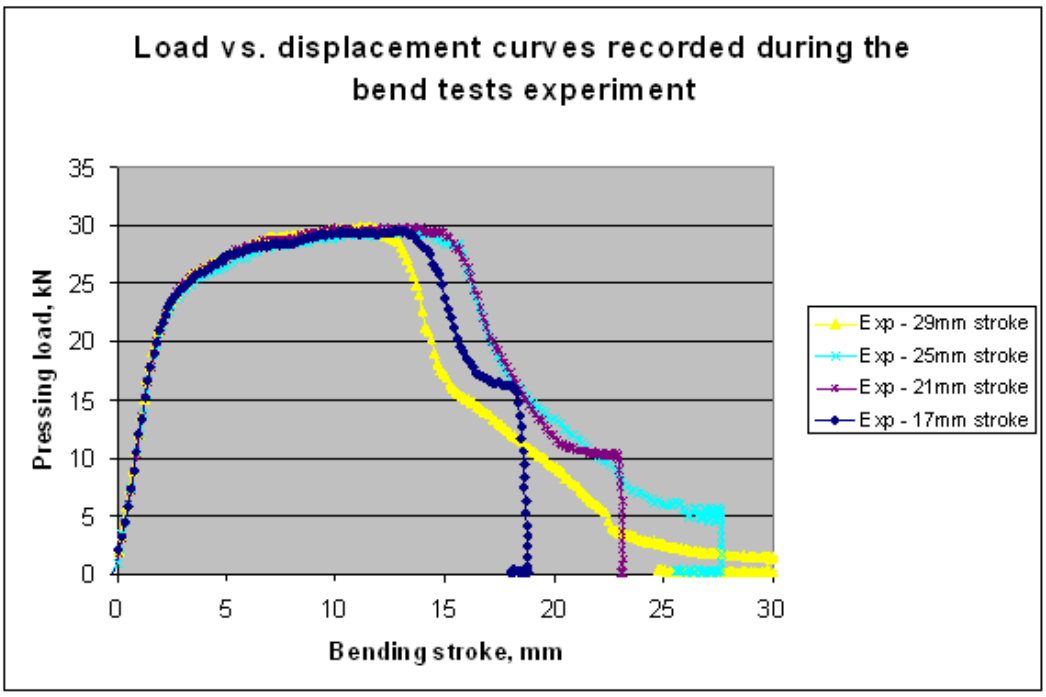


*Figure 2-12: Bend test force-displacement experimental data* [14]

New methods of studying damage initiation have been developed studying the bending moment and are reported to provide more information from the bending force-displacement graph [34]. Troive et al. [34] report that bending forces naturally drop during bending. Thus, a means of studying the bending moment has been developed to study the true loading properties. A bending design in Figure

2-13 has been developed to reduce friction when bending by having die rollers act as the supports. A method was proposed for calculating the bending moment reduction which is more indicative of damage initiation than the bending load drops [34].

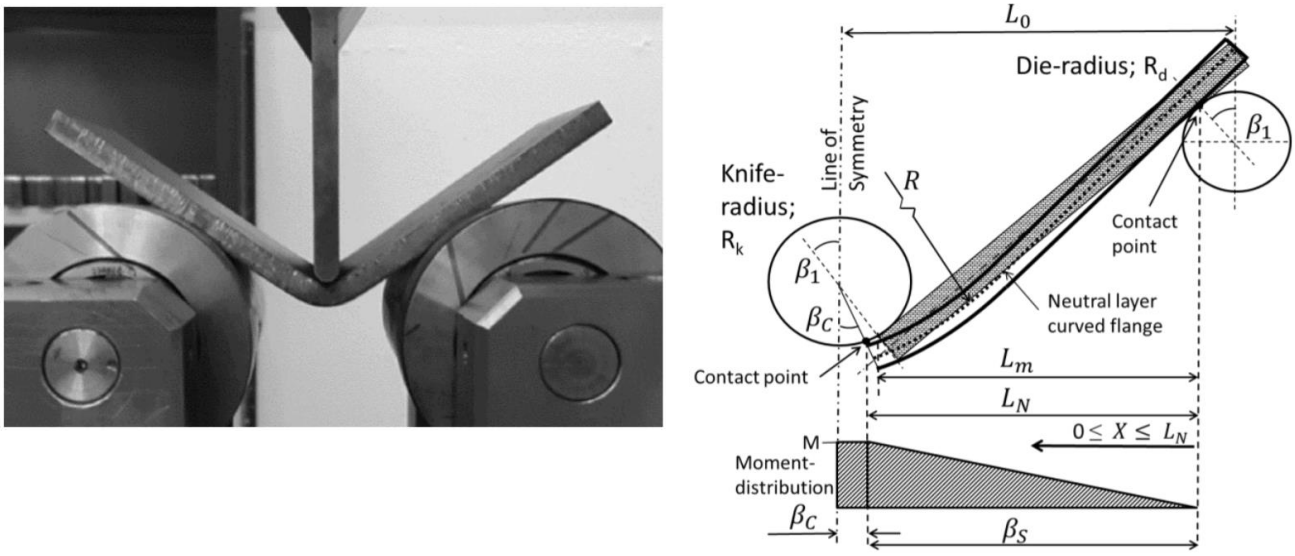


*Figure 2-13: left; Friction-free die roller design with die rollers acting as supports for the bend, right; demonstration of the geometric variables and moment diagram for 3 point air bending* [34].

For initial bending angles then the moment can be:

$$M_0 = \frac{F_y L_0}{2} \qquad \textit{Equation 2}$$

With changing bending angles, the point of contact moves and thus the length over which the moment act varies and has been accounted for by accounting for these geometric changes in bending:

$$M_B = \frac{F_y L_B}{2\cos^2 \alpha_\theta} = \frac{F\left(L_0 - \left(R_f + R_s\right)\sin \alpha_\theta\right)}{2\cos^2 \alpha_\theta} \qquad \textit{Equation 3}$$

To calculate the half bending angle as shown in Figure 2-13, this can be calculated with Equation 4:

$$\alpha_\theta = \sin^{-1}\left(\left(L_0 Q + (S-Q)\sqrt{{L_0}^2 + (S-Q)^2 - Q^2}\right)\left({L_0}^2 + (S-Q)^2\right)^{-1}\right)[rad.] \qquad \textit{Equation 4}$$

Where: $Q = R_f + R_s + T$

The true bending angle has been calculated as:

$$\theta_B = \alpha_\theta - \int \frac{T \sin \alpha_\theta}{L_0 - \left(R_f + R_s\right)\sin \alpha_\theta} \qquad \textit{Equation 5}$$

$$= \frac{\alpha_\theta (R_T + T)}{R_T} - 2TP_2 \frac{\left(\tan^{-1} P_1 - \tan^{-1}\left(P_1 - \tan\left(\frac{\alpha_\theta}{2}\right)\right)\right)}{R_T}$$

Where: $R_T = R_f + R_s$, $P_1 = R_T\left({L_0}^2 - {R_T}^2\right)^{-\frac{1}{2}}$, and $P_2 = L_0\left({L_0}^2 - {R_T}^2\right)^{-\frac{1}{2}}$

While this has been applied in some experiments [27], [34], it involves producing a claimed, frictionless bend test rig as shown in Figure 2-13. This rig is not always representative of real-world bend tests as removal of all friction via a bearing design is not always practical such as in an SEM with a vacuum. Then Equations 2-4 may not be applicable in all bending applications.

As shown in Figure 2-14 while force is increasing due to the moving contact positions the length the force acts on keeps the moment consistent. When analysing the bend test moment curve, when the moment begins to drop the bend test failure is reported to have occurred [34].

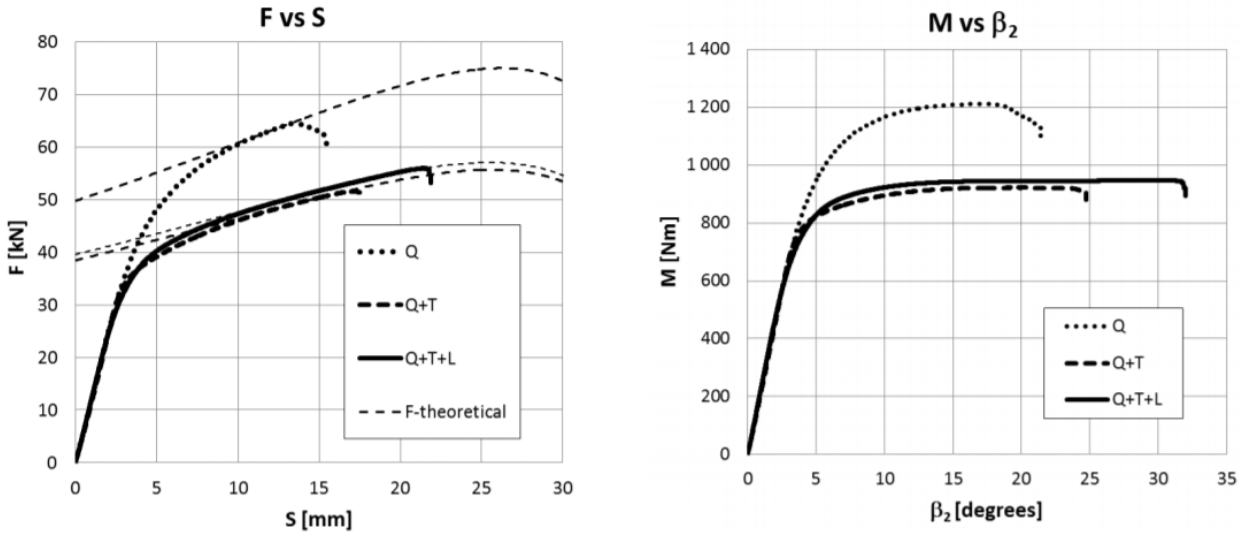


*Figure 2-14: comparison of a force-displacement graph on the left and moment angle graph on the right for bending tests with steel samples, Q; quenched, Q+T; quenched and tempered and Q+T+L quenched, tempered and levelled* [34].

### *2.2.1.1 The anticlastic effect*

When a specimen undergoes bending deformation it is common to only consider the in-plane bending motion. If the 3-dimensional specimen is considered, then due to the tension and compression in the bending plane on either side of the neutral band the material is compressed and tensioned in the other planes respectively. This results in the anticlastic profile in Figure 2-15 where the top surface is promoted into a saddle shape where outside edges are raised and moved further from the neutral axis [35]. Studies have been performed looking at the profiles generated by elastic materials in bending and demonstrate that the effect of the anticlastic behaviour should be considered when designing bend test specimens.

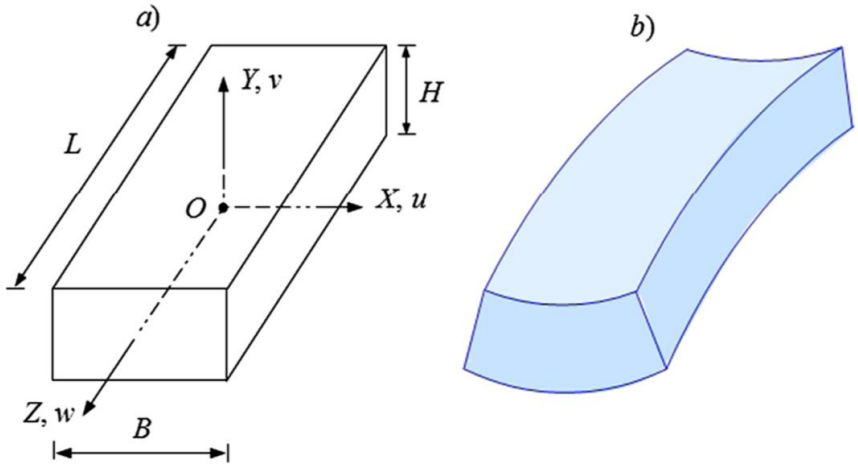


*Figure 2-15: the anticlastic profile of an elastic specimen in bending* [35]

### 2.2.2 Shear localisation and damage

As the UHSS is deformed via 3 point bending shear bands, surface rippling and damage have been reported by Tata Steel [14]. By analysing the samples post-testing with optical microscopes shear bands and surface rippling have been observed in Figure 2-16. The shear bands have consistent properties of being at 45° to the surface, numerous and propagate in both directions. While in other tests such as in Figure 2-17 shear bands and damage have been observed. The crack path is observed to change direction at the intersection of two shear bands.

Shear bands have been observed using optical microscopes in Figure 2-16 these have been seen to be located at depressions at the surface with some of these shear bands showing bifurcation. The shear bands are found at 45° to the surface. Once cracks are generated, they are found to follow shear bands at angles of 45° to the surface.

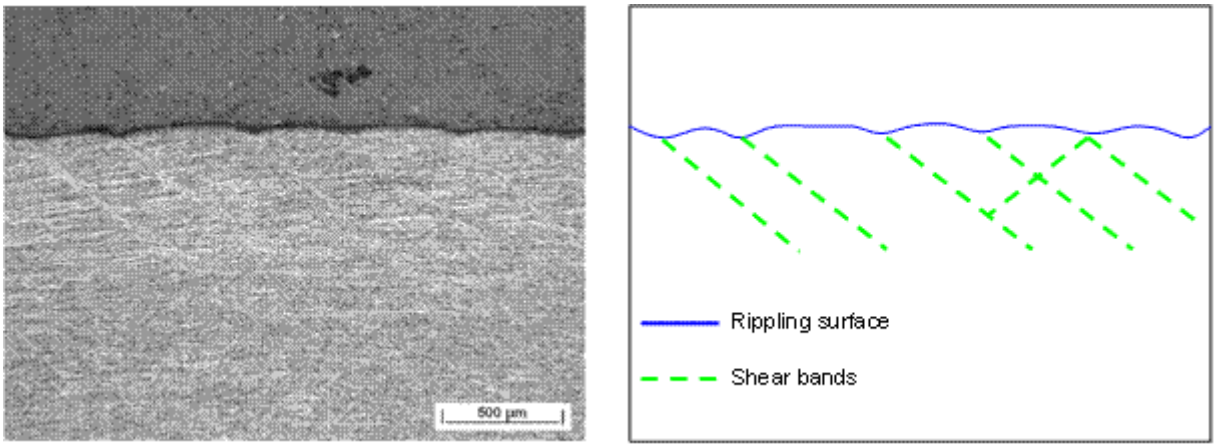


(a) (b)

*Figure 2-16: Surface ripples associated with shear bands (S960, 6mm gauge, 300mm width and 12mm aimed inner bend radius) after bending to 90° (a), and a schematic of the rippling surface and shear bands (b).* [14]

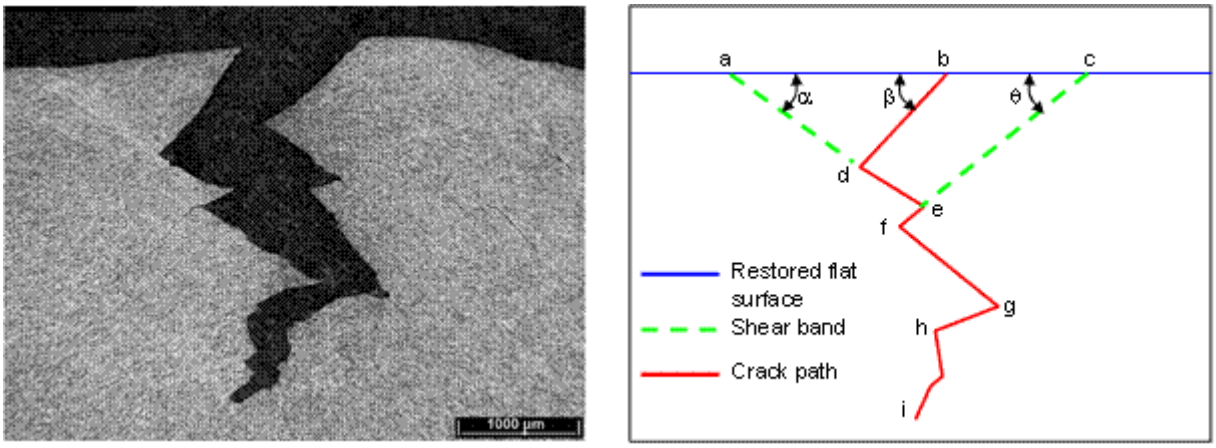


(a) (b)

*Figure 2-17 Etched outer bend surface of S960 sample after bending to 90° (6mm gauge, 25mm width and 30mm former diameter), showing fracture morphology and deformation/strain localisation features (concentrated shear bands) (a), and a schematic of these features projected on to a flat specimen (b).* [14]

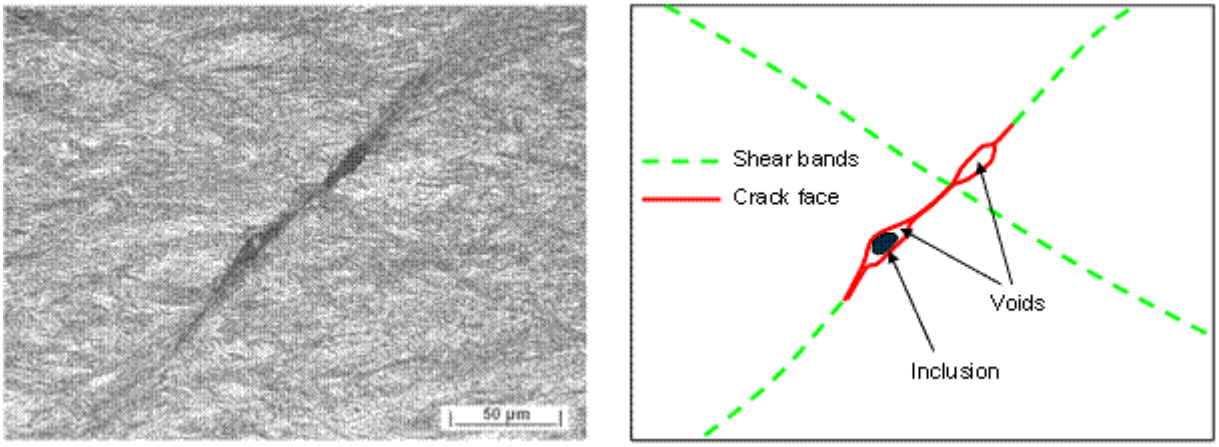


(a) (b)

*Figure 2-18 Voids formed around inclusion within a developed shear band (outer bend of coil 4080-050 sample 25: S960, 8mm gauge, 300mm width and 20mm aimed inner bend radius) after bending to 90° (a), and a schematic of the shear bands with one containing voids formed around an inclusion (b).* [14]

Shear bands are also found at locations of inclusions and voids as found in Figure 2-18. The shear bands run in parallel to the fracture path as shown in Figure 2-17. With these observations, the shear bands need analysis on how they influence failure in bending. However, the micrographs in Figure 2-16-21 lack the high magnification needed to analyse the development of shear bands.

### 2.2.3 Shear bands

The strain localising effect of microstructure in bending is due to the development of shear bands. These are inhomogeneous strain concentrations when a narrow region undergoes plastic flow across several grains but have also been observed within individual grains [36]. Shear bands are promoted when plastic instability occurs commonly seen macroscopically in compression tests [37], tensile tests [36], the rolling of metals [25], [29], [38] and in bending [14], [27], [39]. In compression testing, the specimen is found to bulge and generate shear bands. To better understand this a flow localisation

perimeter $\alpha$ has been derived when studying a compression test in Figure 2-19. When studying compression, the formation of bulging regions through pure compression leads to shear bands being formed leading to a crack forming at the centre of the specimen.

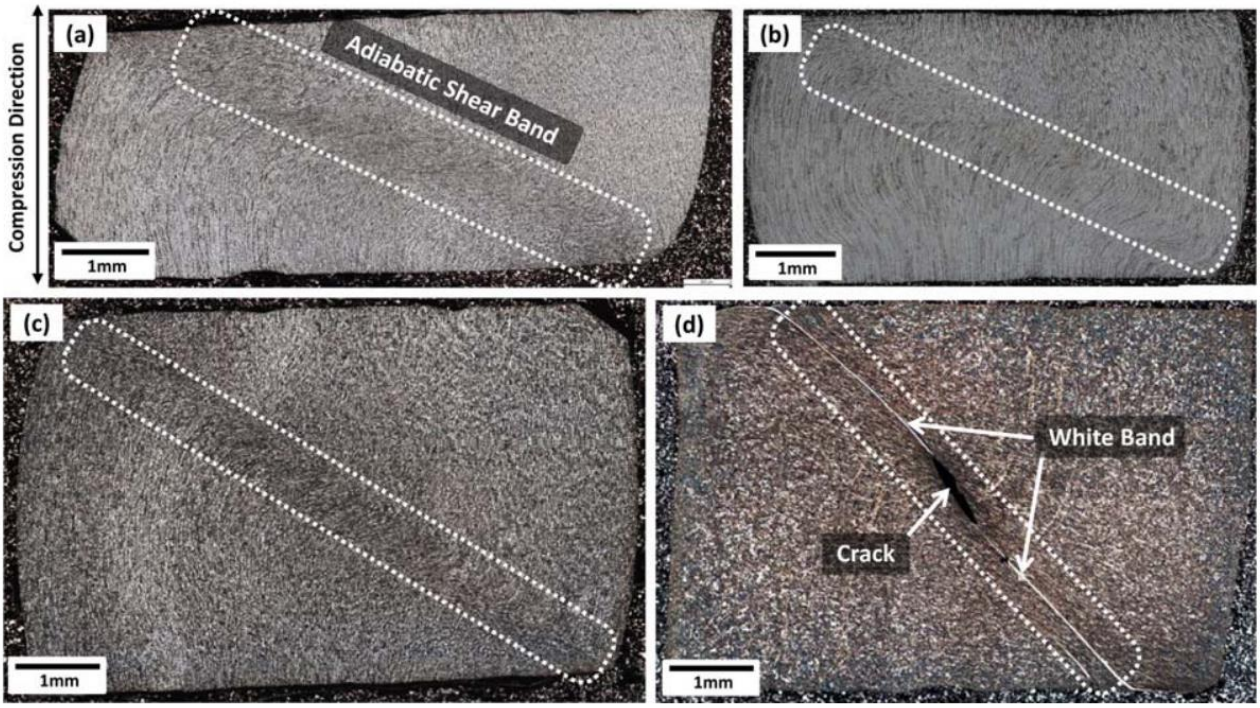


*Figure 2-19: Shear bands developed in compression tests using different carbon alloy quantities, a; 0.2% C, b; 0.4% C, c; 0.6% C, d; 0.8% C* [40].

The instability of crack formation is derived from [37]:

$$\alpha = -\frac{\delta \ln \dot{\varepsilon}}{\delta \varepsilon} = \frac{\gamma' - 1}{m} \qquad \textit{Equation 6}$$

Where $m$ is defined as the rate sensitivity parameter:

$$m = \frac{\partial \ln \sigma}{\delta \ln \dot{\varepsilon}}\Big|_{\varepsilon,T} \qquad \textit{Equation 7}$$

The strain-rate strain-hardening rate is defined as:

$$\gamma' = \left(\frac{1}{\sigma}\frac{d\sigma}{d\varepsilon}\right)\Big|_{\dot{\varepsilon}} \qquad \textit{Equation 8}$$

By analysing this it is found to be affected by strain, strain rate and temperature. So the flow localisation parameter must be defined for a given strain, strain rate and temperature [37]. It is reported that materials that strain harden provide more resistance to shear bands [37].
When the same formula is then recalculated but studying shear stresses instead of compression, the flow localisation parameter changes with the -1 term being removed. This demonstrated that shear bands are promoted more commonly through shear stresses.

$$\alpha = -\frac{\delta \ln \dot{\varepsilon}}{\delta \varepsilon} = \frac{\gamma'}{m} \qquad \textit{Equation 9}$$

When deformation occurs in ductile materials shear (Lüders) bands can be observed. These are a localisation of strain that occur and are often described as two variants, macroscopic shear bands and microscopic shear bands. The macroscopic shear bands (MSBs) are driven by high strain rate, unbalanced heat transfer or poor lubrication of tooling among many factors. These drive macroscale shear bands that are across multiple grains that promote failure in the specimen. Microscale shear bands (μSB) can be considered to be contained within a single grain in the structure of the material measured in micrometres to nanometres [41]. These drive MSBs that are across multiple grains that promote failure in the specimen.

Another study on the promotion of μSBs has been performed with deformation by the equal channel angular pressing (ECAP) process with a range of materials including niobium, ferritic stainless steel and titanium alloy this is typically used as a means of grain refinement via plastic deformation [41]. An equation for the sensitivity derived from applying the Hollomon hardening model in Equation 10 and a shear band compression method was identified by Semiatin et al. [42] in Equation 6 and Equation 8.

$$\sigma = K\varepsilon_p^n \qquad \textit{Equation 10}$$

Together these are combined to become:

$$\alpha = \frac{1 - \frac{n}{\varepsilon_p}}{m} \qquad \textit{Equation 11}$$

This equation was then used to compare with experimental results as shown in Figure 2-20. The $\alpha$ value is found to have a critical value when it increases from 2.5 to 4.5 as found in the titanium alloy and the stainless steel alloy. The author refers to the materials having different properties and that titanium alloys exhibit MSBs at a low $\alpha$ values of 2.5, thus the properties are material-specific and related to grain orientation and properties.

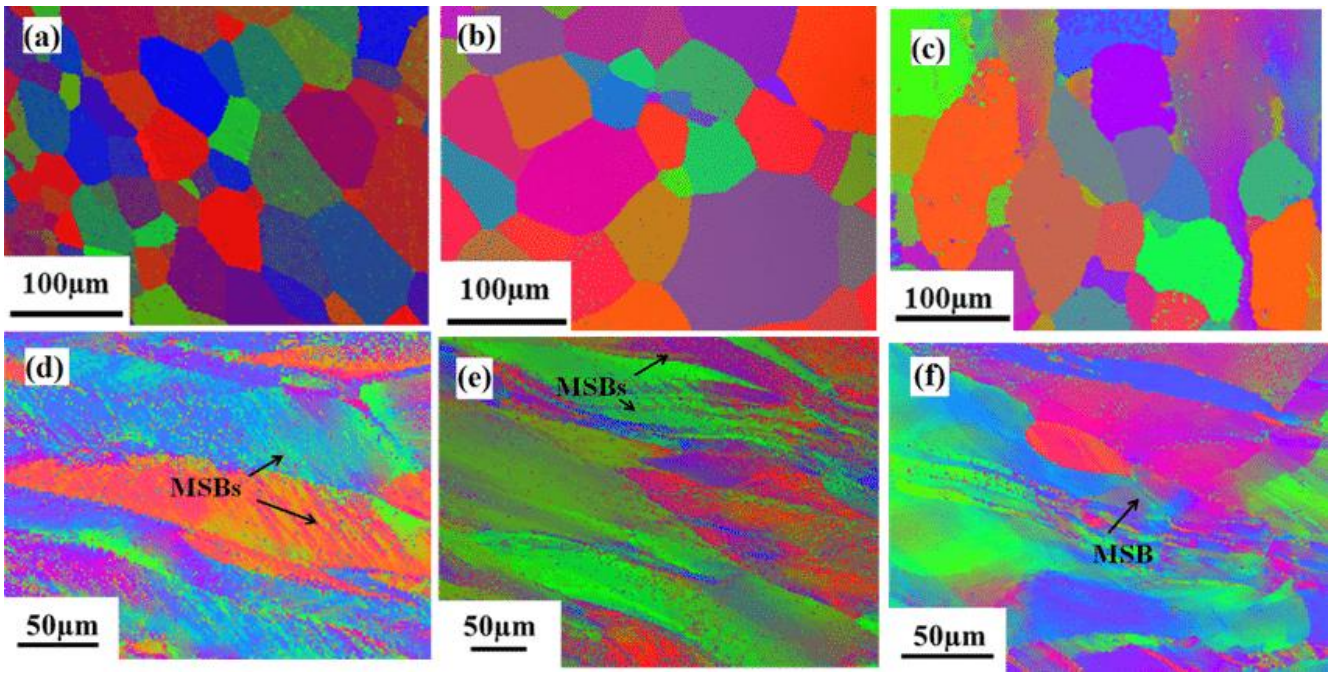


*Figure 2-20: EBSD analysis in the transversal plane, microstructures of annealed a; undeformed Niobium, b; undeformed Fe-20Cr stainless steel, c; undeformed Titanium alloy, d; deformed Niobium, e; deformed Fe-20Cr stainless steel, f; undeformed Titanium alloy* [41].

### 2.2.4 Shear bands in bending

The following sources have been found to promote the formation of shear bands:

- Hardness [27]
- Microstructures [26], [43]
- Alloys [32], [44]
- Grain size [45]
- Surface roughness [46], [47]
- Textures [26], [32], [47], [48]
- Inclusions and voids [14], [39], [49]–[51]
- Grain boundaries [45], [52]

These properties have been investigated by multiple authors, but they are often interlinked and so in this literature review these influences will be reviewed and an approach to improve bendability will be concluded from current literature.

#### *2.2.4.1 Microscopic shear bands*

Microscopic shear bands are observed in singular grains. By using an optical microscope on relatively large microstructures Dao et al. [46] studied the formation of micro shear bands in aluminium. Shear bands are found to have different sources depending on a variety of properties. When studying the bending of aluminium shear bands are observed from multiple sources as shown in Figure 2-21 and Figure 2-22, where shear bands are observed from both a surface undulation and from the edge of a

microstructure [46]. The undulation acts as a stress raiser promoting the localisation of shear strain. The source of shear bands is suggested to be elongated precipitates on the edge of microstructures causing damage through a similar process to MnS inclusions [46].

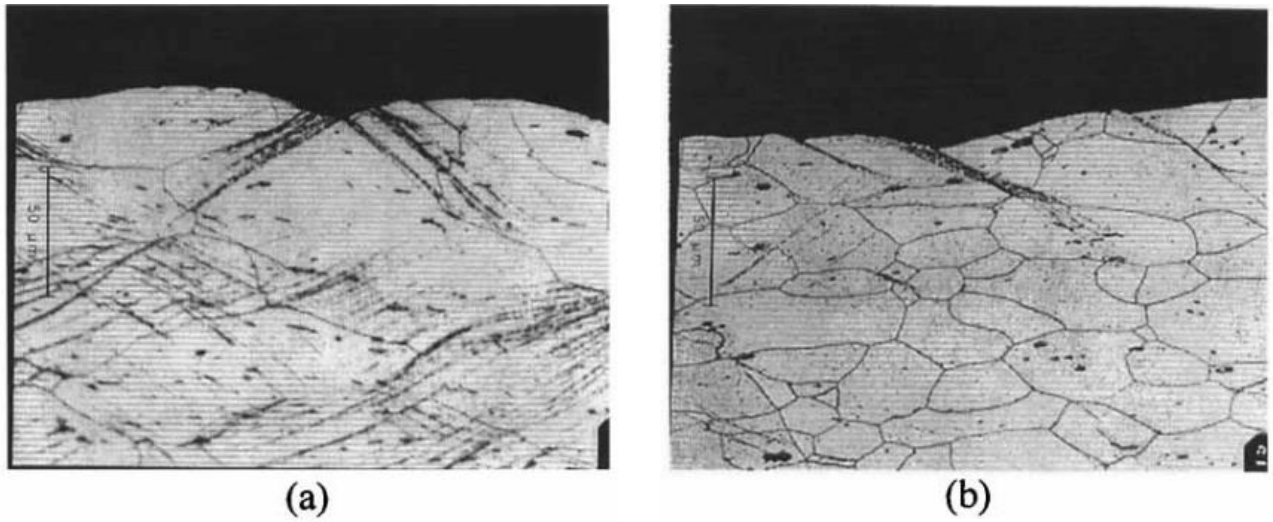


*Figure 2-21: Shear bands propagating in aluminium where in (a) the surface roughening promotes shear bands and in (b) where the edges of the microstructures promote the shear band from the subsurface* [46]

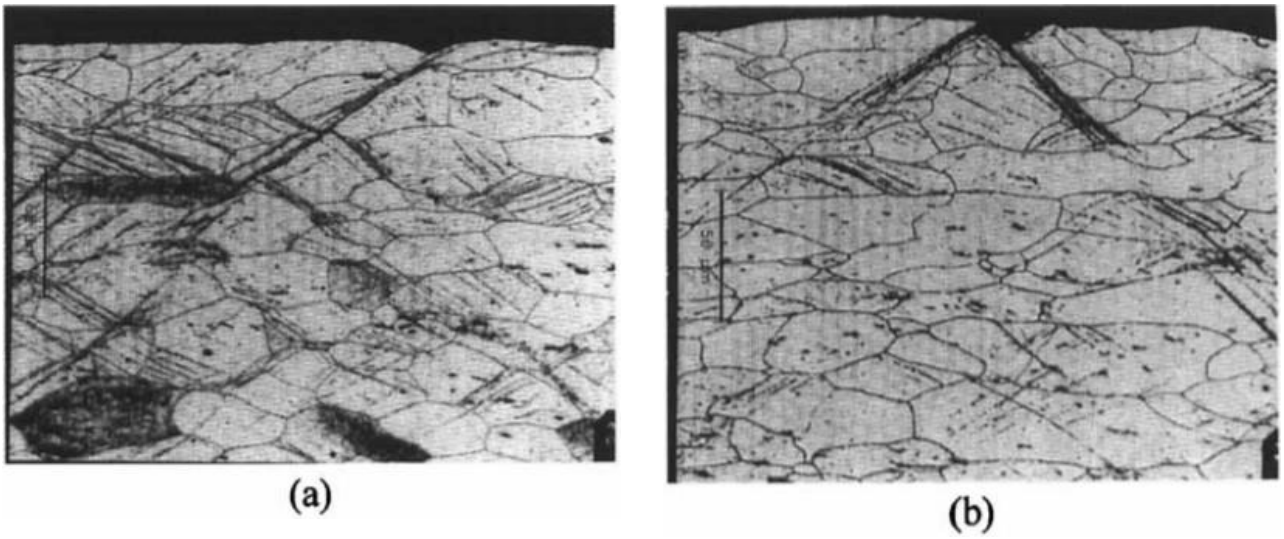


*Figure 2-22: Shear bands promoted under the subsurface with bifurcating subsurface patterns in (a) and discontinuous shear bands in (b)* [46].

These examples show that the surface quality and material cleanliness in production to avoid inclusions are critical to bendability. Hot-rolled steels do not have perfectly smooth surfaces but the grain sizes observed in these aluminium specimens are significantly larger than the UHSS materials. So, the same response to inclusions and surface conditions may not be representative in UHSS.
The shear bands can be observed to be at around 45 degrees to the top surface. Some regions in both Figure 2-21 and Figure 2-22, do not show shear bands while others do. A better understanding of the mechanisms driving this would improve the understanding of bendability.

### 2.2.5 Damage characterisation

Cracks are generated on the outer surface in the bend by fracture. At the neutral axis, no cracks are generated by the lack of stresses at the centre line and the compression of any cracks and voids in the inner bend region stop failure within this region [53]. Typically with steels, the crack starts at 45° to the surface and changes direction to stay in the region of high stress shown in Figure 2-23.

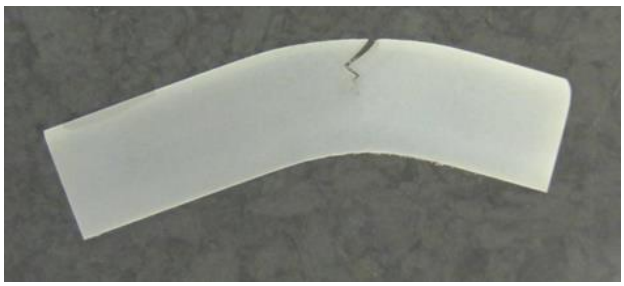

*Figure 2-23: left: S960 steel, 3 point-bending with 13mm stroke* [14].

Once a crack is generated it slows down its propagation as the neutral axis moves towards the inner surface [53]. The damage propagates from the centre of the bend due to this area undergoing a higher triaxiality [5]. This is the ratio of the mean stress over the equivalent stress[54] as shown in Equation 12.

$$\eta = \frac{\sigma_m}{\sigma_{eq}} = \frac{\frac{1}{3}(\sigma_{11} + \sigma_{22} + \sigma_{33})}{\sqrt{\frac{((\sigma_{11} - \sigma_{22})^2 + (\sigma_{33} - \sigma_{11})^2 + 3(\sigma_{12}^2 + \sigma_{23}^2 + \sigma_{31}^2))}{2}}} \quad \textit{Equation 12}$$

Triaxiality is used to study the failure mechanisms depending on the stress state. As shown in Figure 2-24 with low triaxiality shear failure is the typical failure mode while when triaxiality exceeds 0.4 the fractures occur due to the formation of voids. The triaxiality values also vary the equivalent strain to failure, where with high triaxiality a failure can occur at a lower strain than in low triaxiality conditions.

The critical plane strain triaxiality in bending is calculated using Equation 13, where the Lode angle parameter L is set as 0; plane strain condition as shown in Figure 2-25 [5].

$$\cos\left(\frac{\pi}{2}(1 - L)\right) = -\frac{27}{2}\eta\left(\eta^2 - \frac{1}{3}\right) \quad \textit{Equation 13}$$

With this applied to Equation 13 the critical triaxiality of $+1/\sqrt{3}$, 0.58 is found to be the critical plane strain triaxiality. This is when the Lode angle parameter is found to have the most significant effect on fracture strain [55] as shown in Figure 2-25. Where the Lode parameter L is defined in Equation 14, where the principal strains are defined as $\sigma_1, \sigma_2, \sigma_3$ [56]:

$$L = \frac{2\sigma_2 - \sigma_1 - \sigma_3}{\sigma_1 - \sigma_3}$$ *Equation 14*

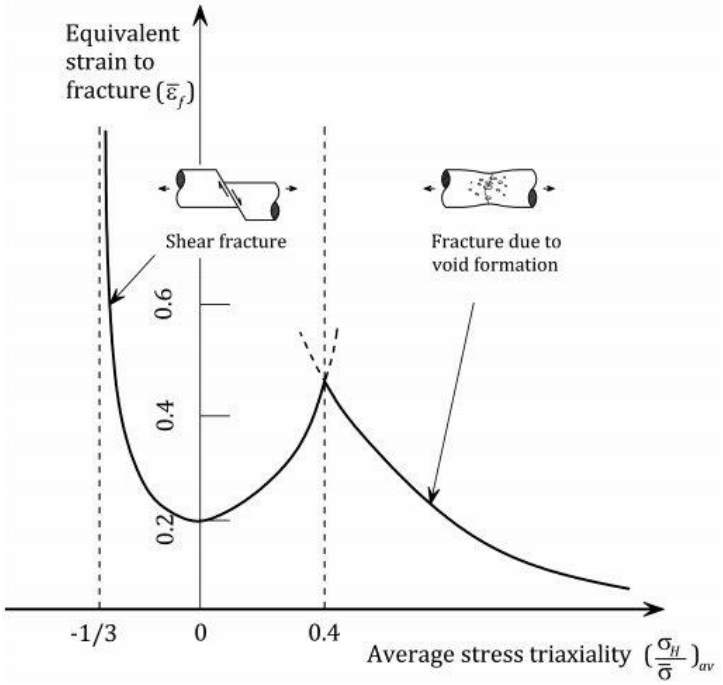


*Figure 2-24; Influence of triaxiality on the failure modes in strain* [57].

Using the equivalent stress, triaxiality and Lode parameter the principle strains have been calculated in Equation 15-17 [58]:

$$\sigma_1 = \left(\eta + \frac{(3-L)}{3\sqrt{L^2+3}}\right)\sigma_{eq}$$ *Equation 15*

$$\sigma_2 = \left(\eta + \frac{2L}{3\sqrt{L^2+3}}\right)\sigma_{eq}$$ *Equation 16*

$$\sigma_3 = \left(\eta - \frac{(3+L)}{3\sqrt{L^2+3}}\right)\sigma_{eq}$$ *Equation 17*

Hence the principal strains can be defined in terms of these 3 parameters $\eta, L$ and $\sigma_{eq}$.

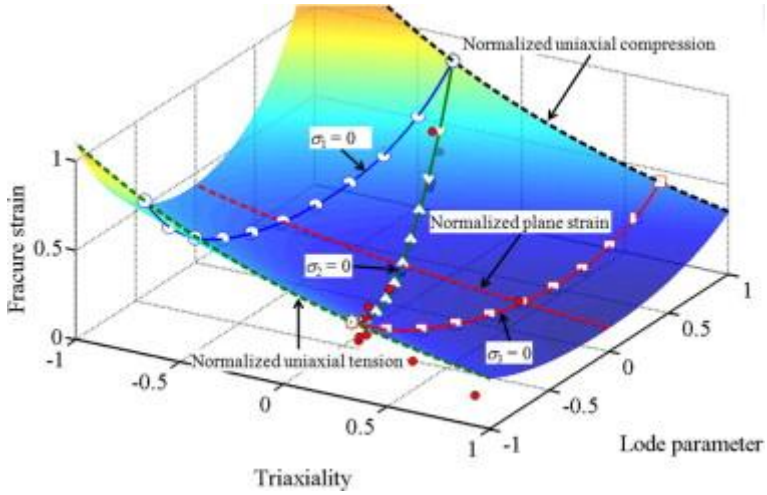

*Figure 2-25: The effect of triaxiality and lode parameter on the fracture strain of Al 2024-T351* [58]

The critical plane strain triaxiality can be exceeded by having a wide specimen as indicated by the finite element modelling results. This will then promote failure at lower strain for wider bend specimens.

There is an increase in triaxiality approaching the edge of the specimens and the BSI standards [5] advise that when studying the damage:

"These edge cracks are not an indication that the test piece failed the bend test as defined in 9.1. Therefore, cracks originating from the edge and extending no more than two thicknesses from the edge shall not be included in the test interpretation of 9.1. However, if the cracks originating from the edge extend more than two times the thickness into the width, then that test piece shall be considered invalid."

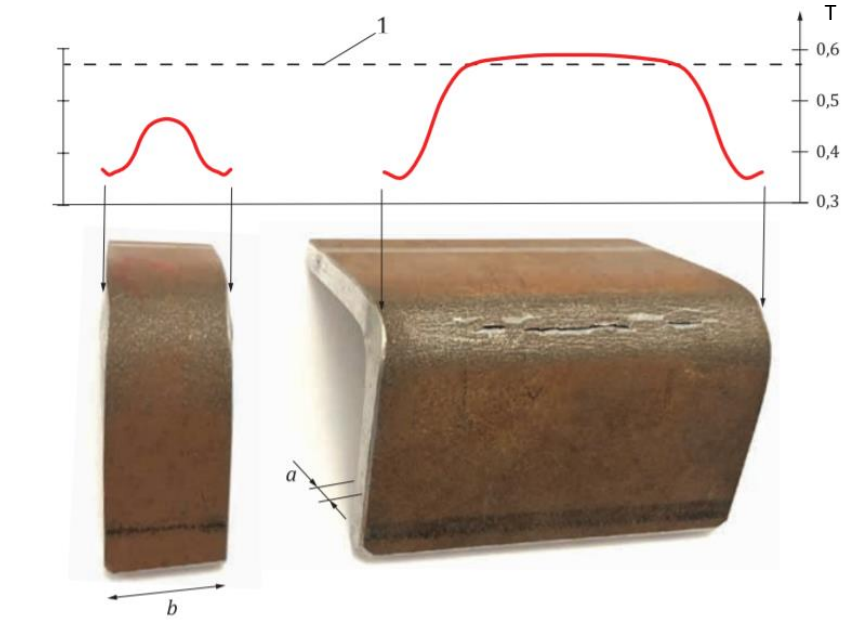


**Key**
T triaxiality factor
1 critical value for plane strain condition

*Figure 2-26: Finite element modelling of the influence of bending specimen width and triaxiality* [5]

It has been found that the total elongation of a tensile test sample has little relation to the bendability of the material [59]. This is due to several factors, such as tensile tests distributing the strain in uniaxial tension over the whole sample, while bending concentrates stress on the tensile and compressive sides of the bend. Some research has suggested that the strain-hardening coefficient has a good correlation with bendability [60].

Research has found bendability to be anisotropic in high strength steels where the orientation of bending to the rolling direction [14], [61]. The face placed in tension can also change bendability due

to materials demonstrating anisotropic properties [14]. This is undesirable for a manufacturer bending this product as they will have to consider the orientation to optimise bendability.

An assessment of edge crack sensitivity after punch forming steel has been performed prior by Tsoupis et al. [62]. As shown in Figure 2-27, damage increases with lower $r_i/T$ values denoted as c in the figure, while the fracture zone (FZ) and burnish zone (BZ) is caused by the punch process, with the FZ promoting increasing damage. Additionally, orientation is found to be important to orientate the bend axis to be parallel to the RD.

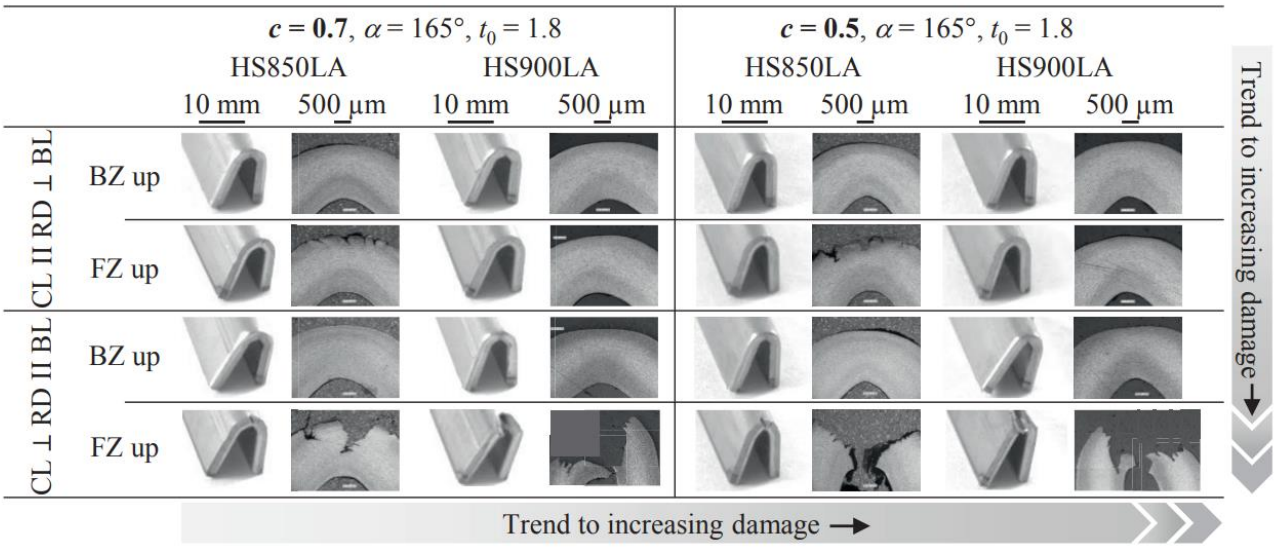


*Figure 2-27: Optical microscope imaging of 3 point bend tests on the punched regions with different $r_i/T$ values, c, with the bend axis in parallel to the RD: II and TD:⊥, orientated with the burnish (BZ) or fracture (FZ) zones are in tension* [62].

These were found combined with brittle and ductile fractures in the sheared regions from punch forming.

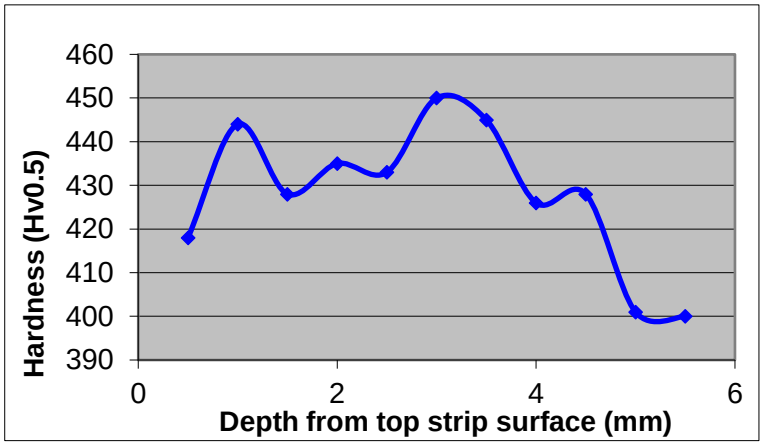


*Figure 2-28: Through the thickness hardness test results on S960 steel* [14]

The hardness values vary through the thickness of an S960 steel sample in bending and are not always symmetrical about the centre as shown in Figure 2-28. With a softer surface on the underside

of this steel, bendability is found to improve bendability then the bottom surface is placed in tension[14].

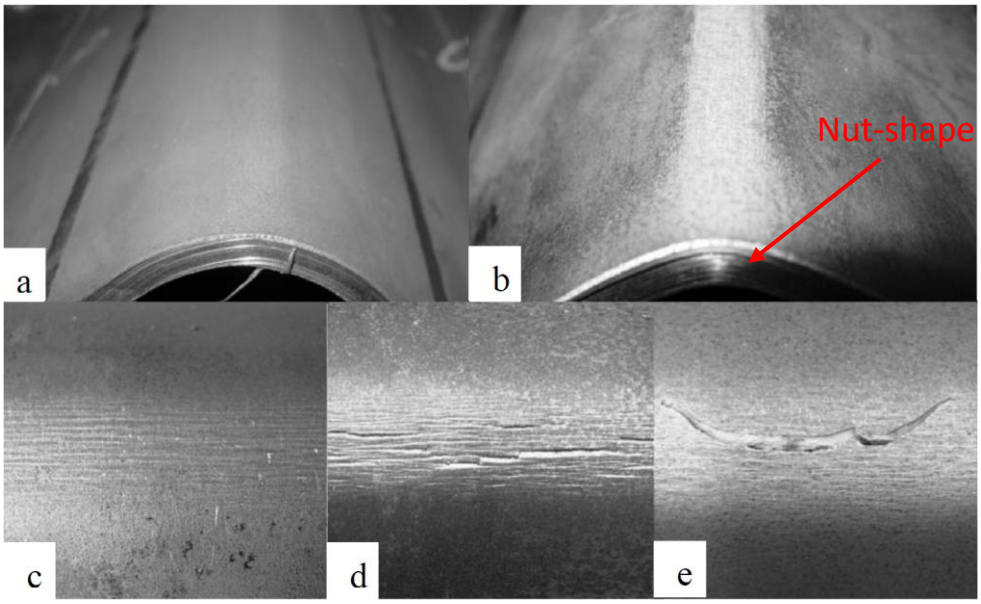


*Figure 2-29: Visual inspection method for identifying bending failures, a, Flawless bend, b, nut-shape, c, surface waviness, d, surface cracks and e, cracks coalesce* [63].

The visible damage, when the sample is bent, is shown in Figure 2-29. They are often spotted in sequence on a sample. One of the initial signs of poor bendability is a nut shape, where a gap forms between the specimen and tooling. This is when the radius of the inner bend becomes smaller than the tooling, this effectively lowers the $r_i/T$ increasing strain. Figure 2-29(b) shows a nut shape in the bend profile. Then in Figure 2-29 (c) a surface waviness is shown suggesting a concentration of strains, followed by Figure 2-29 (d) where these waves propagate to cracks which are then concentrated into a single failure in Figure 2-29 (e).

Another insight into the failure mode of AHSS, a family of steels that include UHSS [64], in bending is provided by Kaupper et al [65]. in Figure 2-30. This shows a similar deformation development as Figure 2-29 showing this is a deformation progression for bending and is not specific to one type of steel.

Shear bands are observed in both examples. It suggests that the development of damage in bending can be arrested at different stages of strain localisation in bending.

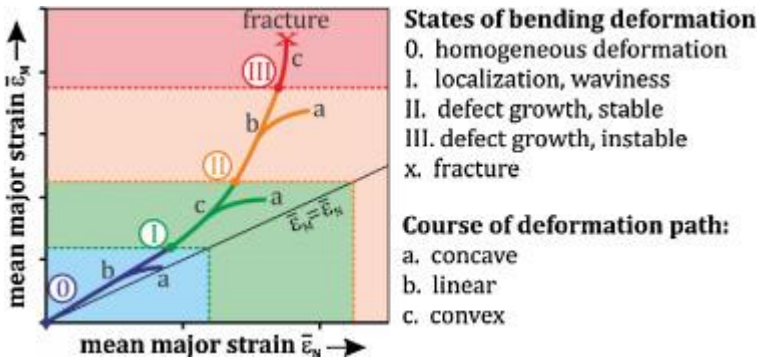


*Figure 2-30: deformation development in bending for AHSS, steel* [65]

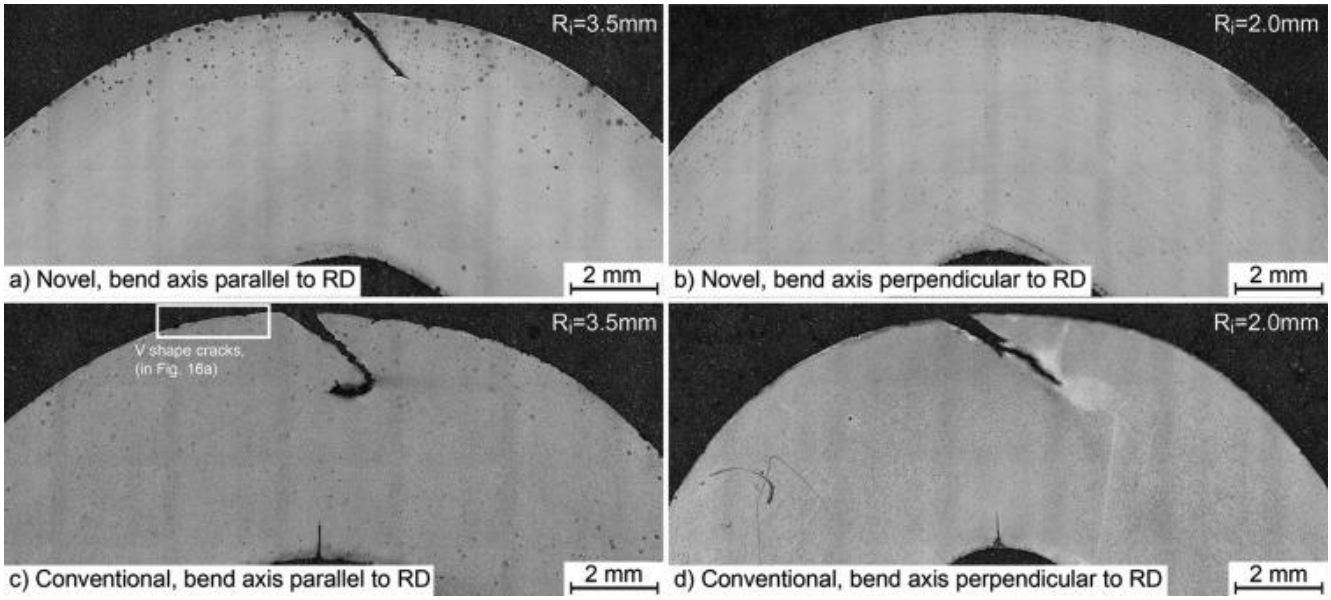


*Figure 2-31: Bending tests for 6mm thick hot-rolled novel a, and b, and conventional c, and d, steel specimens orientated parallel and perpendicular to the RD, using different internal radius tooling, $R_i$.* [27]

Damage studied by authors is performed with qualitative analysis of fracture paths, shear bands, surface notches and deformation. However quantitative analysis of the development of shear bands and damage propagation in terms of strain localisation was not studied. It was found that with AHSS and UHSS steels the bend axis is found to improve bendability when aligned with the TD as shown in Figure 2-31.

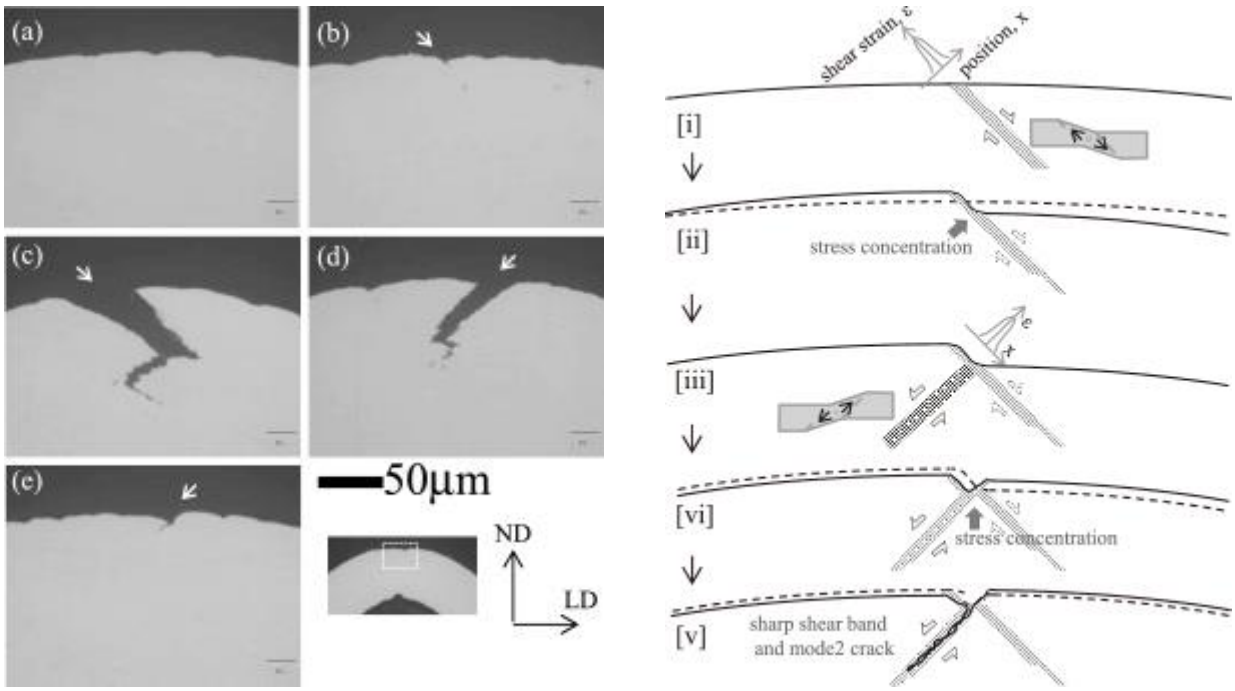


*Figure 2-32: Examples of bend test results by H. Kaneko et al., left, bend test specimens post-test with 0 radius tooling used with varied properties with copper alloy with mass% of alloys added: a-d, 3.8% Ni alloy, e, 2.3% Ni alloy. White arrows indicate crack initiation positions at the surface, right, Shear band propagation and damage development process as seen on the left image* [47].

Research has been performed on the bendability of Ni-Si copper by H. Kaneko et al. [47] who produced an excellent diagram of the shear band development in Figure 2-32. This shows how the shear band produces a surface step (ii), this produces a stress concentration and a new shear band (iii), this generated a surface notch further increasing the stress concentration as the lowest energy path is found via the shear band (vi) followed by crack propagation (v).

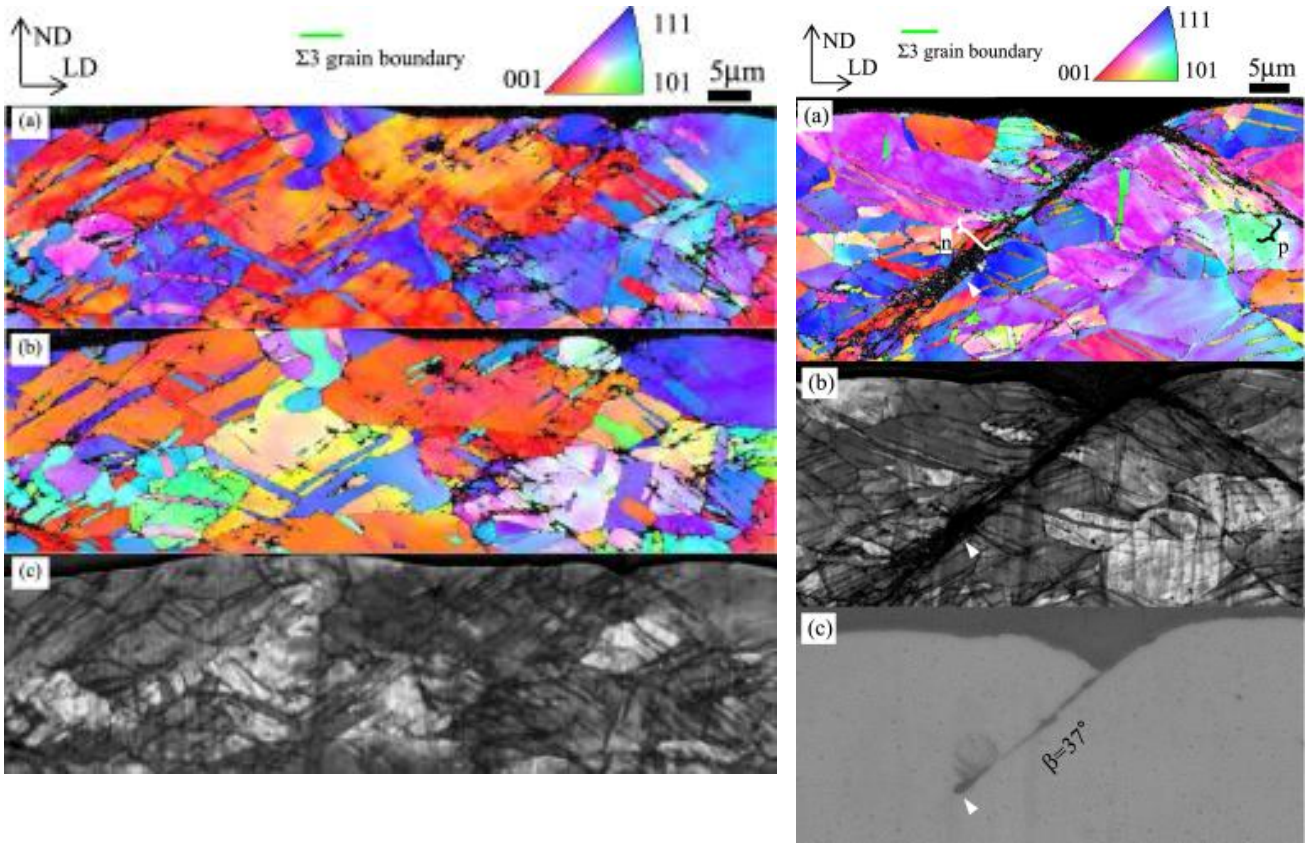


Figure 2-33: EBSD analysis of samples post bend test using the same bend test geometry, left offering good bendability, right a randomly orientated specimen resulting in poor bendability. Left Image a; crystal orientation in the RD, image b; crystal orientation in TD, c; image quality map. Right image, a; crystal orientation in the RD, b image quality map, c; optical microscope image of the crack. The n and p denote the negative and positive shear band orientations. [47]

When analysing the effect of texture, it has been found that randomly orientated microstructures as found in the right specimen in Figure 2-33 provide poor bendability. This promotes the surface step then a notch that promotes crack propagation. This was also allowing the propagation of micro shear bands to develop under small strains that coalesce into macro shear bands. While the left-hand sample in Figure 2-33 is shown to have a cubic orientation and resists the development of shear bands. It is found in copper that the RD-rotated Cube orientation {012}<100> resists the formation of shear bans while the BR orientation {362}<853> was found to improve bendability [47]. Since copper has typically excellent ductility, the propagation of shear bands and their development are likely to have a different failure mechanism than in UHSS.

### 2.2.6 Bendability and Surface quality

The surface finish of the sample provides the surface over which the maximum bending strain will be applied and as such any imperfection in this region acts as a stress raiser and lower the bendability of the material. Experimental [66] and modelling [67] approaches have shown that roughness impacts bendability. During bending the surface quality typically deteriorates further as notches form at the location of shear bands intersecting at the surface of the bend. The influence of the quality of the

surface finish and how notches and shear bands propagate has not been explored experimentally and a study of this would generate novelty.

## 2.3 Bending of Ultra High Strength Steels

The bendability of materials is dictated by many material properties both macroscopic and microscopic. The transition from a stable bend with negligible localisation of deformation to localised deformation normally in the form of shear bands is the priority of this work. Many material properties have been linked to bendability as covered in section 2.2.4. A more detailed analysis of work performed on UHSS is required to understand material-specific properties and if these differ from the norm.

Early work to understand the limits of bendability found that MnS and red scale inclusions have a significant effect on the bendability of martensitic and bainitic steel. These have been shown to cause anisotropic bendability of the material [39], [49], [50]. MnS inclusions are due to their shape localising strain acting as a stress raiser. While red scale acts as an insulator and changes the microstructures to upper bainite and martensite that have poor bendability [50].

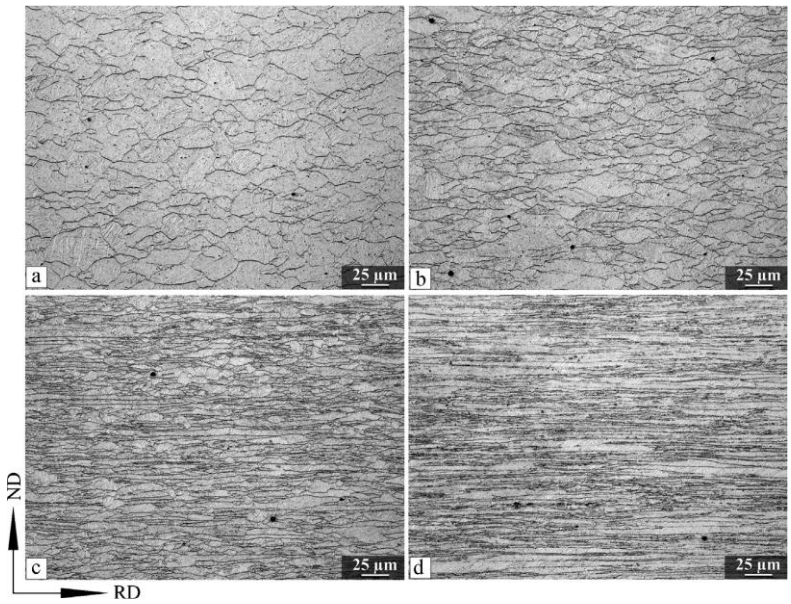


*Figure 2-34: Austenite grain structures of Steel A as seen in RD–ND sections at quarter thickness with $R_{tot}$ 23% (a), 44% (b), 56%(c) and 79% (d)* [43]

Research is then done to change the surface and subsurface properties. As described in section 2.2.1 the highest strain is within these regions. Changing the hot rolling parameters and lowering the finish rolling temperature below the recrystallisation temperature promotes a rolling reduction ($R_{tot}$). This is where the ratio between the width of the microstructures and the thickness is often described as pancaking. This is achieved in the steel as shown in Figure 2-34. This generates softer ferritic and granular bainitic phases promoted in the surface and subsurface regions [43].

At high levels of $R_{tot}$ the steel is found to be highly anisotropic and bending perpendicular to rolling direction is poor. Failure is found in an upper bainite region below the surface while the softer polygonal ferrite layer doesn't crack [26].

It is reported that this anisotropic behaviour is due to the {112}<111>$_\alpha$ texture of the steel having a geometric softness in one direction [32]. This texture has been promoted by increasing $R_{tot}$ [26], but this, in turn, promotes softer microstructures and reduced hardness that are linked to improving bendability [48]. To achieve this improved bendability, the composition of the steel is found to play a significant role in deciding the effect of increasing $R_{tot}$. By changing alloying elements by adding niobium and calcium alloys new steels are made that have softer ferrite and granular bainite surfaces and sub-surfaces. These are found to offer improved bendability of $r_i/T$ at 1 and 1.75 in perpendicular and parallel respectively with the bend axis to the rolling direction for this particular steel [48].

While doing this red scale is discovered on a sample. It is found the red scale causes changes in the microstructure to lower ductility upper bainite from granular bainite in the subsurface region beneath the scale and promotes the {112}<111>$_\alpha$ texture [43]. Both of which are linked to bad bendability and anisotropic properties respectively. Removing the red scale before bending provides no improvement in bendability [43]. This shows how the factors affecting bendability can be linked.

Another method of improving bendability in martensitic steels is by the removal of carbon from the surface and subsurface region within the steel [44]. This results in the creation of a softer microstructure and larger grain sizes in the sub-surface [60], [68].

It is found that having steels with a carbon gradient reduces the stress concentration compared to a sample with no gradient [48]. It is also suggested that the observed brittle failure is due to a crack generated in the martensite in the subsurface, the softer steel at the outer edge not being at its maximum strain. It was found that the steel with a carbon gradient had a higher strain-hardening property, which improves bendability [14], [44], [69].

Despite the insight generated by these studies, the understanding of the initiation of failure concerning strain distributions in the microstructure was not investigated This work has been done for other grades of steel.

### 2.3.1 Strain distribution in bending

In bending, as elongation is placed on the outer surface the plastic deformation tends to concentrate in bands [14], [26], [32], [51], [70]. These shear bands originate from the subsurface region [51] and propagate to the surface as the bending stroke increases [14]. These eventually form a bifurcating

pattern of shear bands [14], [51]. The number of shear bands does not increase until a crack has initiated and are found to pass through inclusions and voids [51].

The shear bands are reported to be more prominent in steel with a large number of inclusions or a strong {112}<111>$_\alpha$ texture when bending with the bend axis parallel to the transverse direction [26], [32], [51]. The latter cause is due to a geometric softening from the texture when strained in this direction [26]. This is reported to reduce bendability by concentrating the strain in bands and causing failure before the bulk material strain is used [26].

No anisotropic behaviour is mentioned in the Tata Steel report on the generation of shear bands and no analysis of textures are performed [26].

The shear bands in all cases are examined after the bending test and from the side profile. The use of insitu tensile or bending interrupted tests observed by SEMs has not been used for these compositions of steel.

## 2.4 FE modelling

Finite Element Modelling (FEM) has become a common method of studying the formation of shear bands concerning strain distributions while verifying these results with experimental results. Many authors have simulated the promotion of shear bands studying a range of materials, modelling approaches, and loading scenarios have been used by authors.

### 2.4.1 Shear bands

Early work using an isotropic elastic-plastic flow theory modelling approach, Von Mises yield criterion and linear work hardening has shown that necking in tensile testing can be successfully modelled but the model remained too stable to promote shear bands [71]. Due to this, means have been researched to add instability to models to promote shear bands.

One of these approaches is the application of the Gurson–Tvergaard–Needleman (GTN) porous metal plasticity model by Wen et al [14] modelling an S960 high strength steel in bending. A 2D model in-plane strain is shown to be accurate as compared to the 3D model due to a sufficiently large width to thickness ratio. Without the GTN model, no shear bands are present. By applying the GTN model with a high-density mesh, shear bands nucleate from the subsurface region and are found to be similar to those found experimentally as seen in Figure 2-35. The application of the GTN model is used as a means of promoting instability in the model. The meshing is a critical factor affecting the generation of shear bands in Figure 2-36. These bands are found to concentrate the strain from 1.9 to 6 times the nominal strain. This limits the bendability of the material due to exhausting the local material elongation [14].

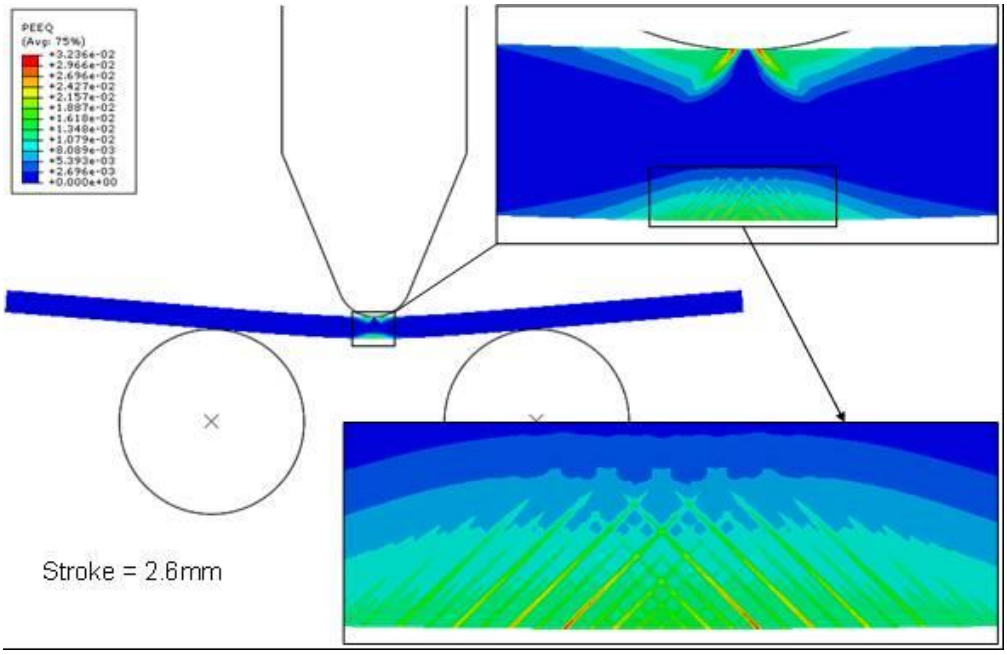


*Figure 2-35: FE prediction of shear band formation shown by the equivalent plastic strain localisation in bend test of S960 steel under 2.6mm stroke (max. nominal strain = 1.7%)* [14].

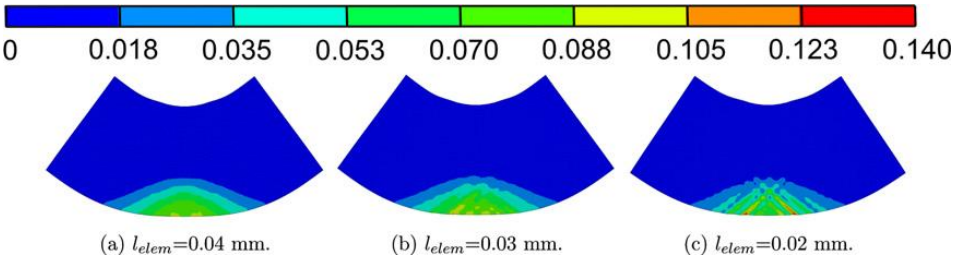


*Figure 2-36: The impact of mesh size on strain localisation when the punch displacement is 10.2mm* [72].

DP steels have also been modelled in FEM. These too are found to generate shear bands in bending and in tensile tests [36], [72]–[74]. These show that high stresses concentrate in martensite and that inhomogeneous strain in the ferrite leads to failure in the martensite or at martensite-ferrite phase boundaries.

FEM has also been performed on analysing shear bands in Samarium cobalt ($SmCo_5$) magnets [45]. By modelling varied grain sizes, it is found that shear bands are promoted with larger grain sizes as shown in Figure 2-37. Luo et al. also highlights that this material has an inverse Hall Petch effect [45]. This makes it difficult to compare to more typical materials that adhere to the Hall Petch effect such as in steels. The development of shear bands due to back stress from stress raisers at microstructural intersections are shown in Figure 2-37. These then promote a shear band that becomes more dominant with reductions in the grain size with the increasing strain found inversely proportional to the grain size.

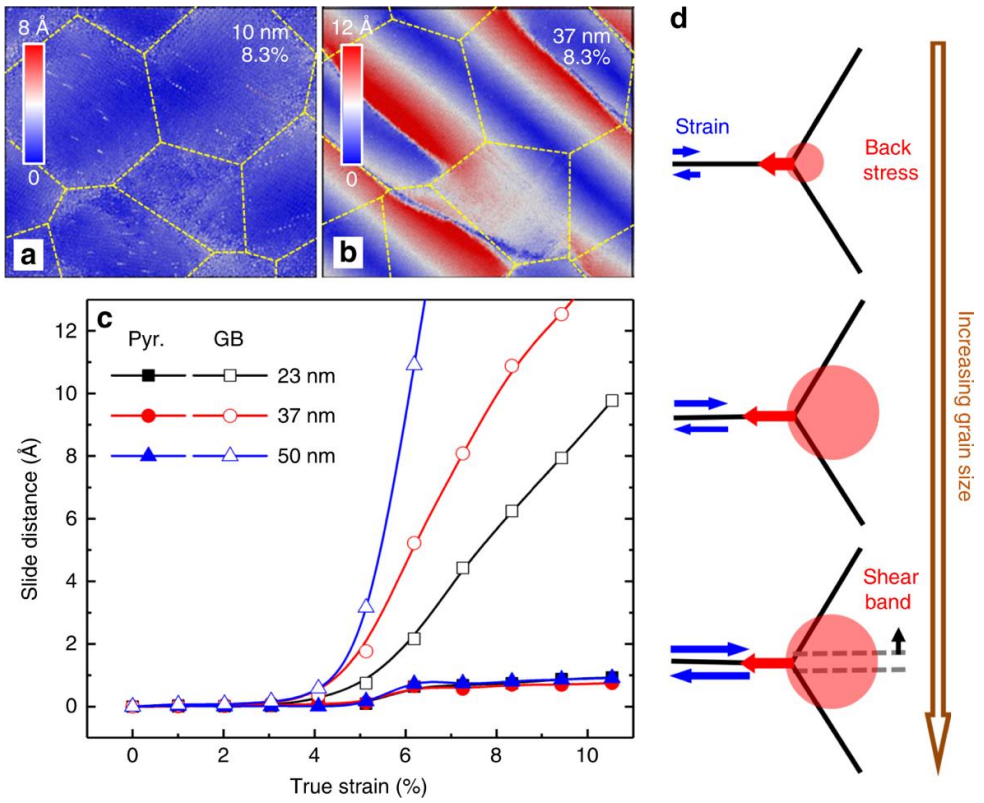


*Figure 2-37: Demonstration of grain size variance on strain localisation, a and b, demonstrate the strain localisation when applying 8.3% strain to a, 10nm grain size and b, 37nm grain size, c, Graph of grain size variance analysis with strain development d, illustration of the shear band development via back stress* [45].

FEM work has a limited scope of using one steel and does not consider bending anisotropy of these steels. No model applied to a martensitic or bainitic steel bending simulates softer phases at the surface of the bend.

### 2.4.2 Modelling microstructures

As defined in section 2.1, the choices made in the production of steel can create different microstructures each with different characteristics due to their transformation kinetics. When modelling these microstructures at a high level of detail these differing microstructures must be accounted for. To do so microstructures have been simulated by many authors to improve FEM accuracy.

Publications by Muhammad et al have used LS Dyna to simulate textures in aluminium alloys with the addition of cladding taken from the centre of a bend [52], [75]. The work shows the development of macroscopic shear bands in an unclad specimen in Figure 2-38 with shear bands found to propagate in a transgranular manner along grain boundaries. It is suggested that the shear bands follow low energy paths that promote failure. The development of shear bands is also found to promote surface undulations which further increase stress localisation and lower the energy required to generate shear bands [52].

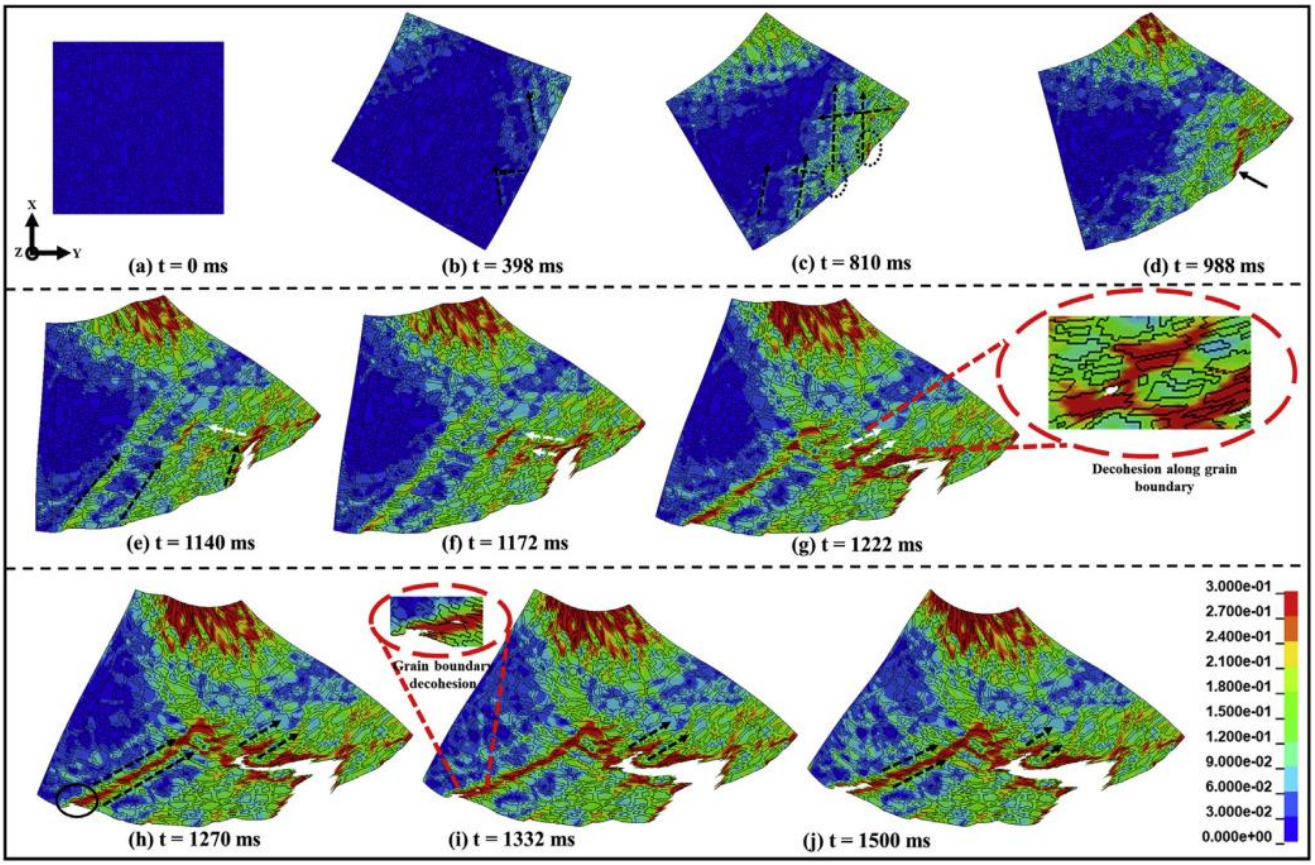


*Figure 2-38: The effective strain causing propagation of shear bands at a range of displacements in a model of an aluminium alloy* [52].

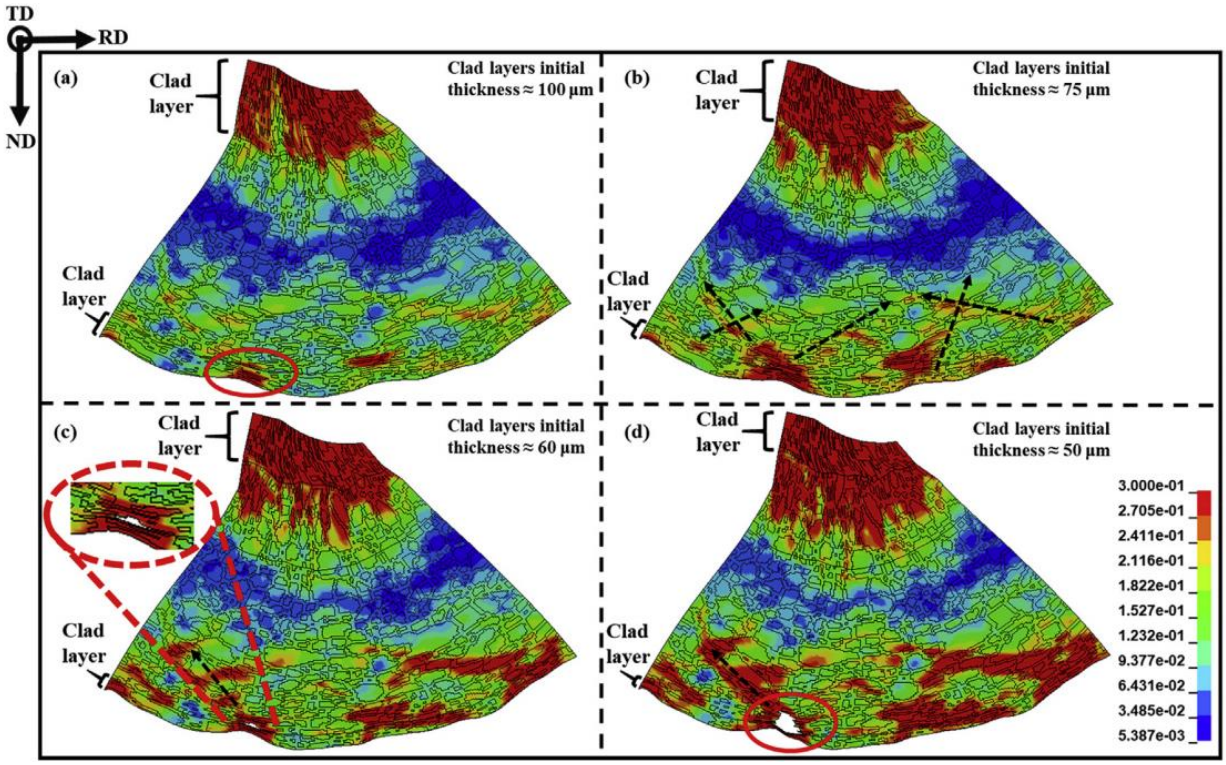


*Figure 2-39: The effective strain distribution for the same displacement with varied cladding thicknesses in an LS-Dyna model with the bulk material consisting of aluminium alloy* [52]

To analyse the effect of a softer layer at the top and bottom a model was produced with varied cladding thickness in Figure 2-39. It is found in the modelling the cladding does not fail using the

damage model applied, therefore the damage is found to initiate in the subsurface bulk aluminium alloy. This was found to be promoted by macro shear bands. This does seem to suggest that a softer 10% thickness layer at both surfaces can resist shear band development.

In other work, Kuroda et al. used crystal plasticity models in hot-rolled aluminium alloys. The cube texture is the optimal texture for resisting the formation of shear bands but goes further and states that no shear bands should be generated when the strain is parallel to TD and in-plane strain. When reorientated to put the strain parallel with RD the texture that best resists this is the Goss texture, {110}<001>.

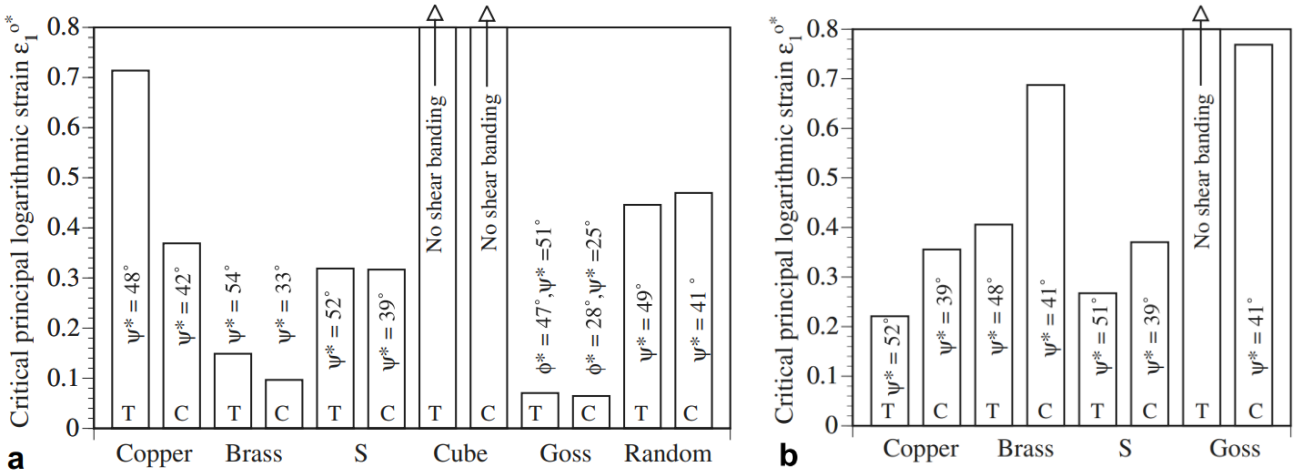


*Figure 2-40: an analysis of shear bands formed in a simulation of textures when the strain is a. parallel to the RD, T for tension and C for compression or b. perpendicular to the RD* [67]

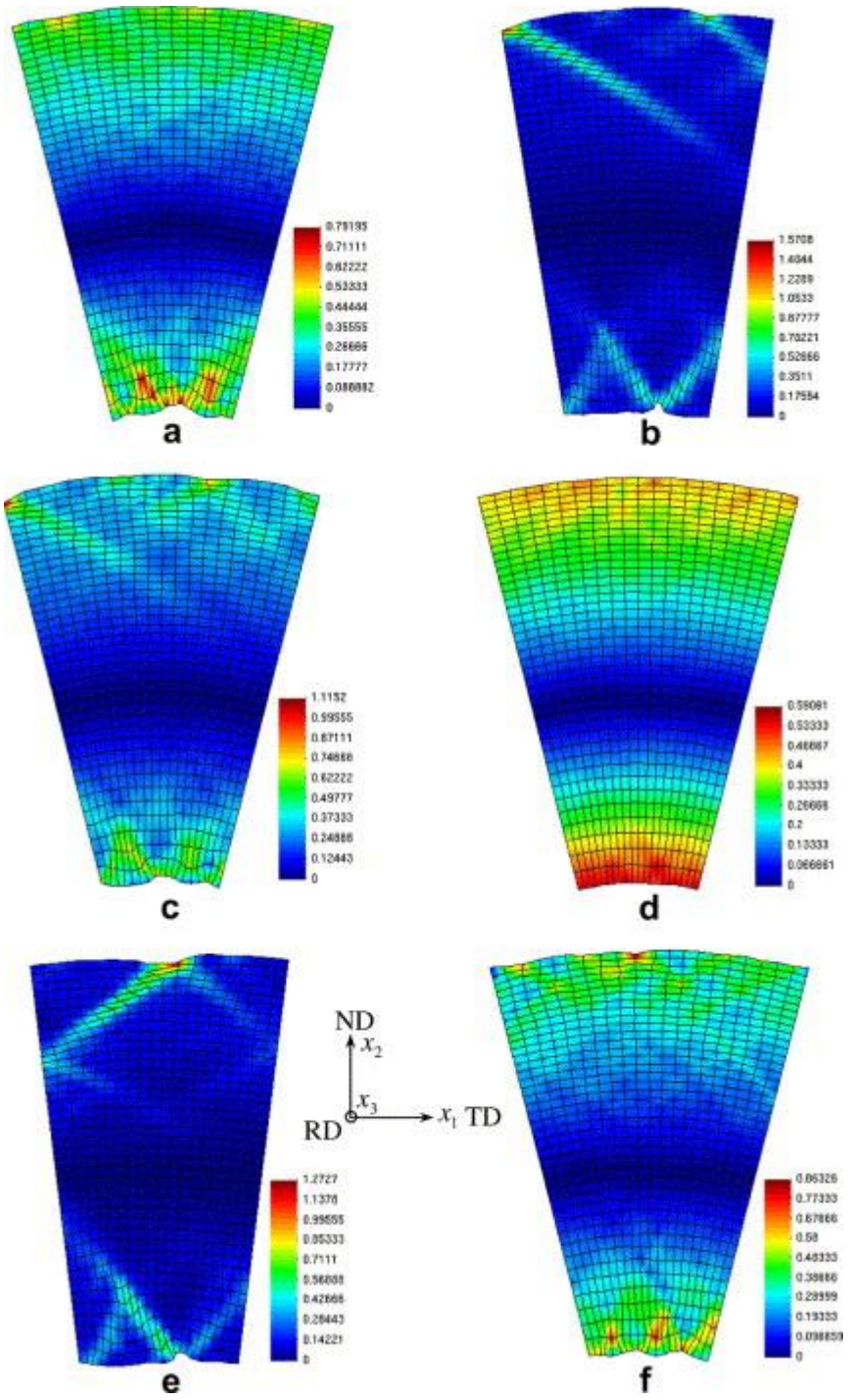


*Figure 2-41: Deformed meshes in bending, bend axis parallel to the RD, $\alpha$ = 90°: a; Copper ( $\theta$ H0/L0 = 1.00), b; Brass ( $\theta$ H0/L0 = 0.648), c; S ( $\theta$ H0/L0 = 1.01), d; Cube ( $\theta$ H0/L0 = 1.00), e; Goss ( $\theta$ H0/L0 = 0.494), f; Random ( $\theta$ H0/L0 = 1.00)* [67].

When the bend axis is parallel with the RD both cube and copper textures offer excellent resistance to shear bands in Figure 2-41. The cube texture results in the shear bands being more numerous but lower in strain intensity and do not propagate very deep into the material.

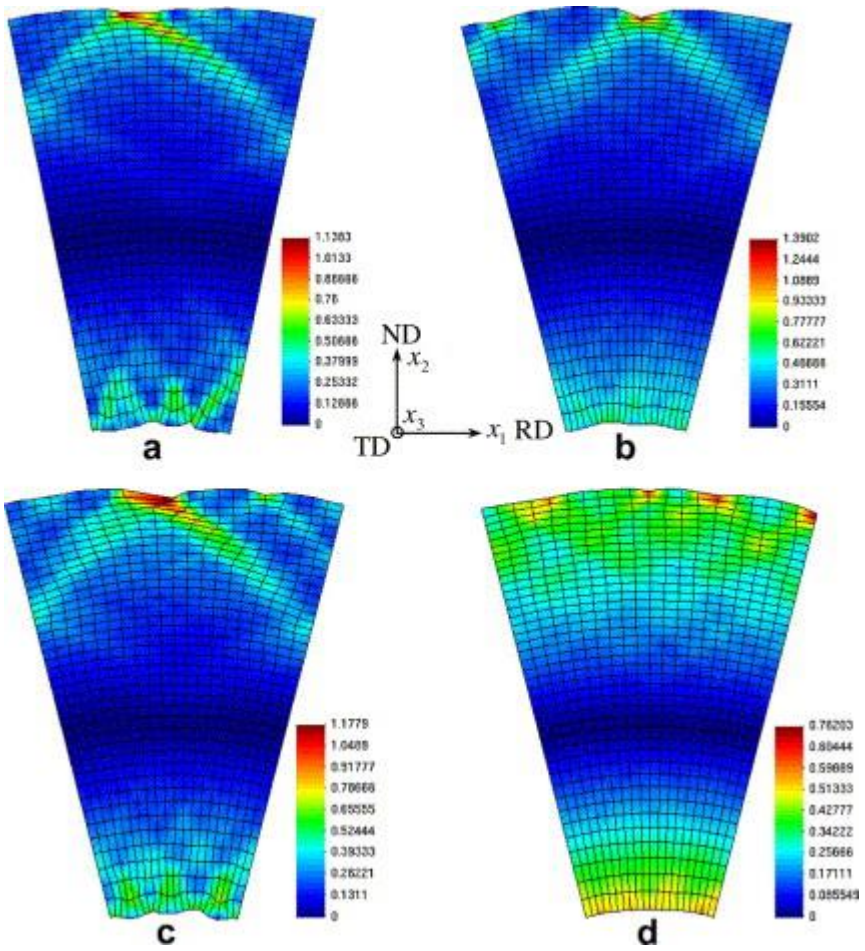


*Figure 2-42: Deformed meshes in bending, bend axis parallel to the RD* [67]

With the bend axis perpendicular to the RD, the best texture to resist shear bands is the Goss texture. Similar work by Muhammad et al. using crystal plasticity has also been performed, this is limited in scope to only performing bending axis perpendicular to RD but uses 3D modelling compared to the plane strain assumed by Kuroda et al. This allowed a comparison between Figure 2-40 and Figure 2-44, the bend angle at failure is greatest for copper with Goss and Brass being superior to the aluminium's texture in Figure 2-44. This doesn't agree with Figure 2-40 which shows Brass and Goss to have poor resistance to shear bands. It should be considered these graphs are looking at bending until failure in Figure 2-44 and directional strain and the development of shear bands in Figure 2-40. Therefore, the specimen may have shear bands in bending but won't be considered a failure until the author deems it as such. As such the development of shear bands should be considered independently of the failure in bending.

While both Figure 2-41 and Figure 2-42 offer useful insight it is idealised with only 1 or 2 textures considered. So, the effect of small variations away from these idealised materials could have significant effects on bendability.

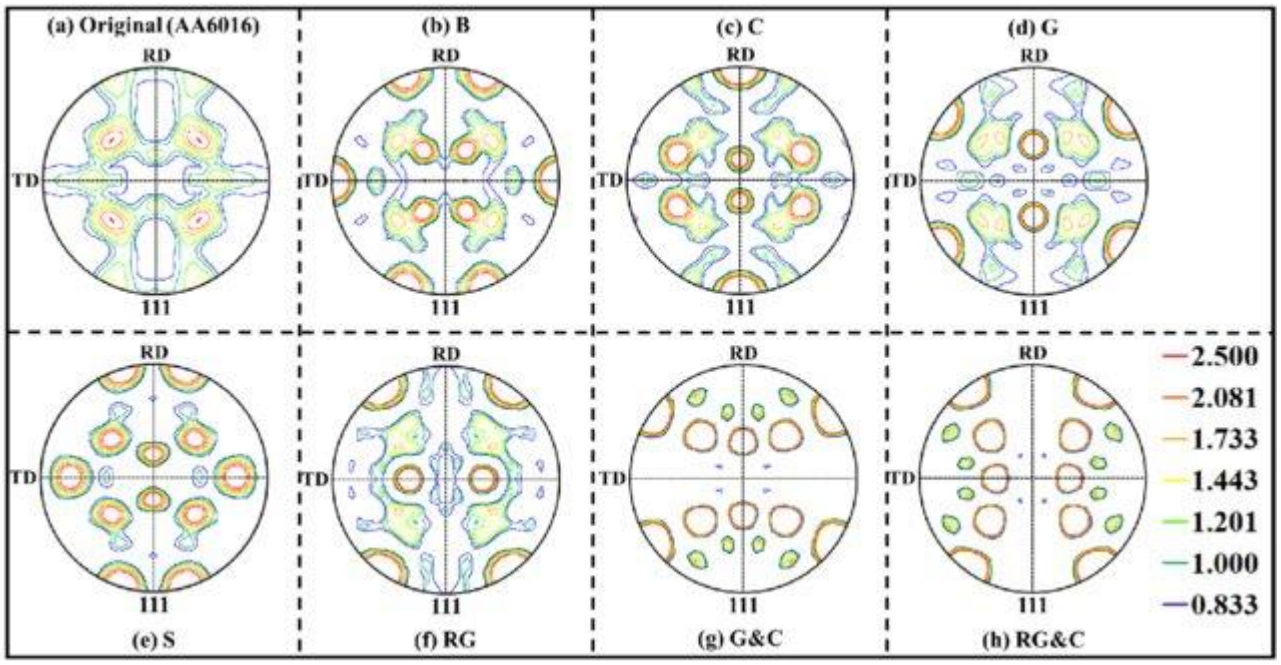


*Figure 2-43: <111> pole figures used for synthetic microstructures in aluminium alloys in bending simulations by Muhammad et al. a, Aluminium alloy texture, b, Brass, c, Copper, d, Goss, e, S texture, f, Rotated Goss, g, 50% Goss and 50% Cube, h, 50% Rotated Goss and 50% cube* [52].

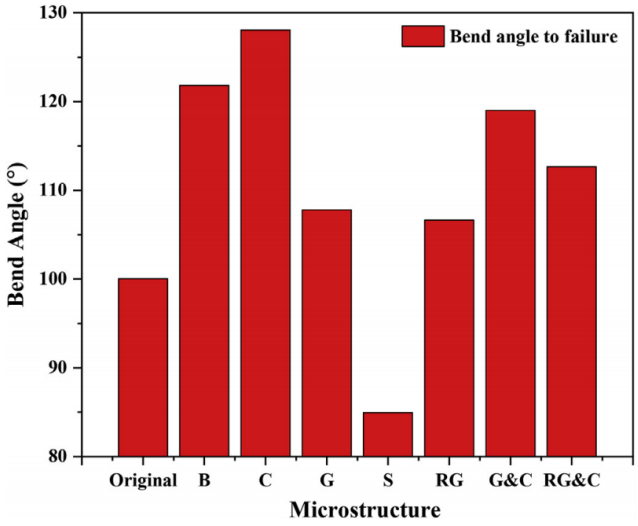


*Figure 2-44: Bend angle to failure for a range of simulated microstructural textures as shown in with bend axis perpendicular to RD Figure 2-43* [52].

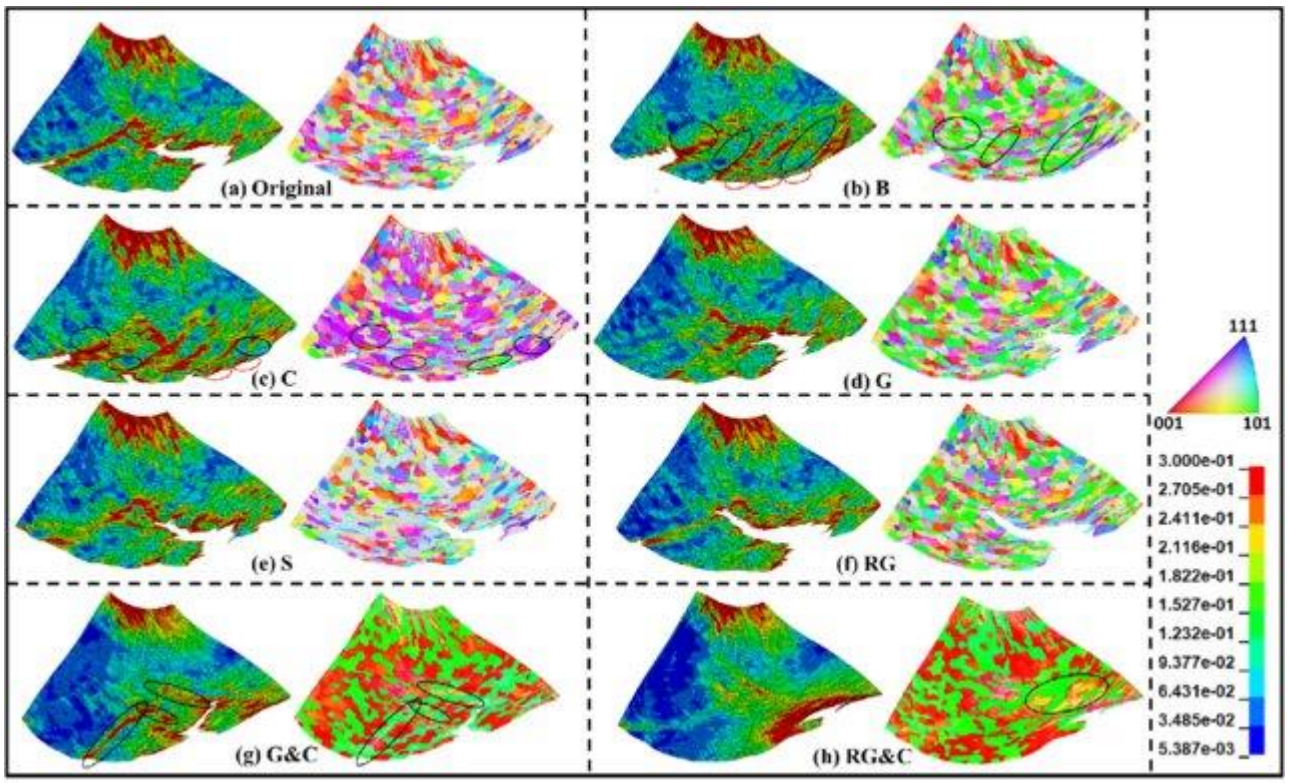


*Figure 2-45: deformed FEM meshing with a. effective strain distribution and b. texture evolution during bending with bend axis perpendicular to RD* [52].

In bending the Goss and the rotated Goss texture is found to promote shear bands and damage to initiate at microstructures boundaries while the cube texture is found to resist the shear bands and damage initiation when added to the Goss and rotated Goss textures [52].

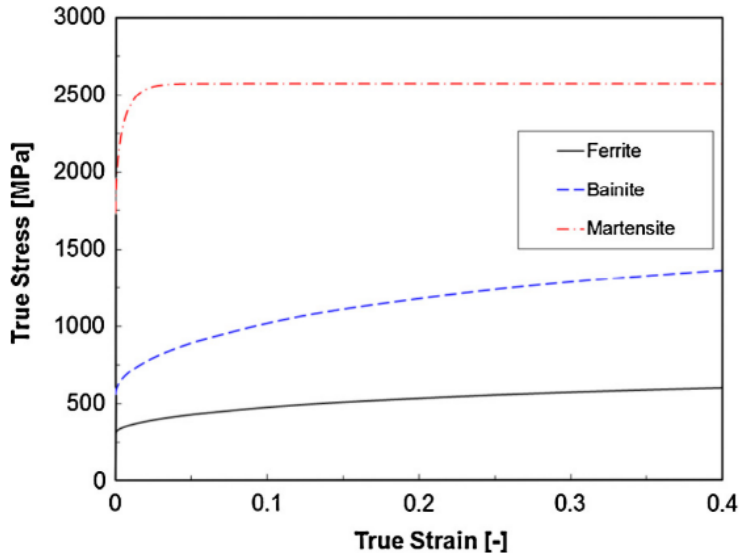


*Figure 2-46: True stress-strain curves for different microstructures in steels developed from dislocation-based modelling* [76]

Publications by Ramazani et al. has found when modelling microstructures in bending using the material properties in Figure 2-46 that due to the work hardening capabilities of bainite when in bending this improved bendability [76].

## 2.5 Alternative bending geometry

While the typical bend test specimen geometry has been defined by the ASTM and BSI [4], [5], this is optimised for analysis of the bendability of the material to observe cracks in specimen post bend test. Bend test rigs for observation are typically observed from the view shown in Figure 2-47, image b. This limits observation to only view the low triaxiality outside the edge of the bend. A novel specimen design was developed by Mishnaevsky et al. to observe the central location with high triaxiality in bending [91].

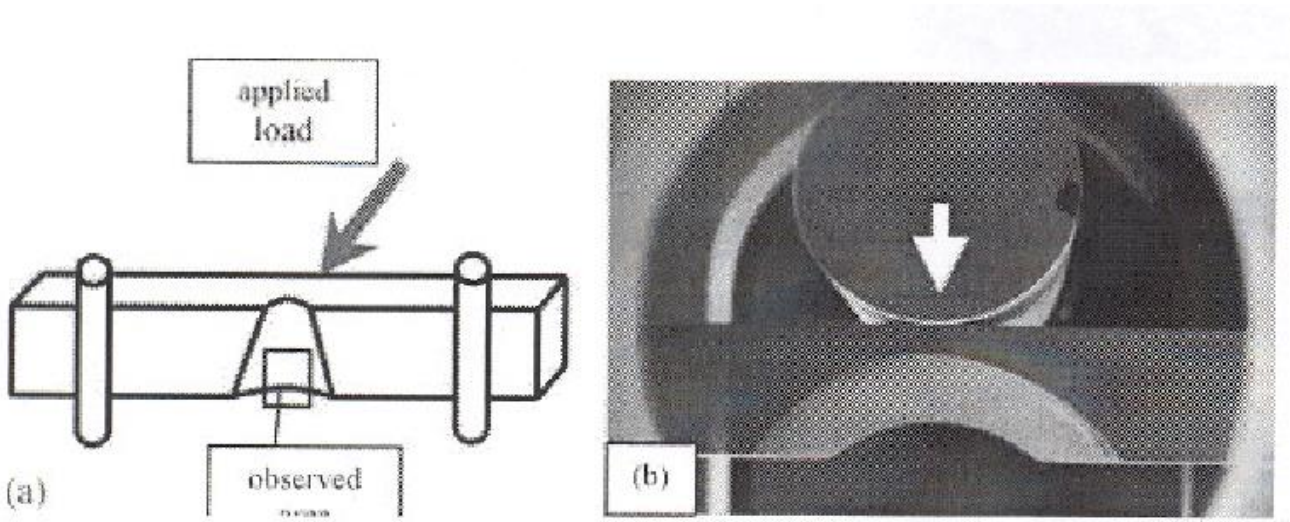


*Figure 2-47: Bend test geometry with notched design with, a; the schematic of the specimen, tooling and observation area b; view of the specimen from the SEM* [91].

In this approach, the observed bend test region was polished and etched to observe cracking in carbides when in bending. Cracks are found to generate at locations of larger carbides as shown in Figure 2-48. These then propagate into the matrix of the material and lead to failure.

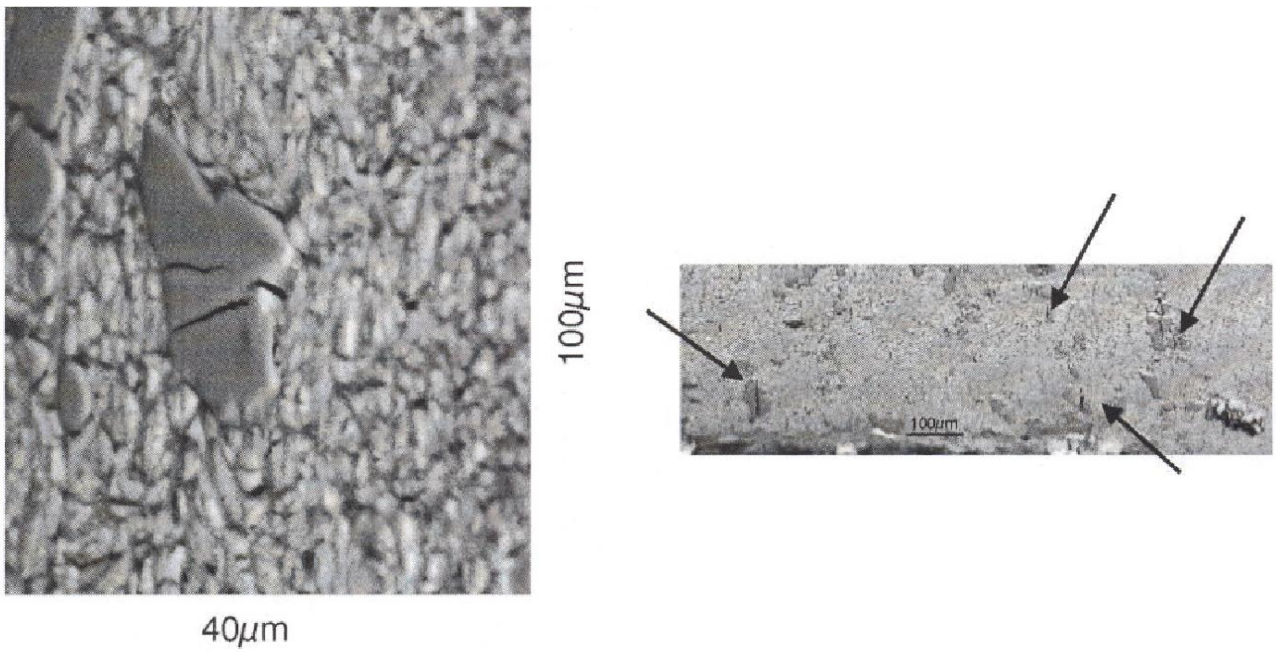


*Figure 2-48: cracks propagating in carbides in the observed region as shown in Figure 2-47.*

This approach shows that the observation of bending can be changed for specific uses by the modification of the specimen. An analysis of alternative bending geometries to localise strain in bending should be performed.

## 2.6 Summary of Literature review

Shear bands are a common process by which materials with low hardenability localise strain and promote material flow. This promotes geometric softening which reduces the hardening properties of the material. Shear bands are found to promote failures when bending UHSS. Publications have proposed a range of approaches to improve the bendability of materials these include:

- Refining microstructures [26], [43]
- Reducing surface hardness [46], [47]
- Promote lower bainite and ferrite microstructures near the surface to reduce hardness and increase work hardening capacity. [26], [76]
- Reducing rolling typically {111} and in particular <112>{111} textures [32], [43]
- Introduce Goss, <110>{001} textures to improve bendability. [52], [67]
- Improving hardenability of the steel (n and m) [37], [41], [42]
- Removing inclusions by producing clean steel. [14], [92]
- Reducing surface roughness, improving surface quality to remove stress raisers. [46], [47]

The primary mechanisms to resist bendability seem to be due to the work hardening properties of materials and/or local microstructures and texture in the top and bottom 10% of the strip or sheet are key to improving bendability [52]. These combined with other factors such as the grain size [45],

surface quality [46], [47] and cleanliness of the material [14], [92] all contribute to the bendability of UHSS.

Despite these studies covered in the literature, there is still a lack of understanding about the formation and development of shear bands in bending.

A novel methodology has therefore been developed in this work to generate new insight into the initiation and propagation of shear bands leading to damage and failure in UHSS. A new bending test rig working inside a scanning electron microscope and enabling very large deformation of such steels has been designed and manufactured to study the formation of shear bands in the microstructure with quantification of strain distributions and their evolution up to failure using DIC. Using this with a novel sample preparation approach has enabled key insights into material properties impacting bendability and the formation of shear bands.

# 3 Experimental & Finite Element Modelling methodology

To develop a comprehensive understanding of the bendability of UHSS a wide range of techniques have been deployed to explore macro and microscopic material properties that provide insight into the mechanisms affecting the bendability of UHSS.

The unique challenges of producing micro-scale test specimens mean that sample production and preparation require extensive planning to optimise for testing. Then the tooling and operation required changing and optimising respectively for the bend testing. To achieve this and bring benefits to the whole process.

## 3.1 Testing Methodology

The testing methods were developed to study shear bands and damage and evolved and changed through the project. To clarify this process the following chapters are aiming to achieve the following aims and outcomes. These helped develop novelty through the research and linked the work to literature to understand how this was conceived.

| Chapter | Aims | Outcomes |
|---|---|---|
| Sample production | Identify the most appropriate process to produce specimens to minimise their impacts on later trials | Informed the need for sample preparation to remove HEZ from the EDM profiled specimens as found in work by Navas and Ekmekci et al. [93], [94]. |
| Sample preparation | Develop a suitable means to observe the UHSS's microstructure and remove any regions impacted by the sample production.<br>Post pandemic the sample production method was changed to batch production and so the methodology had to be adapted again. | Successfully produced specimens for tensile testing and bending used in insitu tests. Post pandemic this was improved to batch production with the implementation of the vacuum storage vessel. This improved work output while reducing lab hours. |
| Applications of insitu testing in SEMs | To develop an understanding of what has been performed with insitu | Using specimen and tooling geometry special developed for the SEM insitu |

| | | |
|---|---|---|
| | testing and how this can be applied in the project. | testing the results can be improved and develop novelty. |
| SEM in situ test module | Describe the basic use and limitations of the insitu bend test module to observe insitu bend test results similar to those achieved by Ghadbeigi et al. where the microstructure and their plastic strains were studied [36], [73]. | Optimised the use of the bend and tensile test for the trials and used the work to develop new tooling to increase the strain in bend testing. |
| Experimental | Understand material properties of the UHSS at a microscopic level of detail using a range of techniques. | Micro and nano indentation were used as key techniques to understand how hardness varied at the surface of the hot-rolled steel known to be a key variable impacting bendability [46], [47]. This informed the bend testing that the surface preparation could be used to remove different depths to change the hardness at the tensile face in 3 point bending. This also removed surface roughness removing another variable. It was found that EBSD was difficult to perform on this material and so was aborted at this stage. |
| Tensile testing | How the process of tensile tests was performed at macroscale and microscale to provide data for FEM to progress the FEM work performed by Tata Steel [14]. This also allows the development of strains in micro tests to also be studied as performed by Ghadbeigi et al. [36], [73]. | The use of tensile testing allowed material models to be generated for FEM. This also provided experimental results to compare the initiation of damage with the same processes in bending. While also acting as a validation for the bend testing results as found in chapter 5. |

| | | |
|---|---|---|
| FEM | To develop a methodology to test the impact of different material properties and surface topography on the formation of shear bands in FEM as performed by Muhammad et al. [52]. | 2D modelling of the bend test using sub modelling developed a means of increasing the mesh density without a significant increase in compute time. This enabled the development of shear bands that could be studied when compared to when they initiate in other stress states [37], [41]. |

## 3.2 Sample production

Throughout the project, specimens are required that have geometries to suit testing methods. The hot-rolled steel is produced in strip sheets then cut into panels of manageable size to handle. To produce these samples from this plate presents difficulties as machining results in thermo-plastically deformed regions resulting in residual stresses. To consider the optimal method of profiling specimens a literature review was performed on the influence of machining on material properties. As shown in Figure 3-1 and Figure 3-2, machining methods influence both the residual stresses and microstructure of steels. This shows the importance of understanding their influence in the production of the specimen. Using X-ray diffraction the strains on latices are measured in the microstructure of the specimen, the residual stress can be calculated [93].

Using X-ray diffraction various authors have studied the influence of machining methods and parameters

It is found that Electro Discharge Machining (EDM) promotes a very significant heating effect, this produces high residual stress of up to 800 MPa at a shallow depth of less than 100µm. The top surface is also found to contain a hard brittle layer known as the white etching layer. This is produced by the rapid melting and resolidification of the metal giving it a brittle hard surface layer. It has been found through this process stresses up to the UTS are reached and cause cracking in the white etching layer [95]. By optimising the process a finishing step can reduce the residual stresses but the overall effect on depth is not very significant.

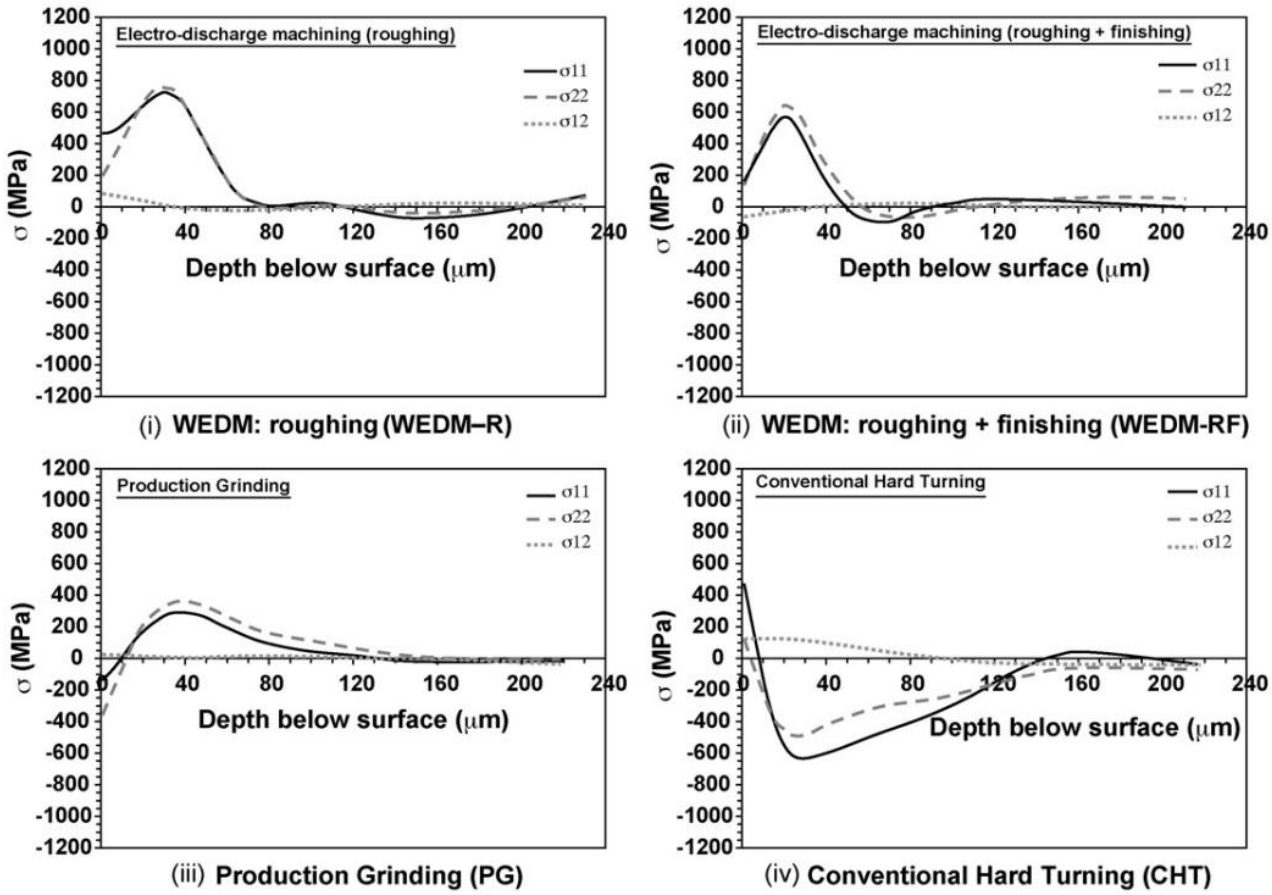


*Figure 3-1 Residual stress depth profiles measured via X-ray diffraction in AISI O1 tool steel.* [93]

Production grinding is found to produce compressive and tensile stresses at different depths of the machining, this is due to the combination of compressive force and heat being generated by the machining process. The compressive force provided by the wheel onto the material surface imparts local compressive residual stress at the surface while the heat generated promotes tensile stresses. While production grinding has significantly lower residual stresses than EDM it has more depth of 120µm. Hard turning generates heat at the surface producing tensile residual stresses then the plastic deformation promotes compressive stresses at the subsurface depth to 160µm.

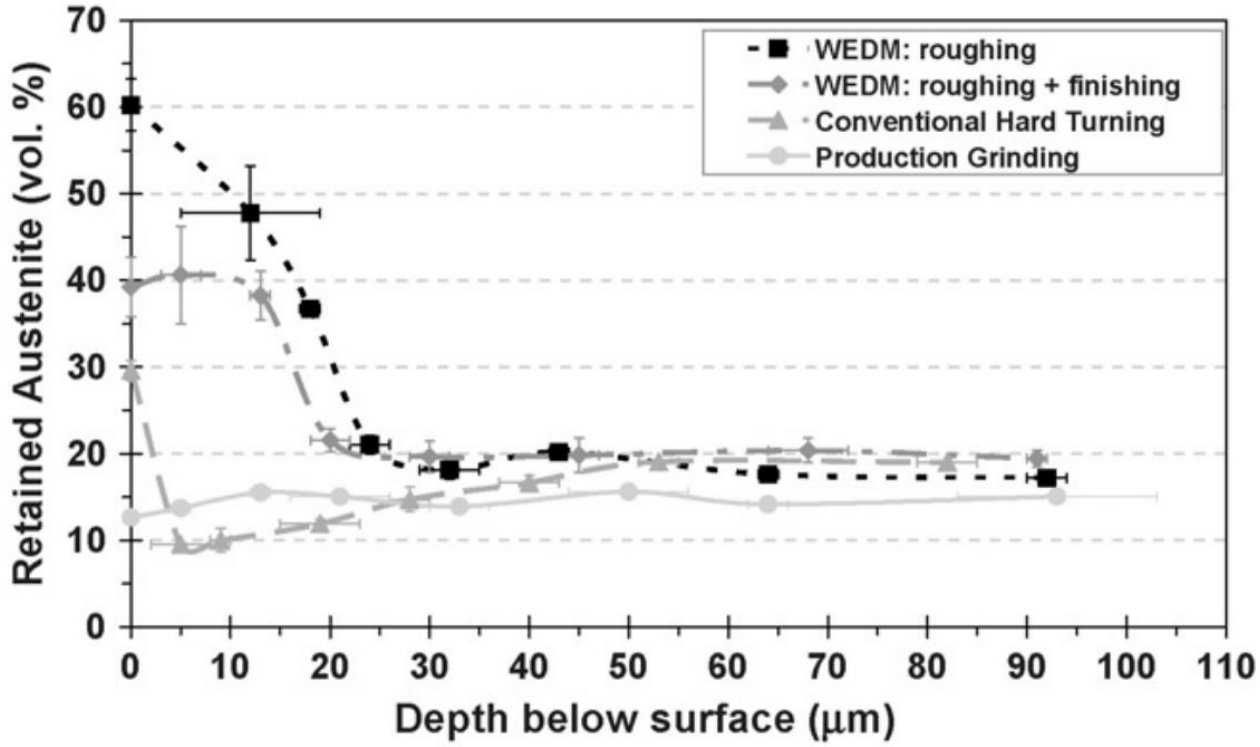


*Figure 3-2: The retained austenite across unit depths using different machining depths* [93]

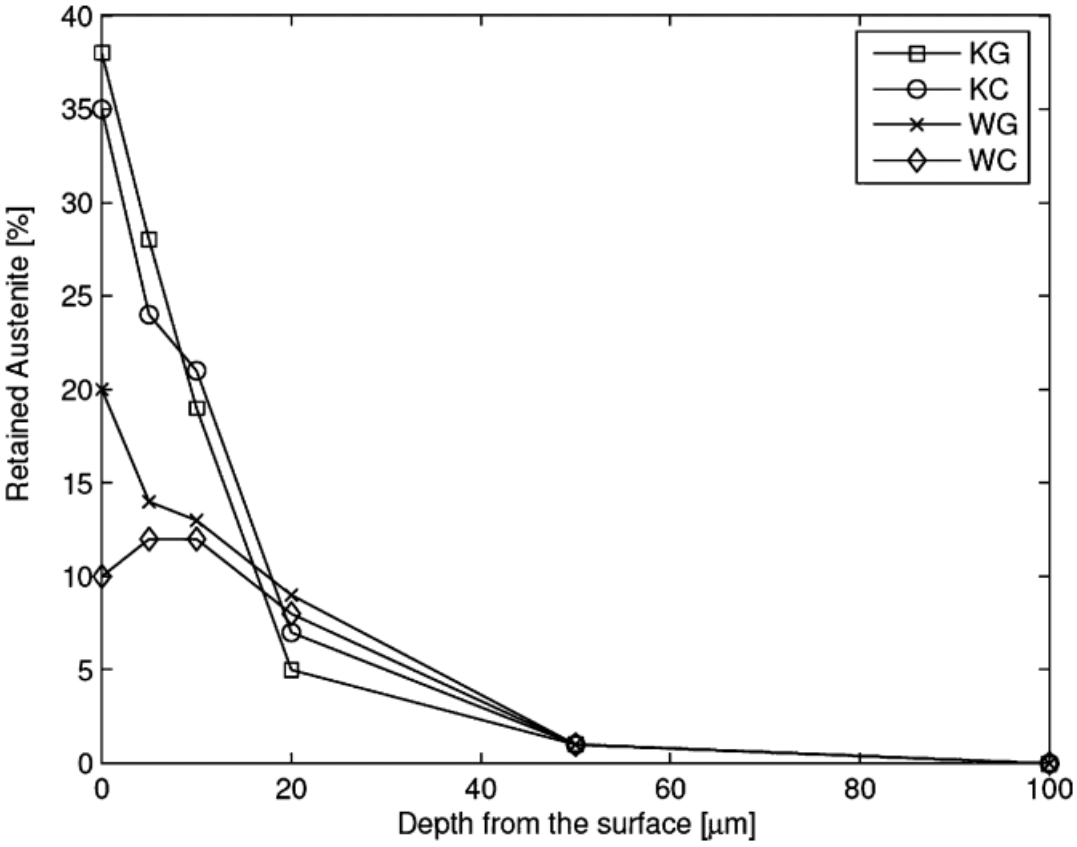


*Figure 3-3: Change in percentage of retained austenite to depth using various electrodes and dielectric components. samples KG: Kerosine dielectric and Graphite electrode, KC: Kerosine dielectric and Copper electrode, WG: Water dielectric and Graphite electrode, WC: Water dielectric and Copper electrode* [94].

While the residual stresses must be minimised so must the influence on microstructure. As shown in Figure 3-2 the change in microstructures corresponds with the influence of the heat-affected zone. In Figure 3-3 it is shown that wire spark eroding influences the microstructures but by varying the electrode and dielectric the changes in microstructures from machining get affected. This is likely due to changes in the heating and cooling properties of electrode and dielectric promoting different heat-affected zones. Comparing the ratio of vol of affected austenite from machining from Figure 3-2 and Figure 3-3 suggests that 60% change in volume of austinite is a large variation in microstructures from wire spark erosion [93],[94].

While these results are going to vary with materials, machining process and parameters they will still affect the results for UHSS. Also, because we are using microscopic analysis of the material and will be observing regions near the machined surface it is of great importance to minimise or eliminate the effects of machining. For this reason, the samples were profiled with wire spark eroded to generate profiles before having the sample ground and polished to remove the affected region of 0.2mm. Production grinding will be used to remove bulk thickness from some regions to retain flatness and parallelism while having minimal effect on the residual stresses and microstructures. Regions close to the region of interest will have material removed by grinding on an Automet 250 Pro, having been mounted in Bakelite the specimens will be ground and polished using either a central force or individual force head for bulk (>0.2mm) or local (≤0.2mm) depth removal, respectively.

### 3.2.1 Sample orientation

To limit the scope of this project and keep testing consistent the bend test specimens will be produced with the bend axis parallel to the rolling direction as shown in Figure 3-4. This will put the TD in tension and is reported to produce inferior bendability to align the bend axis perpendicular to the bend axis. When this project started it was identified the aim to promote shear bands and damage and this was agreed with Tata Steel and prioritised.

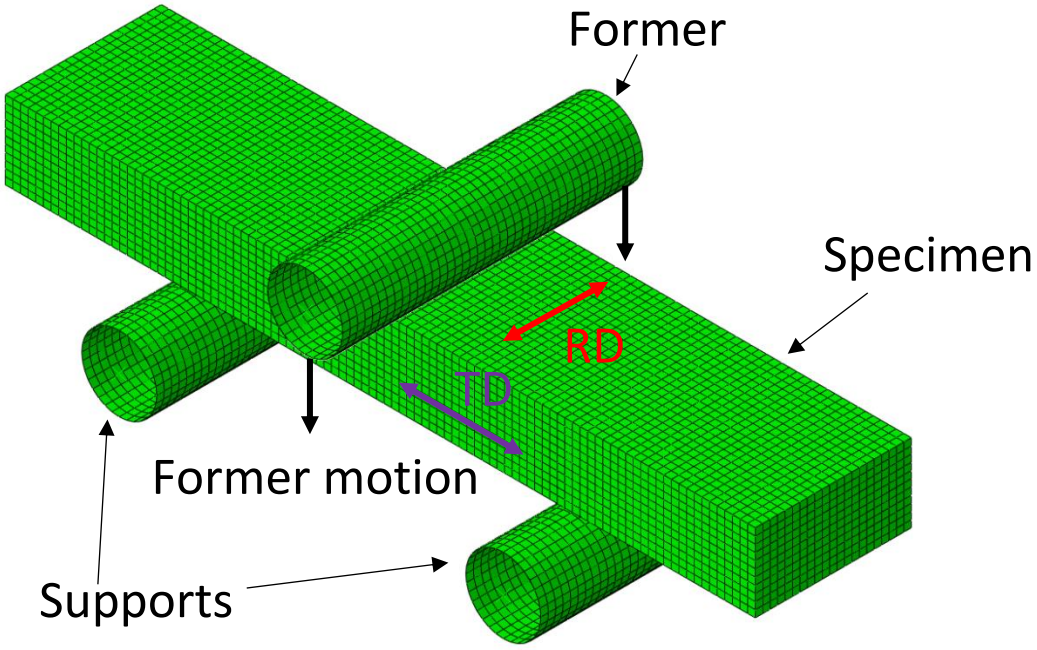


*Figure 3-4: diagram of the sample orientation in bending with respect to the rolling and transverse directions.*

## 3.3 Sample preparation

To produce high-quality SEM micrographs and strain maps, sample preparation had to be of a very high standard. This allows the observation of the microstructure of the material as it deforms free from scratches, defects, and residual stresses. Often when producing a sample for SEM analysis only a single region of good surface preparation is needed and so the field of view can be moved to find a good quality region of sample preparation. Whereas when performing mechanical testing, specimens observed by SEM the field of view is often restricted to specific locations of interest making sample preparation for the whole specimen crucial to a successful test. To achieve this the methods were adapted throughout the project to optimise the sample preparation, this worked in conjunction with sample design and newly redesigned tooling to optimise the sample preparation.

### 3.3.1 Sample preparation method

To produce high-quality SEM micrographs the samples have to be prepared such that the microstructure can be easily identifiable. These microstructures have been used to produce DIC, requiring the microstructures to be observable by the SEM. The contrast in the micrographs has to be optimised to observe the microstructures. The following chapters cover the processes used to prepare samples, as well as the settings and methods used.

#### *3.3.1.1 Sample cutting*

If a sample is of a difficult or too large a geometry the specimen can be cut down with an abrasive cutting wheel. This is performed with the Struers Secotom. The sample is clamped and an abrasive

cut off wheel is used to section the part. These could then be used for observation with SEMs or optical microscopy of a smaller sectioned sample or to undergo further sample preparation as described below.

#### *3.3.1.2 Sample mounting*

Samples are mounted in a conductive compression mounting compound to maximise conductivity to avoid localised charging from the electron beam, the mountings are 1’1/4 inch diameter. These were pressurised to 290 bar and heated to 180°C in a Buehler SimpliMet 1000 v3 automated mounting press in Figure 3-5. This will form the compression mounting compound into a solid mounting holding the sample and retaining edge profiles on the samples during grinding. Mounted specimens bring significant benefits to the process of sample preparation, these include:

- 1’ ¼ inch diameter mountings fit both the centre force and individual force heads. This enables the AutoMet to be used in an automated function removing the variables of hand grinding and user error, while also allowing the use of batch production of up to 6 specimens at the same time.
- The mountings protect the edges of the samples from edge rounding. This is of great importance with sample edges being observed in bending.
- The mounting is retained in the head and keeps the orientation of the specimen the same throughout sample preparation.


*Figure 3-5: Buehler SimpliMet 1000 v3 automated mounting press*

After samples have had preparation complete in the mounting they are often required to be broken out. To do so a hacksaw and vice is used to weaken the mounting before it is broken out with a mounting extraction tool as shown in Figure 3-6.

*Figure 3-6: Method of breaking samples out of mountings, top left; clamping before sawing with hand saws, top right; specimen with cuts from sawing to weaken the mounting, bottom; mounted specimen wrapped in cotton wool and paper towels to protect the surface and retain mounting fragments in the mounting breaking clamp.*

#### 3.3.1.2.1 Measurements

To measure dimensions of up to 150mm with precision throughout the project a J-Bonest digital calliper [96] was purchased and used. This calliper has a maximum measurement of 150mm and has an error as specified in Table 3-1.

| J-Bonest digital calliper | Measurements (mm) | |
|---|---|---|
| Measurement size | <100 | 100-≤150 |
| Error | ±0.02 | ±0.03 |

*Table 3-1: Error for the J-Bonest digital calliper*

This is used to take measurements of specimens, tooling and mounted specimens among many applications.

#### *3.3.1.3 Standard sample grinding and polishing methodology*

To prepare samples effectively the samples are ground and polished using an AutoMet 250 Pro automated grinding and polishing machine. The automation features the head that can have 1'1/4 inch diameter mounted specimens loaded and then polished with consistent load applied onto the specimen throughout each grinding and polishing phase. The machine is as standard a multi-force head allowing loads to be distributed individually on the samples. An alternative central force head has also been used for bulk material removal. This has the benefit of holding mountings flat, provides improved parallelism compared to the multi force head.

To perform the grinding a graduated set of Silicon carbide abrasive papers are used from coarse; P240 to fine; P1200. The papers were used in the following steps:

1. P240 grit
2. P400 grit
3. P800 grit
4. P1200 grit

Each paper was used for one minute until the scratches left by the previous paper has been removed. A grade of paper can be repeated with a new grinding paper used if the previous scratches were not removed. Each grinding paper is only used for one minute this is because the sharp edges of the silicon carbide are lost in this time of usage.

The following settings are used to operate the AutoMet for the multi force head:

- Force mode: Single
- Force: 15N per sample
- Plate Speed: 121 rpm (never use a multiple of the head speed to use the full grinding paper)
- Head Speed: 60 rpm
- The plate rotation direction was changed at each paper to allow easy analysis of scratches being removed at each step.

When performing hand polishing the settings used are identical but with myself applying the force to the specimen and holding it in position.

#### *3.3.1.4 Sample depth removal process*

For the final tests' material depth was to be removed from the top surface of the bend test samples. These samples were produced with excess thickness to allow the samples to be ground down to meet the desired thickness set in bend test thickness design.

To remove material equally the standard approach was changed. A specialised sample holder was obtained from Buhler and to be used in conjunction with the central force setting. This was not found to fit in the Automet machines and caused multiple delays. To alleviate this a new approach was developed with different settings to retain flatness in the specimens while using the standard equipment it was advised the relative rotation speeds between the head and platen to be made as close as possible. As such the platen and head speed were made almost identical with the only difference to move the grinding paper relative to the sample to use all the abrasives in the paper.

To remove the head some different settings are used on the AutoMet to make it compatible and optimise the parallelism by reducing the speed difference between the plate and head:

- Force mode: Central
- Force: This is a total, so; $15N \times number\ of\ samples\ loaded$
- Platen Speed: 61 rpm
- Head Speed: 60 rpm
- The plate rotation stays as comparative throughout.

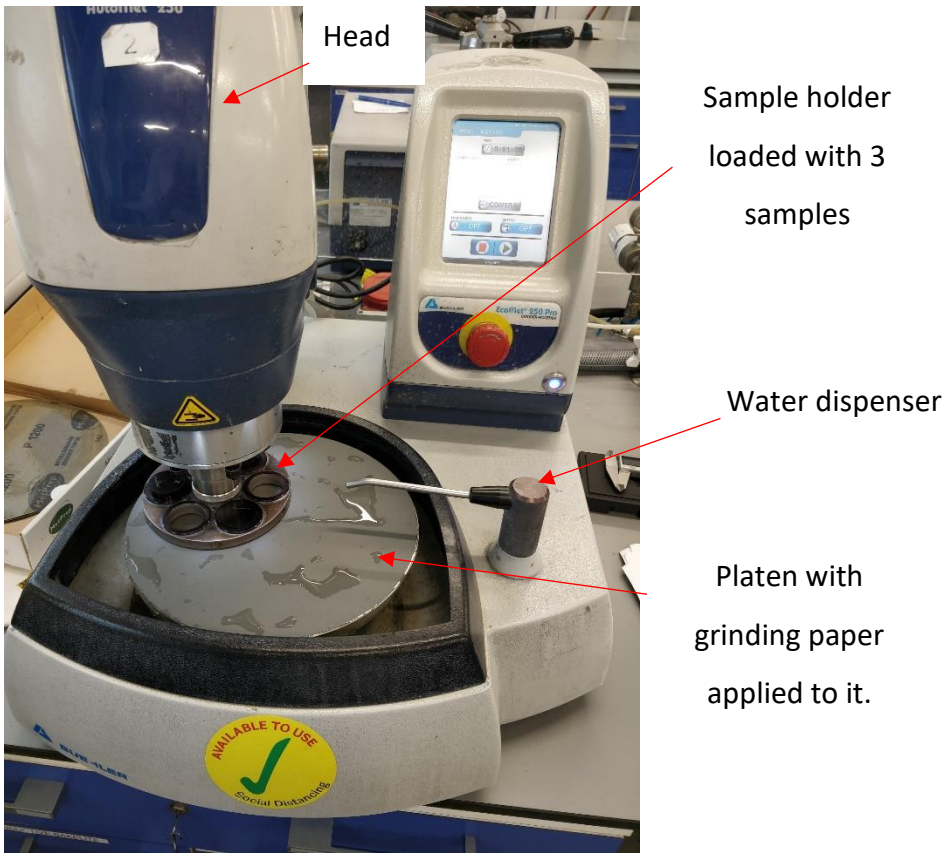


*Figure 3-7: Buehler Automet 250 Pro with 3 mounted specimens set up with grinding paper.*

To perform the final polishing two grades of water-based diamond suspensions are used with a compatible cloth as suggested by the supplier. These grades are used in descending order:

- 6µm Monocrystalline water-based diamond suspension used with the MetPrep Ltd. Plano, napless cloth
- 1µm Monocrystalline water-based diamond suspension used with the MetPrep Ltd. Trounoir, velvet cloth

These were used for 5 minutes each. If scratches were observed or other imperfections from sample preparation the sample was returned to the grinding phase with a P1200 paper used, then returned to the polishing stages.

#### *3.3.1.5 Sample preparation for EBSD*

For preparing a sample for EBSD the sample cannot be etched as it must have any deformation due to polishing on the surface removed. To achieve this a colloidal silica compound is used, MasterMet with 0.06µm polishing grit and 10.5pH it produces a chemical-mechanical polished surface suitable for EBSD analysis [97].

The sample is prepared for EBSD analysis by making the sample a suitable geometry to fit in the EBSD mounting head and then it is ground and polished as described in section 3.3.1.3. An additional set of steps are taken at the final 1µm polishing stage, as this should be reduced to 2.5 minutes to retain

specimen flatness. The Trounoir cloth has a nap that can cause a sample to lose flatness. While the subsequent use of a colloidal silica polishing compound does additional polishing so less time is required with the 1µm polishing stage.

- Force: Single
- Method: comparative rotating
- Force: 20N per sample (extra force to keep in the inclusions in the sample)
- Platen Speed: 61 rpm. The number is odd so that the whole paper is used.
- Head Speed: 60 rpm
- 10-minute polish time
- Final 10 seconds a prewash is performed by pouring a 1-litre beaker of water onto the platen to wash a majority of the colloidal silica compound to avoid the compound crystalising.
- Wash the specimen for 5 minutes under a tap.
- Place in an ultrasound bath in a beaker of isopropanol and vibrate in the ultrasound bath for 20 minutes

After this was performed the specimen was stored in a small container submerged in isopropanol and EBSD analysis was performed that day on the specimen.

#### *3.3.1.6 Sample etching*

To observe the microstructure the steel was etched with a 2% nital solution. The 1µm polished specimens were placed into the 2% nital solution for 5-second increments being washed in isopropanol between each application of nital. The typical time for the application of 2% nital total is 35 seconds, with some variance depending on the strength of the solution.

### 3.3.2 Sample storage

When storing samples, a toolbox is used for temporary storage with the samples wrapped in cotton wool for protection and transported but for the longer-term storage of specimens that were already ground, polished and etched were kept in a vacuum desiccator to reduce oxidation and extend the useable life span of the samples. This allowed the samples to be prepared in batches of up to 6 at a time. This resulted in more efficient production and lower cost of samples and testing to be performed on consecutive days without sample preparation being performed the day before the test.

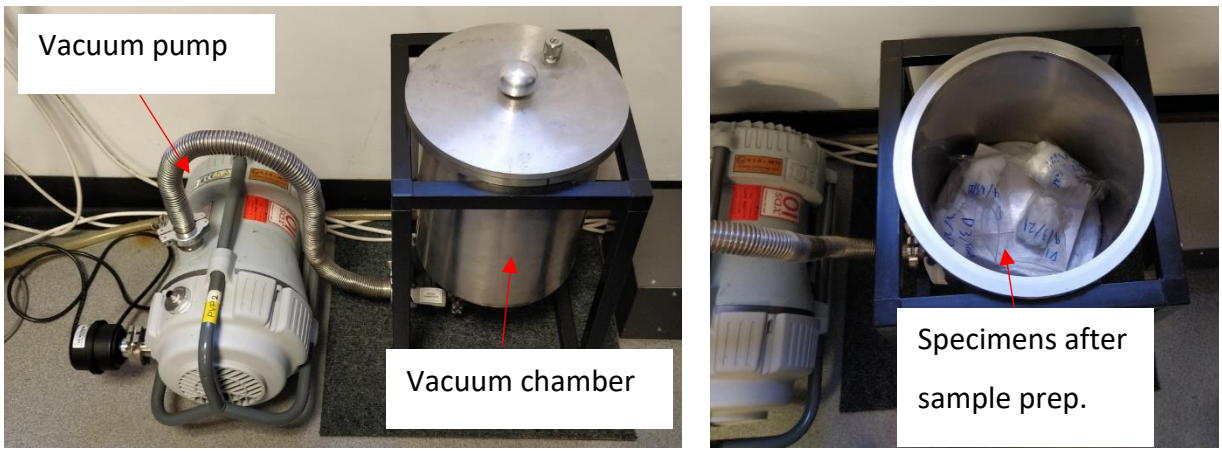


*Figure 3-8: Vacuum desiccator on the left with the chamber open with the lid removed on the right showing the specimens contained within.*

## 3.4 Applications of insitu testing in SEMs

SEMs have been used since the 1930s producing micrographs but the procedure of performing mechanical testing within the SEM and observing images is a relatively recent application starting in the 1970s [77]. Here specialised mechanical loading stages and specimens would be placed within the SEMs chamber and the microstructure and features can be observed. These are then deformed while being observed by the SEM. To study the strain in these tests different approaches have been taken.


*Figure 3-9: Deformed micro-grids: (a) recovered sample, α = 0°, γ = 1; (b) as-rolled sample, α = 0° , γ = 1: (c) as-rolled sample, α = 60 °, γ = 0.25.* [78]

A simple approach for visualising deformation can be achieved with the use of micro-grids, here by using a masking, beam and gold coating technique [79].

Small scale mechanical testing is a popular use of insitu SEM with a variety of scales used. Small scale tests have been designed for SEMs as a means of analysing material properties at a microscopic scale. A popular method of performing tensile tests in the SEM is to use the force transducers and displacement measurement within a stage. Here the specimen is larger with gauge volumes of 2mm long, 2mm wide and 1.5mm thick in a dog bone profile. This requires an electric motor actuated module with larger displacements and force transducer and displacement in the module to obtain stress-strain analysis specially designed for use within vacuum chambers typically used in SEMs.

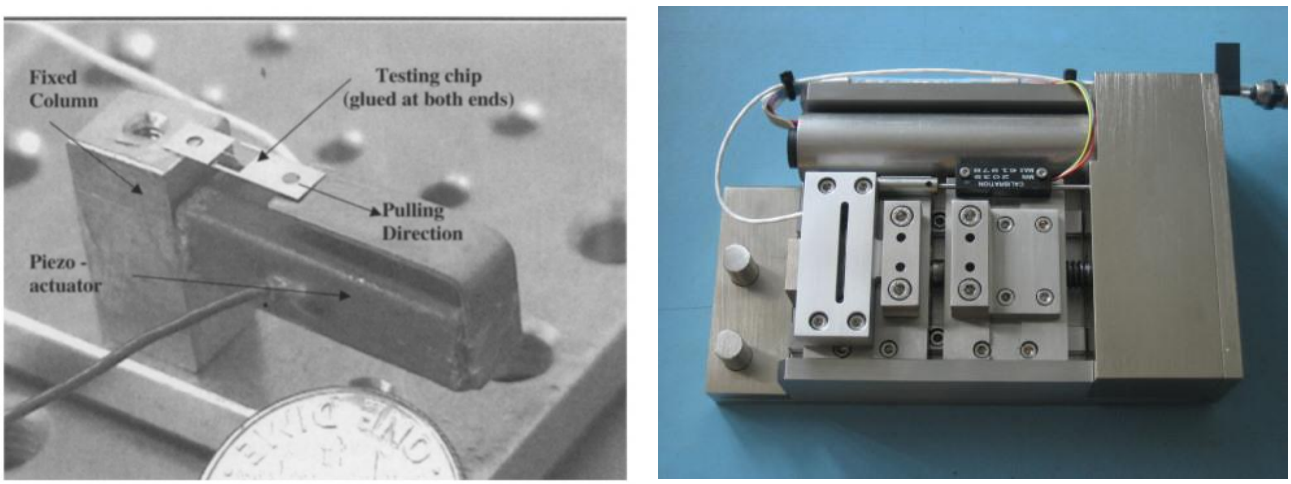


*Figure 3-10: In situ tensile test stages, left; a piezoelectric actuated tensile tester for use with a testing chip* [80]*, right; an electric motor driven tensile tester* [81].

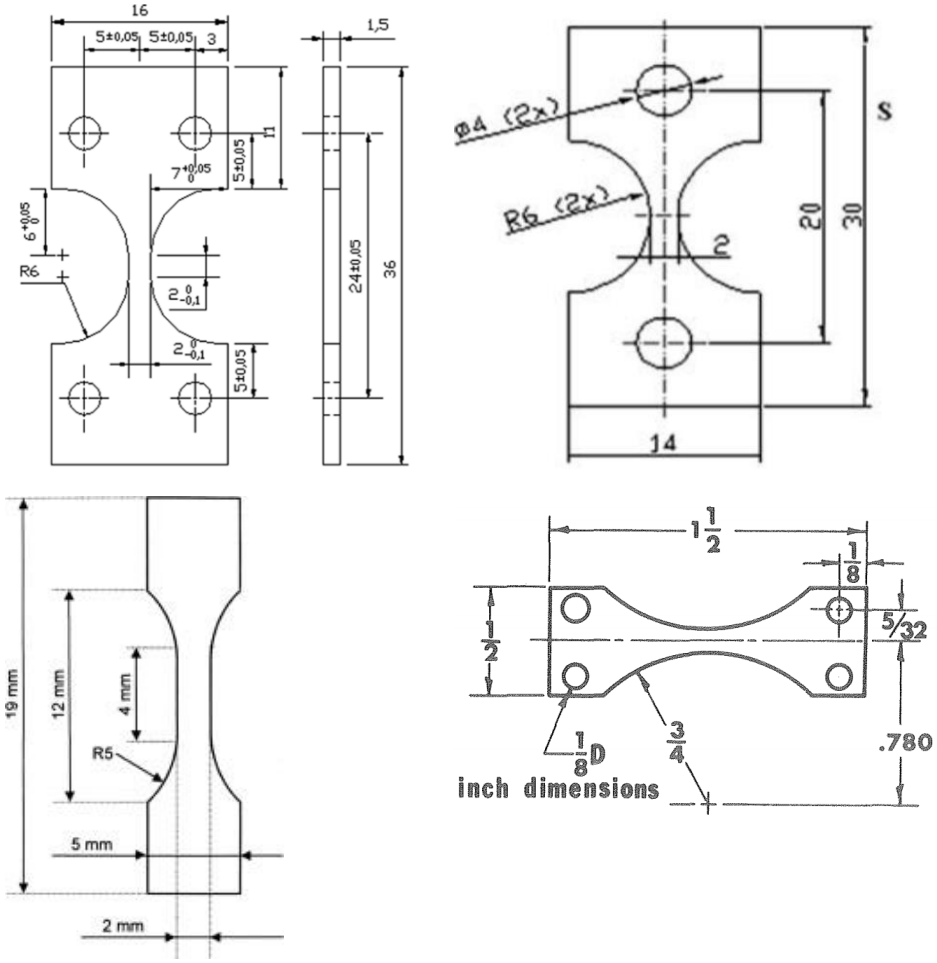


*Figure 3-11: Insitu tensile test specimens for tensile test modules, top left; H. Ghadbeigi, 2010* [73]*, top right; S. B. Hosseini, 2007* [82]*; bottom left; A.Ramazani, 2013* [83]*; bottom right, A. C. Bell 1974* [77].

The use of the electric motor driven tensile test unit simplifies the test specimen design as shown in Figure 3-11. These specimens tend to differ from standard tensile test specimens [84] as they have shortened gauge lengths. These are used to reduce the area over which elongation and failure will nucleate to retain it in the field of view of the SEM during the test as done in the top left specimen in Figure 3-11. This geometry does have some limitations in that the elongation is found to be 5 times

those found in standard bulk tensile tests [36]. The role of the SEM in an insitu test is to observe microstructures as they undergo deformation and damage [36], [73], [77], [82]. This improves the understanding of the failure mechanisms in these materials as the microstructural feature leading to failure can be studied. This information is valuable to developing new materials to avoid these weaknesses and remove defects.

As well as observing the location or failure and deformation the measurement of localised strain is of great interest especially when combined with analysis of damage and deformation. Many methods have been developed to observe strain, early methods use microgrids as shown in Figure 3-9. Using layers of photoresist resin and the SEM beam to remove the resin a gold grid is deposited on the surface. This technique has been used to study strain as the movement of the grids can be calculated. Another popular method to study full-field strain is to use digital image correlation (DIC) as shown in Figure 3-12. DIC operates by tracking the displacement of identifiable patterns and converting these into strain maps. This is done by taking an image before and after strain is applied, the first image is broken up into subsets of specified size each must contain an identifiable pattern as shown in Figure 3-12. These subsets are then found in the second image with the applied strain, this results in a deformation being found that can then be plotted as a strain field. The sizing of these subsets has a significant effect on the error in DIC calculations, this is because as subsets become smaller the number of identifiable patterns decreases increasing the error and chances of not correlating with a deformed image[85] As shown in Figure 3-14 the standard deviation of results is inversely proportional to the subset size. So the calculation settings and subset size have a significant effect upon error [85].

Patterns can be naturally occurring, produced, or applied, a popular method is to spray paint a speckled pattern on macroscale specimens. An ideal speckled pattern should have speckles that are 3-5 pixels, ideally of identical size [86]. With this application of DIC, the method of obtaining an identifiable pattern is the problem.

One method that has been developed by H. Ghadbeigi et al. [73] is the use of the etched microstructure this is used as the identifiable pattern. To perform this the size of the microstructure defines the optimum magnification to use to set the speckle size as such.

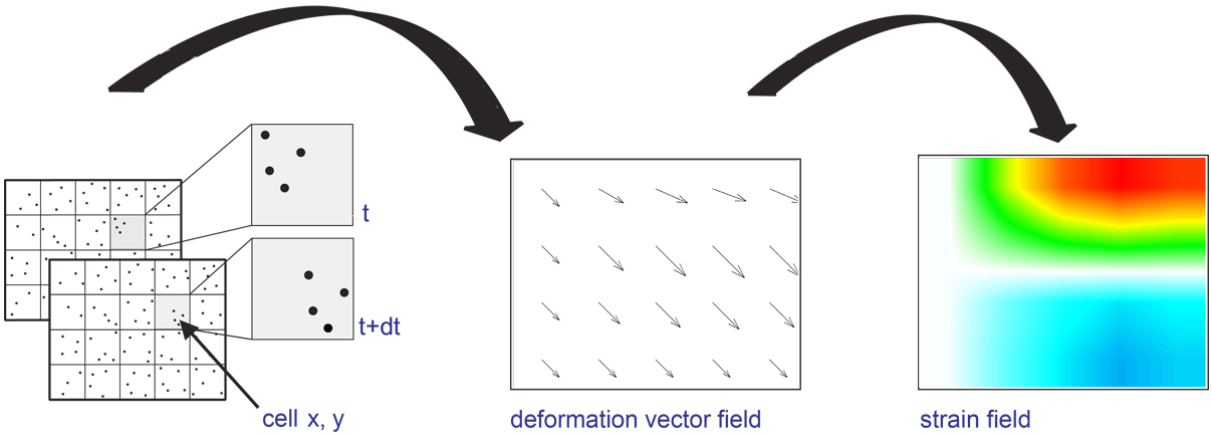


*Figure 3-12: Demonstration of DIC calculation method* [87]

### 3.4.1 Error in insitu SEM DIC testing

To validate this technique, a tensile test was performed with both microgrids and DIC using the microstructure of the specimen [88]. When comparing these techniques, it was found that the DIC has an average error of 16% but this increases to 34% at localised regions of high strain. There are some factors to consider from this publication that make it not applicable to the validation of all insitu testing with DIC:

- The magnification used to obtain micrographs is 500x, a range of magnifications should have been analysed and the effect on error quantified.
- The material is DP600 steel, this provides the pattern for DIC and will be specific to this experiment.
- The microgrid will be interfering with the microstructure the DIC is using to correlate which is not often used in conjunction with an etched microstructure used in other publications. Comparing DIC results between using microstructures and microstructures with microgrids are not the same due to them obscuring the microstructure.
- With SEM imaging the user has control of variables including, focus, magnification, contrast and brightness which can vary during use by trying to observe the microgrids and microstructures in every micrograph. Some degree of user error must be considered.
- The DIC algorithms have been updated with new software by LaVision and the user can influence the settings used to increase the accuracy and precision of the strain values. Follow up work reprocessing the same micrographs using the latest DaVis revision and algorithms to resolve the DIC and compare with previous work would increase the relevance to more recent publications.

- The SEM and sample quality and features will impact the imaging there are many sources of error such as beam drift [88], [89]. A method of reducing this error has been developed using a multiple image integration method [89]. Another is image quality, and this can be a limiting quality when using higher magnifications and varies with the SEM and sample being used.

For these reasons, the error should be considered and validated where possible in the DIC analysis when using SEMs for strain analysis.

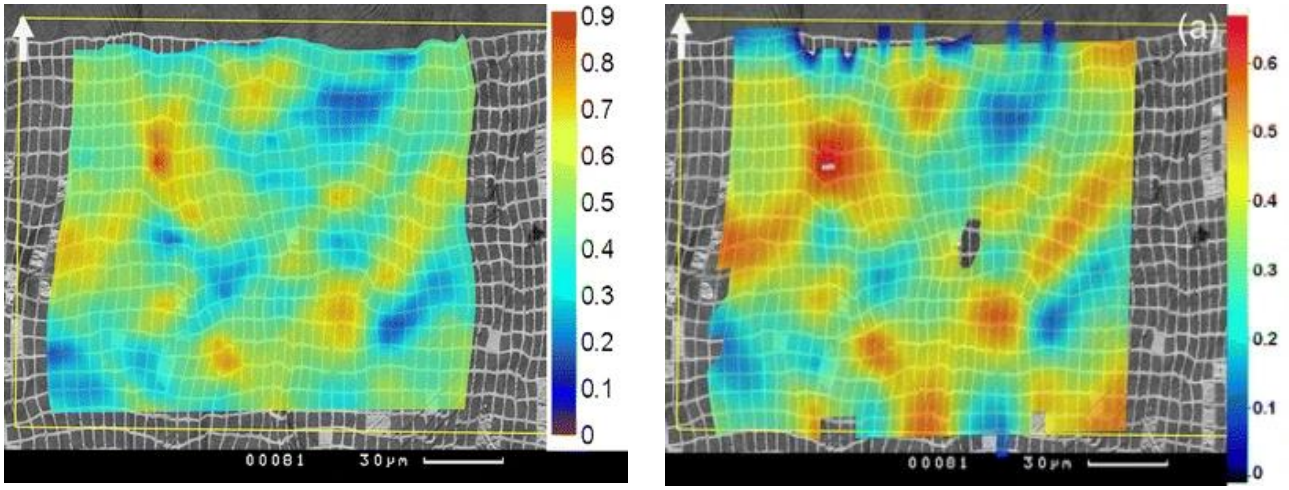


*Figure 3-13: True in-plane strain maps in the loading direction (shown by the white arrow), left: analysis of the deformed microgrids, right: DIC results* [88].

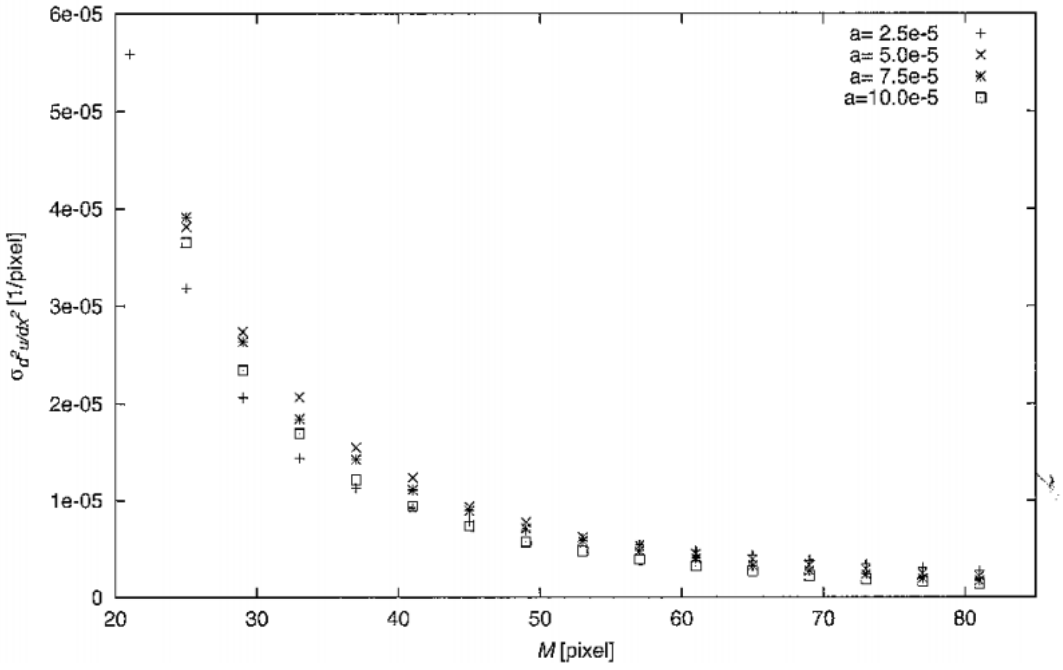


*Figure 3-14: Standard deviation plotted against subset size (M, in this graph) for a range of curvatures for second-order shape functions* [85].

## 3.4.2 Shear bands found with insitu SEM DIC testing

When studying the strain using an interrupted tensile test using the lop left specimen in Figure 3-11 with SEM imaging as shown in Figure 3-15. This is with an AHSS called dual-phase, DP names as it has

2 phases, ferrite and martensite. During the trial performed by Ghadbeigi et al., the strain localises as shear bands at around 45° to the direction of the applied strain. Shear bands are observed to propagate at 22% elongation, DIC is used to find strains of around 20% at the initiation of shear bands in the ferrite. These intensify as the elongation increases [73]. While Alharbi et al. found that damage is observed to occur in the martensite, with it cracking as shown in Figure 3-16 [36]. The strain builds up at the martensite ferrite interface as the martensite resists the high strain found in the ferrite and eventually cracks the martensite as the stresses increase from the difference in strain. The strain is found to be

The DIC technique processed from micrographs from SEMs observing interrupted insitu tests offers a highly detailed analysis of the development of strain at a microstructural level of detail.

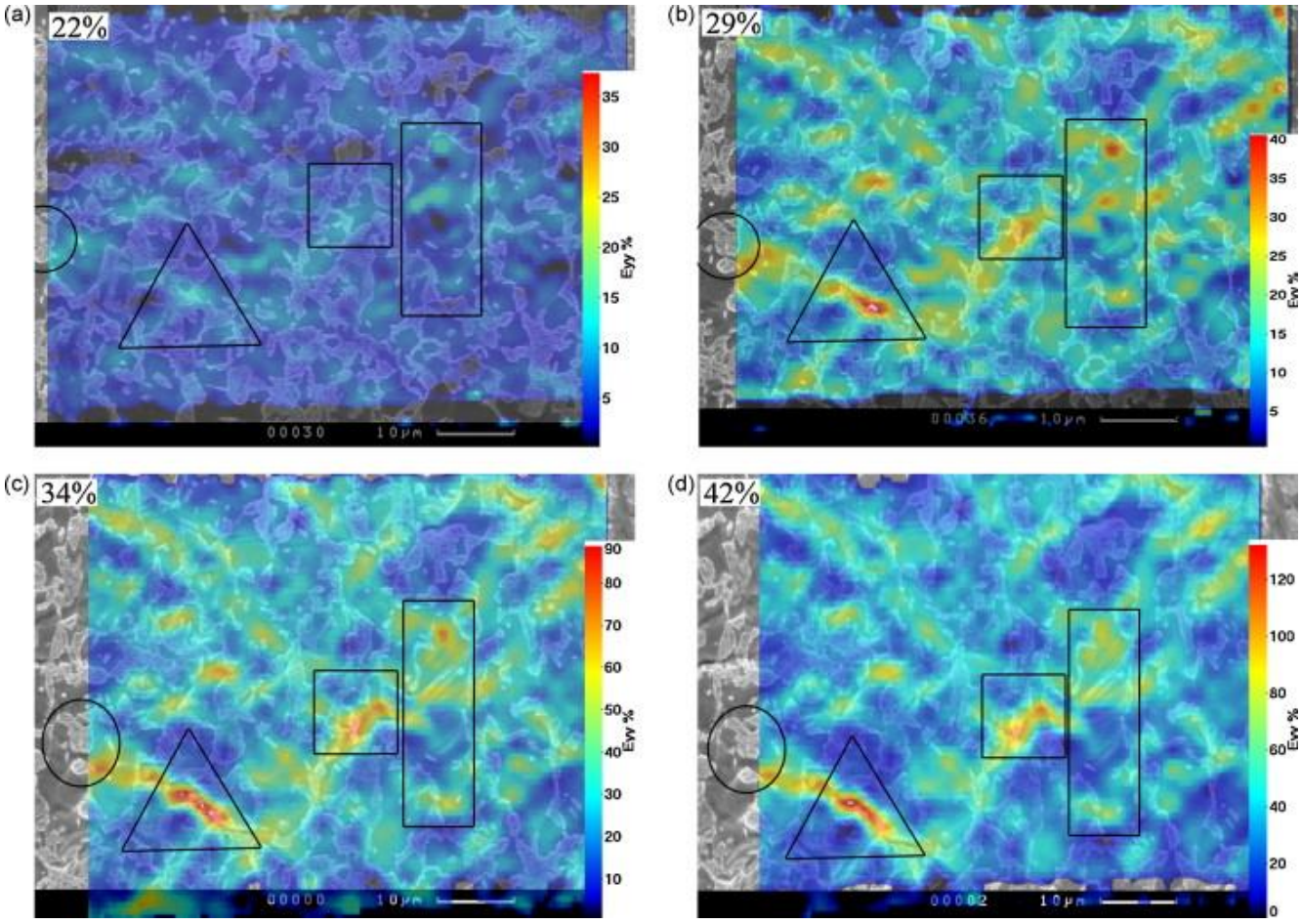


*Figure 3-15: DP1000 steel in the tensile testing area observed with an SEM and post-processed with DIC. a, 18% strain applied, b, the same region with 29% strain applied c, 34% strain applied, d, 42% strain applied (the tensile direction is vertical on these pictures).* [73]

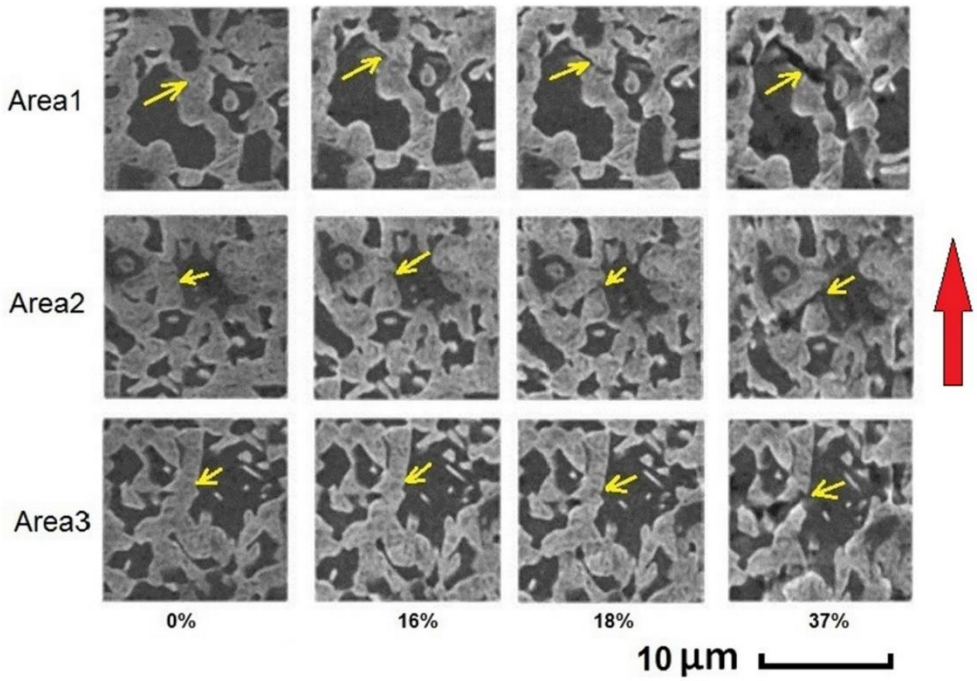


*Figure 3-16: Micrographs of DP1000 steel with yellow arrows highlighting the localisation fracture in the martensite with the applied strain in (%) applied to the specimen, the red arrow indicates the force direction* [36].

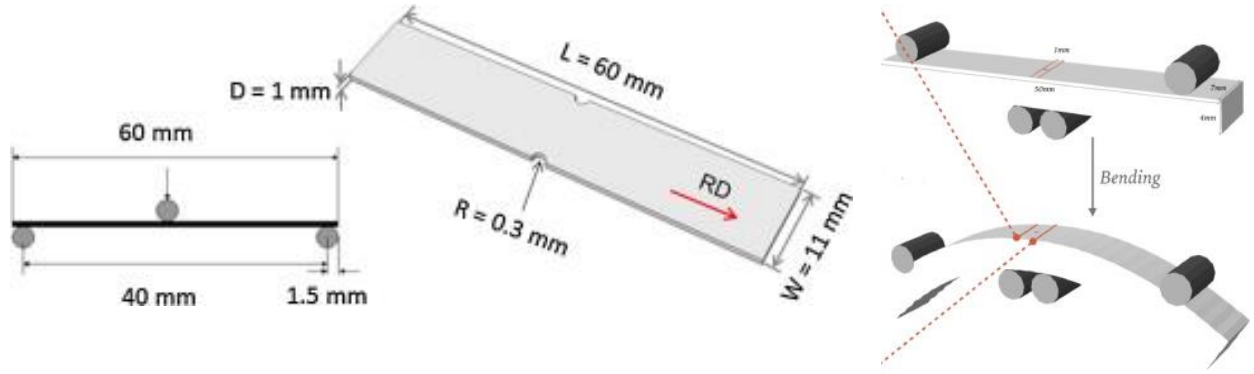


*Figure 3-17: Insitu bend test geometries used in SEMs, left; 3 point bend testing geometry with notches with DP steel* [83]*, right; 4 point bending geometry with aluminium in cyclic loading* [90].

Insitu bend test modules have also been developed for bend testing. This has been of use in flexural and cyclic loading tests. DP steel was bend tested to observe damage initiation in bending, it is found the failure of martensite is due to cracking from the high stresses from the local plasticity of ferrite [83].

In the 4-point insitu bend test, the specimen has a hole in the centre which promotes a stress concentration at the edges of the hole. This is used as a means of validating a crystal plasticity model when used in conjunction with EBSD. DIC is also applied using images obtained from the maximum amplitude of the cyclic loading cycle [90].

## 3.5 SEM in situ test module

To observe plasticity and damage occurring at a microstructural level of detail specialised modules have been developed to be compatible with SEM vacuum chambers and have a means of transferring the control of the module and extracting the force-displacement data.

### 3.5.1 Deben test module

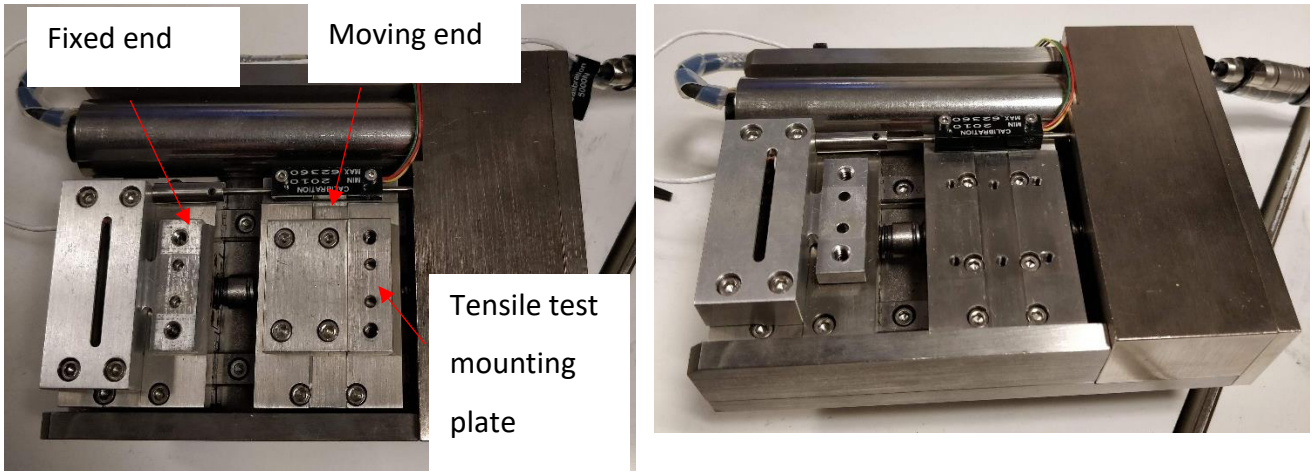


*Figure 3-18: The Deben tensile and horizontal bend test module with no tooling.*

The same module is used for bending and tensile tests with the module having a 5KN maximum load. The module outputs a force and displacement feed and is controlled remotely by the Microtest software on the image capture computer. The tests were run with the following procedure:

1. Load specimen, the specimen was positioned centrally in the bend tooling and orientated to position the specimens polished face to face towards the SEM with careful orientation to position the correct face in tension.
2. Set the test settings: data acquisition rate to 0.5 seconds and displacement rate.
3. Start the module and preload the specimen to 30N to hold the specimen in position so that the module can be loaded without the sample moving out of the tooling.
4. Open the Camscan S2 chamber door and insert the Deben module, fitting in place and tightening a grub screw.
5. Close the Camscan S2 chamber door and generate a vacuum.
6. When a sufficient vacuum is achieved the bend test proceeds.
7. Micrographs are obtained with no displacement in a particular region identified by the user. An on-screen marker is placed on the position of an easily identifiable microstructural feature.
8. A displacement step is performed while the identified microstructural feature is tracked during the movement.
9. Micrographs are obtained of the identified region after each displacement step.

10. Steps 8 and 9 are repeated until the test is complete.
11. The module is then removed from the chamber by repressurising it and opening the chamber door to access the Deben module, loosening the grub screw and removing the module.
12. The chamber door is closed and the vacuum is generated.
13. The sample is removed from the module by running the module in reverse. This unloads the specimen if it has not completely fractured and brings the module back to its home position.

#### *3.5.1.1 Tensile test*

The tensile test setup uses a Deben clamp system. This uses pins and a clamp arraignment to position the specimens. The same procedure is used as in bending with a preload of 30N used to hold the specimen in place. The displacement rate was set to 0.1mm per minute as the specimen was found to fail after only 1-1.5mm displacement.

#### *3.5.1.2 Bend test*

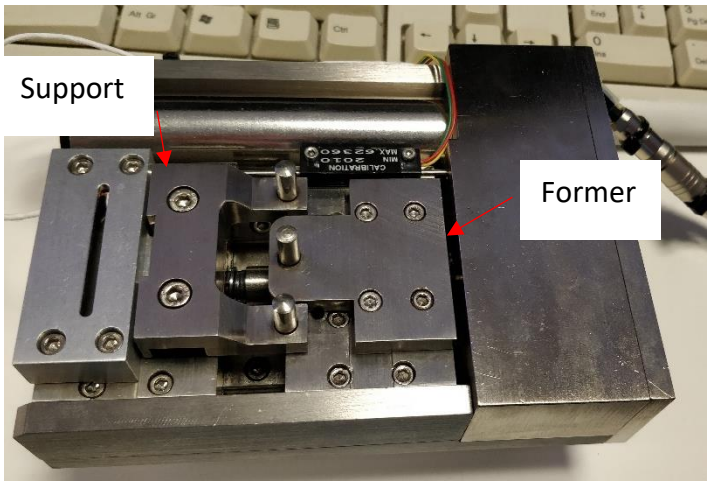


*Figure 3-19: The Deben tensile and horizontal bend test module with the original 5mm diameter bend test tooling.*

The bend test used a variety of tooling throughout the author's project. The methodology is as described above. The displacement rate is changed to 0.5mm per minute as the test displacement often exceeds 2mm to above 5mm in some tests.

#### *3.5.1.3 Changes to the methodology due to errors*

Some software and hardware errors were found to occur during the authors time operating the Camscan S2 SEM and Deben module which required some workarounds to be applied to remove or reduce the likelihood of these errors occurring.

##### 3.5.1.3.1 Rasterization compression

After completing the micro tensile tests, it was found that imaging errors were sometimes found in the SEM micrographs. As shown in Figure 3-20, strain in tension and compression of up to 10% can be found in some micrographs. This is likely due to errors in rasterising the micrograph but another

cause could be the relaxation of the specimen after displacement interruptions. This would cause the specimen to move relative to the SEM image acquisition which was recorded to take 2.5 minutes per image. Though this would not explain why then the compression regions were only in the YY direction in images and it also compressed the image information section in the cut-off.

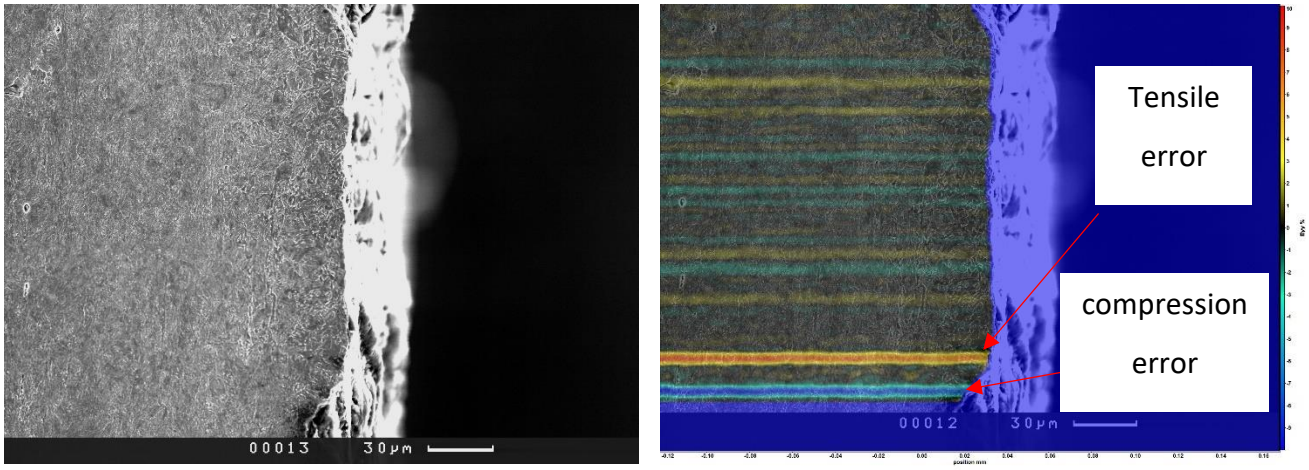


*Figure 3-20: YY compression effect in Camscan S2 SEM micrograph, left, no compression, right compression visible in the highlighted region.*

To reduce the likelihood of this occurring 2 micrographs were always taken rather than 1 at every displacement step. The author also learned to look for signs of compressed regions and text in the YY direction while operating the Camscan SEM. Thus, the likelihood of having 2 errors in subsequent images is reduced. This extended the experiment length but was viable due to the costs of sample production, preparation and SEM booking.

#### 3.5.1.3.2 Saving data error

Due to the extended testing duration to obtain many micrographs. Before lockdown tests were run for up to 10 hours which resulted in saving data becoming a problem. This occurred when the image acquisition computer was running for longer than 5-8 hours it would stop saving data. This was found at the end of a bend test and hence the final images were not saved, and no warning was provided to the author. Hence this led to a significant loss in data until the missing image numbers were noticed. To stop this occurring the test practice was changed with an enforced shutdown of the computer at lunchtime 4-5 hours after start-up of the computer. The Deben module data is saved as part 1 and part 2, these are combined post-test by using the position value in the Deben module data .mtr files when exported into Microsoft Excel.

#### 3.5.1.3.3 Data overflow error

Due to a test failure, the methodology was changed for the final bend tests with the polished surfaces. During the displacement interruption to obtain the micrograph a “data overflow” error

message appeared in the Microtest software. This caused the data for that test period to be lost and the whole test to be repeated which was deemed as unacceptable.

To avoid this occurring again the test setting was changed from “continuing to record data after stop” to “stop recording data after stop”. That way data acquisition is limited to only when displacements are performed and reduces the likelihood of a data overflow occurring.

## 3.6 Experimental

### 3.6.1 Material

During the project work, two materials were used in testing been used. These were both S960 graded UHSS hot-rolled strip steel provided by Tata Steel. Both have been annealed after the hot rolling process but only the 17DF4/1 is levelled after decoiling. The S960 grading indicates that the steel should yield more than 960 MPa. The steel is provided in 6mm and 3mm thicknesses with different production methods.

| Material code | Material grade | Thickness (mm) | Production process |
|---|---|---|---|
| 14TG26 | S960 | 6 | Bundle annealed, No levelling |
| 17DF4/1 | S960 | 3 | Bundle annealed, levelled |

*Table 3-2: Material provided by Tata Steel Europe.*

The tests were initially performed with the 14TG26 sample as this was obtained before the 17DF4/1. The 17DF4/1 sample was prioritised as this was their latest UHSS product. Work with 14TG26 was aborted with the transfer to using smaller diameter bend test tooling to make better use of the thinner 17DF4/1 material.

The materials are known to be martensitic with some bainite expected to be found at the top surface. The strain-hardening coefficient, n and strain rate hardening coefficient m, were both expected to be small, with the n value to be found and m expected to be 0.01.

### 3.6.2 Hardness indentation

#### *3.6.2.1 Microhardness indentation*

Microhardness indentation is a semi destructive means of analysing material hardness across multiple grains that can be qualitatively associated with other material properties such as tensile strength. Using a Struers DuraScan 70 Vickers diamond-tipped indenter a force is transmitted through a mounted specimen. This specimen was prepared in the same manner as described in Sample mounting and Standard sample grinding and polishing. No etching was performed on the specimen as dictated by the ASTM standard [98]. This provided a flat size of the resulting indent can then be calculated using an optical microscope. Indentations were arranged in an array pattern to

correspond with a difference in depths graduating in units of 150µm with 10 indentations per depth to provide averaging and removing erroneous results. The indentations were spaced at 150µm from one another to avoid the plastic deformation from indentations impacting each other. They are spaced at ≥2.5 Vickers diagonal width as shown in Figure 3-22.

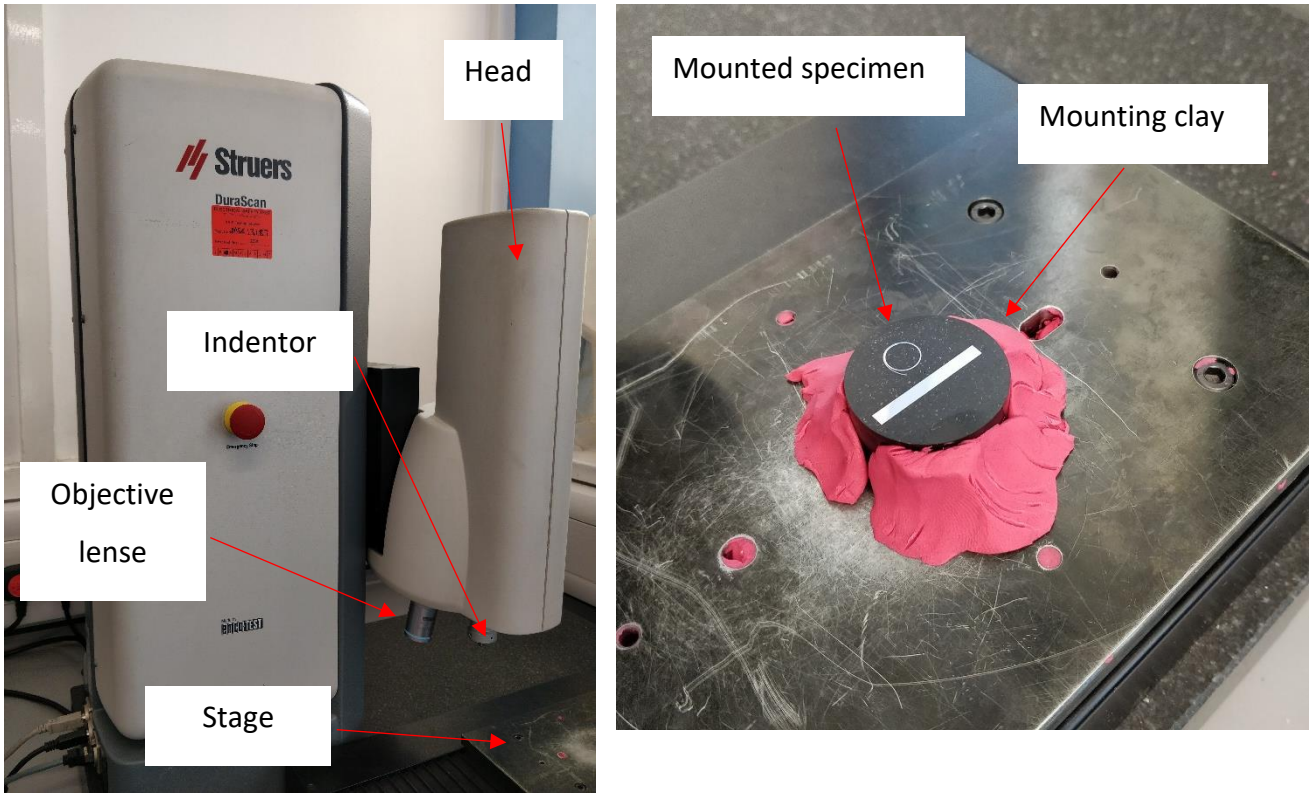


*Figure 3-21: Left: Struers DuraScan 70 micro indenter, right: the mounted bend test specimen positioned on the stage with mounting clay.*

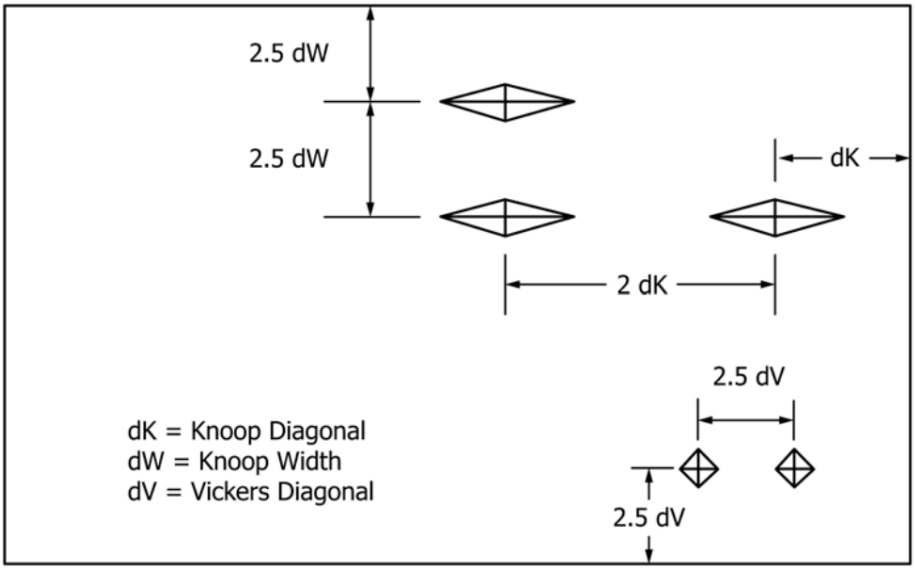


*Figure 3-22: ASTM diagram of Knoop and Vickers indentation spacing relative to each other and the specimen edge* [98].

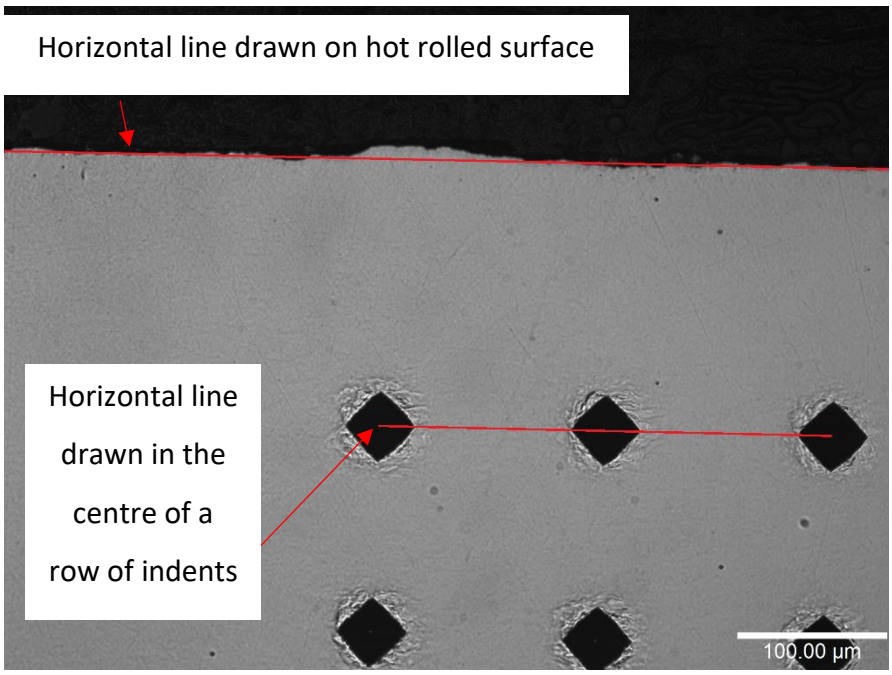


*Figure 3-23: Optical microscope image of the micro indentation array from microhardness testing with lines added for calculating the depth from the surface.*

Indentations were obtained with a weight of 0.5 Kg or 4.9N, which is the maximum load of the DuraScan 70 to maximise the size of the indentations to reduce error. These were then observed with a 40x objective lens and software used to calculate the hardness value using the following formula [99]:

$$HV = \frac{0.102\left(2F\left(\sin\frac{136°}{2}\right)\right)}{d^2}$$ *Equation 18*

Where $d$ is the mean of the diagonals of the indentation. This is automatically identified by the camera and adjusted if erroneous. The indentation is applied and held for X seconds then removed. Using Equation 18 the area of the indent is calculated this is known as the area of the residual impression, $A_r$.

### 3.6.3 Nano hardness indentation

Another means of performing hardness indentation but at a microscopic level of detail is to use a nanoindentation method. Here a Berkovitch 3 face pyramid indenter of face angle 142.3° was used. The Berkovitch indenter is loaded into the sample, held, then unloaded. The force and displacement are recorded and from these, the effective Young's modulus and hardness can be derived with the deformation assumed to be elastic.

For a perfect Berkovich, C value is 24.5, so the area of indentation is [99]:

$$A_c = 24.5{h_{max}}^2$$ *Equation 19*

Due to imperfections in the Berkovich profile, the value is calibrated varying the C value by using a calibration sample.

This is done by fitting the unloading curve to the power-law relation [100]:

$$F = C\left(h - h_f\right)^{m_i} \quad \textit{Equation 20}$$

In this, $F$ is the indenter load while $C$ and $m_i$ are fitting parameters, $h$ is the depth and $h_f$ is the residual depth. Residual depth is the depth at which the loading is zero. Using this the unloading stiffness, $S_h$ is calculated:

$$S_h = m_i C\left(h_{max} - h_f\right)^{m_i - 1} \quad \textit{Equation 21}$$

Where the $h_{max}$ is the maximum depth of the indenter. The contact depth, $h_c$ is then derived:

$$h_c = h_{max} - \frac{\varepsilon_h F_{max}}{S} \quad \textit{Equation 22}$$

With the value calculated for the stiffness and an experimentally derived value for $\varepsilon_h$, which varies with geometry used and is 0.75 with a Berkovich indentor [101]. With the contact depth defined this can be calculated. The area of contact, $A_c$ can be derived with Equation 19. Thus, the nanoindentation hardness, $H_n$ can be defined as:

$$H_n = \frac{F_{max}}{A_c} \quad \textit{Equation 23}$$

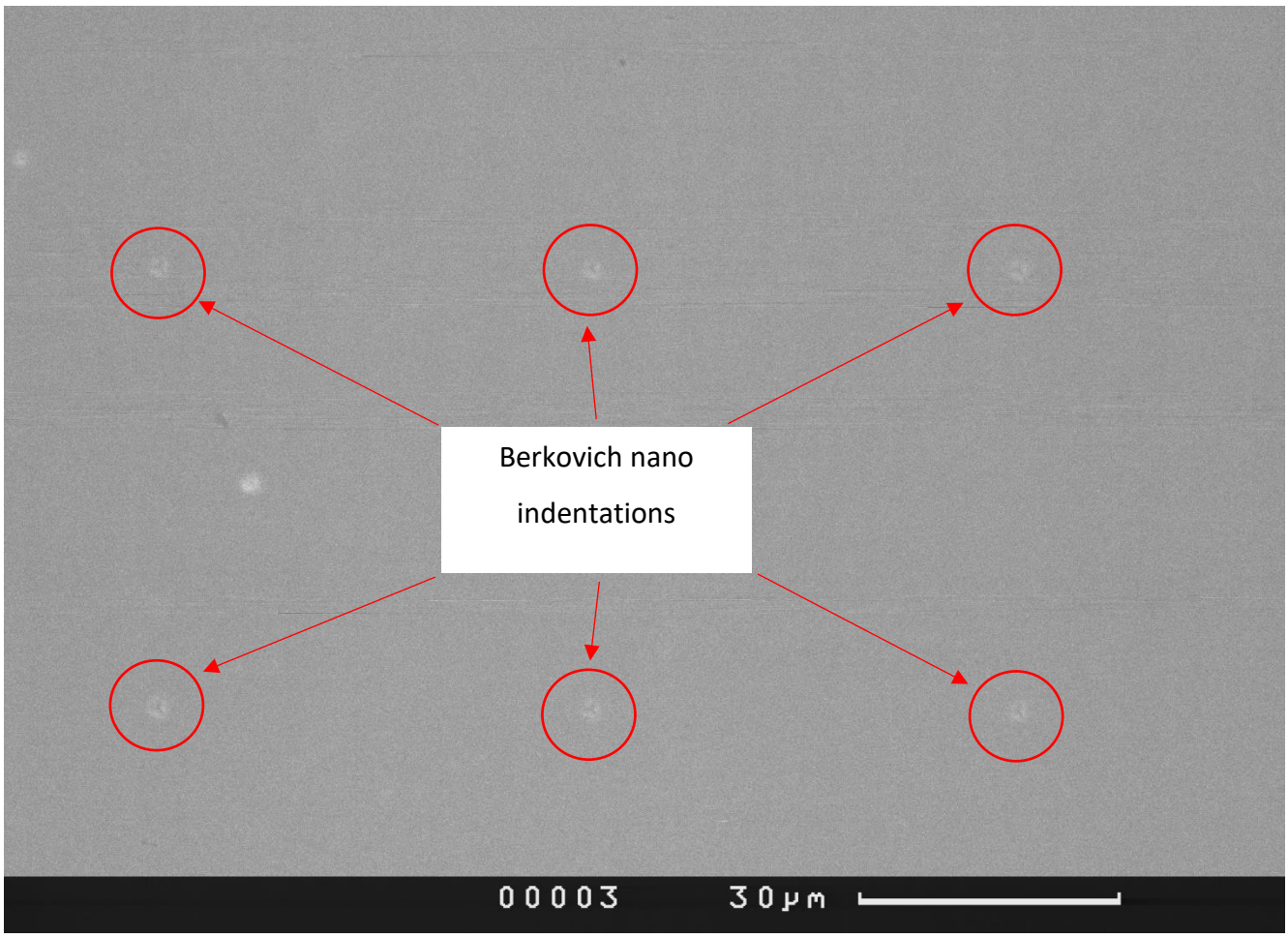


*Figure 3-24: Camscan S2 SEM 800x magnification micrograph of Berkovitch nanoindentations in S960 steel.*

Using a Hysteron TI Premier a load of 13000µN was applied to the specimen. To load the specimen, they are placed on magnetic sample holders and placed on a magnetic plate. The indenter is then calibrated by performing a set of indentations on a calibration sample. This is then used to indent the sample in an array pattern as defined by the user.

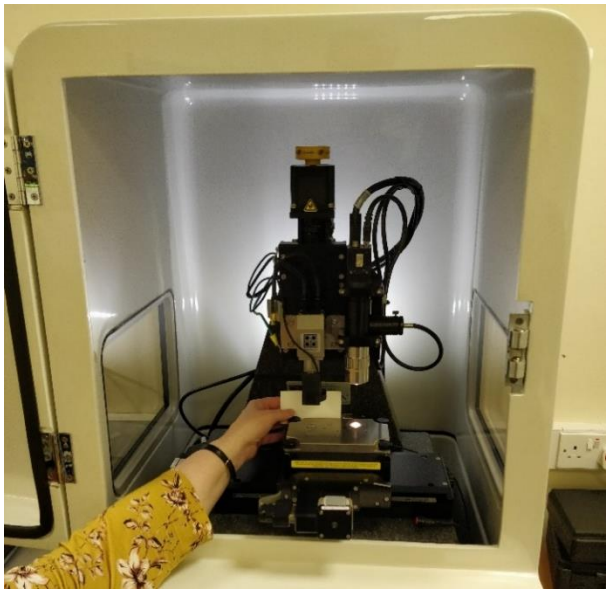

*Figure 3-25: Hysteron TI Premier nano indenter*

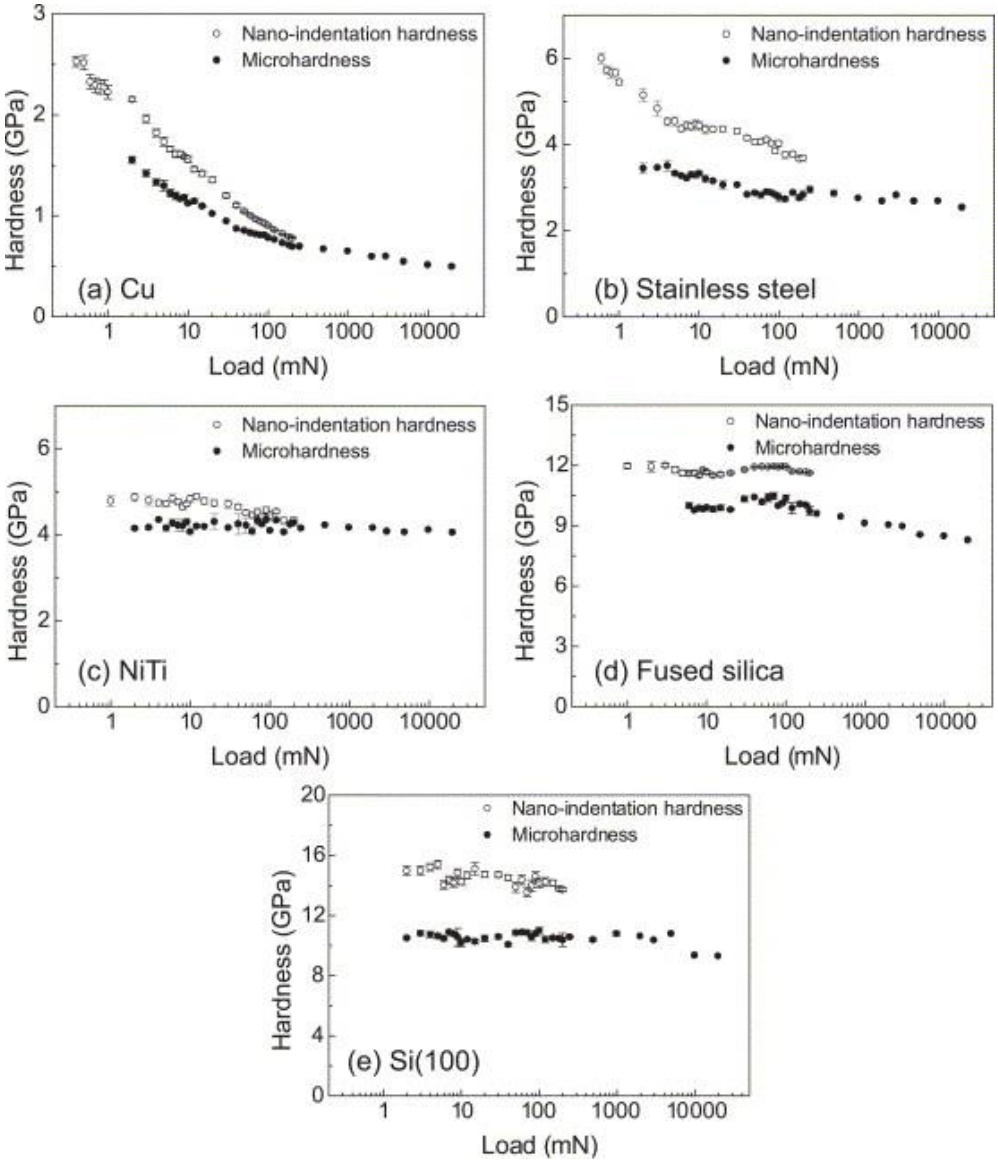


*Figure 3-26: Comparison between Nano and micro indentation hardness results for Copper (Cu), Stainless steel, Nickle Titanium (NiTi), Fused silica and silicon.* [102]

While micro and nanoindentation hardness investigate the hardness of materials it is important to consider that some materials show a size effect with increasing loads reducing their hardness measurements such as in copper and stainless steel. Whereas in all the materials there is a significant variance between the nano and micro-indentation with the former always being harder than the latter. It is found a variance of 10-30% greater hardness for nano-indentation hardness than microhardness [102]. This variance is due to the use of projected contact area $A_c$ and residual contact area $A_r$. where the projected area is always smaller than the residual area. As there is an assumption of elastic deformation in the calculation of projected contact area $A_c$.

So in summary the micro and nano hardness values are not directly comparable and the nano-indentation hardness values should be treated as a qualitative set of results while the microhardness test results can be treated as quantitative.

### 3.6.4 SEM imaging

For high magnification imaging scanning electron microscopes are used to study prepared specimens. Scanning electron microscopes can be used to observe samples typically with a Secondary Electron (SE) detector as this provided this highest detail and contrast for DIC analysis. These are first prepared for observation with samples preparation performed on them as defined in Sample preparation and Sample storage

#### *3.6.4.1 Camscan S2 SEM*

The Camscan SEM was used extensively in this project as it is compatible with the Deben modules for tensile testing, horizontal bending and a vertical bend test module. The Camscan S2 SEM is a tungsten filament SEM with image quality comparable to the tabletop SEM. The SEM has a large chamber with a mounting compatible with the Deben modules and is used as the means of observing interrupted tensile and bending tests, typically using magnifications of 2000x or less.

This SEM has secondary electron (SE) and backscatter electron detectors (BSE) operating. The operation of the SEM is demanding on the user as the controls are analogue with some digital aids not being available. The Camscan S2 does not feature autofocus or brightness and contrast functions as found on most modern SEMs. Thus, the image quality is more dependent on user knowledge and skill.

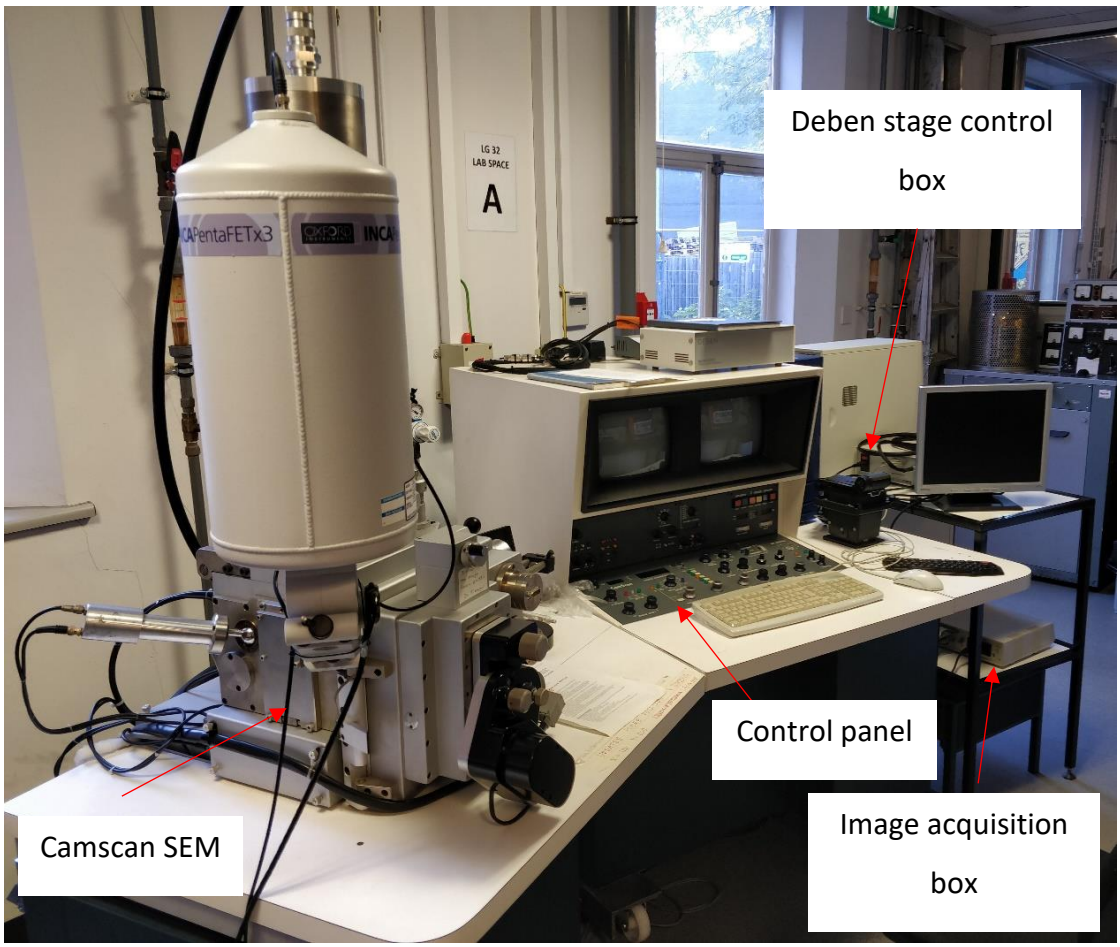


*Figure 3-27: Camscan S2 SEM, view of the SEM, the control panel, SEM displays, computer monitor, imaging box and Deben control box.*

### *3.6.4.2 Hitachi TM3030 Plus SEM*

The Hitachi TM3030 Plus SEM is used for the analysis of small samples and has a low image quality for SEMs like that achieved on the Camscan S2. It has both SE and BSE detectors but also features digital controls with autofocus, auto-brightness and contrast capabilities lowering the user skill level required. The SEM is of a much smaller size and as such has a smaller chamber so samples must be appropriately sized often being cut to size as described in Sample cutting. This SEM is ideal for simple imaging requirements at up to 2000x when using small sample sizes.

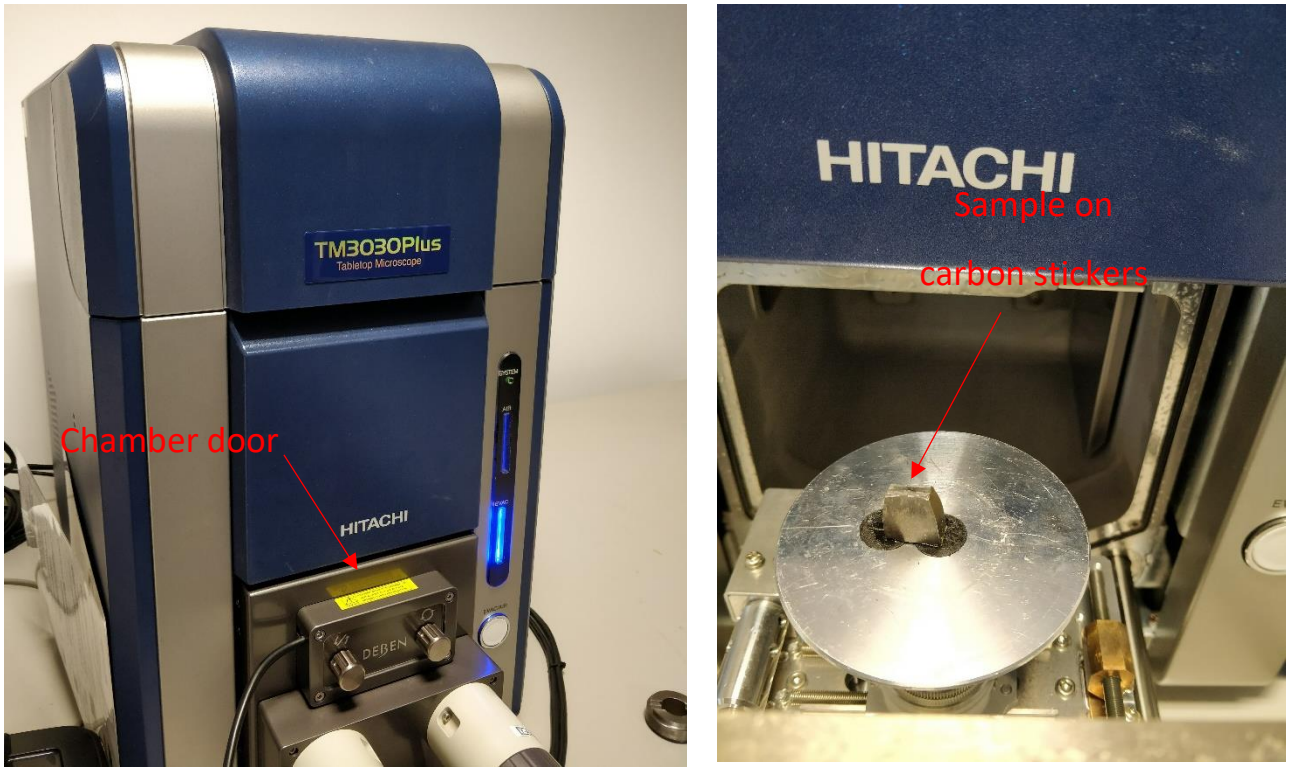


*Figure 3-28: Hitachi TM3030 Plus SEM with on the left the SEM and on the right the chamber open with a sample being inserted.*

### *3.6.4.3 FEI Sirion SEM*

For Electron backscatter Diffraction (EBSD) analysis the FEI Sirion was used. This SEM has the sensors required for performing EBSD to study the texture of the steel. This was used in the project for EBSD analysis only.

### *3.6.4.4 FEI Inspect F50*

This is used for high magnification SEM imaging and has sensors for SE, BSE EBSD and Energy-dispersive X-ray spectroscopy (EDS). EDS can be used to identify materials at a microscopic level of detail by detecting the energy of the X-Rays. The FEI Inspect F50 could obtain high-quality micrographs at magnifications of up to 80,000x. The SEM also had modern digital controls and autofocus and contrast functions.

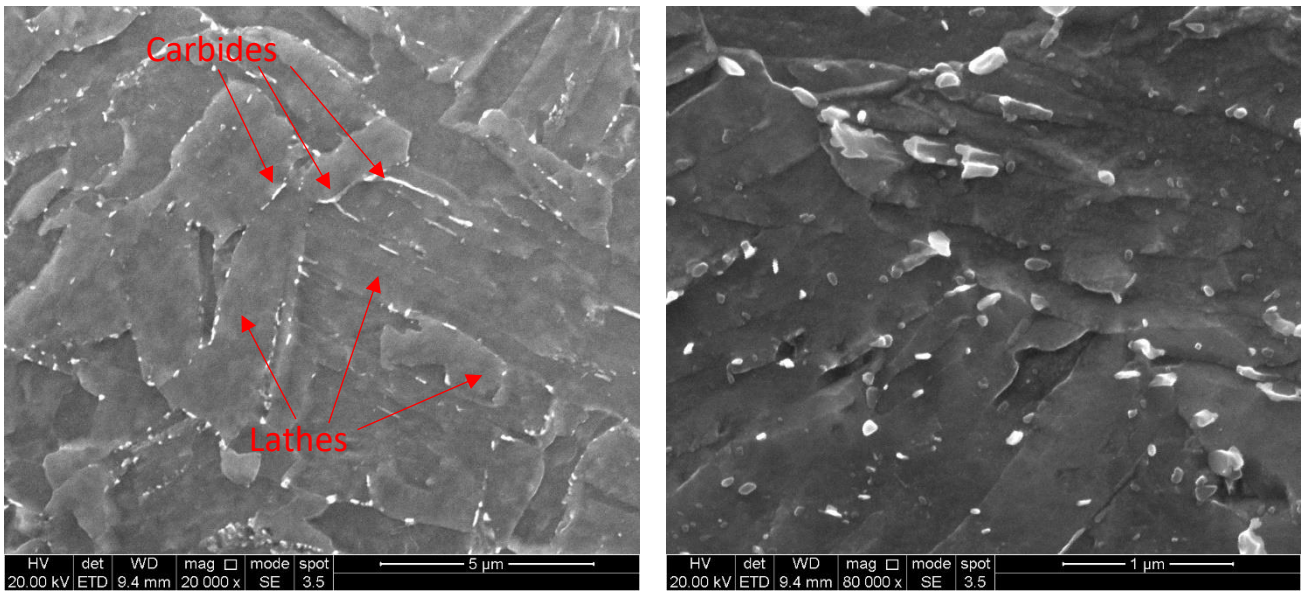


*Figure 3-29: SEM micrographs from the FEI inspect F50 of the 14TG26 sample at on the left, 20,000x micrograph and right, 80,000x micrograph.*

### 3.6.5 EBSD

EBSD analysis was performed with the FEI Sirion SEM as this contained the sensors required for capturing the Kikuchi patterns. The samples were prepared the same day as the experiment as described in section 3.3.1.5 and transported in a vial full of isopropanol to restrict any corrosion. EBSD was attempted on the 14TG26 sample and it was found impossible at the UOS to prepare to a high-quality finish and obtain 80% or higher data pattern acquisition rate considered high enough to have good quality EBSD analysis. Some advice was taken from Warwick University but their facilities were not available at the UOS and newer EBSD produced higher quality scanning.

The UHSS samples were difficult to study due to the deformation-induced martensitic transformation causing the lower quality EBSD. This is because the BCC expected is deformed and other methods of identifying this using image quality methods were not possible at the University of Sheffield.

## 3.7 Tensile testing

To obtain material properties tensile tests were performed to obtain data for modelling the bendability of UHSS.

### 3.7.1 Macroscale

Tata Steel supplied strip steel in various forms and thicknesses. These required differing geometries and testing methods. The tensile test samples were designed to meet the ASTM E8 standards [84] as shown in Figure 3-30 and Figure 3-31. The tensile tests performed on the 14TG26 specimens were 6mm thick as shown in Figure 3-30. To perform this tensile test a load of greater than 25KN was

required so the Mayes 4 100KN tensile tester was used. Due to the lack of training with 3D DIC at the time of testing 2D DIC was used with a LaVision system as described in section 3.7.1.1.1

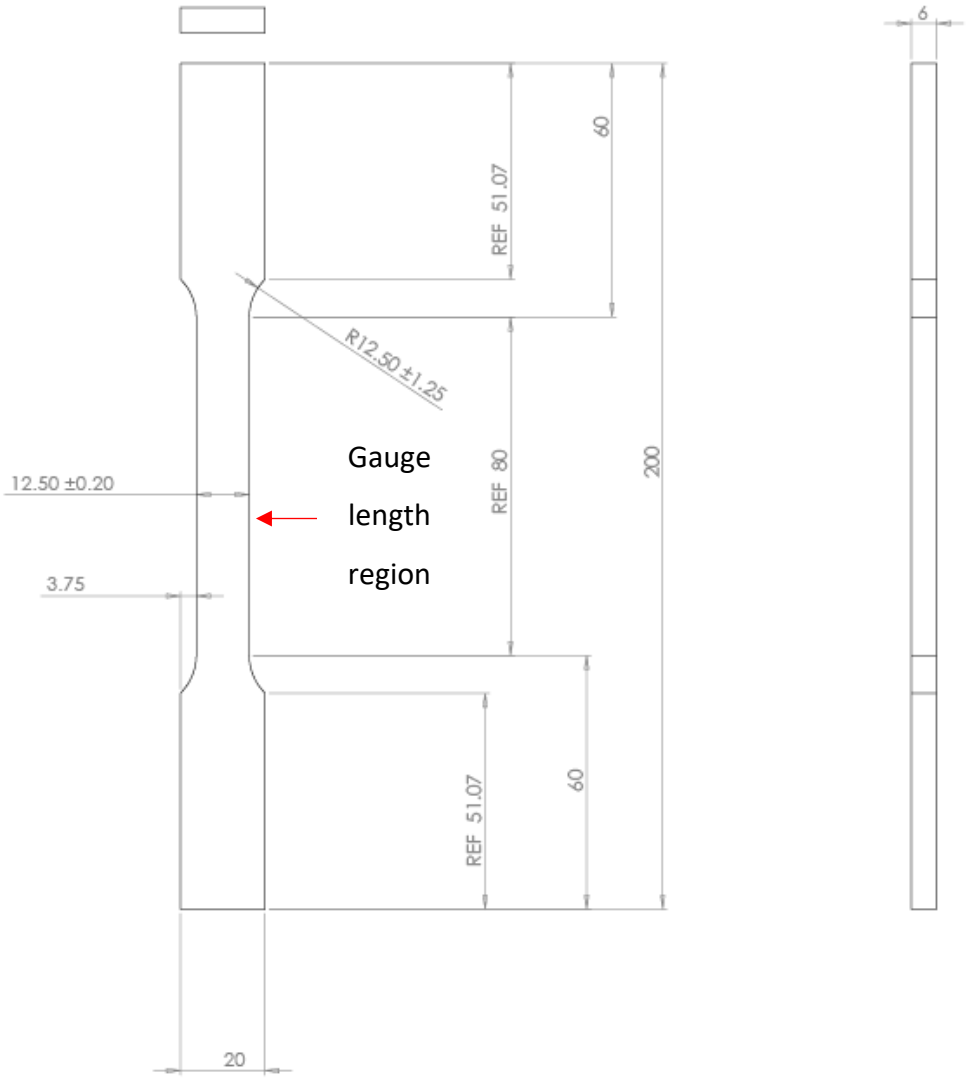


*Figure 3-30: Tensile test design for plate 14TG26, 6mm thickness S960 UHSS, 12.5mm wide, gauge length as specified by the ASTM* [84]

Tensile tests for the 17DF4/1 material as in Figure 3-31 were performed at a macroscale using Tinius Olsen 25KN tensile tester. This was used in conjunction with a 3D DIC system to measure strain distributions as described in 3.7.1.1.2. This allowed the strain field to be analysed post-test with DIC and then virtual strain gauges to be positioned at the gauge length to study elongation.

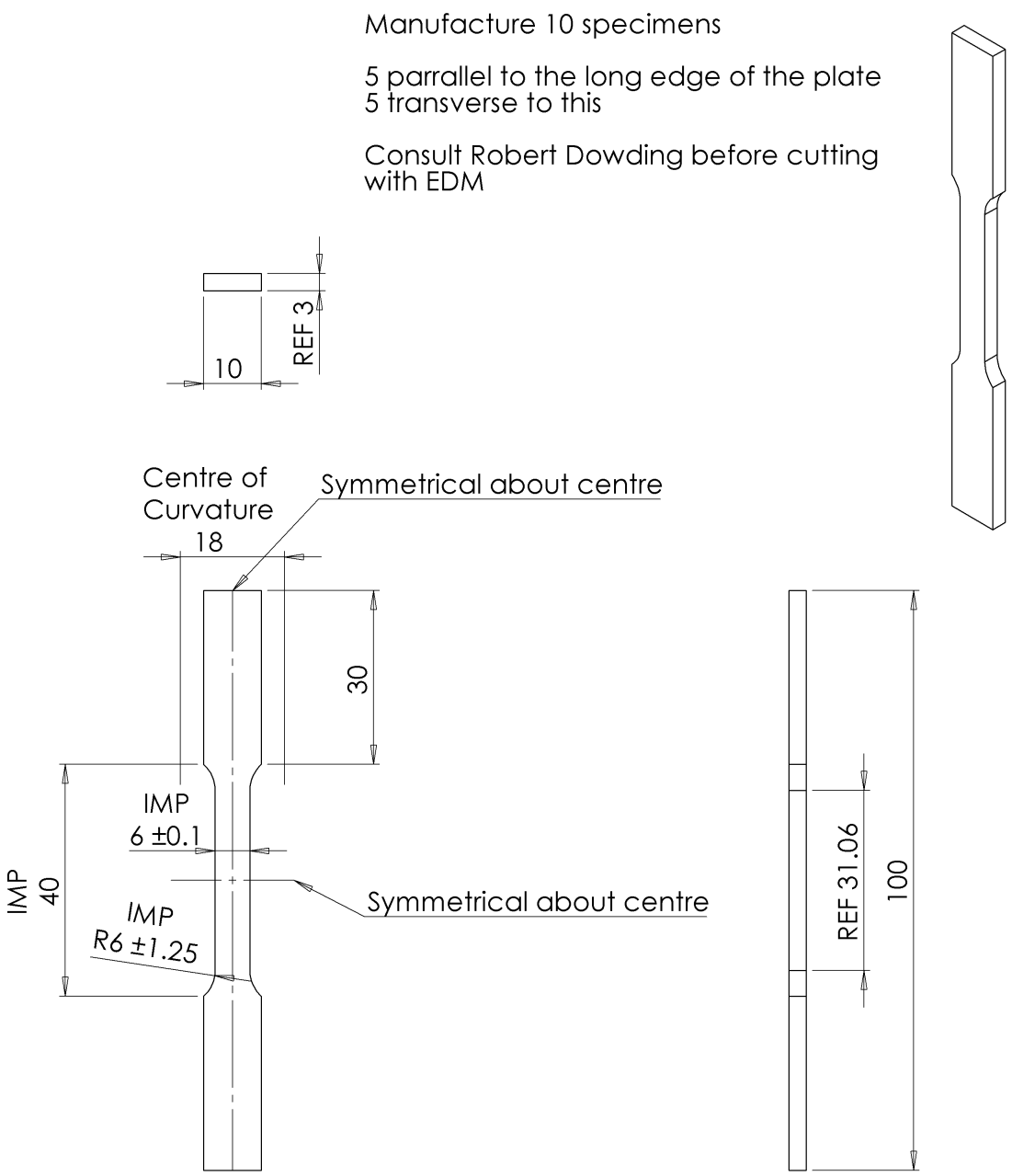


*Figure 3-31: Tensile test design for plate 17DF41, 3mm thickness S960 UHSS, 6mm wide, gauge length as specified by the ASTM* [84]

To find the strain at fracture the fractured specimens were measured with a digital micrometre at both the edges and the centre of the specimens as described by S. Adamczak and uses Equation 24 [21].

$$A_s = \frac{(w_s + w_s')(t_s + t_s')}{4} \qquad \textit{Equation 24}$$

The fracture area, $A_s$ is calculated with the dimensions as shown in Figure 3-32, where the edge width and edge thickness are $w_s$ and $t_s$ respectively. The central necked measurements of the width and thickness are $w_s'$ and $t_s'$ respectively.

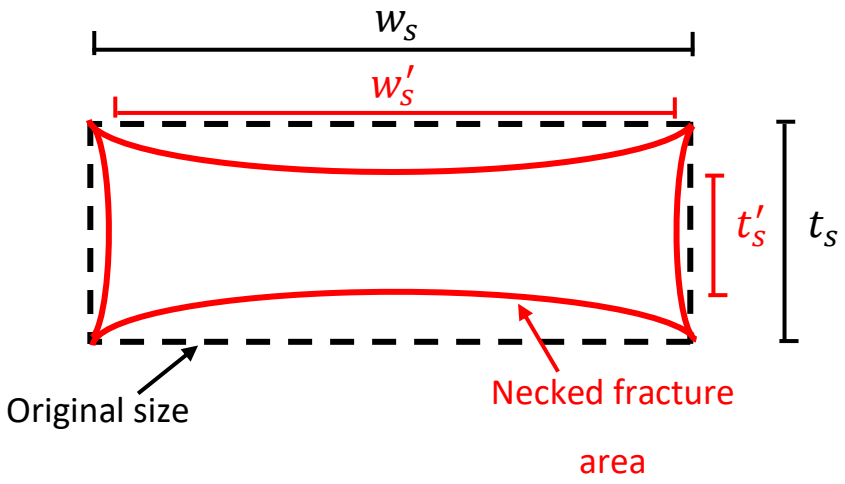


*Figure 3-32: diagram for the measurement of a fractured tensile test specimen.*

This data was measured 3 times for each dimension with each test and the result from TD4 was excluded due to it having the highest fracture load and largest area from the tests.

To generate the strain-hardening value the method as described by B. Yngve [103] where the log stress log strain graph is produced to find the gradient to calculate the strain-hardening coefficient, n. In this instance, the strain-hardening coefficient from plasticity and the fracture was found.

### *3.7.1.1 Testing Apparatus*

The testing is performed with 2 electromechanical tensile testers due to the different load requirements and advantages of better force sensitivity at low loads with the Tinius Olsen 25KN

#### 3.7.1.1.1 Mayes 4 tensile tester

The Mayes 4 tensile tester is an electromechanical tensile tester. This was modified to output force and displacement output voltage as requested by the author. This was recorded with the ADC converter and recorded for the LaVision DaVis software.

The highest load capable tensile tester was used for 12.5mm width specimens with loads exceeding 25KN up to 100KN. The specimens are wire spark eroded (EDM) profiled and inserted into the wedge grips. The wedge grips on the Mayes 4 were problematic as they often loosened after use and the author may have overtightened the chuck tool by using a metal tube to tighten the wedge grips further onto the specimen after repeated specimen drops with risk of damaging the speckle pattern applied to the surface.

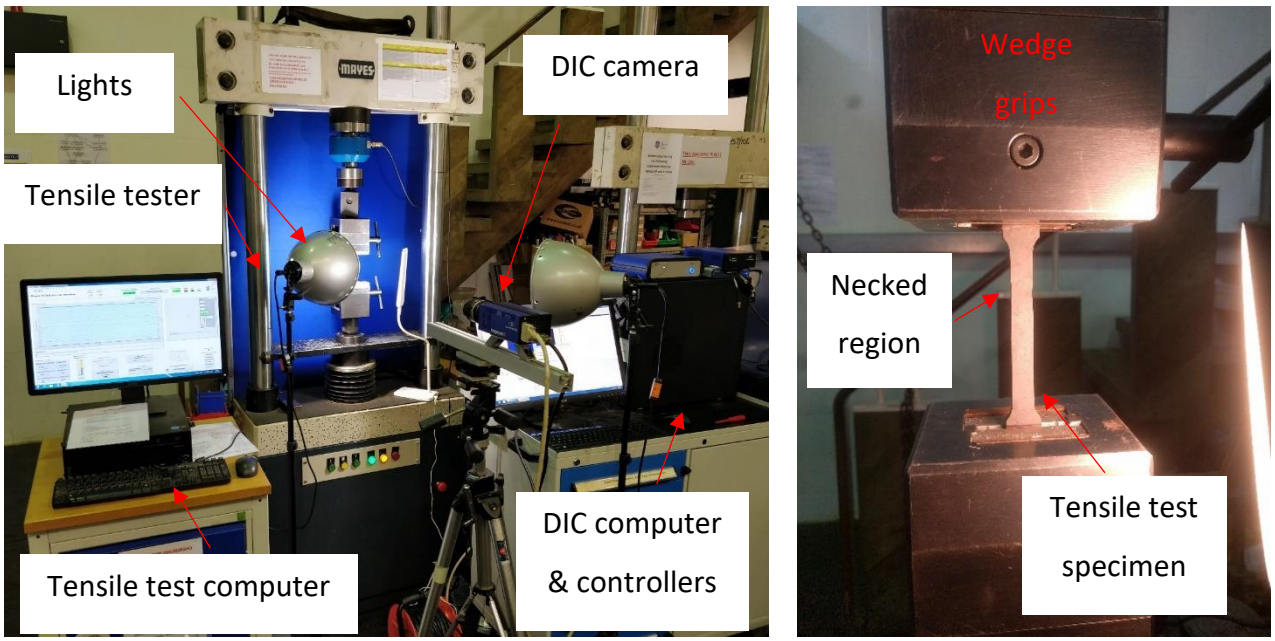


*Figure 3-33: Tensile test was performed with the Mayes 4 tensile tester with the LaVision Imager Pro X 2D DIC system with ADC data log. Left, the equipment was set up for a tensile test, right, the wedge grips holding a specimen with no speckle pattern as a trial, underload with necking occurring.*

#### 3.7.1.1.2 Tinius Olsen 25KN

The Tinius Olsen 25KN H25I S electromechanical tensile tester was used for smaller 6mm width by 3mm thick specimens. It also had the necessary tooling to perform bend testing with 10mm dia tooling as shown in the right image in Figure 3-34. The Tinius Olsen 25KN tensile tester features voltage output for the force and displacement outputs. This was recorded with an ADC and transferred to the DIC recording computer running VIC snap.

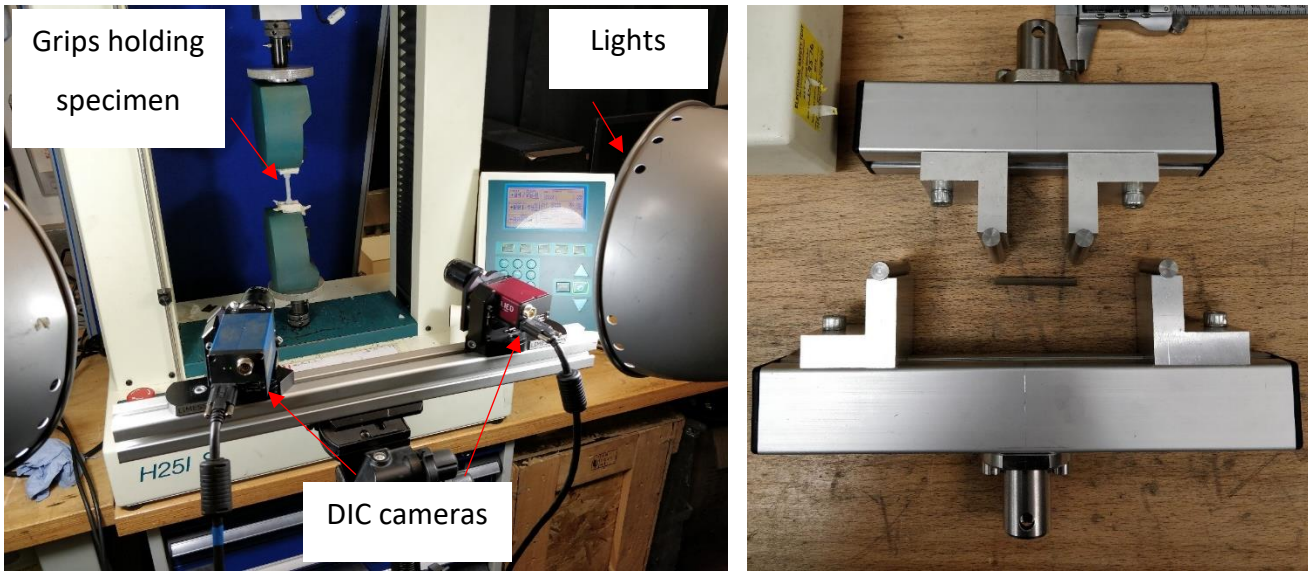


*Figure 3-34: The Tinius Olsen tensile tester, left, 3D DIC tensile test setup with a specimen loaded into the wedge grips, right, 3 or 4 point bend test tooling compatible with the Tinius Olsen 25KN tensile tester.*

#### *3.7.1.2 DIC*

The use of DIC is to study the motion or deformation of specimens. This is typically done with images produced with cameras and has found many applications in industry and academia. This approach processes the displacement of random identifiable patterns and discretises the first image into subsets, each subset is studied as a variation in contrast and the same pattern is then found in the next image in the set. This process is repeated, and the displacement and strain of the subsets were calculated. Depending on the algorithm used the subsets being found can be from the first image ideally before deformation, a summation of the images if the first image cannot be correlated with the later images or a process of comparing the previous image to the next. Each algorithm has more inherent error than the last.

The ideal speckled pattern should have speckles that are 3-5 pixels of identical size [86]. In most applications, the use of speckles can be adjusted by simply repainting the specimen. This wasn't practical on SEM samples due to the sunk costs of sample preparation and SEM bookings. So high sample preparation quality is critical to microscopic DIC to provide the best quality microstructural patterns to observe for later post-processing with DIC.

When using 2D DIC such as with the SEM the micrographs should be on a flat plane and placed parallel to the specimen. If a specimen is misaligned this will add error to the results. The brightness and contrast should be adjusted to maximise the contrast of the speckles without under or oversaturating regions. This can be checked when recording images within VIC snap and DaVis, whereas when using the SEM this is not possible as the SEM can only show a line contrast plot at the central region.

The lighting should be as bright as possible. This enables shorter exposure times on the cameras and reduces error from the motion of the specimen. The lighting can cause problems with reflections on any shiny surfaces. This can lead to errors in calculating the results with DIC. To avoid this masking tape was used to mask off areas where reflections were being generated.

This DaVis software benefits from using a wide range of functions and capabilities that allow the accurate analysis of strain. The difference between macroscopic strain analysis and microscopic analysis is that due to the highly localised plasticity observed in the microstructures during deformation in micrographs the patterns observed in the first micrograph cannot be found in the deformed specimen micrographs. Therefore, a different algorithm is used where the sum of differences is used as shown in Figure 3-35. This causes a higher error due to the summation of error through the calculations but allows strain analysis of the highly localised strain as observed in micrographs [104].

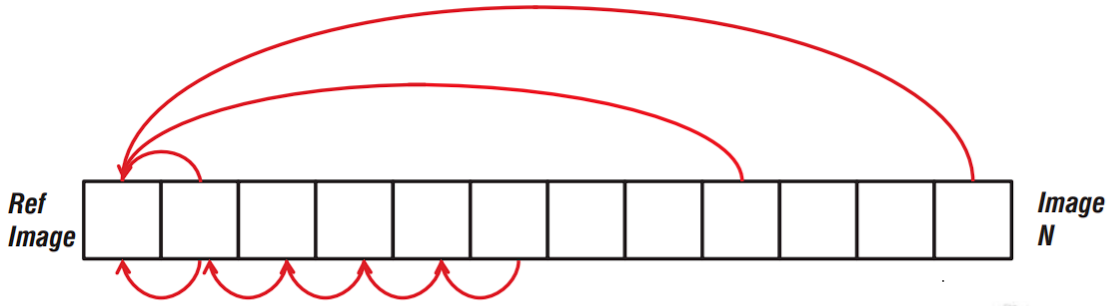


*Figure 3-35: diagram for the sum of differential displacement mode* [104].

#### 3.7.1.2.1 Error

To study the error with DIC several images will be obtained with the specimen stationary with the specimen preloaded. These are then processed with the same settings as used in the microscale DIC and the maximum variation in strain found.

The DIC approach is to use spray paint as the medium of indicating the strain, this is applied in the following steps:

1. A key for the paint to bind to the specimen is produced by grinding the specimen with P400 grinding paper.
2. The specimen is cleaned to remove dirt and debris from grinding, acetone was used in our application.
3. A coat of matt white paint is sprayed onto the specimens to produce a high contrast to the dark speckles. This is as thin as possible to keep the strain on the paint the same as the specimen. A matt paint is used to reduce reflections that cause errors in the DIC analysis. This is left to dry for 30 minutes.
4. A matt black spray paint is used to spray speckles on the specimen, black is used to provide the maximum contrast with the white. This is applied by careful application of consistent size of speckles to attempt to keep the pattern of a 3-5 pixel size when observed by the camera and randomly positioned. This is left for 30 minutes for the paint to set.
5. Once the paint has dried on the specimen, it must be used within 24 hours to stop the paint from losing ductility and cracking when the specimen is strained before failure. If the speckle pattern was not of a good standard or unused after a day, acetone is used to remove it with paper towels. Steps 3 and 4 are repeated to produce a useable specimen for DIC.

It was also found that to stop reflections from shiny or reflective surfaces masking tape was used to cover these to avoid them reflecting onto the specimen and causing localised brighter regions on the specimen. A blue pinboard was used as a background for the tensile and bending tests using the

Mayes 4 and Tinius Olsen 25KN tensile tester. This was to keep any movement in the background and any reflections from reflective surfaces out of the view of the DIC camera/s.

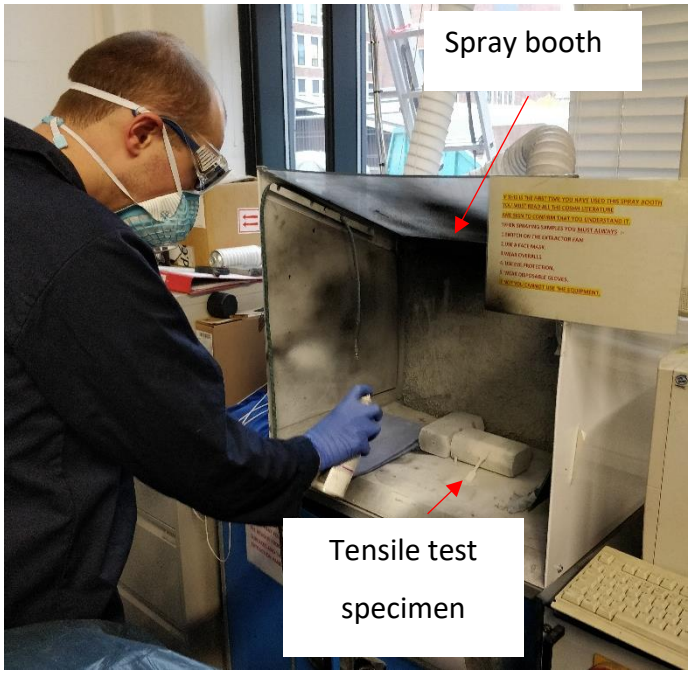


*Figure 3-36: Robert Dowding spray painting a tensile test specimen in the Lea Lab spray booth.*

#### 3.7.1.2.2 2D DIC

The simplest form of DIC uses a single camera as shown in Figure 3-33. The specimen is positioned squarely facing the LaVision Imager Pro X camera. Using this approach, it is not possible to directly analyse the out of plane displacement. In plastically deformed materials a method has been used to approximate this where the sum of the plastic strains total to zero. If strain in 2 planes is known the out of plane strain can be calculated. When used in macroscale the DIC algorithm used is a comparison to the first image. This causes the lowest error due to it using no summation of other results but is limited to applications where the deformed DIC pattern is identifiable when analysed compared with the first [104].

#### 3.7.1.2.3 3D DIC (more detail on the camera positions)

To study out of plane motion 2 or more cameras are used to study the motion of a specimen in 3 planes as shown in Figure 3-37. To perform this a calibration is required in which a calibration plate is produced. This is a pattern printed onto a flat rigid plate. This is then displayed in the field of view Limess Q-400-3D cameras in various positions within the area the specimen is positioned with 50 or more images acquired using VIC snap, a calibration can be performed by the DIC to calculate the pixel error. Once this was performed the cameras cannot be moved until the testing is complete.

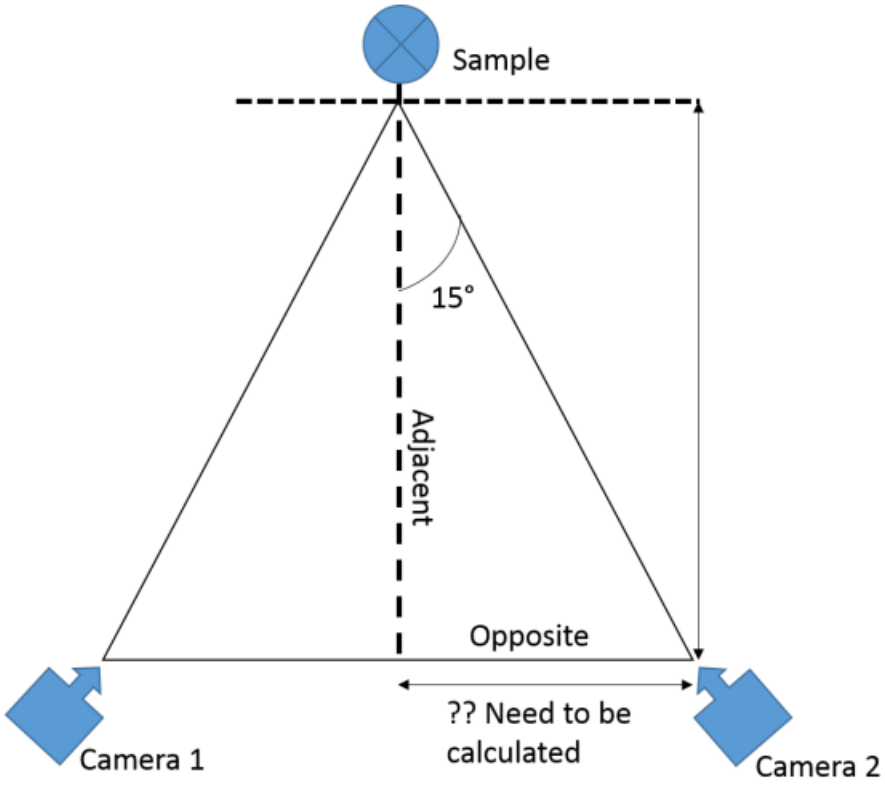


*Figure 3-37: diagram of how 3D DIC cameras are set up to view a specimen.*

A series of tests can then be performed with the specimens being replaced as long as the equipment is not moved. The camera was set up in the calibration in the settings as shown in Table 3-3, Table 3-4, Table 3-5. The angles shown in Table 3-4 were minimised with the beta angle aimed to be 30° to replicate the geometry as shown in Figure 3-37. The Tx dimension is the adjacent, Ty is out of plane and Tz is the opposite if referring to Figure 3-37.

| | Camera 1 | Camera 2 |
|---|---|---|
| Centre x (pixels) | 1208.28 | 1241.85 |
| Centre y (pixels) | 1050.75 | 1025.85 |
| Focal length x (pixels) | 16447.3 | 16466.8 |
| Focal length y (pixels) | 16447.3 | 16466.8 |
| Skew | 0 | 0 |
| Kappa 1 | 0.100282 | 0.230012 |
| Kappa 2 | -19.5382 | -33.8411 |
| Average magnification (pixel/mm) | 37.1775 | 37.6724 |
| Minimum magnification (pixel/mm) | 36.4175 | 36.8601 |
| Maximum magnification (pixel/mm) | 38.0126 | 38.6648 |

*Table 3-3: 3D DIC calibration settings found with the calibration settings for the settings on each camera*

| | Alpha | Beta | Gamma |
|---|---|---|---|
| Camera angles (°) | -0.560792 | 30.5378 | -0.839788 |

*Table 3-4: 3D DIC calibration settings found with the calibration settings for the angles used*

| | Tx | Ty | Tz |
|---|---|---|---|
| Distance (mm) | -226.58 | -0.312557 | 58.1716 |

*Table 3-5: 3D DIC calibration settings for the*

The settings used in 3D DIC were a subset of 29 pixels and a step size of 7 pixels. The error score from the calibration was 0.043 pixels.

### 3.7.2 Microscale

The geometry for tensile testing was designed by Ghadbeigi et al. [73] as shown in Figure 3-38, this geometry was developed to localise the deformation into a specific location to observe strain and damage initiation in specimens microstructure. Due to this design approach, the specimens have a larger elongation at failure of 5 times the size of a standard ASTM specimen [36].

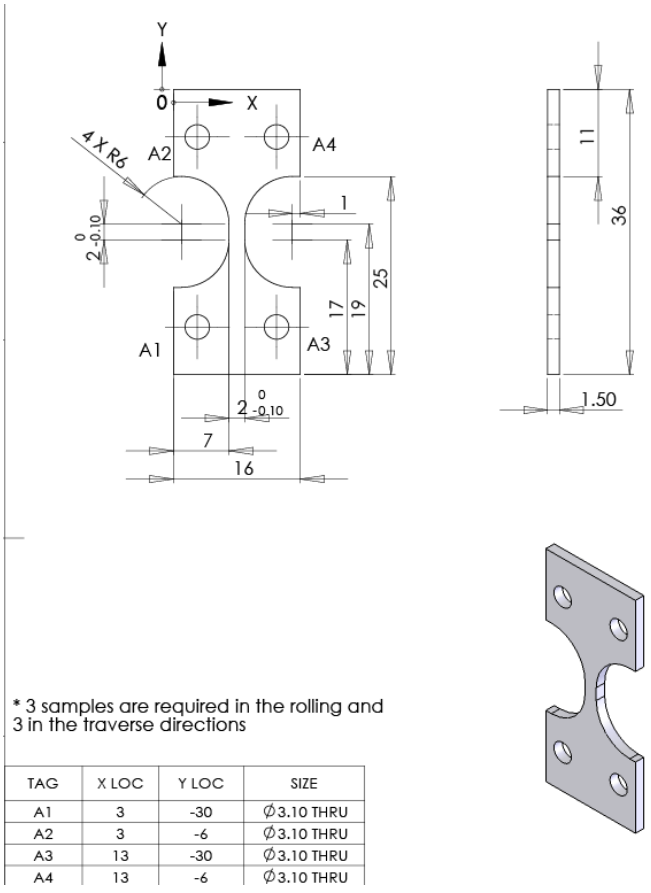


*Figure 3-38: Specimen design for SEM tensile testing in the Deben tensile and horizontal bend test module as designed by H. Ghadbeigi [36]*

#### *3.7.2.1 Testing Apparatus*

The tensile testing is performed with the Deben tensile test module. This module has a 5KN load limit and 10mm maximum displacement. The tensile test adaptor plate and clamps are loaded onto the

module allowing 4, 3mm diameter pins to locate the tensile test specimen in the 4, 3.1mm diameter holes as shown in Figure 3-38. This is then clamped into position using 4 screws pressing down onto the top clamps one at each specimen ends. This restrains the specimen and a preload of 30N is applied before inserting the specimen into the SEM. The preload holds the specimen in a static position allowing the first micrograph to be taken at a position and then that position is easily tracked with the subsequent displacements between interruptions. This also has the added benefit of making any displacement considered to promote strain with little to no slack in the system.

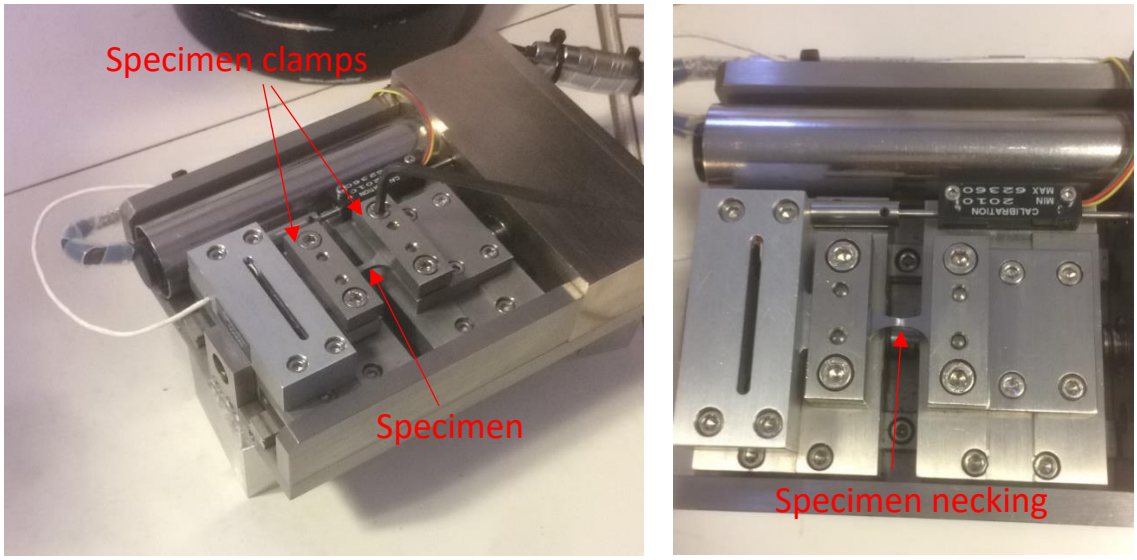


*Figure 3-39: Deben tensile and horizontal bend test module with the tensile test tooling and specimen. Left; Tightening the screws on the tensile test holder, Right: necking occurring in the centre of the tensile test specimen.*

## 3.8 Post bend test analysis

### 3.8.1 Micrograph Shear band counting

To get a better understanding of shear bands and how they develop a method of counting the shear bands from both tests have been explored. Two different methods were used:

- Count the shear bands manually from the images
- Find the peak strain points in a DIC strain data output plot

To perform both of these the 200x magnification images were used as this produced high-quality micrographs which resulted in a low error in the DIC calculation as demonstrated later in DIC error analysis. This also had a large enough field of view to view a statistically relevant number of shear bands in a single test.

To count the shear bands the overlay on the DIC was changed to a black and white colour palette with the settings changed to set strain from minimum to maximum for each image. This was to remove less significant shear bands and check if the intensity of shear bands changed through the bending test. If it is less than the median of the minimum and maximum strain value, it is considered

an insignificant shear band and is ignored. Another rule is that shear bands will only be counted if the band intersects with the surface of the specimen within the field of view.

### 3.8.2 Numerical shear band counting

Another means of checking shear bands is to study the DIC data extract. This was exported out of DaVis and post-processed in Excel. This resulted in a large matrix of results to study requiring a methodology to identify the shear bands. To do this a flat line of data was extracted at each depth in both the polished top surface specimen and the 0.6mm depth polished specimen. Using this data the average strain was identified for each depth per unit displacement. This was used as the minimum a peak would need to exceed to be considered a significant shear band and get counted.

## 3.9 FEM

Using Abaqus 6.14 [105] FEM have been used to simulate tests to validate work and develop a better understanding of bendability and the development of shear bands.

### 3.9.1 2D modelling

#### *3.9.1.1 Material models*

To test the effect of varying material properties, FEM was used with a selection of materials. These were based on the Hollomon strain-hardening model [106] in Equation 25:

$$\sigma_T = K\varepsilon_T^n \qquad \textit{Equation 25}$$

Here K is the material hardening, $\sigma_T$ and $\varepsilon_T$ are the true stress and strain respectively and $n$ is the strain-hardening coefficient. Using the elastic limit prescribed by the S960 material designation in UHSS of 960MPa. Then 3 different $n$ values are used to vary the plastic properties. To simulate a suitable range of properties the n values were chosen as 0.05, 0.1 and 0.2 these have been calculated in Figure 3-40 in 10% true strain steps to 100% true strain. This is to allow the strain to be high enough to simulate microstructural properties in simulations of small-scale tests.

To generate a material model for the 17DF4/1 material this first involves using the averaged true stress-strain and then the fracture stress was calculated using the measured area of the fractured specimen in the necked region and corresponded this with the final recorded force measurement during the tensile test. Using the gradient between the peak true stress point and the fracture stress the strain-hardening coefficient $n$ was calculated by finding the gradient between these points in a log stress-strain graph as described by B. Yngve et al [103].

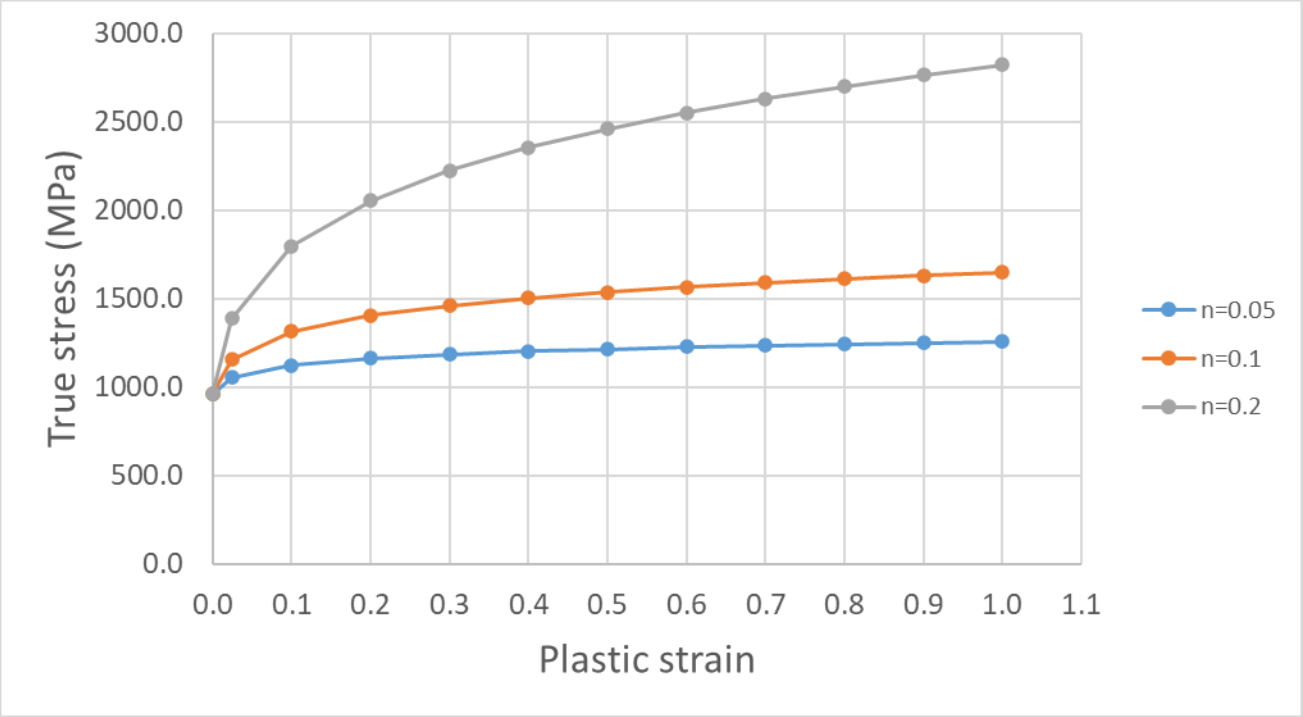


*Figure 3-40: Hollomon material model simulation.*

### *3.9.1.2 Flat specimen modelling design*

A simulation of the 2D bending was performed in Abaqus 6.14 [105] with the specimen designed in Solidworks [107]. Solidworks was used as it has improved CAD tools than provided in Abaqus and was used as a means of developing the flat specimens in Figure 3-41, but also the surface waviness specimens used to simulate surface roughness in section 3.9.1.3. The tooling was designed to have the same geometry as used in the 2.5mm diameter gen 1 and 2 tooling as shown in Figure 4-35 was reproduced in the FEM in Figure 3-41.

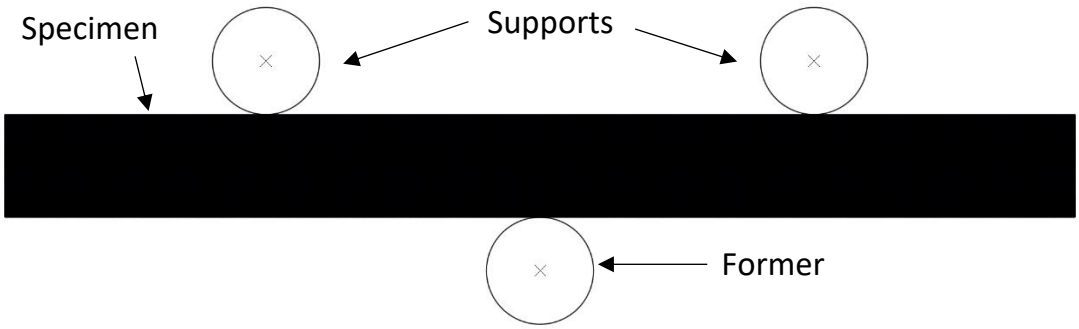


*Figure 3-41: Global bending mesh geometry before deformation*

Using the material models as defined in section 3.9.1.1 the mesh is produced using a plane stress element CPS4R on the specimen with the sizing shown in Table 3-6. While the rigid elements R2D2 were used for the tooling and are only modelling the circumference of the pin to limit element count. A friction coefficient of 0.3 in a penalty coulomb friction model was used to replicate the conditions found in bending with the steel-on-steel contact as used by Tata Steel [14]. The contact used the

surface-to-surface discretisation method with finite sliding and surfaces and the supports and formers were set as masters and the faces of the specimen in contact with each of these were set as slaves as shown in Figure 3-42. To bend the specimen a displacement in the positive Y direction is added to the former with this broken into 2 steps. The first step acts as a small preload and stabilisation step with a 0.01mm displacement with an automatic stabilisation applied. This acts as damping and is then removed in the second step with an additional 4mm of displacement resulting in a total displacement of 4.01mm of motion from the former. In both steps, non-linear geometry was switched on. The results being presented doesn't consider the results for the first displacement step with stabilisation. This removes the need to consider the impact of the damping on these simulations.

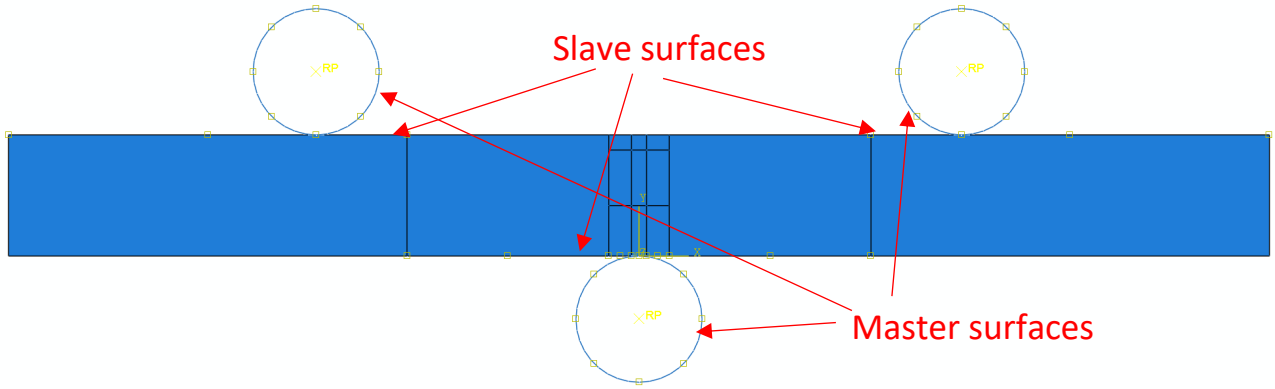


*Figure 3-42: contact interactions in the 2D bending simulations.*

The 2D model uses submodeling to allow a refinement in the mesh with a reduction in computation time as the simulation area is reduced, reducing the number of elements and the contact between the specimen and tooling is removed after the global model is simulated. The submodels are driven by the displacement of boundary conditions to match those movements in the model driving it. The relative motion was set to 0.01 to limit deviations from the model driving the submodel. The boundary conditions for these are shown in Figure 3-43, where the global model has boundary conditions on the former with that having a positive Y displacement, and the supports are both under the encastre boundary condition. The first submodel has boundary conditions on the left, right and bottom boundaries to replicate the movement of the same boundaries in the global model. Which was similar to the second submodel with the left, right and bottom boundaries to replicate the movement of the same boundaries in the first submodel.

| Model | Driven by | Element size | Area |
|---|---|---|---|

| | | | |
|---|---|---|---|
| Global model | NA | 0.02mm, 20µm | Full geometry, 2.4mm by 25mm long specimen, 3 2.5mm diameter |
| First submodel | Global model | 0.004mm, 4µm | Central of the top region of bending in tension, 1.2mm wide by 1.4mm deep |
| Second submodel | First submodel | 0.0008mm, 0.8µm | Central of the top region of bending in tension, 0.3mm wide by 0.3mm deep |

*Table 3-6: 2D modelling meshing and geometry data*

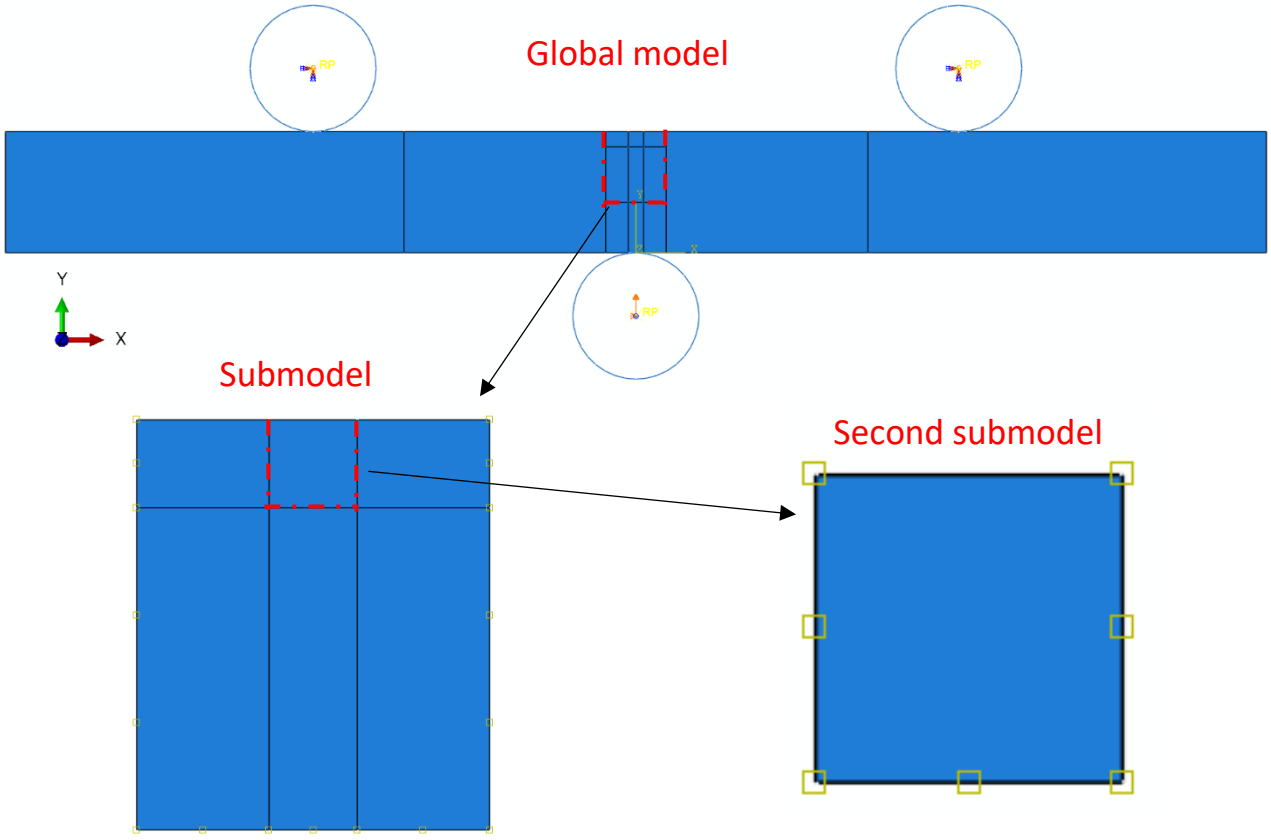


*Figure 3-43: 2D FEM boundary conditions set on top: global model, bottom left, first submodel, bottom right, second submodel.*

To study the effects of mesh sizing a mesh convergence study was performed with both the global model and first submodel since these were used in this thesis. The data was captured from the same point at the centre of the bend with the strain. The material model used was the data obtained from

the 16TG26 true stress-strain curve. The test was not performed with a refined mesh as used in most tests as this methodology was not followed in this work due to its impact on promoting strains in specific locations. This was exactly what was being avoided as such the refinements were all performed globally. This resulted in the results as shown in Figure 3-44 for the global model and Figure 3-45 for the sub-model. These were for the global and sub-models at 1mm and 0.5mm respectively before the strain localising in shear bands. This was found to occur at smaller displacements with smaller meshes. Due to how close the results are to each other for both models they are considered converged in this application.

Mesh sizes were selected as shown in Table 3-6 at 0.02mm for the global mesh because the computational time to perform this simulation was only an hour. While offering high mesh density and detail for the results. The mesh for the sub-model was sized at a fifth of the size of the global mesh at Tata Steels advice and so was used in this simulation. This resulted in the mesh on the sub-model being 0.004mm in size.

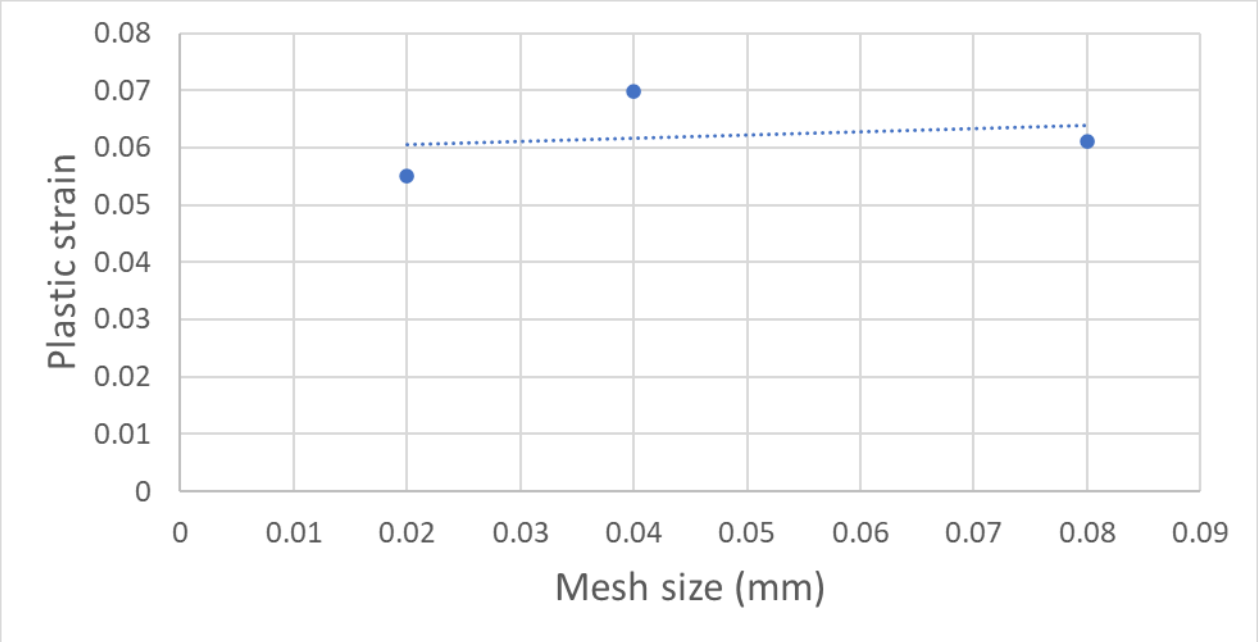


*Figure 3-44: Global model mesh convergence graph*

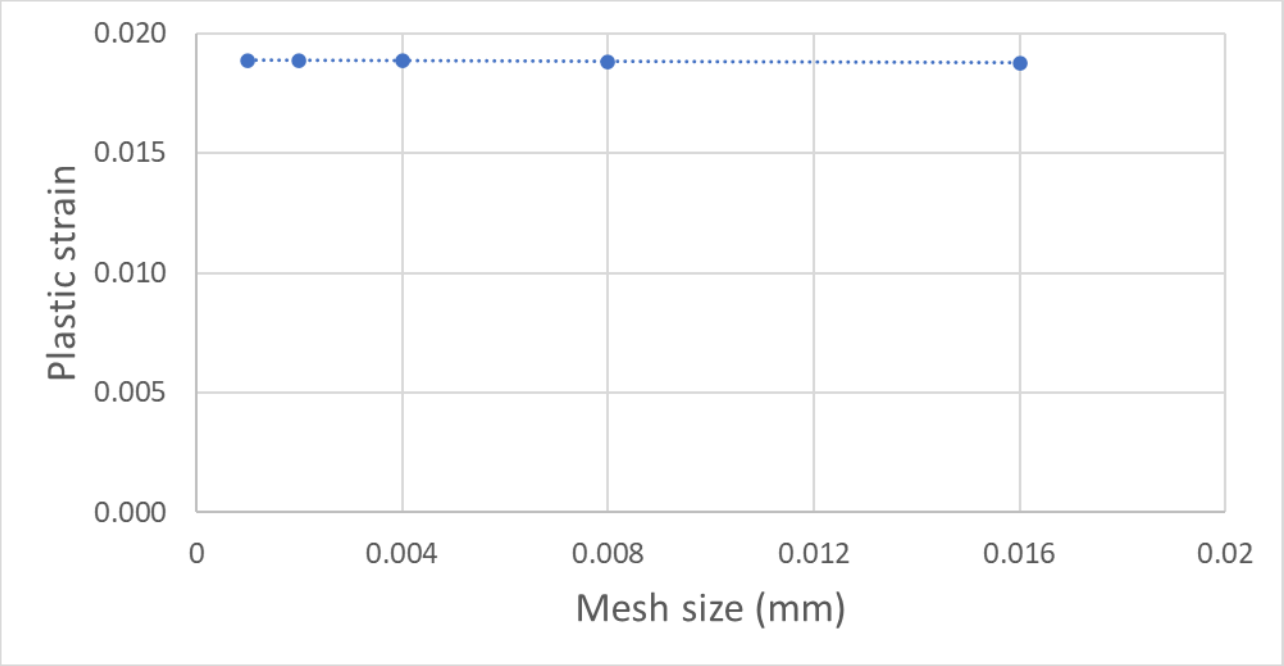


*Figure 3-45: Sub-model mesh convergence graph*

### *3.9.1.3 Wavy top surface specimen design*

An analysis of the hot-rolled top surface of the 17DF4/1 specimen resulted in an average top surface roughness being found to have a depth of 6µm and a period of 72µm being found to be the average surface waviness in the methodology as shown in *Figure 3-46*. This was used as a useful insight into the

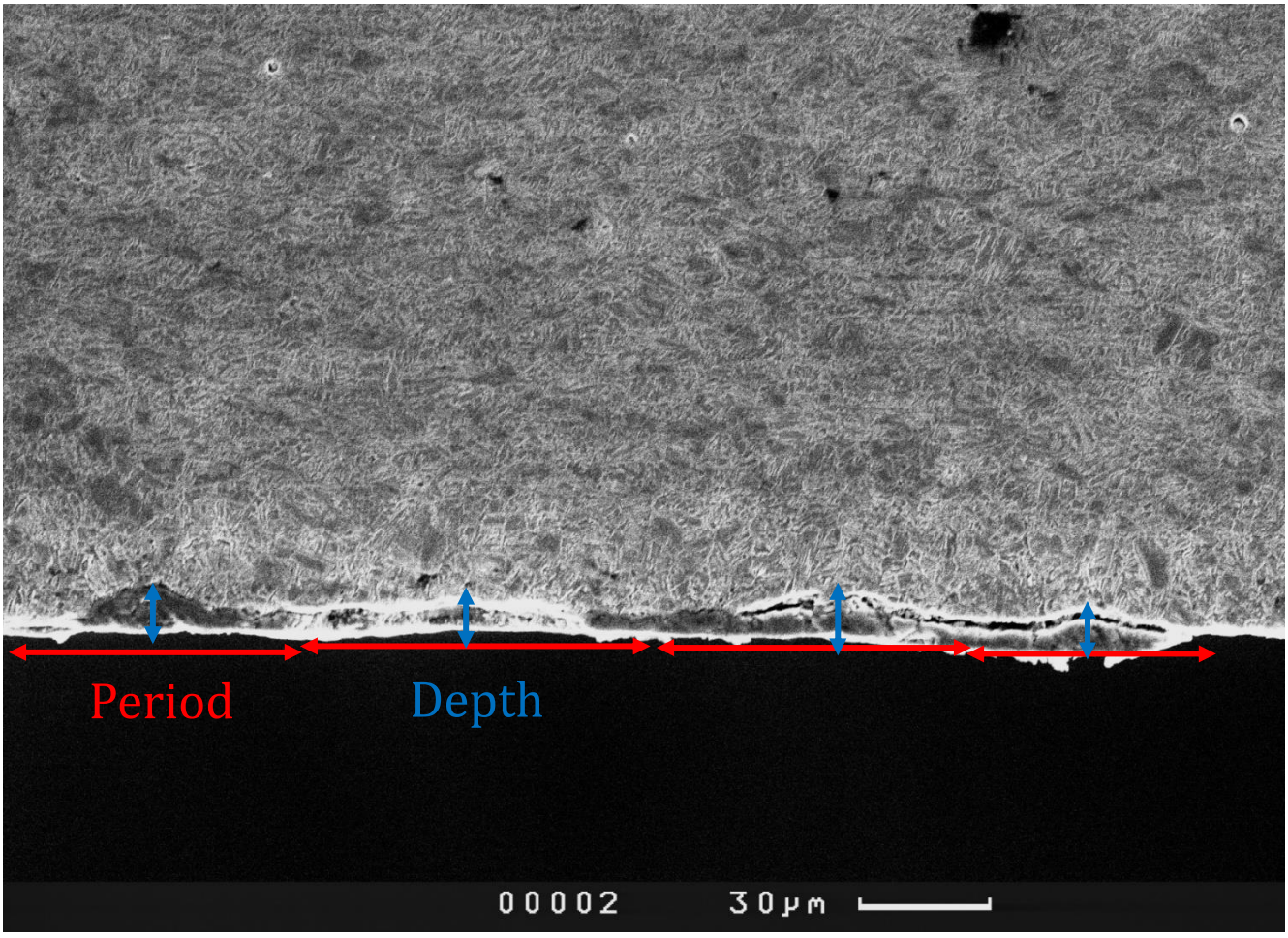

To study these a global model, first and second submodel were developed with the meshing and parameters the same as defined in sections 3.9.1.1 and 3.9.1.2. The geometry varied with the flat specimens by adding a surface waviness. To simplify the problem a single geometry for the global model and first submodel was used. These consisted of the geometry shown in Figure 3-47 and Figure 3-48, where the period and depth are 100µm and 10µm respectively to limit the numbers of models to compute. This geometry was selected as it was the middle of both the period and depth settings to be used in the second submodels as shown in Figure 3-49 and Figure 3-50. This allowed the effect of period and depth variations on the localisation of strain in bending.

*Figure 3-46: Micrograph showing how the surface waviness and period was identified in a 17DF4/1 sample*

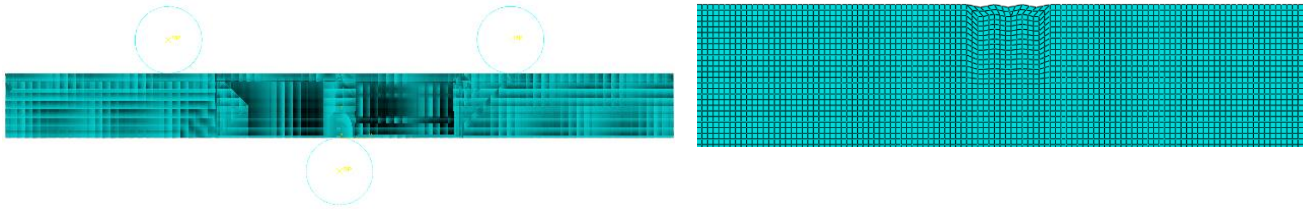

*Figure 3-47: Global model for surface waviness mesh with 100µm period and 10µm depth.*

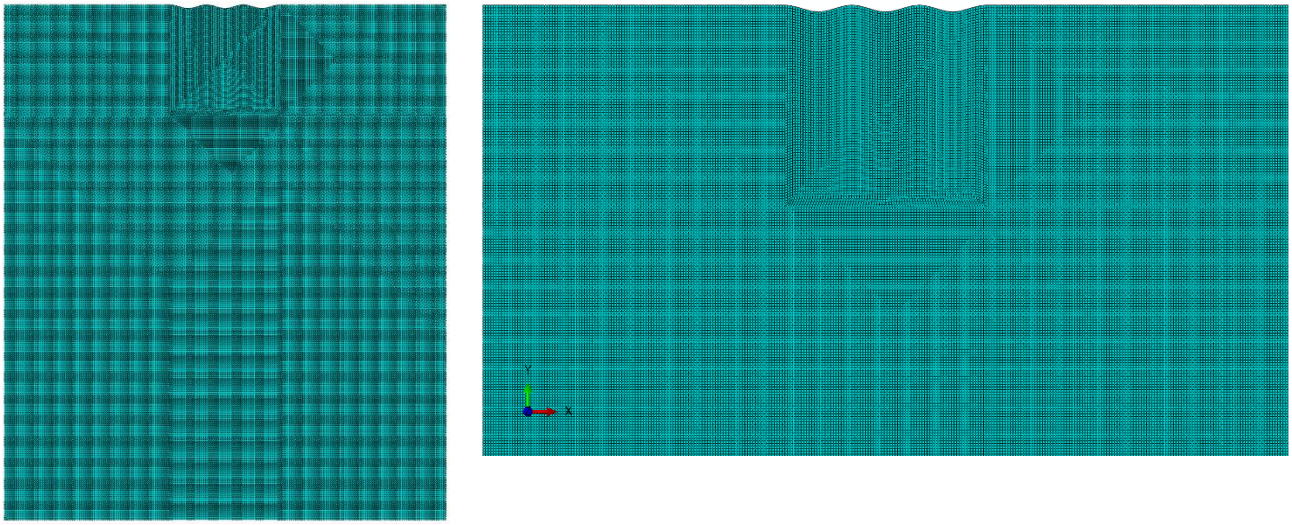

*Figure 3-48: The first submodel for surface waviness mesh with 100µm period and 10µm depth.*

As such a model for a range of surface waviness factors were explored with varied dimensions with periods of 75µm, 100µm and 150µm with a depth of 10µm tested in Figure 3-49. As well as using the same period of 100µm to test varied depths of 5µm, 10µm and 20µm in Figure 3-50. The material used in this application was the experimentally derived data from 17DF4/1 as shown in  Tensile test force-displacement graphs for 17DF4/1.

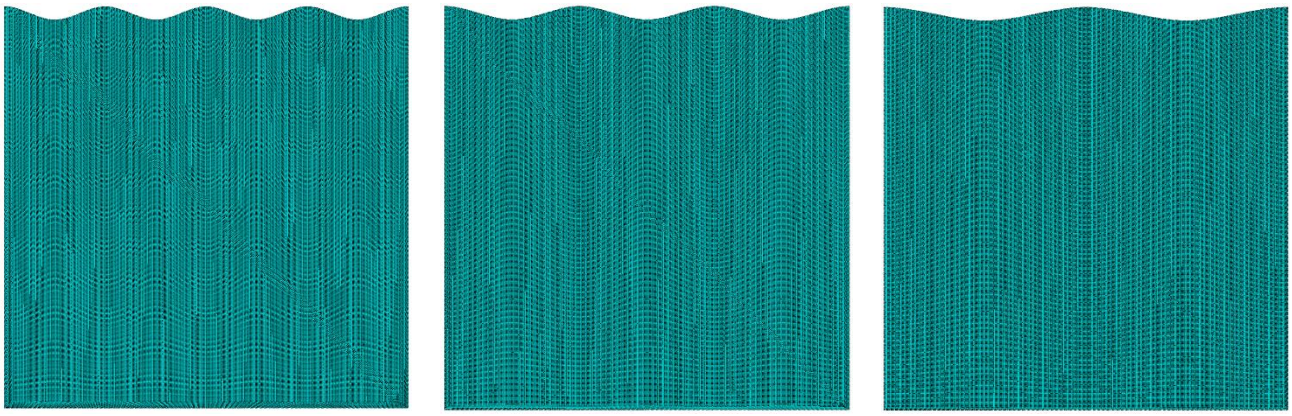

*Figure 3-49: The second submodel for surface waviness meshes with 10µm depth, left, 75µm period, middle, 100µm period, right, 150µm period*

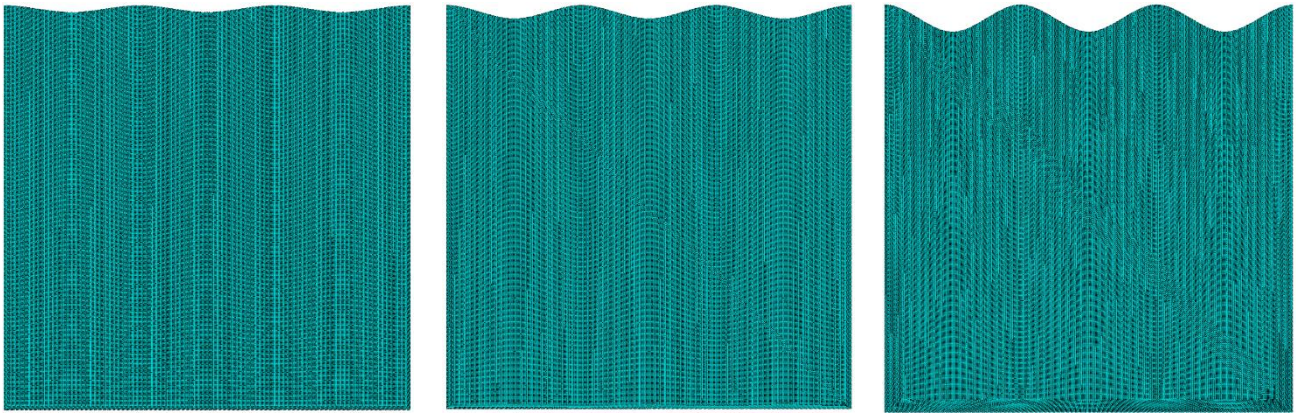

*Figure 3-50: The second submodel for surface waviness meshes with 100µm period, left, 5µm depth, middle, 10µm depth, right, 20µm depth.*

## 3.10 Summary of methodology

The sample preparation techniques have been improved by changing the sample preparation process to using batch production. The new approach to flatten bend test specimens using a material depth removal step removes the roughness variable for bend testing. This brings the specimens as close as possible to being a perfectly flat bend test specimen as found in FEM. The FEM is a basic but efficient means of studying local strain and will be used to compare with the experimental results.

A combined methodology to study the local bendability of UHSS will be developed and these techniques will be applied to produce novel research and results.

# 4 Tooling and specimen design and methodology

Due to the material properties of UHSS and the limitations of the existing designs. New tooling and specimen designs have been developed to improve the insight into the development of shear bands and damage initiation. The process to develop these was to first study the design of the Deben tooling. This was done by measuring them, recreating them in the Solidworks CAD package [107] and then simulating their use in Abaqus FEM [105]. This allowed the strain and deflection of the tooling to be studied. As well as the localisation of stresses and consider improvements to the design. This included the need to increase strain in the specimen to improve the likelihood of damage occurring in bend tests. This also showed that this design had been taken to its limit with the use of thicker specimens of up to 4.25mm in thickness.

To improve the testing results 2 generations of tooling were developed. The first was less innovative and used in the same orientation as the Deben tooling. This was developed in CAD and in FEM to confirm it operated as expected. It was found this tooling was not suitable for testing but the position of the former and support was retained and used in the second generation tooling. This changed the orientation of the tooling and resolved the issues with the first generation tooling. This was done by deploying new materials to resist plastic deformation and using replaceable parts. Combining this with a resised specimen enabled a very high strain to be applied to the specimen in bending.

## 4.1 Horizontal bend testing with Deben tooling

### 4.1.1 Microscale

Horizontal bend testing was performed using the Deben tensile and bend test module. This came supplied with bend test tooling and was initially used to test the bendability of the UHSS.

#### *4.1.1.1 Testing Apparatus*

The Deben bend test tooling has the geometry as shown in Figure 4-1. The span between the supports is 37mm this is larger than the ASTM specifies for the bend test with 5mm diameter tooling when using the equations as shown in Figure 2-11 with a 4.25mm thickness specimen the span would need to be between 20.6mm and 24.9mm. Significantly smaller than the width found in the Deben 5mm diameter tooling at 37mm.

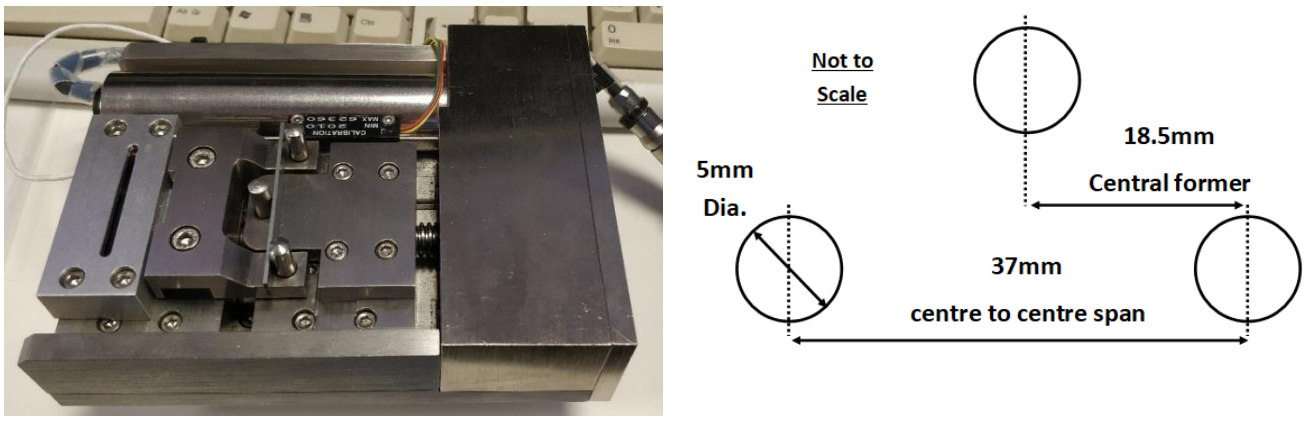


*Figure 4-1: Left; Image of the Deben bend test module with the Deben bend test tooling and 1mm thick bend test specimen loaded into it, right; diagram of the Deben bend test geometry.*

#### *4.1.1.2 Standard bend test geometry*

Bend tests were performed with the Deben standard bend test geometry. This was done to promote shear bands and damage. The geometry was as shown in Figure 4-1, while this geometry is suitable for bend testing it has the following problems:

- Large radius pins of 2.5mm in size result in a high $r_i/T$ ratio limiting the testing of bendability.
- The gap for the specimen loading is limited to 4.5mm
- The 4.5mm gap means smaller specimens have a lower maximum displacement as the module only has 10mm maximum displacement.
- The geometry does not conform with ASTM standards therefore the tests do not comply with other experimental approaches
- The large specimens and diameters of pins result in a larger bend to be observed that cannot be observed with a single micrograph in the Camscan SEM.
- The tooling was used in tension, this meant the tooling was not as stiff as in compression as it drew the specimen through the tooling which is explored in Second Generation 2.5mm diameter tooling.
- The pins are not replaceable, when plasticity or wear deforms the working surfaces the whole support or former would need to be modified or replaced.

Due to these limitations of the Deben tooling geometry, the bend test results did not promote enough deformation to test the bendability of the UHSS. Specimens were redesigned to increase the specimen thickness and retested, but it was concluded new tooling geometry would improve the testing procedure.

#### *4.1.1.3 Deben Tooling FEA Design analysis*

The approach used to design was to study the Deben tooling to understand the design and loading on this tooling then produce new tooling to mimic it and incorporate the improvements needed. The

tooling and specimens were designed in Solidworks by measuring dimensions from the Deben tooling. By doing this an accurate assembly of the bend test module was created. This was useful to check the fitment of updated tooling designs at a later stage but was also used to simulate the tooling in FEM.

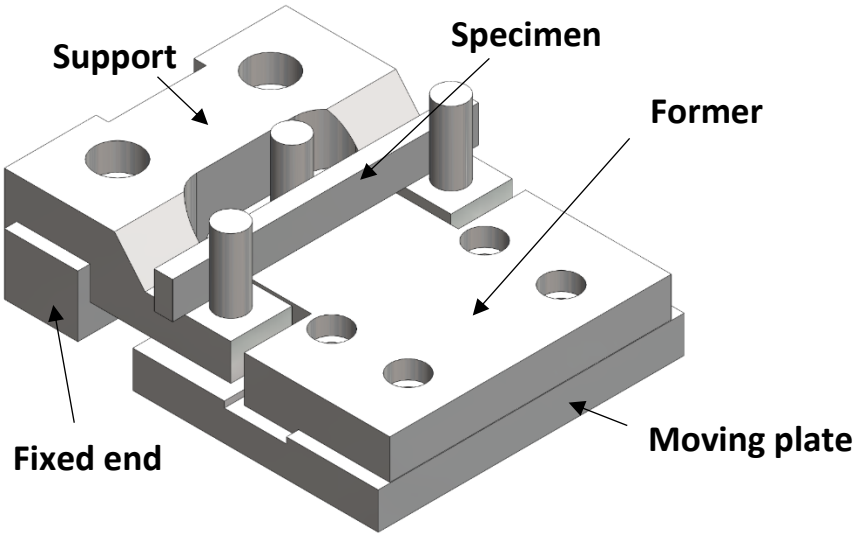


*Figure 4-2: Solidworks* [107] *assembly of the Deben bend test tooling, showing the support, former and mounting plates.*

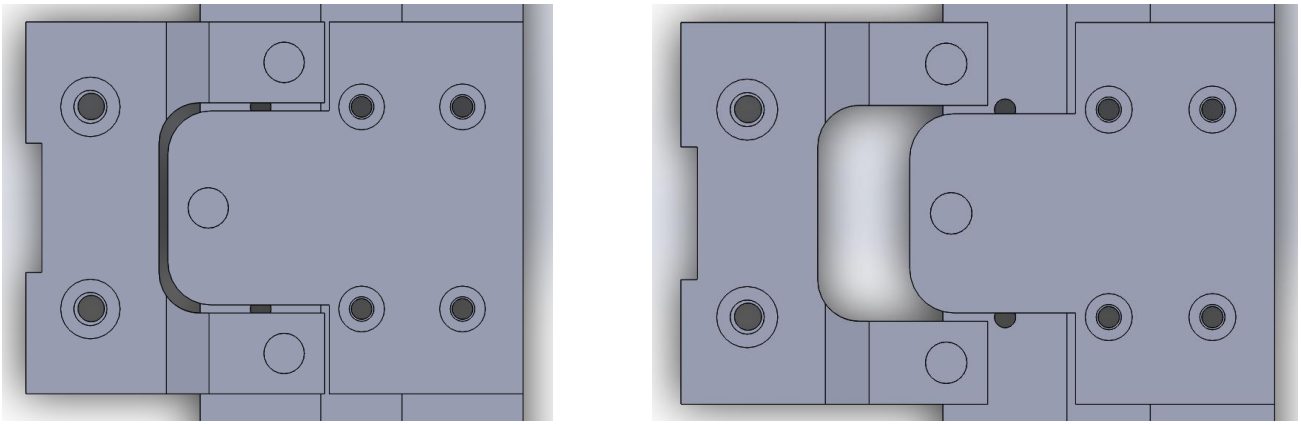

*Figure 4-3: Solidworks drawing from the top view of the tooling showing the home position at 0 displacement on the left and full displacement of 10mm on the right.*

This would provide details on the stresses and strains on the design and provide insights for later designs. These were then imported into Abaqus [105] as a Step file. The model is a static, general model in Abaqus/standard as the effects of strain rate were deemed to be low enough to use a static model. The 4.25mm thick specimen was then added to the model to apply the load of the design shown in the right image of Figure 4-5. The specimen with the same geometry was bend tested to perform a validation of the model with the force-displacement curves and a qualitative assessment of the specimen as a comparison with the model.

The geometry of the specimens was imported from Solidworks. The tooling required sectioning as in its original form it could not have meshed as shown in Figure 4-4. A sectioning approach was used to

convert the single complex geometry into smaller simple geometry elements that could be meshed in a structured method with hexagonal elements. This optimised the mesh quality and provided localised regions the mesh can be refined. Thanks to sectioning, hexagonal elements have been used with element C3D8R used for all parts. This element is a continuum model element, C3 with 8 nodes, D8, this is simplified to a single central integration point with reduced integration, R. Two material models were used in the simulations, an elastic model is applied to the tooling, while an elastic-plastic model is used for the bend test specimen. The plastic data was extracted from a tensile test with the 6mm tensile test specimen in a transverse orientation. These results were tested and found to be an accurate representation of a tensile test force-displacement curve.

| | Tooling material model | Specimen material model |
|---|---|---|
| Youngs modulus, $E$ (GPa) | 210 | 210 |
| Poisson's ratio, $\nu$ | 0.3 | 0.3 |

*Table 4-1: Elastic material properties used for the tooling and the bend test simulation*

| Stress (MPa) | Plastic strain |
|---|---|
| 1044 | 0 |
| 1051 | 0.001 |
| 1055 | 0.0021 |
| 1060 | 0.0037 |
| 1065 | 0.0069 |
| 1070 | 0.0102 |
| 1075 | 0.0135 |
| 1080 | 0.0167 |
| 1085 | 0.02 |
| 1091 | 0.0239 |
| 1095 | 0.0272 |
| 1100 | 0.0314 |
| 1103 | 0.0337 |

*Table 4-2: Plastic material data extracted from transverse tensile tests for 14TG26.*

These models were assembled as shown in Figure 4-8, where the specimen is in contact with the tooling and the tooling is in the identical position as measured in the Deben module. The front view shows there is a 0.5mm gap between the former and the specimen. This was to allow space for an anticlastic profile due to plastic deformation in bending to stop an additional contact region between the specimen and body of the former. The specimen was supported by the body of the support before bending on both sides. No lubrication is applied to the tooling or specimen to avoid contamination of the SEM chamber.

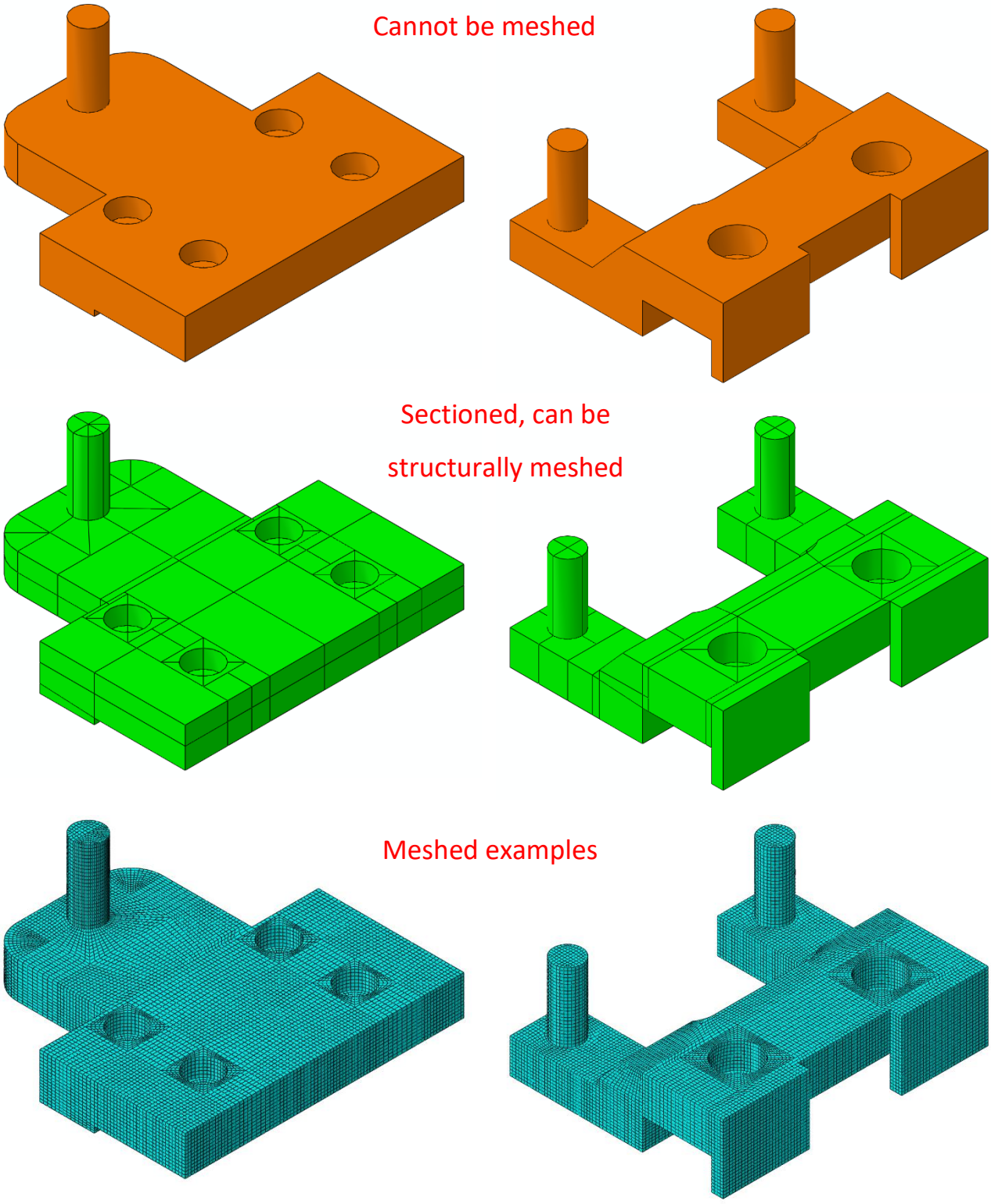


*Figure 4-4: Figures showing the approach to meshing parts with the former on the left and support on the right, the top row is the imported step file coloured orange to show it could not have meshed. The middle row shows the tooling after a sectioning approach is used to enable meshing of the tooling. The bottom row is the meshed tooling.*

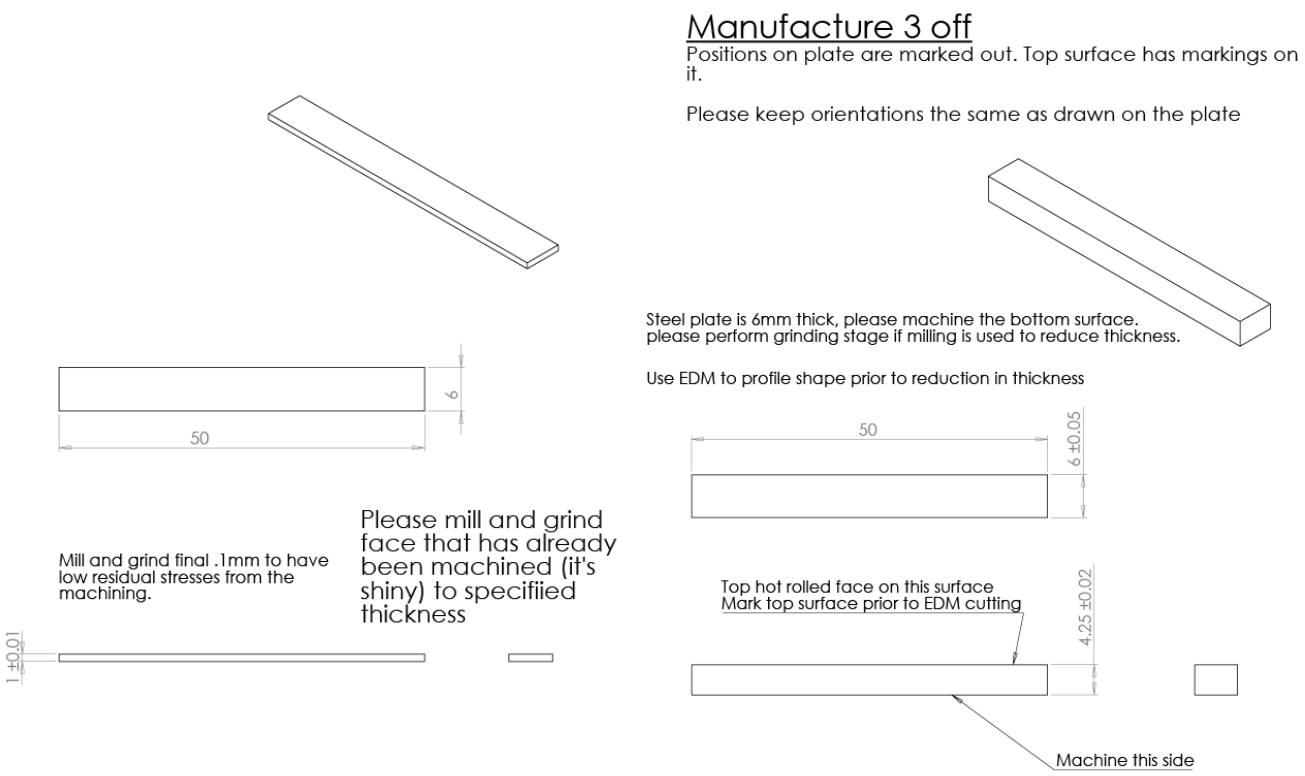


*Figure 4-5: Drawings used to produce bend test specimens for the Deben 5mm diameter tooling, left, 1mm specimens, right 4.25mm specimens*

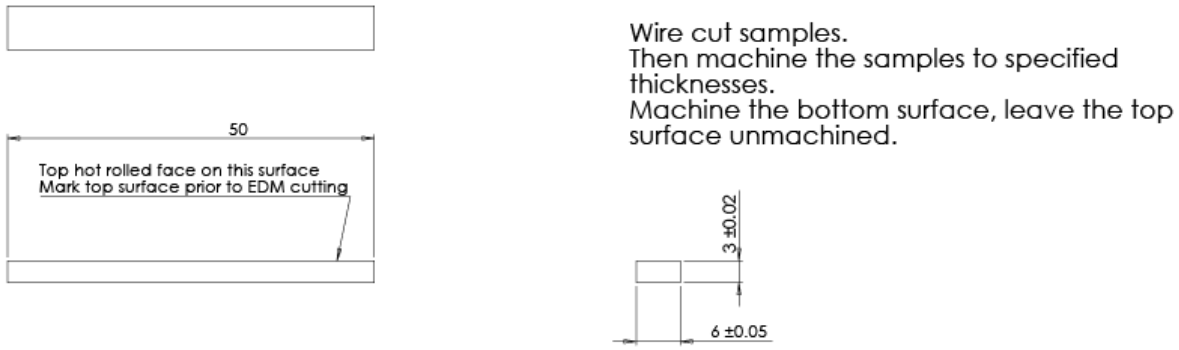


*Figure 4-6: Drawing for the production of 3mm thickness bend test specimen design for the Deben 5mm diameter tooling.*

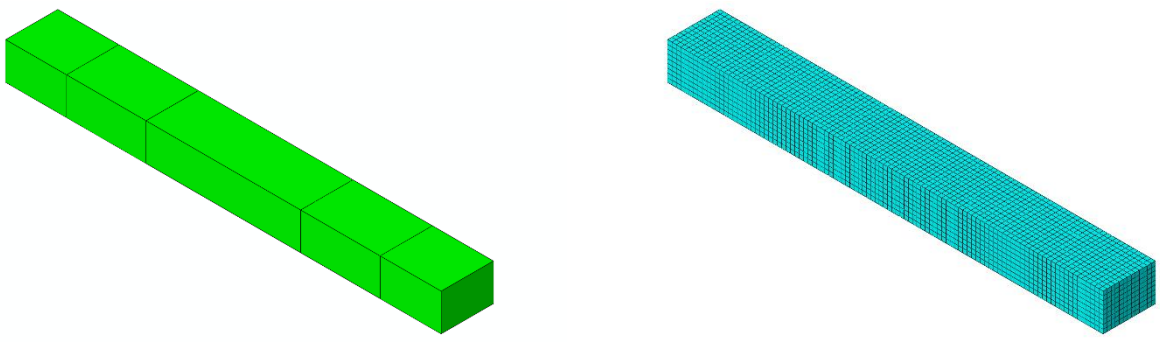

*Figure 4-7: 4.25mm thickness bend test specimen, left: sectioned, right: meshed*

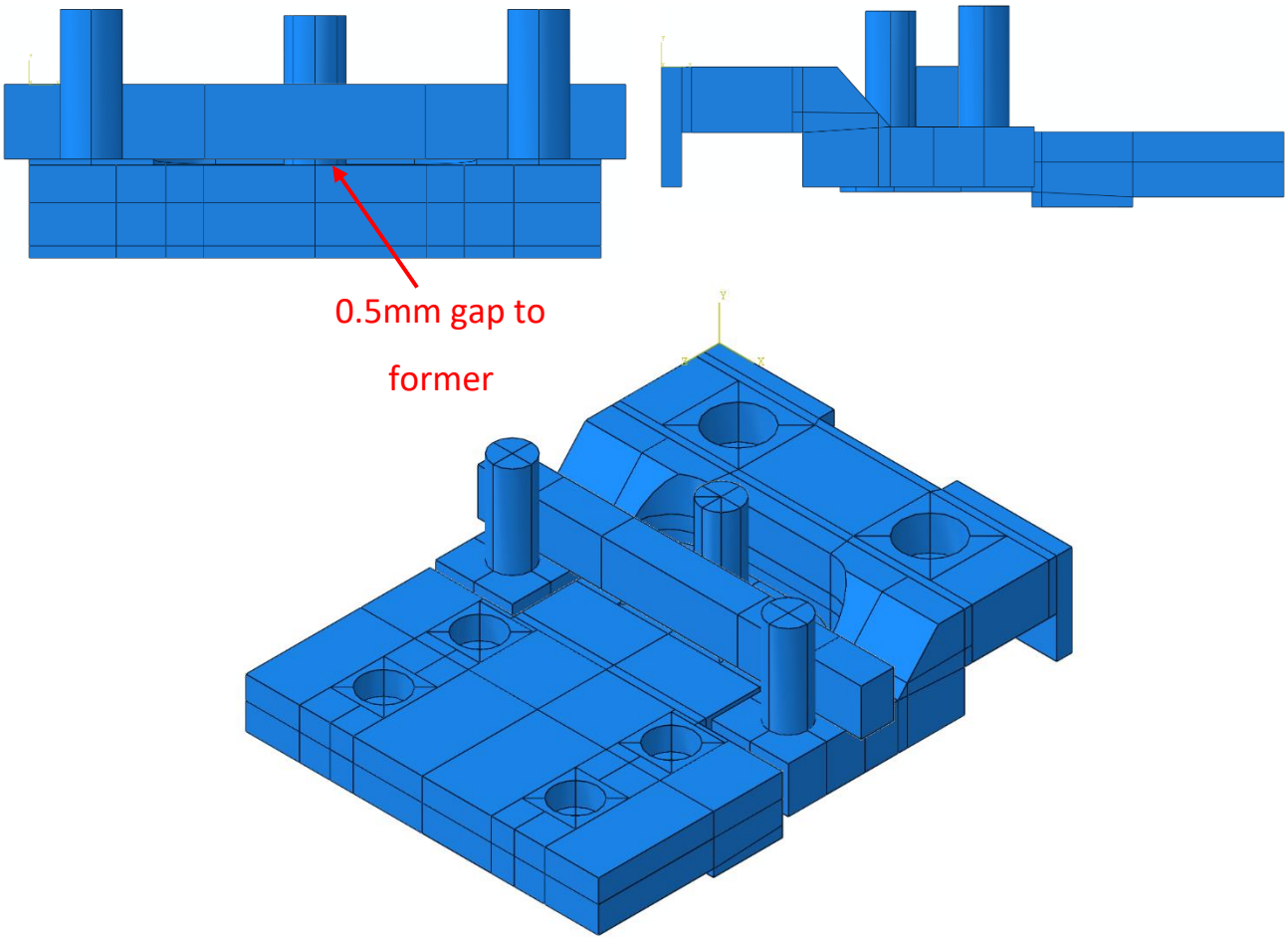


*Figure 4-8: The Deben tooling and 4.25mm thick bend test specimen assembled after sectioning in Abaqus, top left front view, top right, side view and bottom, Isometric view.*

To mesh the former support and specimen a global mesh size of 0.5mm was used as this provided an acceptable computation time of 2 hours. This was refined to a more detailed mesh on the pins with 0.25mm elements on the pin faces and a coarser global mesh of 0.75mm used elsewhere to reduce computation time. The specimen was retained at 0.5mm global mesh to reduce computation time.

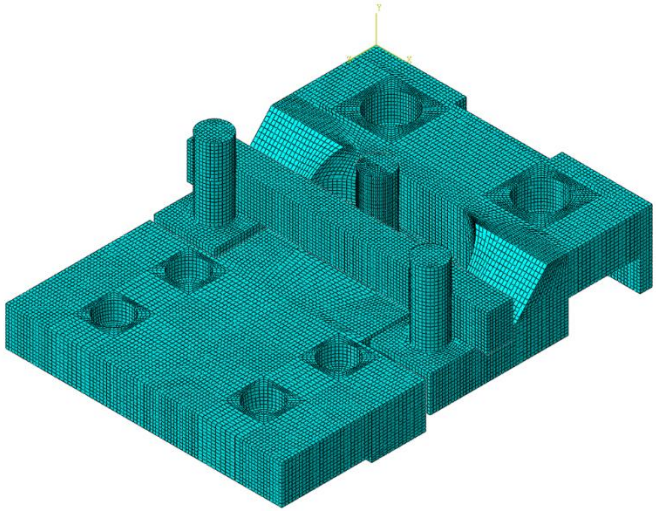

*Figure 4-9: Meshed assembled bend test tooling with 4.25mm thickness specimen*

To replicate the contact regions in testing regions are simulated for contact using the surface to surface discretisation method in Abaqus. Surfaces are selected as pairs for each region, the master surface was selected as the tooling and slave as the specimen as shown in Figure 4-10. Finite sliding was found to allow for the specimen the movement required for bending accurately. Friction was simulated using the penalty method with the friction coefficient of 0.3 used as the contact is steel on steel contact. This was found to be too low when compared to literature but was used in Tata Steel internally. This was also found to produce the most accurate bending force-displacement curve as shown in Figure 4-12.

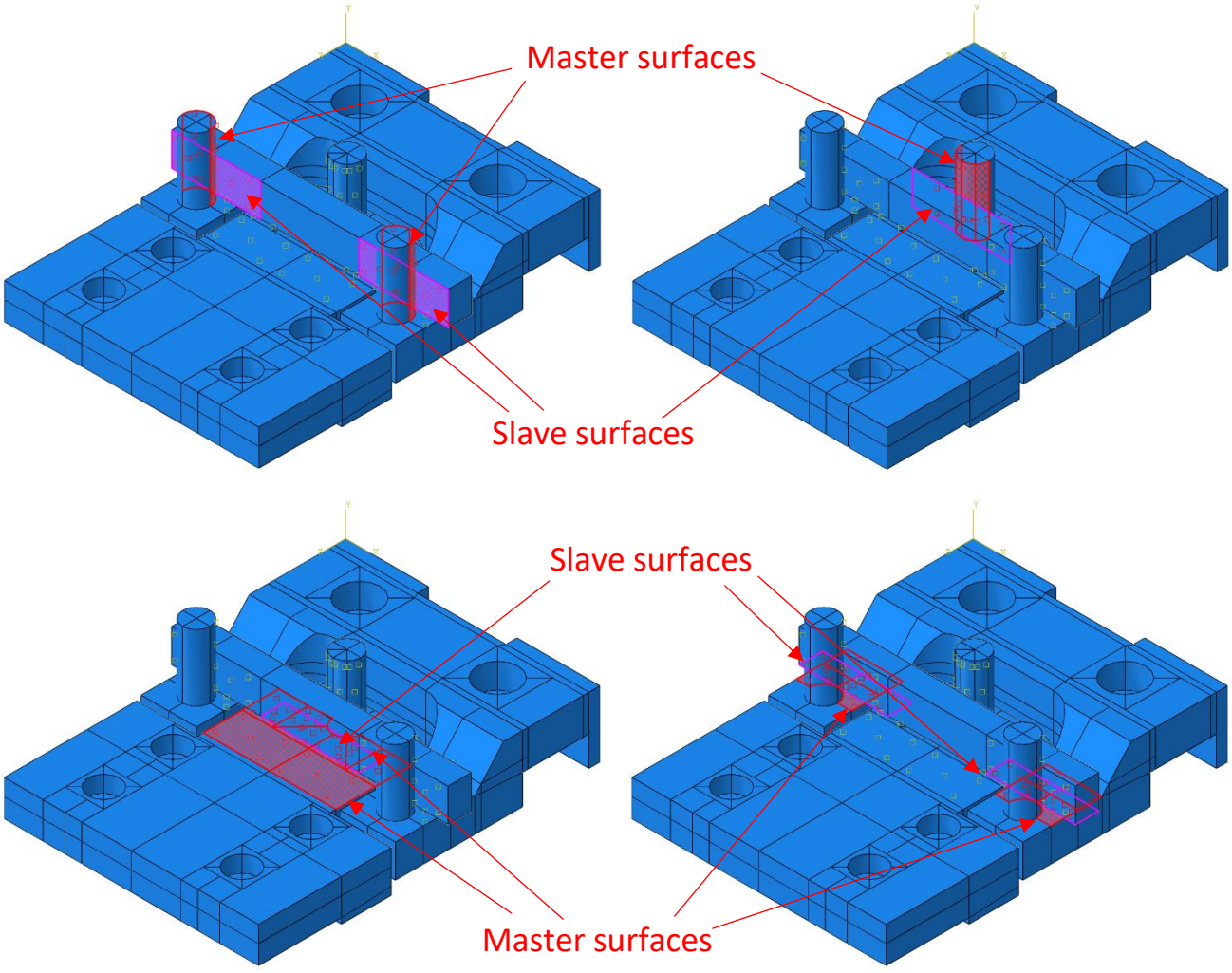


*Figure 4-10: Contact surfaces with the former, support and specimen interactions selected. The master surfaces are in red, the slaves are in purple. Top left, the supports and the specimen, Top right, the former and the specimen, bottom left the former body and the bottom horizontal surface of the specimen, bottom right, the support body and the bottom horizontal face of the specimen.*

To constrain the model in a manner that is representative of the real tooling the following boundary conditions are applied. To reduce computational time and improve stability the initial interaction and movement of 0.05mm has damping applied with automatic stabilisation, this damping is then removed for the second step with 10mm of displacement, in the same manner as described in 2D modelling.

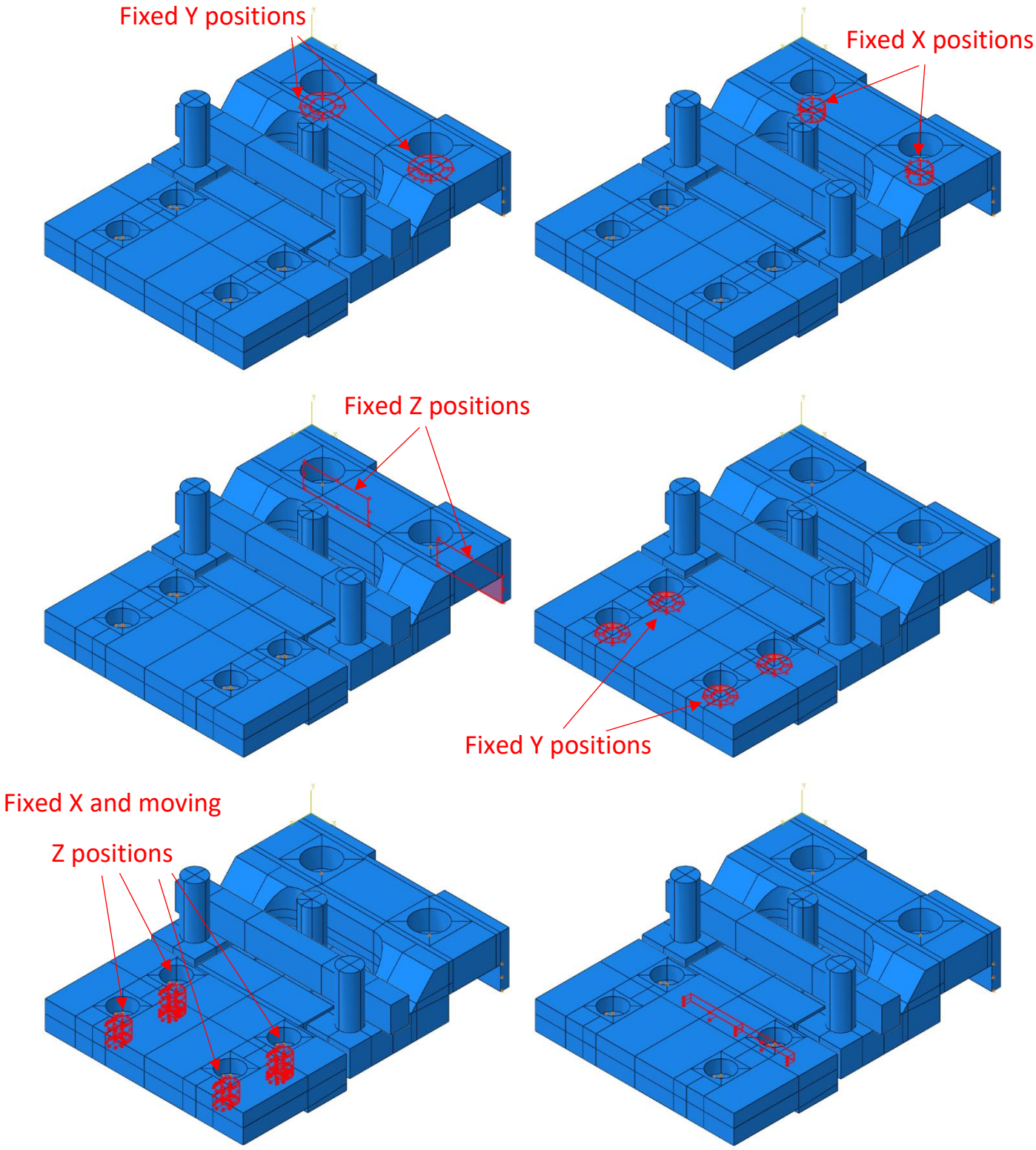


*Figure 4-11: Boundary conditions (BC) set for the Deben tooling assembly, top left; Support BC for fixed Y direction, Top right; Support BC for fixed X direction, Middle left; Support BC for the fixed Z direction, Middle right; Former BC for fixed Y direction, Bottom left; Former BC for fixed X direction and moving Z, Bottom right; Former BC for moving Z.*

The former and support are fully constrained as shown in Figure 4-11. While the bend test specimen is not constrained and moves freely but the friction acts as the stabilisation.

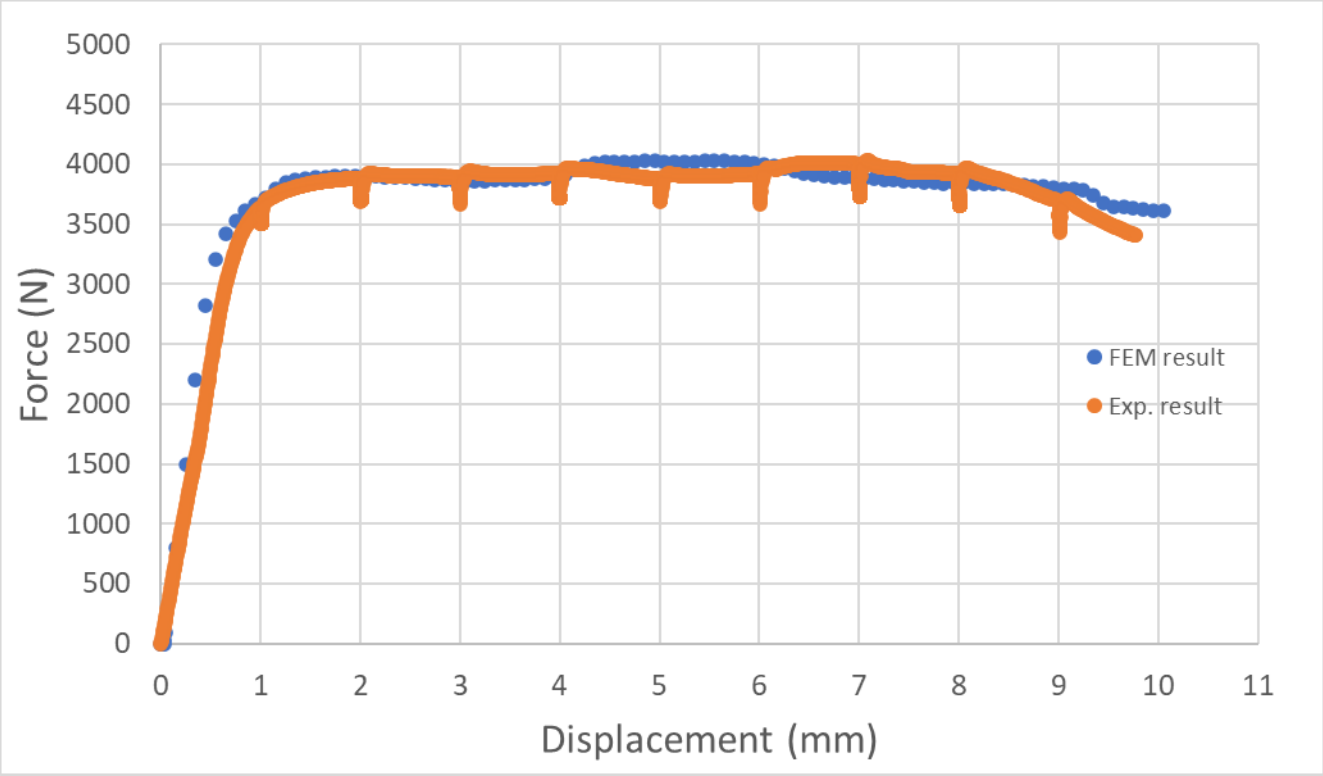


*Figure 4-12: Comparison of FEM bend test results and experimental results.*

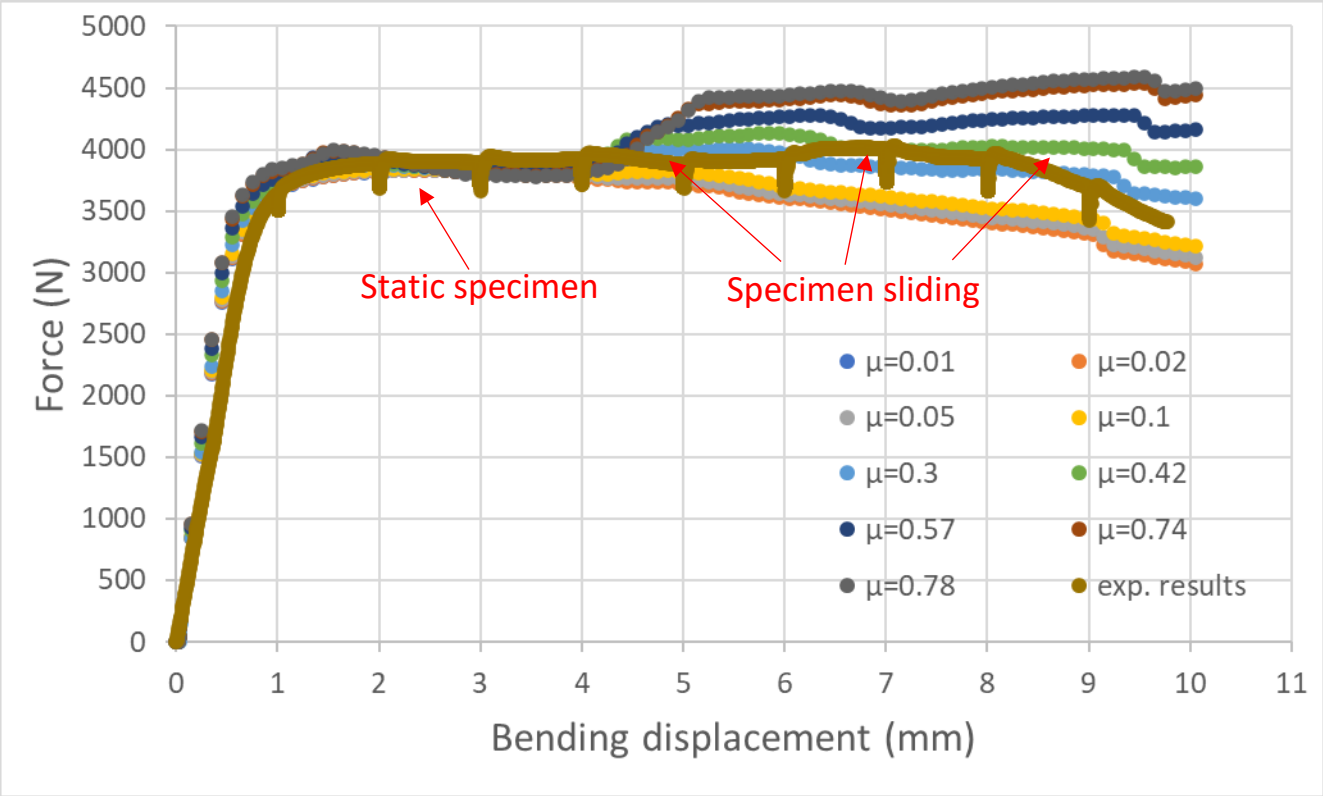


*Figure 4-13: comparison of different friction coefficients used in modelling*

As shown in Figure 4-12 the FEM bend test and the force-displacement curves show a strong correlation. The loading phase is not as steep in the experiment likely due to the stiffness of the Deben module not being considered in the FEM. No failure mode is included in the model hence the

force drop is not replicated past 8mm displacement in the FEM. A difference between the simulation and the tests were found at between 4 and 6mm of displacement where there is a force increase in the simulation and drop in the experimental results.

It has been reported that the final force increase in modelling is not representative for experimental bending loads [34] although for model validation rather than material analysis this was suitable. The simulation also allowed an analysis of the interaction between the tooling and bend test specimen and those found experimentally.

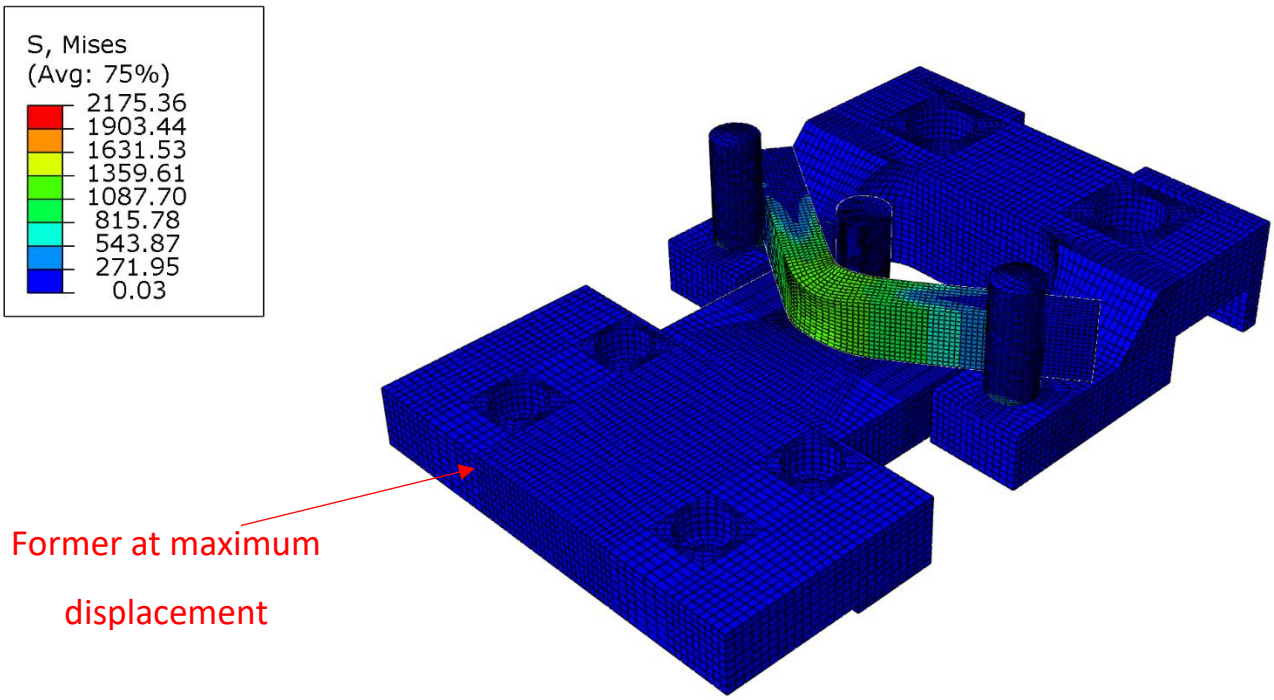


*Figure 4-14: Isometric view of bend test at 10.05mm of displacement, displaying the von mises stress on the parts.*

The bending of the specimen promotes high stresses of over 2100MPa as shown in Figure 4-14. Although the high-stress point is indicated it is not visible in this view and the locations of high stress are found on the contact positions these can be found at the centre of the former where it is in contact with the specimen with stresses of up to 1609 MPa. This is acceptable stress for tool steel of less than 2GPa.

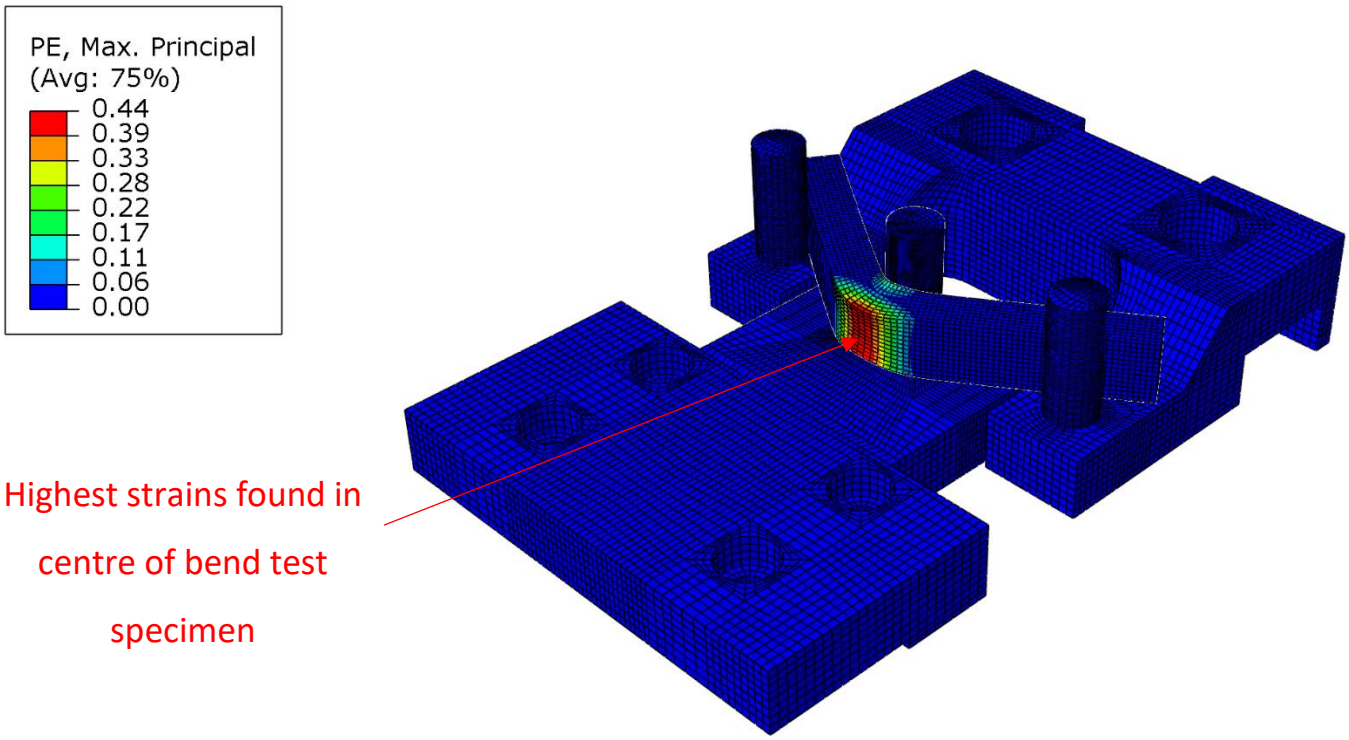


*Figure 4-15: Isometric view of bend test at 10.05mm of displacement, displaying the maximum principal strain on the parts.*

The bend test specimen undergoes high strain with the region in tension getting an elastic-plastic strain of up to 0.44 in Figure 4-15. The specimen deforms plastically so is less stiff than the tooling since it uses the data from Table 4-2.

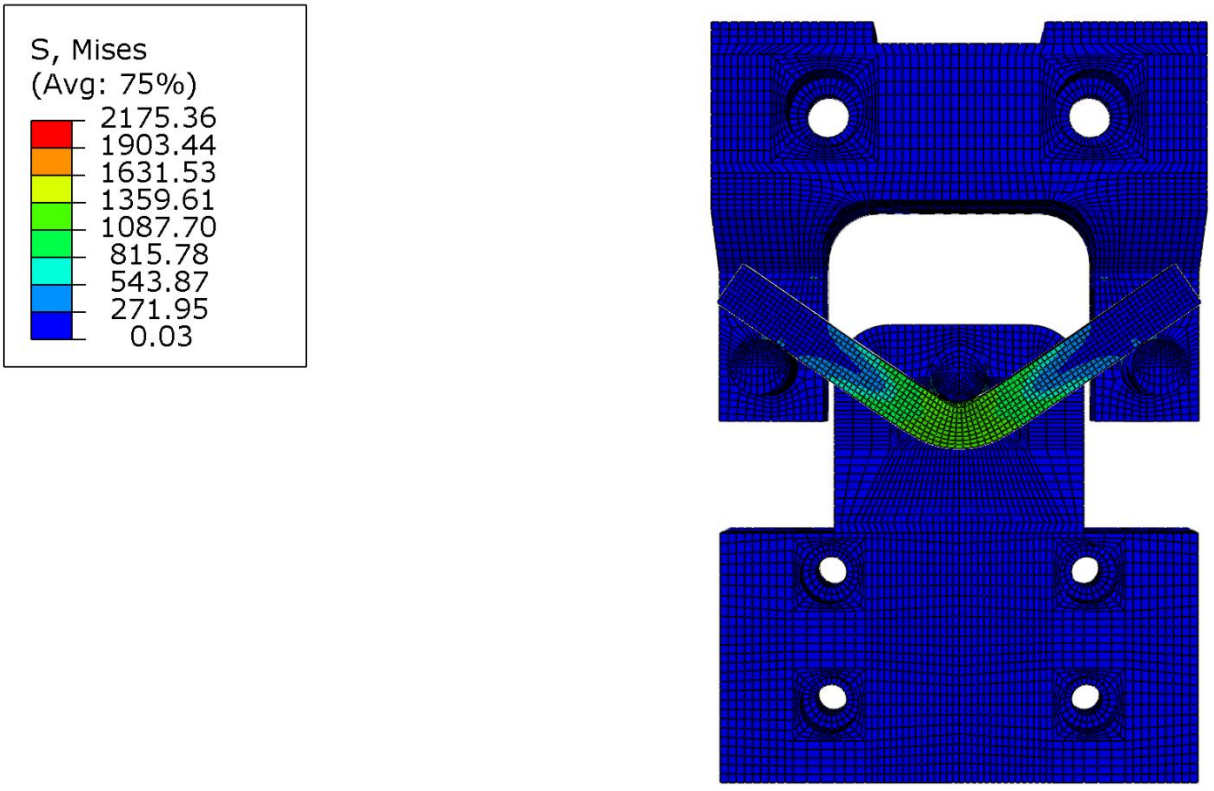


*Figure 4-16: Top view of bend test at 10.05mm of displacement, displaying the von mises stress on the parts.*

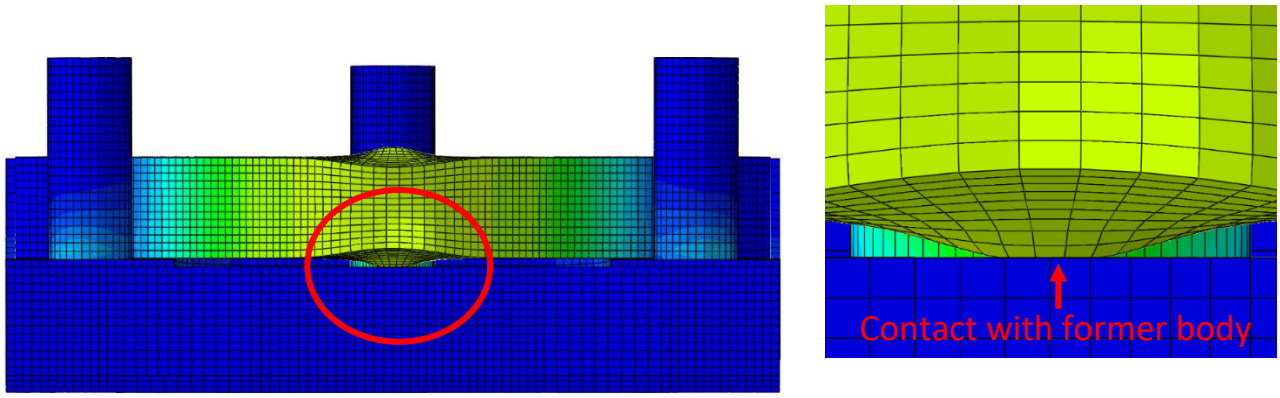


*Figure 4-17: Front view of bend test at 10.05mm of displacement, displaying the von mises stress on the parts with left, an overview of the parts and right, zoomed-in view at the specimen making contact with the tooling.*

When viewed from the front in Figure 4-17, it is shown that at the full displacement of 10.05mm due to anticlastic flow the compression region expands in thickness. This makes contact with the body of the former.

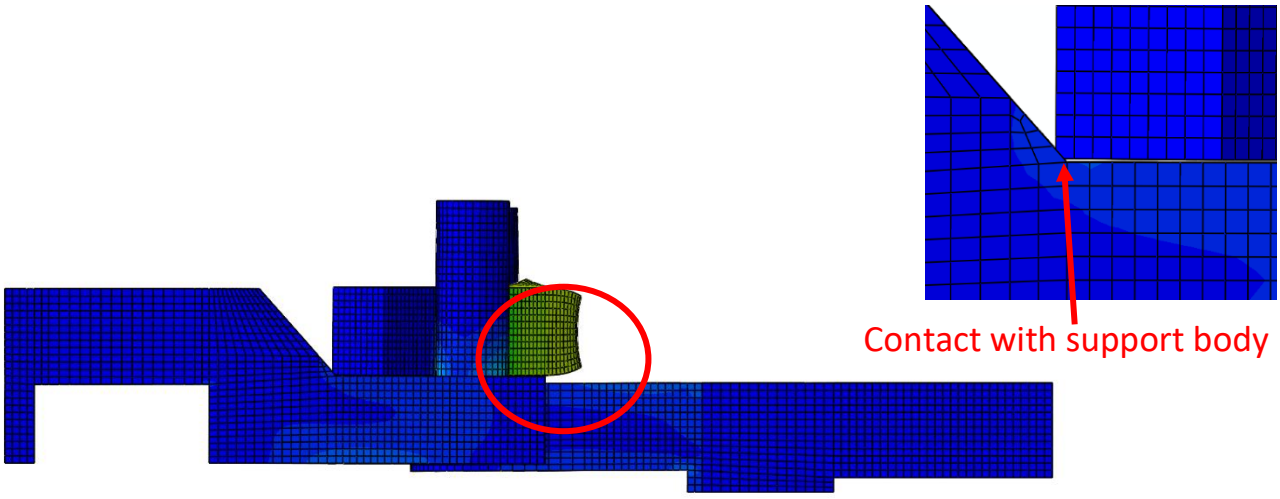


*Figure 4-18: Side view of bend test at 10.05mm of displacement, displaying the von mises stress on the parts with a zoomed-in view of the specimen making contact with the support.*

Another pair of contact points were found in the FEM in Figure 4-18 at the leg of the bend test specimen at maximum displacement. This is due to the thickness and length of the specimen and the geometry of the support body having the slope too close to the specimen.

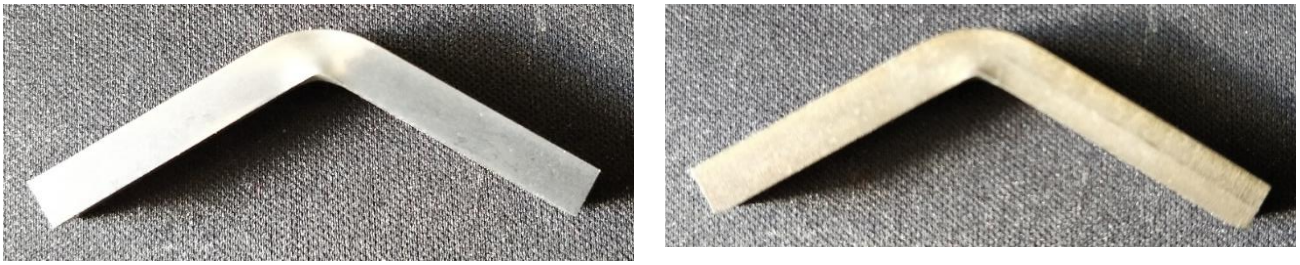

*Figure 4-19: images of a 4.25mm thickness bend test specimen post-test at 10mm displacement, left; the horizontal face of the bend test specimen, polished and etched, right, the horizontal underside of the bend test specimen, rough from EDM machining.*

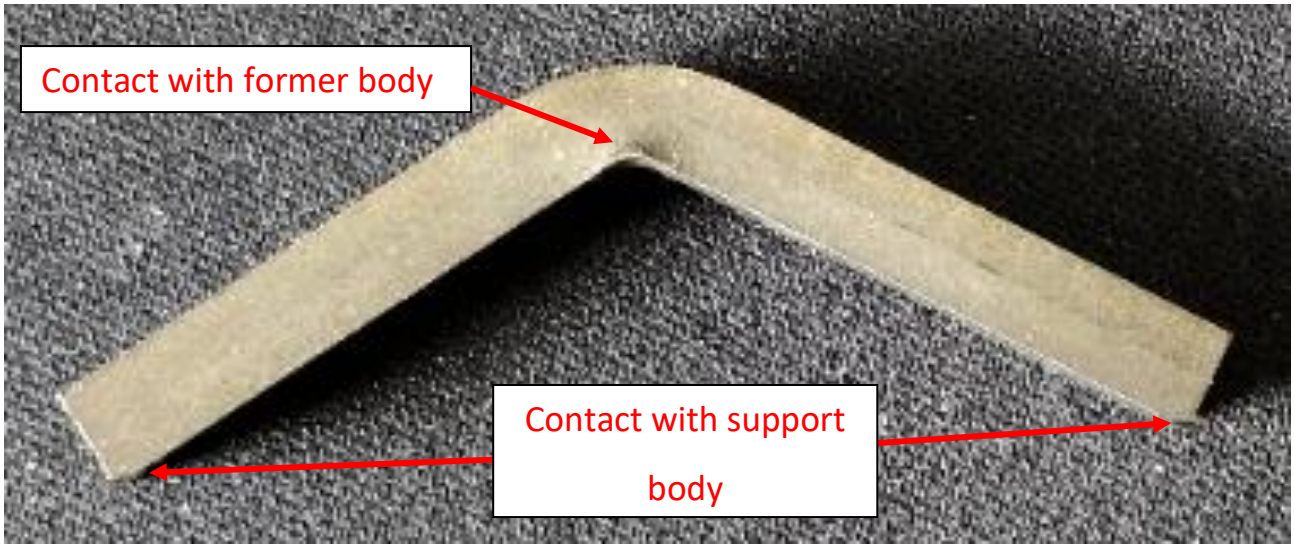


*Figure 4-20: underside side profile showing the points that the support and former bodies have interacted with the specimens.*

By performing FEM and experimental bend tests the contact points can be compared to those found in modelling. The points of contact found in Figure 4-17 and Figure 4-18 are replicated in the sample in Figure 4-20. This combined with the strong correlation with the force-displacement graph in Figure 4-12 shows the tooling dimensions and FEM produced were accurate and as such was used in a similar approach to design new tooling. Before this, an analysis of the stiffness and stress is performed to understand the stresses and set suitable limits on future designs.

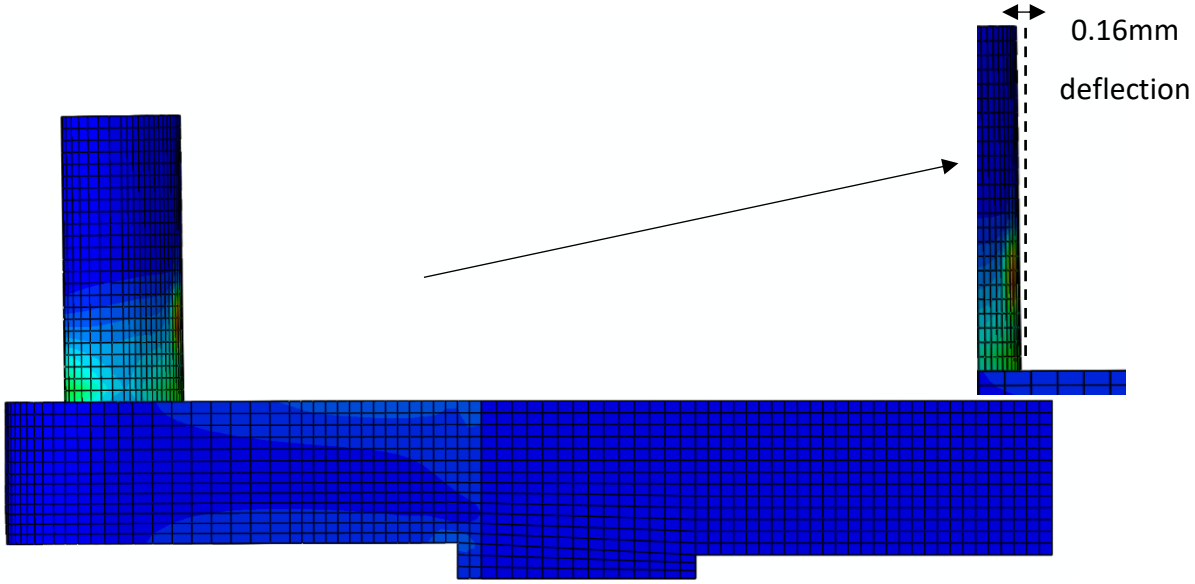


*Figure 4-21: Side profile of the former at 10.05mm displacement, with the zoomed-in region showing the deflection measurement.*

The Deben tooling used a tension setting causing the tooling to deflect under load. The measured deflection at the top of the pin relative to the bottom was found to be 0.16mm.

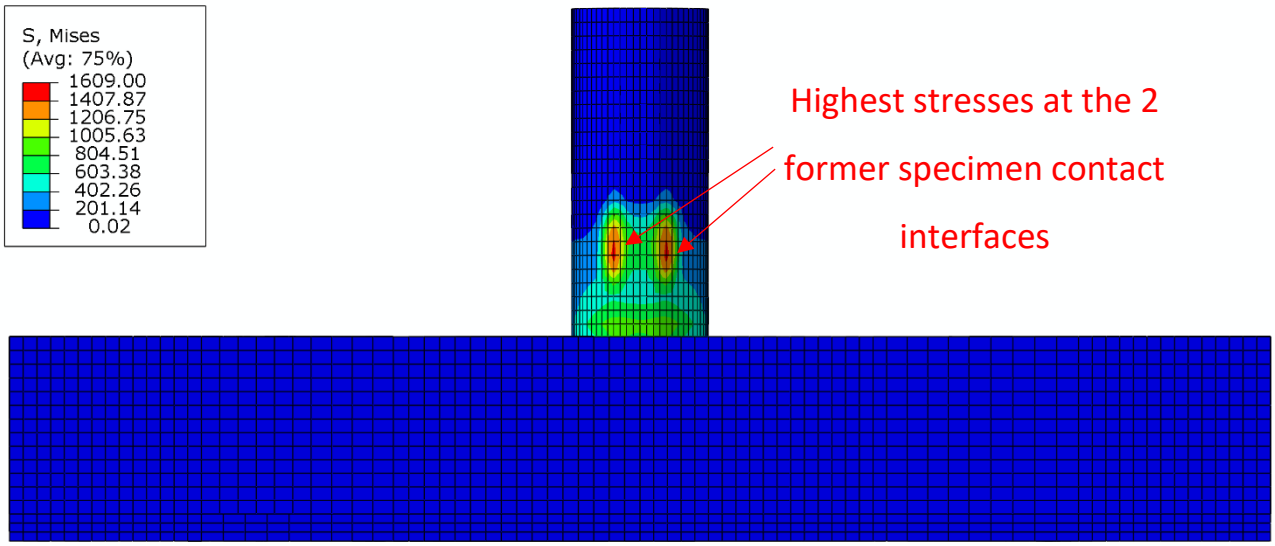


*Figure 4-22: Front view of bend test former at 10.05mm displacement with the bend test specimen removed.*

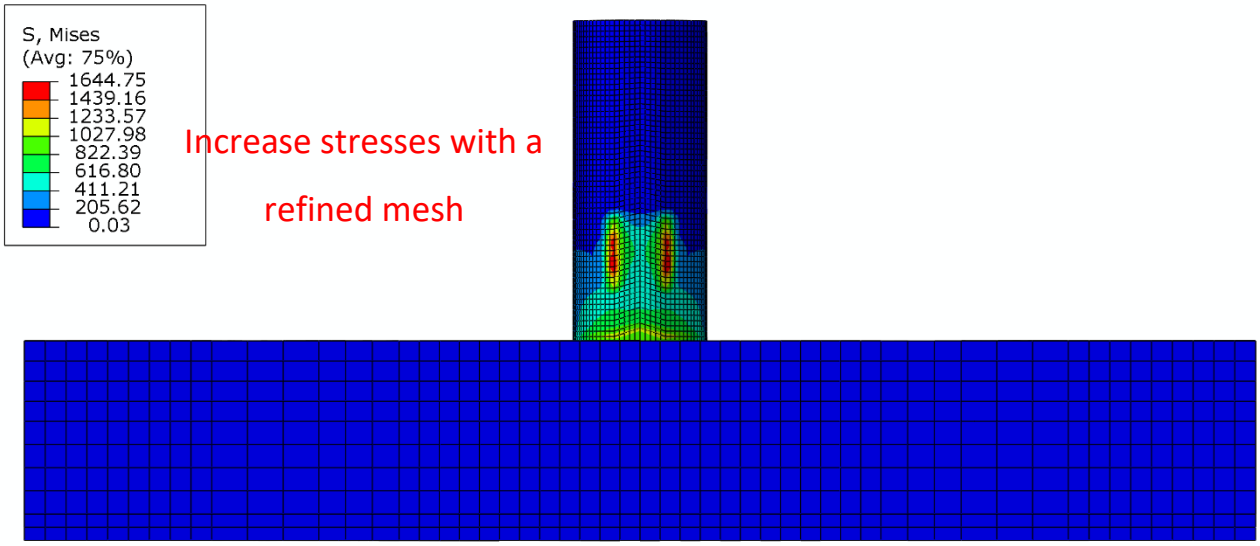


*Figure 4-23: Front view of bend test former at 10.05mm displacement with the bend test specimen removed with a refined surface of 0.25mm in size.*

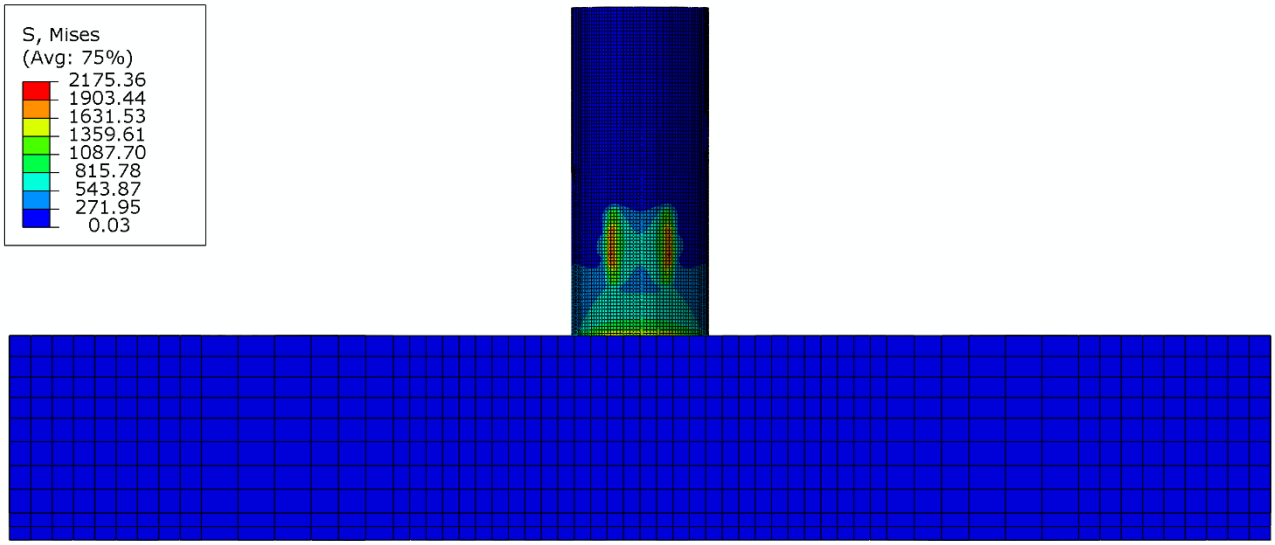

*Figure 4-24: Front view of bend test former at 10.05mm displacement with the bend test specimen removed with a refined surface of 0.125mm in size.*

Through modelling analysis, the peak stresses are achieved on the tooling through bending and while the bending occurs the point of contact starts at the centre of the specimen then bifurcates into two contact patches on the centre line of the former. This generates 4-points of contact bearing a closer resemblance to a 4-point bending process. The centre section of the bend then has a smaller radius to the pin. The highest stresses are found at the end of the test when friction or sliding from contact increases the localised stresses. By using a refined mesh localised on the pin contact surface the stress is localised and increases with the reduced mesh sizes. This didn't occur linearly with smaller mesh sizing as shown in Figure 4-22, Figure 4-23 and Figure 4-24. While the mesh of the surface was refined a similar refinement was not performed on the bend test specimen to avoid increasing the computation time. A study of the stiffness of the former was performed, by analysing the angle of the former pin as it was loaded by the 4.25mm thickness specimen. This found that the angle of deflection is $1.93 \times 10^{-4}$ °/N.

This modelling has provided a basis to investigate new bend designs using a design imported from Solidworks and using the same methods outlined in this chapter.

### 4.1.2 Revised tooling geometry

Performing bend testing the bend test tooling geometry was found to be a limiting factor. As previously discussed, the radius of the tooling and thickness of the specimen was reported to be the primary variables in the bendability of metals as known as the r/T ratio with a lower ratio without specimen failure being preferential. Therefore, the tooling can be devised to either maximise specimen thickness, reduce the radius or compromise both. As such an FEA study was performed with different radius tooling to assess the viability of changing bending radii.

The first simulation used was a bending simulation with 10mm diameter tooling. The same width between the supports of 37mm was used as found in the Deben tooling. The same specimen thickness of 4.25mm was used as the loading is expected to be similar to that used with a 5mm diameter. The change in tooling dimensions resulted in an increase to the r/T ratio to 1.18 but brings the geometry closer to conforming with the ASTM standards with the spacing intending to be between 30.6mm and 34.9mm.

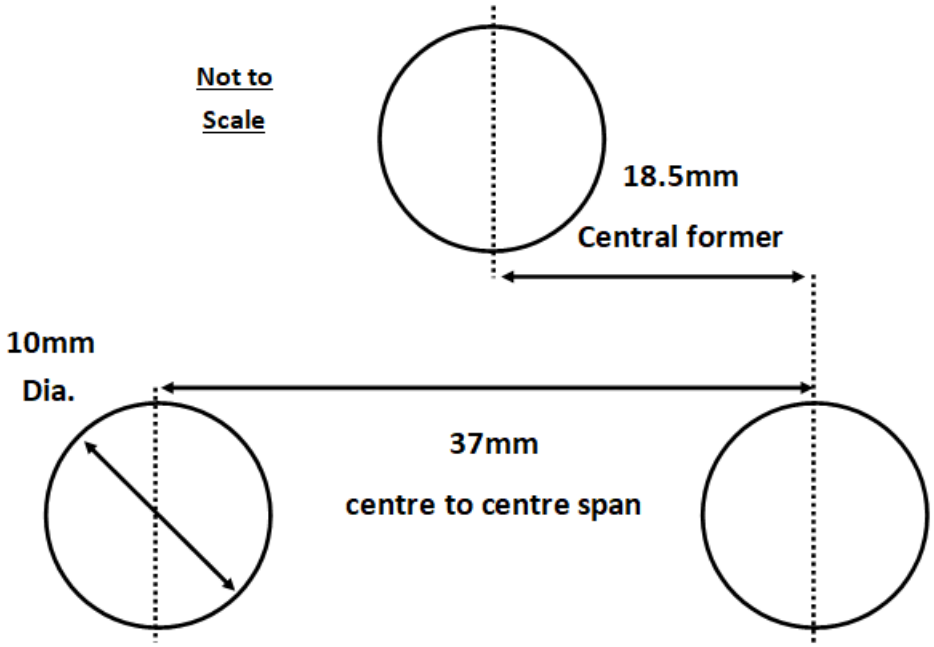


*Figure 4-25: The bend test geometry used in simulations and validated in the Tinius Olsen tensile tester.*

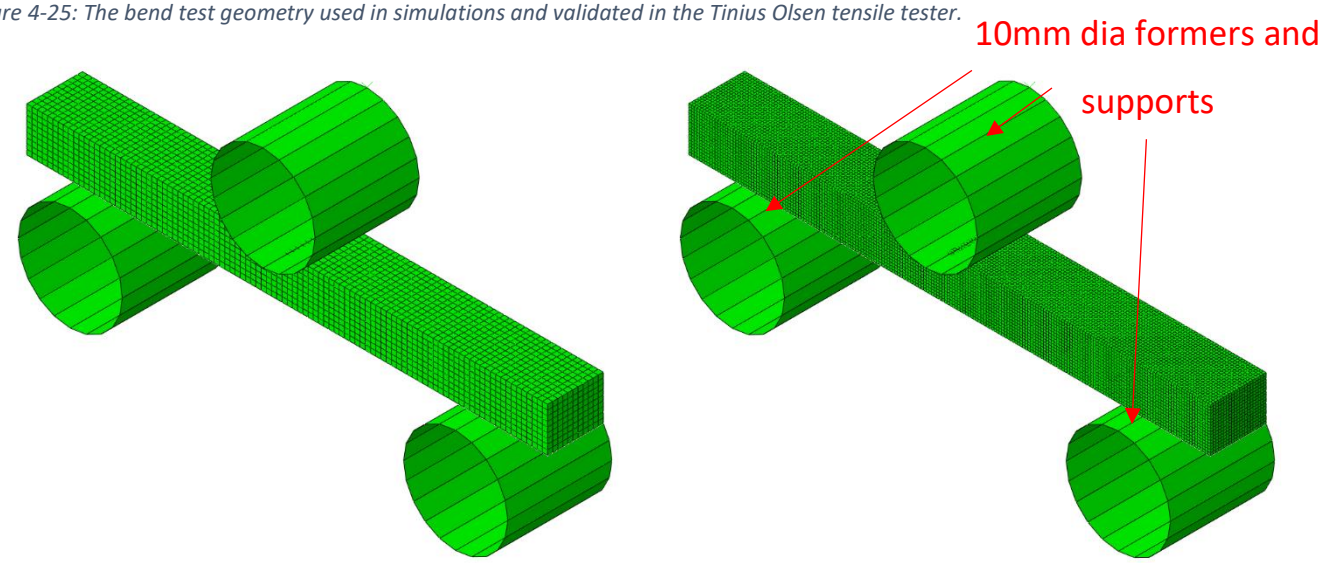


*Figure 4-26: mesh of the 10mm diameter tooling with the 4.25mm thickness, left: 0.5mm mesh, right 0.25mm mesh*

To lower the computational load the rigid tooling was modelled with analytical geometry. The material and meshing parameters are identical as used in the specimen in simulating the Deben tooling.

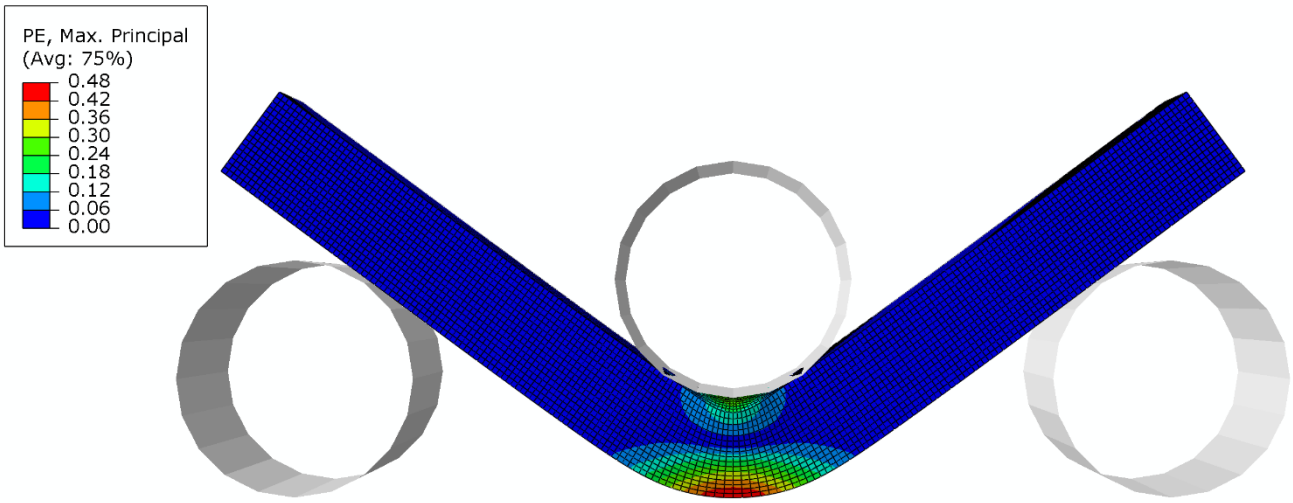


*Figure 4-27: Side view of 10mm diameter tooling with 10.05mm displacement, 0.25mm mesh, maximum principal strain.*

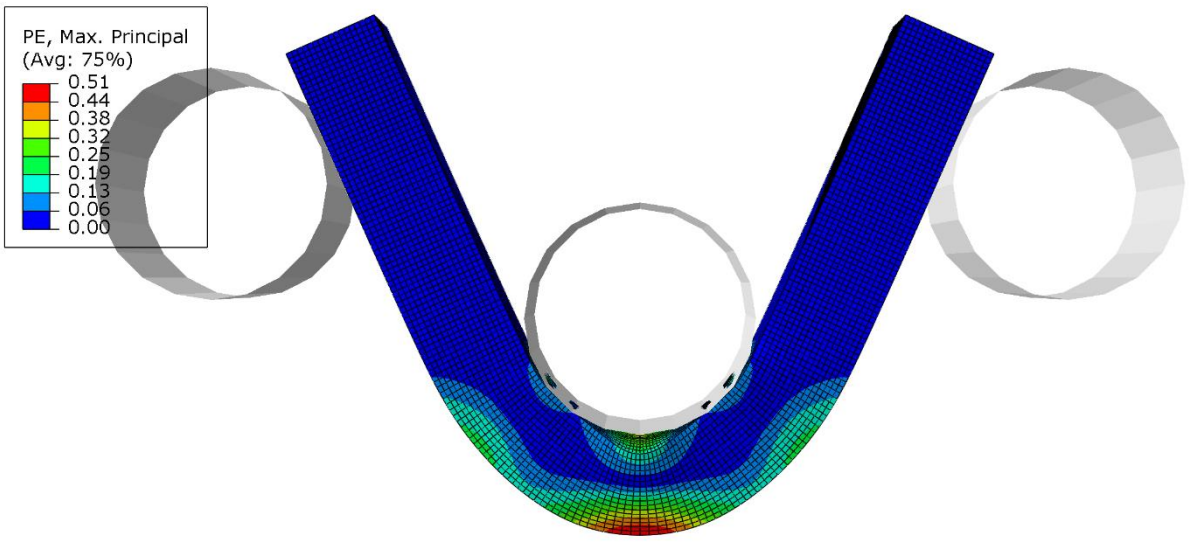


*Figure 4-28: Side view of 10mm diameter tooling with 20.05mm displacement, 0.25mm mesh, maximum principal strain.*

To replicate the FEM bend test the 10mm diameter tooling as shown in the right image in Figure 3-34 was used to perform a 3 point bend test with the Tinius Olsen 25KN tensile tester. This served as a validation for the simulation.

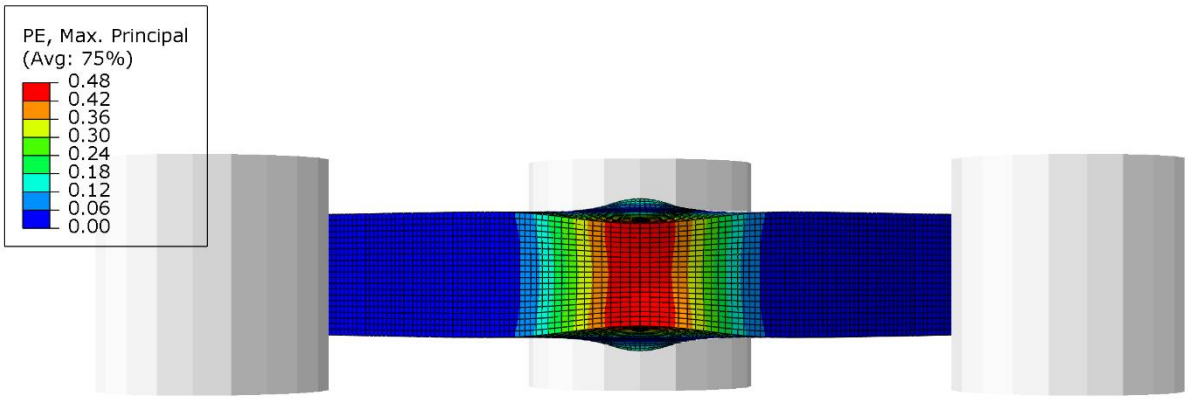


*Figure 4-29: Bottom view of 10mm diameter tooling with 10.05mm displacement, 0.25mm mesh, maximum principal strain.*

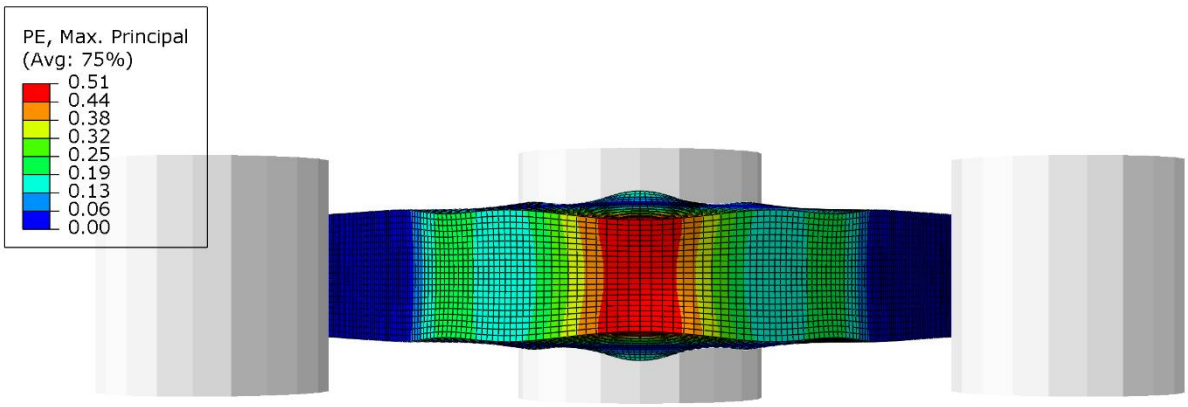


*Figure 4-30: Bottom view of 10mm diameter tooling with 20.05mm displacement, 0.25mm mesh, maximum principal strain.*

When deforming the specimen over a 20mm displacement the strain development of peak strain is not linear. It increases to a near-maximum at 10mm displacement. This occurs as a central bent region is promoted with high stress in this region as shown in Figure 4-31. As the displacement increases above 10mm the stress intensifies away from the centre of the specimen and strain is found to increase in these regions.

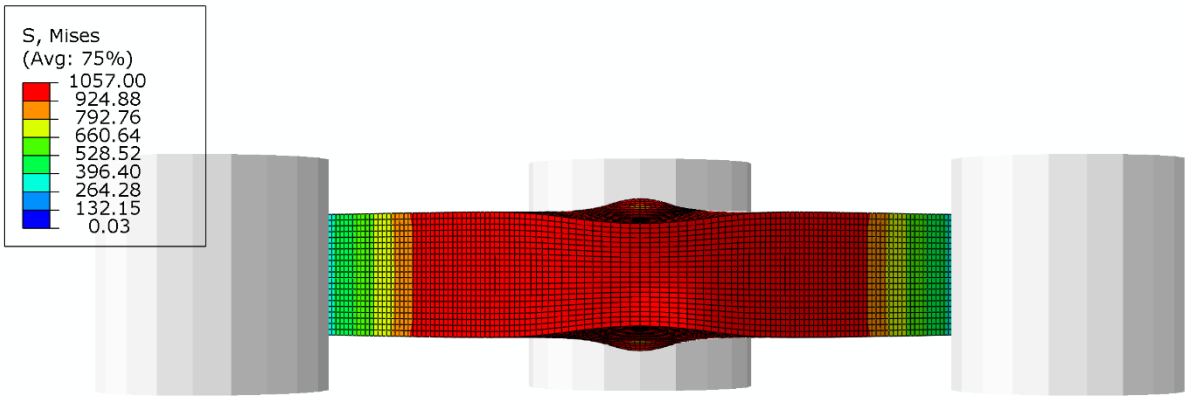


*Figure 4-31: Bottom view of 10mm diameter tooling with 10.05mm displacement, 0.25mm mesh, Von Mises Stress (MPa).*

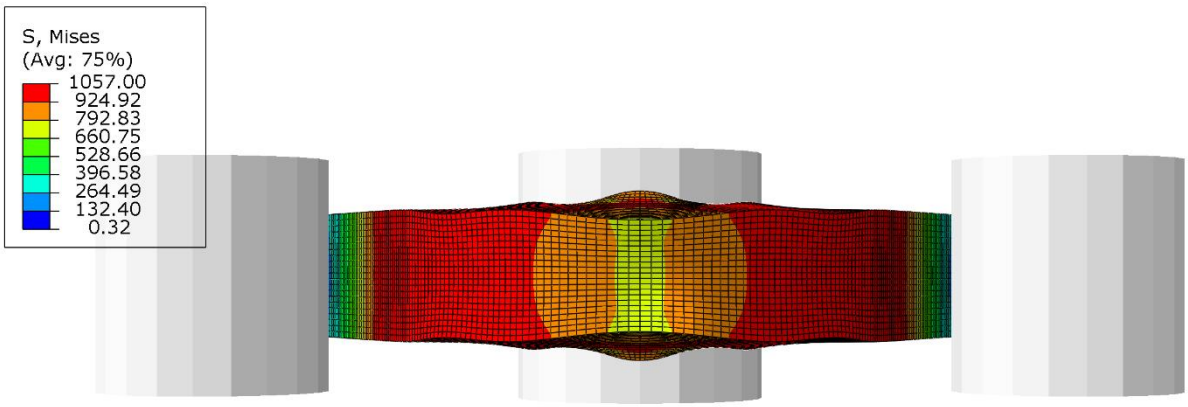


*Figure 4-32: Bottom view of 10mm diameter tooling with 20.05mm displacement, 0.25mm mesh, Von Mises Stress (MPa).*

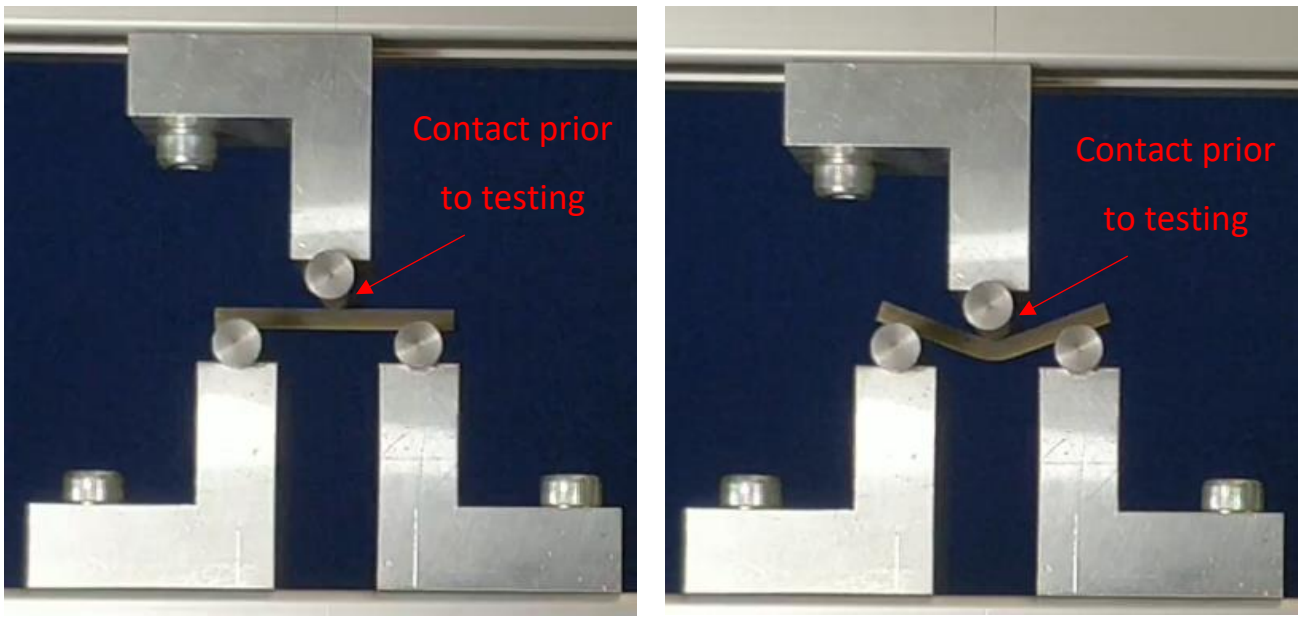

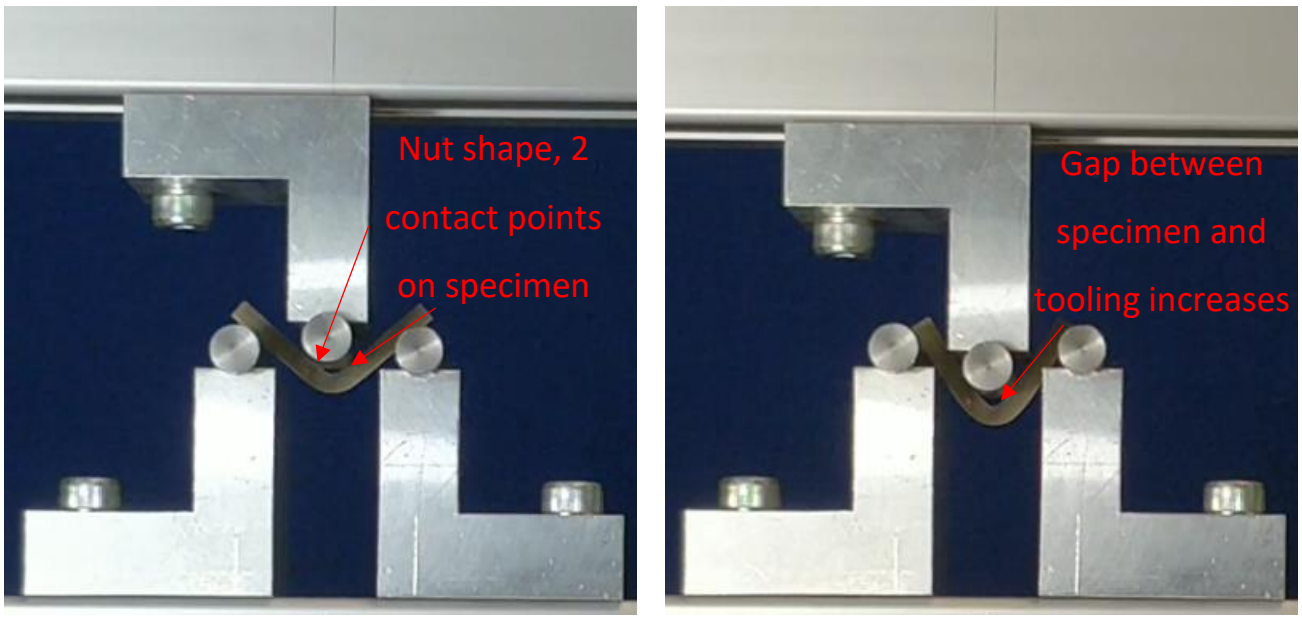


*Figure 4-33: Images captured while recording the 10mm diameter tooling bend test, top left; 0mm displacement, top right; 6mm, bottom left; 12mm and bottom right; 18mm.*

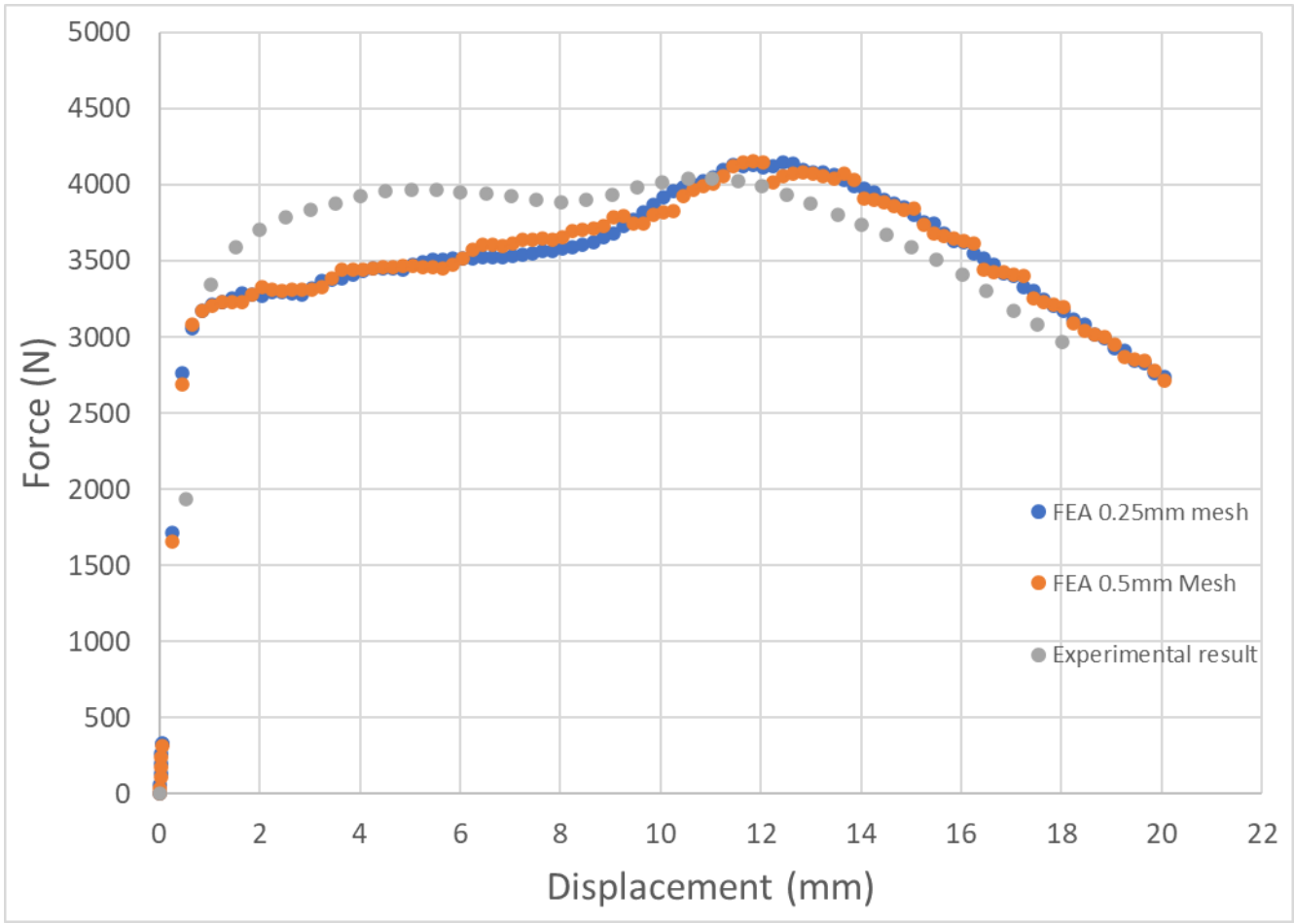


*Figure 4-34: 10mm tooling bend test force-displacement graph with 2 FEA results with a 0.25mm and 0.5mm global mesh on the specimen and the experimental result*

The experimental results and simulations are not found to correlate as strongly as found with the 5mm diameter tooling as shown in Figure 4-34. The profile of both the simulations and experiments show a loading phase and then peak force after 10-12mm of displacement.

The discrepancies between the model and the results are likely due to the basic material model derived from tensile test results. The larger radius tooling cause a larger top surface region to deform plastically and as such, the difference between the loading scenarios in bending and tensile testing was too significant. The second peak was far more significant in the FEM. As previously shown in Figure 4-13, the friction coefficient is found to affect the loading in the later stages of bending. The friction coefficient may be incorrect in this instance as the tooling may have had some residual lubrication as is the correct operation in most uses of 3 point bending.

### 4.1.3 2.5mm diameter tooling

To study the effect of using a smaller pin diameter and geometry that conformed with the ASTM standards a new specimen geometry was developed. To have both a reduced pin size to decrease the $r_i/T$ ratio and to reduce the specimen size. This assisted in conforming with the ASTM standards with a smaller diameter tooling a smaller span being required.

This also allowed a thinner specimen to be used. This was beneficial as the 17DF4/1 material delivered was 3mm thick. As such having a thinner specimen to lower bending loads was required. Using this approach, a new tooling and specimen geometry was developed to meet the ASTM design specifications.

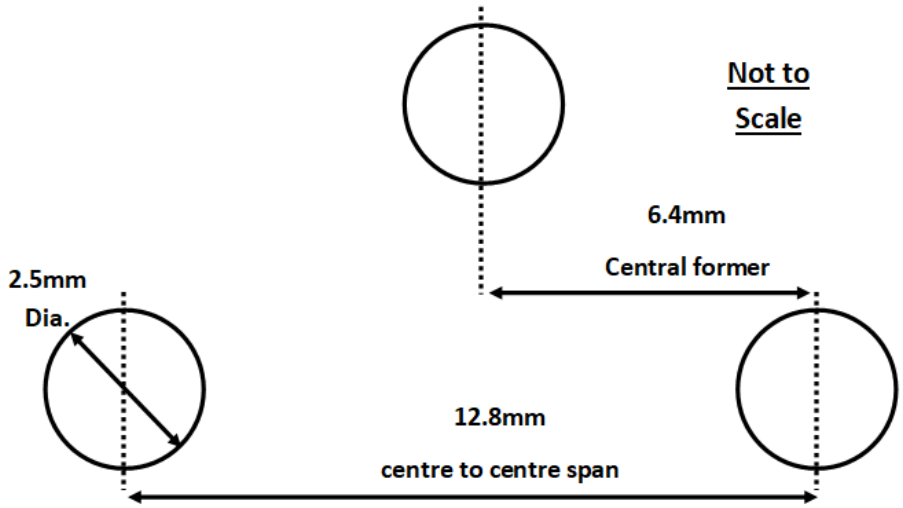


*Figure 4-35: 2.5mm dia. bend test tooling geometry.*

This bend test geometry was then processed through a series of modelling approaches. Initially, the simulations were run with rigid tooling as shown in Figure 4-36. This is primarily used to analyse the strain on the specimen and have the best example of sample plasticity. Using a mesh for both the tooling and specimen of size 0.25mm. The same approach to setting contact and interactions were used as shown in Figure 4-10 where the tooling is set as the master and specimen slave. The same coulomb penalty friction of 0.3 was applied with the damping factor applied to the first 0.05mm of

displacement. This was removed for the subsequent step with the 10mm displacement. The results presented are only at the second step with no damping turned on to avoid the influence of damping on the results.

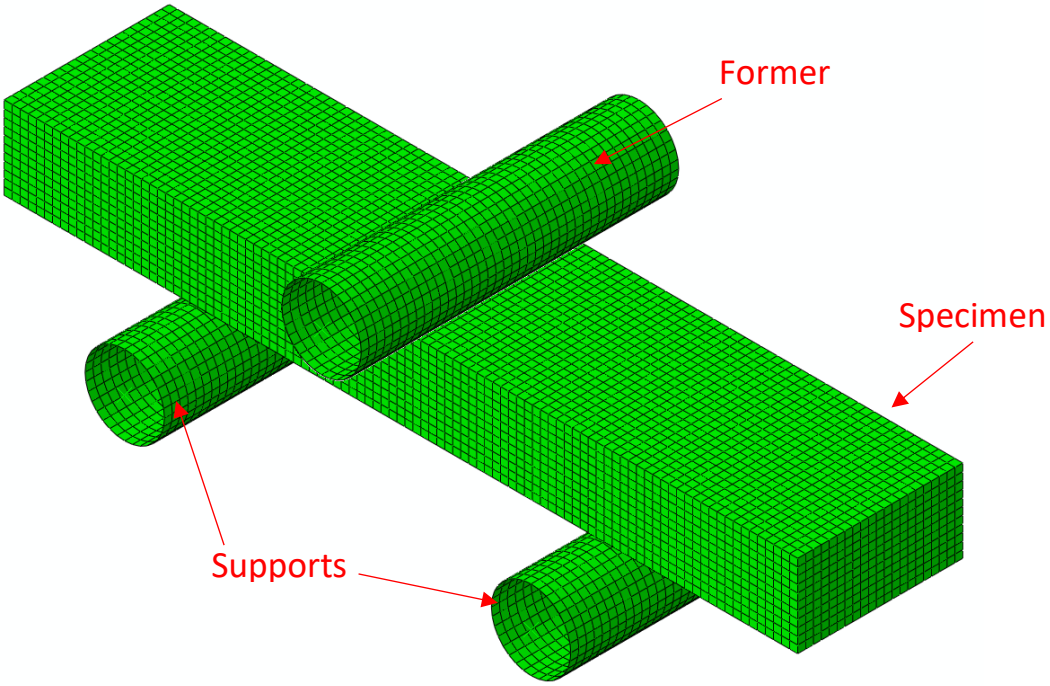


*Figure 4-36: Isometric view of mesh for the 2.5mm diameter tooling with a 12.8mm centre to centre spacing. The specimen is 2.4mm thick and 5.0mm wide.*

To ensure the tooling and specimen was compatible with the Deben horizontal bend test module the bending loads had to remain under 5KN. As such a range of specimens with geometries of 2.4mm, 2.5mm and 2.7mm thickness while being 4.8mm, 5.0mm and 5.0mm wide respectively were simulated in bending with the tooling geometry as shown in Figure 4-36. These were simulated using material data from Table 4-1 and Table 4-2 and run with the same mesh size. These resulted in the force-displacement curves in Figure 4-37. The 2.7mm thick specimen reached 5829N in load and so was not suitable for this design. The 2.5mm and 2.4mm thickness specimens were both under 5000N at 4861N and 4158N respectively. Due to how close the 2.5mm thickness specimen load was to 5000N it was also considered unsuitable for the Deben module. The 2.4mm thick specimen used with the 12.8mm centre to centre support span and 2.5mm diameter former is suitable for the ASTM and BSI [4], [5] standard bend test geometry in Figure 2-11.

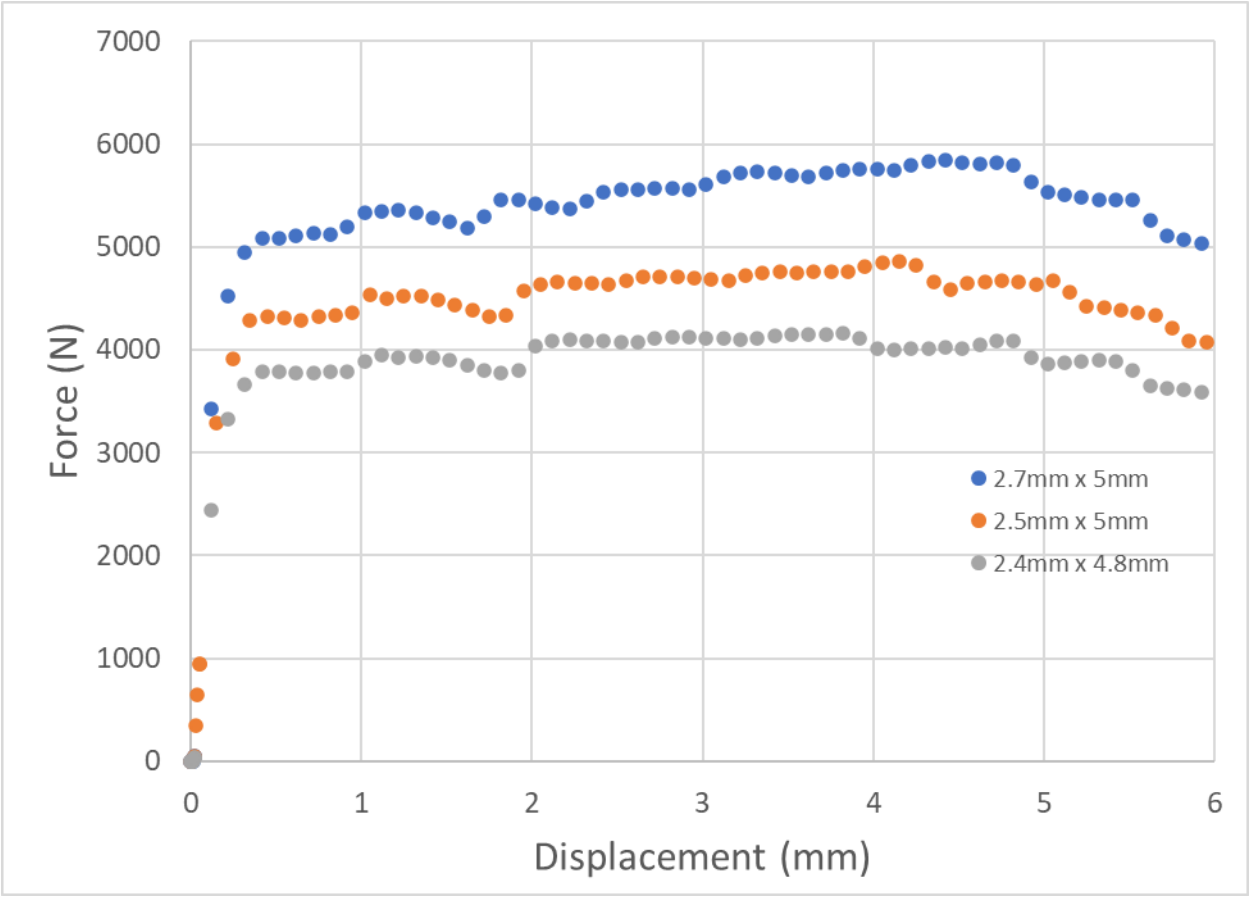


*Figure 4-37: Force-displacement graphs for the tooling geometry as shown in Figure 4-35 for different specimen geometries.*

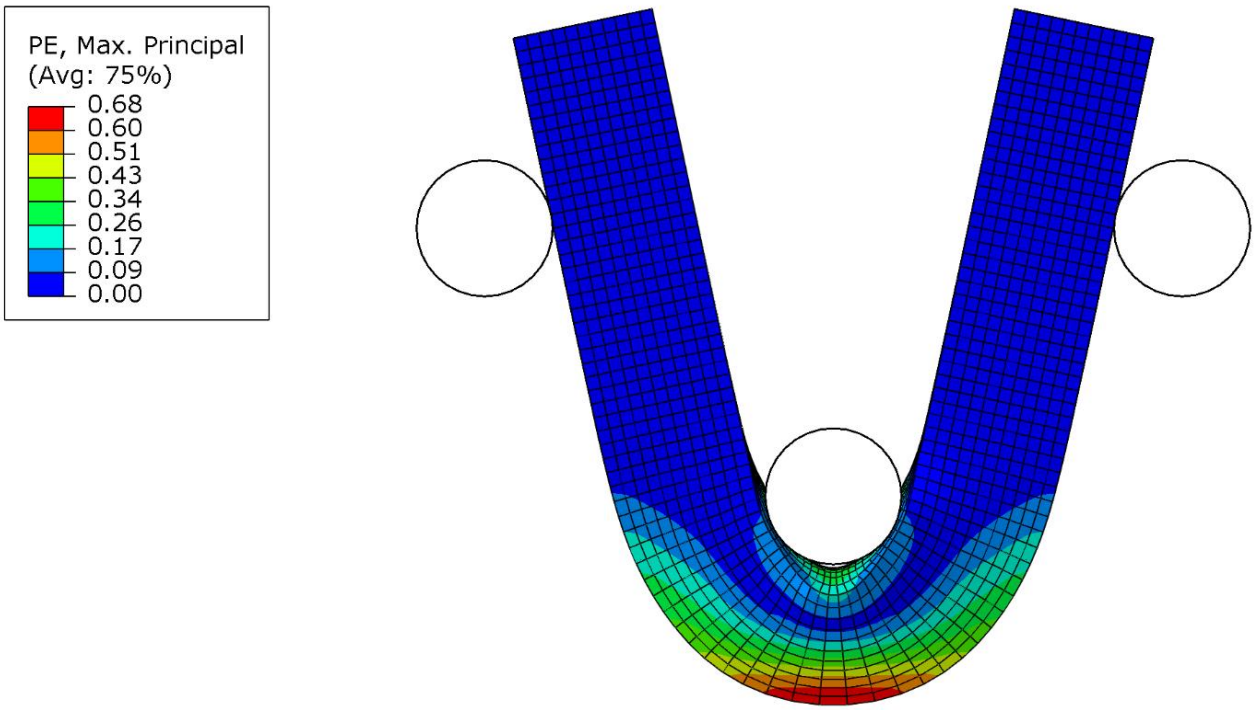


*Figure 4-38: side view of bend test the 2.5mm diameter tooling, 10,05mm displacement, 0.25mm mesh, displaying the maximum principal plastic strain.*

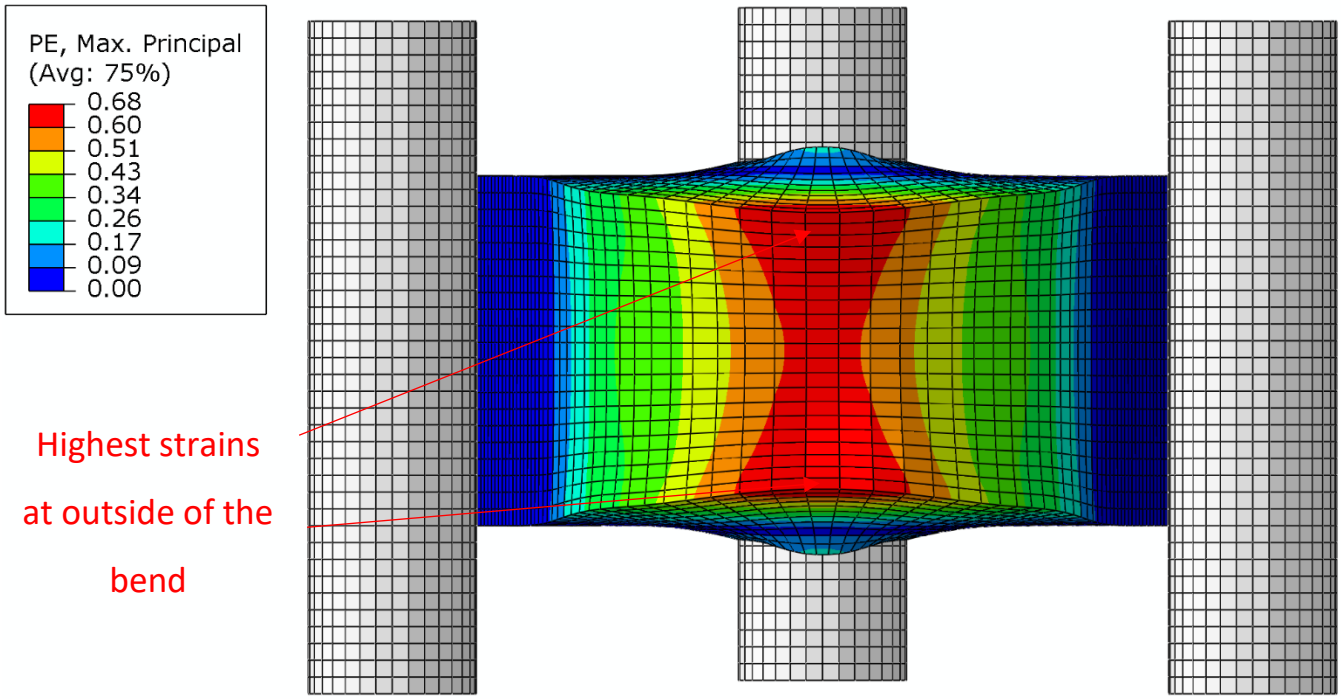


*Figure 4-39: Bottom view of bend test the 2.5mm diameter tooling, 10,05mm displacement, 0.25mm mesh, displaying the maximum principal plastic strain.*

Strain is found to be at a maximum of 0.688 at the outside edges of the specimen due to the anticlastic profile. The centre of the specimen is compressed, and the sides flare out. This effectively increases the thickness of the specimen at the edges and the distance from the neutral bending plane for these regions, increasing the strain.

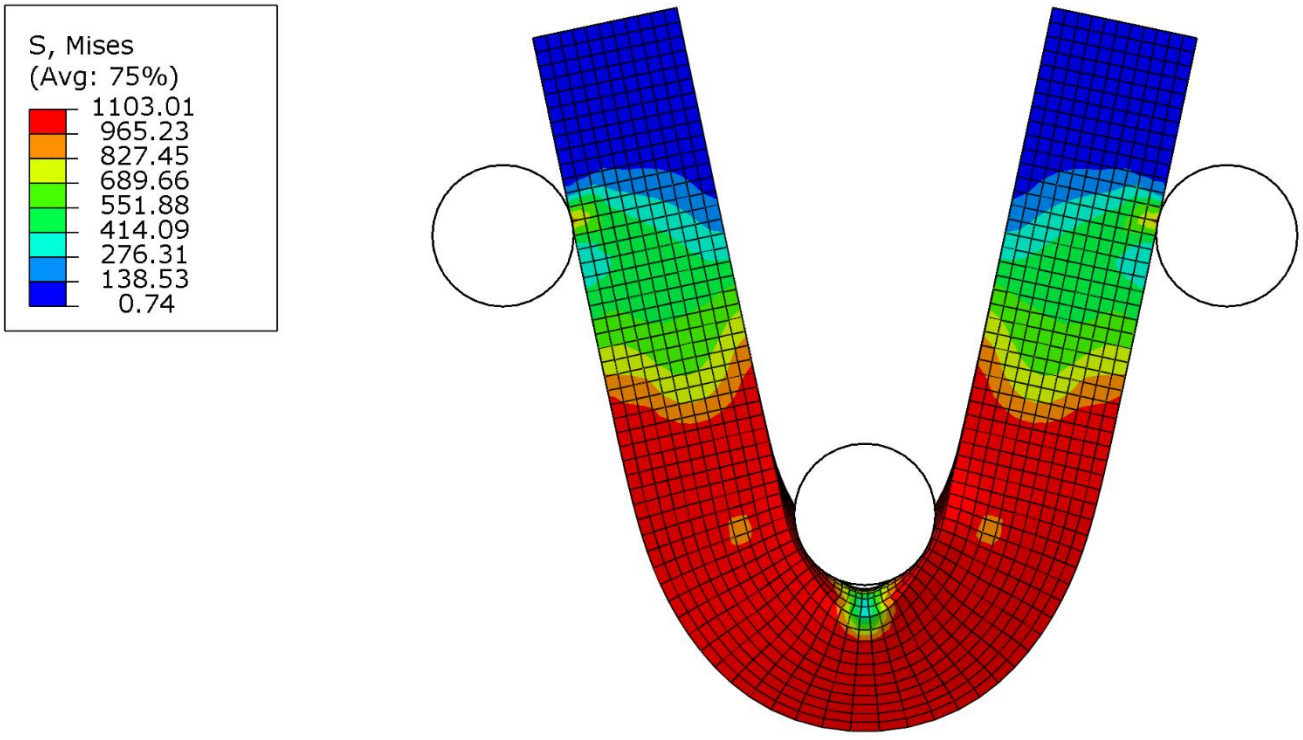


*Figure 4-40: side view of bend test the 2.5mm diameter tooling, 10,05mm displacement, 0.25mm mesh, displaying the Von Mises Stress.*

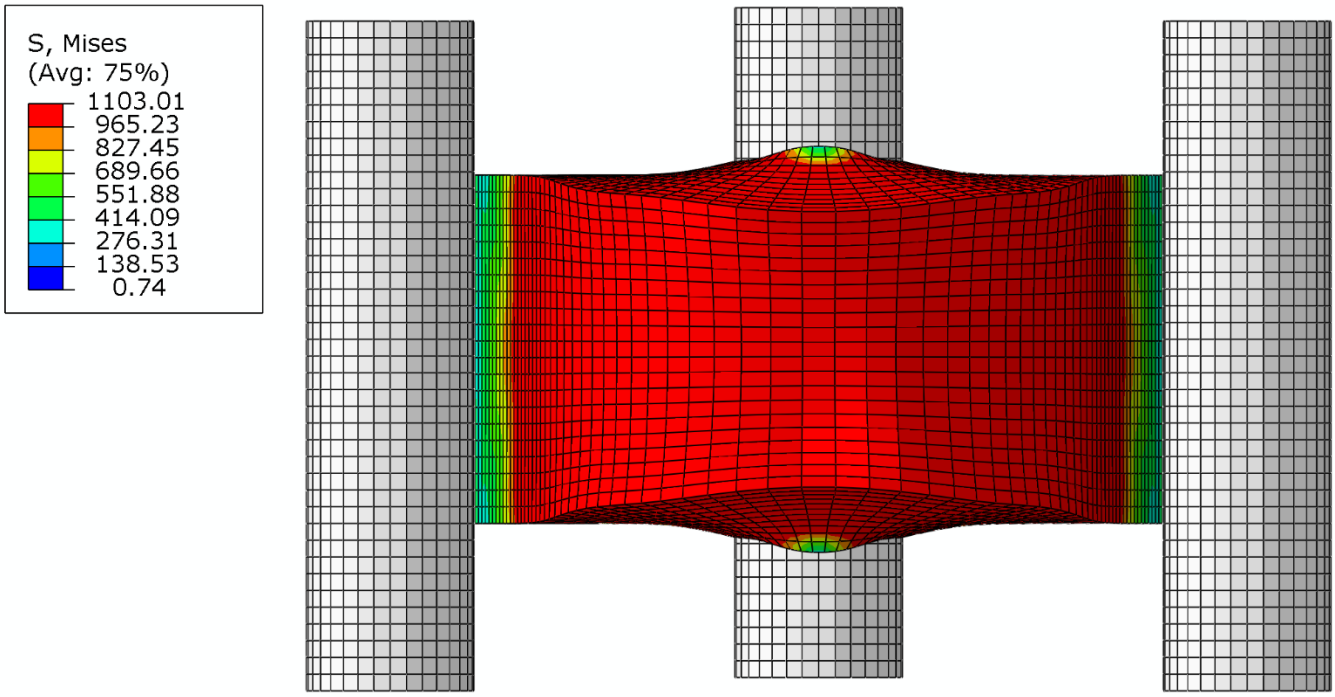


*Figure 4-41: Bottom view of bend test the 2.5mm diameter tooling, 10,05mm displacement, 0.25mm mesh, displaying the Von Mises Stress.*

To simulate this bend tests were simulated with 10mm, 5mm and 2.5mm dia tooling. Both 10mm and 5mm tooling bend tests were replicated with experiments to act as validation for the models. By using the same material model in all the simulations analysis of the strain generated in bending was developed.

The simulations found that the bend tests were split into 3 phases:

1. Loading, largely elastic transitioning into plastic deformation occurs as the specimen is loaded until it begins to bend.
2. The specimen remains in contact with the former and plastically deforms around the former. The specimen is held static as the friction on the supports stops the specimen from moving. The specimen undergoes a vast majority of plastic strain at this point
3. As the specimen bends the contact patch on the support moves. At a specific angle, likely influenced by the force and friction coefficient the specimen begins to slide on the support pins. This results in a very small increase in the peak plastic strain values but can develop new areas of strain always from the maximum strain point.

The first tooling design was the same design rationale as used by Deben in their tooling. This would have a 2.5mm diameter pin welded onto the tooling body and the module would be set in tension mode. To simplify this the pin was simply modelled as elastic steel with the boundary conditions to replicate the tooling body. The contact settings are set up with a friction coefficient of 0.3. The model is simplified to study tooling stiffness and specimen strain.

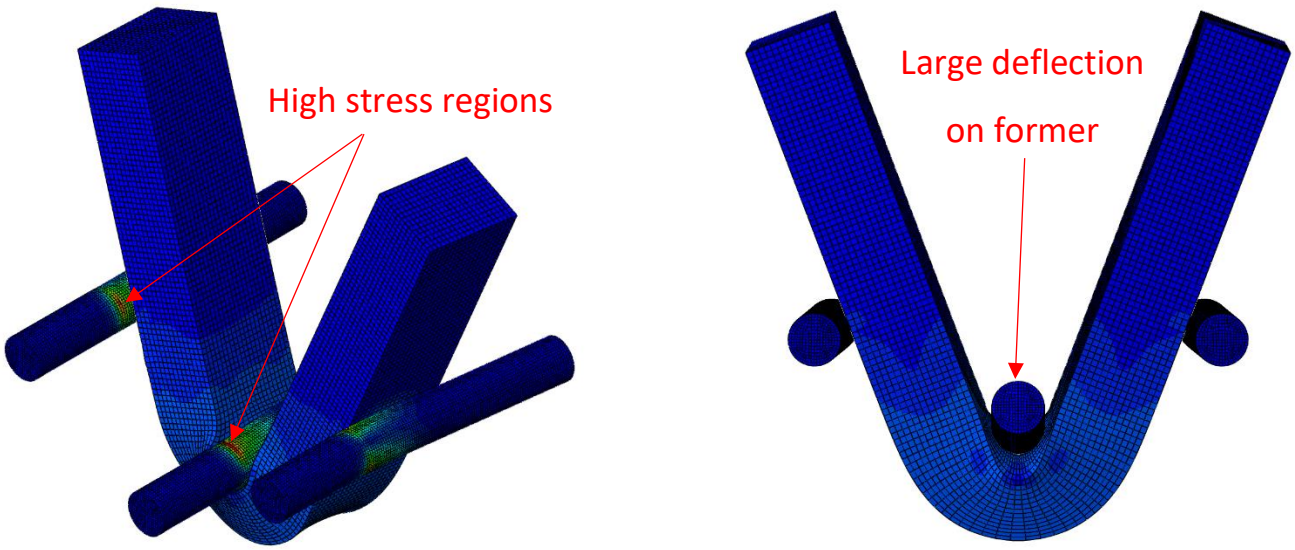


*Figure 4-42: isometric view of elastic 2.5mm pin design at 10.05mm displacement with Von Mises in MPa*

As shown in Figure 4-42 when at full displacement due to the boundary conditions replicating the effect of being welded into the tooling body the stress is localised in the tooling forming a hinge on the outside with compression in view. The highest stress was found at 7.02mm displacement of 22,000MPa, thus far exceeding any suitable material ability to retain elasticity. The largest pin deflection was found to also be at 7.02mm displacement. This was measured as 1.95mm and 8° angle when comparing the fixed end compared to the bent end of the pin.

Additionally, as shown in the right image in Figure 4-42 when viewed from the side view, the same as that observed from the SEM when using the Deben horizontal bend and tensile test module. the tool deflection is found to be significant enough to change the formation of strain in the bend test specimen. These examples show that using the same design with a 2.5mm diameter pin as the Deben tooling is not suitable for this test. Therefore, a new tooling design was required to increase tooling rigidity and reduce the stresses to find a suitable material to remain in elastic deformation when under load.

When comparing the results, it was decided to use a smaller radius for the following reasons:

- The bend test results in a higher strain of around 50% higher than the Deben tooling
- It enabled smaller specimens, resulting in less expensive sample production while using less sample material.
- The bend is smaller and as such a better overview of the bend can be produced by using the Camscan S2 SEM on its minimum magnification of 20x.
- Smaller radii reduce the need to have a large displacement when conforming with the ASTM bend test geometry standards. The module only has 10mm of displacement, so this problem is resolved.

- The smaller specimen size allowed different sample preparation methods to be used. This enabled cheaper automated sample preparation with higher sample quality.

This also brings the following problems:

- The smaller radii increase contact stresses.
- Smaller radii mean that there is less material to resist bending forces if using the same design as the original Deben bend test.

The benefits of using a smaller radius outweighed the problems, so a design for using 2.5mm diameter tooling was developed and used the ASTM standard geometry with a new design to retain improved stiffness compared to the Deben design.

## 4.2 First-generation 2.5mm diameter tooling

New tooling provided a benefit, but a holistic approach was taken to assess design improvements to the tooling and specimen design. With tooling and specimen design being optimised together a new design approach was used. Studying bending loads, specimen geometry and ASTM guidance a specimen of 2.6mm thickness and 5.2mm width or twice thickness was used with a length of 25mm. 25mm was used as it was ample to span the 12.8mm gap in bending and allowed the specimen to be positioned precisely centred during the experiment but without the legs striking tooling. An additional benefit is the specimen was small enough to fit in the castings of size 1 1/4”, this then allows the specimens to be prepared using the automated sample preparation using an AutoMet. Due to the increased stresses, the simulation in Figure 4-38 has shown that copying the design approach from the Deben tooling is not a suitable approach. This would not have a necessary rigidity for bend testing as shown in Figure 4-42. Therefore, a new design was developed which incorporated the design of smaller specimens with a length of only 25mm, half of the previous design and a reduced thickness to allow the tests to be performed at a load below 5KN to operate in the Deben module.

To improve stiffness the pin was reprofiled to elongate it and widen it away from the contact surface. This was to increase its second moment of area to resist the stresses from bending. These were developed as a series of prototype designs that were simulated and developed until a suitable design was developed that was manufactured within the Sheffield University Mechanical Engineering Workshop and withstand the bending loads. The tensile test approach was retained to be confident of the specimen fitment and keep the design consistent with the Deben tooling. To improve the rigidity of the tooling each part was designed to be produced from a single piece of steel.

Due to the higher stresses expected from having a smaller contact area a high strength material is required. To achieve this D2 tool steel was used as it is machinable, strong and with high wear and abrasion resistance. It is often used in press tooling for these properties as well as having a high compression strength, so was an ideal material for this application. Heat treatment was considered to increase the strength further but with the varied thicknesses in the geometry of the tooling could crack through varied cooling and with machining and material costs already input it was deemed as not being suitable.

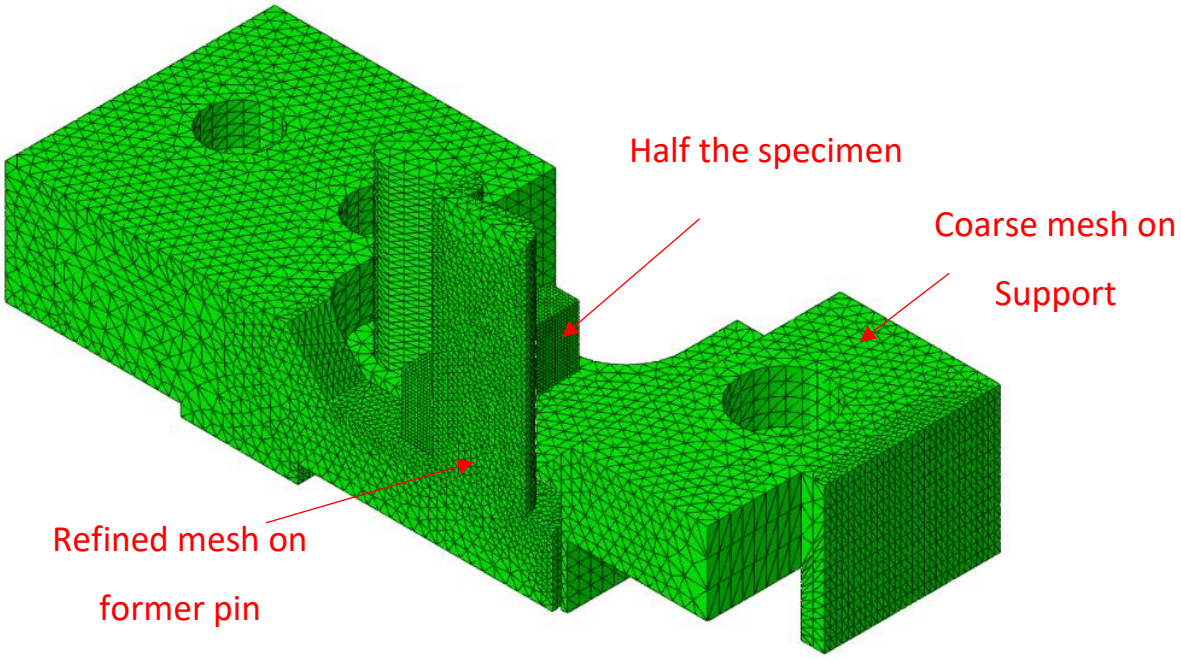


*Figure 4-43: Isometric view of gen 1 tooling mesh with a refined mesh on the central former pin region.*

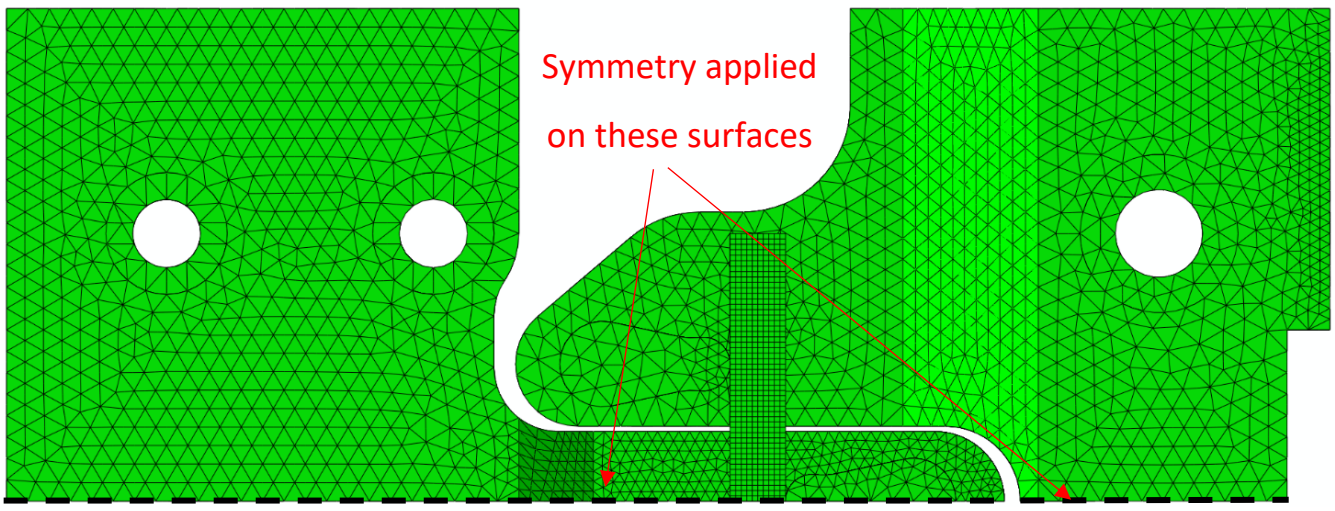


*Figure 4-44: Top view of the meshed tooling and specimen assembly.*

Due to the complex geometry tetragonal C3D4 meshing was found to provide a simple method of producing structured meshed tooling. The specimen remained a heptagonal element meshed specimen with element C3D8R. The tool material was assumed to be fully elastic while the specimen

used the elastic-plastic data from Table 4-1 and Table 4-2. Another simplification for this model was the use of symmetrical boundary conditions along the centre of the support, former and specimen. The same interactions and boundary conditions were used as shown in Figure 4-10 and Figure 4-11 but only half of the number of boundary conditions and a single support interaction due to the symmetry.

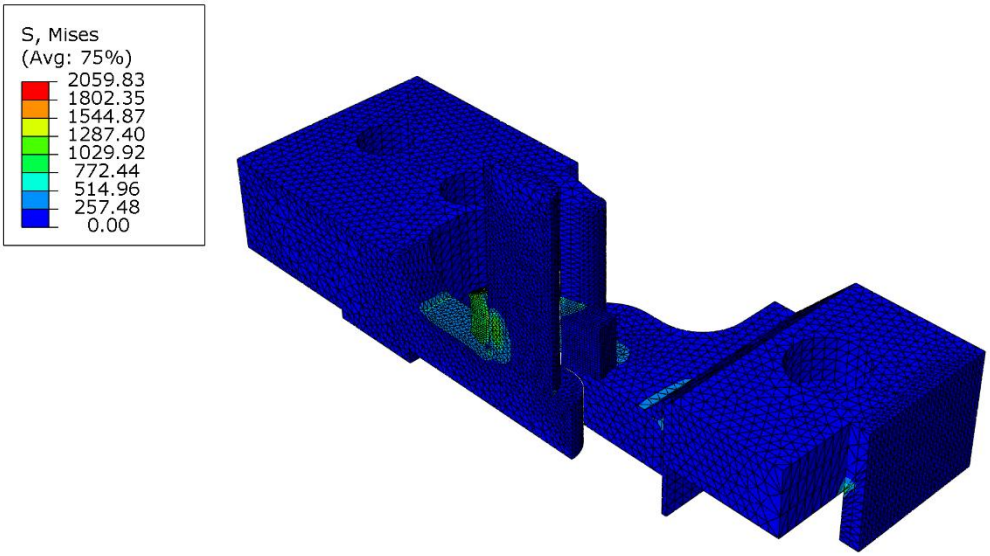


*Figure 4-45: FEM displaying the von mises stress with the specimen visible, a coarse mesh of 0.25mm size at the former face at 10.05mm displacement.*

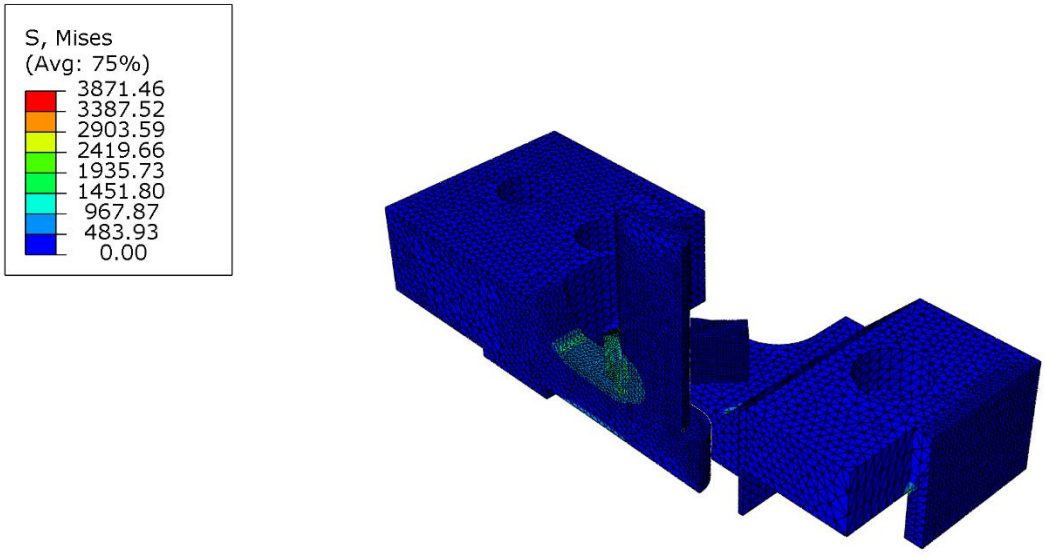


*Figure 4-46 FEM displaying the von mises stress, a mesh of 0.25mm size at the former face at 4.25mm displacement*

When a coarse mesh is applied the stress is higher than found in the 5mm diameter tooling exceeding 2GPa but when studied at a lower displacement this is found to increase further to above 3GPa. Further examination of the deformation noted that the central former had a noticeable deflection. Due to a reduction in thickness of the former body the moment from bending acted on the former and caused a deflection.

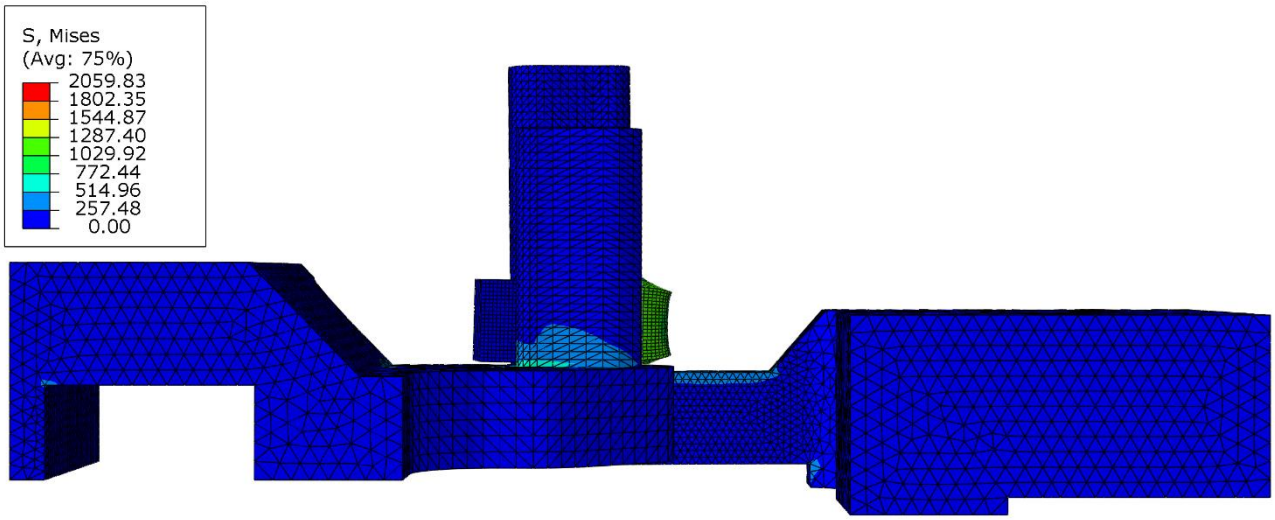


*Figure 4-47: Side profile view of the support, former and specimen with a coarse 0.25mm mesh at 10.05mm displacement.*

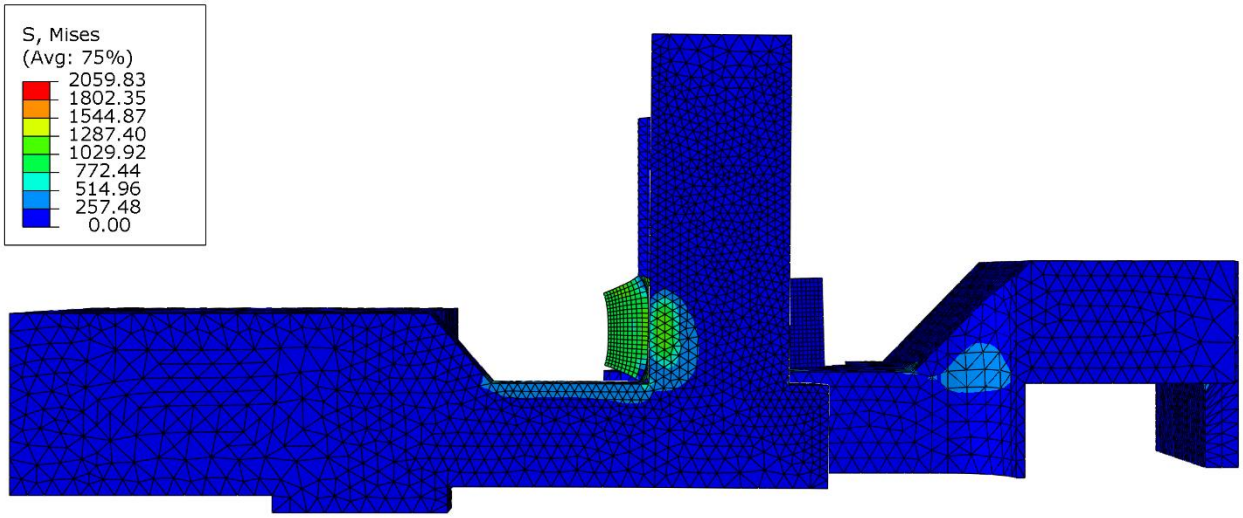


*Figure 4-48: Symmetry side profile view of the support, former and specimen with a coarse 0.25mm mesh at 10.05mm displacement.*

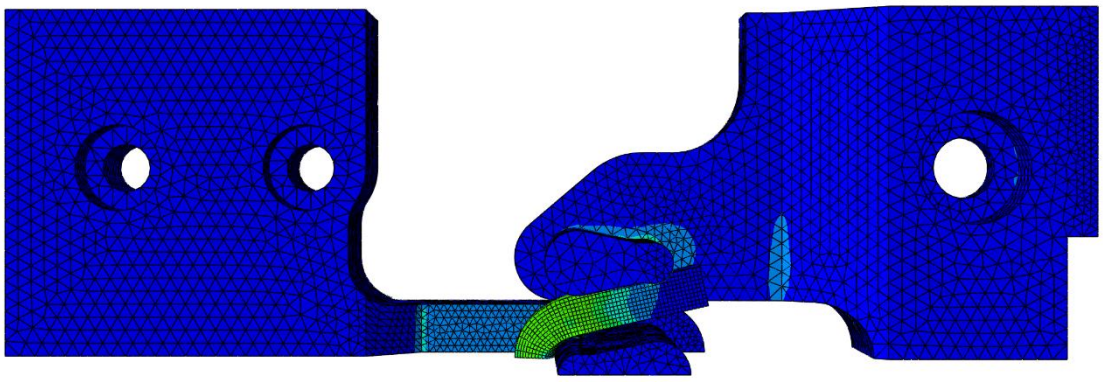

*Figure 4-49: Top view of the support, former and specimen with a coarse 0.25mm mesh at 10.05mm displacement.*

This tooling was deemed acceptable and used initially for several tests over which the deflection of the tooling moved the centre of the bend in the specimen and the high stresses caused wear on the tool face. When the stiffness of the tooling is studied in FEM it was found to be 35% less stiff than the Deben 5mm diameter tooling at $3 \times 10^{-4}$ °/N.

## 4.3 Second Generation 2.5mm diameter tooling

As the first set of new tooling was found to have problems with stiffness and deflection. Also, the contact stresses were causing local deformation on the former and support surfaces which would influence bend test results. To resolve this a new set of tooling were designed with these featured improvements which resolved these issues. These features included:

- Reversing the tooling orientation allows the tooling to improve the stiffness of the tooling by supporting the bending specimen.
- Tooling inserts for contact with the bend test specimen.

This approach required a redesign of the tooling and repositioning of the interfaces. To simplify the design a standard size insert is shared between the support and former, two used in the support and one in the former. Due to the small size of the insert, these were produced from more specialist materials. Technical ceramics and high-speed steel were considered for this role. Due to concerns about the brittle properties of ceramics and their poor characteristics in tension, it was decided to use high-speed steel. High-speed steels were found to have a compressive yield exceeding 3000MPa [108] and are commonly used in tooling. By producing these as inserts they are replaceable. These inserts were wire spark eroded out of a billet and press-fit into the support and former bodies to produce the completed tooling.

The body of the support or former was designed to retain the inserts. The design of these parts was simplified to save costs in production with flat faces and with as few complex shapes as possible. This was also produced with wire spark eroding and manufactured from D2 tool steel for its excellent tooling properties described in 4.2. To produce the slot for press-fitting the inserts a hole is drilled into the centre of the slot to then allow the wire to be fed through to erode the slot profile.

### 4.3.1 FEA of the second-generation tooling

To simulate the tooling different approaches were taken as each piece of tooling now consisted of different parts. The first approach taken was to produce a smaller slot than the tooling this then caused an interference fit. This could then be simulated with a step to relax the nodes at the start of the step and then instigate contact through the step progressively. Using the next steps to promote bending as performed in sections 4.1 and 4.2. This was not found to be possible with this approach as it would not resolve due to the stability of the bending simulation. The combination of bending with an unconstrained specimen and tooling only held in place by interference fit resulted in the solution not resolving. Transferring the model to Abaqus Explicit may have computed a result but the stability of the model would have led to questions on its accuracy.

As similar work had been performed when simulating the first generation tooling the model was broken into smaller parts and considered in a few models.

To effectively model this, different modelling approaches were used. The first was to model only the inserts as shown in Figure 4-50. This simplified the model to avoid instability problems. A rigid flat plate was added to simulate friction with the support tool body with a Coulomb penalty friction of 0.3 as used previously.

The purpose was to simulate the stresses on both the inserts and the tooling bodies containing them to validate the design. The tooling was elastic as defined in Table 4-1 while the specimen used the elastic-plastic data from Table 4-1 and Table 4-2.

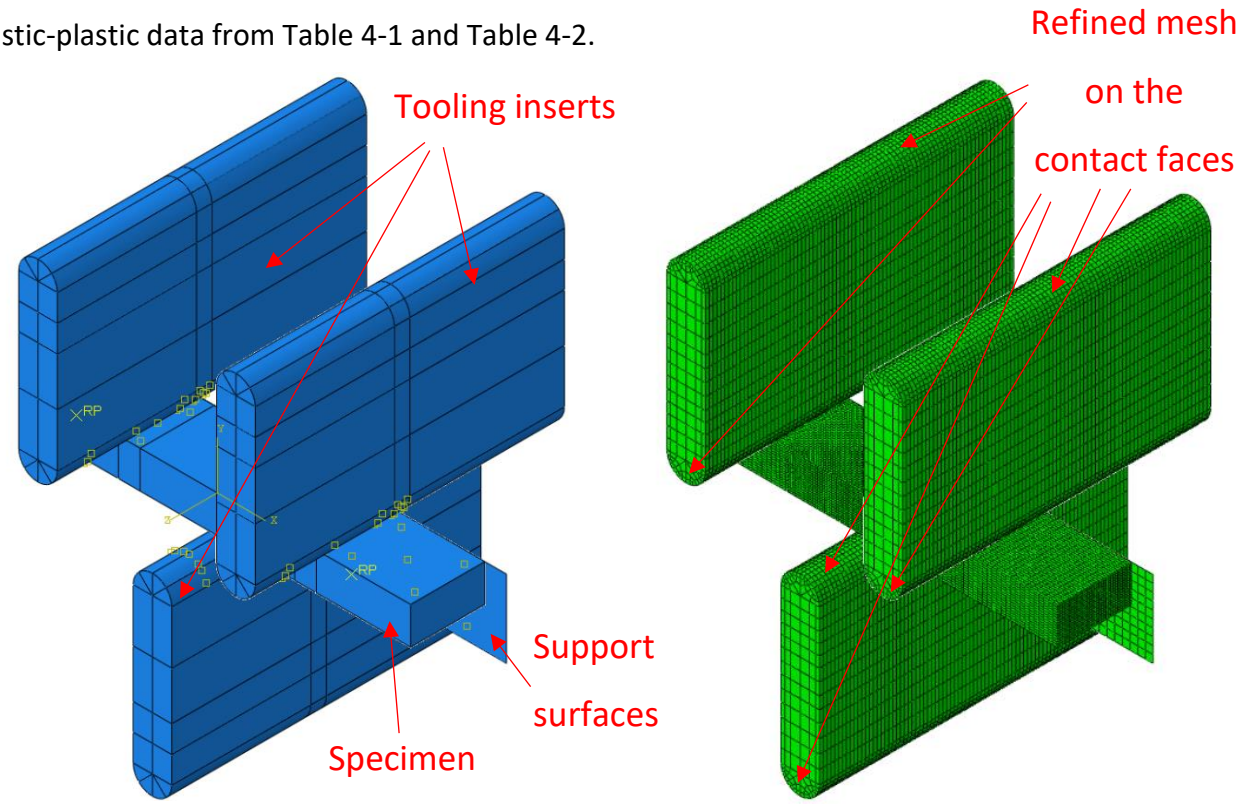


*Figure 4-50:The assembly for the bend test with elastic tooling inserts and 2.4mm thick bend test specimen, left, interactions between the sectioned tooling and the specimen, right, meshed assembly with 0.125mm mesh on the contact faces and the specimen and 0.5mm on the regions of the pin with no contact.*

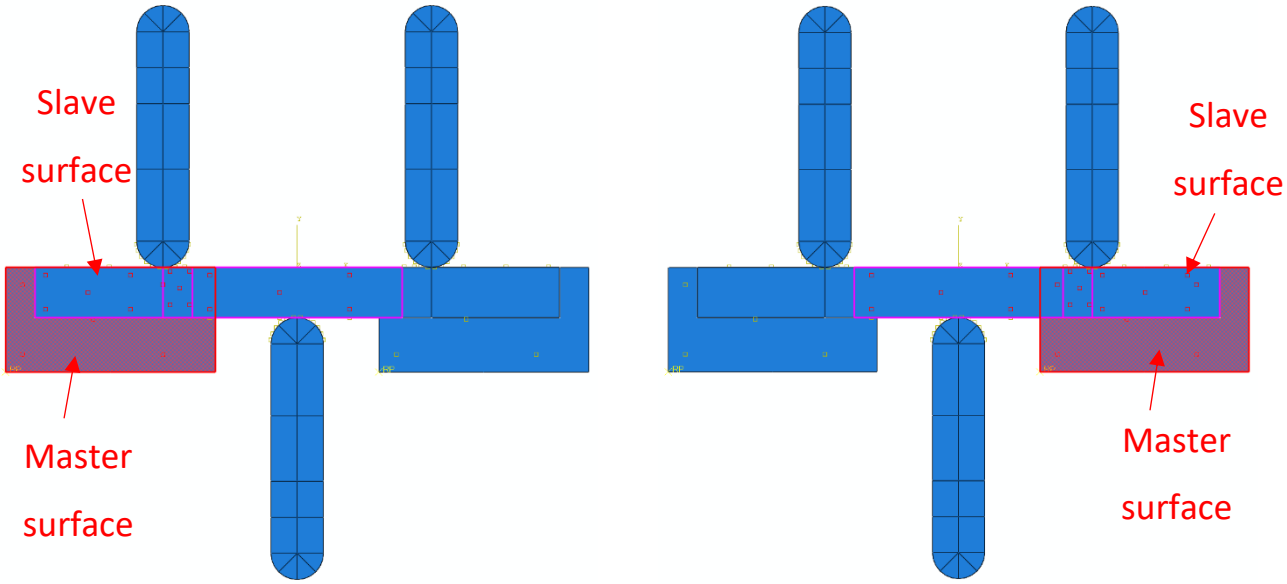


*Figure 4-51: Discrete sheet interaction settings with the red master and purple slave.*

The mesh is detailed around the contact faces at a size of 0.125mm and 0.5mm in regions of less interest as shown in Figure 4-50. The simulation was run with boundary conditions to be as close to the fitment of the tool body as possible. This resulted in the localised build-up of stresses on the front face similar to other tooling types. These stresses drop as the displacement increases resulting in stress and deformation as shown in Figure 4-53.

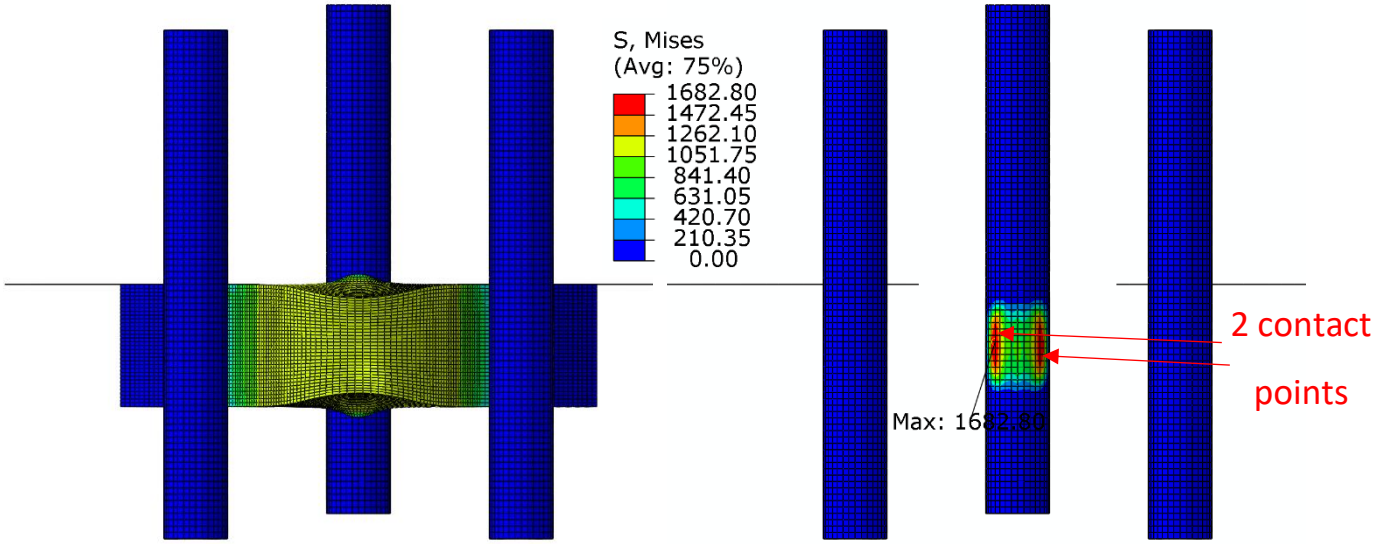


*Figure 4-52: Peak stress at 2.5mm displacement, left, front view with former, supports and the specimen, front view with former and supports with the specimen removed.*

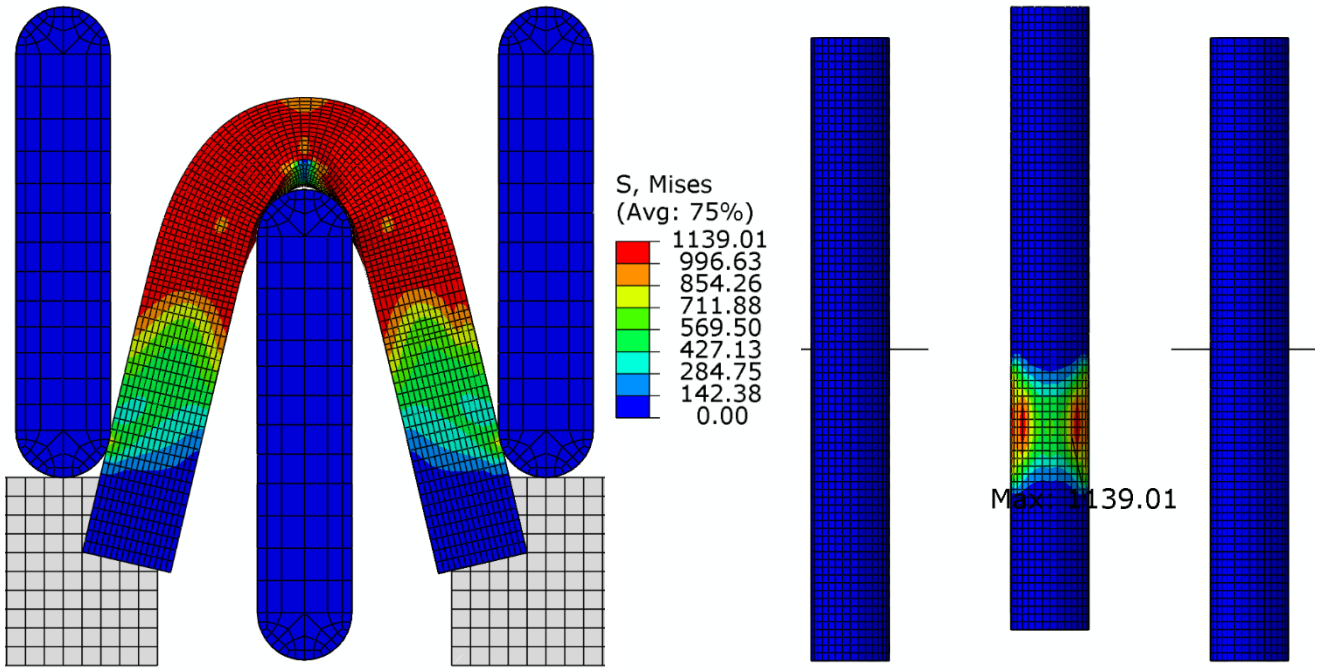


*Figure 4-53: Von mises stress on the tooling at maximum displacement, left, top view with former, supports and the specimen, right, front view with the specimen removed.*

To simulate the inserts being press-fit and how they transfer the load onto the tooling body. This region is of interest because it will validate the use of inserts. To achieve this an interference fit was introduced to simulate the press-fit insert in the local tool body. The former body is cut down to only be the region retaining the insert. To promote the compression fit the size of the inserts radius was oversized by 3 thousandths of a micron relative to the hole. The interference fit option was selected on Abaqus that relaxes the locations of nodes then moves until they interfere over a step. Due to instability displacement boundary conditions were avoided, so a load was added to the former face. Only the former was simulated as this undergoes twice the load of each support insert. The simulation of the former was used to assess the transfer of loads and contact stresses from the former insert to the tool body. The materials are all elastic with the material properties as described in Table 4-1.

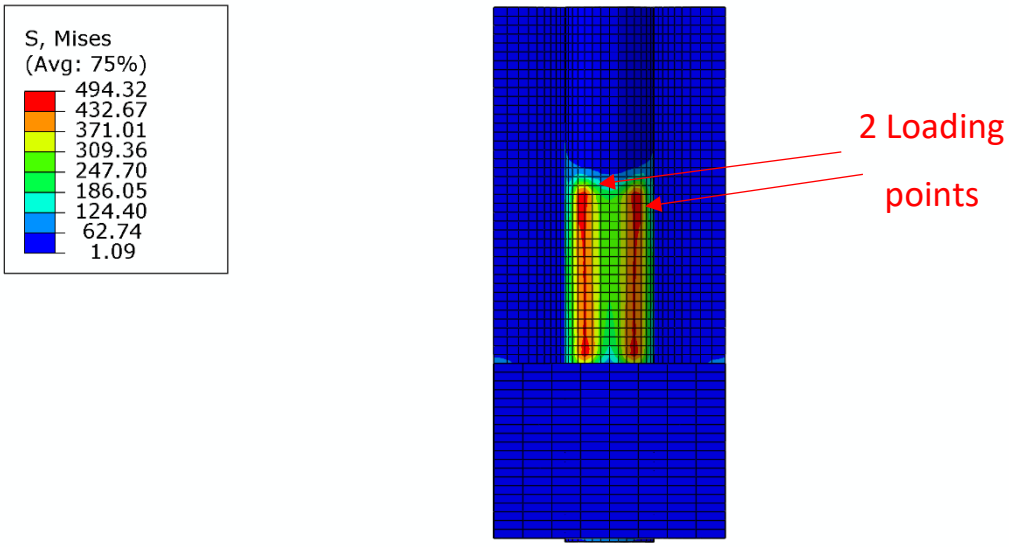


*Figure 4-54: Insert and sectioned former with 5KN load applied to the front face promoting the highest stresses, front view*

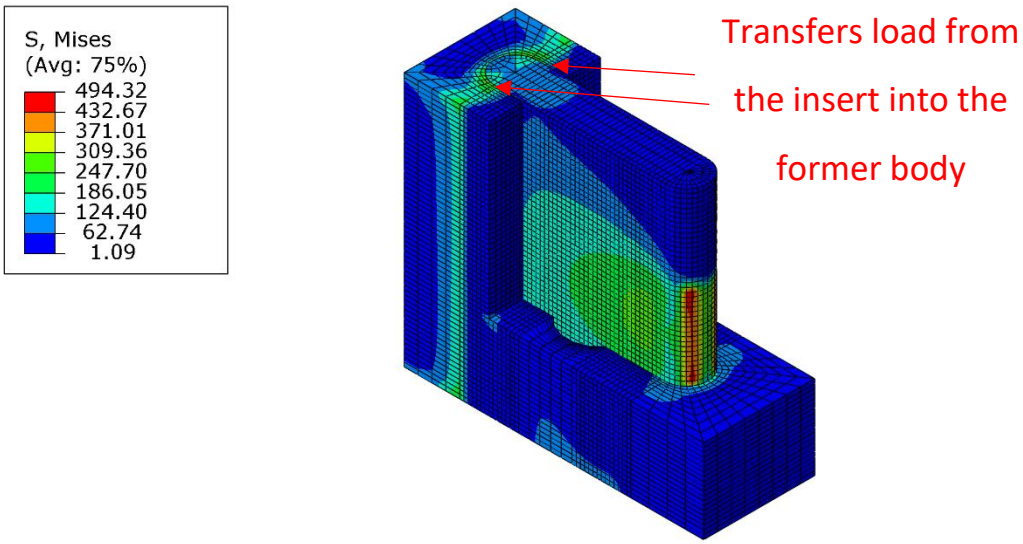


*Figure 4-55: Insert and sectioned former with 5KN load applied to the front face promoting the highest stresses, isometric view*

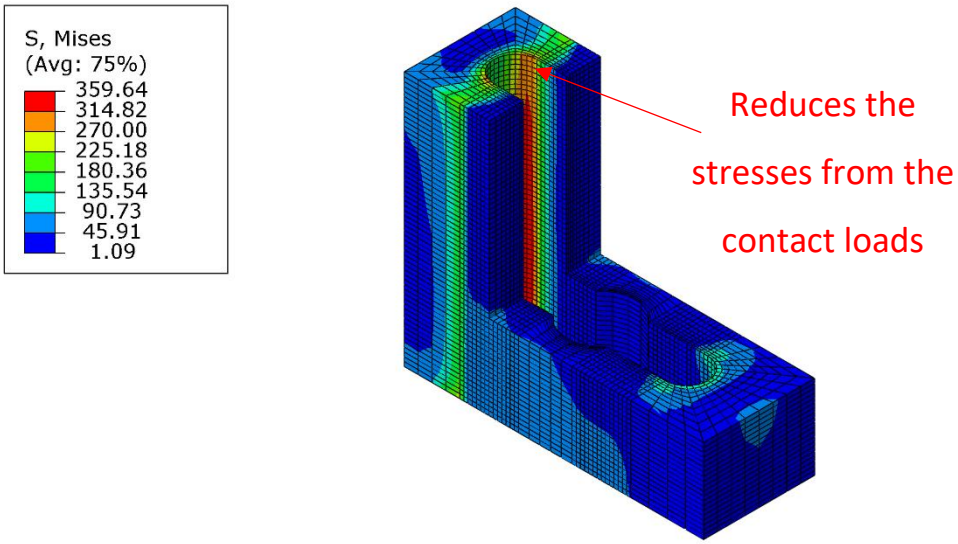


*Figure 4-56: Sectioned former with 5KN load applied to the front face promoting the highest stresses, isometric view.*

As can be seen in Figure 4-54 and Figure 4-55, the force of 5KN is applied to the insert tool face. This promotes stress of nearly 500 MPa. This is redistributed onto the former body with lower stress of 360MPa this is due to a better distribution of strains and shows that the inserts will act as a means of protecting the body of the former from contact loads.

The final FEM simulation was a simplification of the inserts, former and support bodies by treating the former and insert as one part and 2 inserts and support as one part. This has the benefit of increasing stability enough to perform a simulation of a bend test as performed in sections 4.1.1.3 and 4.2 and compare it to these results. The former and support were both sectioned and then meshed with C3D8R elements using the material as outlined in Table 4-1. The bend test specimen is an elastic-plastic material with properties from Table 4-1 and Table 4-2. A global mesh of 0.5mm was applied with a mesh on the specimen and the tool face of 0.25mm.

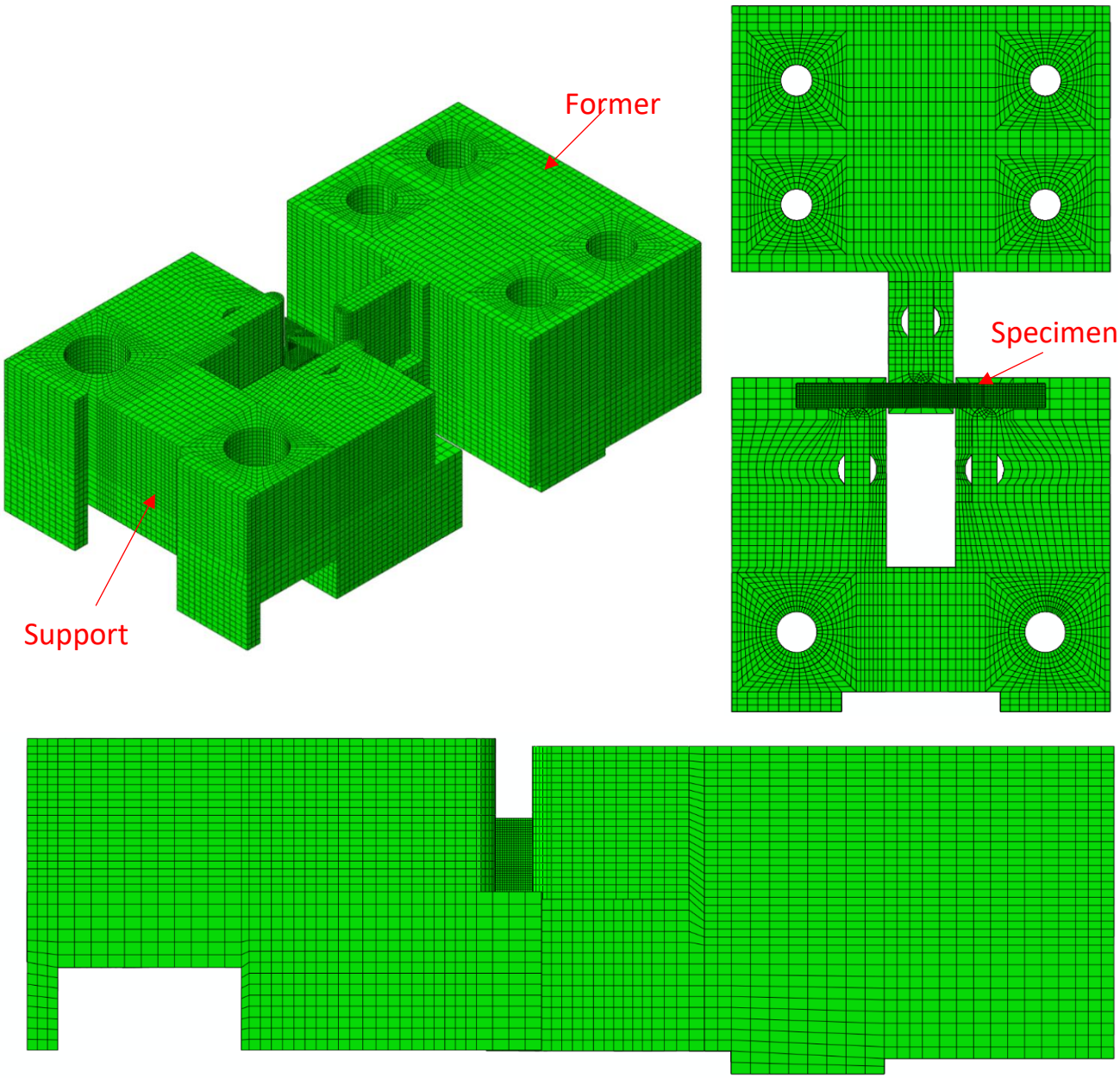


*Figure 4-57: Views of the meshed 2nd generation 3 point bend test tooling and specimen assembly, top left is the orthogonal view, top right is the top view, bottom is the side profile.*

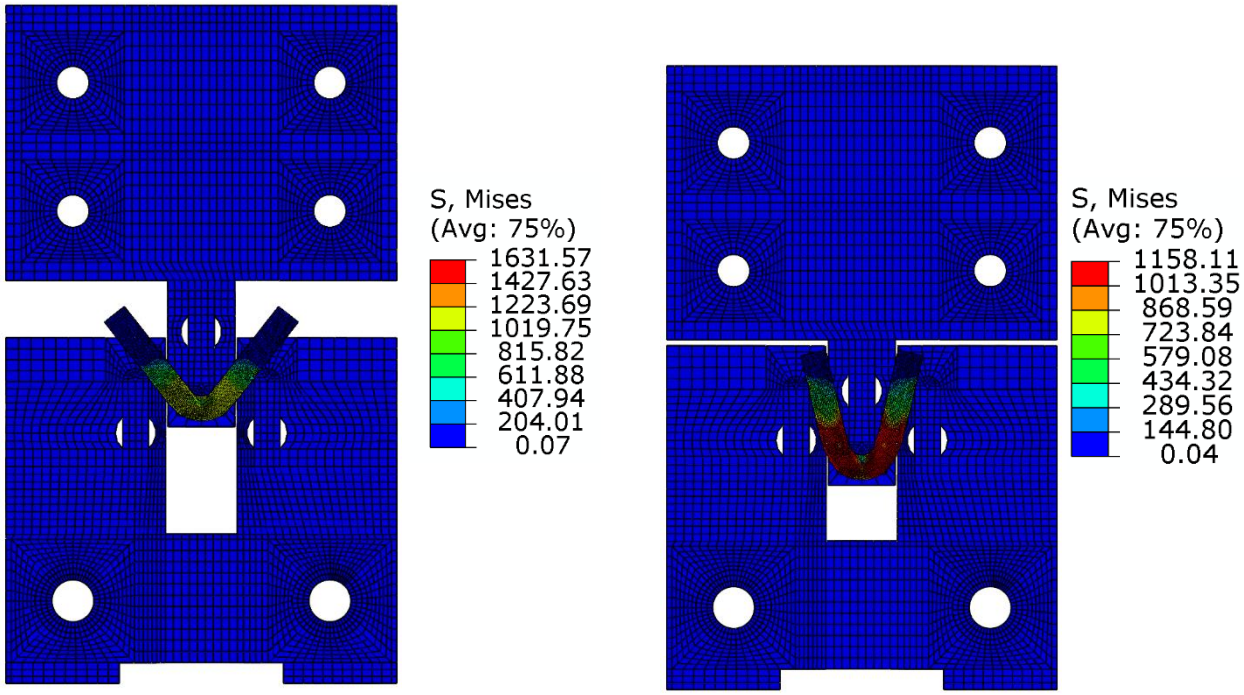


*Figure 4-58: Top view of bending with von mises stress, left, 5mm displacement, right, 10mm displacement*

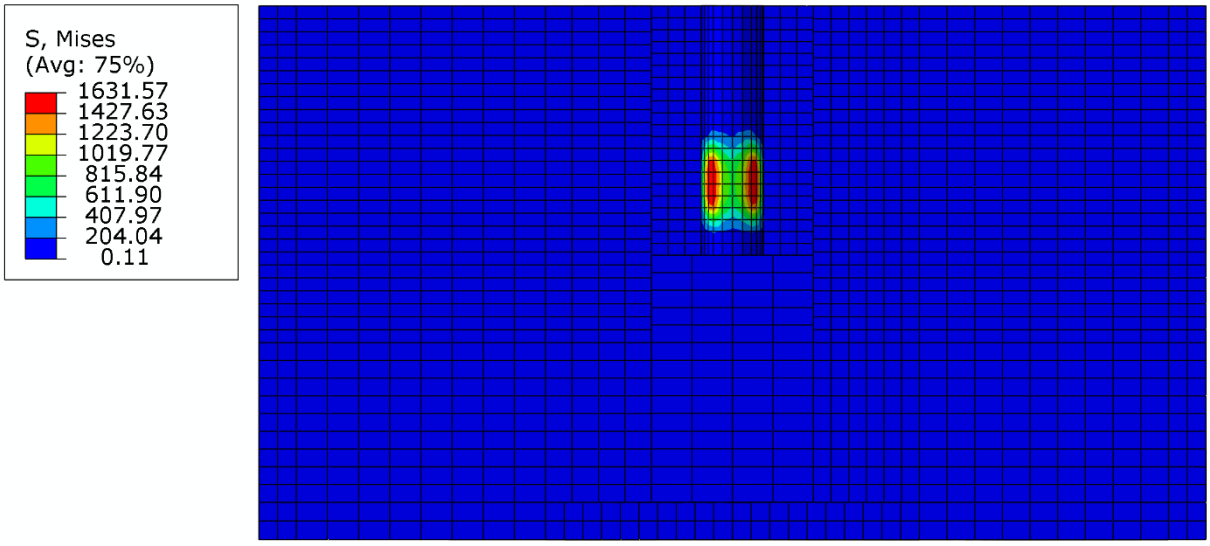


*Figure 4-59: Front face of the former with the specimen and support removed, at 5mm displacement.*

The high stresses found at 5mm displacement in Figure 4-59 are close to those found in Figure 4-52 at 2.5mm displacement. No visible sign of deflection is noticed on the tooling after simulations are run. When the stiffness was calculated it was found to be 80 times stiffer than the Deben 5mm diameter tooling. The testing found the tooling had a stiffness of $2.39 \times 10^{-6}$ °/N. By having the material to support the pin face in compression the tooling stiffness is increased significantly. The high stresses on the inserts will be accounted for by manufacturing the inserts out of high-speed steel.

## 4.4 Angled bend test geometry

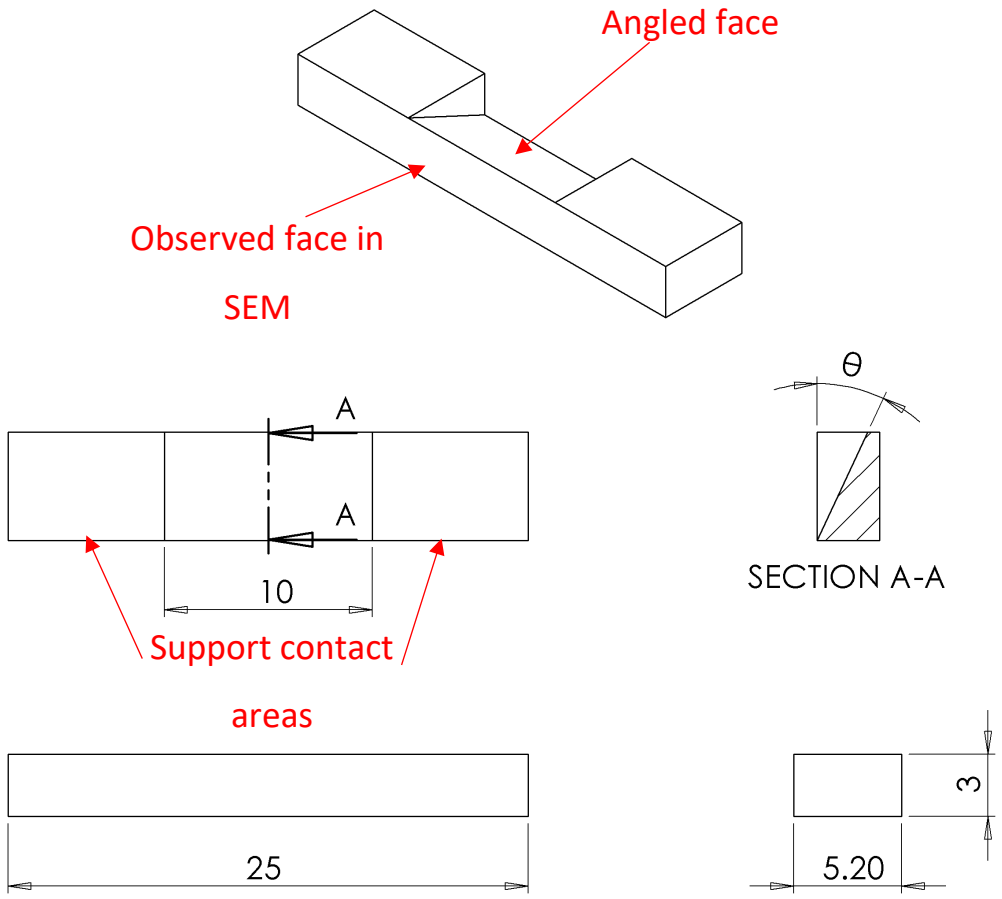


*Figure 4-60: Bend test specimen geometry with angled geometry.*

Having performed bend testing on rectangular bend test specimens they were found to promote shear bands observed at the centre of the horizontal bend test surface. The bend test caused a significant drop in the load, but no damage is observed at the horizontal face.

Due to these tests being performed without any damage being observed, a study into the development of a geometry promoting shear bands and damage in bend testing was performed with knowledge of other geometries used in bending tests [91]. This was used in conjunction with the anticlastic effect as described in section 2.2.1.1 and an increase in triaxiality at the edge of the specimen as shown in Figure 2-26 could be combined and promote an observable edge damage effect. This resulted in the generation of the angled bend test geometry in Figure 4-60.

To study design a new bending geometry a study was performed with parameters varied to promote damage in the observed horizontal region as shown in Figure 4-61. To achieve this a combination of high strain and triaxiality at the horizontal surface. With these considerations, the concept of an angled bend test specimen was developed. A range of angled profiles was simulated with a varying θ angle from 0-25° in 5° increments.

Using an elastic-plastic data set obtained by performing tensile tests a continuum model is produced in Abaqus. The tooling supports and former were a shell of rigid discrete elements with contact and a Coulomb friction model applied at the tool-specimen interfaces. Displacement of up to 10mm is then applied to the former deforming the specimen in the bend test models.

The specimen was intended to be observed from the horizontal view with the horizontal surface in Figure 4-60 observed by the SEM, to impart strain and damage observed in the tensile region. The design was developed to use the angled profile to promote a larger distance from the neutral axis in bending at the observed horizontal face with the acute corner edge in tension. When computing the models, a significant amount of out of plane deformation is observed from the horizontal face. Strain is concentrated at the edges of the specimen; this is due to the anticlastic profile on the top surface as the specimen was compressed on the tensile strain region on the top surface. This promotes the peak strain values at the observed horizontal edge.

As the former deforms the specimen the contact region changes from a single central location to two independent points of contact. These contact regions diverge from the central location as the former deforms the bend test specimen. As the deformation progresses the specimen develops other notable features including:

- Expansion and contraction of the width of the compression and tensile faces respectively due to these stresses.
- The neutral axis moves towards the compressive side as the material is deformed by the bending stresses adjusting the central material area position.
- Increasing the specimen angle reduces the bending force.
- With larger angles, the specimen begins to move along the supports and begin to slide.

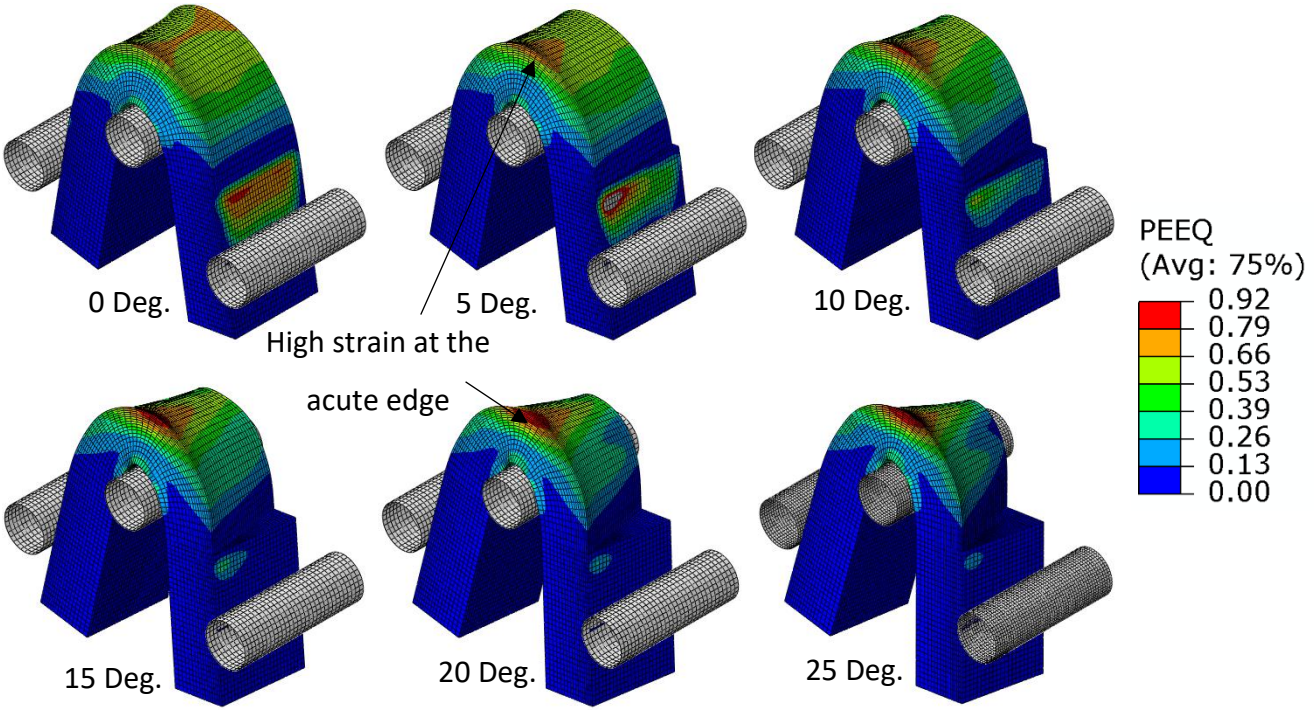


*Figure 4-61: Isometric view of angled bend test geometry with PEEQ strain with specimens from 0-25 degrees of angle.*

By varying the angled profile of the bend test specimen the location of maximum strain and the intensity of the strain is affected in Figure 4-61. To analyse this further the strain is analysed at the point of highest strain in each test in Table 4-3.

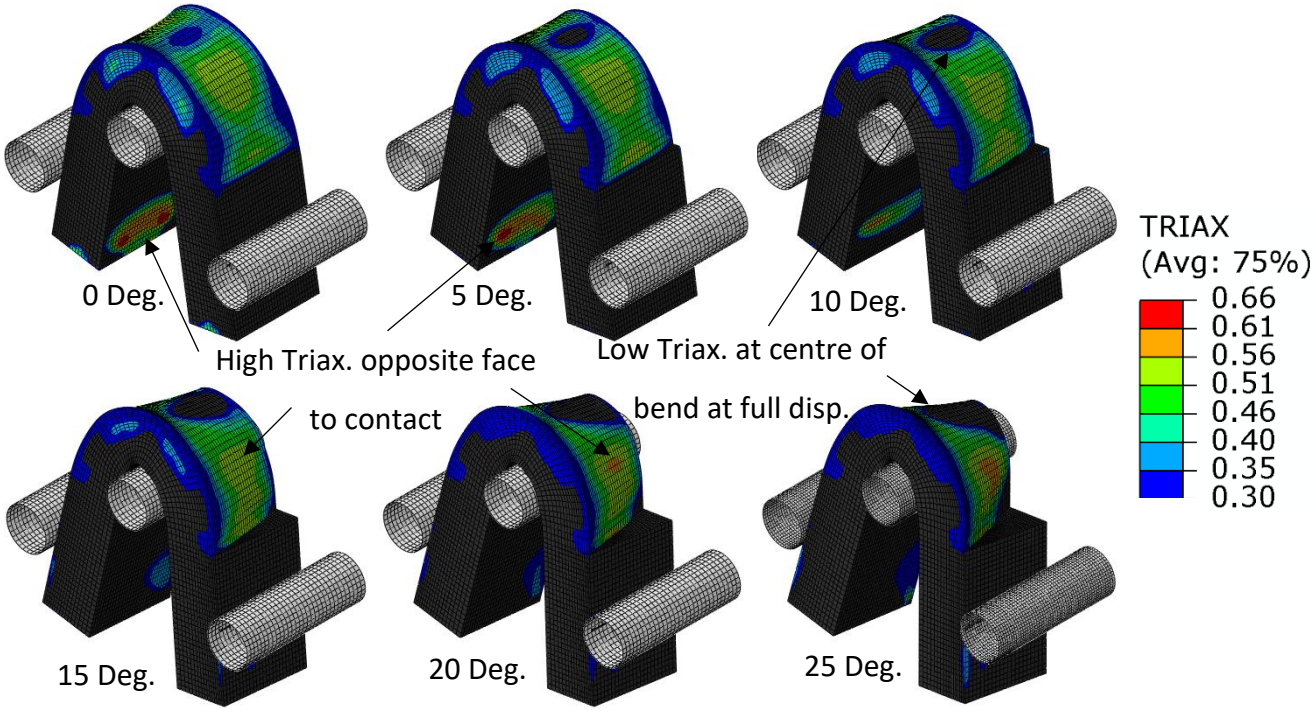


*Figure 4-62: Isometric view of angled bend test geometry with triaxiality of specimens from 0-25 degrees of angle.*

While the centre of the bend localises the high strain and increase through the test the triaxiality is very consistent at 0.33 throughout the test. This shows that damage located in this region is dictated

by the high strain and not due to any change in loading. This region is also at the same triaxiality as standard tensile tests.

| | Strain at $\theta$ angle | | | | | |
|---|---|---|---|---|---|---|
| Displacement (mm) | 0° | 5° | 10° | 15° | 20° | 25° |
| 1 | 0.157 | 0.164 | 0.168 | 0.172 | 0.175 | 0.180 |
| 2 | 0.346 | 0.359 | 0.370 | 0.381 | 0.390 | 0.400 |
| 3 | 0.539 | 0.561 | 0.580 | 0.599 | 0.614 | 0.630 |
| 4 | 0.666 | 0.707 | 0.746 | 0.783 | 0.812 | 0.834 |

*Table 4-3: Strain values at the centre of the horizontal edge in PEEQ from Abaqus, location shown in Figure 4-63.*

While the thickness of the specimens remains consistent throughout the strain increases as the angle increases. As shown in Table 4-3 strain is highly linked to the angle of the specimen. The reason for this is the anticlastic profile promoting a localised strain at the central edge of the specimen. As the anticlastic profile is generated it increases the relative thickness of the specimen at the angled edge making the distance from the neutral band greater. This then intensifies the strain in this region this is demonstrated in Figure 4-63.

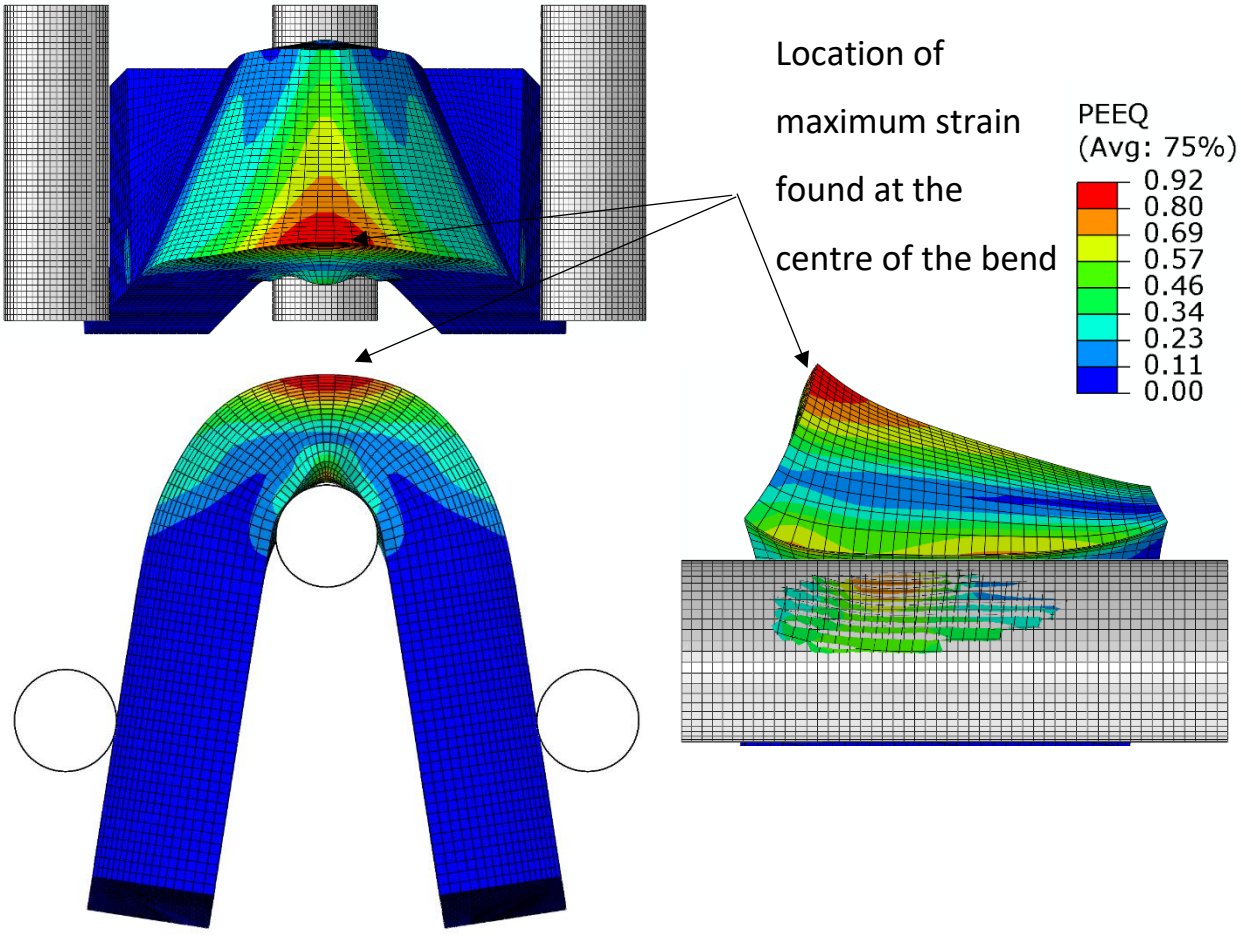

*Figure 4-63: 25° angled specimen, Θ bent to 10mm displacement, top left is the horizontal face, bottom left is a view of the angled profile of the top surface, bottom right is a section view through the centre of the horizontal face.*

The neutral axis can be observed in the test in the section view in Figure 4-63. This is clearest at the narrowest edge as the elements are smallest through the thickness. At the horizontal face the

As higher angled specimens are used the following properties are observed:

- As the angle is increased the contact patch moves towards the thicker section of the angled specimen.
- Increasing the angle of the specimen increases the strain as the angle works together with the anticlastic profile to increase the vertical height of the edge. This results in higher strains as it is further from the neutral axis.

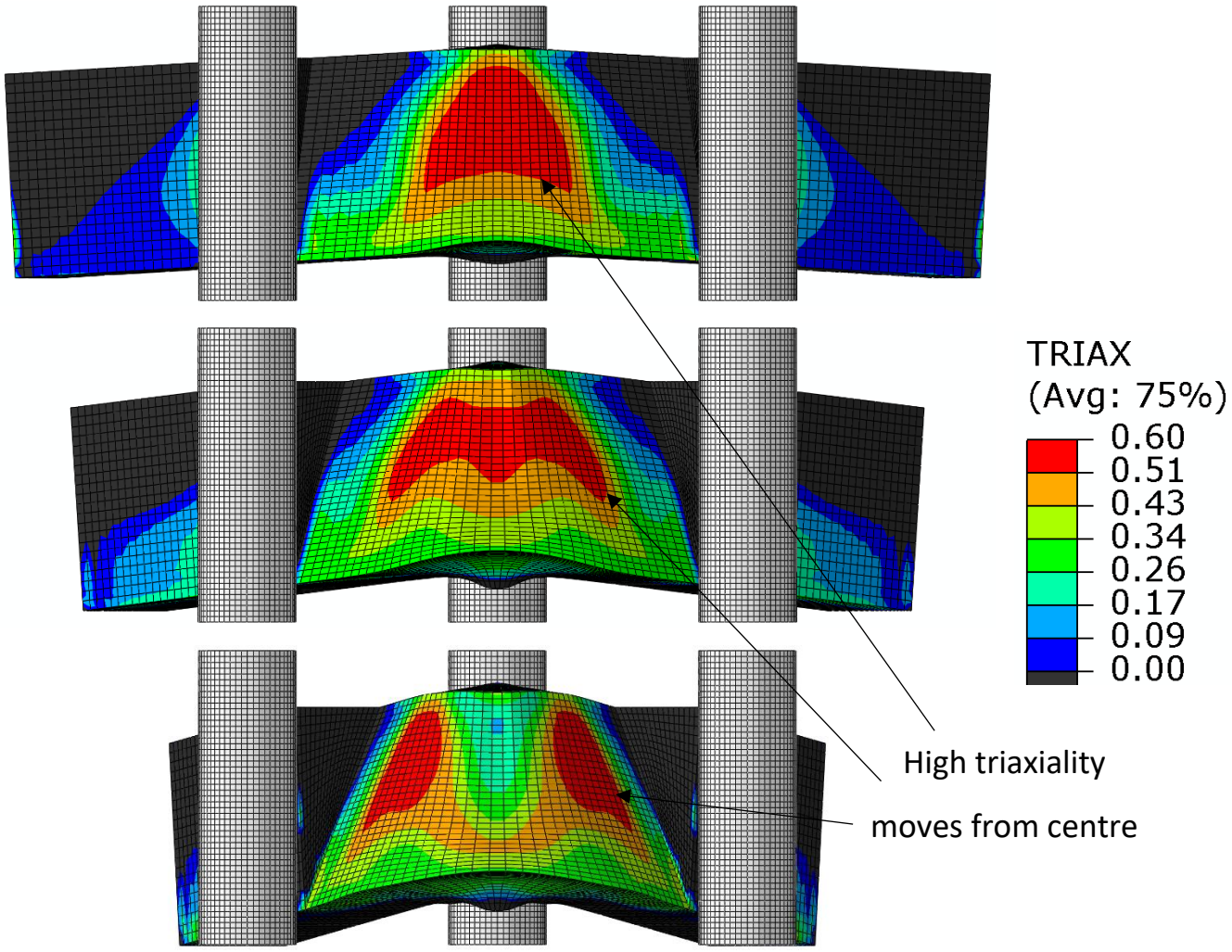


*Figure 4-64: FEM of 25° angled bend test showing the movement of triaxiality during bending. The top image is at 2mm displacement, the middle image is at 4mm displacement, the bottom image is at 6mm displacement.*

The triaxiality of the angled bend test specimen is very different to that found in the standard bend test geometry. With no angle, $\theta = 0°$ the region of highest triaxiality is found to be at the centre of the bend at plane strain, this then moves off centre as larger displacements are applied. With the 25°

Figure 4-64 the maximum triaxiality is found to move off centre as larger displacements are applied. The author considers the movement of the regions of high triaxiality due to the deformation of the specimen and movement of contact patches changing the loading state in the test during the test. This might cause the damage to be promoted in different locations through the range of motion of the bend test.

Due to the increased localisation of the strain at the observed horizontal face and the consistent but low triaxiality at the same face with higher values found to fluctuate along the angled face, the damage is expected to occur in 2 locations. At the high strain low triaxiality tensile portion of the horizontal face and the high triaxiality, lower strain area on the angled face. The observed horizontal face is the priority for this work.

## 4.5 Summary of tooling and specimen design and methodology

A new methodology for performing bend tests has been developed using new tooling and specimen design, simulated in FEM and produced in the University of Sheffield. The new specimen and tooling comply with ASTM and BSI standards with only specimen width being limited due to the maximum module load of 5KN. The specimen in horizontal bending will be viewed on the horizontal face and in-plane stress that should not change stress triaxiality in that region. This allows many benefits to the testing methodology such as:

- Increased tooling stiffness
- Longer tooling life, with replaceable inserts to maintain the same geometry after tool face wear and abrasion from bending
- Smaller bends required a smaller FOV for the SEM during bend testing
- Higher strains 50% greater than previous 5mm diameter tooling
- Smaller specimens allow them to be mounted to use batch production in sample preparation.

With the smaller specimens allowing them to be mounted this new tooling and specimen has been integrated with a new sample production method with batch production. Additionally, the removal of rough hot-rolled top surfaces is reported to introduce stress raisers in bending that could impact the bendability of the UHSS.

As such the bendability of UHSS at the side profile can be observed with greater detail and precision than ever before. This will enable the observation and study of the initiation of shear bands and how they develop during bending and can promote damage.

A novel specimen design has also been developed for bend testing with an angled profile. This has been shown to promote higher strains near the edge due to the anticlastic profile in bending. The

triaxiality has also been shown to be localised in the central region of the specimen but acts independently of the high strain edge. Thus, the observer has 2 regions of interest to observe during the bend test. One high strain region with a triaxiality of 0.33 and a high triaxiality of 0.6 and a low strain region.

# 5 Results

Using the methodologies shown previously results were produced to identify the material properties in UHSS that initiates sheat bands and damage initiation. This led to a series of experiments to identify material properties. Then promote shear bands in bending and identify the initiation of shear bands using the insitu bend test technique. This is supplemented by FEM results to assist in identifying these mechanisms.

## 5.1 Tensile testing

Tensile tests were performed at macro and micro scales. The macroscale results were used to identify the material properties of the UHSS. While the microscale tests were used in the SEM in interrupted tensile tests. This enabled the observation of the microstructure while under tensile loading. Both provided insights into the material properties and its failure modes in tensile testing. The material data was used in the FEM for the material models used in the Modelling results.

### 5.1.1 Macroscale

Tensile testing was performed on sample 1 on the Mayes 4 100KN electromechanical tensile tester as described in the methodology. The samples used in this application were the 14TG26 sample using the 12.5mm wide EDM profiled design as specified by the ASTM suitable for use with 6mm thick specimens. 2D DIC with a single camera was used and results were recorded and processed on DaVis 8 software. To analyse the strain 3 centrally positioned virtual strain gauges located at the start and end of the gauge length and averaged as in the same manner as Figure 5-11 and Figure 5-12.
For 17DF4/1 samples tensile tests were performed with a 6mm wide ASTM specimen design which is suitable for 3mm thick specimens. Specimens were profiled with EDM and tests were performed on the Tinius Olsen 25KN tensile tester. 3D DIC measurements were captured with VIC SNAP and the results were processed with VIC 3D 8 software. The strain values are found by also averaging 3 centrally positioned virtual strain gauges.

#### 5.1.1.1 *Tensile test force-displacement graphs for 14TG26*

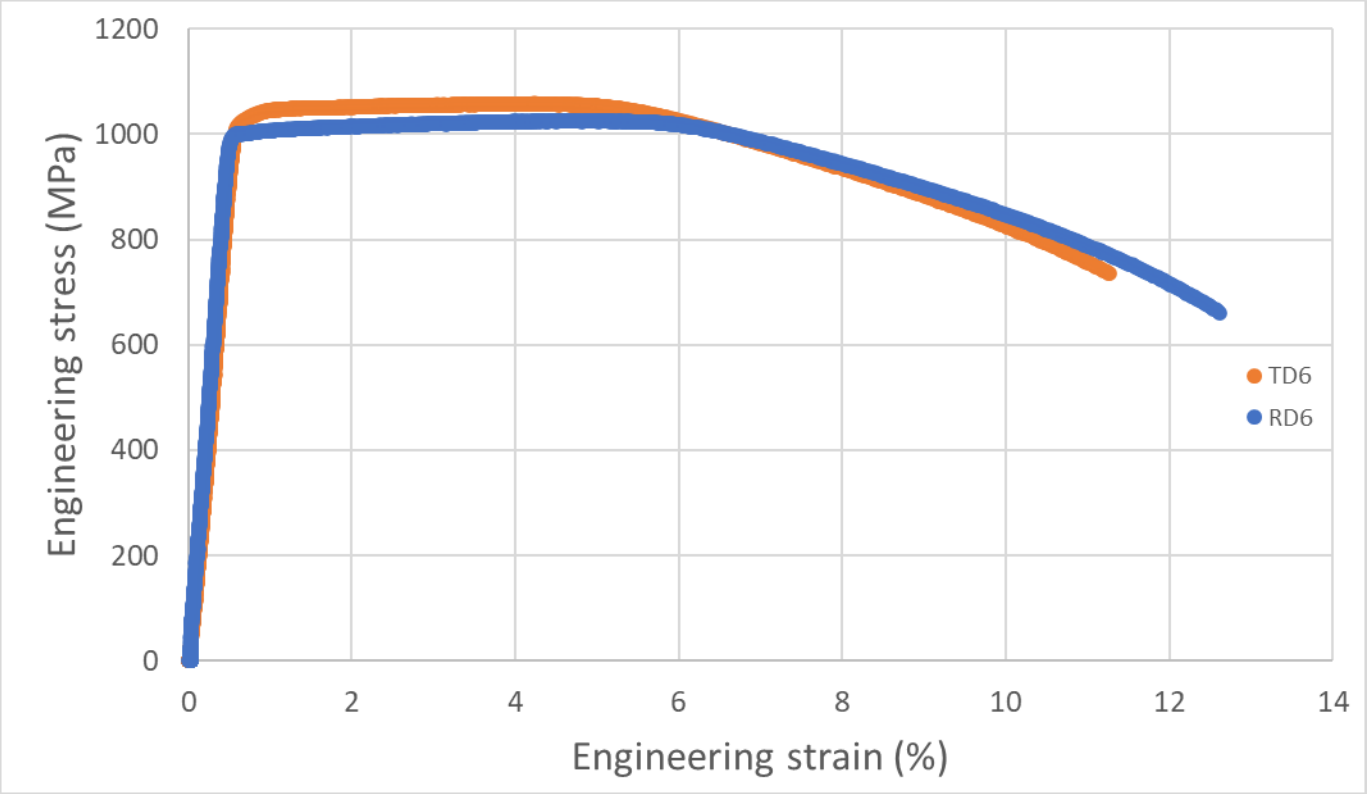


*Figure 5-1: Engineering stress-strain curves for 14TG26 tensile tests.*

In tensile testing, the 14TG26 material in RD is found to have better ductility than in the TD with a lower Yield and UTS but improved elongation properties, Figure 5-1. The RD test found a sharp transition from elasticity to plasticity. Material mechanical properties extracted from these tests are shown in Table 5-1.

| | Youngs Mod. E (GPa) | Yield 0.2%(MPa) | UTS (MPa) | Elongation (%) |
|---|---|---|---|---|
| RD6 | 213.1 | 1001 | 1026 | 12.6 |
| TD6 | 180.5 | 1036 | 1059 | 11.3 |

*Table 5-1: Material properties data for 14TG26 data*

The true stress-strain curves are shown in Figure 5-2 and the fracture points. These were calculated by measuring the area of the fracture surface and the final point before the sudden force drop due to failure fracture points were found so the final stress point was calculated.

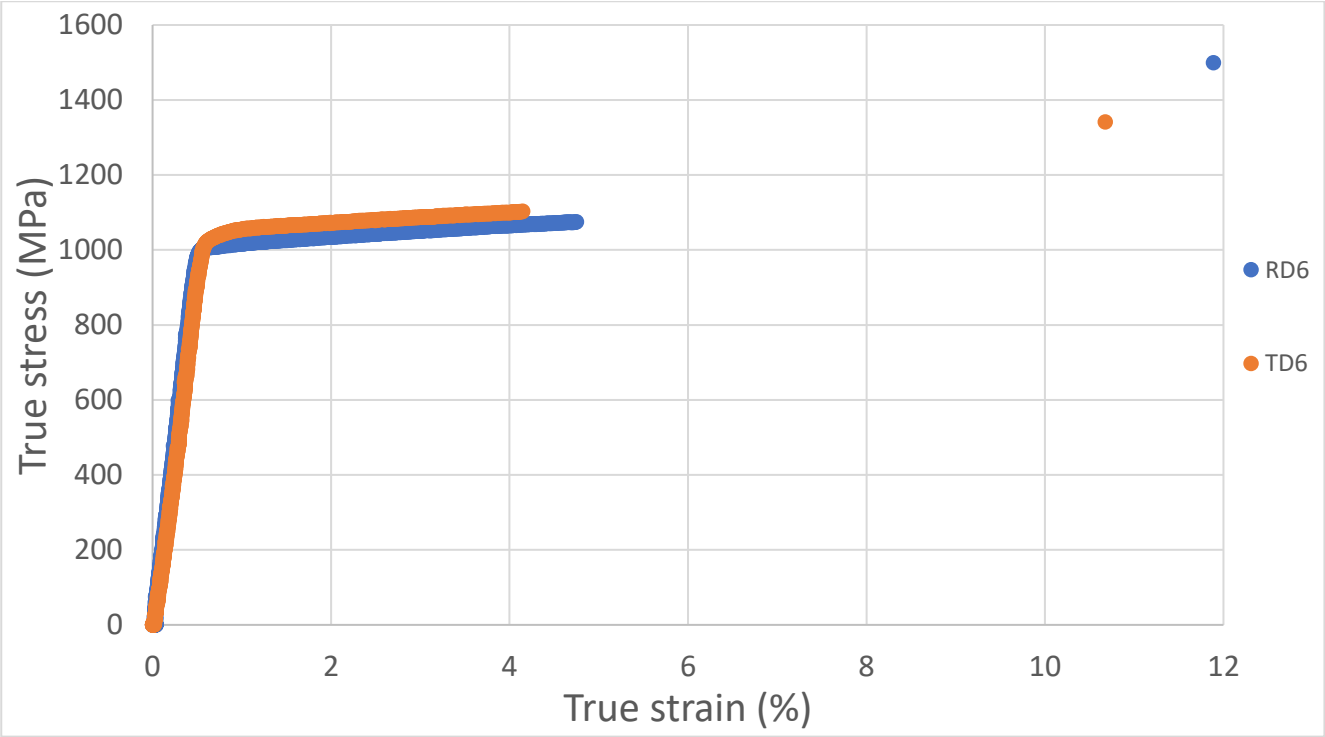


*Figure 5-2: True stress-strain curves for 14TG26 tensile tests with fracture points*

### *5.1.1.2 14TG26 DIC images*

Tensile tests with the UHSS steel were performed and found that the RD had better ductility and elongation than TD. The DIC images at failure are shown in Figure 5-3, where the necking region can be observed. The strain over most of the gauge length in both tests is found to be only 5% while in the necked regions the maximum strain is found to be 60% or higher.

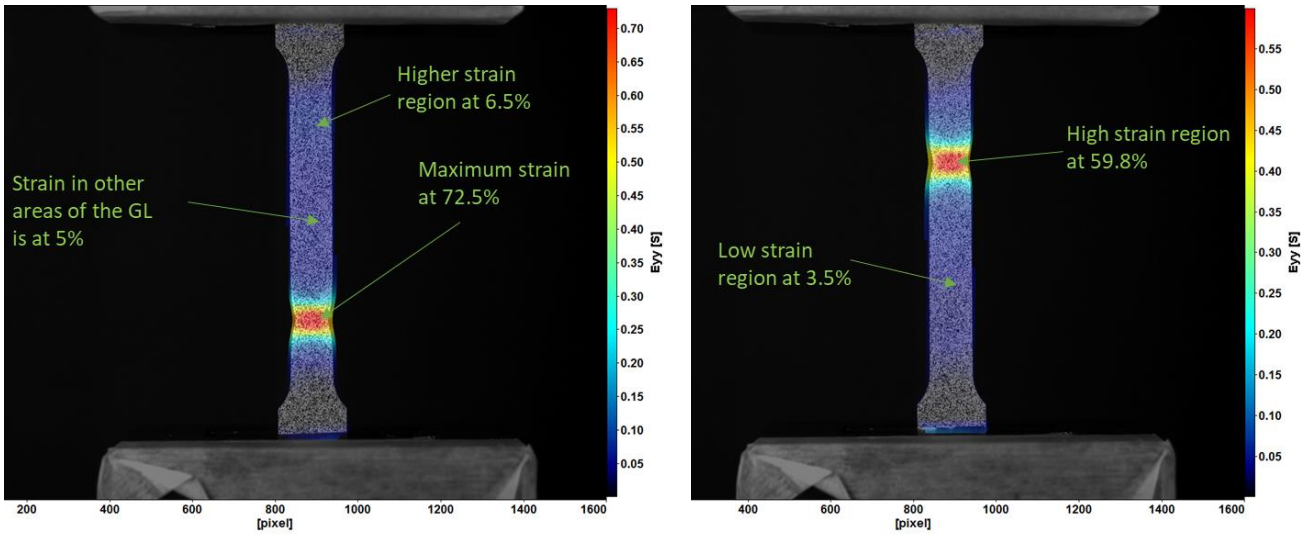


*Figure 5-3: The last image before failure during the tensile test, left RD6, right, TD6*

### 5.1.1.3 *Tensile test force-displacement graphs for 17DF4/1*

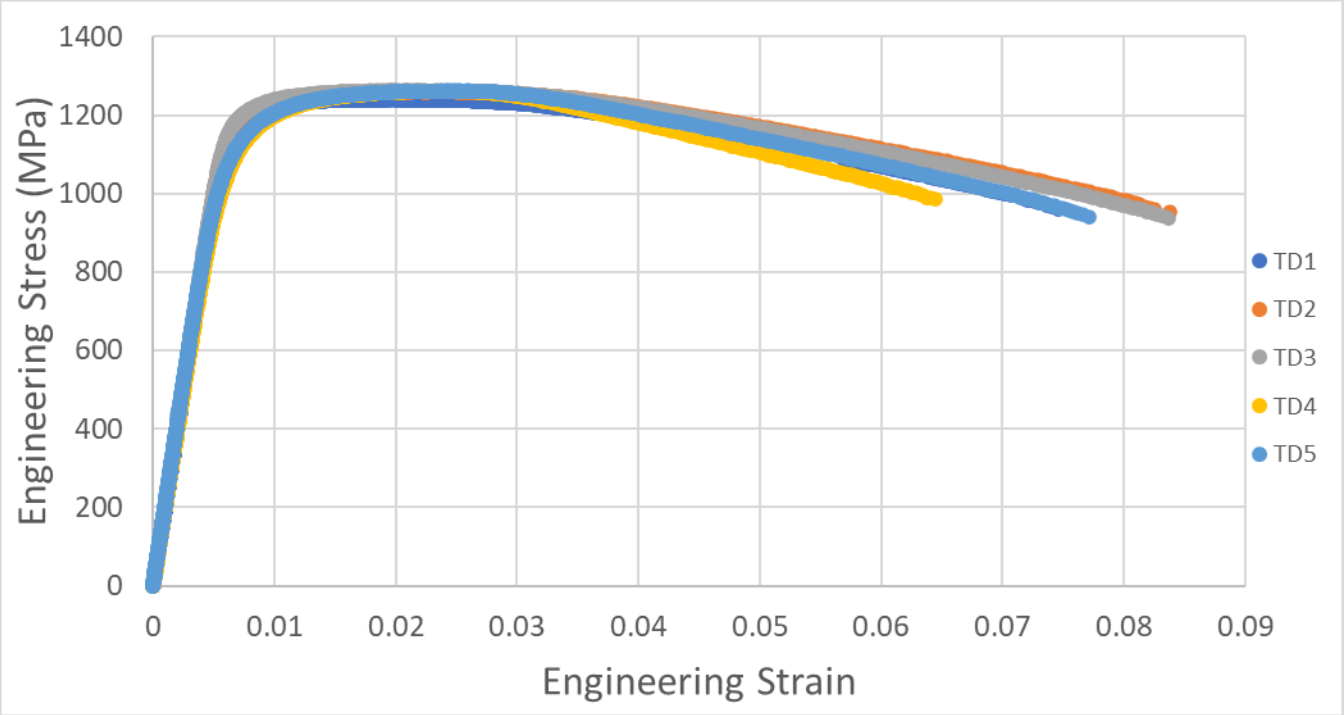


*Figure 5-4: Engineering stress-strain curves for 17DF4/1 tensile tests.*

The 17DF4/1 sample is found to have lower ductility than the 14TG26 sample. It was also found that TD4 resulted in significantly less ductile results than the other tests with tensile elongation failure found to be less than 0.065 strain while all others exceeded 0.07 and had different curve profile than found in the other tests. This was removed from the results used for generating the average of these tests.

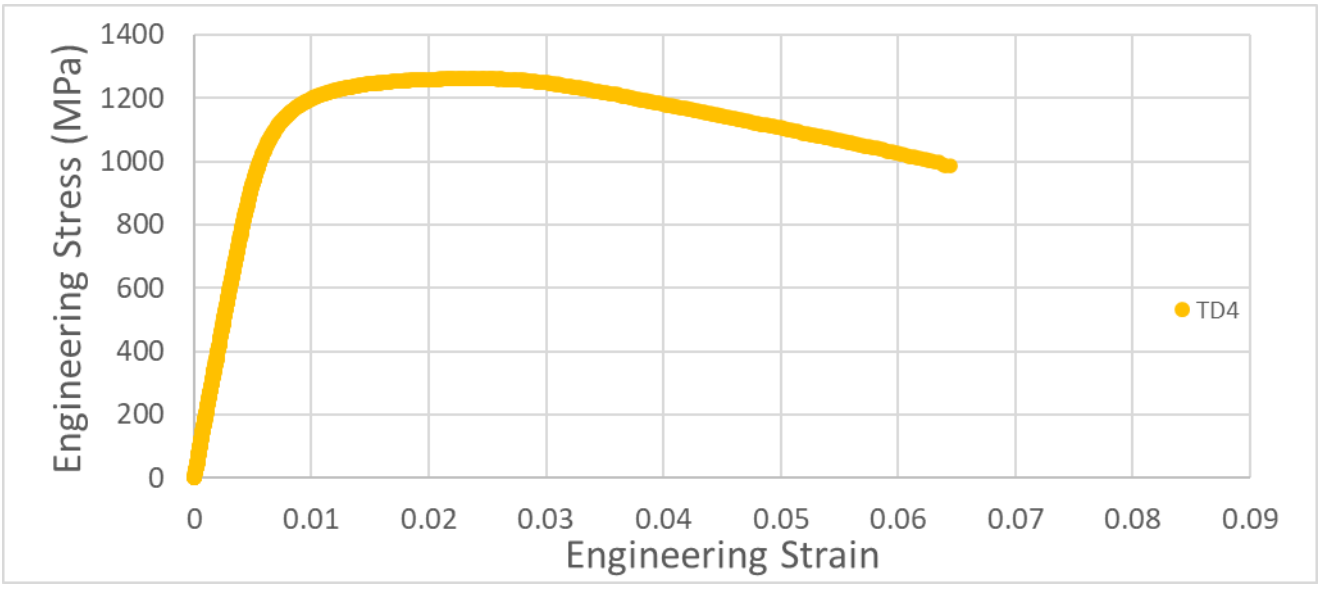


*Figure 5-5: Engineering stress-strain curve for TD4, 17DF4/1 tensile test.*

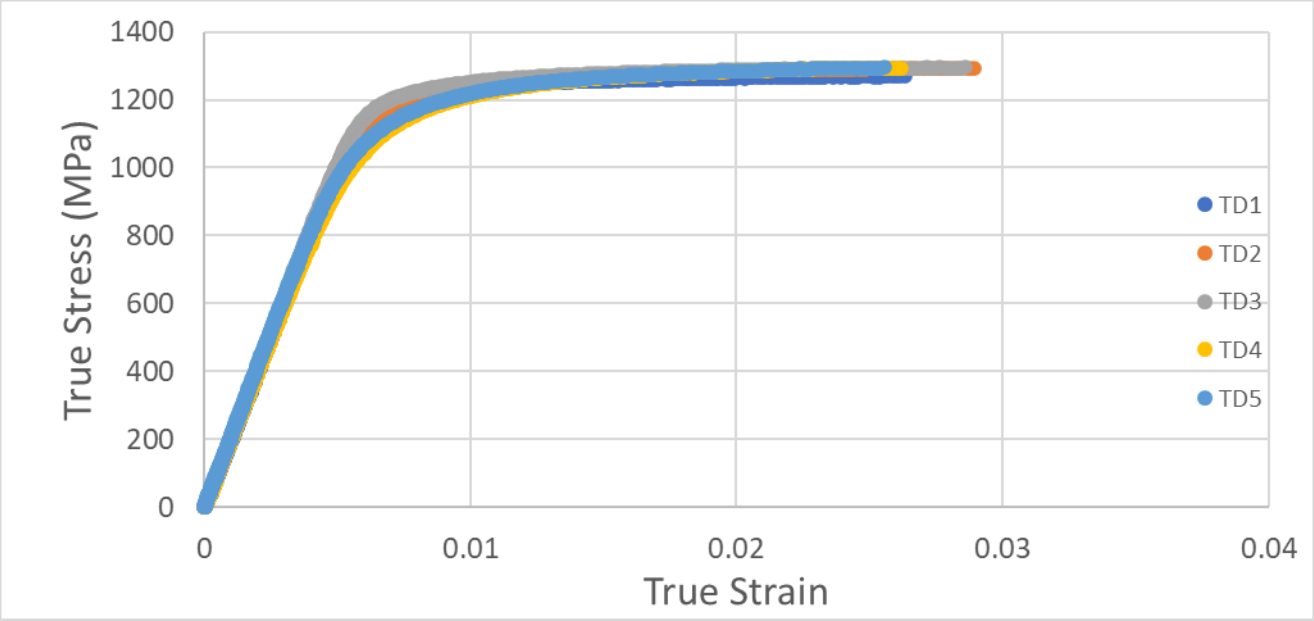


*Figure 5-6: True stress-strain curves for 17DF4/1 tensile tests.*

To produce the averaging curve the data as shown in Figure 5-7 data was compressed by assessing stress every 0.001 strain increase, this was to simplify calculations and to simplify the curve for use in FEM. To do this a data point was taken from each set of data every 0.001 unit of strain. To do this accurately linear interpolation was used as shown in Equation 26:

$$y = y_0 + (x - x_0)\frac{y_1 - y_0}{x_1 - x_0} \qquad \textit{Equation 26}$$

This was used to position the y point at a specific position on x. This was applied to all the stress train curves generating the data in Figure 5-6. To find the stress at each 0.001 increase of strain, linear interpolation was applied. The data from test TD1-5 had this performed. TD4 was excluded as it was considered an anomaly from both its lack of ductility and high strength when compared to the other results.

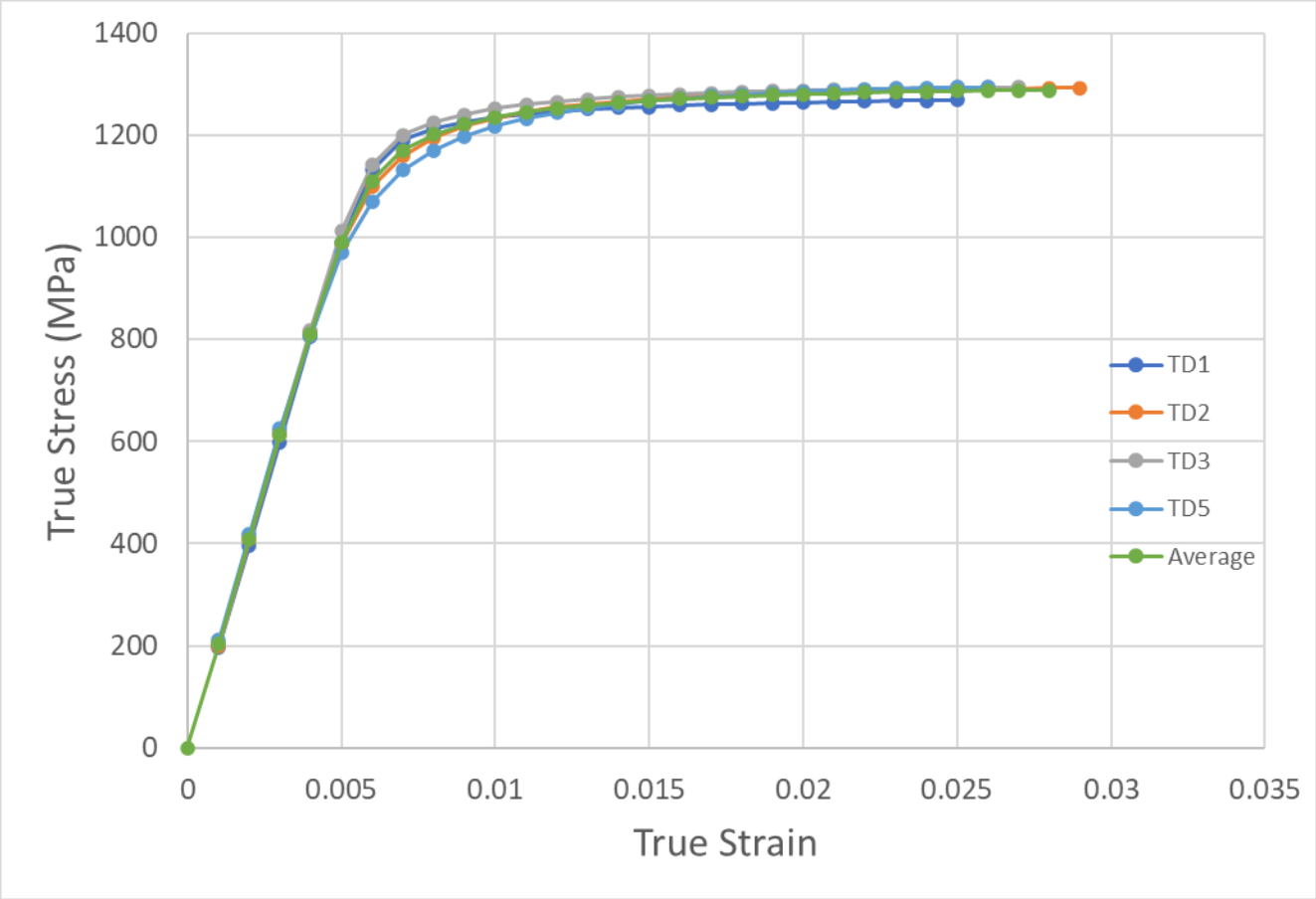


*Figure 5-7: True stress-strain curves for 17DF4/1 tensile tests with averaging.*

The fracture point stress and the strains were averaged and used to produce Figure 5-8.

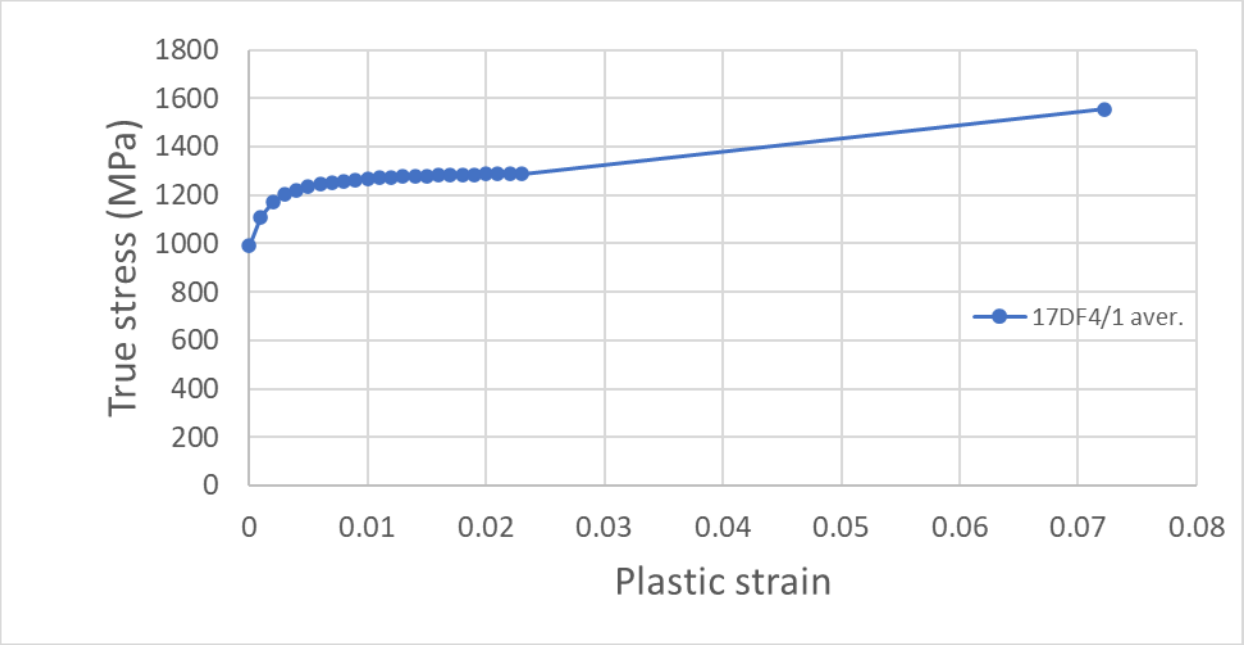


*Figure 5-8: average plastic stress-strain graph for the 17DF4/1 material model with the average fracture point.*

To use this data for FEM for microstructural deformation higher strain values than 0.072 were required with 100% strain being the amount used to allow shear bands to be observed in 2D meshes. To generate this mesh the Hollomon equation as described in section 3.9.1.1 was used. The plasticity

data found a strain-hardening coefficient of 0.0442. While the identification of strain-hardening coefficient at fracture was to use the final point on the true stress-strain graph and the fracture point to find the strain-hardening at fracture. This resulted in a strain-hardening coefficient of n=0.1642 being calculated. This was extrapolated out to 100% strain in 10% strain increments with the plastic data as found in the tensile test as shown in Figure 5-10. This data was used in 2D finite element modelling.

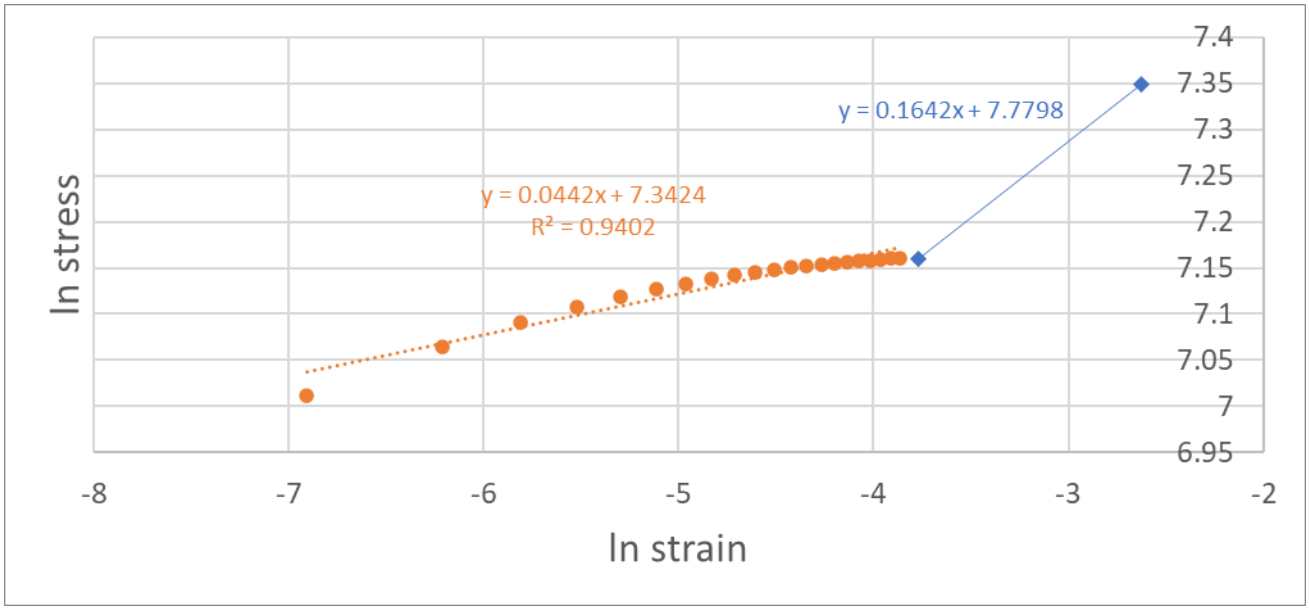


*Figure 5-9: log stress log strain graph for the plastic data and last true stress-strain data point and the average fracture point.*

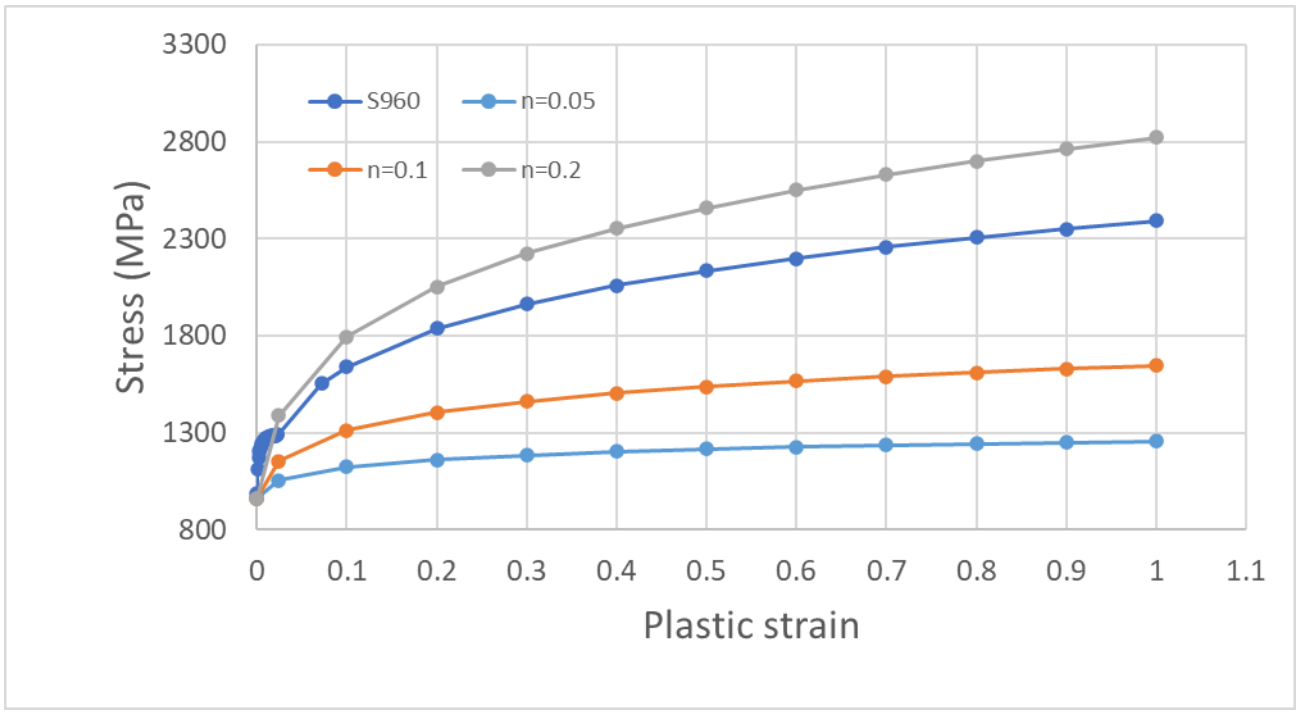


*Figure 5-10: True stress plastic strain graph with the experimentally derived data for 17DF4/1 and the range of material hardening models with different material hardening models as shown in Figure 3-40.*

### *5.1.1.4 DIC images*

The images processed in VIC 3D DIC as described in section 3.7.1.2.3, are shown in Figure 5-11 and Figure 5-12 for the final image in each test before tensile failure. These images allow the analysis of the necked region and how the strain gauges are positioned.

The necked region's peak Eyy strain was found to be between 54% and 55% in tests 1 and 4 respectively and exceeding 60% with 64%, 66% and 68.5% in tests 2, 5 and 3 respectively.

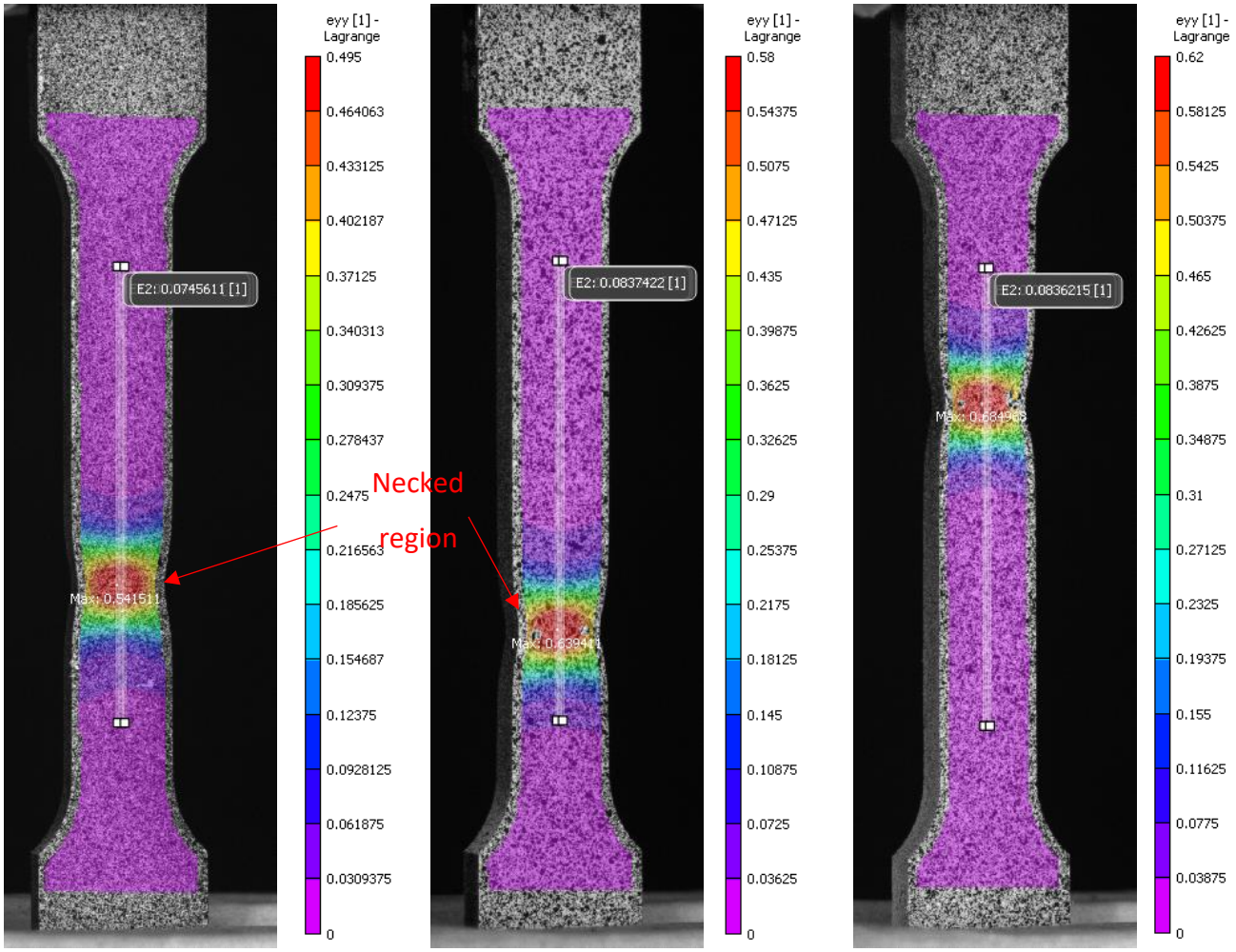


*Figure 5-11: final images before failure with Eyy strain field and virtual strain gauges applied to the surface with: left, TD test 1, middle, TD test 2, right, TD test 3.*

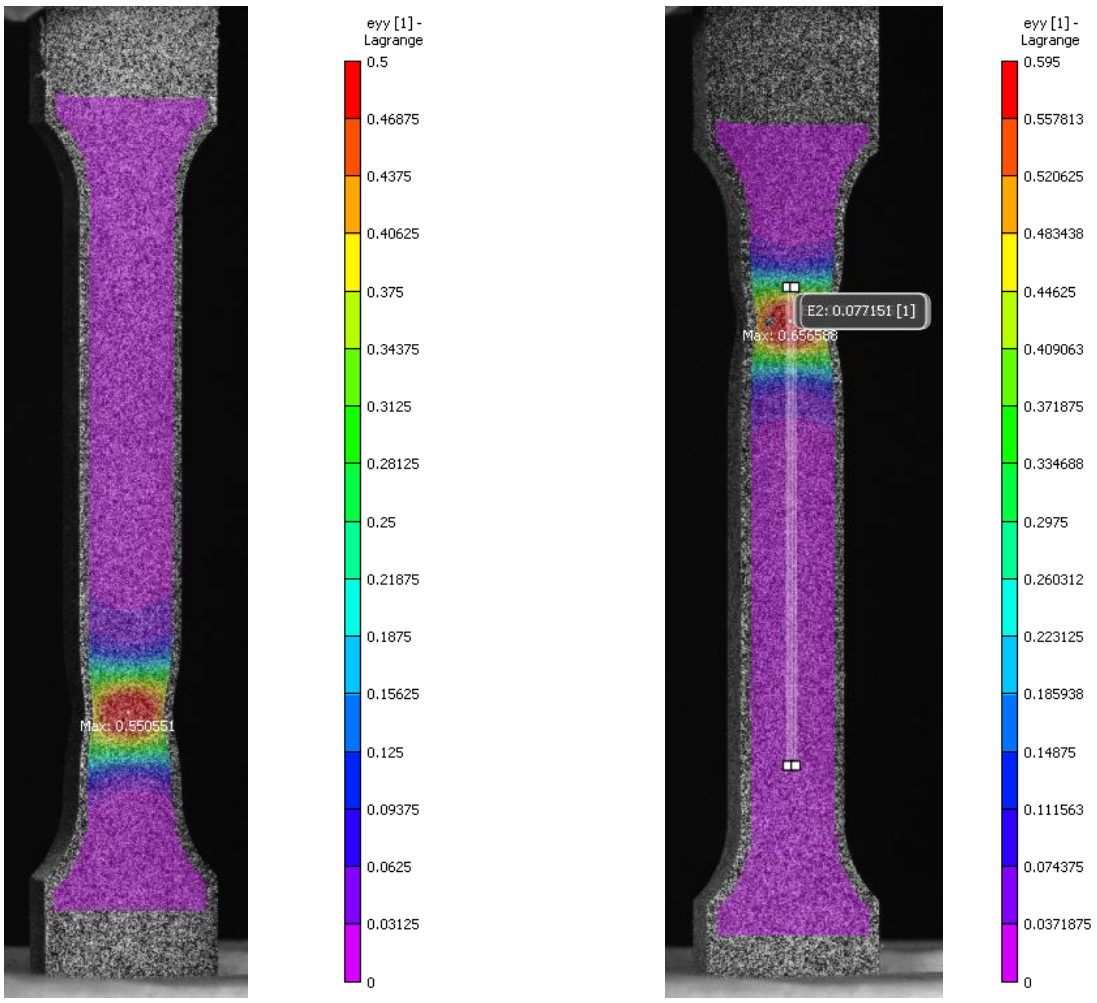


*Figure 5-12: final images before failure with Eyy strain field and virtual strain gauges applied to only TD5 to the surface with: left, TD test 4, right, TD test 5.*

## 5.1.2 Microscale

### *5.1.2.1 Force-displacement graphs*

The force-displacement data is extracted from the Deben module for the tensile test. The results are found to vary significantly Tensile test 1 and tests 2 and 3 were run with different settings. Test 1 was run without interruptions and at a displacement rate of 1mm/min as a trial outside the SEM in a standard tensile test, whereas tests 2 and 3 ran at 0.1mm per minute as interrupted tests within the SEM. The lower strain rate allowed greater control of the interruption points for the operator. This results in different force-displacement curves as shown in Figure 5-13.

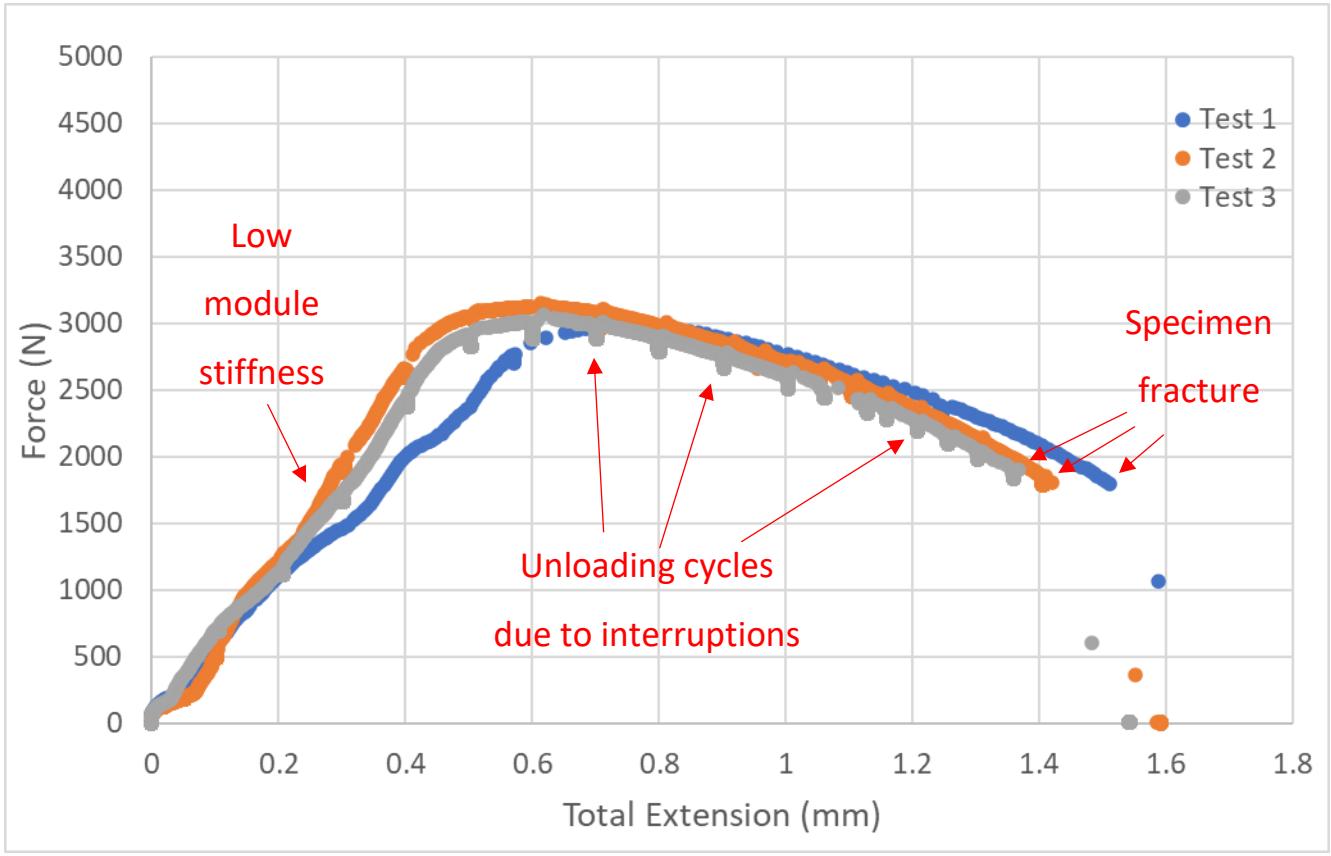


*Figure 5-13: Force-displacement graph from tensile tests in the Deben module.*

#### 5.1.2.1.1 Deben module stiffness correction

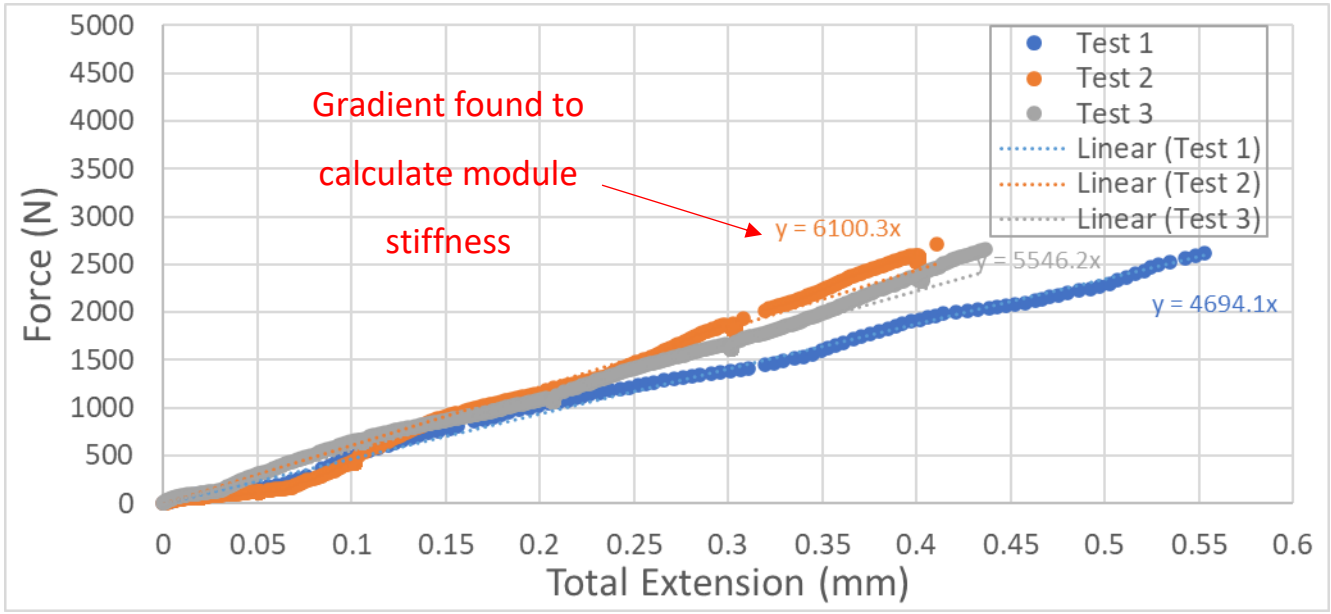


*Figure 5-14: Elastic region analysis of stiffness*

An intercept is set at zero displacement and force. This produced the best quality results compared to using no intercept. This produced the graphs in Figure 5-15 and Figure 5-16. The elastic region is lost as the stiffness correction removes it. This isn't significant as the gauge length is so short relative to its width. While the DIC can only detect plastic strain so this is not a major problem.

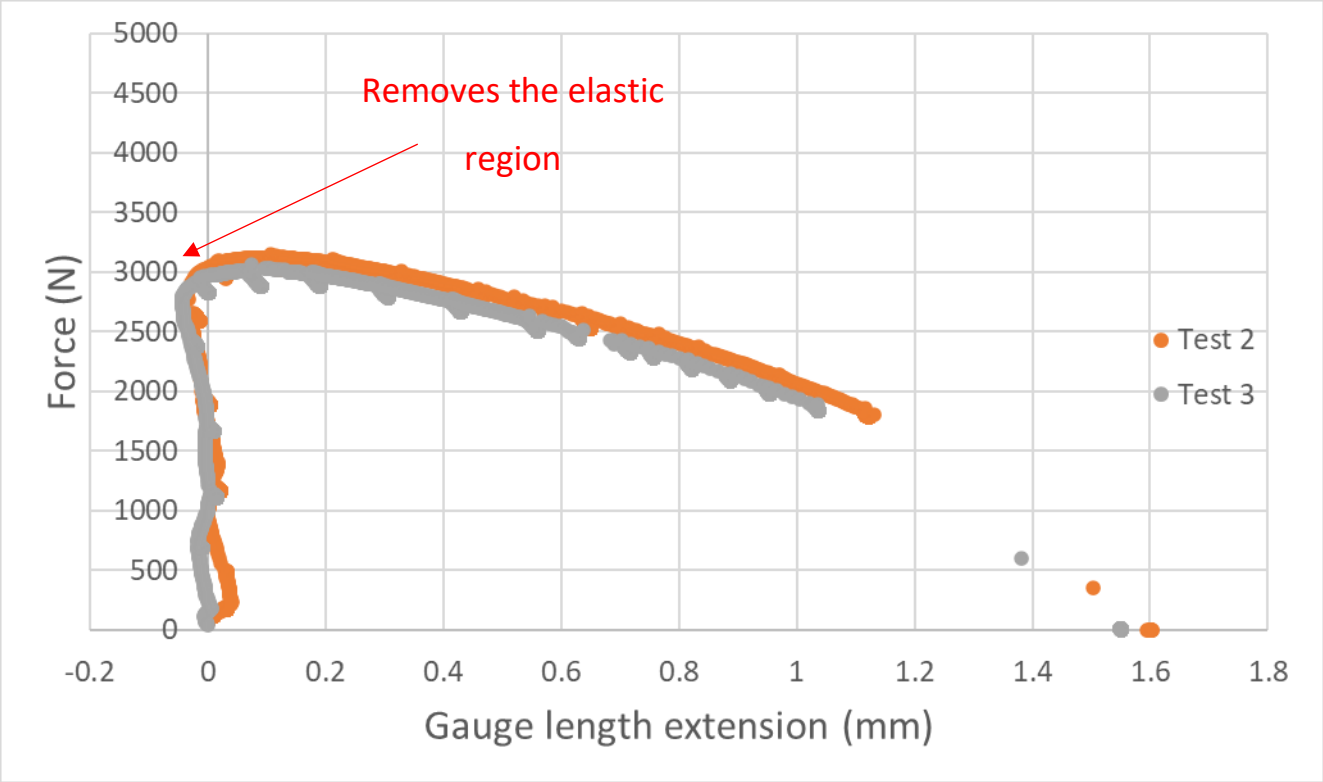


*Figure 5-15: Stiffness adjusted force-displacement graph*

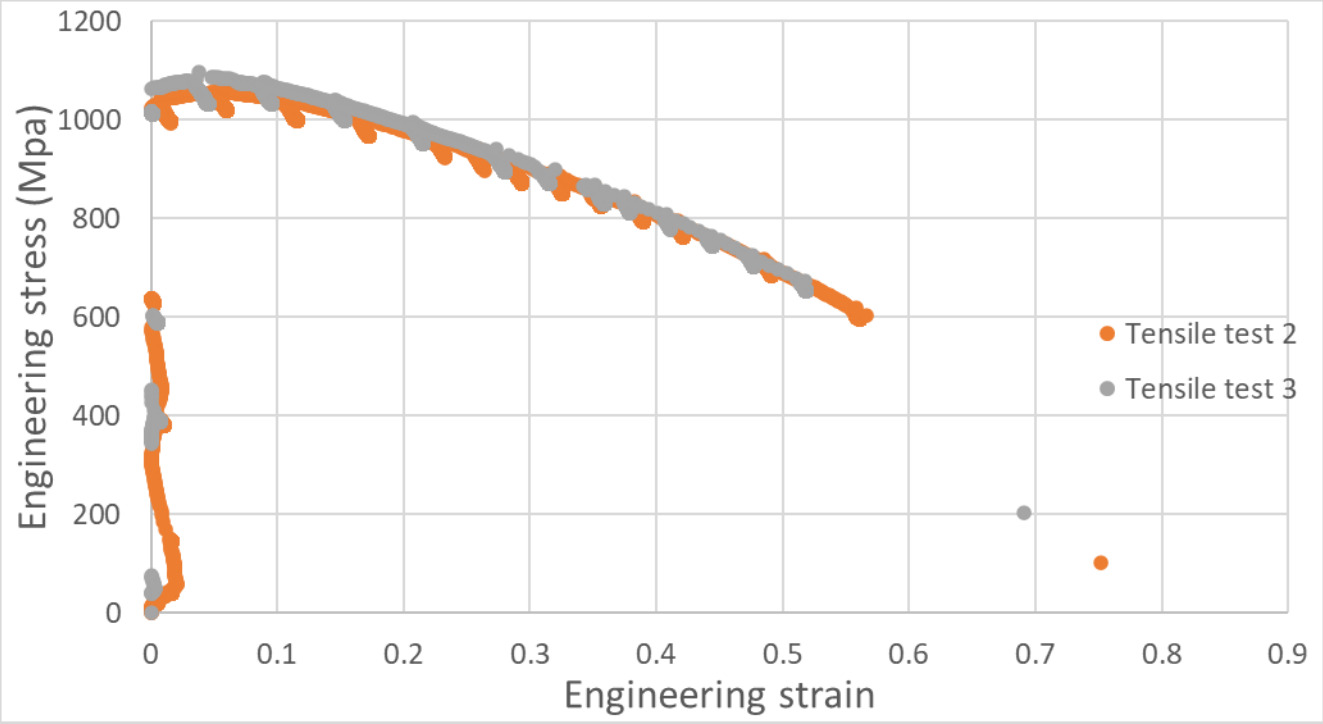


*Figure 5-16: Stiffness adjusted engineering stress-strain graph*

In Figure 5-13 an analysis of total extension against engineering stress is converted into Figure 5-15 by the application of the stiffness calculation. By treating the total extension of the tensile tester, $u_T$, sample, $u_s$ and the module's motion $u_m$ as elastic they can be modelled by Hooke's law where the

force, $F$ is applied on both of the sample and module and their respective stiffness's, for the module, $k_m$ and for the sample, $k_s$.

$$F = k_m u_m = k_s u_s \quad where \quad u_T = u_m + u_s \qquad \textit{Equation 27}$$

In Equation 27 Hooke's law is applied to both the tensile test stage, sample and total extension $u_T$ is shown to be a sum of the extension from the tensile test stage elastic extension $u_m$ and sample gauge length ${u_s}^{GL}$ and outside the gauge length ${u_s}^{OGL}$. The terms excluding the extension of the gauge length are summed into a total module extension term, ${u'}_m$.

$$u_T = u_m + ({u_s}^{OGL} + {u_s}^{GL}) \rightarrow u_T = {u'}_m + {u_s}^{GL} \quad where \quad {u'}_m = u_m + {u_s}^{OGL} \qquad \textit{Equation 28}$$

Using the total extension term in Equation 27, Equation 28 derives the extension of the gauge length area and simplifies the regions outside this down to a single component. Where the sample's stress, $\sigma_s$, Young's modulus, $E$ and strain, $\varepsilon$ as well as the gauge length dimensions; width, $w_s$ thickness $t_s$ and length of the gauge length, $l_s$.

$$\sigma_s = E\varepsilon \equiv \frac{F}{w_s t_s} = E\frac{{u_s}^{GL}}{l_s} \rightarrow {u_s}^{GL} = \frac{F l_s}{E w_s t_s} \qquad \textit{Equation 29}$$

Now by rearranging Young's modulus in Equation 29, a term for the extension of the gauge length can be derived.

$$u_T = \frac{F}{{k'}_m} + \frac{F l_s}{E w_s t_s} \rightarrow {k'}_m = \frac{F}{\left(u_T - \frac{F l_s}{E w_s t_s}\right)} \qquad \textit{Equation 30}$$

By inputting the equations from Equation 27 and Equation 29 into Equation 28, the stiffness for the outside gauge length and tester is derived in Equation 30. By then plotting the force and total extension a stiffness value can be derived for the extension outside the gauge length. Then calculating for every point the extension from this stiffness using Hooke's law the extension in the gauge length can be calculated.

Due to the differences in the test procedure, tensile test 1 has been excluded from the following results. The lines converge between tensile tests 2 and 3 once the stiffness correction value is calculated for each test with the gradient found in the elastic region in
Figure 5-14. This is applied to in Figure 5-15 and Figure 5-16 with results converging when compared to Figure 5-13. Both tests show consistent material behaviour excluding the point of failure.

The strain is calculated for the 2mm gauge length. This shows failure occurred after 58% and 54% for test 2 strain after a significant reduction from their UTS to 620MPa and 680MPa at failure. These strains are exaggerated by the tensile test geometry, previous use of their geometry by Alharbi et al [36] has found they increase the strain by a factor of 5 over a standard tensile test.

To validate the strain calculations markings were placed on the edge of the gauge length using a micrometre being calibrated to half the length of the specimen minus half the gauge length. This is then used to scribe a gauge length marking which is then repeated from the other end of the specimen. Micrographs of the gauge length area at 20x magnification were obtained at each displacement interruption. These were then analysed post-test using Microsoft Paint to identify the position of the line with 3 points taken and averaged to calculate the strain.

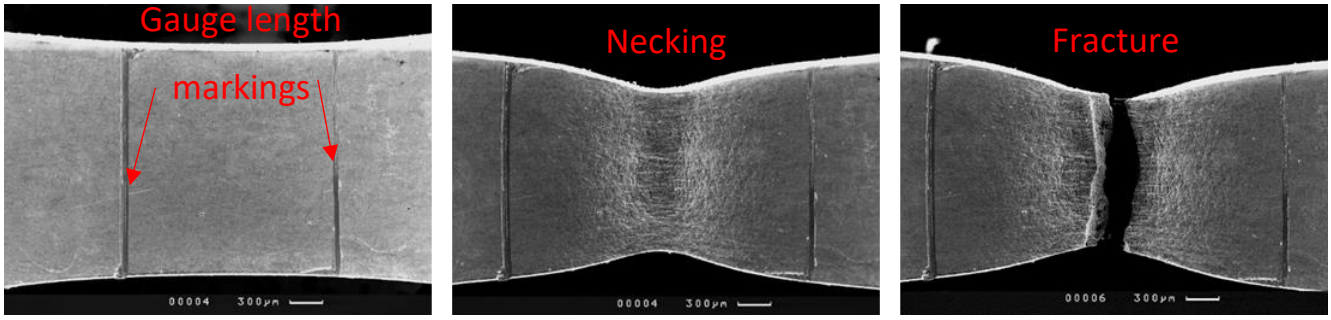


*Figure 5-17: 20x magnification micrographs of the gauge length in the tensile test at no displacement on the left, 1.1mm displacement at the middle and post-failure on the right.*

Using this method of identifying the strain development a comparison to the stiffness adjusted strain values was produced. This allowed the first increase in strain to be calculated. While this does find the initial correction value as found in Figure 5-19, it does not account for the stiffness of the module which will relax as the force is reduced.

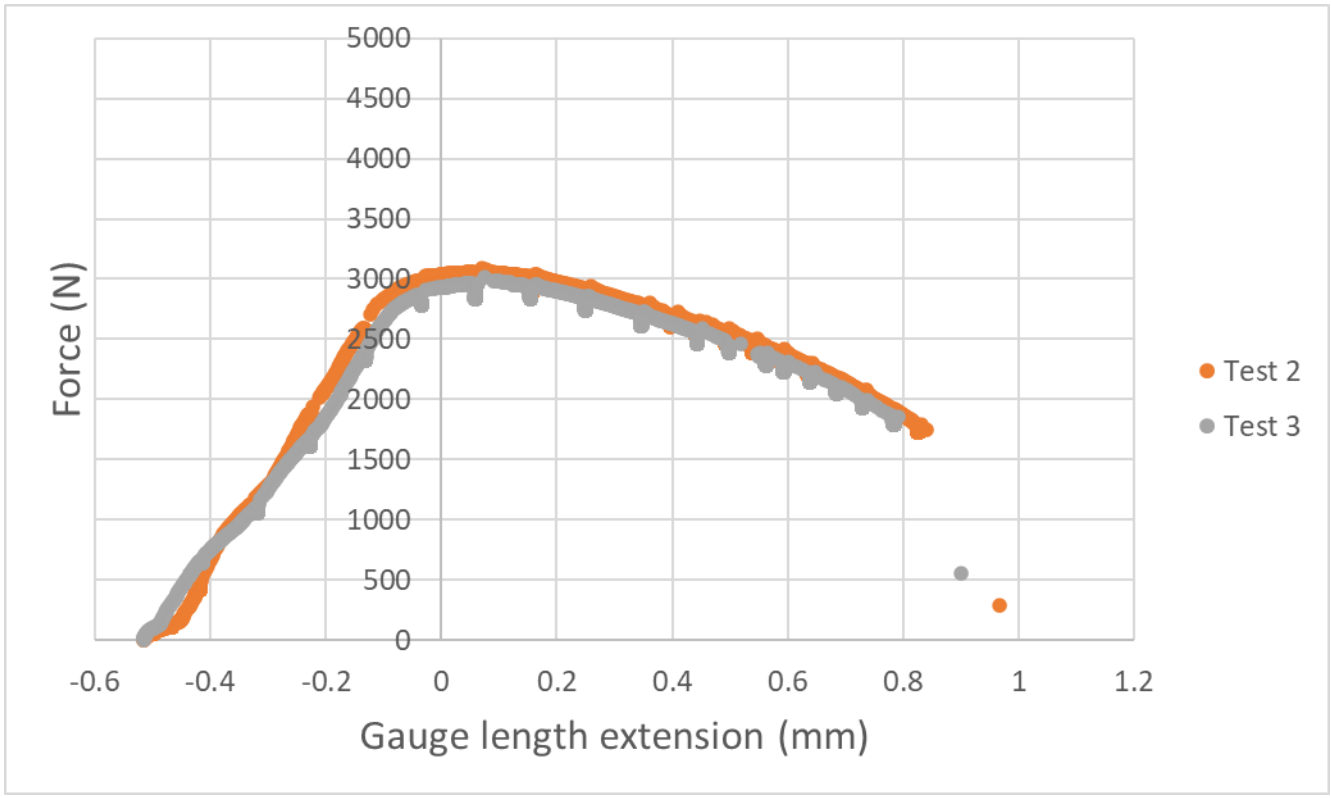


*Figure 5-18: Optically adjusted force gauge length extension graph.*

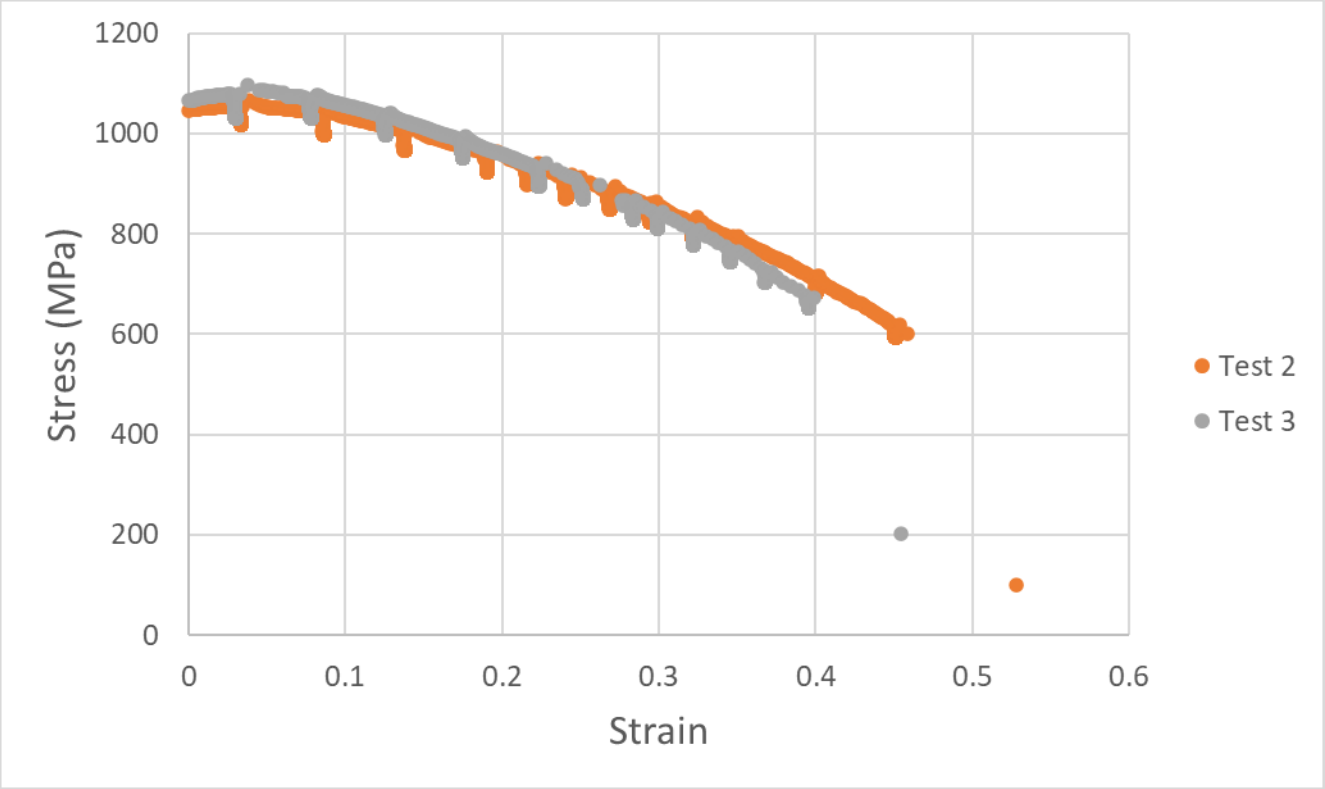


*Figure 5-19: Optically adjusted stress-strain graph for tensile tests 2 and 3 in the SEM.*

### *5.1.2.2 Micrographs*

Using the Camscan S2 SEM micrographs were obtained at the centre of the tensile test specimen in test 2 at 1400x magnification, giving a small field of view of 80.3µm by 54.8µm but have high enough magnification and detail to observe the microstructural strain. The images are taken at interruptions in the tensile test as described in section 3.5.1.1 due to the SEM taking 2.5 minutes to scan a micrograph.

The extension is in the XX direction as shown in image 2. in Figure 5-20. The micrographs show the deformation of the specimen during the test. No significant deformation is shown between images 1. (no displacement), and 2. (0.5mm displacement), with surface roughness becoming visible from image 4. (0.9mm displacement). This increases as the specimen undergo intense plastic strain until failure at just over 1.419mm displacement shortly after the 1.4mm interruption. In image 7. (1.3mm displacement) 2 voids begin to localise promoting voids to the surface in image 7. (1.4mm displacement). The locations of where the voids nucleate are circled in image 7.

*Figure 5-20: Micro tensile test 2*

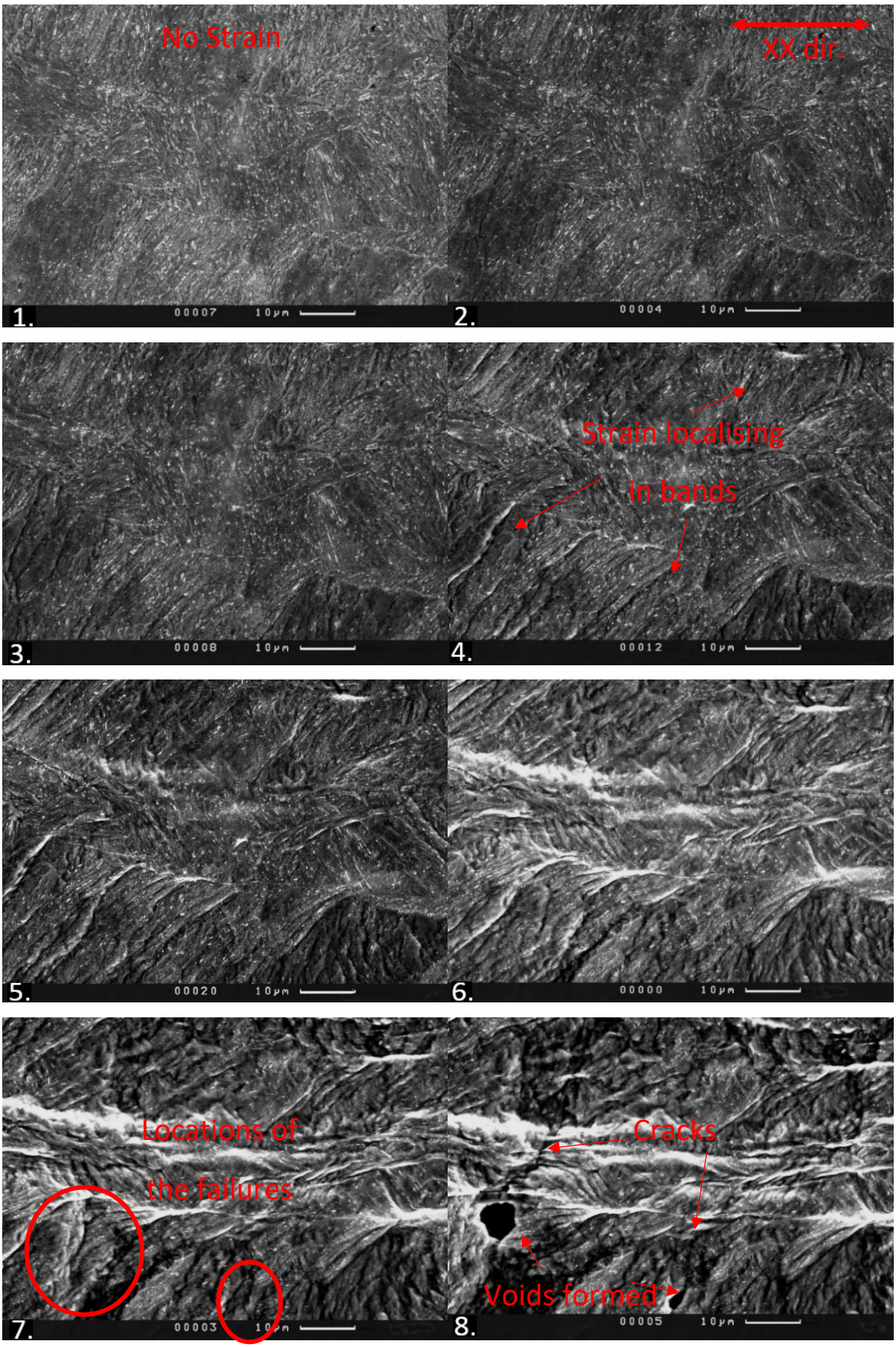


*micrographs at 1400x magnification at the centre of the gauge length. 1. No displacement; 2. 0.5mm displacement; 3. 0.7mm displacement; 4. 0.9mm displacement; 5. 1.0mm displacement; 6. 1.2mm displacement; 7. 1.3mm displacement; 8. 1.4mm displacement.*

#### *5.1.2.3 DIC*

To obtain DIC images these were processed by using the micrographs as shown in Figure 5-20. The settings used for this were a sum of differential settings that sums the strain propagation from previous images, a subset of 31 pixels to identify patterns was used and the overlap of each pattern or step size is 5 pixels. Accurate calculation mode was used with outlier and smoothing filter on.
The strain is found to localise in shear bands at 45° to the strain being applied in the XX direction. The failure is promoted from the centre of the specimen in the subsurface below the image and propagates to the surface observed. By studying the location of failure that was captured in image 7. the strain found at the point of failure has a strain of 150% but is located between a location at Exx 50% strain and 350% strain. The strain in image 7. shows that the specimen has localised strain with very inhomogeneous properties with strain in Exx varying from 25% up to 390% in regions.
The strain was also studied at its maximum shear strain at the same displacement in Figure 5-24. This shows the shear strain in the same locations as Exx, with lows of 15% and peaks of 225% shear strain. The location of the void forming has a strain of 100% shear strain, the local high and low strain points of 225% and 25% shear strain respectively. The locations of the shear bands are found to be static, intensifying as strain is applied until 1.3mm displacement where the shear band in Figure 5-21 the shear band goes perpendicular to the applied strain.
To obtain the images in Figure 5-22 a post-processing method is used to obtain the DIC images in DaVis called Vector Shift Correction VSC, the location of points in the strain map can be identified from the undeformed first image. This allows the area of interest to be traced back to its origin. This also shows in Figure 5-22 that no significant strain is detected by the DIC until 0.5mm displacement due to the lack of stiffness in the Deben tensile test module. Using this technique allowed the location of the failure in the DIC region to be found in Figure 5-23. When this is studied nothing of interest is noted in this region. The failure is originating from the subsurface, so the cause of the strain localisation is not obvious from the surface where it is only coming to the surface. It is likely the cause of the failure would be found in the subsurface.

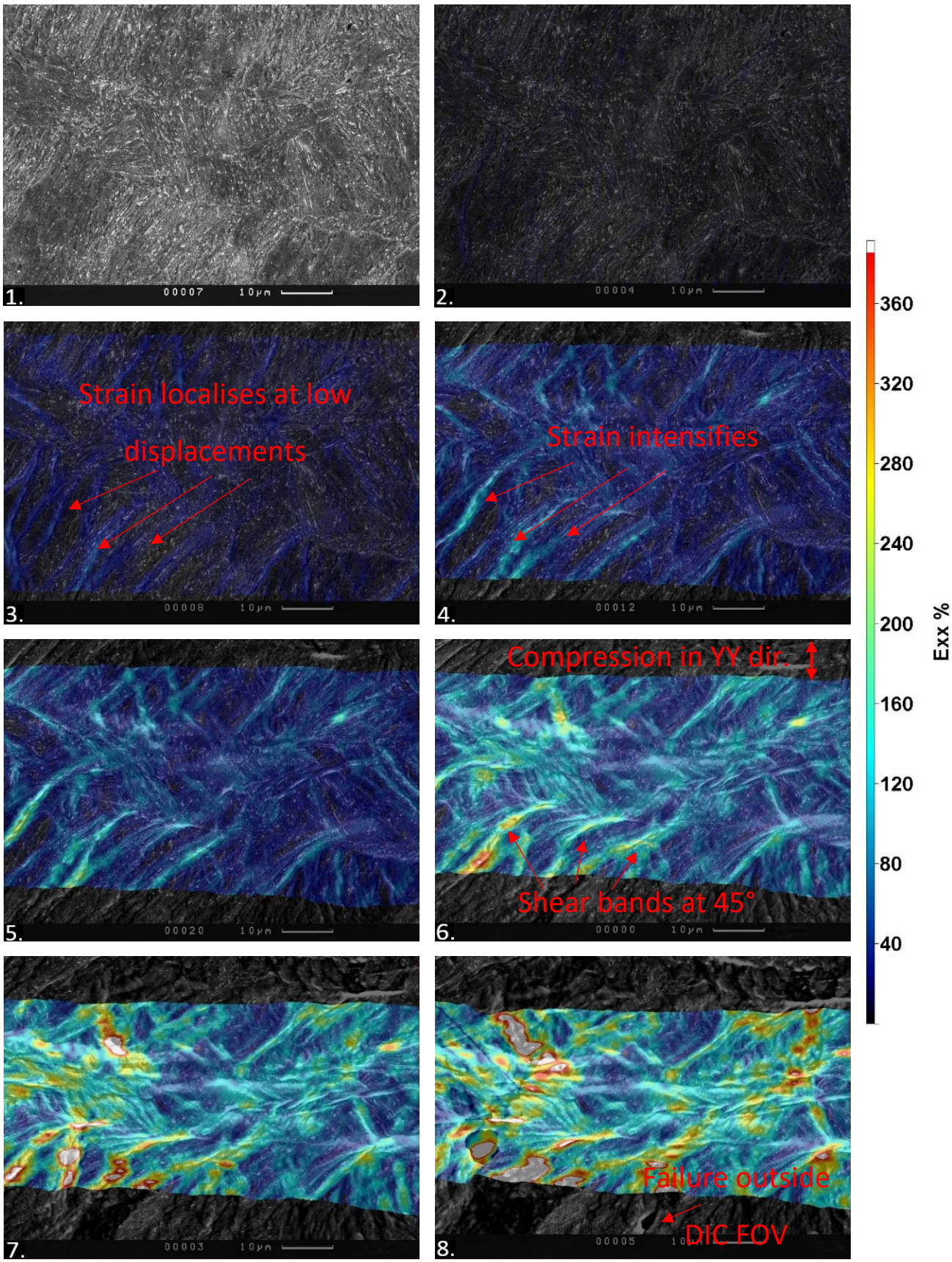


*Figure 5-21: DIC plots on overlaid on micrographs at 1400x magnification at the centre of the gauge length. 1. No displacement; 2. 0.5mm displacement; 3. 0.7mm displacement; 4. 0.9mm displacement; 5. 1.0mm displacement; 6. 1.2mm displacement; 7. 1.3mm displacement; 8. 1.4mm displacement.*

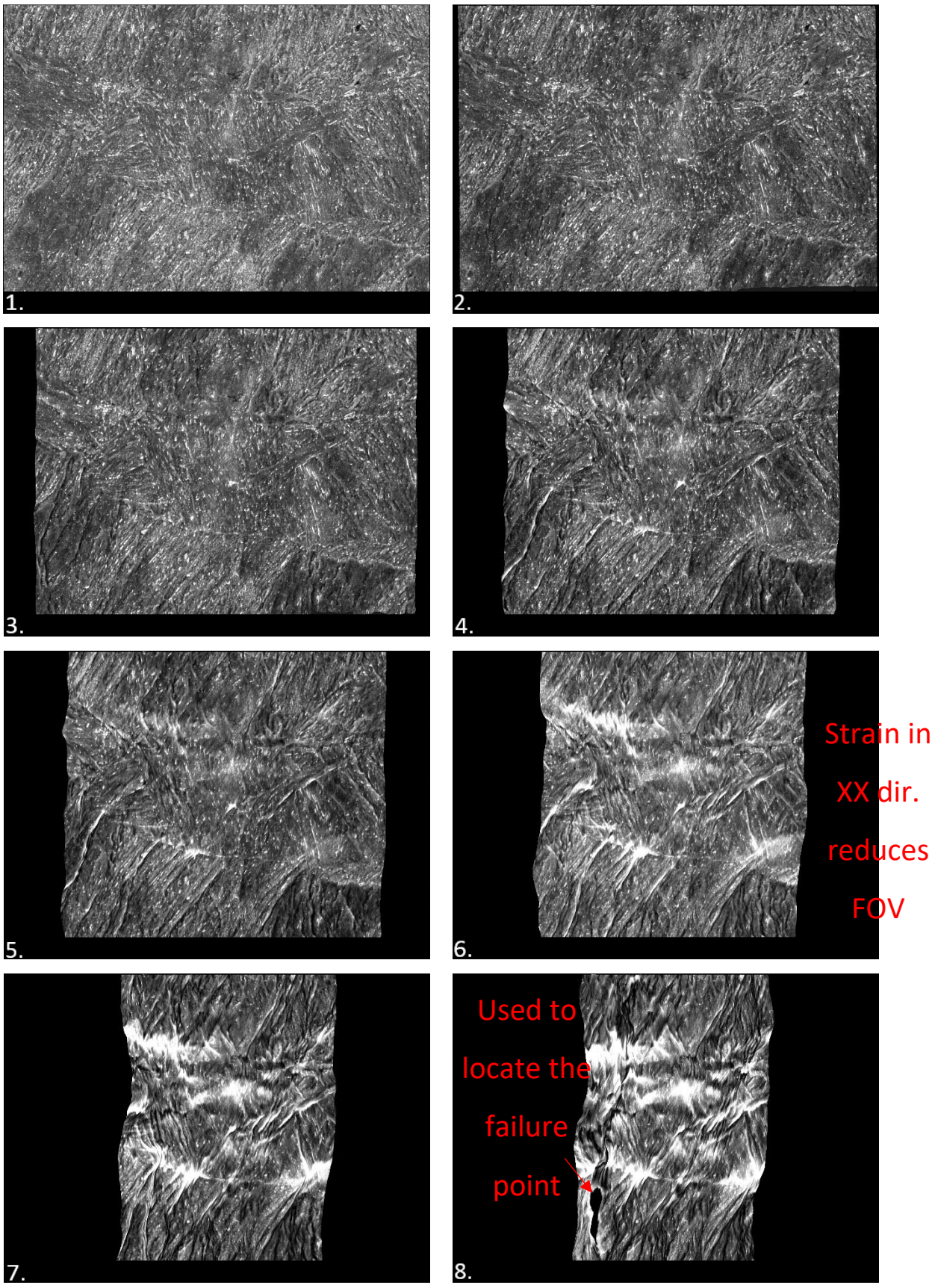


*Figure 5-22: VSC DIC post-processed micrographs at 1400x magnification at the centre of the gauge length. 1. No displacement; 2. 0.5mm displacement; 3. 0.7mm displacement; 4. 0.9mm displacement; 5. 1.0mm displacement; 6. 1.2mm displacement; 7. 1.3mm displacement; 8. 1.4mm displacement*

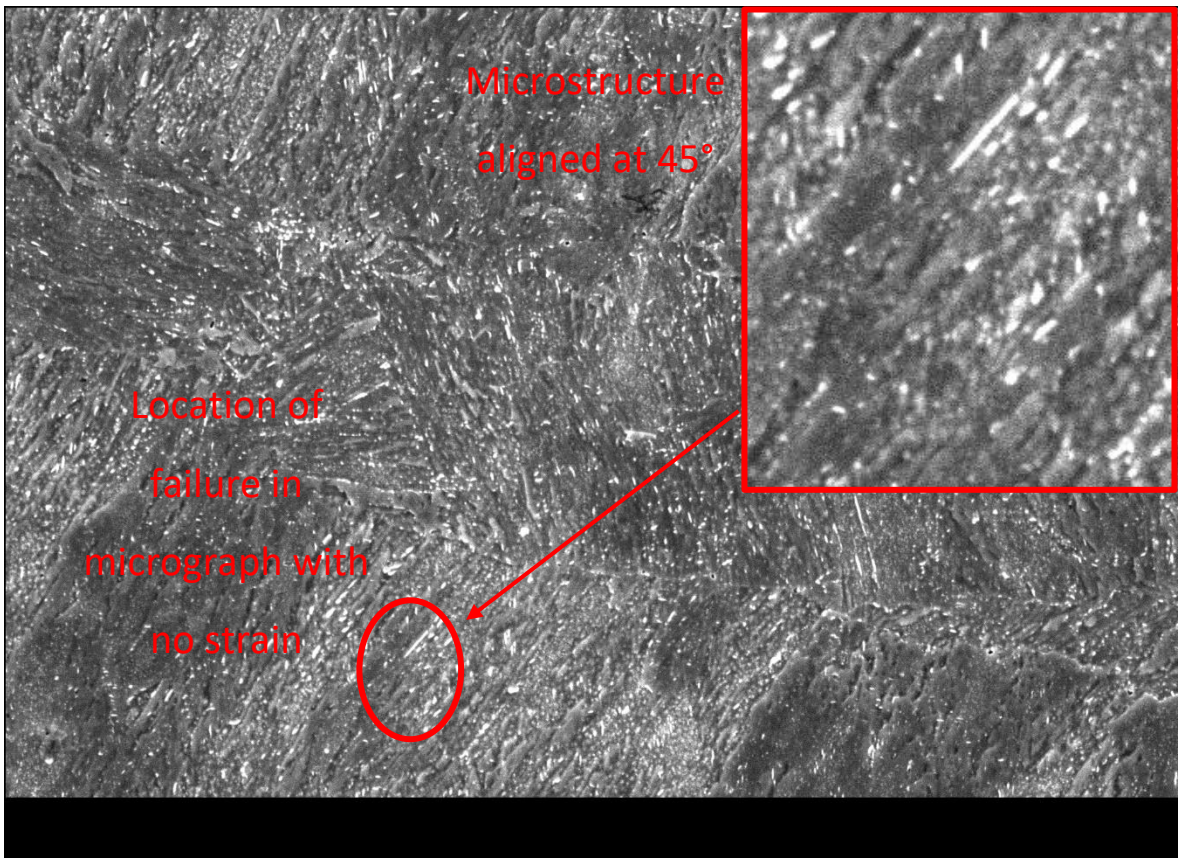


*Figure 5-23: VSC identification of failure zone in the microstructure.*

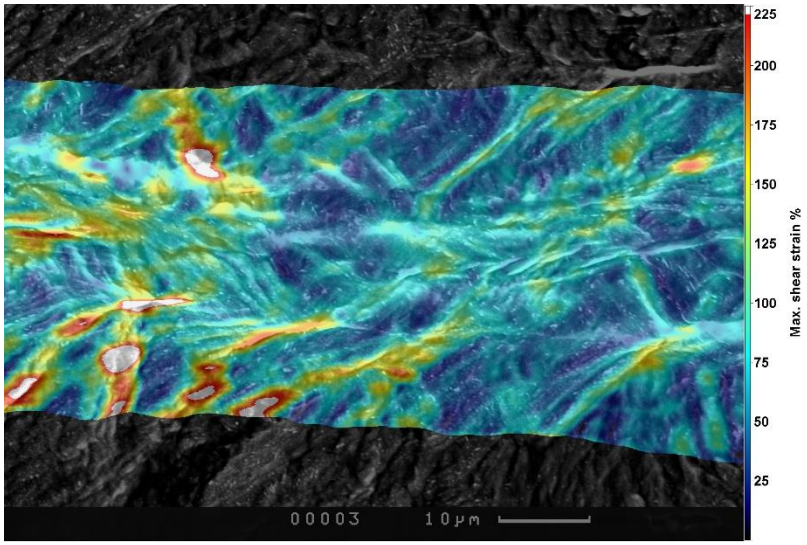


*Figure 5-24: DIC plots overlaid on micrographs at 1400x magnification at the centre of the gauge length at 1.3mm displacement*

### 5.1.3 Microhardness

To study localised material properties and their properties, hardness indentation was used to analyse the variation in hardness through depth. Micro and nano hardness indentation were used as they allowed for analysis of hardness at higher density with smaller indentation and hence closer to the material's top surface.

Using the methods described in Microhardness indentation the hardness is found to vary from the top hot-rolled surface to 0.6mm of depth. The hardness is found to vary by about 20HV in this region. Although due to the size of the indentations their spacing cannot be located closer to each other or nearer the surface to meet the ASTM standards for hardness testing [98]. This causes the top 0.15mm in depth from the surface to not be measured. This region is of particular interest as this is where the DIC images are produced to analyse the formation of shear bands.

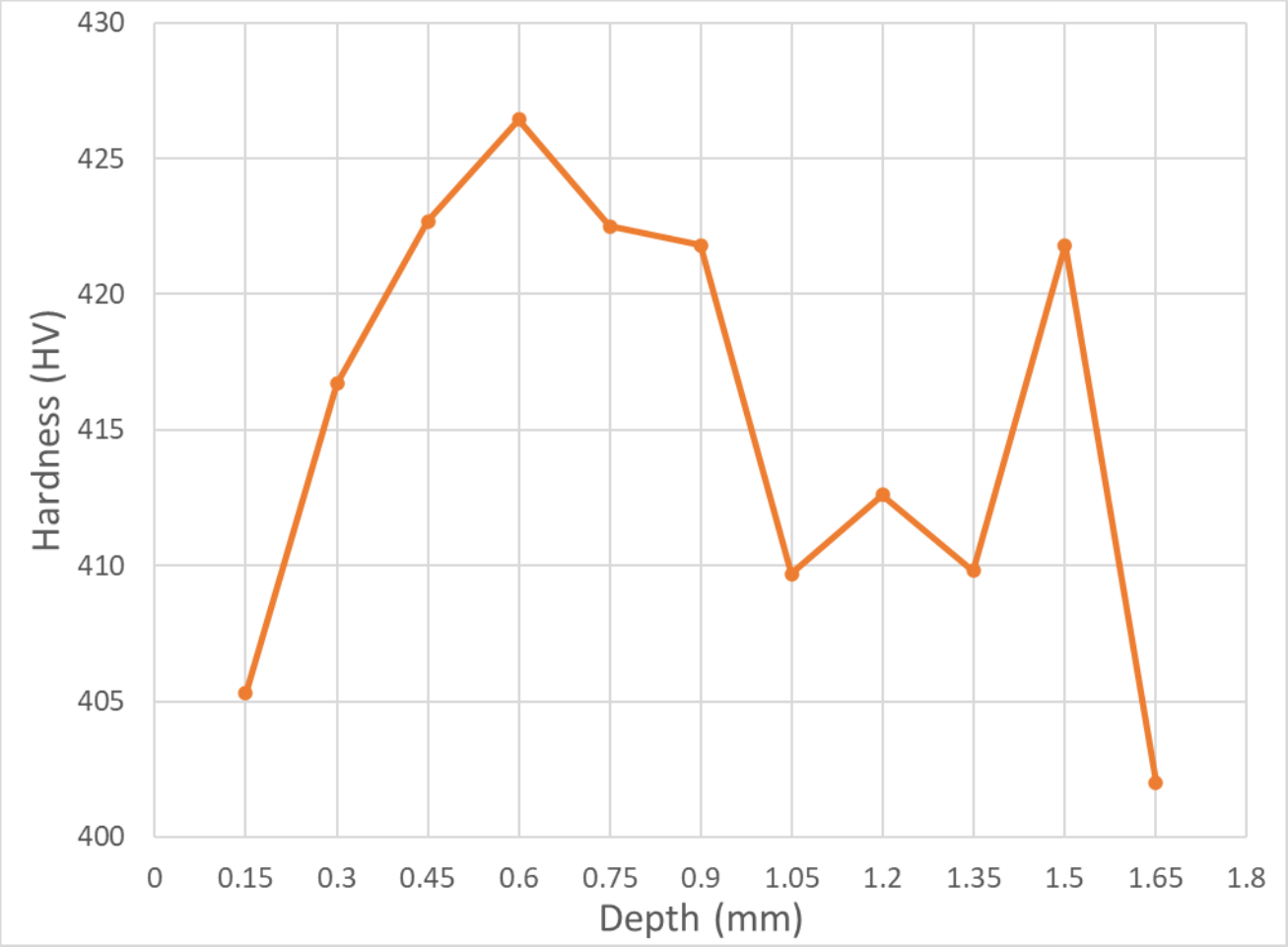


*Figure 5-25: Average microhardness vs depth graph*

### 5.1.4 Nano-hardness

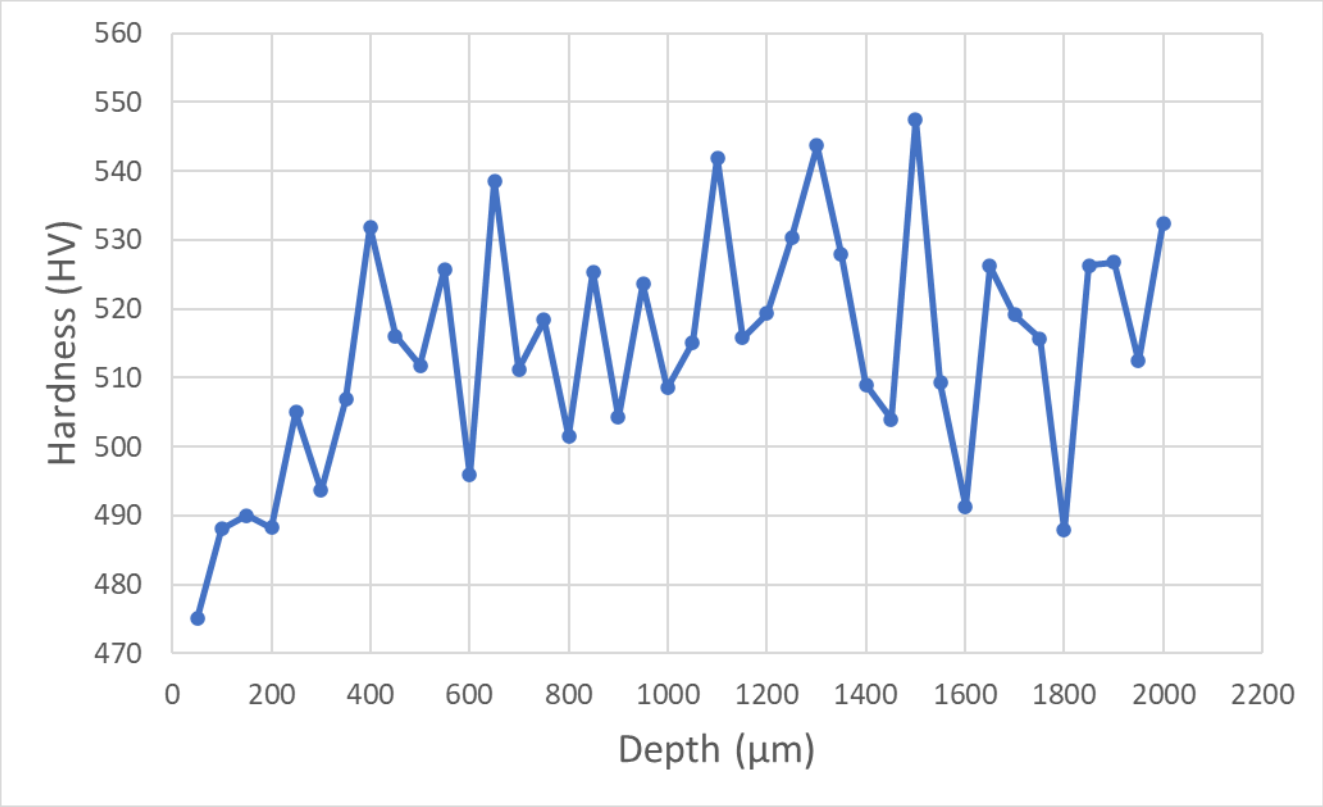


*Figure 5-26: Average nano hardness vs depth graph*

To analyse the depth close to the top surface and space the indentations closer together nano hardness indentation was used. This allowed the indentations to be spaced every 50µm. The nano hardness values were found to vary significantly although the top surface shows a significant drop in hardness from 0.4mm (400µm).

### 5.1.5 Micro vs nano-Hardness comparison

It is found that both micro and nano hardness indicate the steel has a softer top surface with a reduction from 426 HV0.5 at 0.6mm depth to 405 HV0.5 at 0.15mm depth in the micro tests while the nanoindentation tests are at 475 HV at 0.05mm depth and highs of 539 HV at 0.65mm depth. When comparing micro and nano hardness curves they follow a similar pattern but with a difference of around 100HV between those curves. The nano hardness indentations have more noise which is due to tests individual microstructures rather than the larger areas tested with microhardness indentation. Error bars were applied with 2 standard deviations above and below the mean point. This results in a confidence margin of 95.4%.

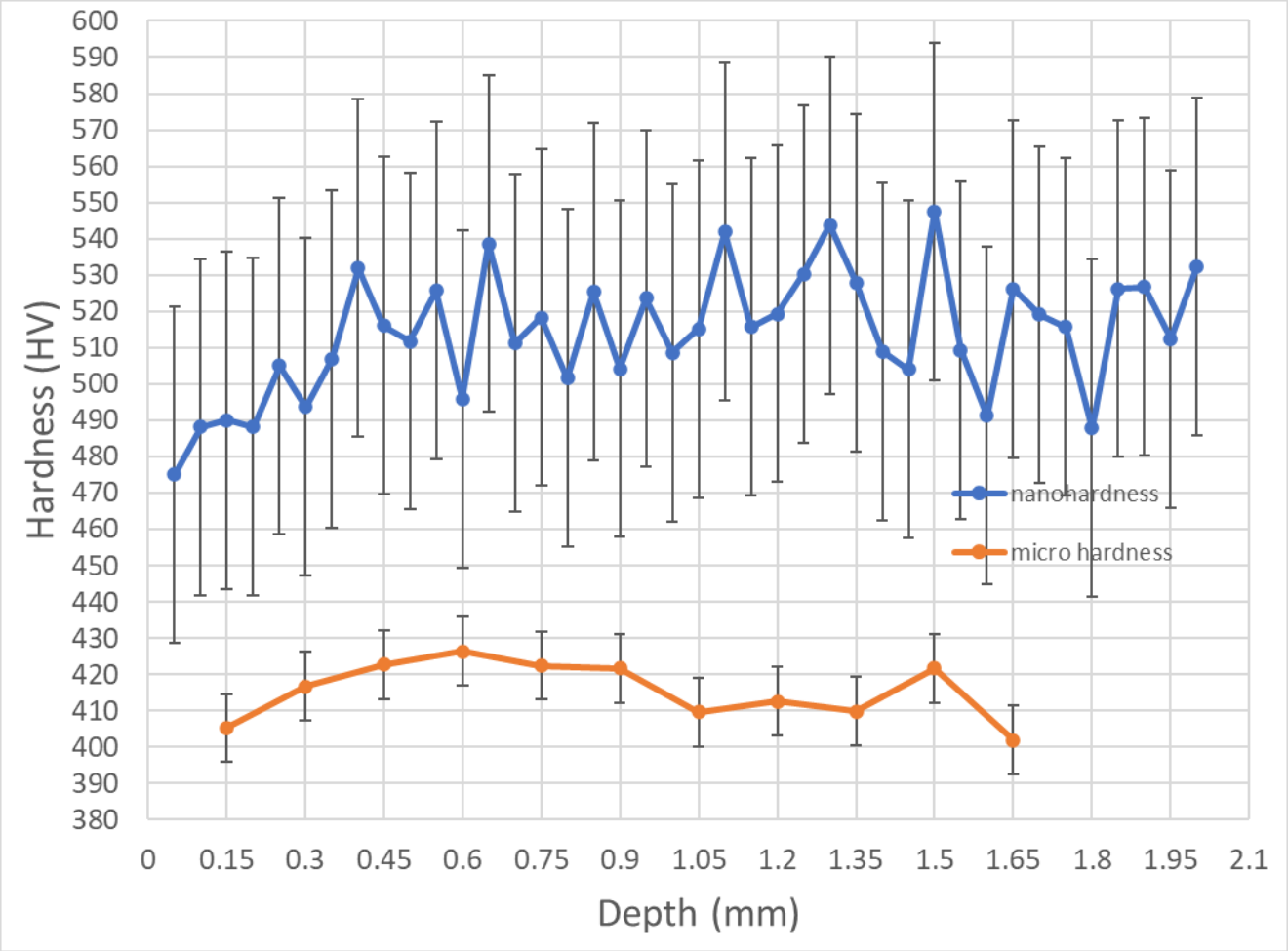


*Figure 5-27: comparison of micro and nano hardness depth profiles*

## 5.2 Bend testing

### 5.2.1 Deben 5mm diameter bend test tooling

#### *5.2.1.1 Transverse direction 1mm thickness bend tests*

Initial tests were performed with the 14TG26, 6mm thick sample plate. The specimens were only 1mm thick, produced to an existing design used with DP steel. These were performed primarily to trial the bend test tooling. The loads were very low and did not approach damage. Hence a thicker specimen was designed.

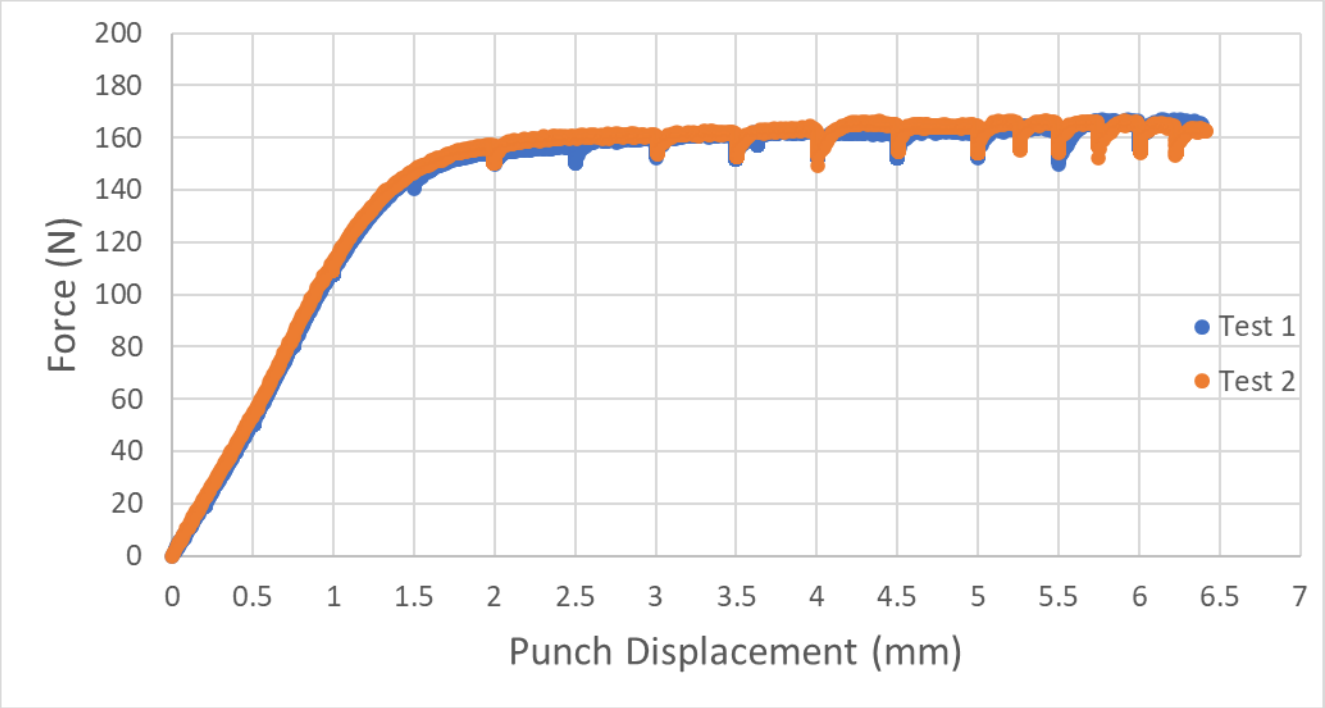


*Figure 5-28: Force-displacement graph for 1mm thickness bend test specimens bent with the Deben bend test tooling in the Deben tensile and horizontal bending module.*

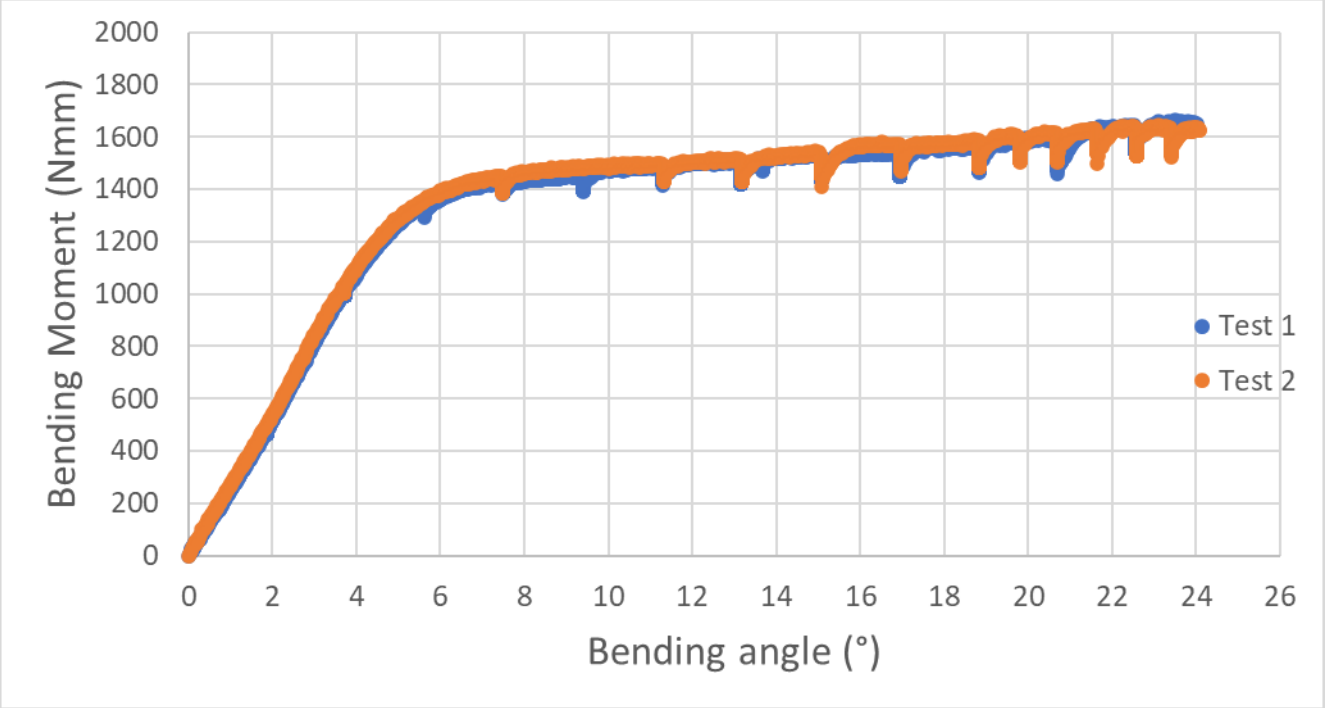


*Figure 5-29: Bending moment bending angle graph for 1mm thickness bend test specimens bent with the Deben bend test tooling in the Deben tensile and horizontal bending module.*

#### *5.2.1.2 3mm thickness transverse direction bend tests*

The 3mm thickness bend tests promoted a force drop not achieved with the 1mm thick specimens when comparing Figure 5-28 and Figure 5-30. Manufactured from the 14TG26 6mm thick plate, the specimens were effectively half the thickness of the plate with the bottom section of the plate

removed. Further analysis of the bending moment graph in Figure 5-31, shows that there is no drop and damage is not being promoted.

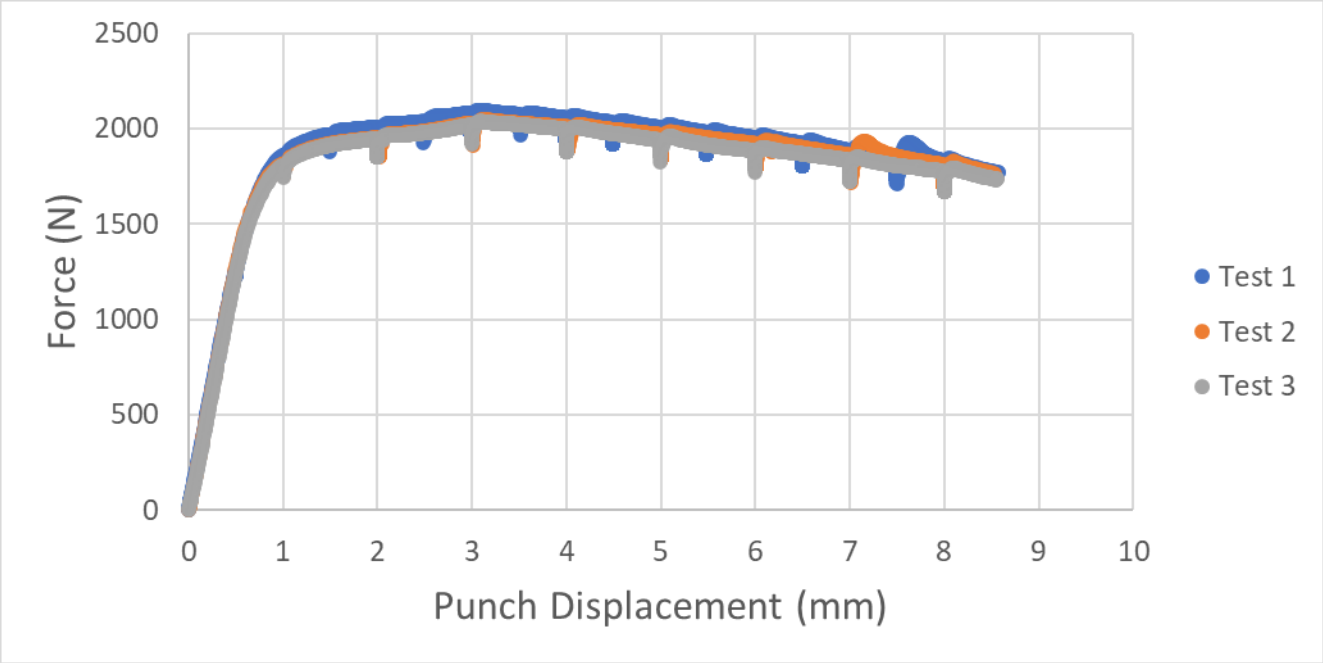


*Figure 5-30: Force-displacement graph for 3mm thickness bend test specimens bent with the Deben bend test tooling in the Deben tensile and horizontal bending module.*

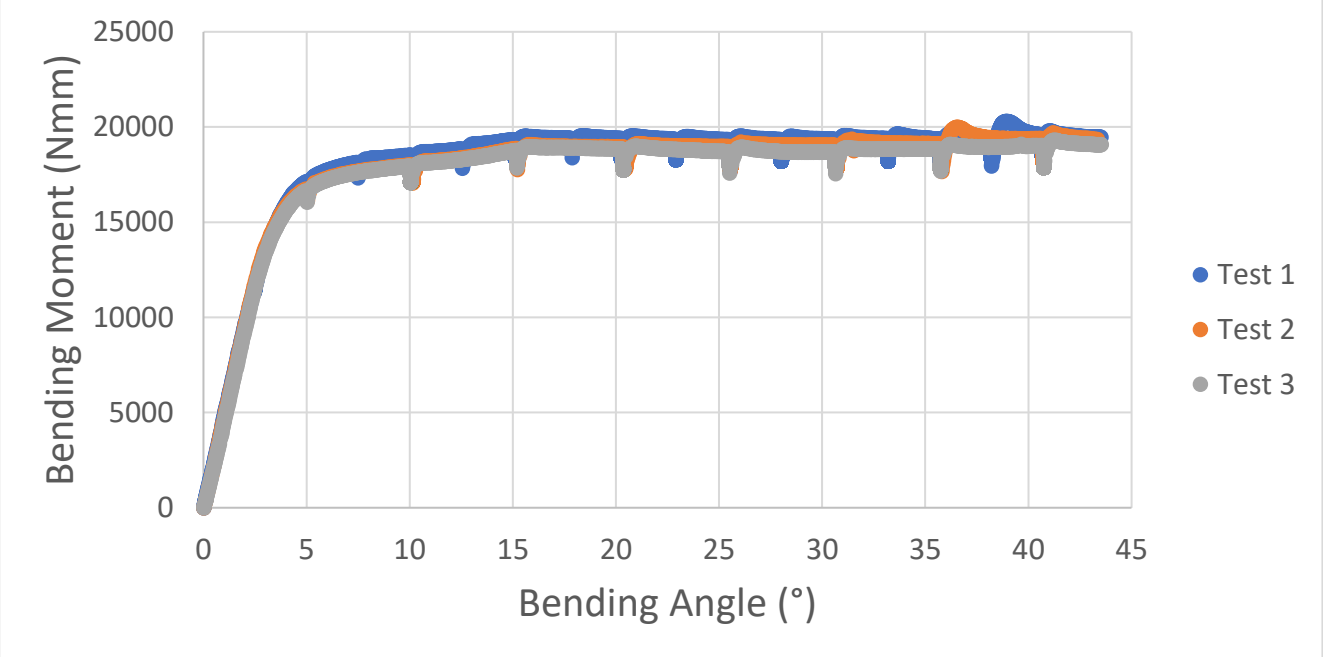


*Figure 5-31: Bending moment bending angle graph for 3mm thickness bend test specimens bent with the Deben bend test tooling in the Deben tensile and horizontal bending module.*

#### 5.2.1.2.1 Micrographs from Deben tooling

While no damage was observed from the force and bending angle a large inclusion, 3.5µm in diameter and a 0.05µm void located near the inclusion as shown in Figure 5-32. The oxide scale is on the surface as the top surface was not polished on this specimen, as the specimen is deformed these

crack and spallate. The inclusion is found to resist compression in the XX direction. While the void collapses and forms a shear band local to the inclusion.

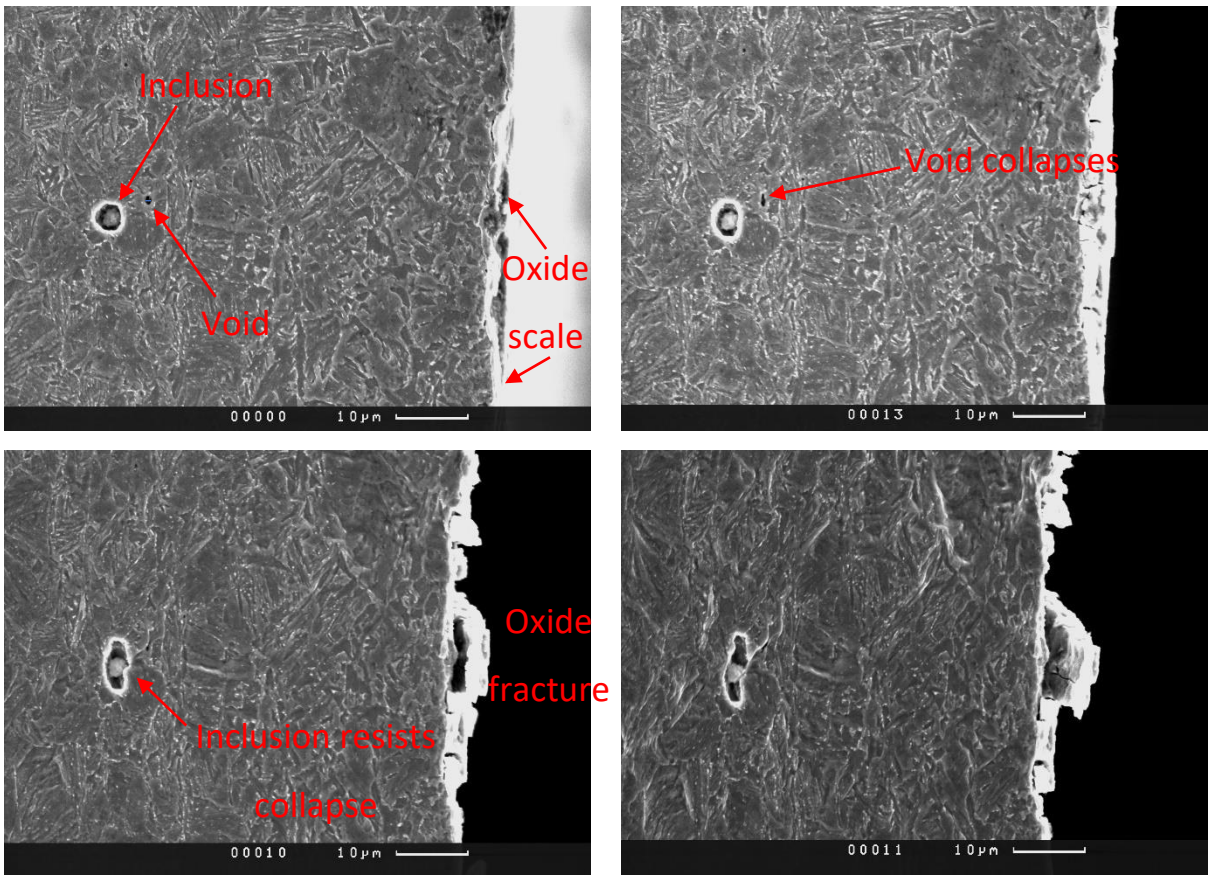


*Figure 5-32: Micrographs from bend test 3 at 1400x, top left, no displacement, top right, 3mm displacement, bottom left, 6mm displacement, bottom right, 8.57mm at maximum module displacement.*

### 5.2.1.3 4.25mm thickness transverse direction bend tests

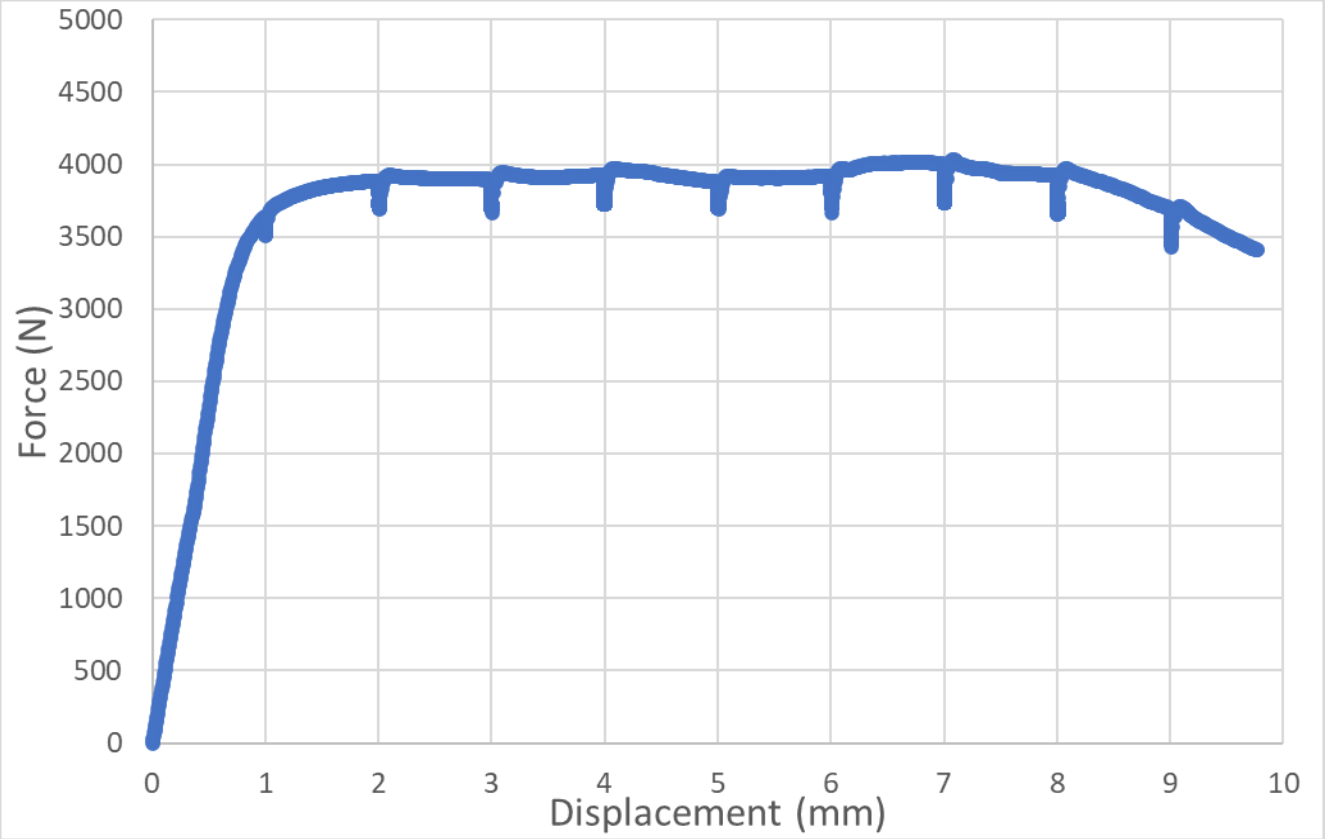


*Figure 5-33: Force-displacement graph for 4.25mm thickness bend test specimens bent with the Deben bend test tooling in the Deben tensile and horizontal bending module.*

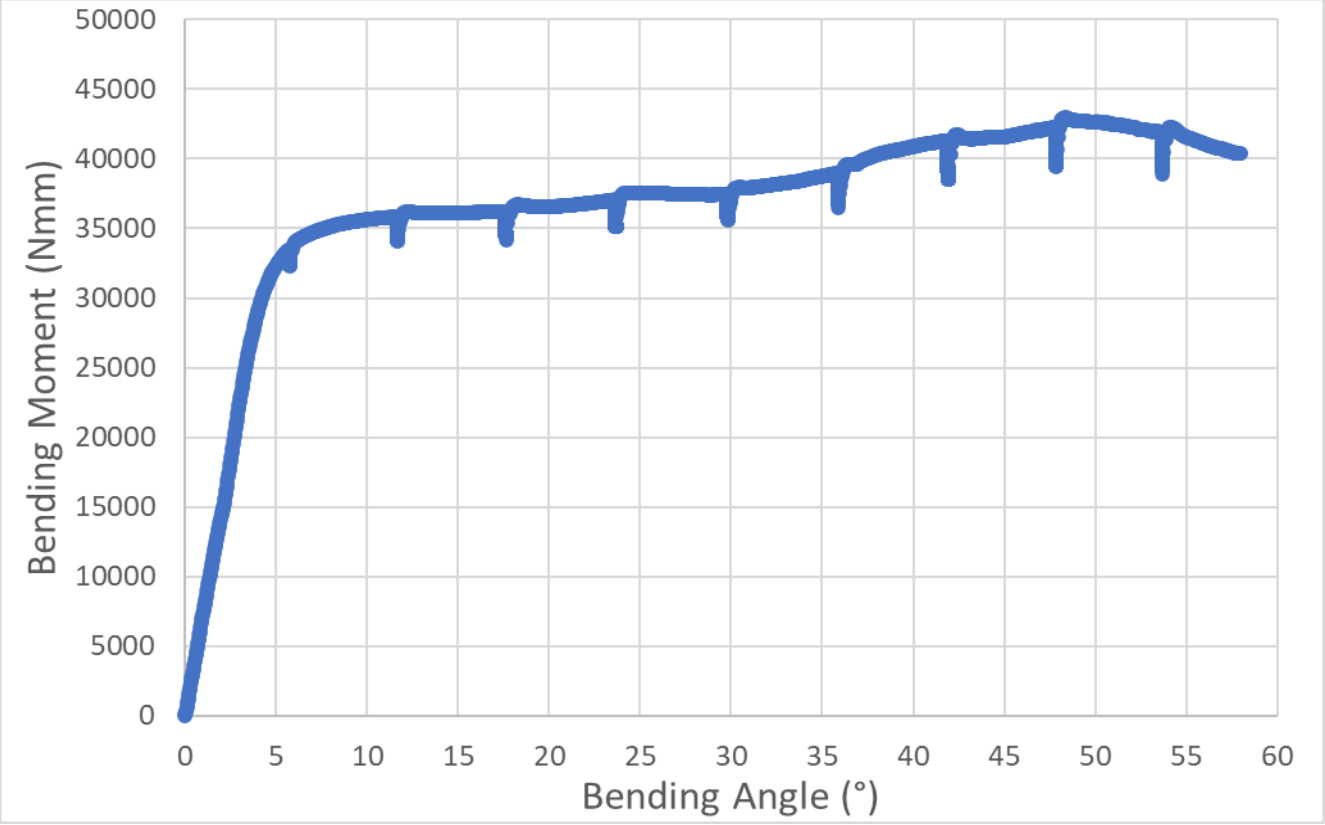


*Figure 5-34: Bending moment bending angle graph for 1mm thickness bend test specimens bent with the Deben bend test tooling in the Deben tensile and horizontal bending module.*

Figure 5-33 it is shown a typical bending curve with the maximum bending load of 4033N achieved at 7.0884mm of punch displacement, resulting in a bending moment of 41750Nmm at 42.4°. This is during a loading phase after the 7mm displacement to acquire micrographs. The load then begins to drop, while this unloading effect occurs, the bending moment increases as shown in Figure 5-34. Until it reaches its peak of 42950Nmm, at a load, displacement and angle of 3966N, 8.095mm and 48.4° respectively. This indicates damage is achieved in this specimen.

This was the final test performed using the Deben bend test tooling as 4.25mm thick specimen made contact with the tooling as shown in Figure 4-20 in section 4.1.1.3. As such this is the only result for this specimen geometry and tooling combination.

## 5.2.2 2.5mm diameter tooling, Gen. 1

Using the 2.5mm diameter tooling a new 2.4mm thick by 4.8mm wide geometry specimens were manufactured from the 17DF4/1 sample. The specimens were manually ground from 2.6mm to 2.4mm thickness and 5mm to 4.8mm in width to remove the region with residual stresses from EDM machining. The new tooling and specimen changed the $r_i/T$ value and drops from 0.59 with the Deben tooling and 4.25mm thickness specimen to 0.52. These are under the maximum $r_i/T$ values recommended by Tata Steel of 1.75. 3 insitu bend tests were performed with interruptions to obtain micrographs.

### *5.2.2.1 Standard geometry specimens*

The force-displacement curves for these specimens are found to be very consistent as shown in Figure 5-35. The maximum load found in each test was, 3862N, 3829N, and 3914N at 3.052mm, 3.073mm and 3.048mm for tests 1-3 respectively. These specimens then have damage and fractures occur after the peak loads. The bending moment and angle curve in Figure 5-36 show that the bending moment increases beyond this point and increases to the same in 13484Nmm, 13600Nmm and 14427Nmm at 3.055mm, 3.316mm and 3.552mm for tests 1-3. Tests 1 and 3 have sudden drops from the maximum moment at 68.5 and 76.3 degrees respectively.

These tests were stopped when the specimen was at 1000N or deemed to have failed by the operator so the last data point is not significant.

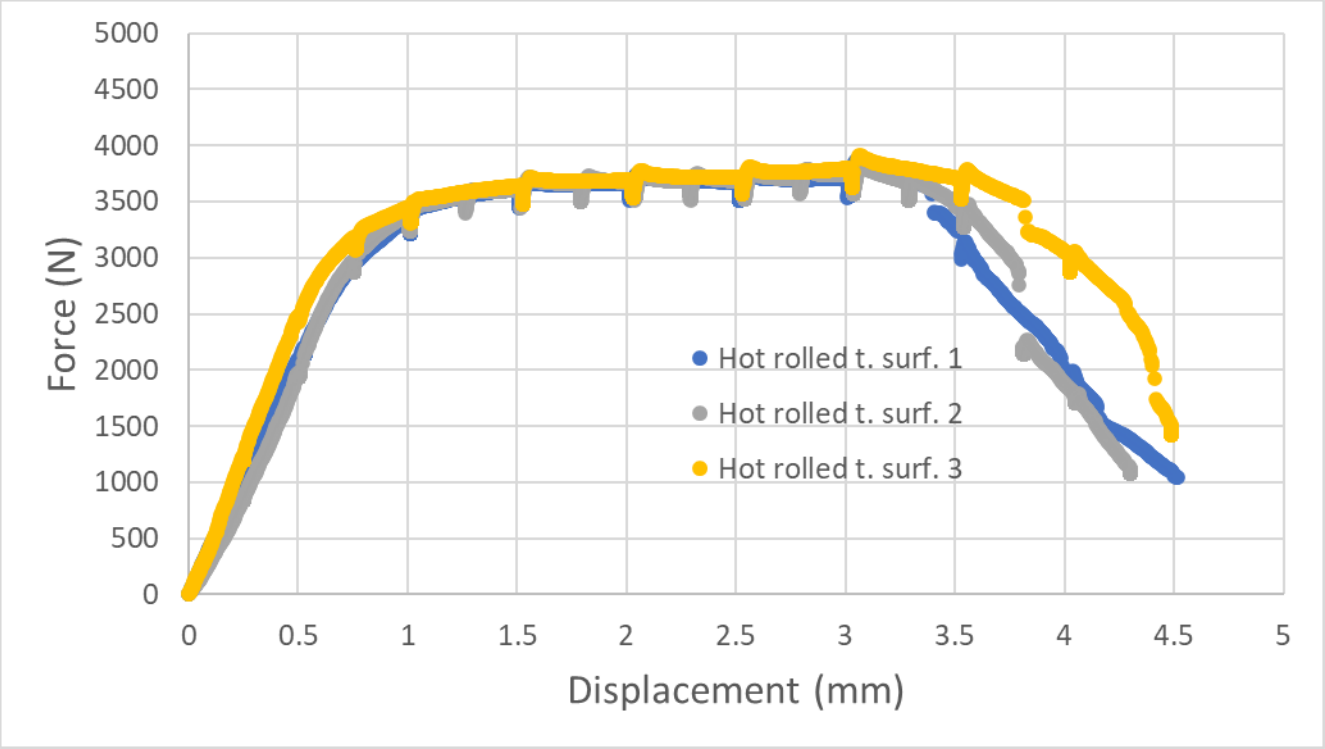


*Figure 5-35: Force-displacement graph for the 2.4mm thick hot-rolled top surface bend test specimens all performed with SEM interruptions.*

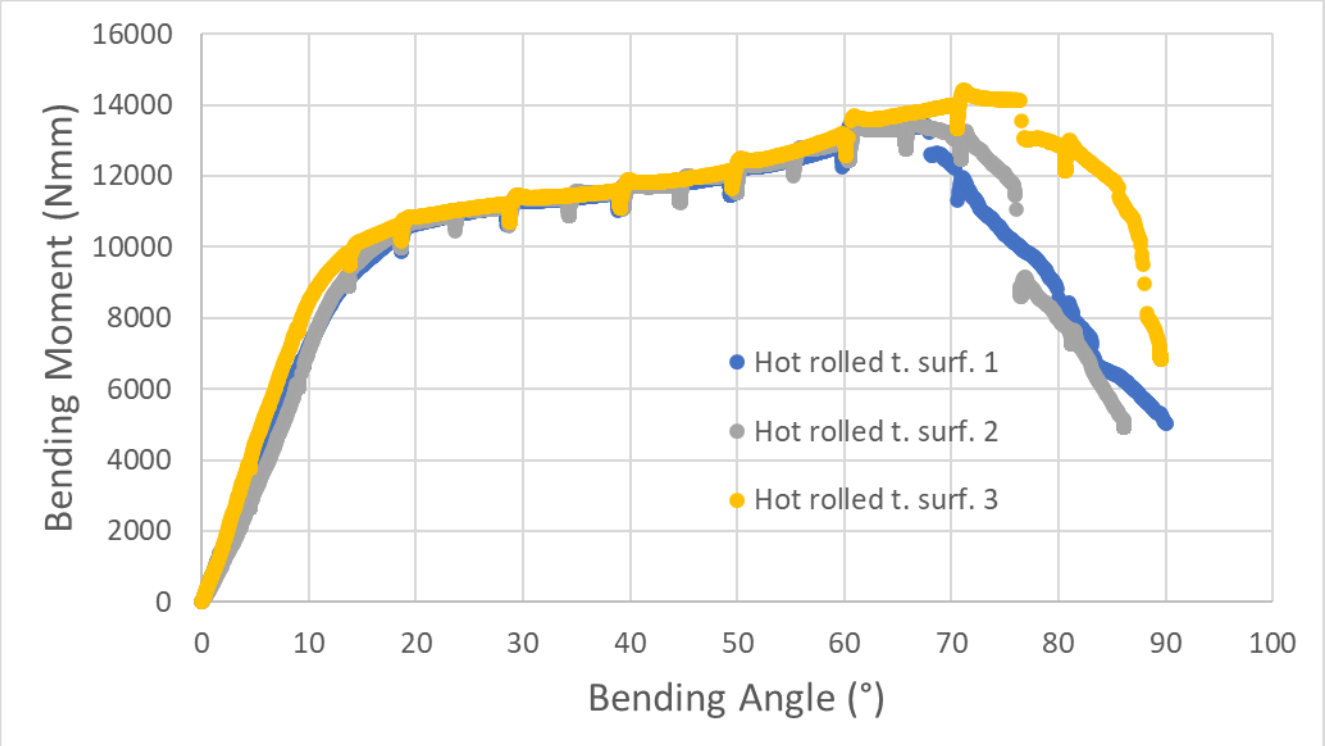


*Figure 5-36: Bending moment bending angle graph for the 2.4mm thick hot-rolled top surface bend test specimens all performed with SEM interruptions.*

### 5.2.3 The angled bend test specimen

The angled bend tests were designed and developed as described in section 4.4 and used with the 2.5mm diameter gen 1 tooling as described in section 4.2. 2 and 17DF4/1 material. Tests were performed with the first being an ex-situ bend test with no interruptions and the second and third insitu within the Camscan SEM with interruptions.

#### *5.2.3.1 25° angled specimens force-displacement graphs*

The force is found to increase for each subsequent test with a double peak load in the first test. The load is found to increase by around 400N per test, 2695N, 3083N and 3474N at 2.187mm, 2.078mm and 1.549mm for tests 1-3 respectively as shown in Figure 5-37. This failed in the load cell after a subsequent test.

Due to the increasing loads reported in Figure 5-37, this impacts the bending moment curve in Figure 5-38, the thickness is varied across the specimen so the author treated it as 3mm thick as it is at its thickest. Test 1 does show that with the second peak the high load causes the large bending moment.

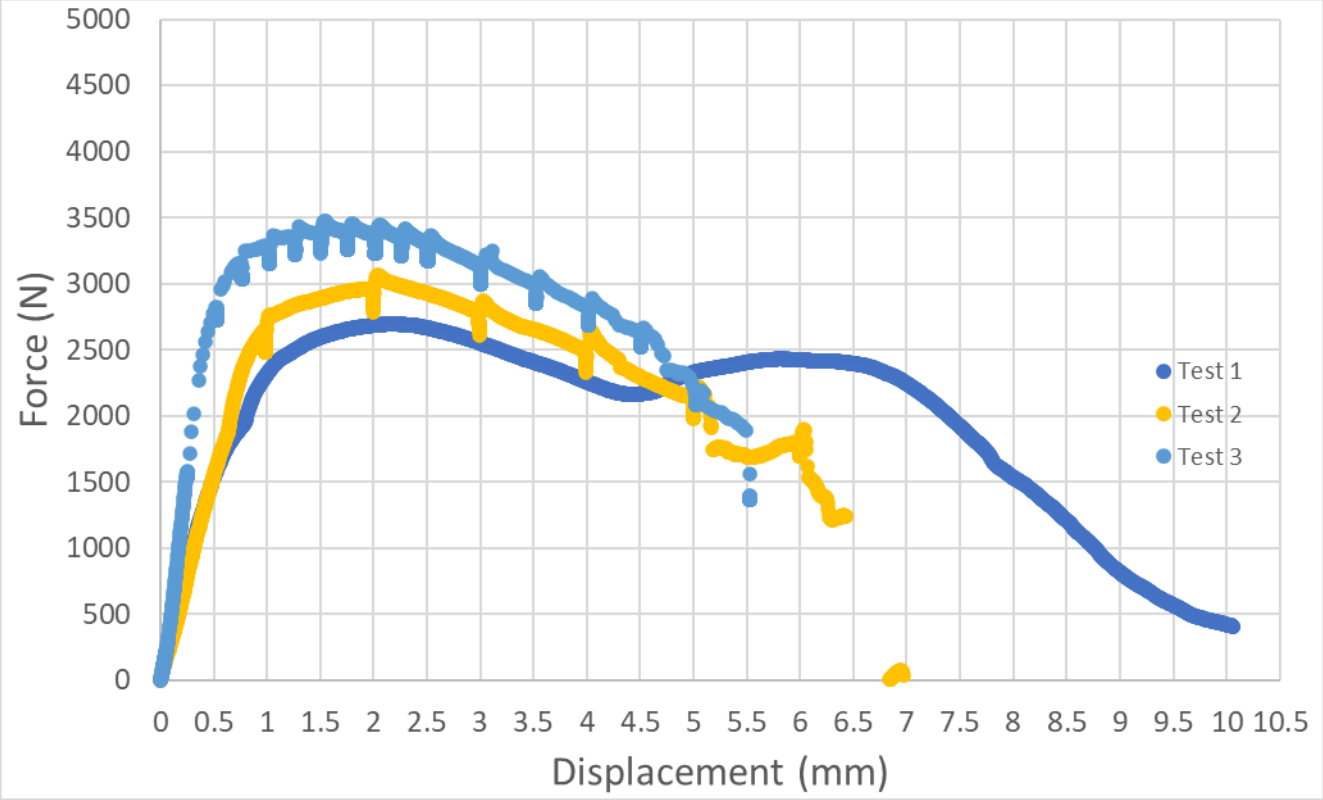


*Figure 5-37: 25° angled bend test force punch displacement graph for tests 1-3*

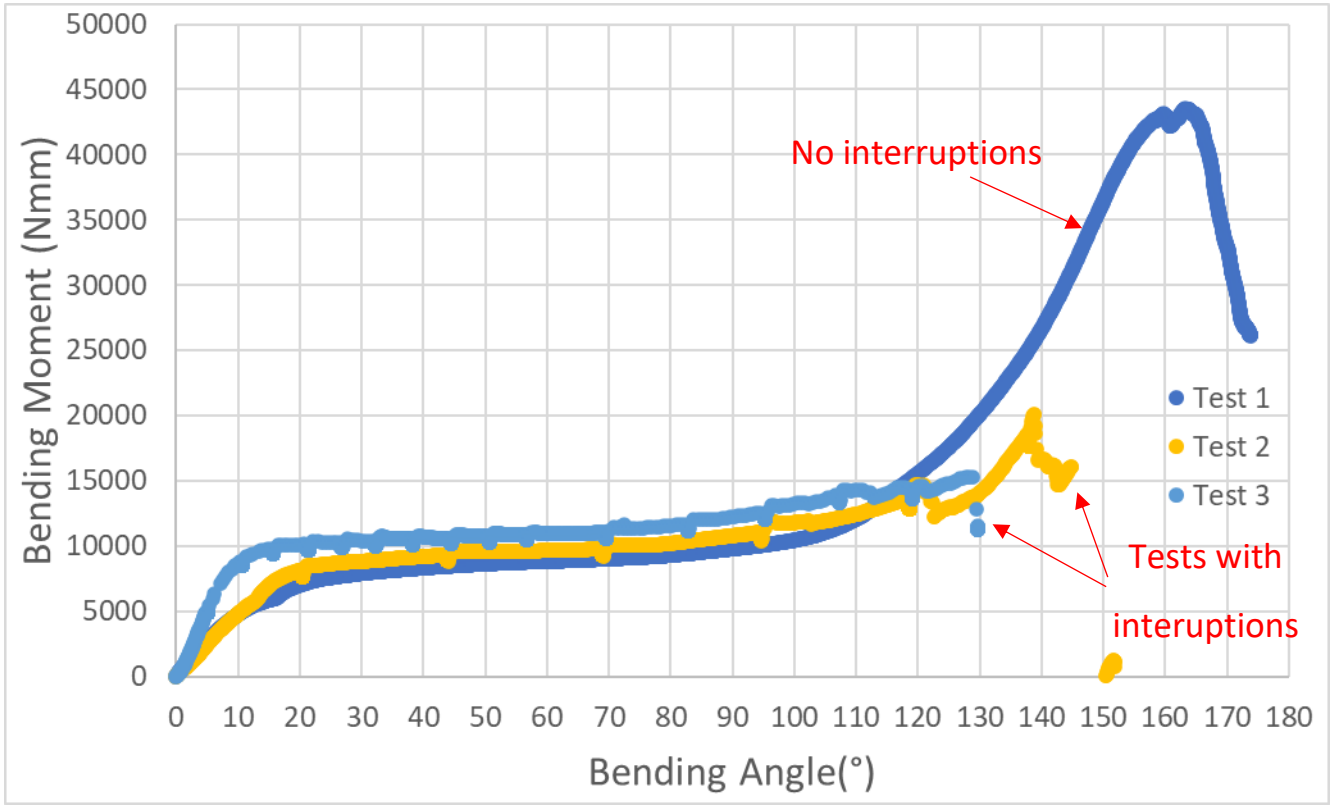


*Figure 5-38: 25° angled bend test bending moment bending angle graph*

### *5.2.3.2 25° angled specimens' micrographs*

Using post-test images in Figure 5-41 and comparing to Figure 5-39 the damage mechanism is found to change from a ductile damage mode to transitioning to a sharp crack. Damage occurs in two regions by different mechanisms as expected from the FEM when comparing Figure 4-64 and Figure 5-41. The larger cracks are in the blue box with triaxiality dominating with lower strain promoting damage generating long cracks are perpendicular to the bending strain and are largest around the centre of the specimen and diminishing until near the horizontal faces. These regions of damage agree with the high triaxiality observed in Figure 4-64, multiple cracks are observed due to the moving triaxiality through the displacement. The secondary region of damage is found at the observed horizontal surface in the red region has strain dominated damage generating cracking at the surface of the bend. These regions were found not to interact and so the observation of the horizontal face can be analysed independently of the central triaxiality based damage.

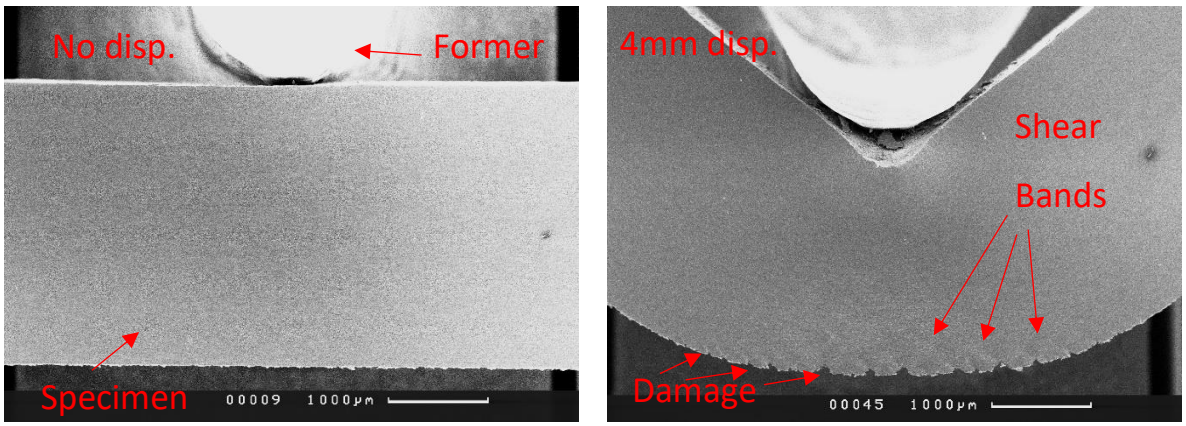


*Figure 5-39: Global view (x20) of the bend test specimen: left, no displacement; right, 4mm displacement in test 3.*

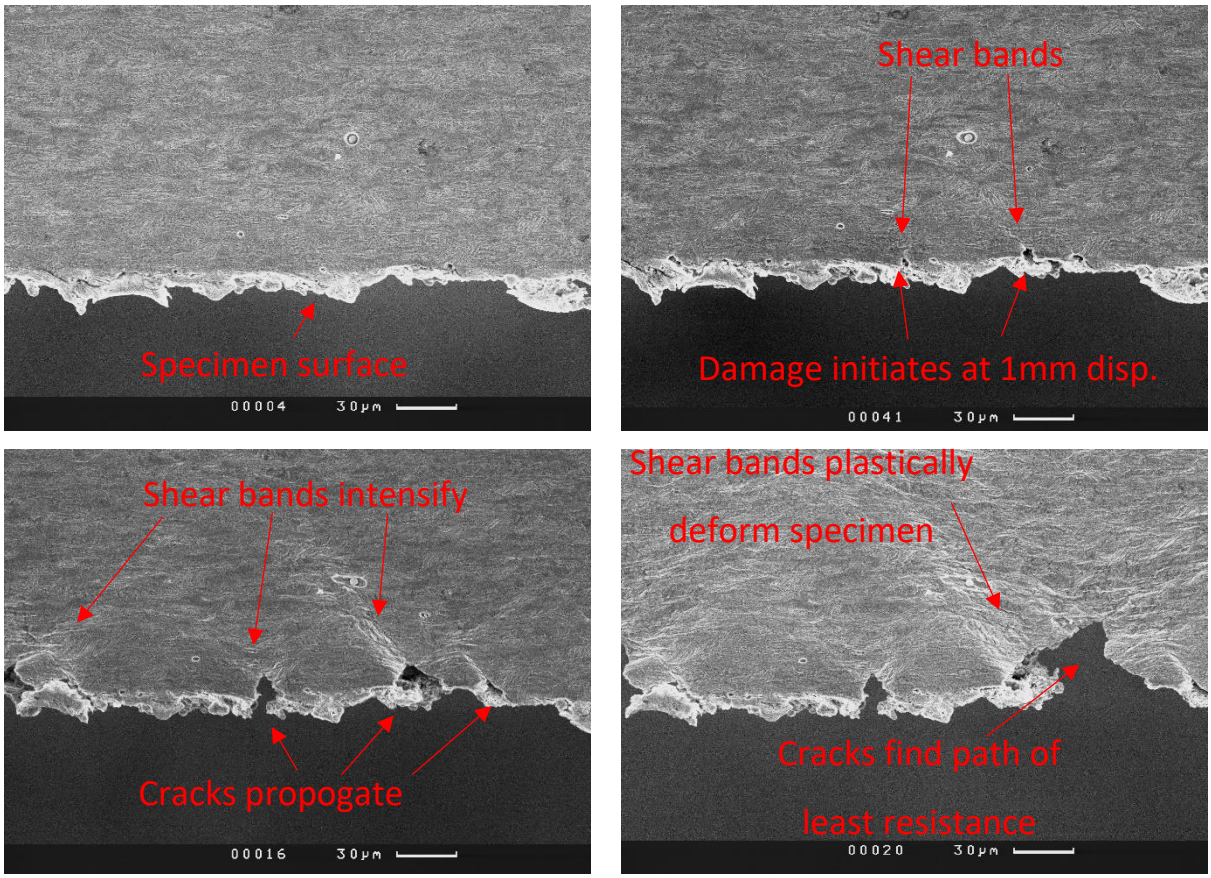


*Figure 5-40: SEM Micrographs of the horizontal face observed in a bend test at 400x magnification for test 3, top left at no displacement, top right 1mm displacement, bottom left 2mm displacement, bottom right 3mm displacement.*

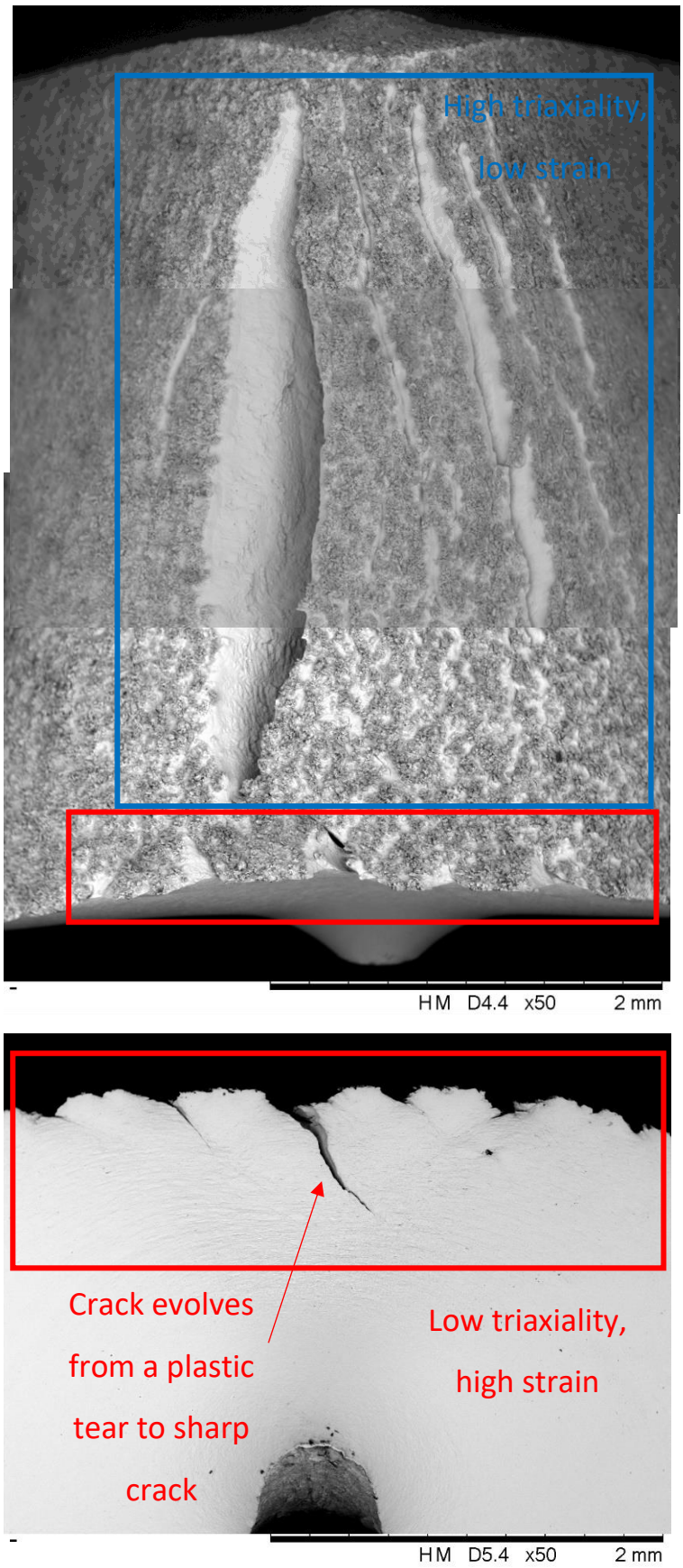


*Figure 5-41: Post-test images of the angled bend test specimen for test 3 obtained with the tabletop SEM: top, Composite SEM micrographs of the top surface of the angled bend test at 50x magnification; bottom, 50x magnification of the horizontal face.*

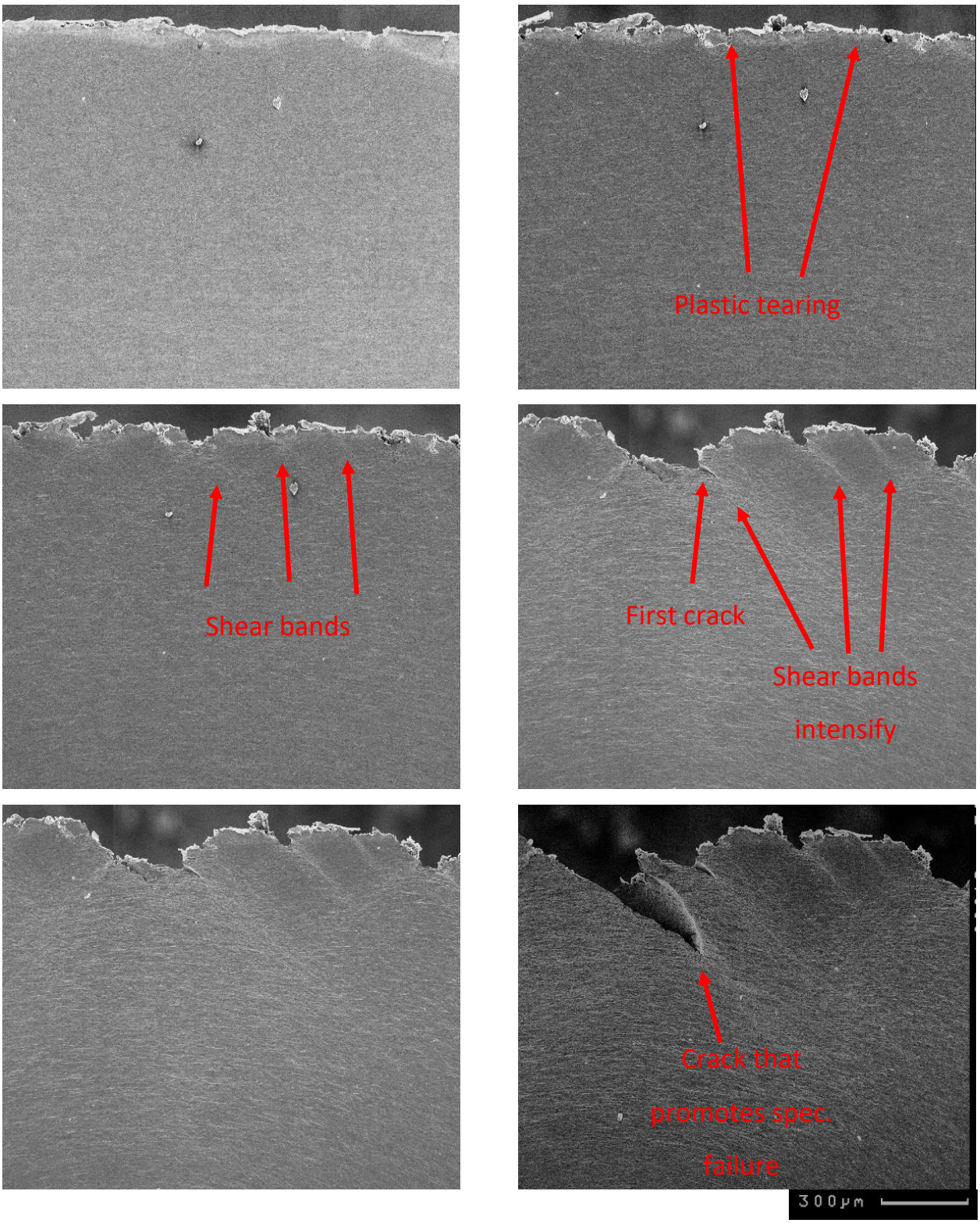


*Figure 5-42: SEM micrographs of the horizontal face at 50x magnification from test 2, top left, no displacement, top right, 2mm displacement, middle left, 3mm displacement, middle right, 4mm displacement, bottom left, 5mm displacement, bottom right, 6mm displacement.*

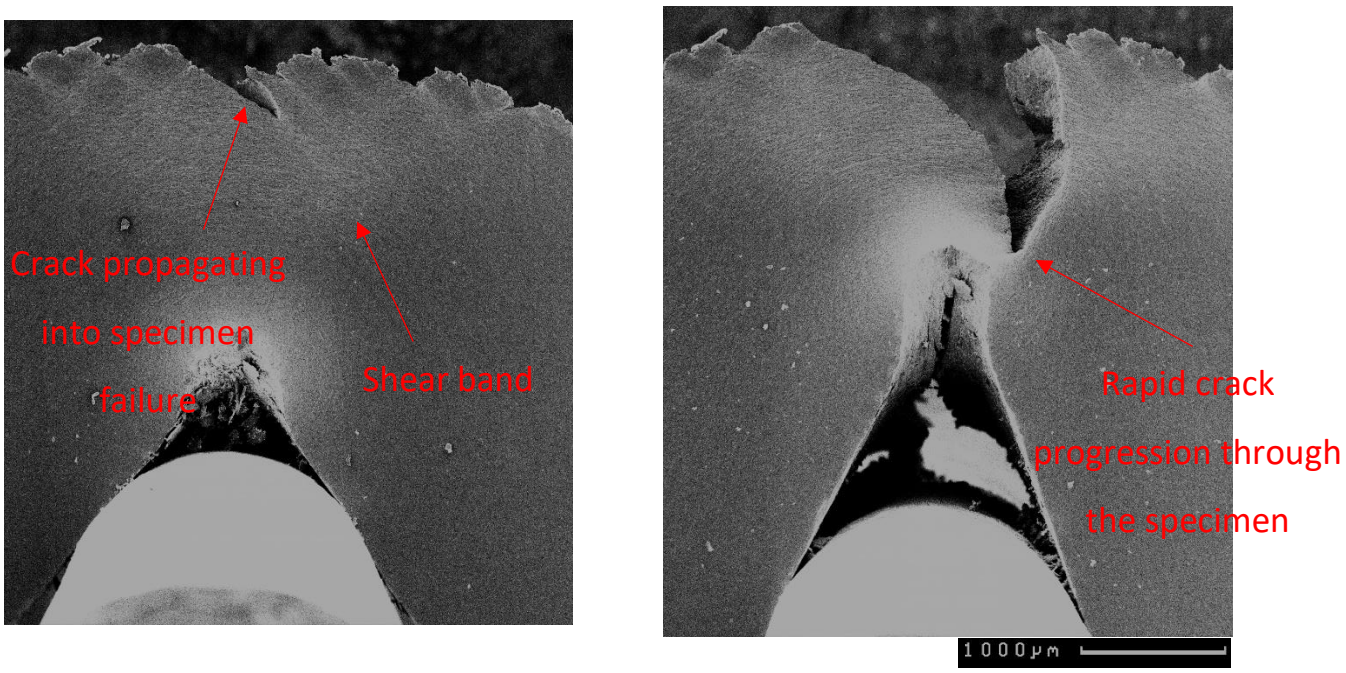


*Figure 5-43: SEM micrographs of the horizontal face at 20x magnification from test 2, left 6mm displacement, right 7mm displacement.*

Using micrographs of the etched surface revealed the martensitic microstructure and can be observed in Figure 5-40. These are then post-processed using DaVis to produce Figure 5-44. In the micrographs, the initial surface is rough due to machining as well as the inclusions. As displacement increases the ductile damage is observed to occur in an unstable pattern. At the crack tip, 2 micro-cracks can be found at 45° to the surface.

The best demonstration of the crack formation in bending is shown found in test 2 as shown in Figure 5-42 and Figure 5-43. In these, the damage is initially plastic tearing at 2mm displacement just as the force-displacement curve in Figure 5-37 begins to drop. At 4mm of displacement the tearing transitions to the promotion of cracks. These quickly promote failure of the specimen at 7mm of displacement as shown in Figure 5-43.

#### *5.2.3.3 25° angled specimens' DIC results*

With DIC applied to the micrographs, the strain maps can be studied only test 3 had the high-quality micrographs required for DIC analysis. The shear bands can be observed and be seen clearly after only 1mm displacement. As displacement is increased the ductile damage propagates into the specimen as do the shear bands at the tip of the crack. The shear bands promote the microcracks at the tip of each crack due to ductile damage. High strains are found in regions of lathe martensite and near inclusions. Neither of these high strain regions was intersected by the crack.

Damage occurs at the surface at 50% strain, but higher strains are found in regions where shear bands intersect, or inclusions are found. These produce strains of up to 275% without causing specimen failure

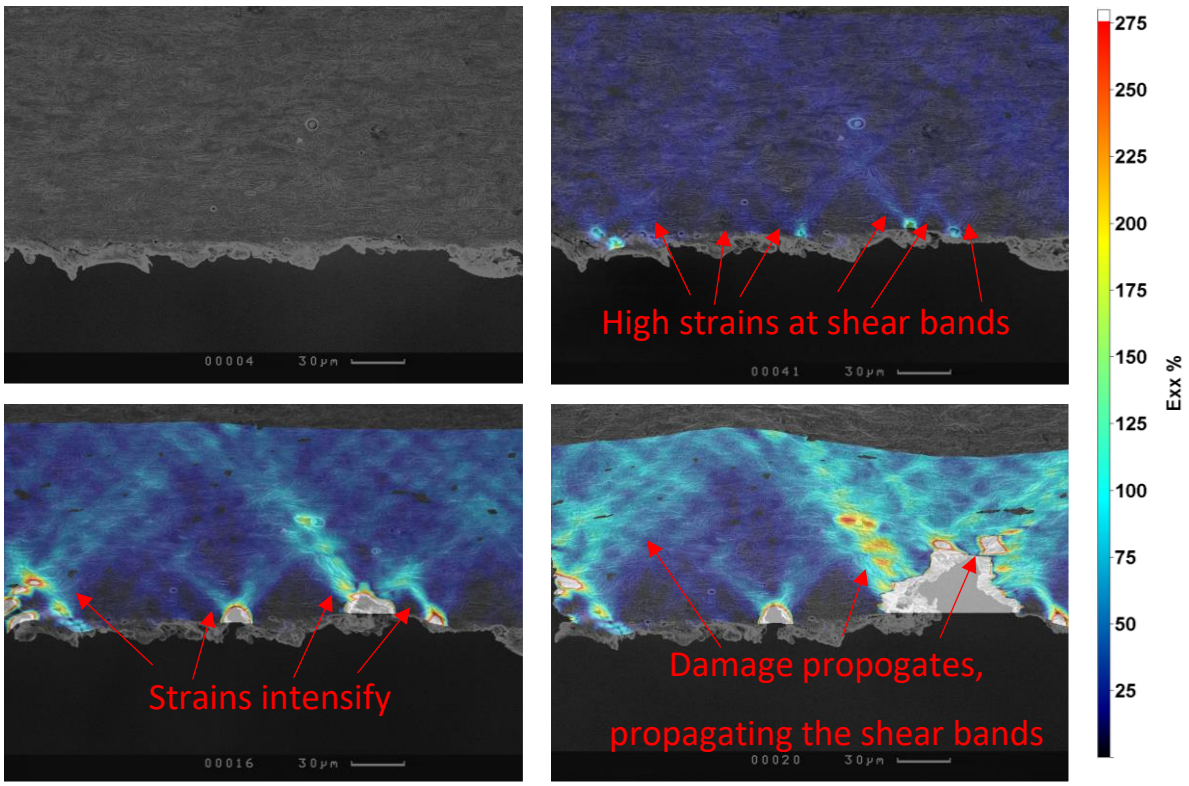


*Figure 5-44: DIC of the SEM micrographs in Figure 5-40, top left at no displacement, top right 1mm displacement, bottom left 2mm displacement, bottom right 3mm displacement.*

## 5.2.4 2.5mm diameter tooling, Gen. 2

Updating to the latest tooling a set of experiments were performed to study the impact of different hardness properties at the top surface and 0.6mm depth surfaces. Both samples had their top surfaces that were put in tension polished to remove any influence from surface roughness. This is because the hot-rolled surface on the top surface would have been impossible to replicate with the 0.6mm depth specimen. Thus that variable was removed by polishing that face with 1µm diamond suspension.

### *5.2.4.1 Polished Top surface sample*

The samples produced by the methods are described in sections 3.3.1.3,3.3.1.4, 3.3.1.6 and 3.3.2. these samples had the top surface polished to remove surface roughness and this variable from bend testing and make the geometry as close as possible to that simulated in FEM. To produce these specimens, controlled material removal had to be performed.

| | Thickness removed (mm) | Target (mm) | Width removed (mm) | Target (mm) |
|---|---|---|---|---|
| Top surface polished 1 | 0.070 | min. possible | 0.125 | 0.200 |
| Top surface polished 2 | 0.080 | min. possible | 0.150 | 0.200 |
| Top surface polished 3 | 0.057 | min. possible | 0.143 | 0.200 |

*Table 5-2: material removal data for the polished top surface specimens.*

The sample preparation material grinding target was to remove a minimal amount of material, this was because the specimen was already 2.4mm thick. The aim was to remove around 0.02mm but the author removed an amount with grinding paper until all the hot rolling roughness was not visible and then performed the polishing. This removed more material than aimed for and resulted in a thinner specimen when compared to the 0.6mm depth specimens.

The width removal was aimed to be 0.2mm to remove any material with residual stresses from the EDM process as found in section 3.2. A new batch sample approach was taken that removed less material than expected and the mounting process caused the specimen to be mounted within the mounting compound that causing the material removal to be exaggerated. So, the true material removal in the width was found to be less than expected.

The 1$^{st}$ specimen was used for the test within the SEM. The force for bending the polished top surface specimens was lower than that required for the 0.6mm specimens as the specimen was thinner due to grinding error.

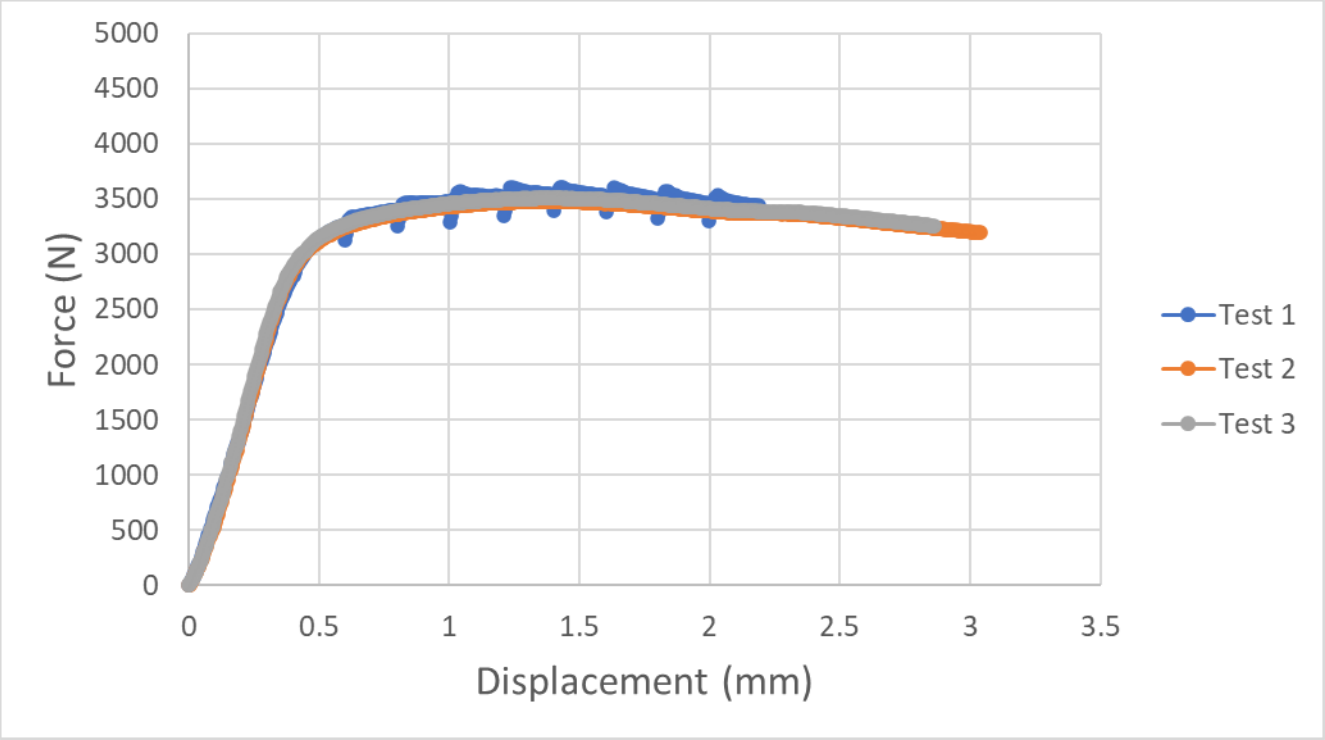


*Figure 5-45: Force-displacement graph for the polished top surface bend test specimens with gen. 2 tooling.*

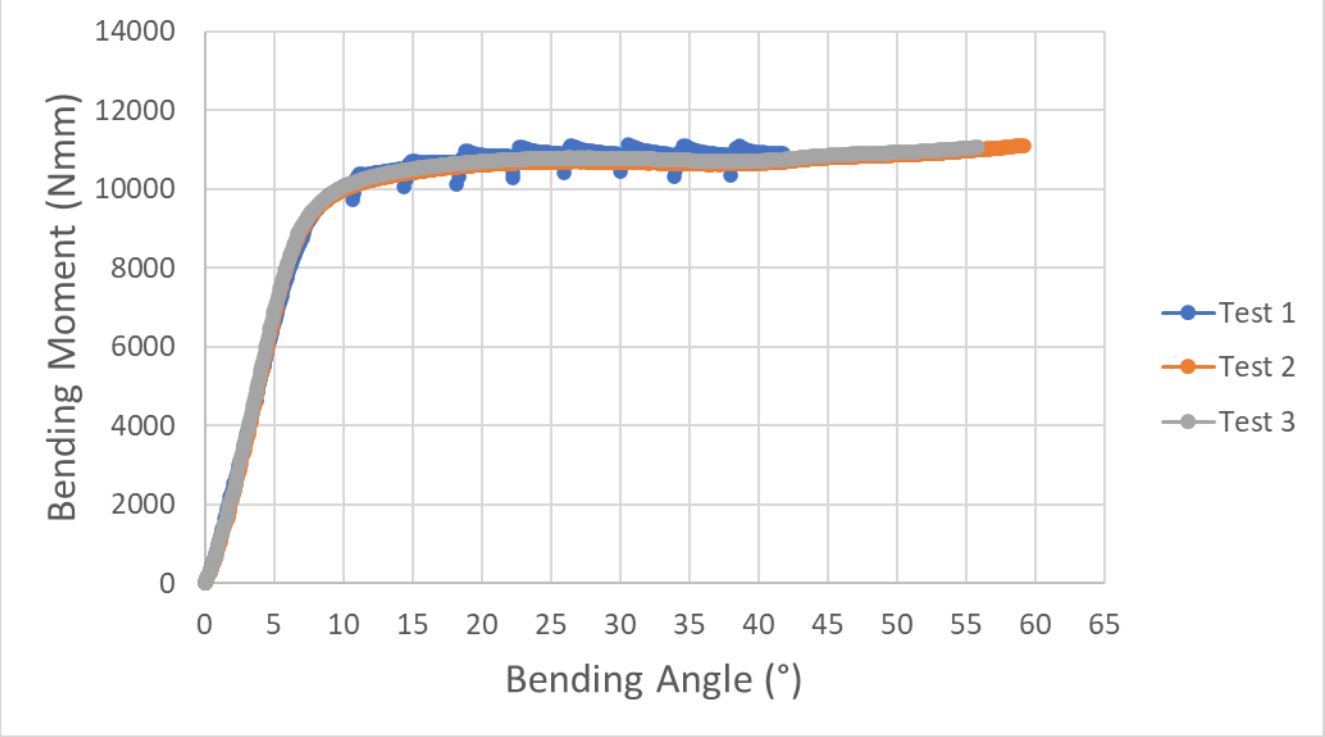


*Figure 5-46: Force bending angle graph for the polished top surface bend test specimens with gen. 2 tooling.*

#### *5.2.4.2 0.6mm depth polished surface specimens*

To manufacture the specimens they were originally oversized at 3mm thick and 5mm wide. This allowed for the targeted 0.6mm thickness removal down to 2.4mm using the method described in section 3.3.1.4. Then the width was reduced to be 2 times the width of 4.8mm using the method

described in 3.3.1.3 and etched with 2% nital as described in section 3.3.1.6. This resulted in the material removal measured in Table 5-3.

The thickness removal was within 0.04mm of the target while the width removal was under target by 0.07 to 0.09mm. The reason for this was the mounting process in section 3.3.1.2 caused the specimen to be buried within the mounting. This resulted in the measurements of material removal from the mounting being erroneous due to a zero error and less material was removed for both the width and thickness than expected.

| | Thickness removed (mm) | Target (mm) | Width removed (mm) | Target (mm) |
|---|---|---|---|---|
| 0.6mm depth polished specimen 1 | 0.565 | 0.6 | 0.131667 | 0.2 |
| 0.6mm depth polished specimen 2 | 0.586667 | 0.6 | 0.135 | 0.2 |
| 0.6mm depth polished specimen 3 | 0.6 | 0.6 | 0.111667 | 0.2 |

*Table 5-3: material removal data for the 0.6mm depth polished surface specimens.*

The bending force for the 0.6mm depth specimens in Figure 5-47 is higher than the top surface as found in Figure 5-45. With the bending force between 3800-4000N at its peak. Due to the higher bending loads and the thicker specimens, this increased the bending moment significantly from 10500Nmm in Figure 5-46 to exceeding 12000Nmm in Figure 5-48.

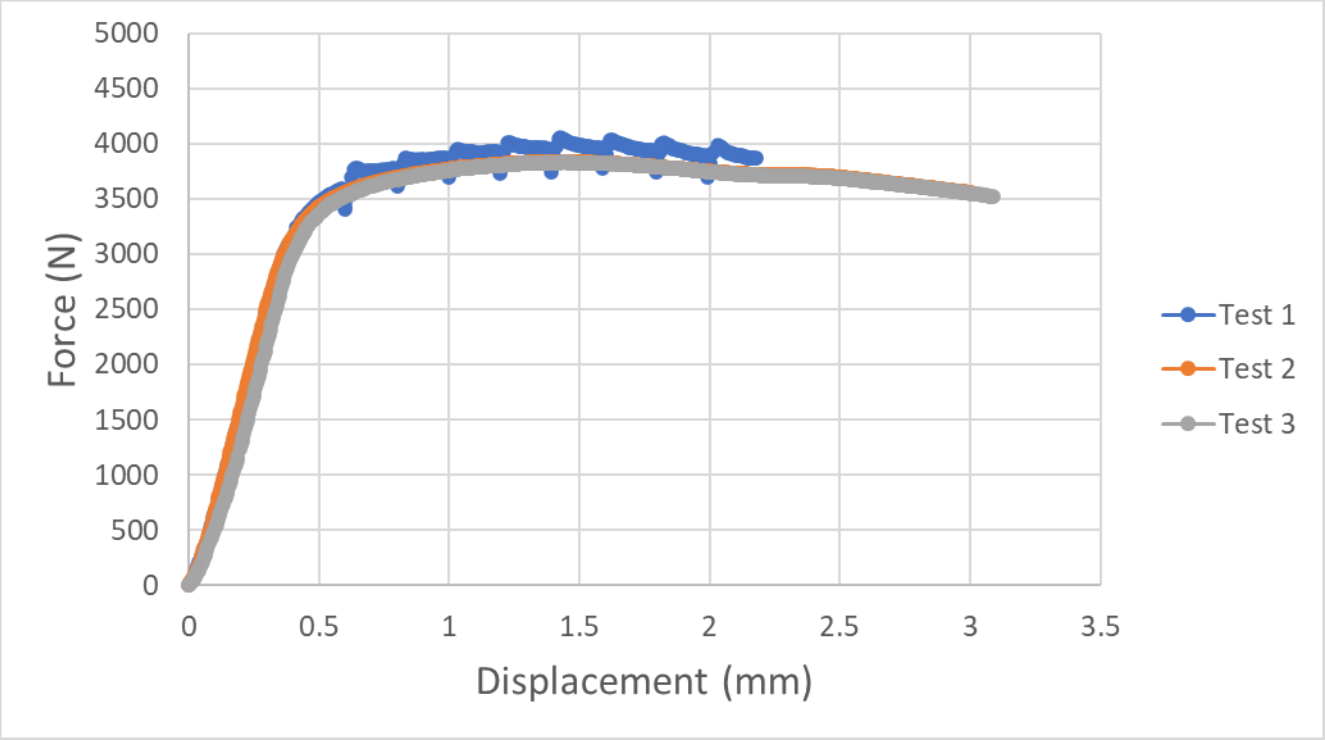


*Figure 5-47: Force-displacement graph for the 0.6mm depth top surface bend test specimens with gen. 2 tooling.*

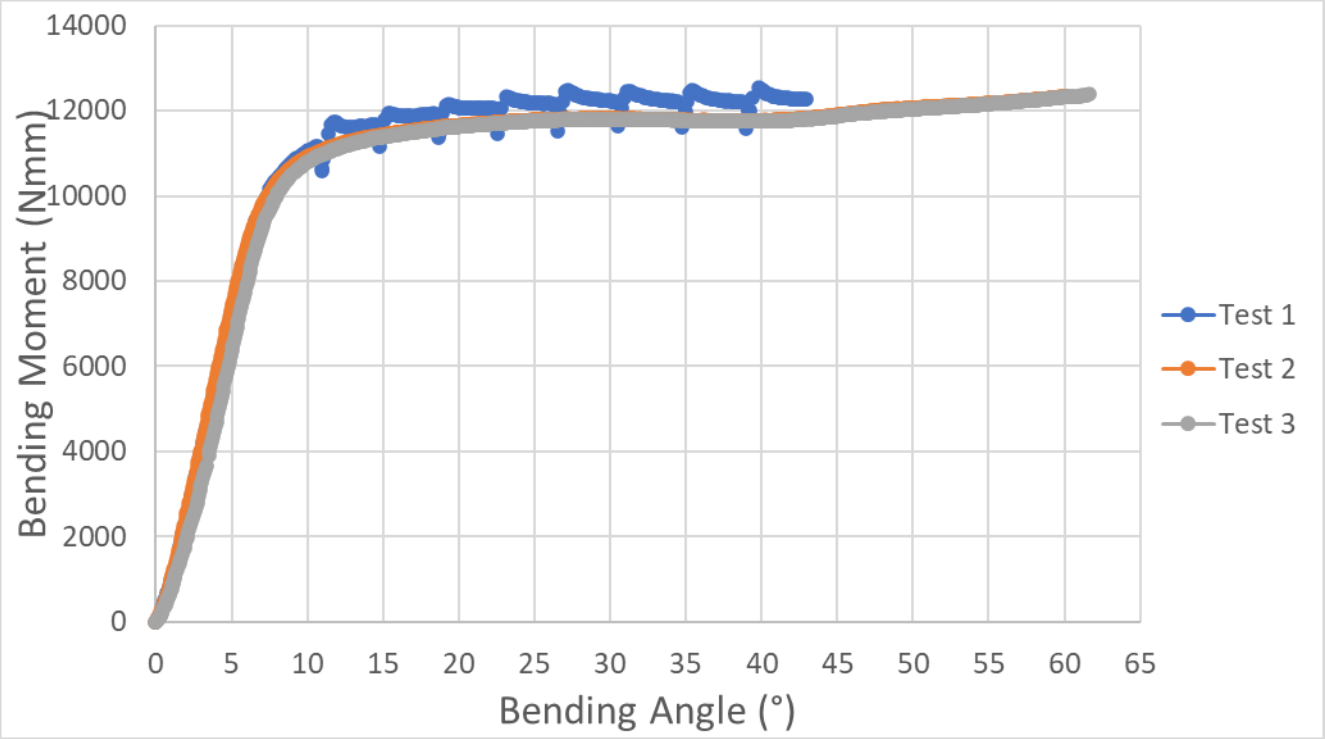


*Figure 5-48: Force bending angle graph for the 0.6mm depth top surface bend test specimens with gen. 2 tooling.*

### *5.2.4.3 Micrographs*

#### 5.2.4.3.1 20x magnification

The micrographs in Figure 5-49 and Figure 5-50 are used as an overview through the test and allowed the study of the bending angle when compared to those found with the bend angle calculations. This has been used in other tests to observe edge cracking, although no damage is observed at this

magnification for either the polished top surface or polished 0.6mm depth specimens in Figure 5-49 and Figure 5-50 respectively.

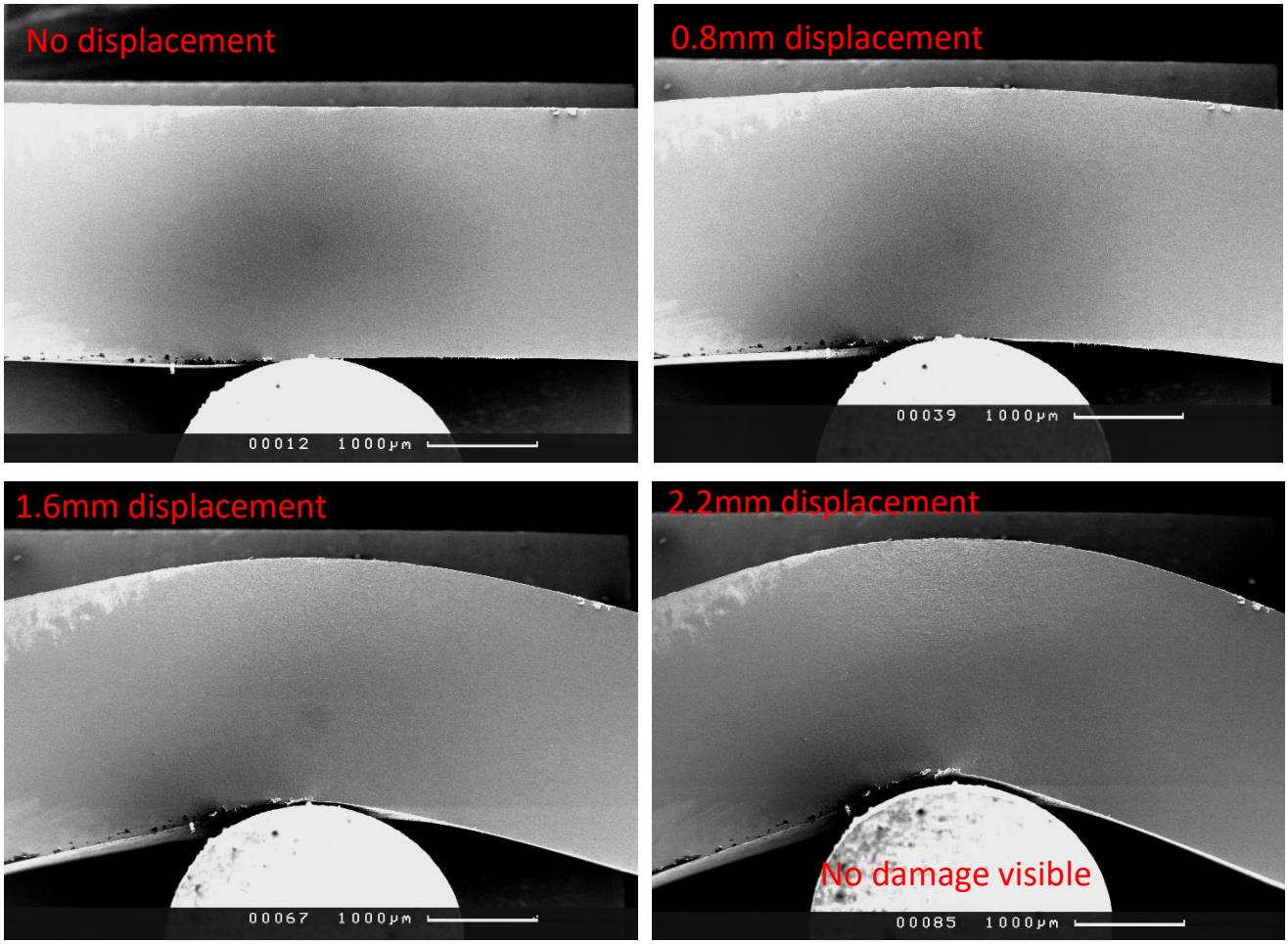


*Figure 5-49: Polished top surface bend test micrographs at 20x magnification overview. Top left, no displacement, Top right, 0.8mm displacement, Bottom left, 1.6mm, bottom right 2.2mm displacement*

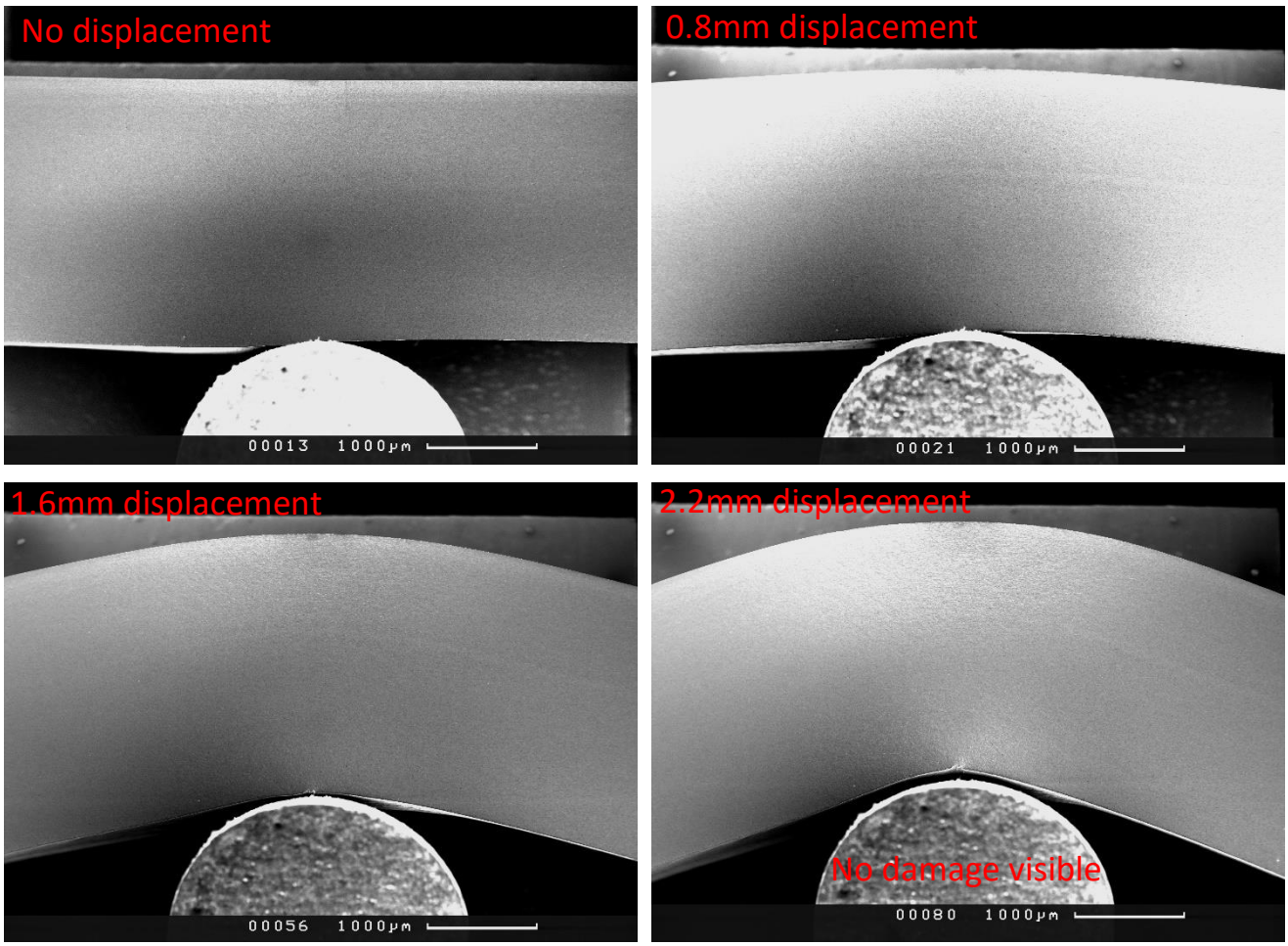


*Figure 5-50: 0.6mm depth polished surface bend test micrographs at 20x magnification overview. Top left, no displacement, Top right, 0.8mm displacement, Bottom left, 1.6mm, bottom right 2.2mm displacement*

#### *5.2.4.4 Validation of bending angle method*

To confirm the accuracy of the bending angle method by L. Troive et al [34], a validation by studying the SEM micrographs has been performed. Due to the tooling lacking the claimed frictionless bending capabilities the bending angle formula does not account for friction. To perform such an analysis three methods of identifying bending angles were used, these were rigid beam theory, optical single contact point analysis and optical 2 point contact. The rigid beam theory is the most basic calculation assuming that contact points are singular and static on both the supports and former. The displacement recorded from the Deben module was used to convert this into basic trigonometric terms. Where the bending angle, $\theta$ is found with the bending depth, $d$ and the width to the centre of the image, $C$ assuming the angle is the same

$$\theta = 2 \times \tan^{-1}\left(\frac{d}{(C)}\right) \qquad \textit{Equation 31}$$

To provide another validation optical analysis methods were also used. These used images at 20x magnification as shown in Figure 5-49, which were then analysed locating the positions by eye to identify the contact point/s on the former and the edge of the specimen in the image extremities.

Two different contact point methodologies were applied. The simplest approach was to assume that a single contact point was at the centre of the former and keep this static throughout the test. In contrast, as described by L. Troive the contact point is expected to bifurcate and become two contact points. When these are overlaid on an SEM micrograph as shown in Figure 5-51 it is shown the single point method is likely to undervalue the bending angle. Whereas the 2 contact points seem to be more representative of the real bending angle but have more reliance on the author to position the contact points correctly.

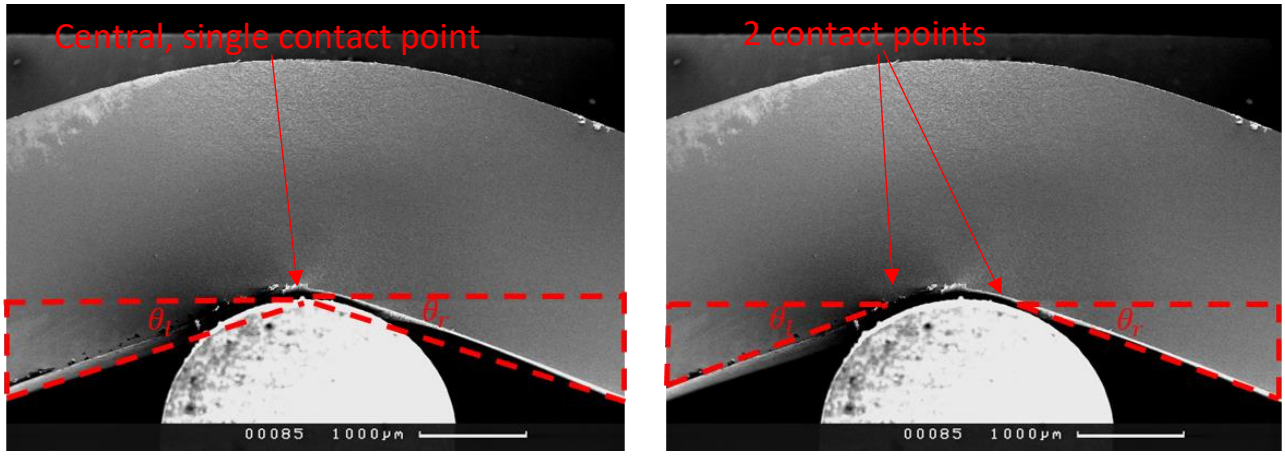


*Figure 5-51: Optical bending analysis diagram projected over the 2.2mm displacement micrograph of the polished top surface specimen. Left: single point contact analysis right: 2-point contact analysis.*

By then summing both left, $\theta_l$ and right, $\theta_r$ angles a bending angle, $\theta$ is found as shown in Figure 5-51

$$\theta = \theta_l + \theta_r \qquad \textit{Equation 32}$$

Using these methods, the bending angle has been plotted for comparison in Figure 5-52

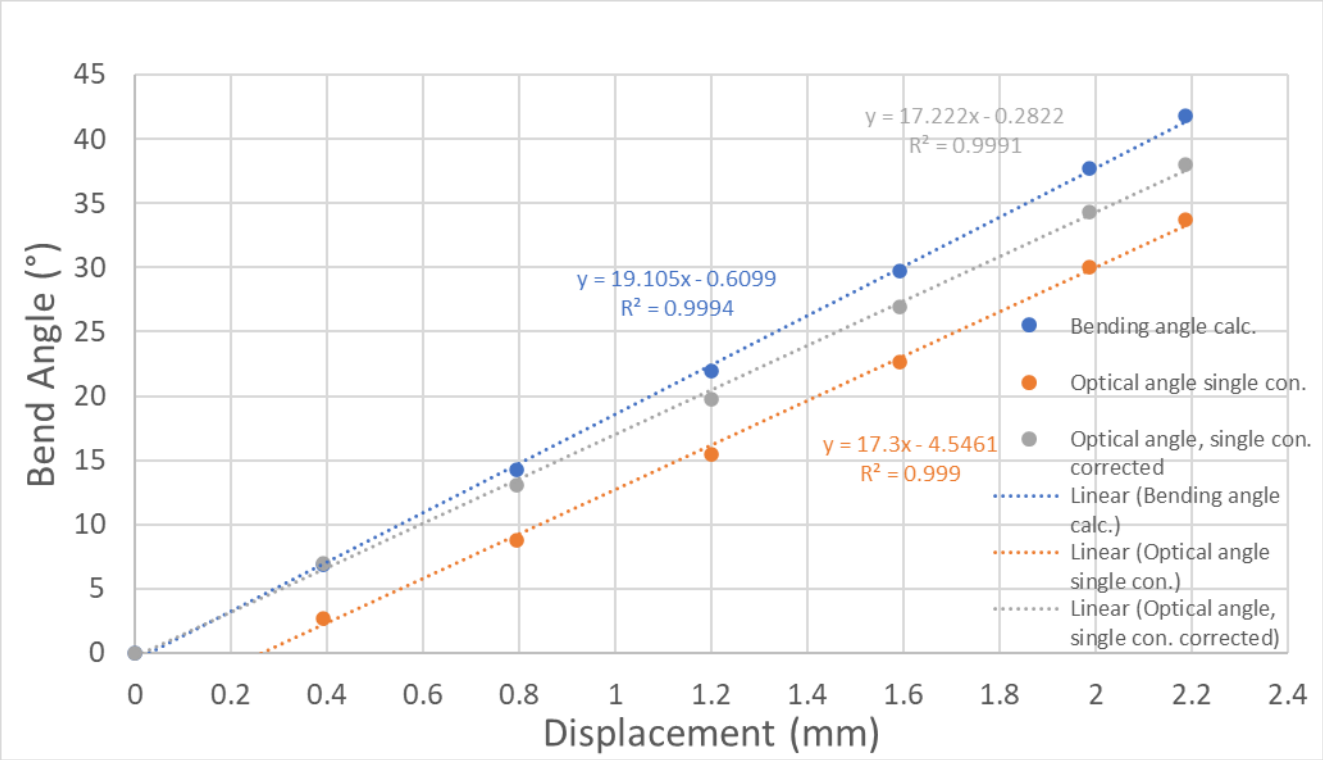


*Figure 5-52: bending angle assessment with optical and numerical analysis with a single contact point.*

When these numerical and optical methods are plotted in Figure 5-52, most of the results are a good approximation to those found by the numerical method by L. Troive et al. except the optical single-point method. This is at a similar gradient but has a zero error. This is found to be due to the perspective of the SEM image which the tooling is closer to the aperture and forward of it. This results in an initial negative bend angle which was then corrected by subtracting the negative angle from the full set of results. This corrects the position of the tooling. When comparing the numerical methods, the rigid beam theory and numerical moving contact position formulas the bending angle is initially the same at lower bending angles but diverges as the contact positions move.

Once the zero error for the optical analysis method has been corrected the line converges on the numerical moving contact formula. Using a single point contact the bend angle is undervalued with increasing displacement. This is due to the moving contact points which are shown in Figure 5-51, which shows why the bending angle was undervalued.

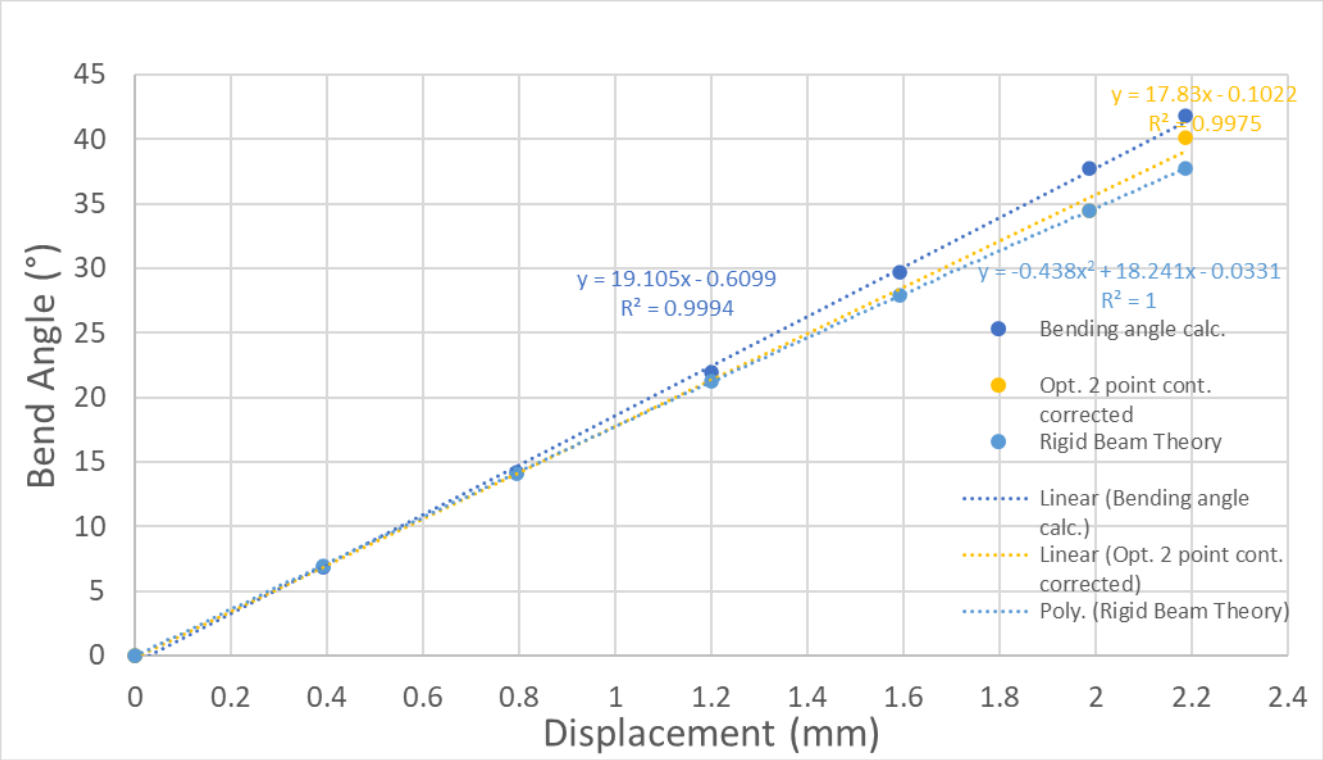


*Figure 5-53: bending angle assessment with optical and numerical analysis with 2 point contact.*

To correct for this 2-point contact was used as shown in Figure 5-54, this corrects the bend angle and is closer to the moving contact points formula. This is limited by only the edge of the bend being observed, the contact points having to be estimated by the author and is difficult due to not being able to observe the support pin contact in the micrographs.

In conclusion, the moving contact point formula by L. Troive et al. is found to be a good approximation of the bending angle found using other methods and will be used through this thesis. Furthermore, the bend testing optical results being a good approximation for the numerical results also suggests that the gen. 2 tooling and module have high stiffness.

#### 5.2.4.4.1 200x magnification, polished top surface specimen, 17DF4/1

The 200 magnification micrographs were used as an overall analysis of the strain development and showed some pitting due to over-etching due to the sample preparation exposing the corner from polishing on 2 faces.

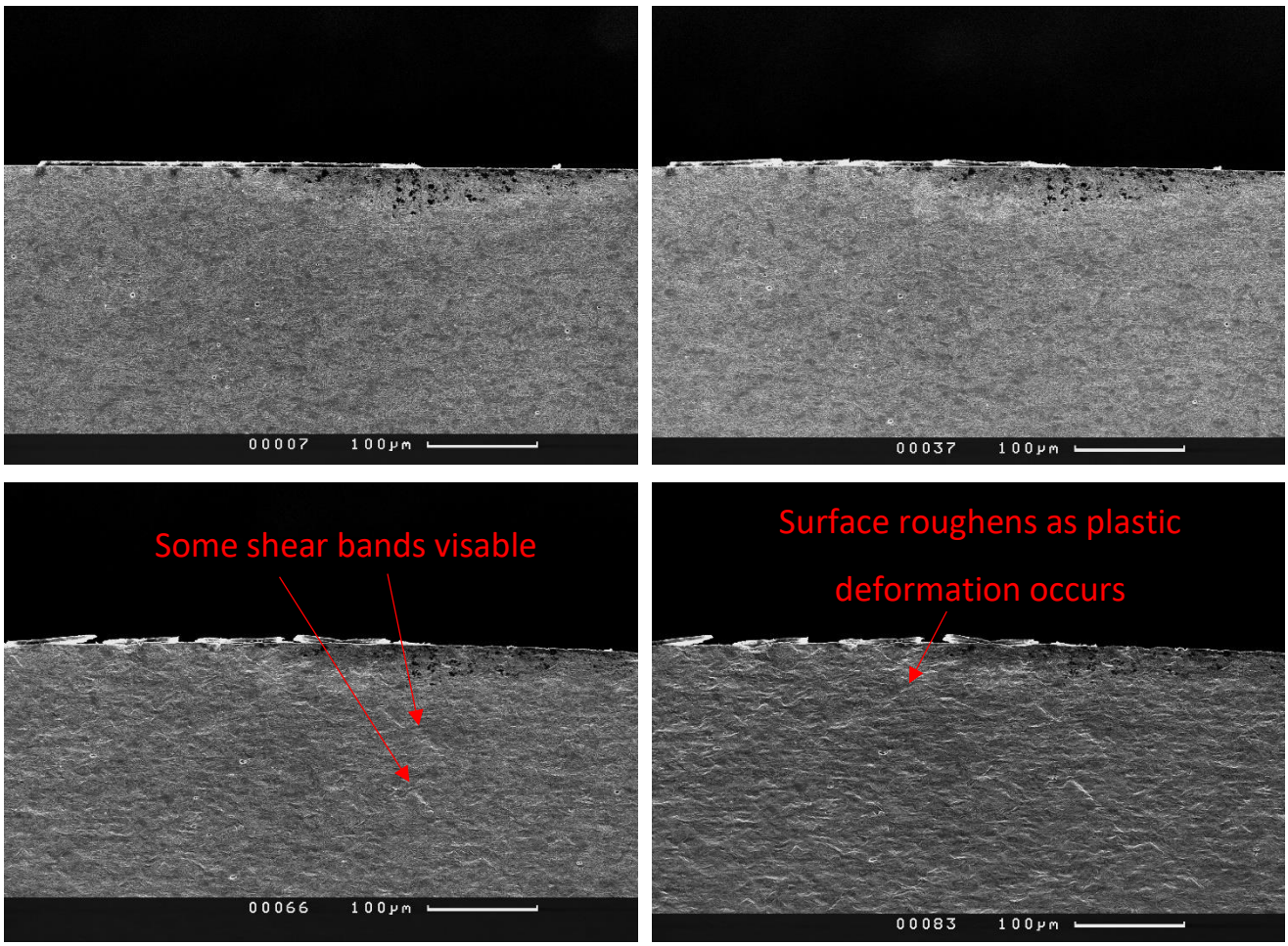


*Figure 5-54: Polished top surface 200x magnification bend test micrographs. Top left, no displacement, Top right, 0.8mm displacement, Bottom left, 1.6mm, bottom right 2.2mm displacement*

The top surface becomes rough as it plastically deforms, and the surface becomes uneven. Some shear bands become visible and can be studied further with DIC.

#### 5.2.4.4.2 200x magnification, 0.6mm depth polished surface specimen, 17DF4/1

The surface of the 0.6mm depth specimen at 2.2 in Figure 5-55 seems visibly rougher than the polished top surface at 2.2mm displacement in Figure 5-54. While shear bands at the top surface are visible in the micrograph in Figure 5-54.

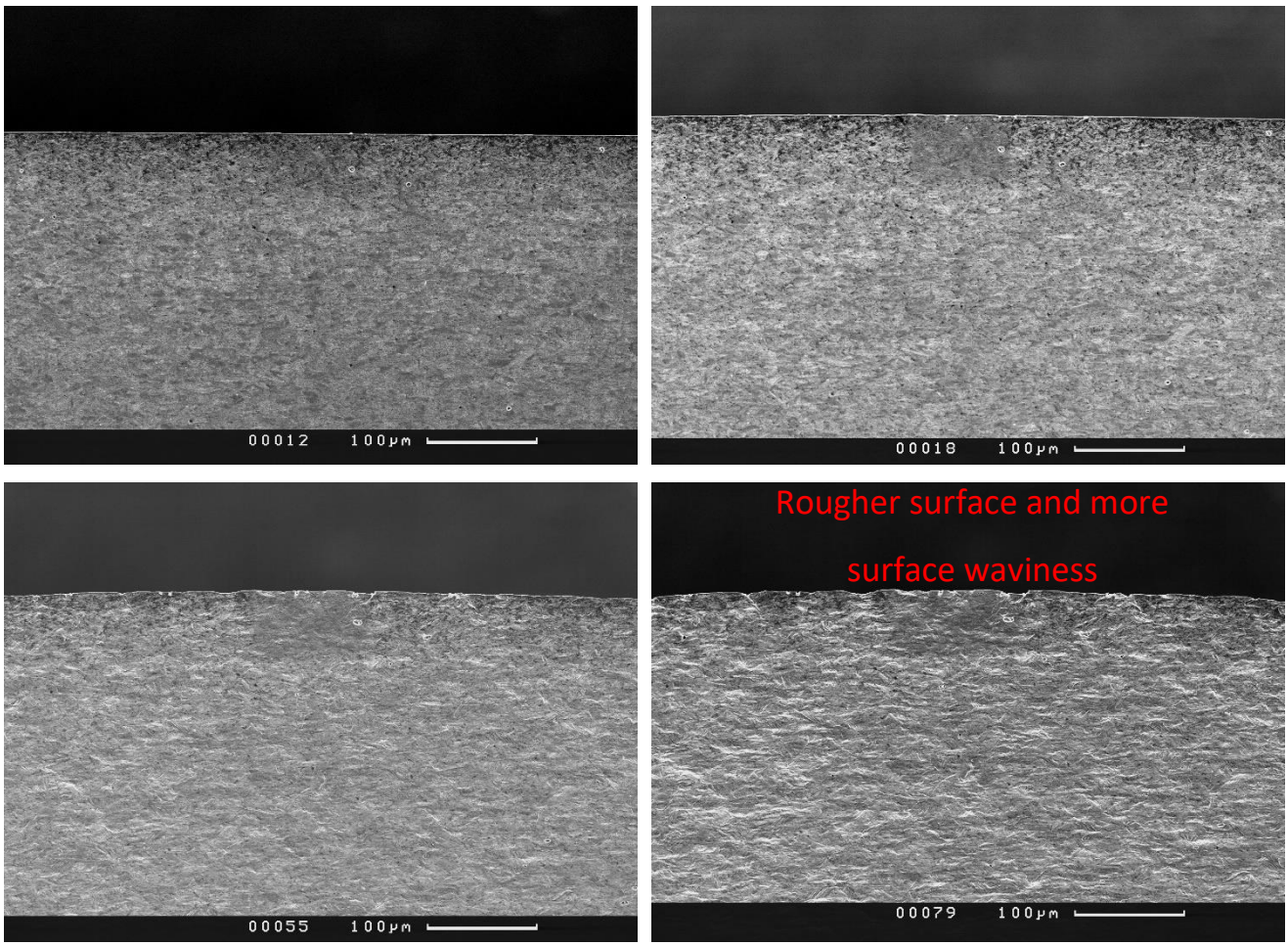


*Figure 5-55: 0.6mm depth polished surface 200x magnification bend test micrographs. Top left, no displacement, Top right, 0.8mm displacement, Bottom left, 1.6mm, bottom right 2.2mm displacement*

#### 5.2.4.4.3 1400x magnification, polished top surface specimen.

The top surface is found to be very flat with a 5µm layer of conductive mounting compound which undergoes spallation when strained. Some areas are found to be over etched near the edge. This is due to being on the edge the chemical reaction is acting on two faces. Strain is observed and the surface visibly roughens through the test. The deformation is found to be plastic deformation.

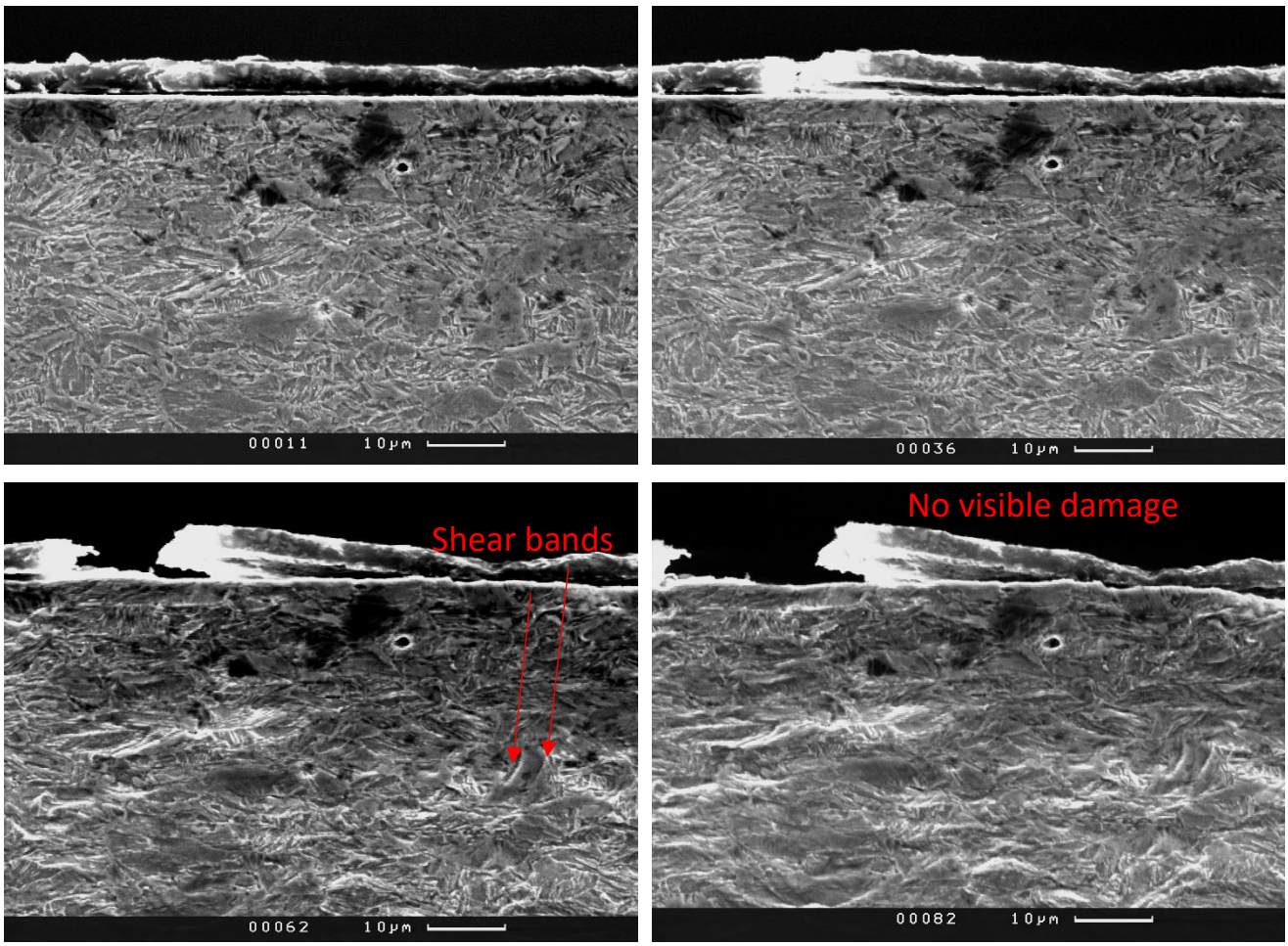


*Figure 5-56: Polished top surface 1400x magnification bend test micrographs. Top left, no displacement, Top right, 0.8mm displacement, Bottom left, 1.6mm, bottom right 2.2mm displacement*

5.2.4.4.4 1400x magnification, 0.6mm depth polished surface specimen.

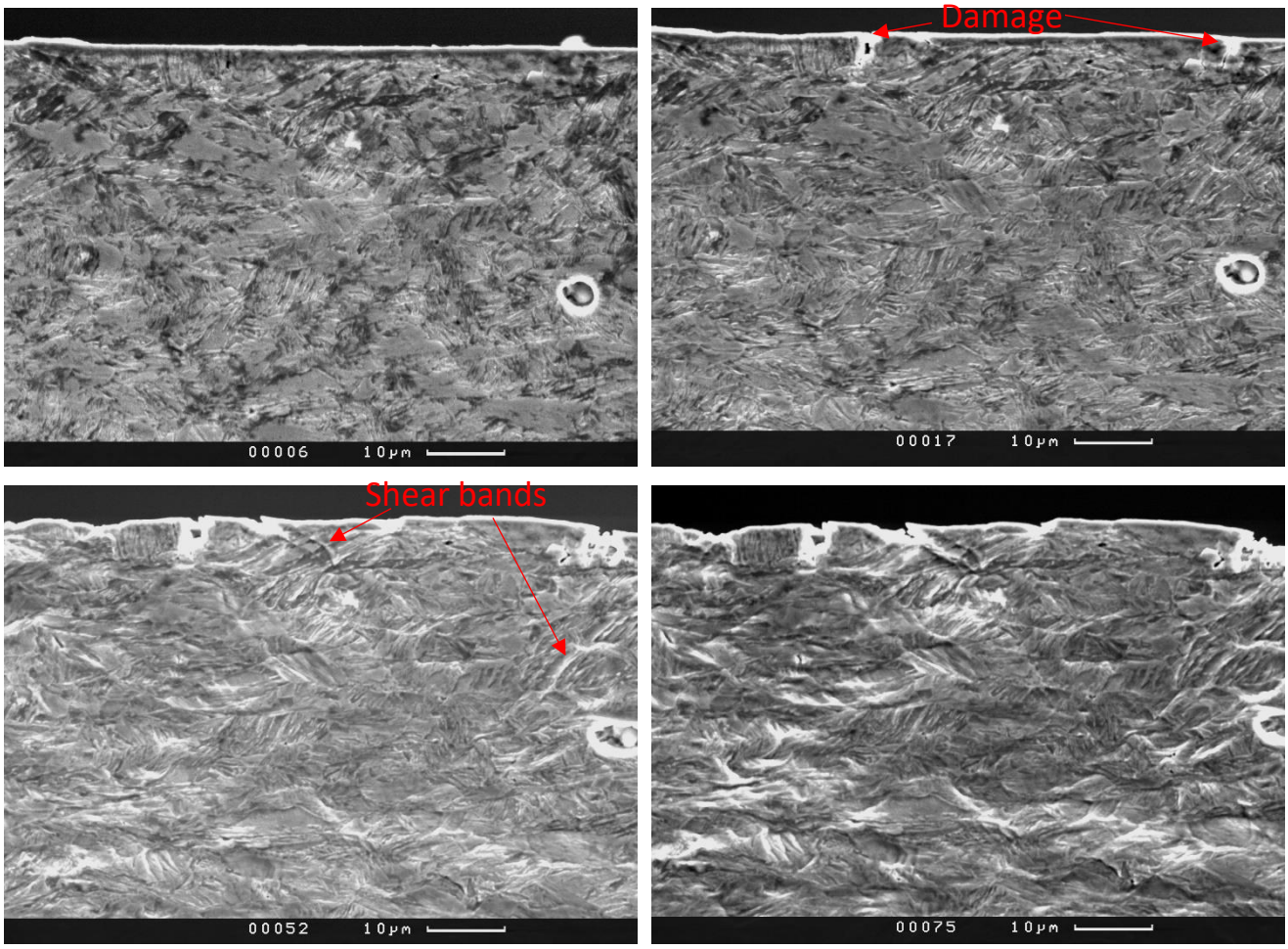


*Figure 5-57: 0.6mm depth polished surface, 1400x magnification bend test micrographs. Top left, no displacement, Top right, 0.8mm displacement, Bottom left, 1.6mm, bottom right 2.2mm displacement*

While the specimen at 0.6mm depth has damage initiate at the top surface at 1.6mm tooling displacement as shown in Figure 5-58

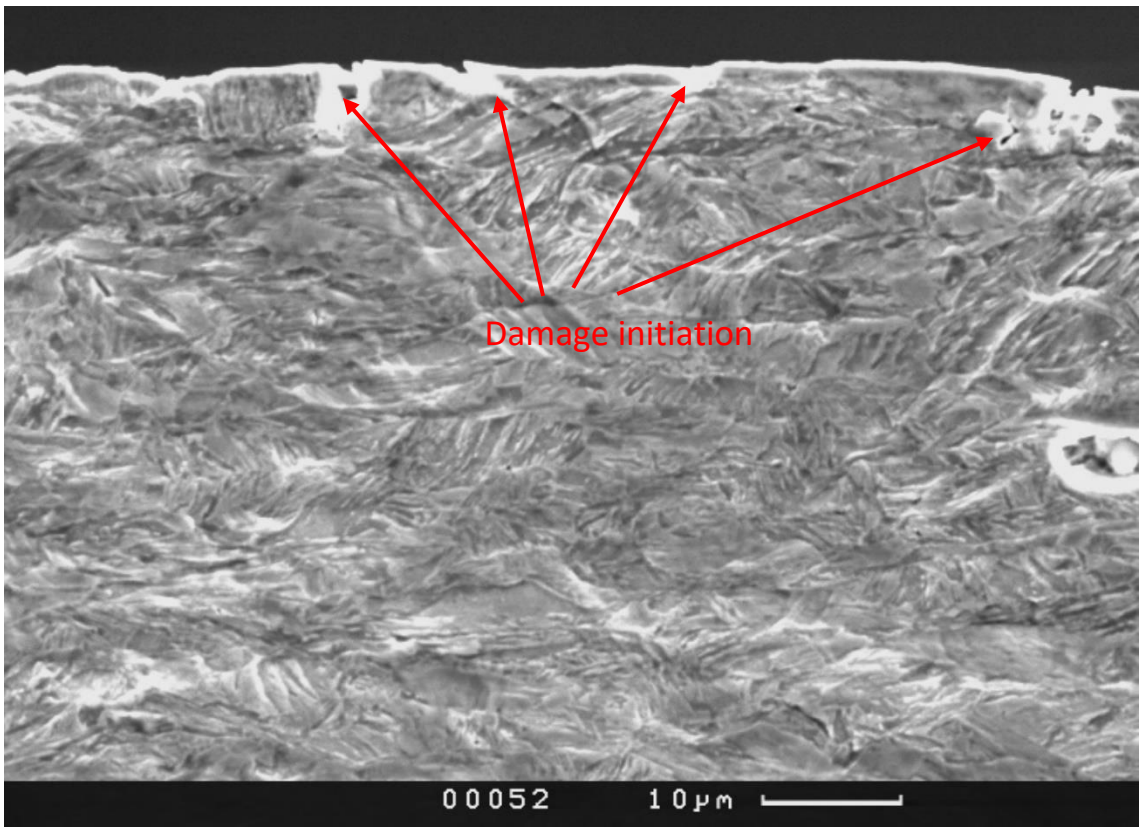


*Figure 5-58: 0.6mm depth polished surface, 1400x bend test at 1.6mm displacement.*

## 5.3 Digital Image Correlation

#### *5.3.1.1 DIC results from Deben tooling*

To study the strain development in bending the micrographs from Figure 5-32 were processed with DIC in Figure 5-59. These find high strain at the inclusion and void as expected, exceeding 150% strain in EYY. Other regions have also been highlighted where the strain along 2 shear bands was found. By examining the micrographs, the microstructures longer grain boundaries are aligned at 45° to the surface. Where they intersect a high strain region exceeding 150% strain is found.

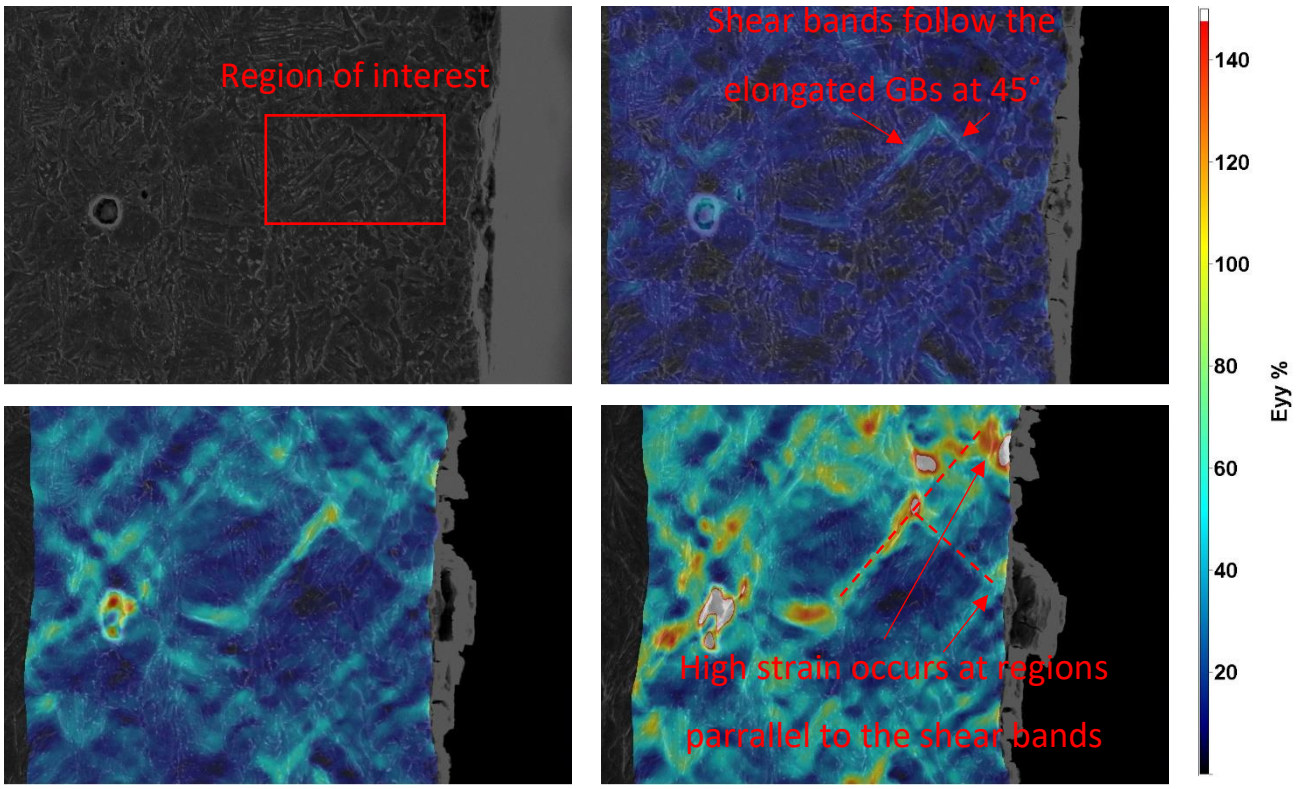


*Figure 5-59: Micrographs from bend test 3 with a 3mm thick specimen at 1400x with DIC strain maps, top left, no displacement, top right, 3mm displacement, bottom left, 6mm displacement, bottom right, 8.57mm at maximum module displacement.*

## 5.3.2 DIC error analysis

Error has been identified as a limitation of the interrupted DIC error analysis by work by H. Ghadbeigi et al. [88]. To optimise the DIC settings to keep error within acceptable bounds an error calibration was performed. A process of maximising detail by getting a compromise between limited averaging with a small subset and low error by using a larger subset.

To perform this, 5 images were obtained at the two magnifications with no movement between these images. Due to the contamination on the specimen, the brightness and contrast were adjusted as the image was found to get darker during the experiments. This happens throughout the experiment so acts as a means of considering this effect on error.

These micrographs were then post-processed in DaVis with the same settings as used in later DIC images in this document. The step size was set to 5 pixels, a mask was set on the image by the author, the algorithm used was a sum of differential type and it was set in accuracy mode as advised by LaVision. These images were studied and the maximum positive and negative strain value in Exx was found for each image set and this is shown in Figure 5-60 and Figure 5-61.

### *5.3.2.1 1400x magnification error*

The error in 1400x is found to follow an inverse relationship between error and subset size. The error is found to be greater in the top surface micrographs as these were a lower quality than the 0.6mm

depth subsurface test micrographs. These varied due to the high degree of user input to optimise imaging with the Camscan S2 SEM. Error is found to be significant with up to 22.5% error measured in the top surface imaging with a subset of 15 pixels. While with the same micrographs the error can drop to 3% error while using a subset of 55 pixels.

To set a suitable compromise the strain measured was found to exceed 100% in some locations at 1400x magnification thus an error of less than 5% was considered acceptable. Thus the subset selected is highlighted in Figure 5-60 as 45 pixels when using 1400x magnification.

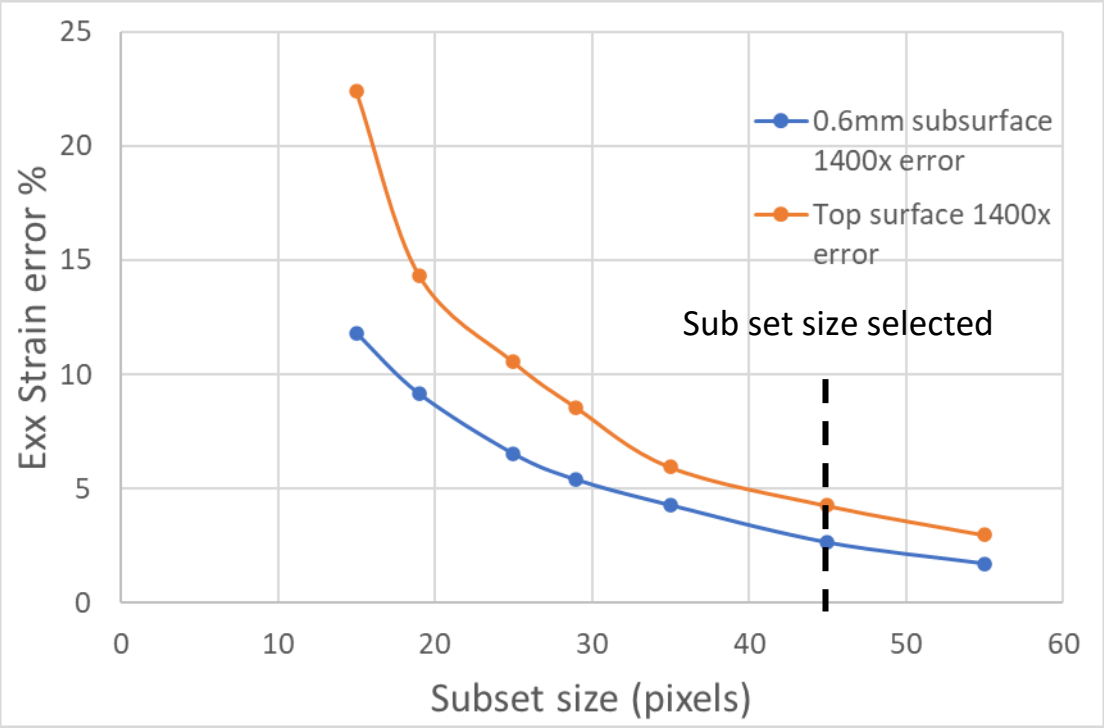


*Figure 5-60: 1400x micrograph DIC error analysis for the polished top surface and 0.6mm depth specimens.*

### *5.3.2.2 200x magnification error*

When using a lower magnification, the error is found to drop significantly while retaining the same inverse profile as described for 1400x. This is likely due to the improved micrograph quality and detail from using a lower magnification. When studying DIC at 200x magnification strain is significantly lower at only 50% or more. So, the error should be attempted to be smaller than for 1400x, as such keeping error below 0.8% was considered suitable and a subset of 29 was chosen to obtain good quality DIC results at 200x magnification.

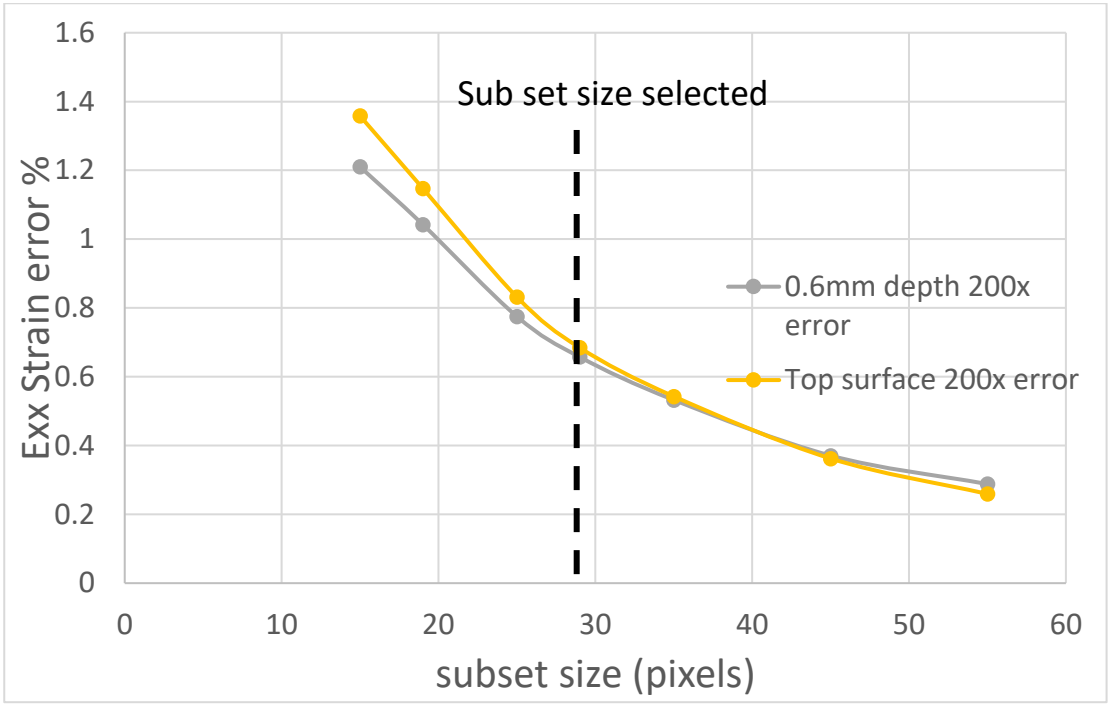


*Figure 5-61: 200x micrograph DIC error analysis*

## 5.3.3 Polished surface results

#### 5.3.3.1.1 Polished top surface 1400x DIC

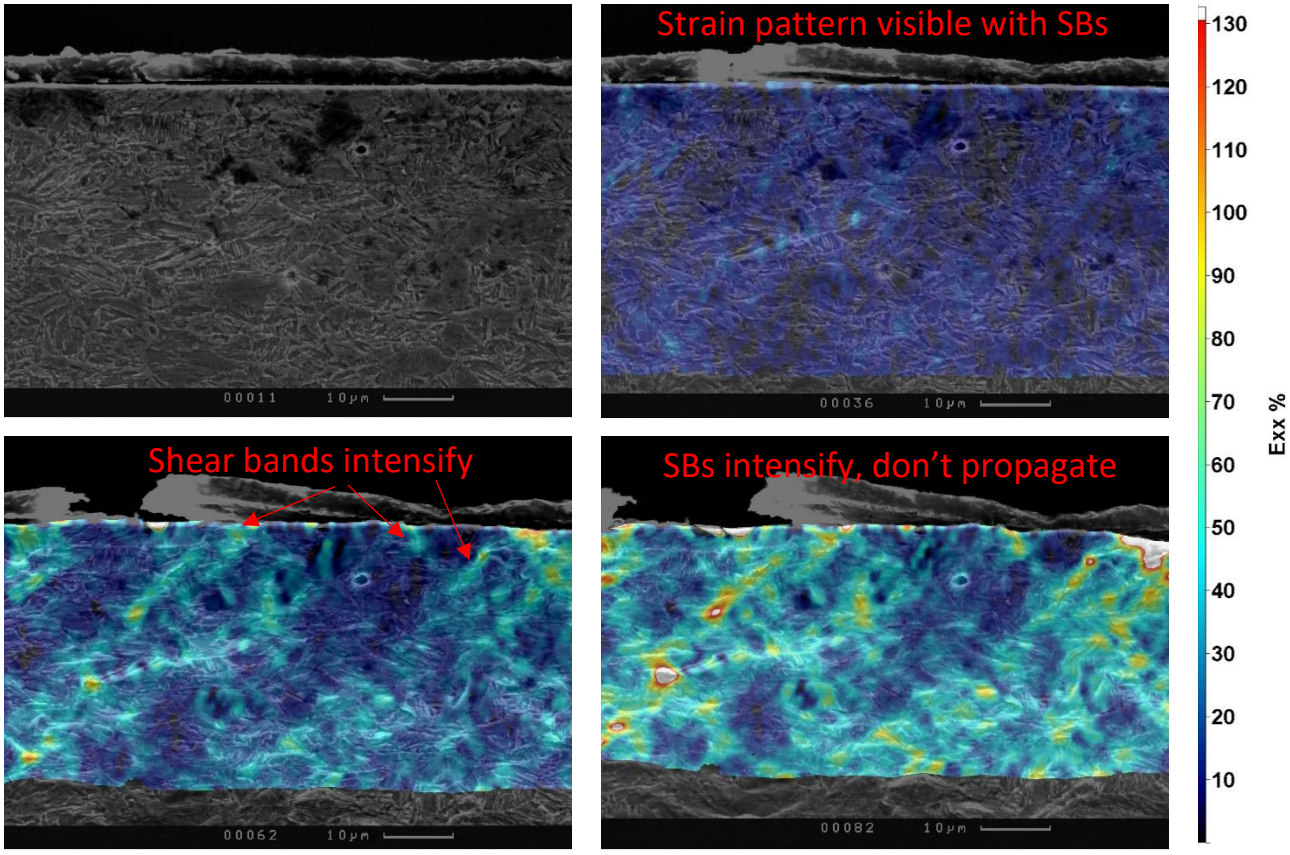


*Figure 5-62: 1400x magnification bend test micrographs with DIC post-processing. Top left, no displacement, Top right, 0.8mm displacement, Bottom left, 1.6mm, bottom right 2.2mm displacement.*

Shear bands are found to propagate at 45 degrees to the top surface. The peak strains are found at the surface where shear bands interact with the high strain top surface as seen with the highlighted squares in Figure 5-63 but also in the subsurface in the triangle highlighted regions. These appear to be found at positions where the shear bands intersect and will be investigated further in the discussion.

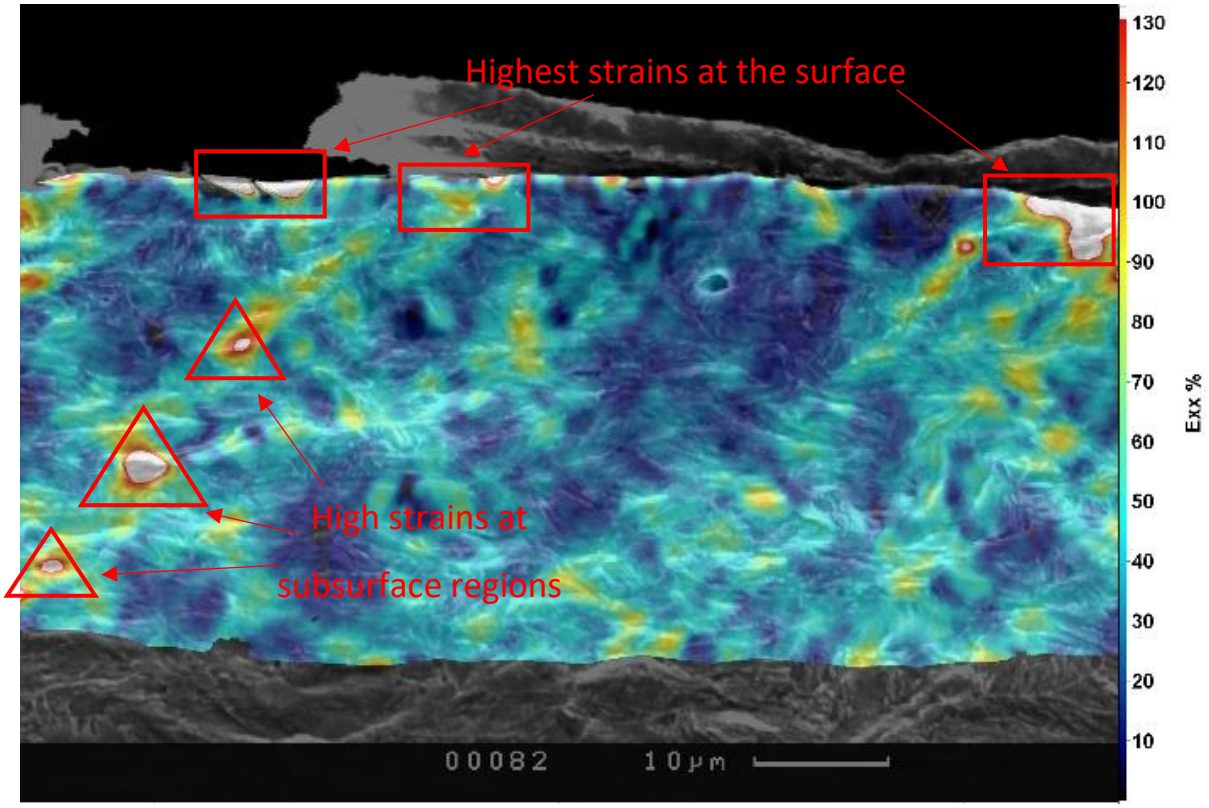


*Figure 5-63: polished top surface depth micrograph with high strain locations highlighted*

#### 5.3.3.1.2 Polished top surface 200x magnification DIC

The polished surface show shear bands appear after the Exx deformation exceeds the error value. Strain is found to propagate in bands at around 45°. These are found to be numerous and intensify neat the surface and where they intersect.

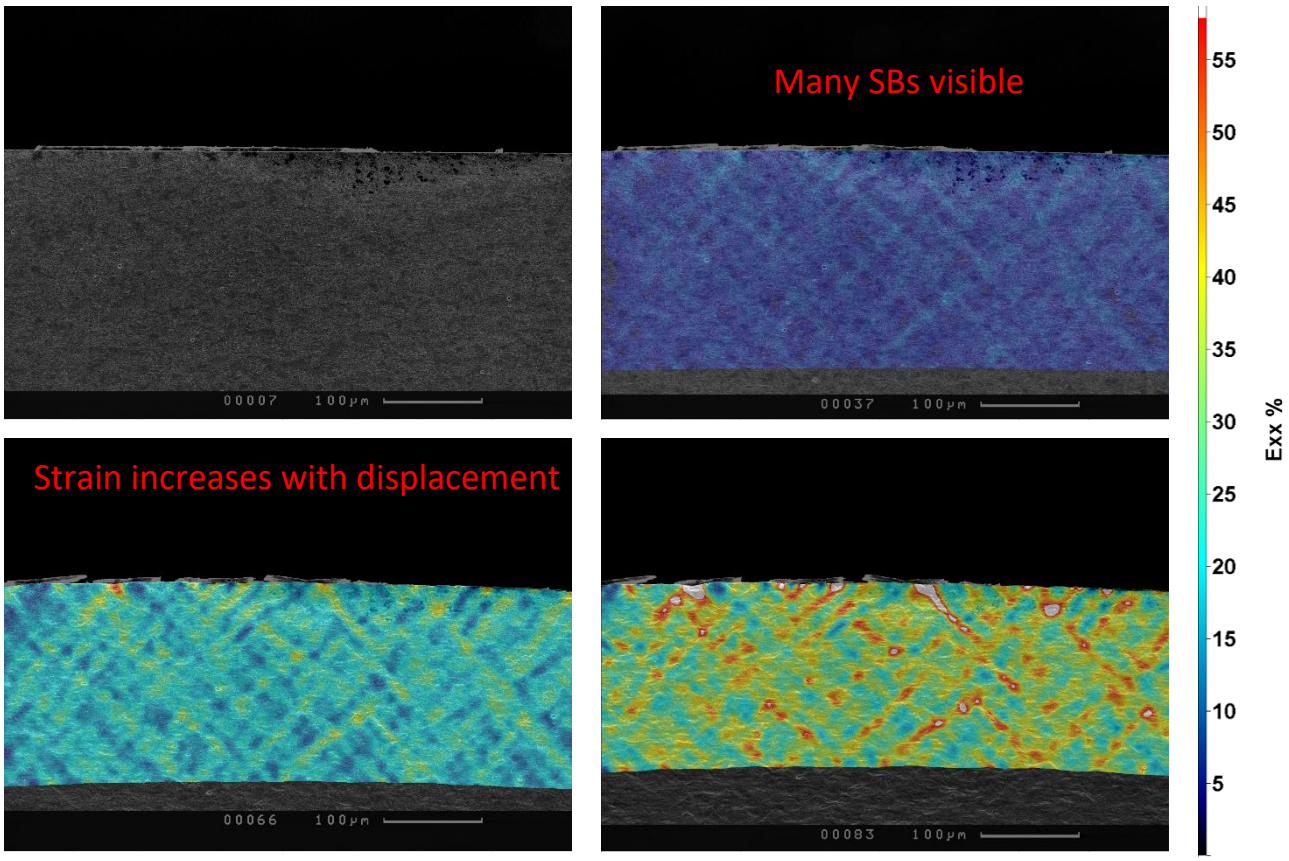


*Figure 5-64: 200x magnification bend test micrographs with DIC post-processing. Top left, no displacement, Top right, 0.8mm displacement, Bottom left, 1.6mm, bottom right 2.2mm displacement*

### *5.3.3.2 0.6mm depth sample*

Shear bands are also observed in the 0.6mm specimen. Damage is observed at the surface of this specimen after 0.8mm displacement. This is investigated further in Figure 5-66, where surface waviness can be observed at 0.4mm displacement and then cracks develop at 0.6mm displacement in Figure 5-67. The shear bands are visible and are found to have a higher strain than those found with the polished surface specimens. A means of assessing the shear bands were required to understand the differences between specimens.

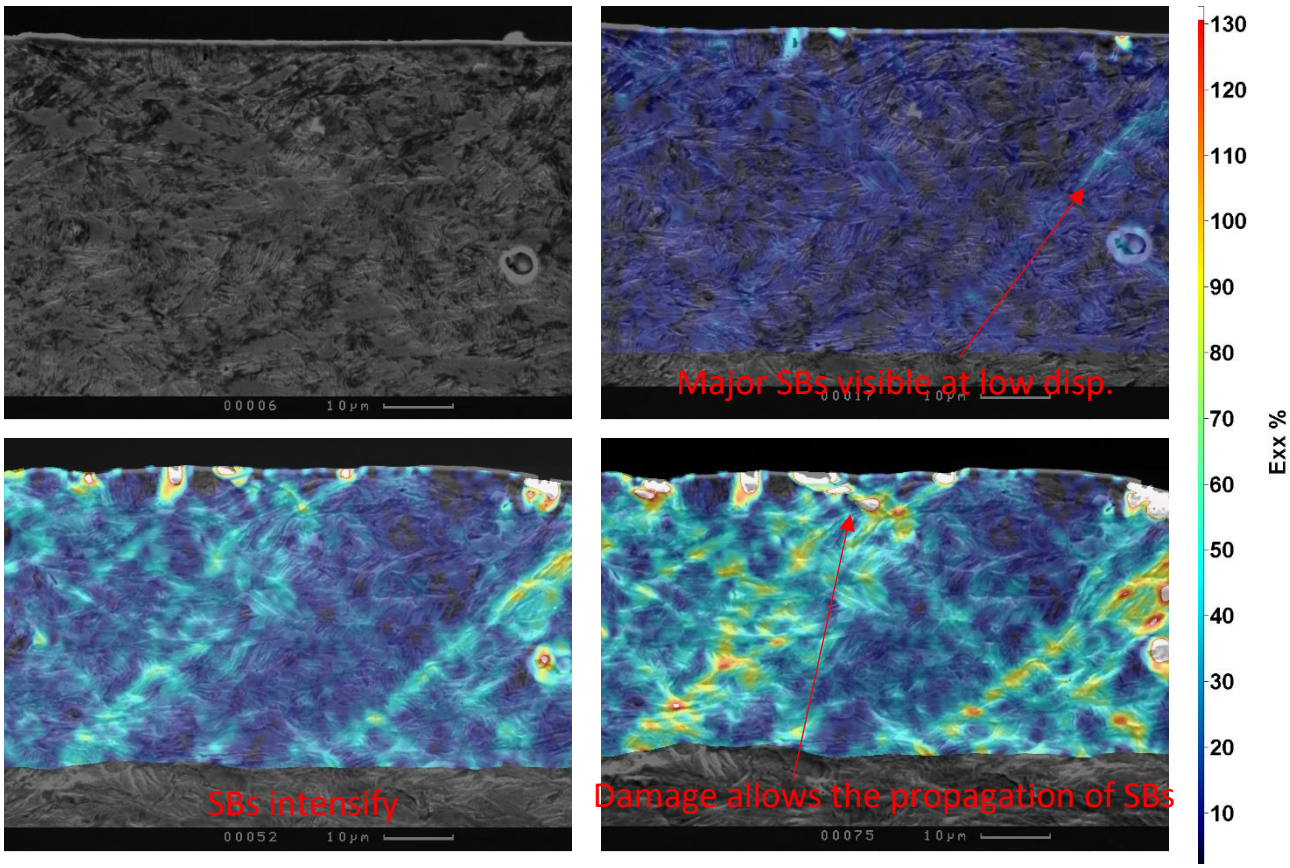


*Figure 5-65: 1400x magnification bend test micrographs with DIC post-processing. Top left, no displacement, Top right, 0.8mm displacement, Bottom left, 1.6mm, bottom right 2.2mm displacement*

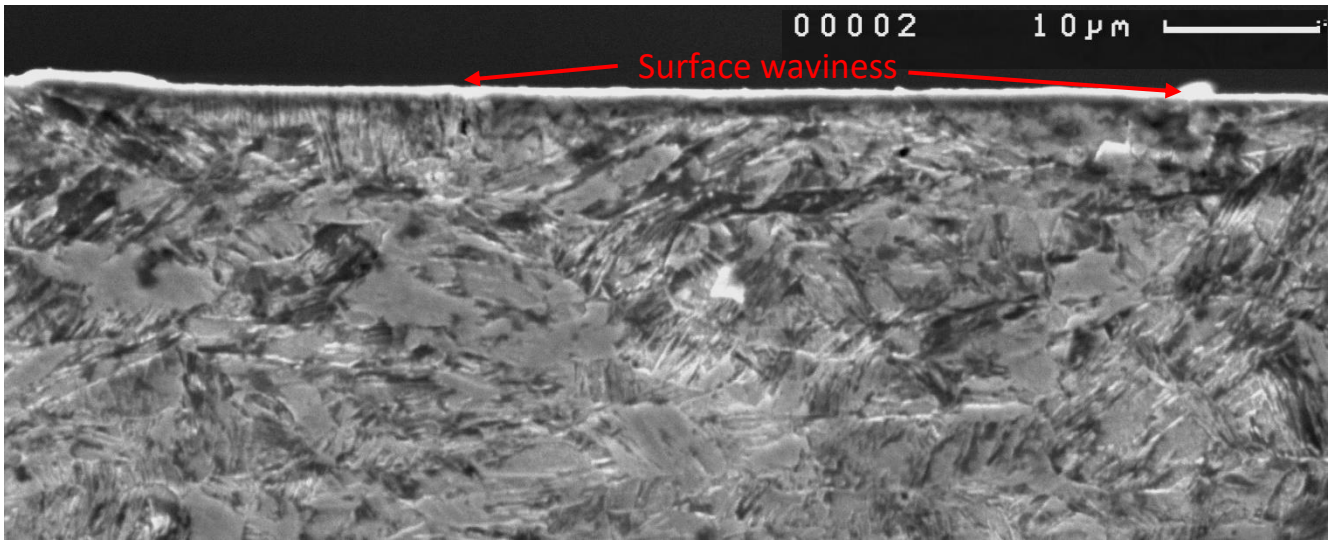


*Figure 5-66: Surface waviness before damage initiation at 0.4mm displacement*

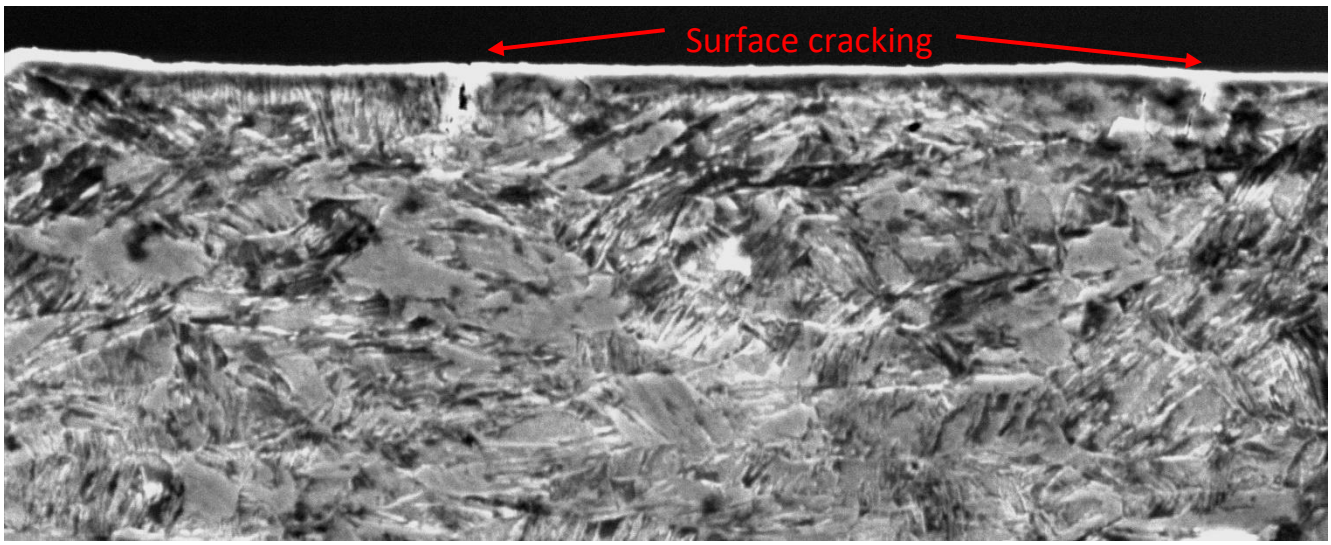


*Figure 5-67: surface cracking at 0.6mm displacement*

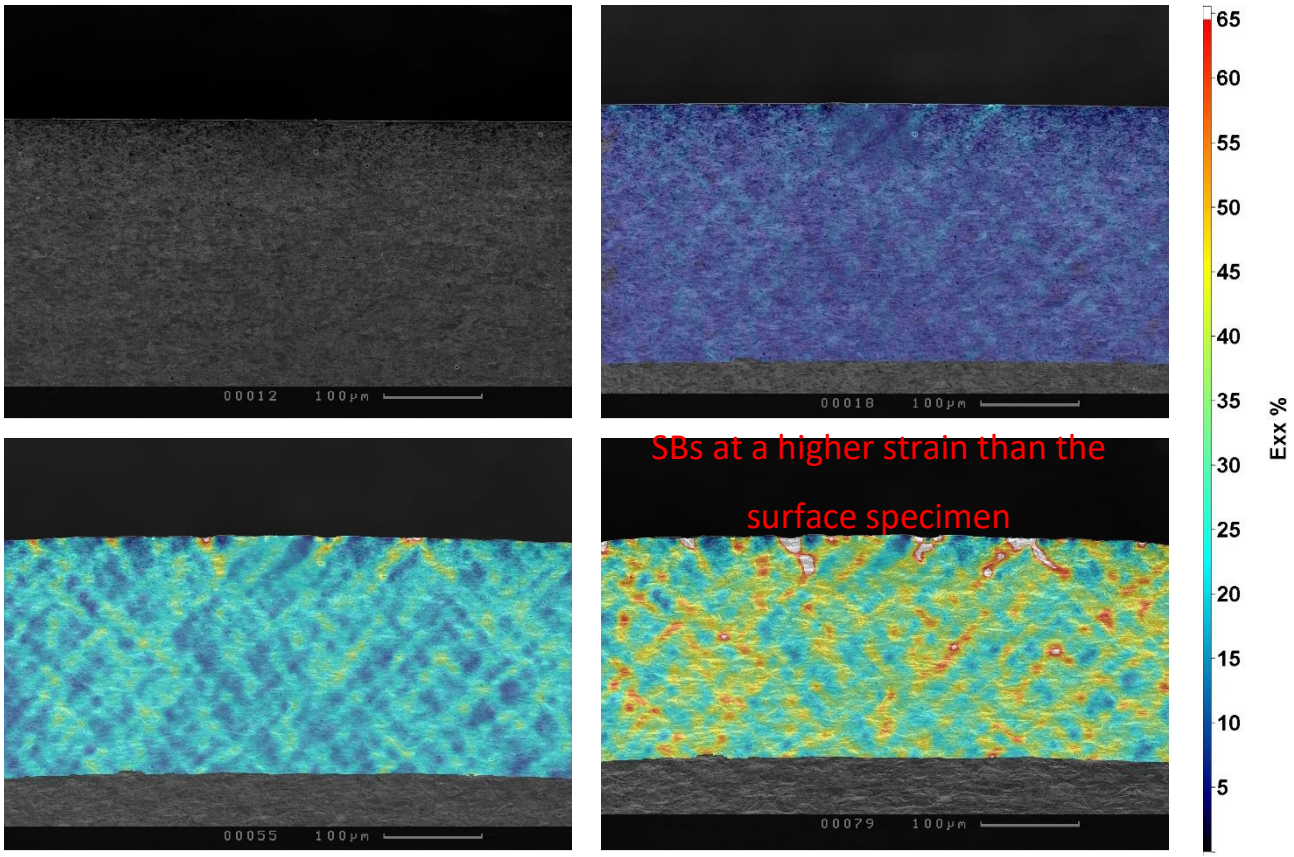


*Figure 5-68: 200x magnification bend test micrographs with DIC post-processing. Top left, no displacement, Top right, 0.8mm displacement, Bottom left, 1.6mm, bottom right 2.2mm displacement*

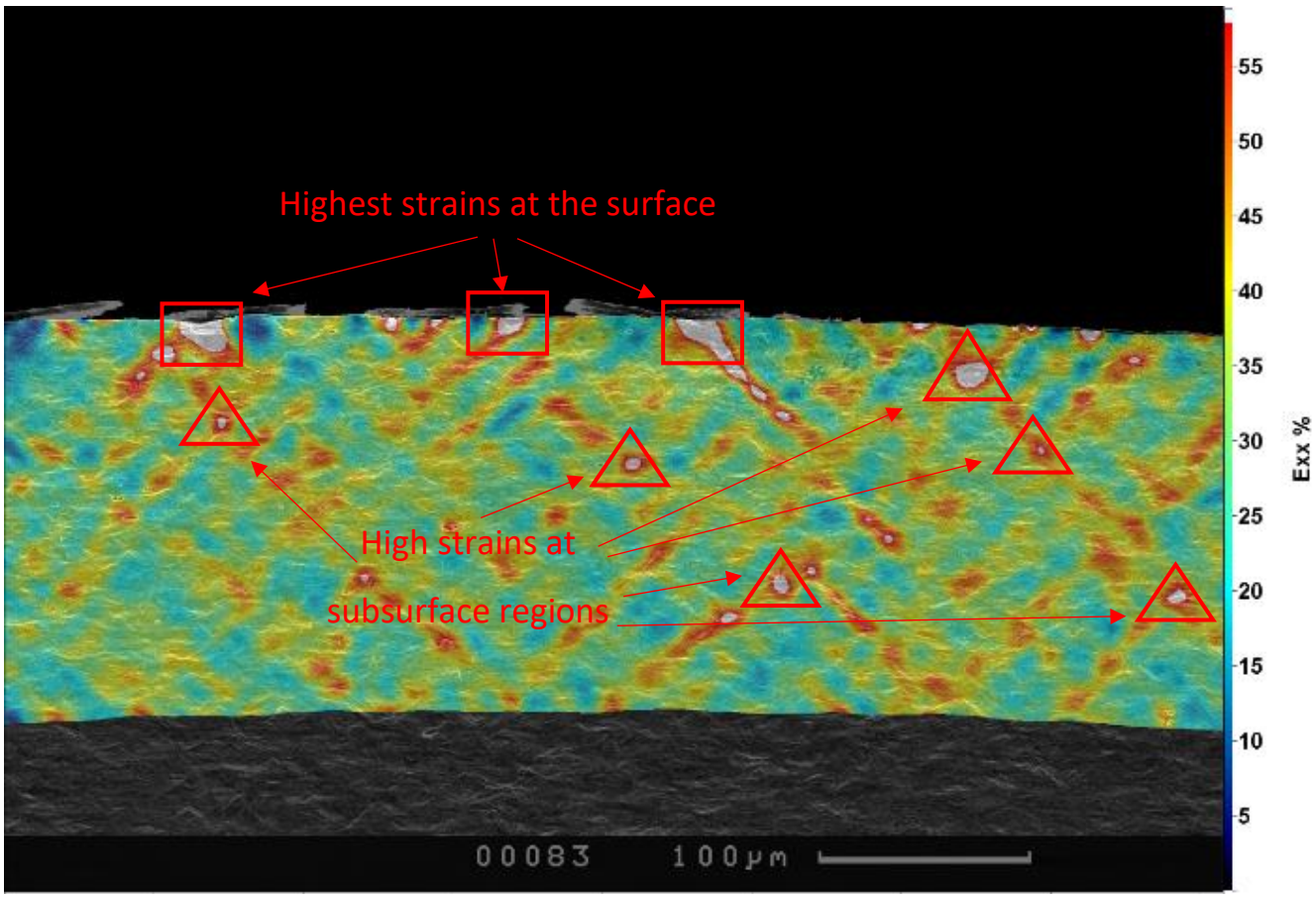


*Figure 5-69: polished 0.6mm depth 200x micrograph with high strain locations highlighted*

Shear bands are found to cause the peak strains at the surface as shown in the rectangles in Figure 5-69. Other strain concentrations are found where shear bands intersect at the triangle areas highlighted in Figure 5-69.

#### 5.3.3.2.1 Shear band images for the polished top surface specimen

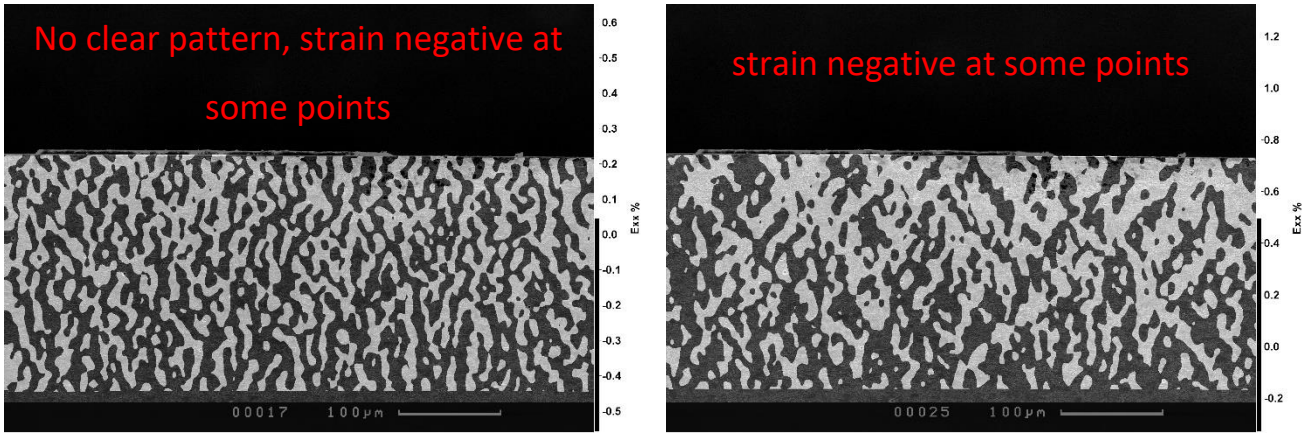


*Figure 5-70: 200x micrographs of the polished top surface with Exx DIC and black and white strain map palette at left, 0.2mm displacement right 0.4mm displacement.*

Due to the DIC calculation error, the images at 0.2 and 0.4mm displacement are found to have negative strain values as shown in Figure 5-70. So, these were not considered for the analysis of shear bands as any pattern associated with it could be due to error.

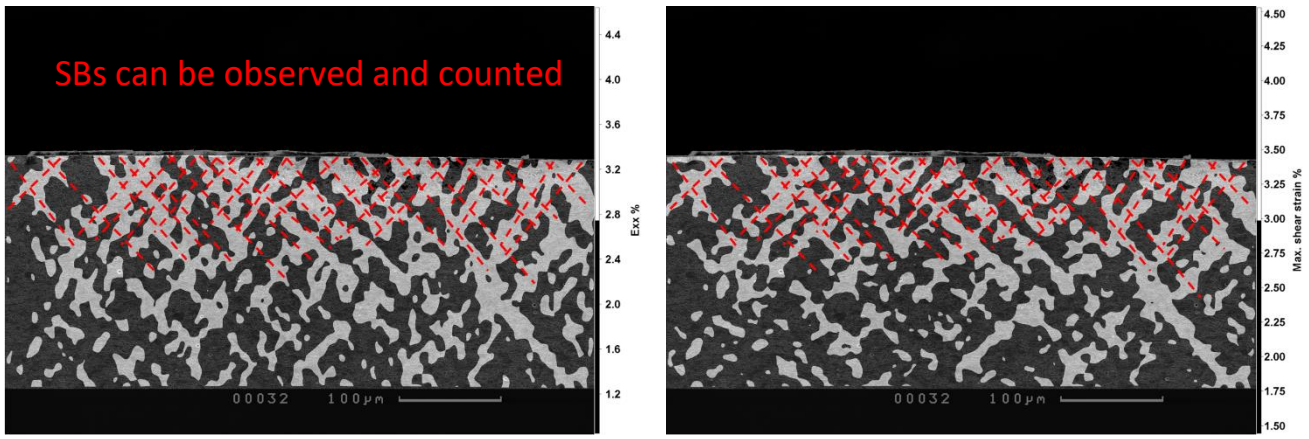


*Figure 5-71: 200x micrographs with the polished top surface with DIC and black and white strain map palette and shear bands are drawn on at 0.6mm displacement, left displaying Exx strain, right, displaying maximum shear strain.*

At 0.6mm displacement, the shear bands become visible in both Exx and the maximum shear strain in Figure 5-71. The shear bands are densely grouped, found every 16µm on average. The shear bands are at around 45° in angle with some deviation due to the shear bands finding the lowest energy route.

When comparing the same micrograph with Exx strain and the maximum shear strain in Figure 5-71 the strain maps are found to be near-identical, showing the shear strain is occurring in the same regions as the strain in tension.

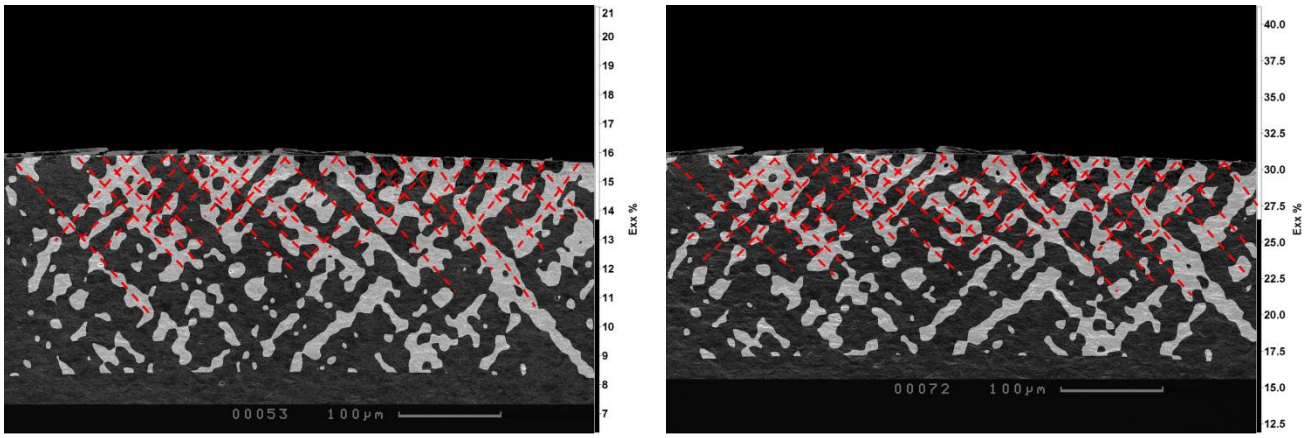


*Figure 5-72: 200x micrographs with the polished top surface with Exx DIC and black and white strain map palette and shear bands were drawn on left, 1.2mm displacement, right, 1.8mm displacement.*

As the displacement increases the shear bands spacing increases to 19µm at 1.2mm in Figure 5-72 and remains at that amount for the rest of the tests with the polished top surface specimen. This is likely due to the left side not having many shear bands observed and so it going outside the FOV with increasing strain doesn't reduce the shear band count very much. Shear bands are found to be stable and the strain magnitude is not found to increase in the shear bands as much as in the 0.6mm depth test.

Many SBs still visible, strain is not localising

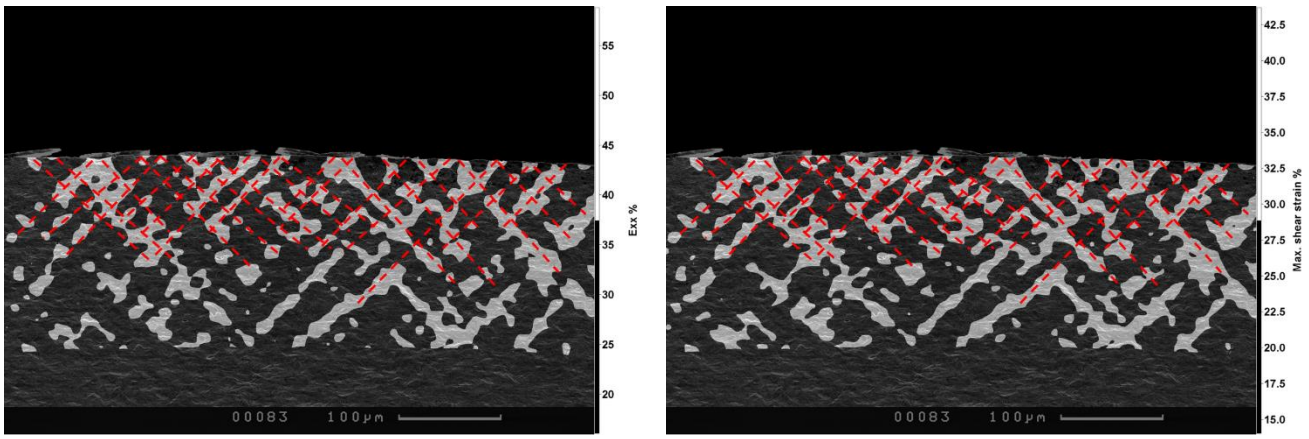


*Figure 5-73: 200x micrographs with polished top surface, black and white strain map palette and shear bands were drawn on at 2.2mm displacement. Left, Exx strain, right, maximum shear strain.*

As previously found in Figure 5-71 the regions of shear and Exx strain are also the same at 2.2mm displacement as shown in Figure 5-73.

5.3.3.2.2 Shear band micrographs for the 0.6mm depth polished surface specimen

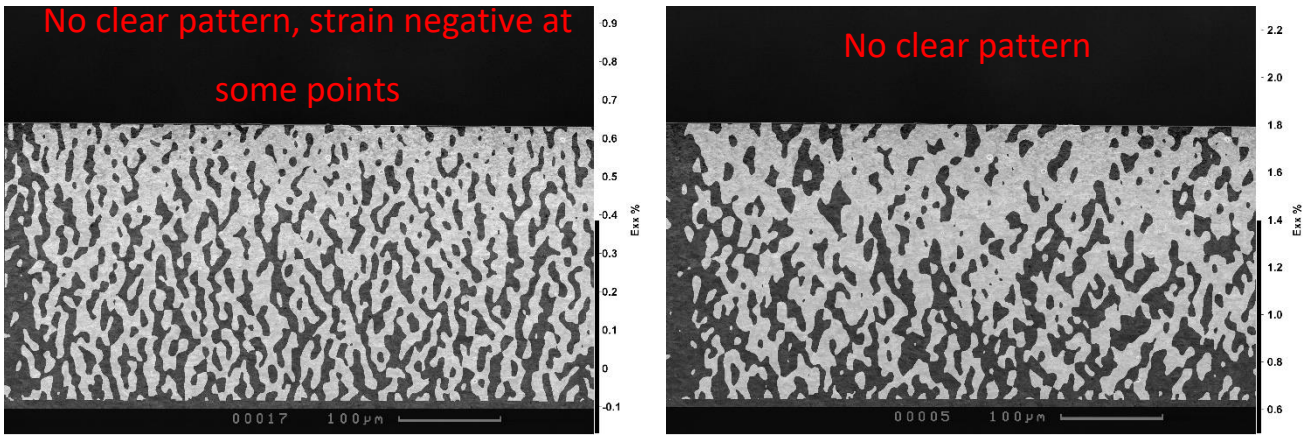


*Figure 5-74: 200x micrographs of the 0.6mm depth surface at left, 0.2mm displacement, right 0.4mm displacement.*

As found in section 5.3.3.2.1, the 0.2mm displacement has too much error and 0.4mm is ignored because the pattern is not easy to differentiate with the low strain values although the error is lower than with the polished top surface specimen.

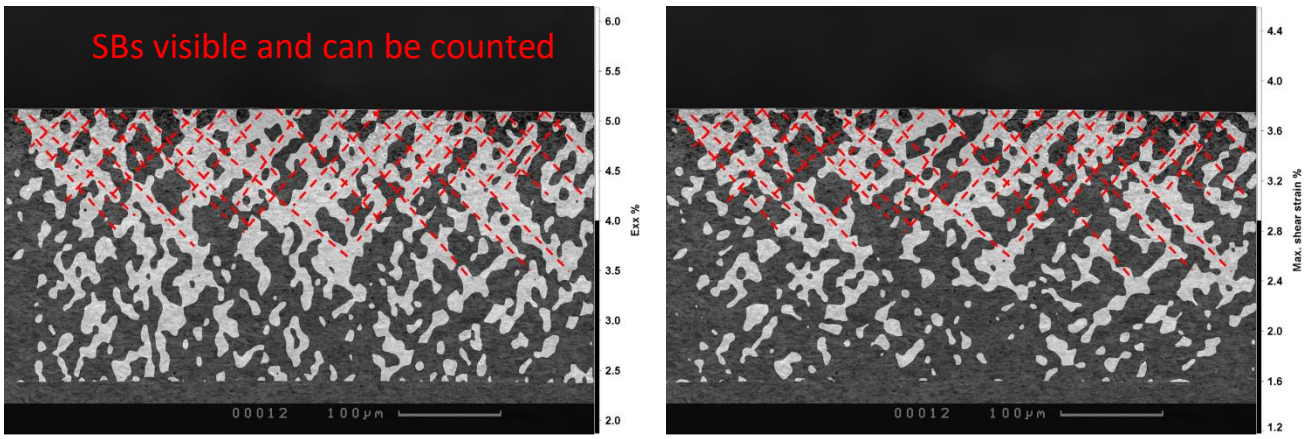


*Figure 5-75: 200x micrographs with 0.6mm depth polished surface post-processed using DIC with black and white strain map palette applied and shear bands were drawn on at 0.6mm displacement, left, Exx strain, right, maximum shear strain.*

At 0.6mm displacement, the shear bands become visible; it is again found that the maximum shear strain is in the same locations as Exx. The shear bands are found to have a slightly larger spacing of 18µm. As the bend test displacement increases the shear bands are found to intensify and some are lost as the maximum strain and median increases. This is due to the damage localising at the top surface causing the DIC to find high strain values in those regions.

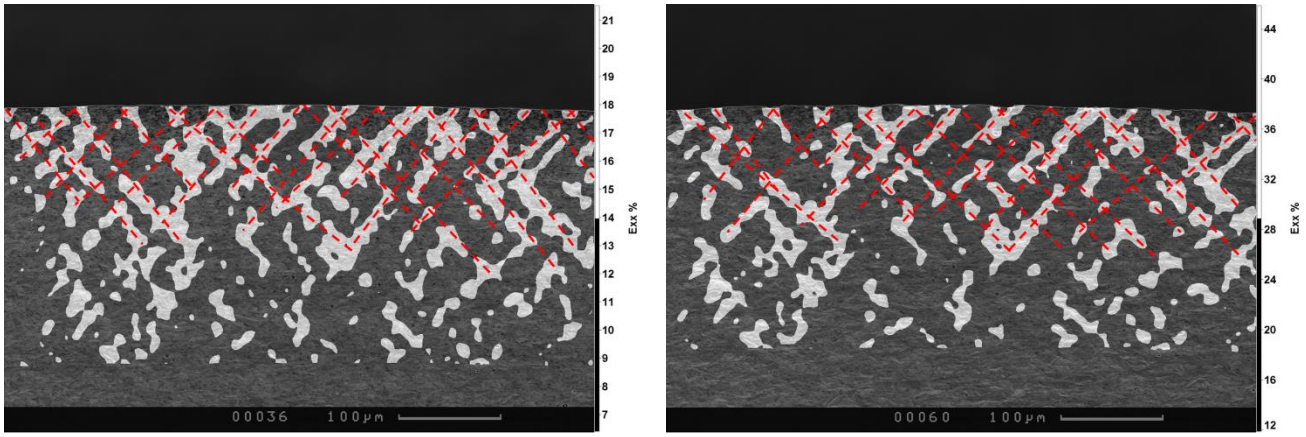


*Figure 5-76: 200x micrographs with 0.6mm depth polished surface with Exx DIC and black and white strain map palette and shear bands were drawn on at left, 1.2mm displacement, right, 1.8mm displacement.*

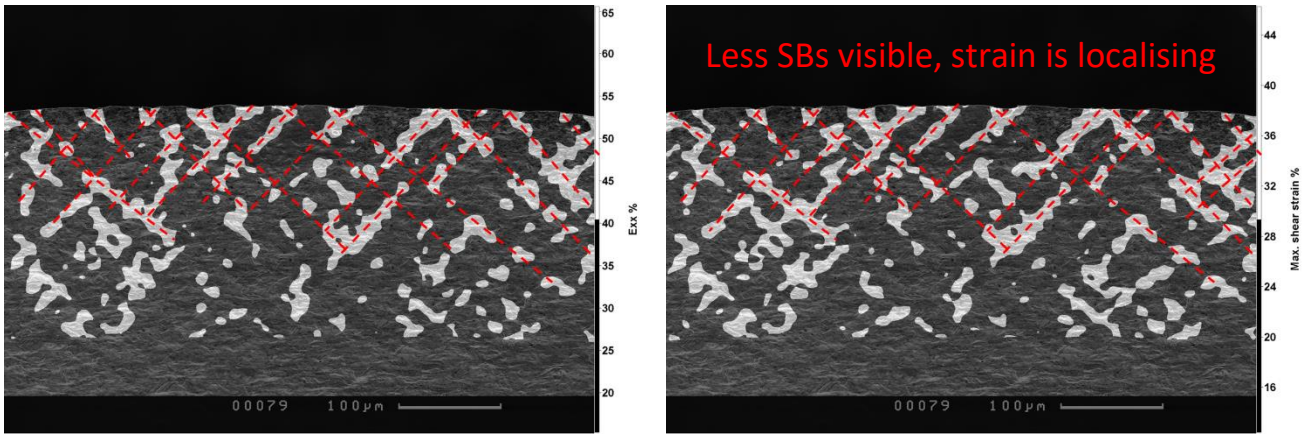


*Figure 5-77: 200x micrographs with 0.6mm depth polished surface post-processed using DIC with black and white strain map palette applied and shear bands were drawn on at 2.2mm displacement, left Exx strain, right, Maximum shear strain.*

### *5.3.3.3 Average shear band spacing*

Using these DIC micrographs and adding the shear band line profiles to them the number of shear bands can be counted. Thus, the dimensions of the micrograph known from the first image using the scale bar can be calculated as 571.4µm. To calculate the shear band spacing, $S_s$ the number of shear bands counted, $N_s$ is divided by the width of the FOV, $W_{xx}$ as shown in Equation 33.

$$S_s = \frac{W_{xx}}{N_s} \qquad \textit{Equation 33}$$

The average shear band spacing is calculated using Equation 33, is used to populate the graph in Figure 5-78 and finds the 0.6mm depth specimen has fewer shear bands and the shear band spacing

increases through the experiment. This increase in shear band spacing is not just due to the changing number of shear bands as during the bend test the specimen is strained in the XX direction causing an increase in the spacing through the experiment.

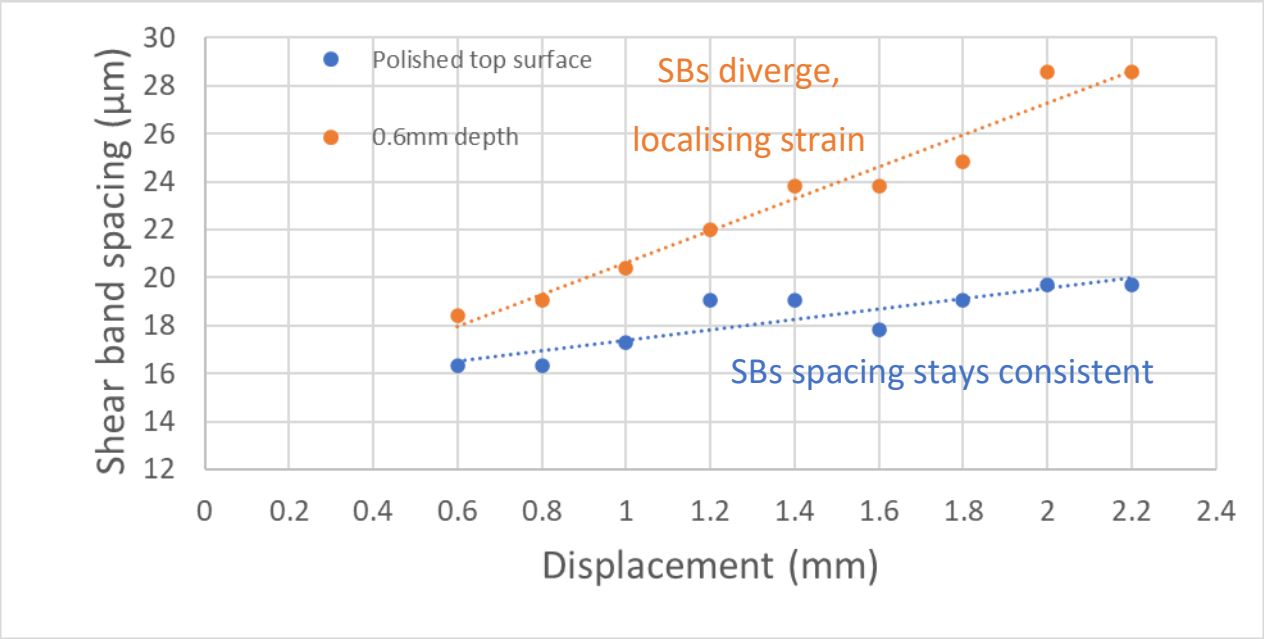


*Figure 5-78: plot of Average shear band spacing vs tooling displacement*

To account for strain in the XX direction the numerical data has been extracted from each step in both tests. The top surface has been identified and the average strain across the top surface, $\varepsilon$ is calculated. The length over which the shear bands were observed was divided by the average strain across the top surface plus 1 to represent the original as calculated in Equation 34.

$$S_S = \frac{W_{xx}}{N_s(1+\varepsilon)} \qquad \textit{Equation 34}$$

This is used to produce Figure 5-79 and shows that the number of shear bands in the more ductile top surface region was more stable and are tending to increase. In contrast, the less ductile 0.6mm depth specimen has fewer shear bands initially and is found to have the strain localised reducing the number of shear bands counted.

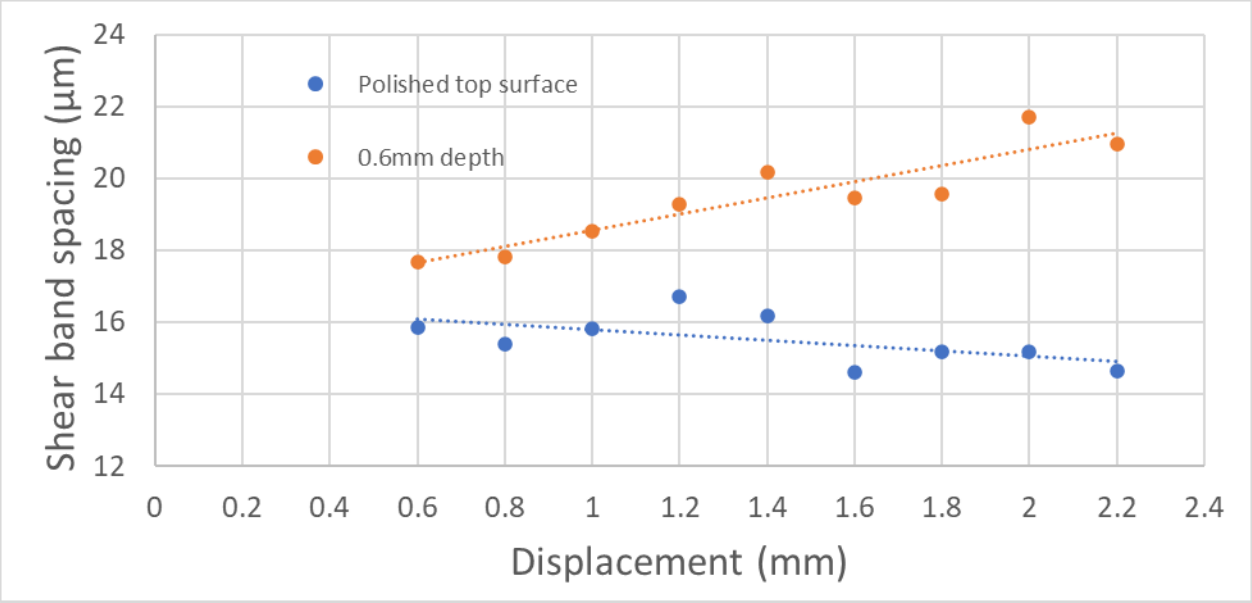


*Figure 5-79: Shear band spacing relative to the first image vs tool displacement.*

### 5.3.4 Strain depth results

Using the methodology described in section 3.8.2 the shear bands peaks can be counted.

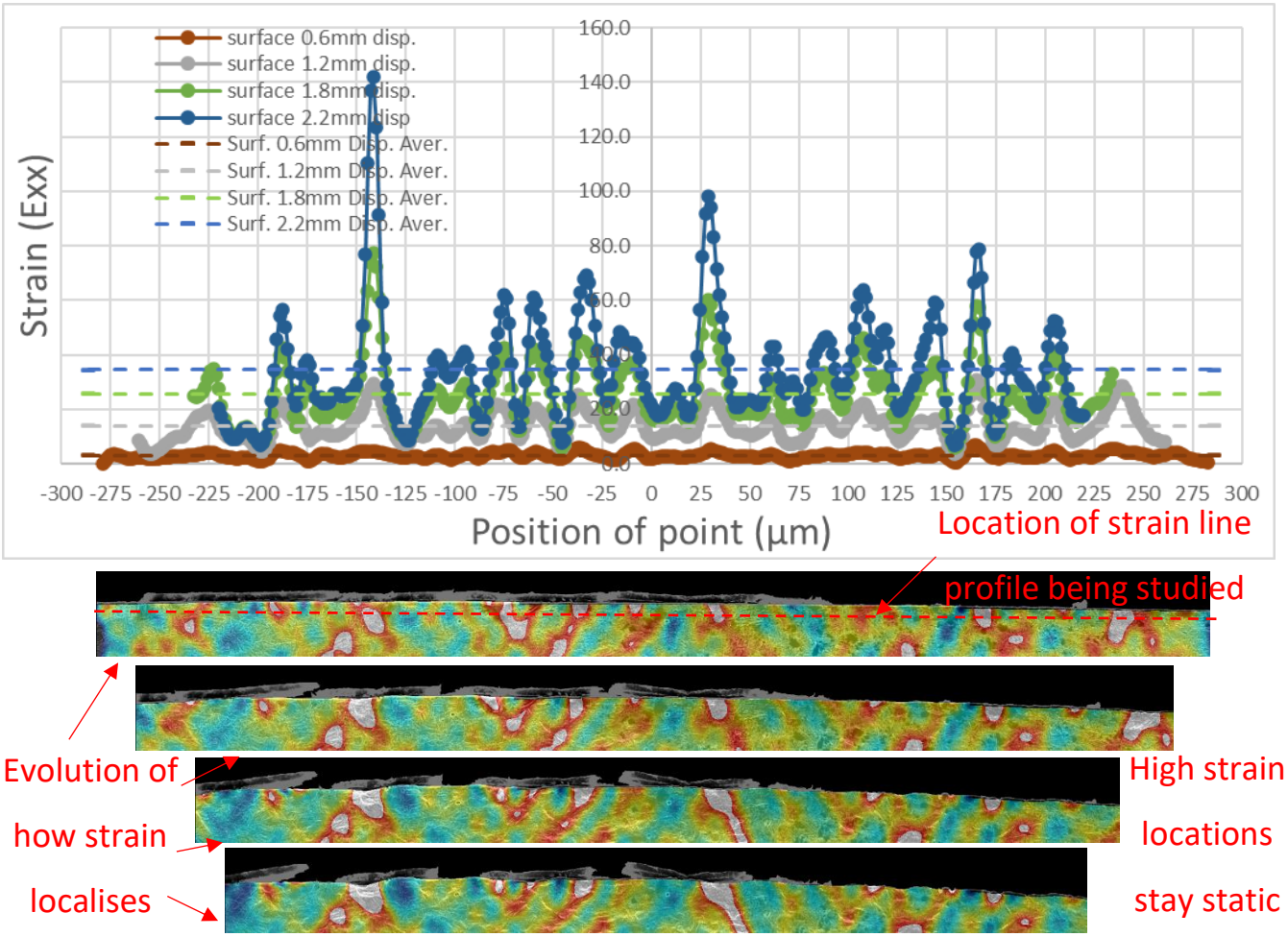


*Figure 5-80: Numerical DIC output from the surface of the polished top surface specimen, with associated DIC images sized to match the size of the DIC data width with a line highlighting the location of the strain analysis.*

In Figure 5-80 and Figure 5-81 the graphs show the strain at the surface of the specimen over the width of the FOV throughout the bend tests. The micrographs under the graph are sized to fit the curve as the original FOV shrinks as the specimen is strained and go out of view. This shows the DIC analysis is accurate as the positions of high strain can be identified and tracked throughout the test. The 0.6mm depth polished specimen has 4 points that exceed 100% strain in Exx at 4 points while in the polished top surface only one point exceeds 100% Exx strain. This shows that damage is found at the top surface of the 0.6mm depth specimen, it should be noted that the thickness of the specimens varied due to the thickness removal process. This meant the 0.6mm depth specimens underwent a higher strain due to the specimen having a greater thickness.

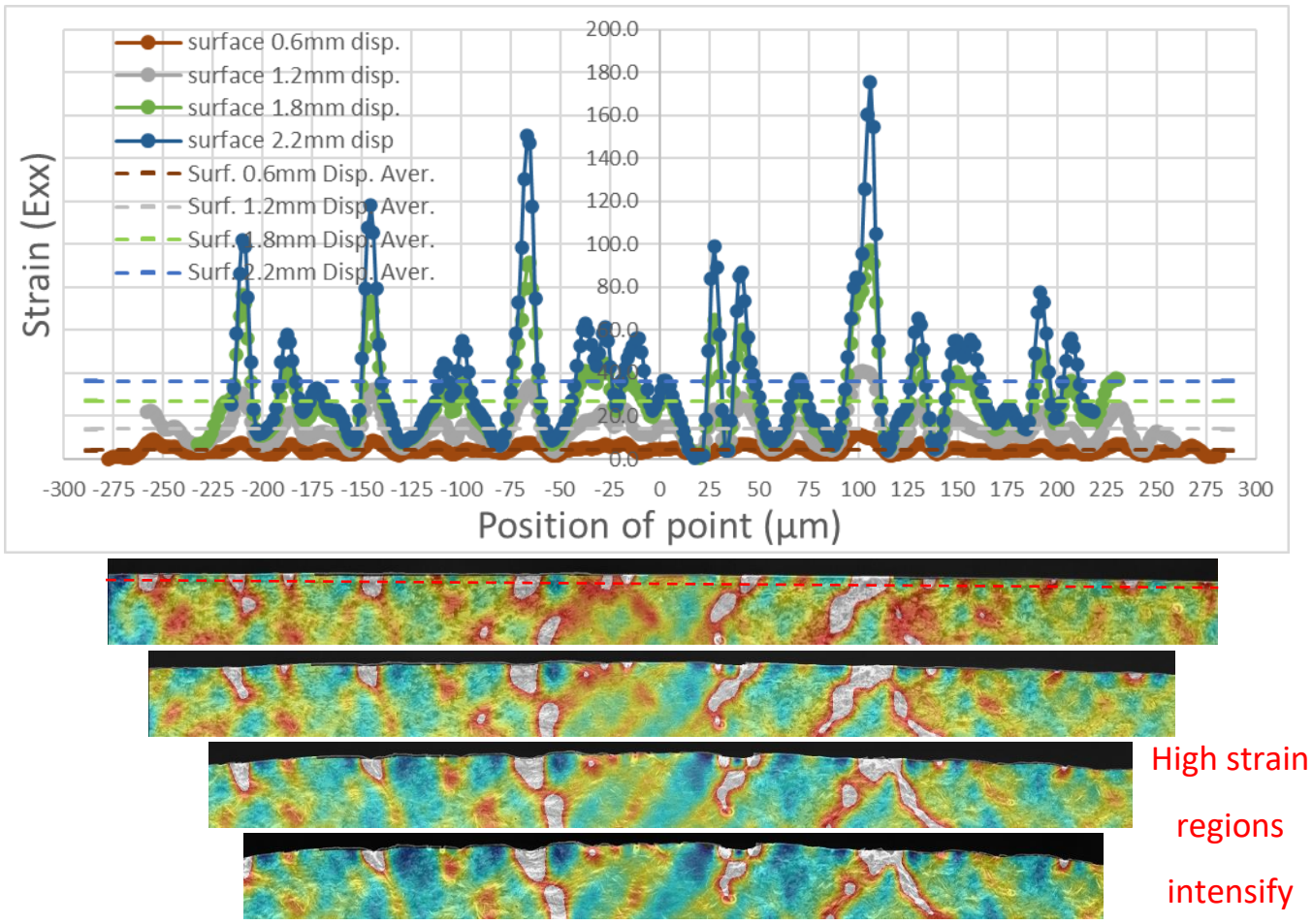


*Figure 5-81: Numerical DIC output from the surface of polished 0.6mm depth specimen, with associated DIC images sized to match the size of the DIC data width.*

The average strain through the depth of the specimen in both tests is shown in Figure 5-82. The average strain is found to be higher for the 0.6mm depth specimen with the strain offset by 1% between the results.

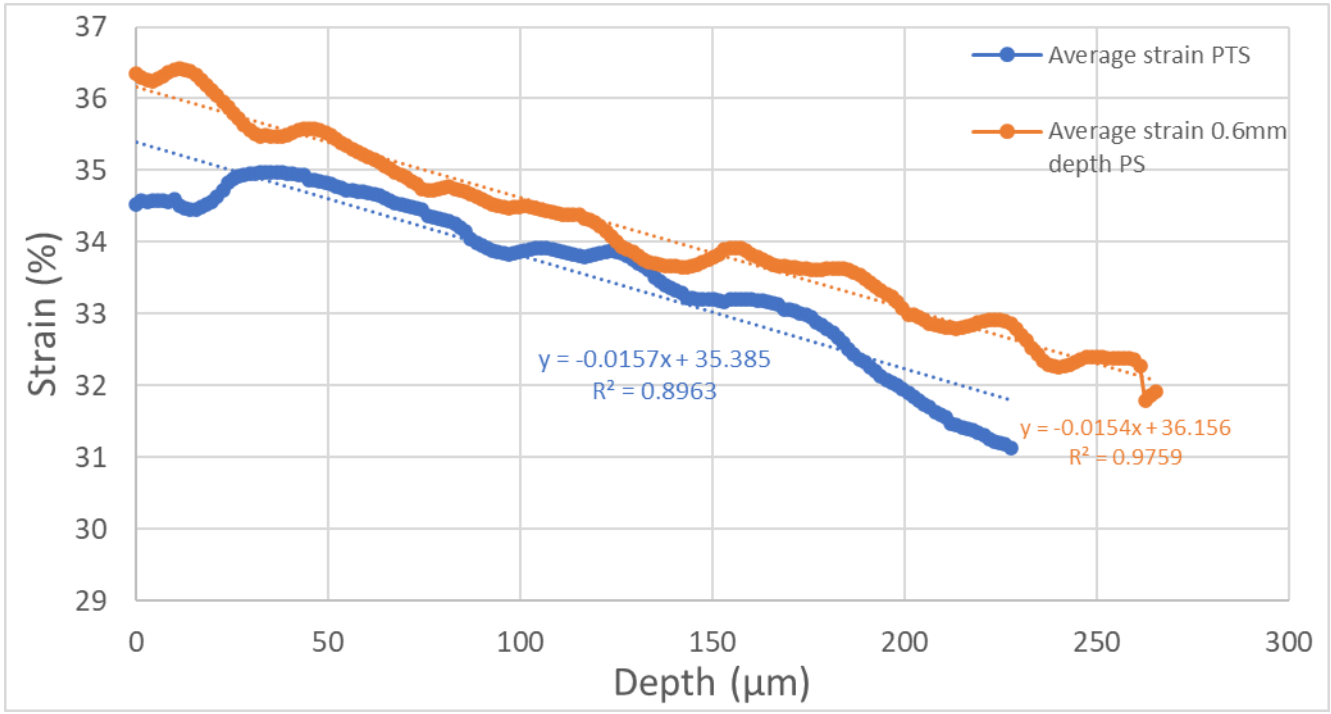


*Figure 5-82: average strain at 2.2mm displacement for the polished top surface specimen, PTS and 0.6mm depth polished surface.*

To study the variation in the strain the standard deviation was studied for the results from Figure 5-82 in Figure 5-83. This showed that the 0.6mm depth specimen had more variations in the strain at the surface but also through the depth when compared to the polished top surface sample.

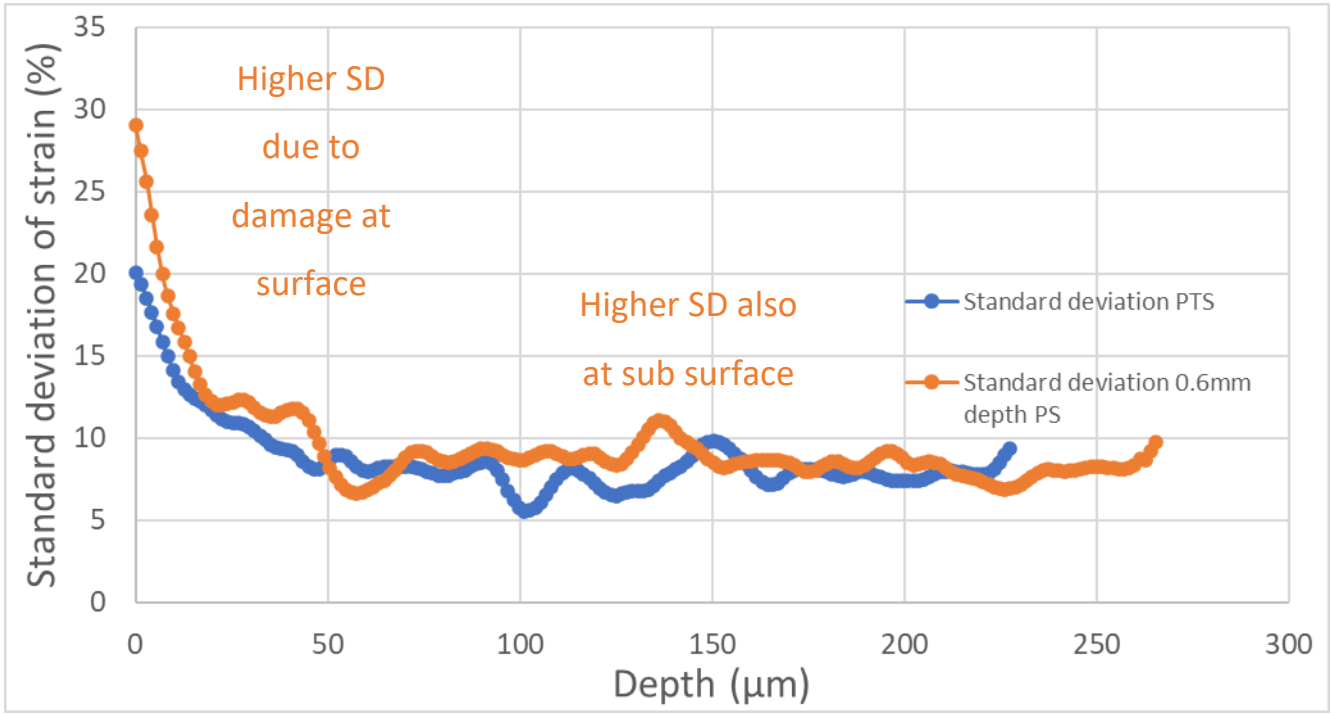


*Figure 5-83: Standard deviation strain at 2.2mm displacement for the polished top surface specimen, PTS and 0.6mm depth polished surface.*

## 5.4 Modelling results

### 5.4.1 Bend testing standard geometry

#### *5.4.1.1 2D Bend testing simulation*

2D FEM bend testing was performed as described in section 3.8.2. a range of materials simulated using material data from Figure 3-40 for the data produced using the Hollomon material hardening model and using the tensile test material data from section 5.1.1.3, the average strain data for sample 17DF4/1 has been studied. The use of material models with up to 100% strain enables the continuum model to deform to the high strains found in insitu tests in the SEM [109]. By continuing to harden they should resist necking and strain localisation and perform better than previous models.

##### 5.4.1.1.1 Shear band generation

The best diagram of how shear bands develop was demonstrated with the n=0.05 material model global model bend test as shown in Figure 5-84. No shear bands are observed from the compression region while the top region in tension develops shear bands at 0.89mm displacement. These localise at increasing displacement until a dominant shear band develops. The maximum strain is always at the top surface. Only the n=0.05 material model developed shear bands in the global model.
Using different material models shows a significant change in the distribution and intensity of strain as shown in Figure 5-85. Where increasing the strain-hardening coefficient, n from 0.05 to 0.2 the strain intensity at the same bending displacement of 0.81mm is halved from 0.16 to 0.08. Also, the strain has a larger area of distribution with a higher strain-hardening coefficient and does not go into the material depth.

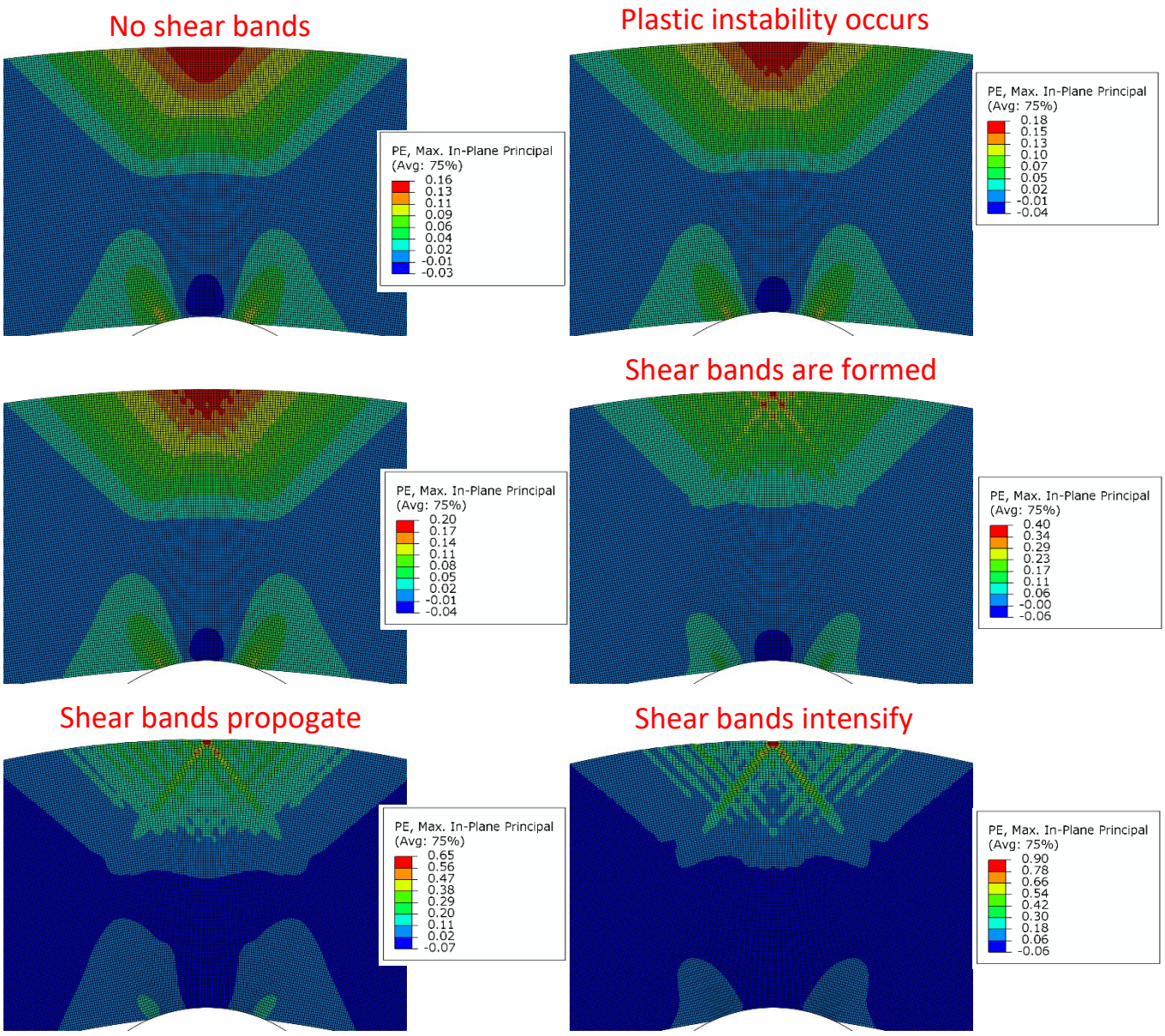


*Figure 5-84: Shear band development plane stress 2D, 3 point bending for n=0.05 material model. Top left, 0.81mm displacement, top right, 0.89mm displacement, middle left, 0.93mm displacement, middle right, 1.21mm displacement, bottom left, 1.41mm displacement, bottom right, 1.61mm displacement.*

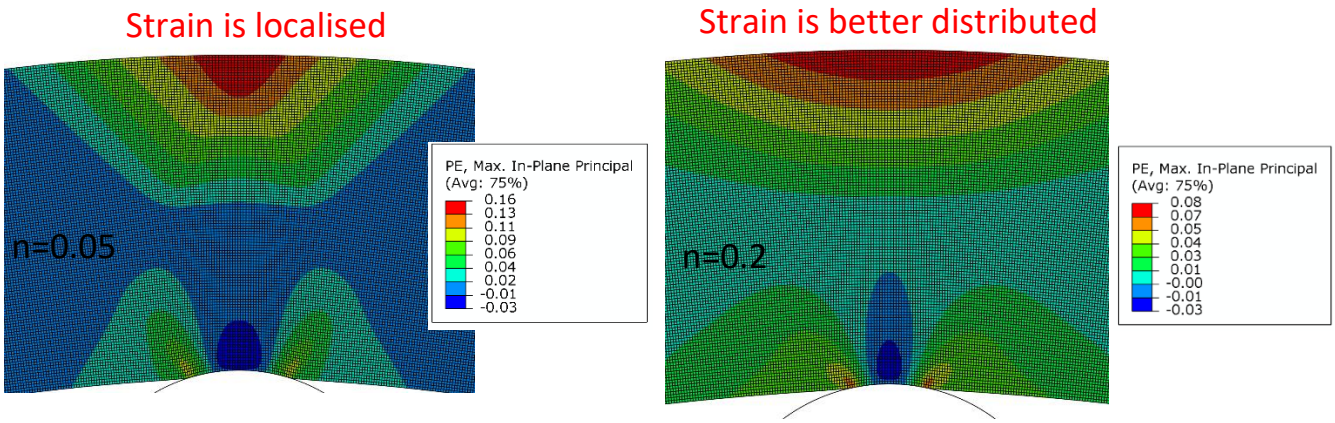


*Figure 5-85: Comparison of the strain location and intensity in the global model for different material models both at 0.81mm displacement left, n=0.05, right n=0.2*

As only the lowest material hardening model developed shear bands the first submodel was run with the mesh 5 times the density of the global model. This resulted in shear bands in all material models up to n=0.2.

### *5.4.1.2 Surface waviness results*

Using the methodology as described in section 3.9.1.3 a series of simulations were run with a surface waviness with the second submodel used to simplify the model. Results for varied periods and depth are shown here while using the same settings.

#### 5.4.1.2.1 Varied period

By varying the period strain is found to localise at different displacements as shown in Figure 5-86 where the final displacement before the plastic strain exceeds the material model's limit is shown. It is found the strain localises with smaller displacements with smaller periods.

Shear bands are not found to localise in all the models with vertical strain localisation becoming dominant in the 75µm period in Figure 5-86. This transitions to shear bands at 150µm period, with 100µm being a combination.

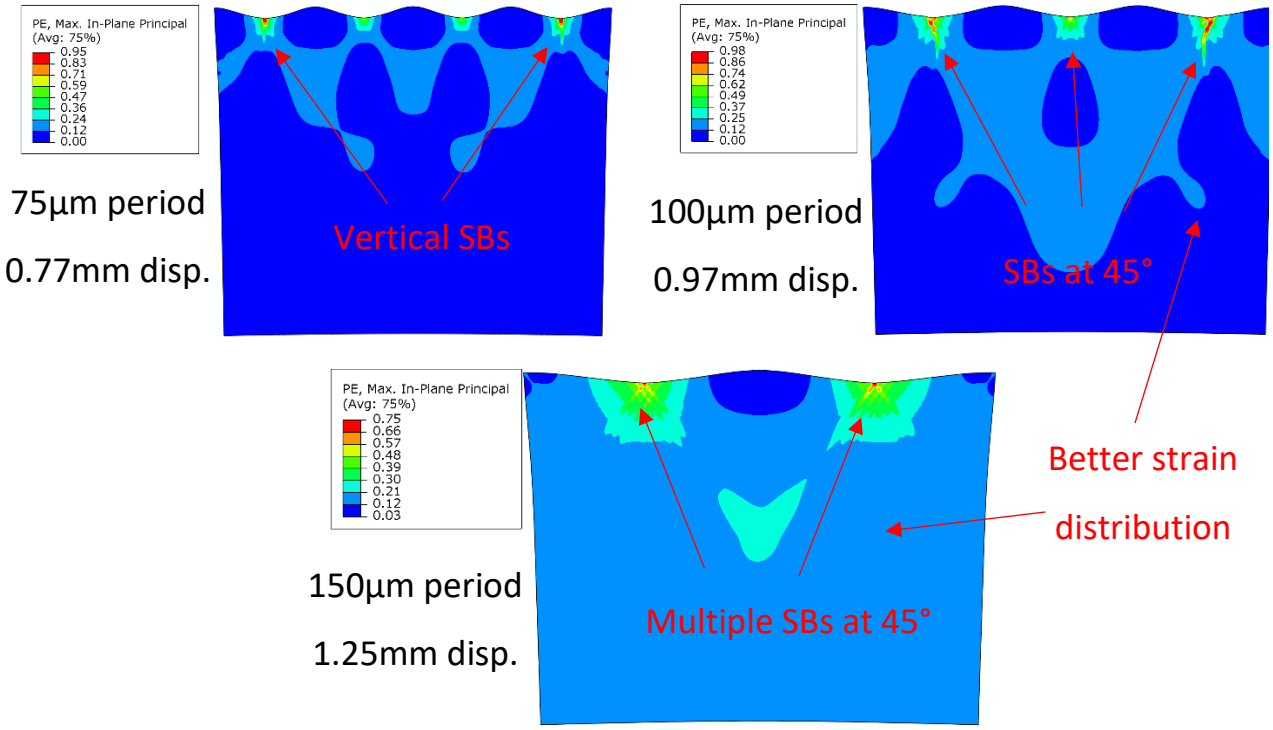


*Figure 5-86: FEM showing the maximum displacement while using the S960 material model, displaying the max in-plane principal plastic strain for the different periods, top left, 75µm period test at 0.77mm displacement, top right, 100µm period test at 0. 97mm displacement, bottom, 150µm period test at 1.25mm displacement.*

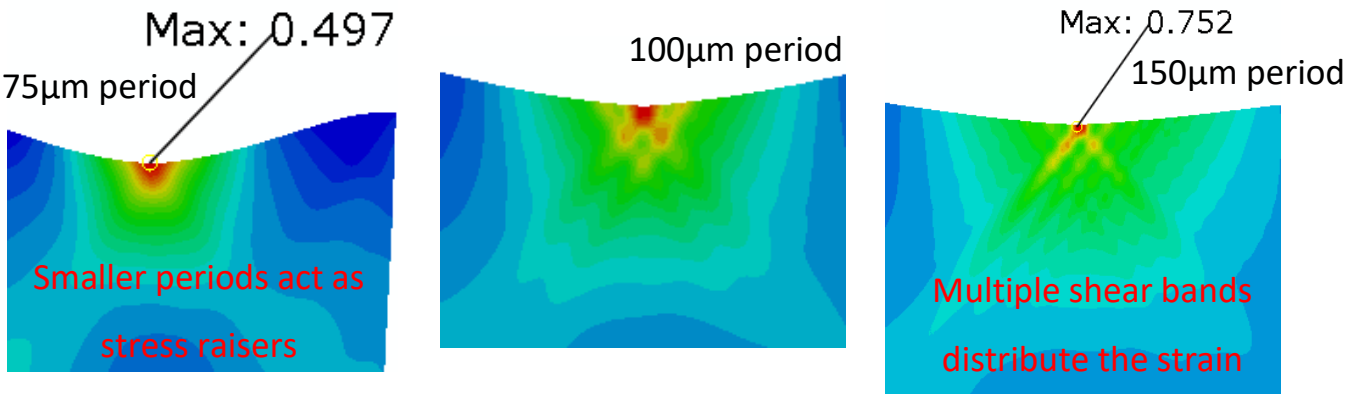


*Figure 5-87: notched region promoting failure shown before failure, left, 75µm period at 0.65mm displacement, middle, 100µm period at 0.89mm displacement, right, 150µm period at 1.21mm displacement*

As shown in Figure 5-87 shear bands are found in both the 100µm and 150µm periods. In the 100µm period model, the notch generates 4 shear bands, while the 150µm notches generate 8 shear bands.

#### 5.4.1.2.2 Varied depth

Another set of FEM varied the depths 5µm, 10µm and 20µm, all with a period of 100µm. These simulations were run and as shown in Figure 5-88. Shear bands are the dominant strain localisation mechanism for both 5µm and 10µm waviness depth models, while the 20µm model promotes vertical strain localisation. This is similar to being found with the 75µm period result found in Figure 5-86.

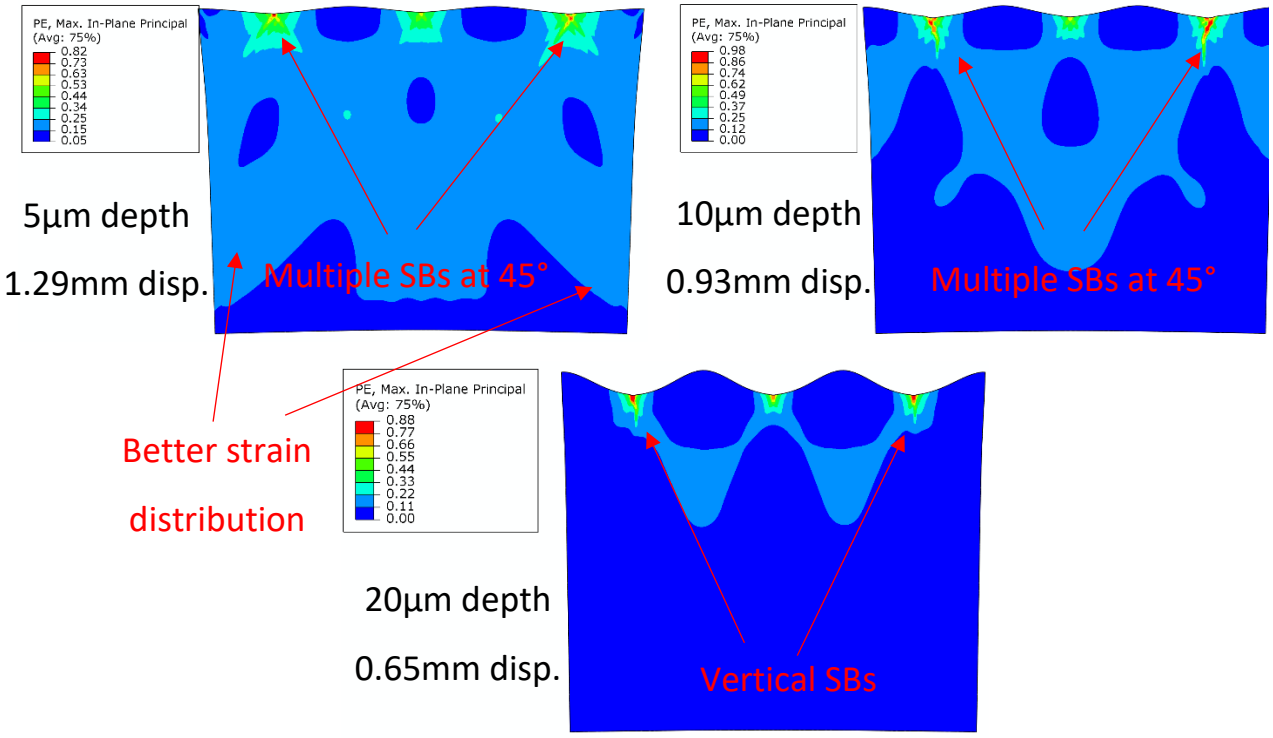


*Figure 5-88: FEM showing the maximum displacement while using the S960 material model, displaying the max in-plane principal plastic strain for the different depths, top left, 5µm depth at 1.29mm displacement, top right, 10µm depth at 0.93mm displacement, bottom, 20µm depth at 0.65mm displacement.*

To compare the effect of the strain localisation from varying the depth of the surface waves, the same displacement of 0.65mm as shown on the 20µm depth specimen in Figure 5-88 is shown for the 5µm and 10µm depth simulations in Figure 5-89. This shows the strain localises from only 22% for a 5µm depth waviness and increases to 35% and 88% for 10µm and 20µm depth waviness respectively.

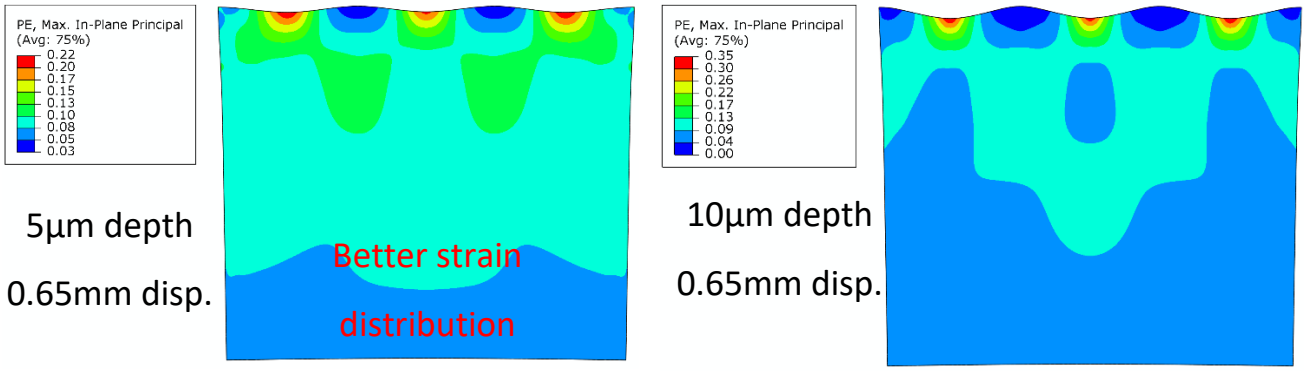


*Figure 5-89: 2D FEM at 0.65mm displacement for, left 5µm depth and right, 10µm depth*

By studying the plastic stain at the penultimate displacement step before exceeding the material model the shear bands can be observed in Figure 5-90. It is found with larger depths, fewer shear bands are promoted. For both 5µm and 10µm depth models 4 shear bands are observed with only 2 being found with the 20µm depth model.

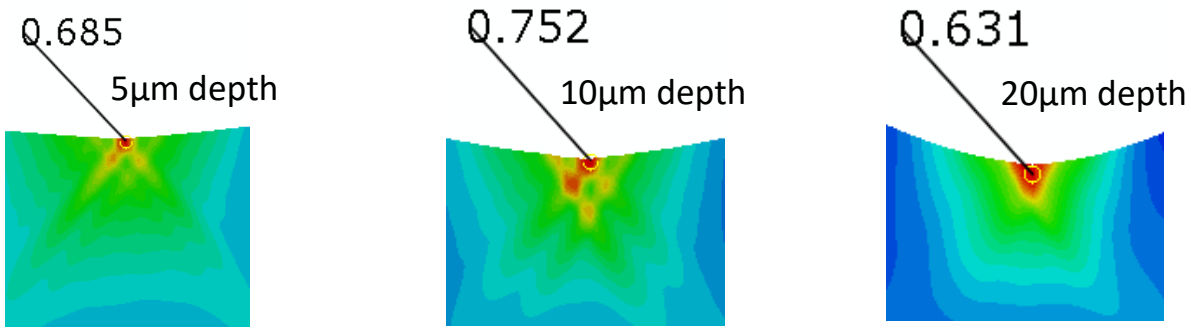


*Figure 5-90: 2D FEM at penultimate displacement step at 0.65mm displacement for, left 5µm depth at 1.25mm displacement, middle, 10µm depth at 0.93mm displacement and right, 20 µm depth at 0.61mm displacement*

## 5.5 Results summary

A wide range of testing has been demonstrated in this chapter using novel methodologies. The use of tensile testing has produced material model data used for FEM. The FEM demonstrates 3 point bending for plane stress. The formation of shear bands is explored with varied Hollomon strain-hardening model and the effect of surface waviness have been explored. This showed how the higher strain-hardening coefficient restricts the formation of shear bands. The surface waviness is found to increase the strain localisation particularly when the period is reduced to 75µm and depth is increased to 20µm.

This work has been complemented by the use of novel tooling and specimen geometry both in terms of the methodology of their production and their design. In the case of the new methodology developed the polished top surface specimens and the 0.6mm depth specimen. The other approach developed a new specimen geometry that demonstrates the advantages of the angled bend test specimen approach. The different depth specimens showed that hardness has an important role on the surfaces of the specimen.

Implementing the novel sample production allowed the comparison between a UHSS with different top surface properties in bend testing.

# 6 Analysis and discussion

## 6.1 Material properties

### 6.1.1 Macroscale tensile

#### *6.1.1.1 UHSS 14TG26*

The 14TG26 UHSS shows very low strain-hardening properties. When this is investigated the angle of the slope before fracture is n=0.03. This low strain-hardening property is linked with the localisation of strain [42] This material was used in a small number of applications and 17DF4/1 became the priority of the work. The only significant work using this material were the microscale tensile tests and the insitu bend tests using the Deben 5mm diameter tooling.

#### *6.1.1.2 UHSS 17DF4/1*

In section 5.1.1.2 the strain in the transverse direction tests is explored as the bend tests are orientated to strain the specimen in the TD plane in bending. The results showed that the 17DF4/1 sample has lower ductility than the 14TG26 sample. The strain-hardening coefficient in plasticity for this material is found to be higher than in 14TG26 at 0.044, leading to fracture. The strain-hardening coefficient increases to 0.1642 in Figure 5-9 between the true stress-strain point and the stress-strain at fracture. The effects of strain-hardening coefficients will be explored in the FEM and analysed further.

### 6.1.2 Microscale tensile

Micro tensile tests with 14TG26 material are found to have a significantly greater extension than found in Macroscale tensile testing, this was as expected due to the very short gauge length in respect to its width. This results in a significant region of the gauge length being in the necked region thus increasing the elongation by a factor of about 5. As shown in Figure 5-21, the failure in the microscale tensile test is observed at a shear band between a point of high strain and low strain. Shear bands have been observed by Ghadbeigi et al. using the same geometry with DP steels [73]. The strain found at the location of the failure is only at 150% strain, while the local high and low strain regions point to a strain gradient promoting the void. The shear strain is found at the same locations as the Exx strain. The shear band can be observed to rotate from an angle of 45° to the applied strain in image 2. of Figure 5-21 to being perpendicular in image 7. The author proposes that as the failure is being promoted from the subsurface the specimens top surface loses rigidity and is observed to deform the specimen to open the void with the Exx strain. The strain gradient suggests that the void formed near a grain boundary between a hard and soft microstructure located at the

surface or subsurface. This caused a failure at the grain boundary between these phases, similar failures have been reported by Alharbi et al. with failures occurring at a ferrite-ferrite interface[36]. The shear bands observed in the tensile test also show that the plastic strain found at a highly plastically deformed necked region can still have significant variations in the strain when analysed at high magnification. The position of the shear bands is not found to change until the rigidity of the specimen allows the shear bands to move shortly before failure. These are found to intensify similarly to the macroscale tensile tests where the necking occurs in regions observed to have higher strain at low displacements. As shown in Figure 5-13 the force drops from a peak load of 1100N to 700N at the 1.3mm displacement, showing the significant loss in rigidity in the specimen.

### 6.1.3 Hardness testing

The 17DF4/1 material produced by Tata Steel Europe was found to have a range of hardness properties through the thickness. It was found to be a variance of 20HV with microhardness and using nano hardness testing the variance increases to 70HV. This is due to both the nano hardness testing being able to be at 50µm from the depth while microhardness was at 150µm. Another key difference is that nanoindentations are localised on microstructures while microhardness tests bulk microstructures. When comparing these results to those obtained by Arola et al. the 17DF4/1 material hardness depth profile is similar to that found in the conventional steel they tested [27].

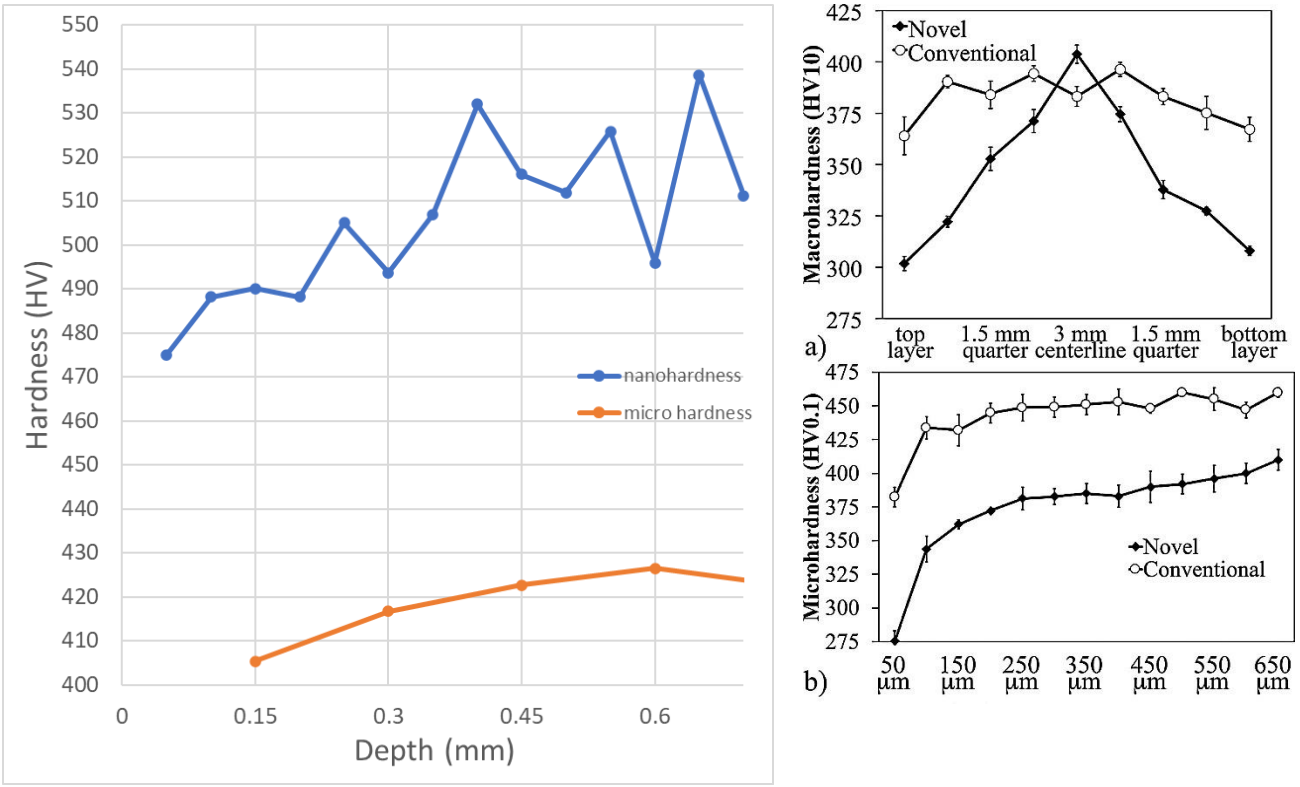


*Figure 6-1: Comparison of hardness testing results between left, 17DF4/1 and right a conventional and novel UHSS by Arola et al.* [27].

As shown in Figure 6-1 the hardness found in microhardness testing is comparable with the conventional UHSS found in literature where the subsurface exceeds 426HV while 17DF4/1 is found to be softer with a sub-surface hardness varying between 405HV and 426HV but were obtained with HV0.5 tests. This could be due to the annealing process applied to 17DF4/1 that has softened the bulk material properties. There were very low hardness measurements found at 50µm depth in both the novel and conventional steels in Arola et al.'s paper [27]. The microhardness was not measured at 50µm depth for 17DF4/1 material. If the nano hardness indentation at 50µm depth is considered, the hardness from those measurements is found to drop from 490HV to 475HV from 150µm to 50µm depth. From that, it can be inferred that the microhardness indentations at 50 µm depth may have been 15HV softer than at 150µm depth. This suggests a microhardness of around 390HV at 50 µm depth. This still well exceeds the 275HV in the novel steel but is close to the 380HV found in the conventional steel by Arola et al. [27]. As such the 17DF4/1 sample shows very similar material properties to the conventional steel.

Due to the size of the indents and the ASTM standards, the microhardness indents could not be positioned closer to the edge. HV0.5 was selected as it was the highest load indentation available for the indenter which could be observed with the objective lens. A smaller load would have increased the error, a higher magnification microscope in the hardness indenter would have allowed better analysis.

As shown in Figure 2-39 with a softer cladding added to the top and bottom 10% of the material the bendability of the material is improved with less strain concentration in bending [52].

## 6.2 Novel bend test methodology

### 6.2.1 Tooling

The development of tooling with a smaller diameter that complies with the ASTM tooling geometry has been designed, manufactured and tested in this project. The stiffness of gen 2 tooling is significantly higher than found in gen 1 tooling due to the change in bend test orientation from a tensile test pulling through the specimen to a compression test pressing the specimen. Replaceable press-fit tooling inserts manufactured from high-speed steel. These were demonstrated to reduce contact stresses on the tooling body. The high strength and wear resistance of HSS results in the tooling having an extended life span and can be exchanged with a new insert once wear or deformation is identified. The use of smaller specimen sizes, localising the deformation in a more localised area required a smaller FOV to observe the bend.

The stiffness was found to be a significant driver in the development of the second generation 2.5mm diameter tooling. The change to a compression test rather than tension test as used with the Deben 5mm diameter tooling allowed improved tooling 80 times stiffer than Deben's. This increase in stiffness is not found in the experimental results as the module stiffness itself is not very high as shown in the microscale tensile tests in section 5.1.2.1.1. A new module would be required to further increase stiffness as the tooling can be considered as stiff as reasonably possible.

### 6.2.2 Sample geometry

The specimen geometry is a compromise between the ASTM and BSI standard design and the limitations imposed by using the Deben test module. Due to the module only having 5KN of load the specimen geometry is a compromise to fulfil both these requirements. The width is limited to 2 times the thickness. While the thickness was 2.4mm to keep the bending load below 5KN. The more compact tooling with the centre of the support pins 12.8mm apart and 2.5mm diameter allowed the specimen to be shortened to 25mm. This allowed the specimen to be mounted in the 1.25 inch diameter mountings and so semi-automated batch production of specimens was used improving the flatness, consistency and lowering the cost of specimen production.

Future work could be used to replace the Deben 5KN horizontal bending and tensile test module with a higher load module. If this can increase to 10KN the specimen width can be increased to 4-5 times the thickness. This would bring it closer to the ASTM standards and increase the central triaxiality in bending. With this application, the same tooling design can be applied and allow for future bend test analysis.

The bend test specimens used in the polished surface tests were found to have different geometry due to their manufacturing process as shown in Table 5-2 and Table 5-3. This resulted in the force-displacement graphs being impacted with a lower force reported for the polished surface bend test in Figure 5-45 when compared to Figure 5-47. This also impacted the bending moment graphs as it relies on the bending force. The bending force depending on the specimen geometry has been calculated by the SSAB bend force calculation in Equation 35 [110]. The bending force in tons, $F_T$ is found from the specimen geometry of width, $w$ and thickness, $T$ and materials ultimate tensile strength, $\sigma_{UTS}$. The other terms are from the tooling geometry of width from the support centre to centre, $W_{cc}$, radius of support, $R_S$ and former, $R_F$. Since the tooling geometry was consistent between the tests, only the specimen geometry variations were considered.

$$F_T = \frac{w \times T^2 \times \sigma_{UTS}}{9800(W_{cc} - R_S - R_F)} \qquad \textit{Equation 35}$$

Using Equation 35 to account for variations in the width and thickness of the specimens caused the force-displacement and bending moment curves to converge.

## 6.3 Microscale bending

### 6.3.1 Shear band formation

As a means of analysing shear band formation, equations have been developed to quantify the expected initiation of shear bands. Using Equation 11 and considering that 4.5 is defined as the critical value for α to produce shear bands [41], Equation 11 has been rearranged to produce Equation 36.

$$\varepsilon_p = \frac{n}{1 - \alpha m} \qquad \textit{Equation 36}$$

Assuming that the sample is fully martensitic with a strain rate hardening coefficient; m=0.01, as recommended by Tata Steel Europe and found to be similar in literature [111], a critical plastic strain, $\varepsilon_{cp}$ can be calculated for a range of strain-hardening coefficients. It is shown that the critical plastic strain, $\varepsilon_{cp}$ increases linearly with increasing strain-hardening coefficients. The critical plastic strain values are sound to be very close to the strain-hardening coefficients due to the low value of m. The m value is known to delay the onset of necking and localisation of strain and is limited by the material in this instance [112].

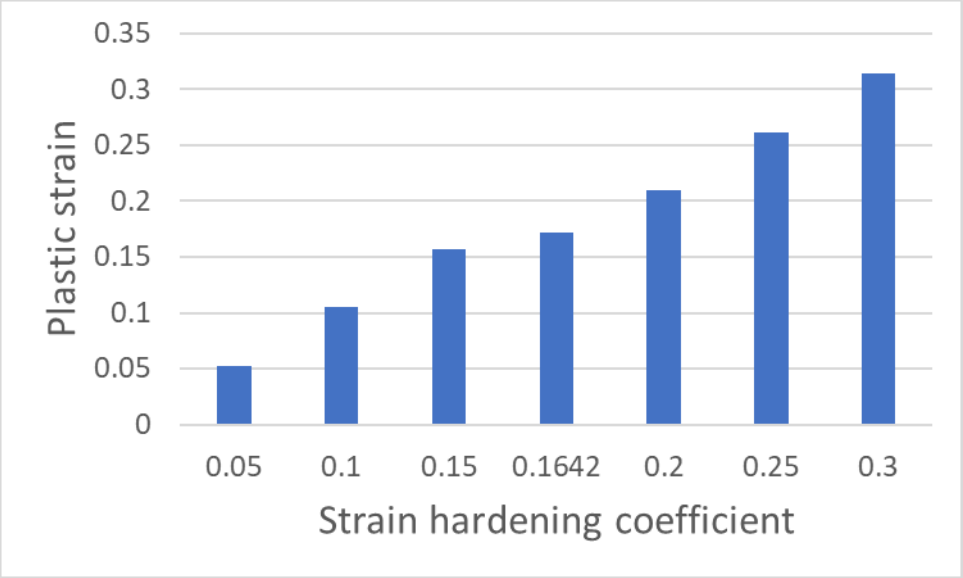


*Figure 6-2: critical plastic strain value for generating shear bands calculated from Equation 36,* [41].

It is important to consider this approximation has been developed for microscopic shear bands formed in the Equal-Channel Angular Pressing, ECAP process using a range of materials not including steel. Also, the critical value for α was found empirically from ECAP so could be different to that

process in bending or with UHSS undergoing plasticity. If an adjustment can be explored for bending a critical value for α in bending of UHSS and develop novelty.

### 6.3.2 Angled bend testing

Developing the new bend test geometry has enabled shear bands, surface waviness and damage to be observed initiating at the horizontal surface. The shear bands promoted are similar to those observed in standard bend tests with UHSS [14]. The use of high magnification SEM micrographs and DIC allow strain maps to be produced throughout the bend test. The UHSS 17DF4/1 has been found to have a softer top surface in the first 400µm of depth in particular as shown in  Error bars were applied with 2 standard deviations above and below the mean point. This results in a confidence margin of 95.4%.

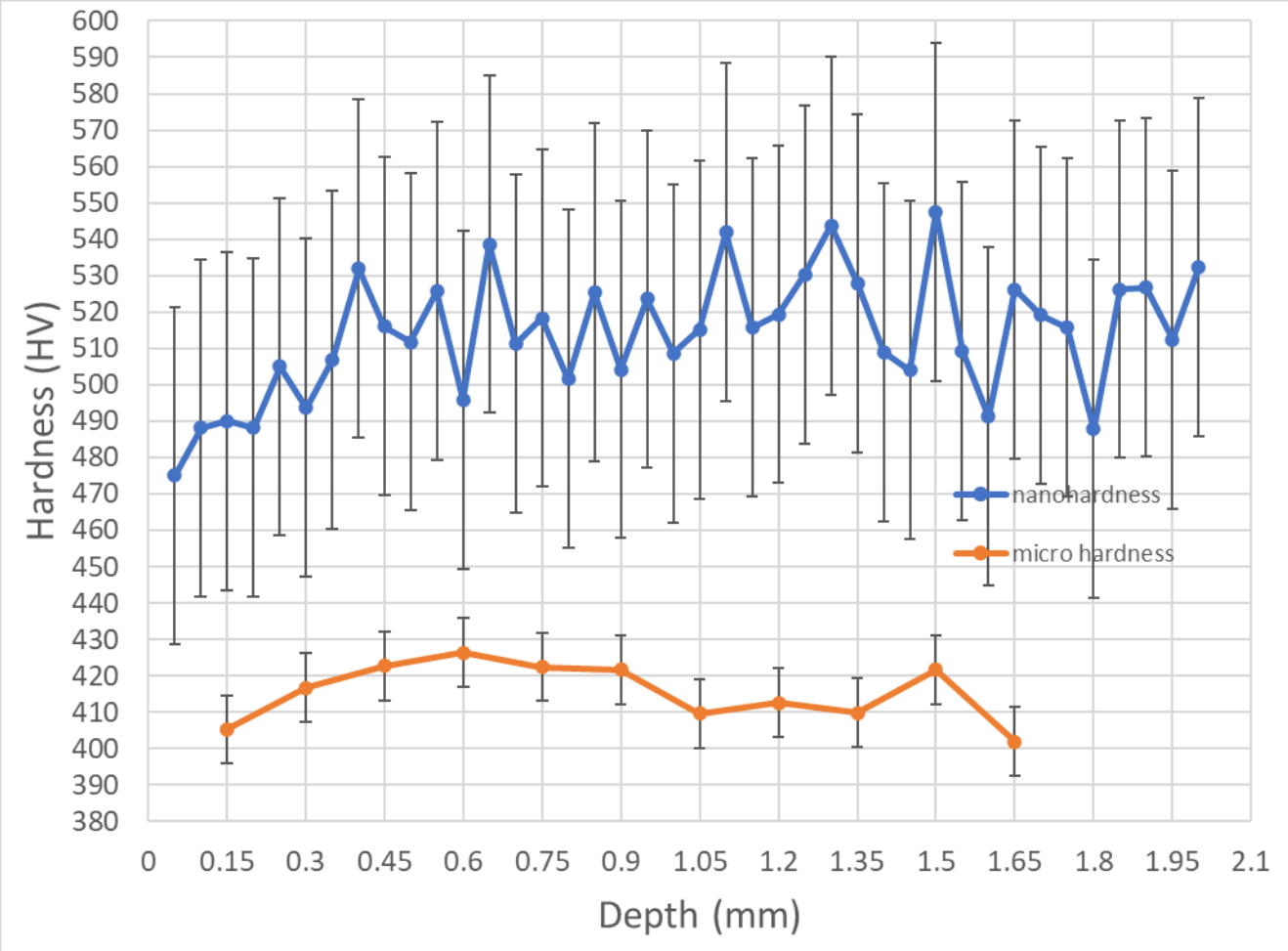


Figure 5-27. The deformation of the specimen can be defined into 4 stages in this test as shown in Figure 5-40, Figure 5-42 and Figure 5-44:

- Elastoplastic deformation of the specimen with no visible damage at small displacements.
- The evolution of shear bands in a bifurcated pattern at 45 degrees to the surface was observed in other experimental work [14]. At the surface, the shear bands microscopic ductile

tearing is found to have initiated a stable failure mechanism while constrained to the top surface.

- The damage propagates through the depth and the material begins to increase in hardness. This combined with the stress raiser of the notch generated by the plastic tearing intensifies the shear bands localising the damage into a sharp crack at 4mm of displacement in Figure 5-42. At the same displacement, the shear bands can be seen to intensify and promote the sharp crack to continue to grow.
- The sharp crack quickly propagates and promotes failure as shown in Figure 5-43. As the stress raiser of the sharp crack and higher hardness below the more ductile 400µm depth destabilises the failure mechanism causing a sudden failure.

The use of the angled bend test technique did cause some problems for the module, the author believes there to be 4 causes:

- The lack of stiffness in the 2.5mm diameter gen 1 tooling allowed a deflection causing a different loading scenario than the module was designed for.
- The centre cutaway section to produce the angled geometry in the specimen was too wide. This approached the location of the support pins in contact with the specimen legs. These contact points may have slipped into the angled region, but the author did not notice this occur. These are small specimens so this may have been missed due to the length of time to remove the specimen.
- The higher thickness further away from the base of the Deben horizontal bend test module would have had an increased moment on the module and may have caused eccentric loading.
- The module stiffness is not very high and has been used in a variety of work some of which it was never designed.

This causes the force-displacement, Figure 5-37 and bending moment angle curves, Figure 5-38, to be impacted and the increasing loads and moments from each test is a result of the force transducer undergoing plasticity. In test 1 in Figure 5-37 a double peak is found at 2.2mm and 6mm of displacement. The author proposes this test exceeded the punch displacement of tests 2 and 3 because it was a trial with no interruptions. The addition of interruptions adds a relaxation and loading cycle at each interruption and is where peak loads can often be found. This causes the standard tests with no interruptions to have higher elongation or punch displacement. In bending this has another significant effect where the strain localises in different regions and then the specimen starts to slide causing a second load peak as shown in Figure 4-13. This promotes a sliding

force; the bending moment calculation assumes frictionless contact. So, the maximum moment in test 1 in Figure 5-38 from the second peak load in Figure 5-37 is not representative of the moment to deform the specimen. This is further complicated by the anticlastic flow effectively increasing the thickness and making the assumption of a 3mm thick specimen incorrect. This might increase the moment through the bend test but would need further investigation.

When studying the initiation of damage in Figure 5-42 the bending load is found to drop as the damage is observed suggesting that in the use of angled bend test specimens the force-displacement curves represent a better identification of damage initiation than the bending moment.

The use of DIC can calculate the strain using the microstructure as a pattern does have too much error to accurately study elastic deformation [88]. Other techniques would need to be applied to further analyse the elastoplastic deformation before damage with smaller displacement intervals used to further lower the error.

As shown in Figure 4-63 the strain is localised due to plasticity whereas in a standard specimen a combination of high strain and triaxiality localises the location of damage producing a single crack. The damage observed appears to occur at 50% strain at the crack tips. This is a third of the strain at failure in micro tensile tests in section 5.1.2.3. The author suggests this is due to the crack causing a stress raiser promoting an extremely localised strain that the DIC cannot detect without the use of very high magnifications and image quality. Work by A. Ramazani et al. cannot be used as a comparison as they perform DIC on the mesoscale, observing cracks initiating at 6.9% strain [83]. This isn't suitable to compare to strain at crack initiation at the microscale. In tensile testing with DP steels, the martensite is found to crack between 14% to 8.6% strain when the microstructure is simulated [36]. This is only simulated and the microstructure is also composed of ferrite and martensite and the former is under higher strains than the martensite promoting failures in debonding and cracking of martensite [36].

### 6.3.3 Shear band analysis

Shear bands were analysed from bending of UHSS at a microscopic level of detail, two magnifications were used which were 200x and 1400x, these allowed different scales to observe the development of shear bands. The study of micro shear bands was performed with the 1400x images to provide the detail to observe the MSBs in the microstructures.

Whereas the lower 200x magnification was used to count shear bands, study the macroscale shear bands and how they develop.

#### *6.3.3.1 Microstructure size effect on micro shear bands*

During bending, micro shear bands were observed in larger microstructures. In Figure 6-3 the development of strain in a large microstructure relative to the others found this was measured as 8µmx 8µm. This can be seen to develop two micro shear bands within the microstructure with the first observed at 1mm displacement and the second at 1.4mm.

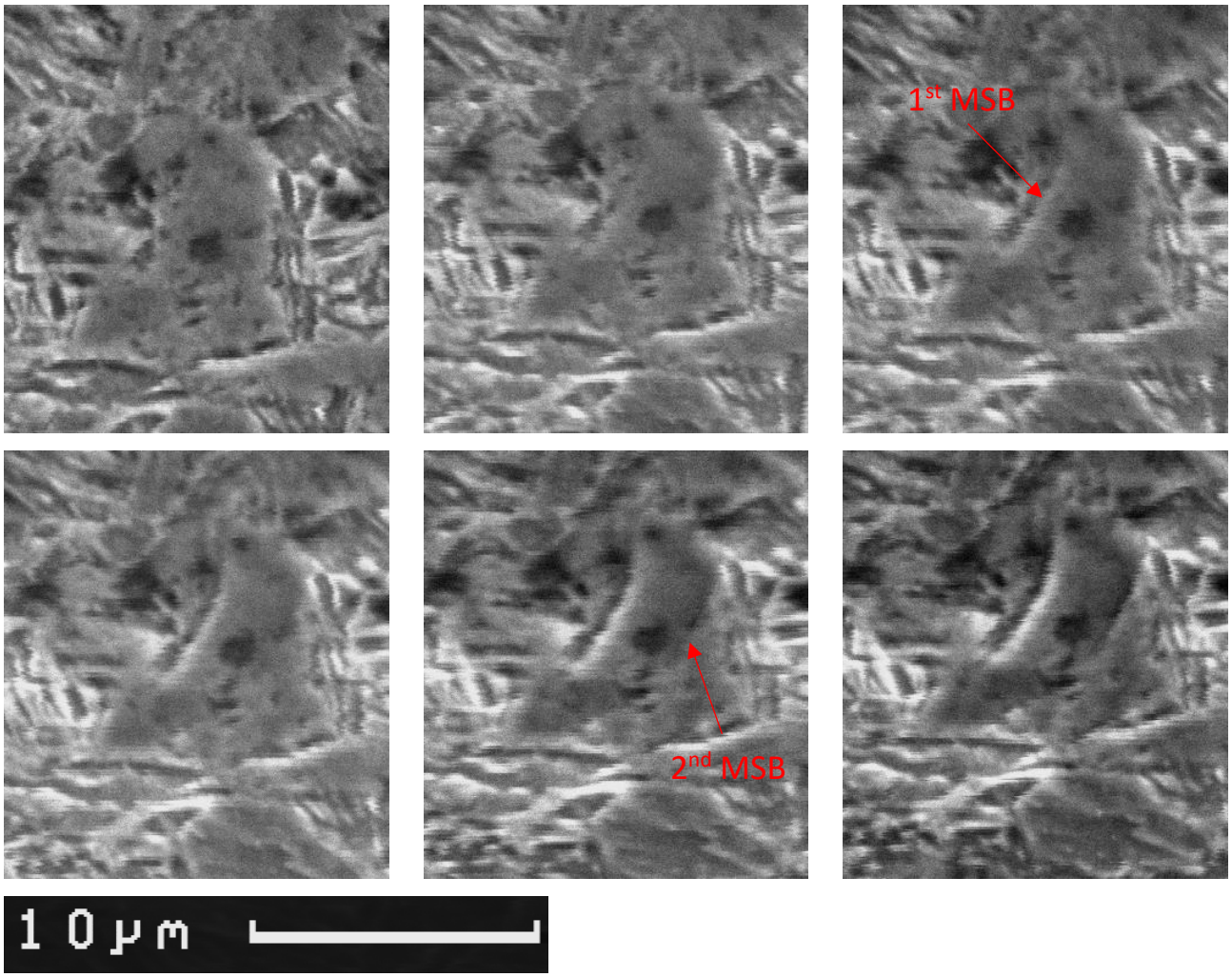


*Figure 6-3: polished top surface 1400x magnification large microstructure deformation, top left; 0mm displacement, top centre; 0.8mm displacement, top right; 1mm displacement, bottom left; 1.2mm displacement, bottom centre; 1.4mm displacement, bottom right; 1.6mm displacement*

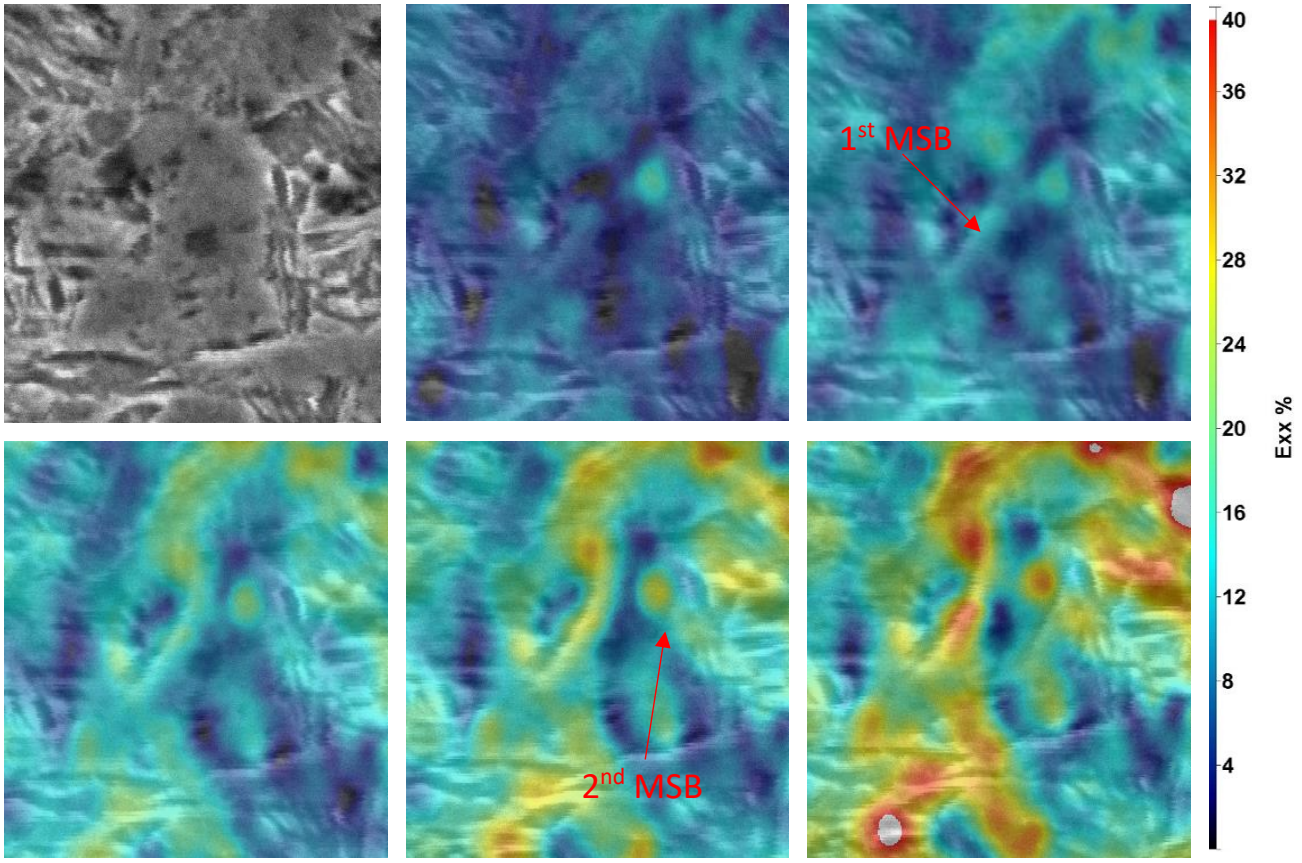


*Figure 6-4: polished top surface 1400x magnification large microstructure deformation with Exx strain map overlay, top left; 0mm displacement, top centre; 0.8mm displacement, top right; 1mm displacement, bottom left; 1.2mm displacement, bottom centre; 1.4mm displacement, bottom right; 1.6mm displacement.*

The majority of shear bands are observed to grow through grain boundaries with smaller microstructures as shown in Figure 6-3. Larger microstructures lower the strain required to promote micro shear bands as described by H. Luo et al [45]. Similar shear bands are observed in larger ferritic microstructures in DP steel in Figure 3-15. The shear bands are at angles of 57° and 62° in the microstructure. The first and second MSBs are found to have been promoted at Exx strains of 12% and 17% respectively and in the maximum shear strains of 8% and 10%. These strains are similar to the 20% strains that form shear bands in ferrite microstructures the tensile testing [73].

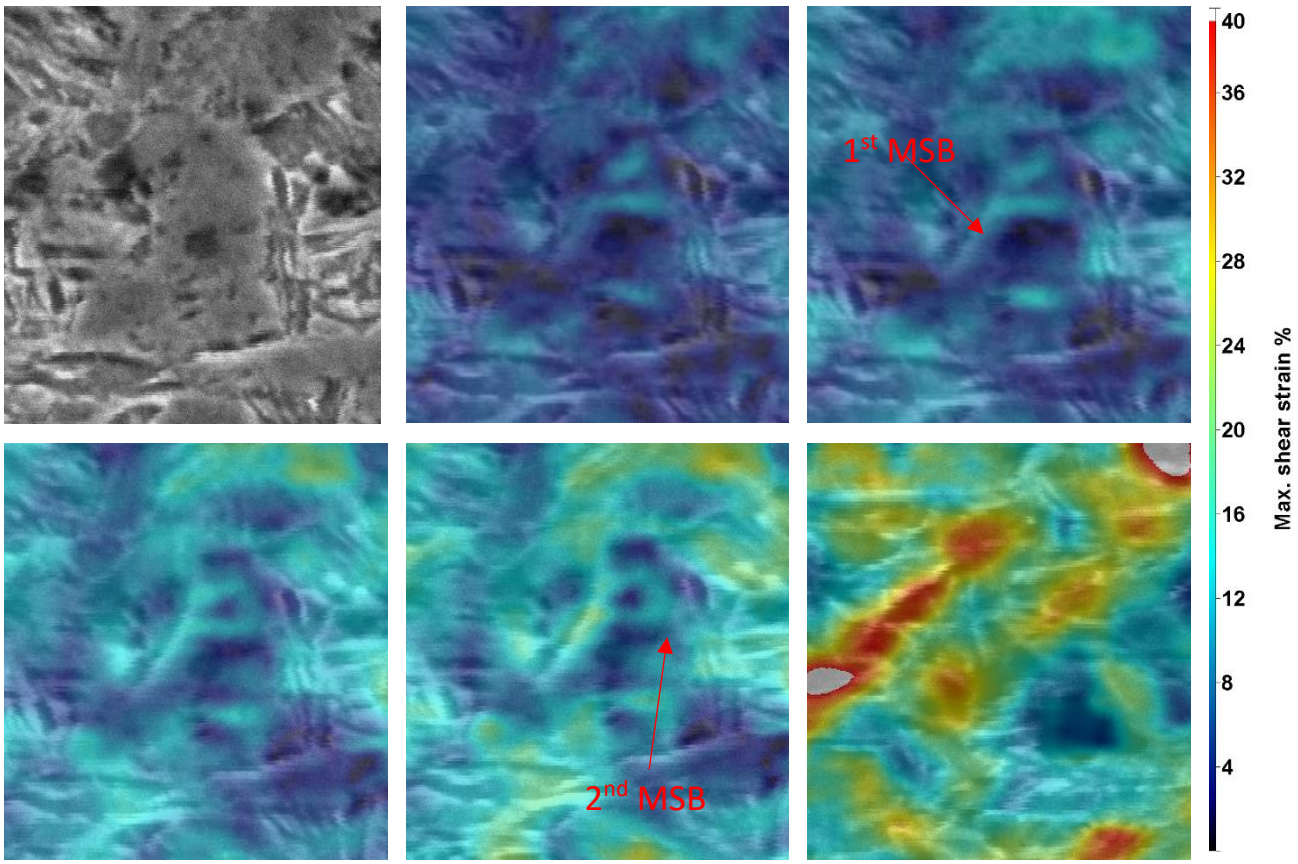


*Figure 6-5: polished top surface 1400x magnification large microstructure deformation with maximum shear strain map overlay, top left; 0mm displacement, top centre; 0.8mm displacement, top right; 1mm displacement, bottom left; 1.2mm displacement, bottom centre; 1.4mm displacement, bottom right; 1.6mm displacement.*

#### *6.3.3.2 Inclusions and voids*

Clean steel has been a priority to avoid inclusions, particularly those consisting of MnS which have been found to reduce bendability. The bending tests in sections 5.2.1.2.1 and 5.3.1.1 show inclusions and a void, the inclusion is found to resist compression in Exx while the void collapses as shown in Figure 5-59. While no failures were found to be located at inclusion the strain localisation due to them causes instability in the specimen by increasing strain locally. The local increase in strain promotes localised softening which then can intensify shear bands by providing a lower energy route. The void collapses and forms as the shear band travels towards the inclusion. At maximum displacement, the void is at 140% and 103% in Eyy and maximum shear strain respectively. The strain at the inclusion is at 270% and 170% in Eyy and maximum shear strain respectively. These far exceed the strain found at other points at the same depth, the highest was found to be 110% and 85% in Eyy and maximum shear strain respectively. Therefore it is expected shear bands will interact with inclusions and voids.

#### *6.3.3.3 Microstructure orientation*

The promotion of macroscale shear bands has been reported to be promoted by microstructural boundaries [45] and promoted along their length [52]. As found in Figure 5-32 and Figure 5-59, the

microstructures were elongated at 45° to the surface in two perpendicular lines that intersect. When bending is applied these features had a long line of grain boundaries to promote the macroscale shear band. This softened the microstructure in this region. This results in a peak high strain point where the shear bands intersect exceeding 150% strain in Figure 5-59. This is also going to locally raise triaxiality at this point further promoting premature failure.

### 6.3.4 Damage initiation

Damage was observed at the surface of the specimen in both the polished top surface specimen and in the 0.6mm depth specimen but have different damage initiation modes.

#### *6.3.4.1 Polished top surface damage initiation, 17DF4/1*

The top polished surface specimen as shown in Figure 6-6 has a shear plastic deformation initiate at the surface. This causes the surface to increase in roughness acting as a stress raiser in a similar process as shown in Figure 2-32 and described by H. Kaneko et al. [47]. Although it only deforms to the displacement processes [i] and [ii] from Figure 2-32, where only a surface step is produced in Figure 6-6.

Analysis with DIC at 0.8mm displacement in Figure 6-7 and Figure 6-8 finds that at the location of the surface shearing the strain before deformation is 20% and 15% in Exx and maximum shear strain respectively. The shearing is at an angle of 57° to the surface and acts in a mode 2 shear failure mode. These strain values are consistent with the strain found in ferrite microstructures in DP steel [73]. This plastic deformation is found to be stable and not lead to a shear band localising and is a similar damage mode as described by M. Kaupper et al. in Figure 2-30 [65]. At high magnification, this surface shearing with a ductile material creates a rough surface that acts as stress raisers but no damage is observed in the specimen beyond the ductile shearing.

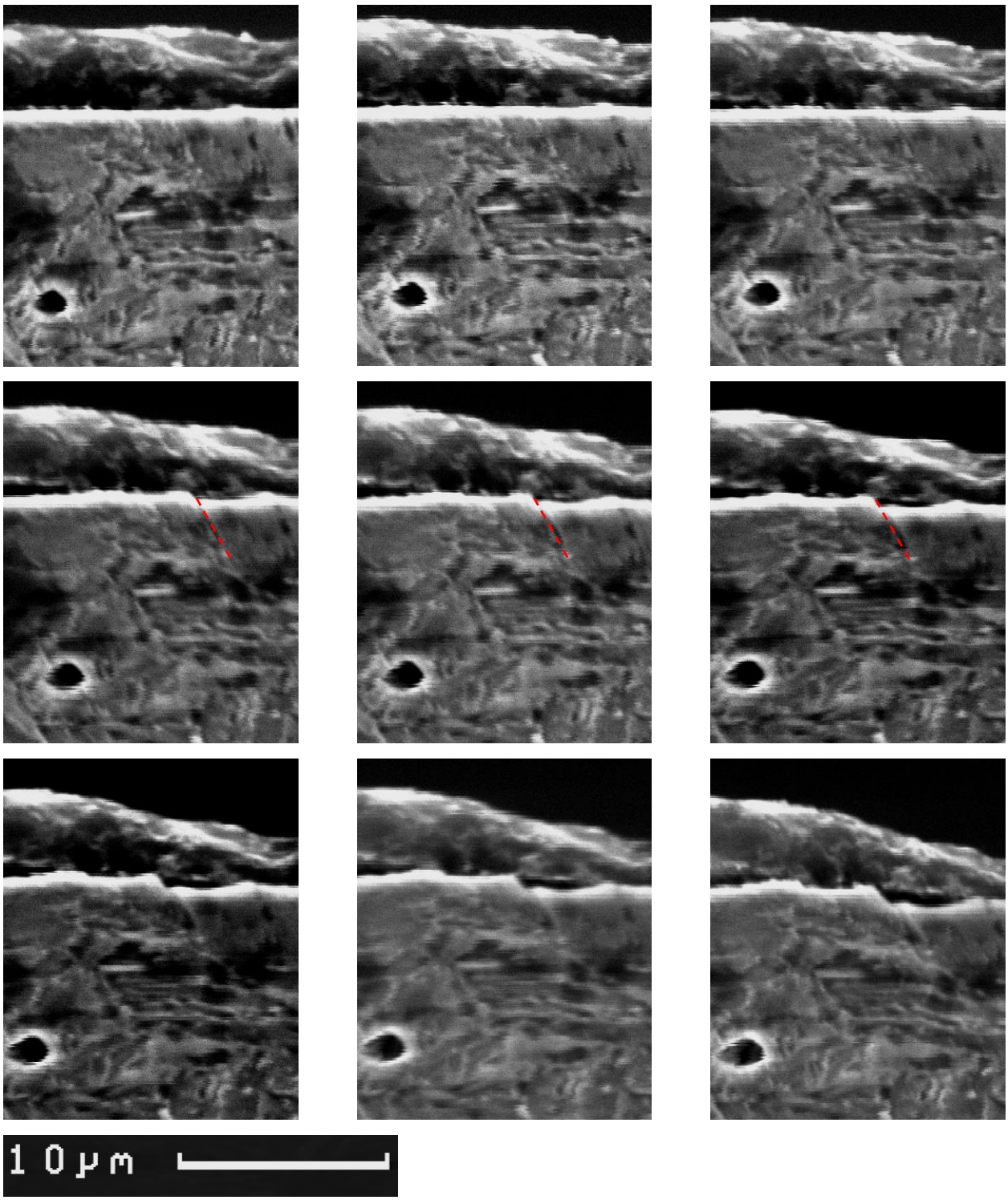


*Figure 6-6: Micrographs at 1400x of the polished top surface localised damage propagation, top left, no displacement, top centre, 0.6mm, top right 0.8mm, middle left 1.0mm, middle centre, 1.2mm, middle right, 1.4mm, bottom left 1.6mm, bottom centre, 1.8mm, bottom right, 2.2mm.*

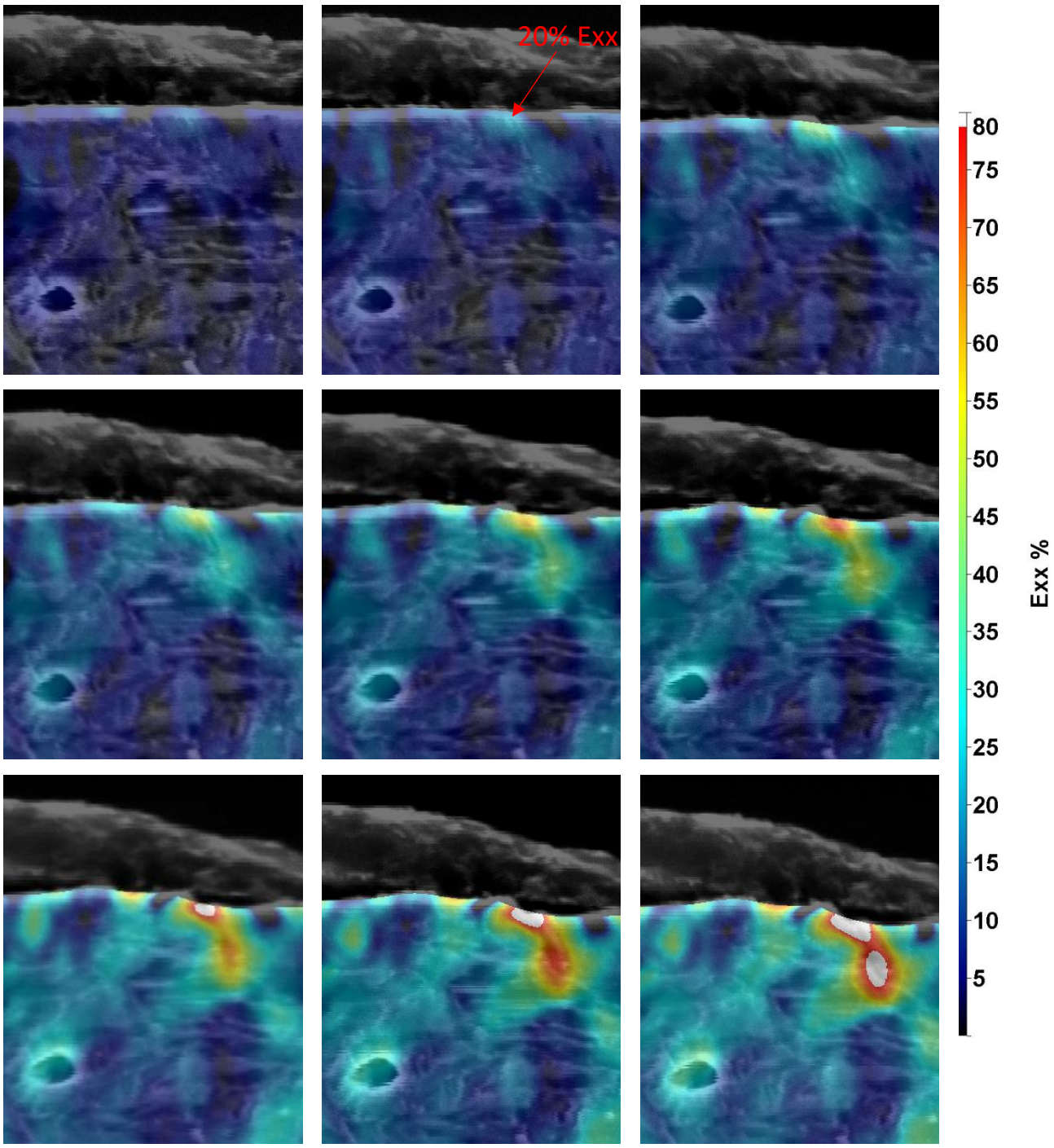


*Figure 6-7: Micrographs AT 1400x magnification of the polished top surface localised damage propagation with Exx strain map overlaid, top left, 0.6mm, top middle, 0.8mm, top right 1.0mm, middle left 1.2mm, middle centre, 1.4mm, middle right, 1.6mm, bottom left 1.8mm, bottom middle, 2.0mm, bottom right, 2.2mm.*

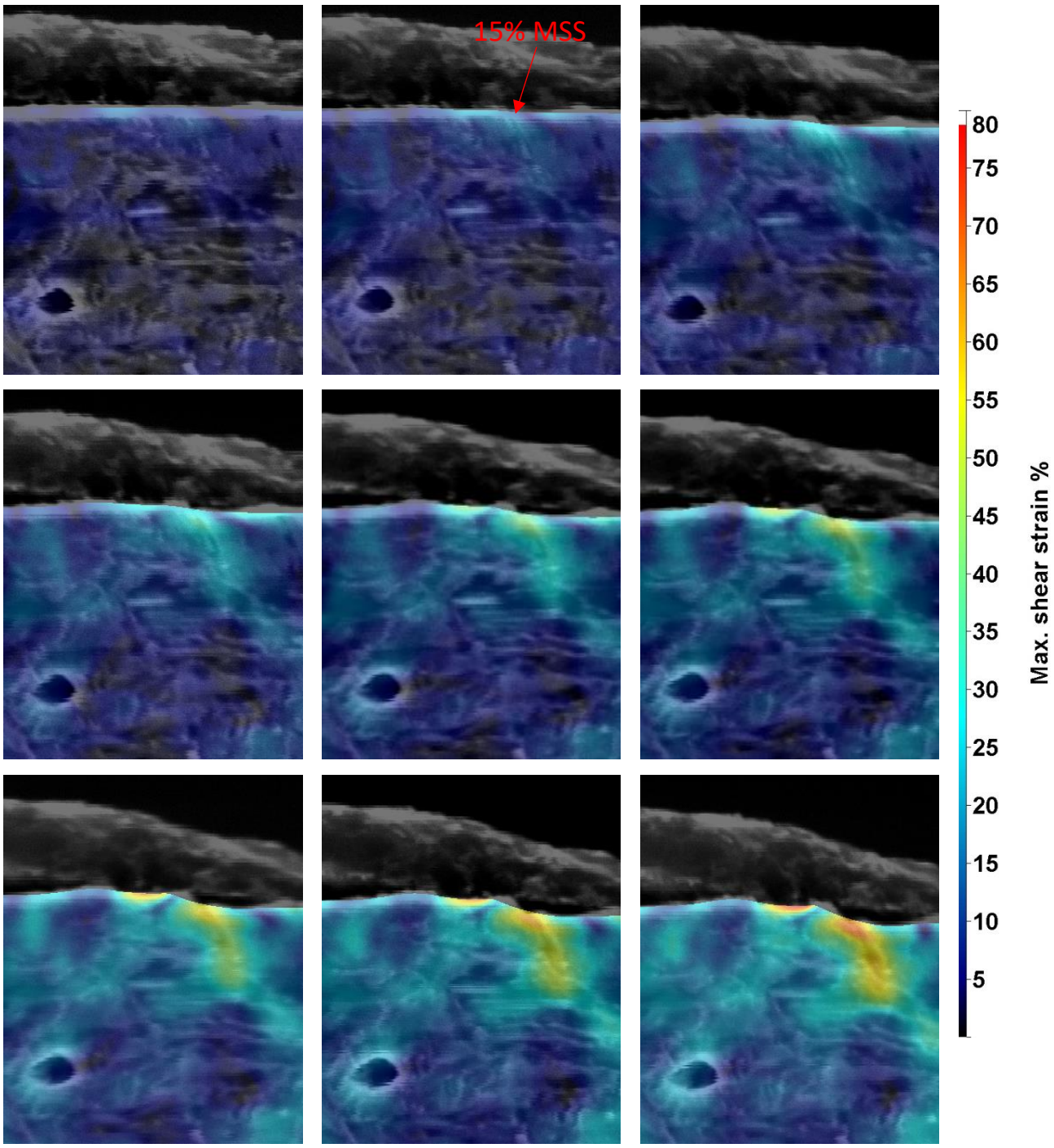


*Figure 6-8: Micrographs AT 1400x magnification of the polished top surface localised damage propagation with the maximum shear strain map overlaid, top left, 0.6mm, top middle, 0.8mm, top right 1.0mm, middle left 1.2mm, middle centre, 1.4mm, middle right, 1.6mm, bottom left 1.8mm, bottom middle, 2.0mm, bottom right, 2.2mm.*

### *6.3.4.2 0.6mm depth polished surface damage initiation, 17DF4/1*

Damage is observed at the top surface of the 0.6mm depth in Figure 6-9 in the 1400x magnification micrographs. This demonstrates the promotion of a shear band and propagates by fracturing a lathe. The shear band propagates at an angle of only 28° to the surface. This meets a lathe and appears to resist the strain, as such a ductile region generates a shear band just above the lathe and attempts to bypass the lathe and re-join the shear band on its original trajectory. The strain intensifies until the

lathe fractures and the shear band continues to propagate further into the material at the same angle as before the lathe resisted it.

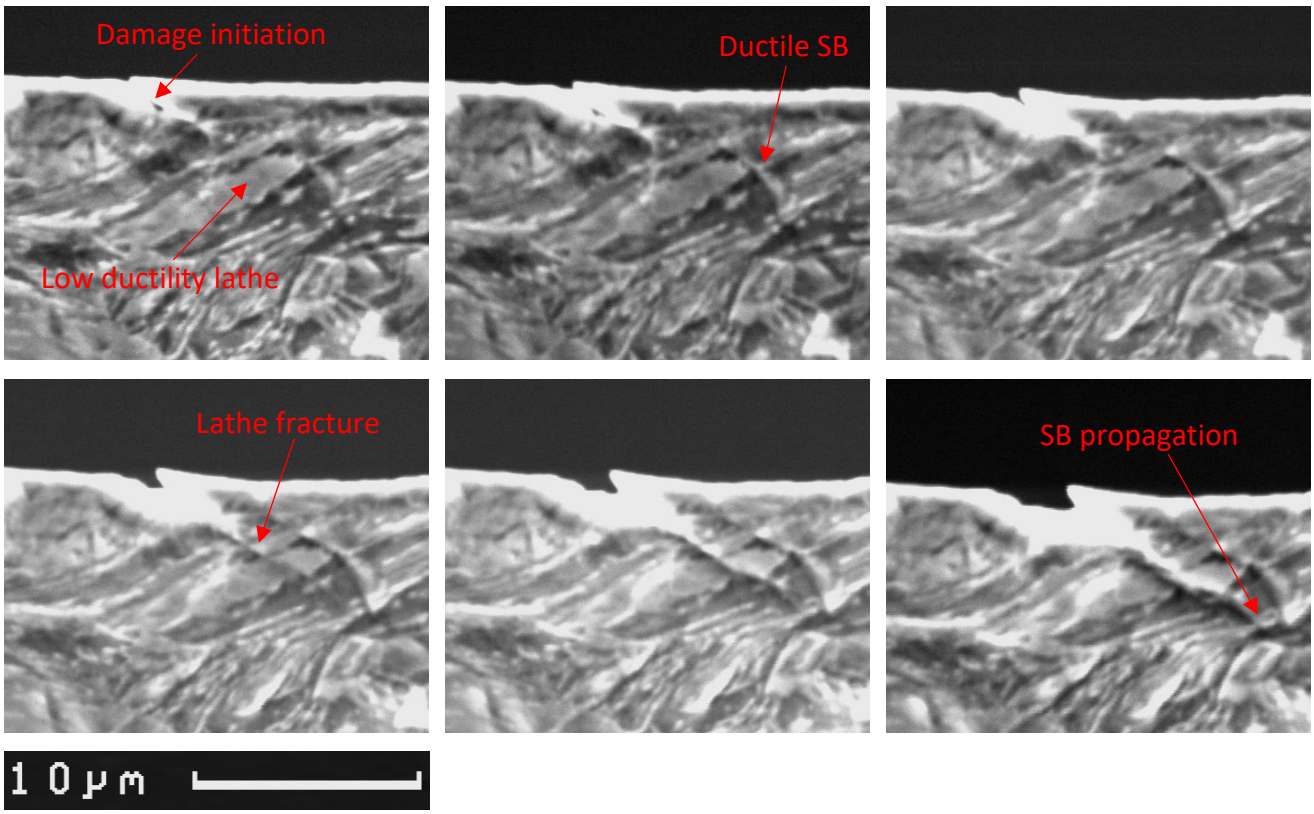


*Figure 6-9: Micrographs of the damage propagation at surface of the 0.6mm depth specimen, top left, 1.0mm, top middle, 1.2mm, top right 1.4mm, bottom left, 1.6mm, bottom middle, 1.8mm, bottom right, 2.0mm.*

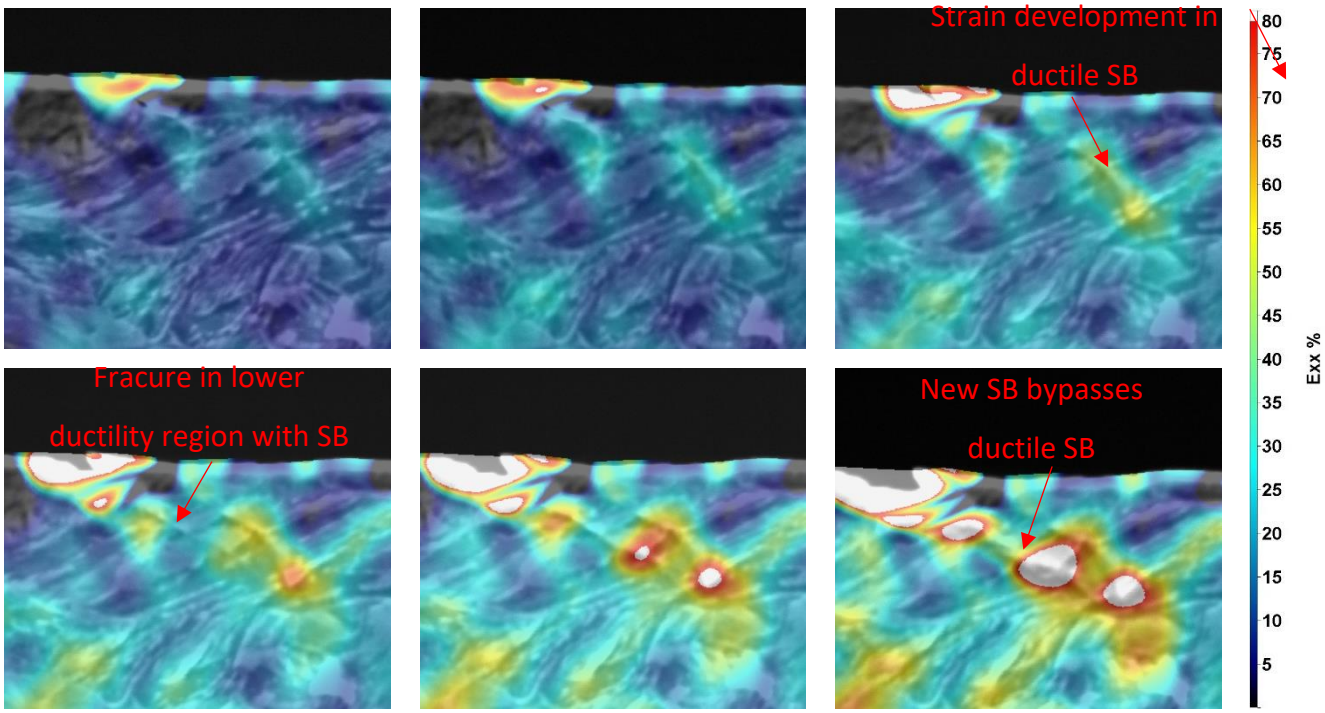


*Figure 6-10: DIC Micrographs showing the Exx of the damage propagation at surface of the 0.6mm depth specimen, top left, 1.0mm, top middle, 1.2mm, top right, 1.4mm, bottom left, 1.6mm, bottom middle, 1.8mm, bottom right, 2.0mm*

To better demonstrate the influence of the shear band localising in this region DIC on that area shows that strain localises near the surface. Generating a sharp crack that acts as a stress raiser in Figure 6-10. Strain is shown to increase near the lathe as the strain bypasses the lathe by going above it. As found in the last micrographs before failure at 1.4mm displacement in Figure 6-12, Exx strain is around 17% in the lathe while it is around 45% at the point the shear band is attempting to bypass the harder martensite lathe. The maximum shear strain in the lathe is 17% and the nearby shear band bypassing the lathe is at 35%. This shows that the shear strain plays a significant role in the failure with it matching the Exx strain in some locations. When the lathe cracks the shear band is only at an angle of 28° from the surface. The high shear strain indicates the failure is a shear mode 2 failure.

This damage mode is similar to those found by A. Ramazani and K. Alharbi et al. [36], [83] as shown in Figure 3-16, where the more ductile ferritic microstructure in the DP steel undergoes significant plasticity while until the martensite cracks.

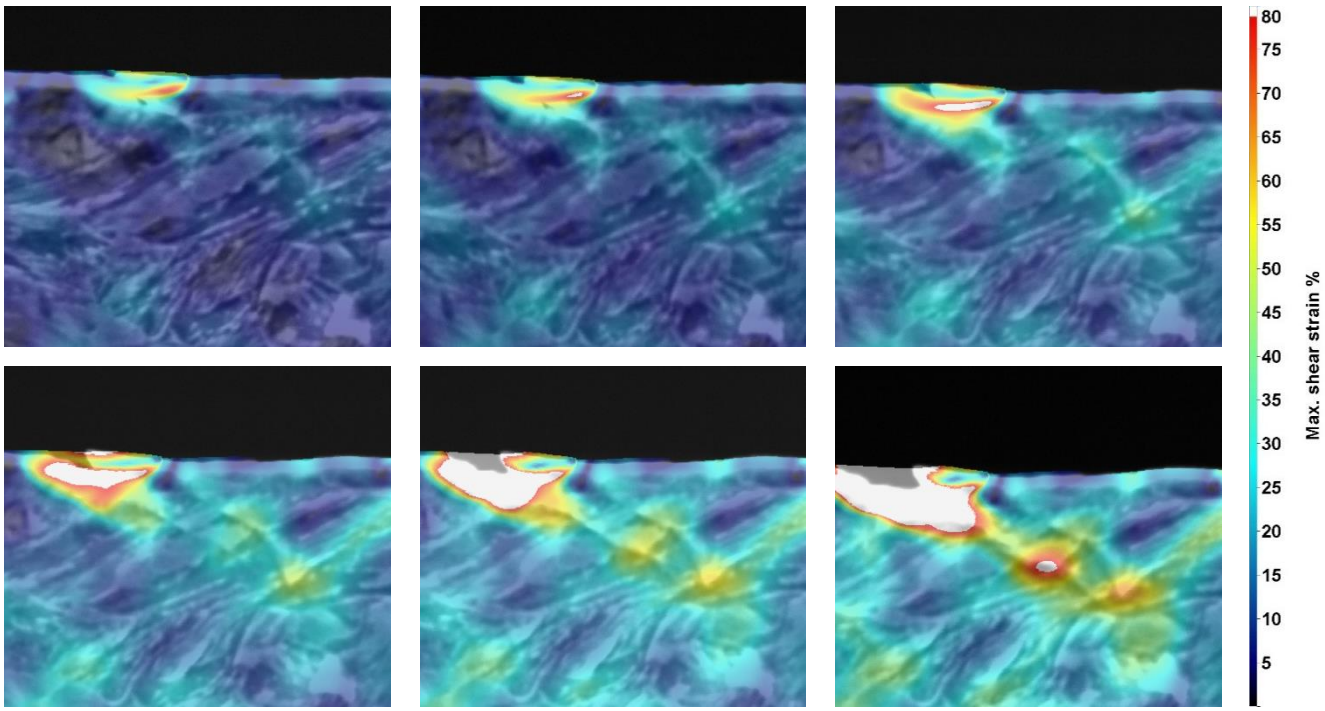


*Figure 6-11: DIC Micrographs showing the maximum shear strain of the damage propagation at surface of the 0.6mm depth specimen, top left, 1.0mm, top middle, 1.2mm, top right 1.4mm, bottom left, 1.6mm, bottom middle, 1.8mm, bottom right, 2.0mm*

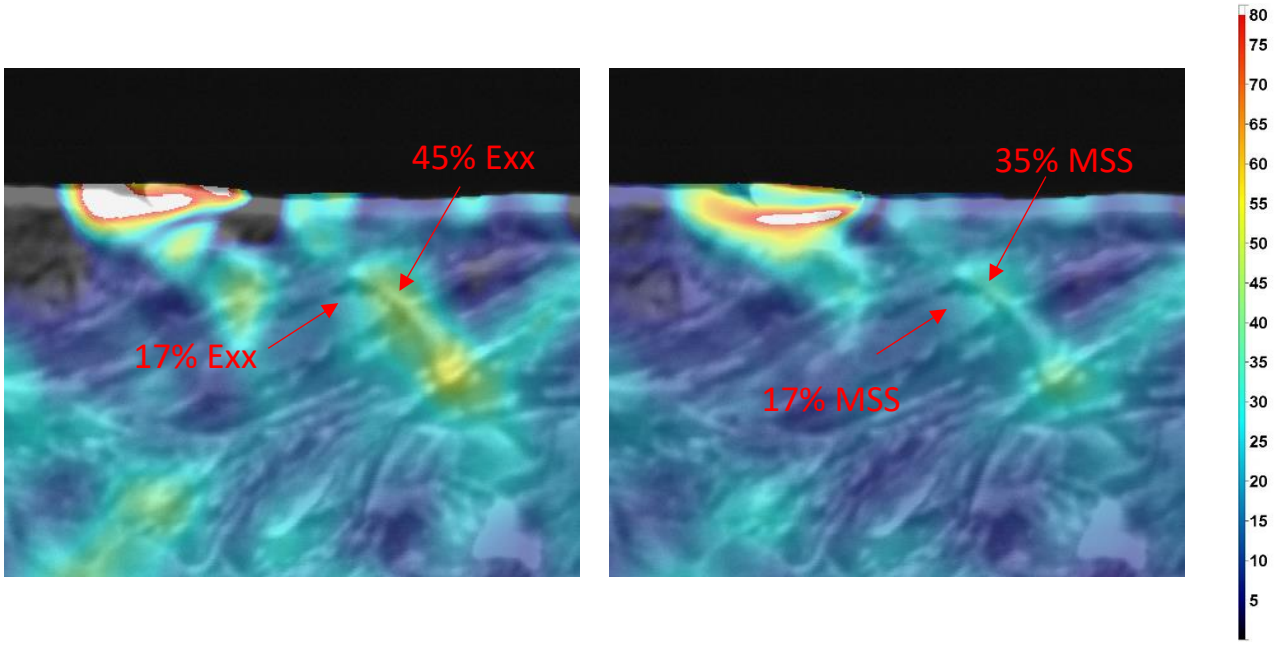


*Figure 6-12: Strain at 1.4mm displacement marked up with the strain before failure Left; Exx, right; maximum shear strain (MSS).*

These figures demonstrate the limitations of martensite in the bending of UHSS. Some authors have sought to change the surface microstructures from martensite to more ductile microstructures of bainite or ferrite [26], [43].

#### *6.3.4.3 Polished surface strain depth analysis*

In Figure 5-77 the average strain is found to be consistent along the depth for both specimens. This is because the bending force is promoting these strains to which the material has enough ductility to bend with varying amounts of success. Whereas in Figure 5-83 the increased strain localisation in the 0.6mm depth specimen at the surface where the fractures have occurred is higher than the plastic deformation found in the polished top surface. The strain is also found to be further localised in the subsurface for the 0.6mm depth specimen. This demonstrates poor bendability as these localised strains will promote plastic instability. The softer surface of the material seems to result in a more homogenous strain distribution. The textural effects of hot rolling could also be impacting the crystallographic orientation and so a more random texture should be expected at 0.6mm depth. The author considers that the lower ductility found at 0.6mm depth results in the fractures. These have been shown to produce sharp cracks which act as stress raisers. This causes instability and inhomogeneous strain in the specimen which produces poor bendability.

### 6.3.5 2D plane stress FEM analysis

The 2D plane stress simulations were selected as these should be representative of the results observed in the plane stress state observed at the surface of the specimen in the insitu bend tests. As described in 5.4.1.1.1 with low strain rate hardening models shear bands are observed in plane stress

in bending. It was also found that with smaller mesh sizing that the shear bands became prevalent in higher strain rate hardening models. It has been found by S. Wen et al. that smaller mesh sizing promotes the development of shear bands in FEM [14].

The modelling results show shear bands in Figure 6-13 demonstrate that with increasing strain-hardening coefficient the shear bands move further from the centre.

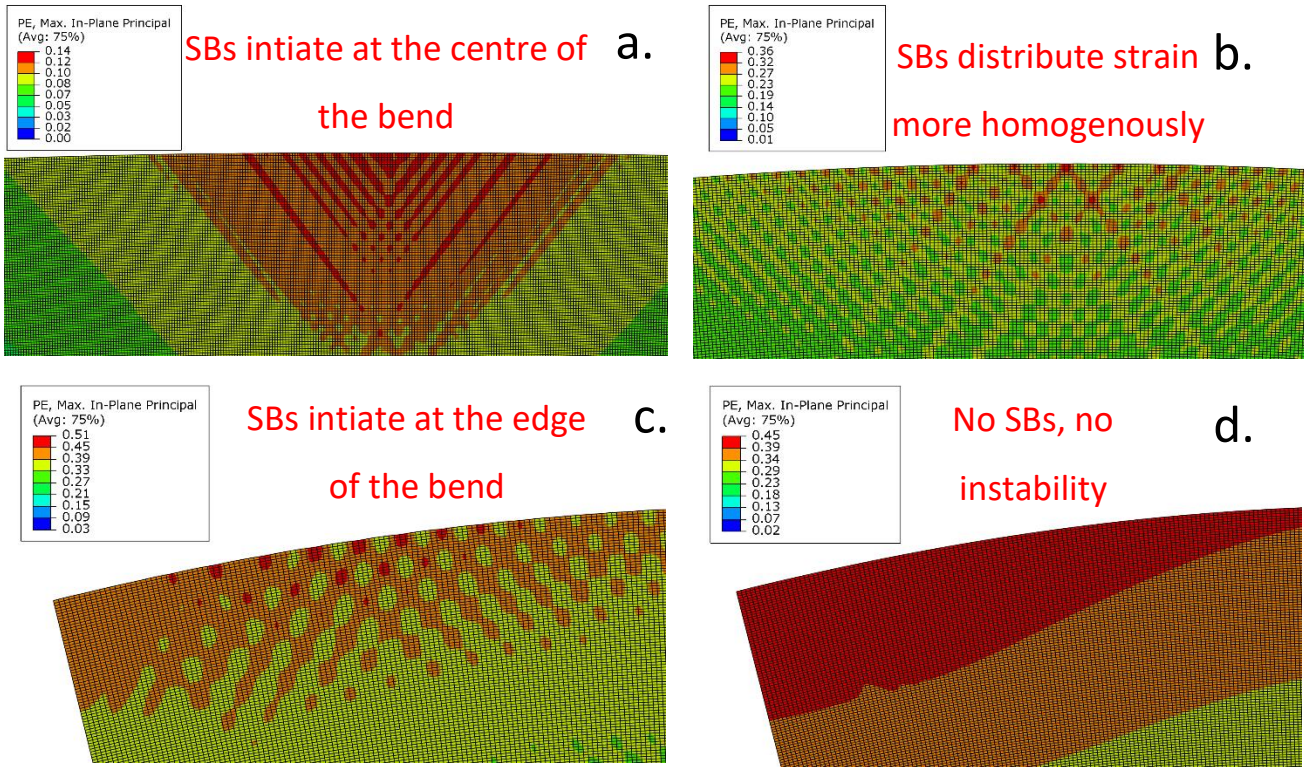


*Figure 6-13: images used to count shear bands from the first submodels. a., n=0.05 at 0.65mm displacement, b., n=0.1 at 2.33 displacement, c., 17DF4/1 at 4.01mm displacement and d., n=0.2 at 4.01mm displacement.*

Using the images extracted from Abaqus in Figure 6-13, the shear bands were counted, and the distance was measured from the unstrained length. This makes these values comparable with the results from Figure 5-79. As shown in Table 6-1 the global model only produces shear bands for the lowest material hardening coefficient of n=0.05. Even then the shear band spacing is found to be large at 72µm compared to anything found experimentally.

| | Global model shear band count | | |
|---|---|---|---|
| Mat. Model | No. shear bands | Length (µm) | Shear band spacing (µm) |
| n=0.05 | 21 | 1520 | 72.38095 |
| n=0.1 | 0 | | |
| 17DF4/1 | 0 | | |
| n=0.2 | 0 | | |

*Table 6-1: Global model shear band count spacing analysis, number of shear bands, length over which the shear bands were counted and average shear band spacing.*

When the first submodel is used the shear bands become visible as shown in Figure 6-13. These were counted by the author and the shear band spacing was similar to those found experimentally in Figure 5-79. For this reason, a second submodel was considered unnecessary as the first submodel results were close to those found experimentally.

| | First submodel shear band count | | | |
|---|---|---|---|---|
| Mat. model | Displacement (mm) | No. shear bands | Length (μm) | Shear band spacing (μm) |
| n=0.05 | 0.61 | 24 | 606.64 | 25.28 |
| n=0.1 | 1.95 | 46 | 574.78 | 12.50 |
| 17DF4/1 | 0.25 | 17 | 375.15 | 22.07 |
| 17DF4/1 | 2.93 | 28 | 466.05 | 16.64 |
| n=0.2 | | 0 | | |

*Table 6-2: first submodel shear band count spacing analysis, displacement shear bands are observed, number of shear bands, length over which the shear bands were counted and average shear band spacing.*

To better understand why shear bands are formed. An analysis of the strain when the shear bands were produced was developed by studying the FEM results. These strains at shear band initiation in Table 6-3 are found to be double those predicted with Equation 36 in Figure 6-2, suggesting that the α value is not calibrated for FEM bending.

| | First submodel shear band strain analysis | |
|---|---|---|
| Mat. model | Displacement (mm) | Maximum strain at shear band initiation |
| n=0.05 | 0.61 | 0.111 |
| n=0.1 | 1.95 | 0.228 |
| 17DF4/1 | 0.25 | 0.0268 |
| 17DF4/1 | 2.93 | 0.364 |
| n=0.2 | | |

*Table 6-3: first submodel strain when producing shear bands.*

Most material models only have a single strain, after which shear bands are produced and remain. The material model for 17DF4/1 did not conform to this and as shown in Figure 6-14 the shear bands are found to propagate at 0.25mm displacement then disappear at higher displacements.
When the region with shear bands was analysed it was found it had a strain value of between 0.0167 and 0.0235. Then they disappear when the strain exceeds 0.0235 when using this material model. This is because of the use of 2 material models and a fracture point, and the gradient of the stress-strain curves at these points as shown in Figure 6-15. The material then has no shear bands until the stress-strain curve gradient is low enough on the stress-strain graph at higher displacements as

shown in Figure 6-16. Studying the point at which the material model allows a shear band to localise the gradient at each of these points was found in Table 6-4. This shows a gradient of less than 1000MPa/strain can initialise shear bands. Other analyses of the n=0.2 material model find it has a gradient of 585MPa/strain at its final data point and yet this doesn't show significant signs of shear bands. The author considers that the stress-strain gradient has an effect as a sudden drop as found in the material model for 17DF4/1 promotes a sudden strong initialisation of shear bands. This has the biggest effect early on in the bend test as the strain is focused on the centre of the specimen. This then changes as the single central point of high strain becomes 2 points of contact in bending when the specimen transfers into a quasi 4 point bend sharing the deformation energy in 2 points on the specimen. In this process, it can resist the instability of shear bands by having already deformed into a more stable deformation process. This quasi 4 point bending process requires more of the surface to become unstable thus needing a lower stress-strain gradient that is material based.

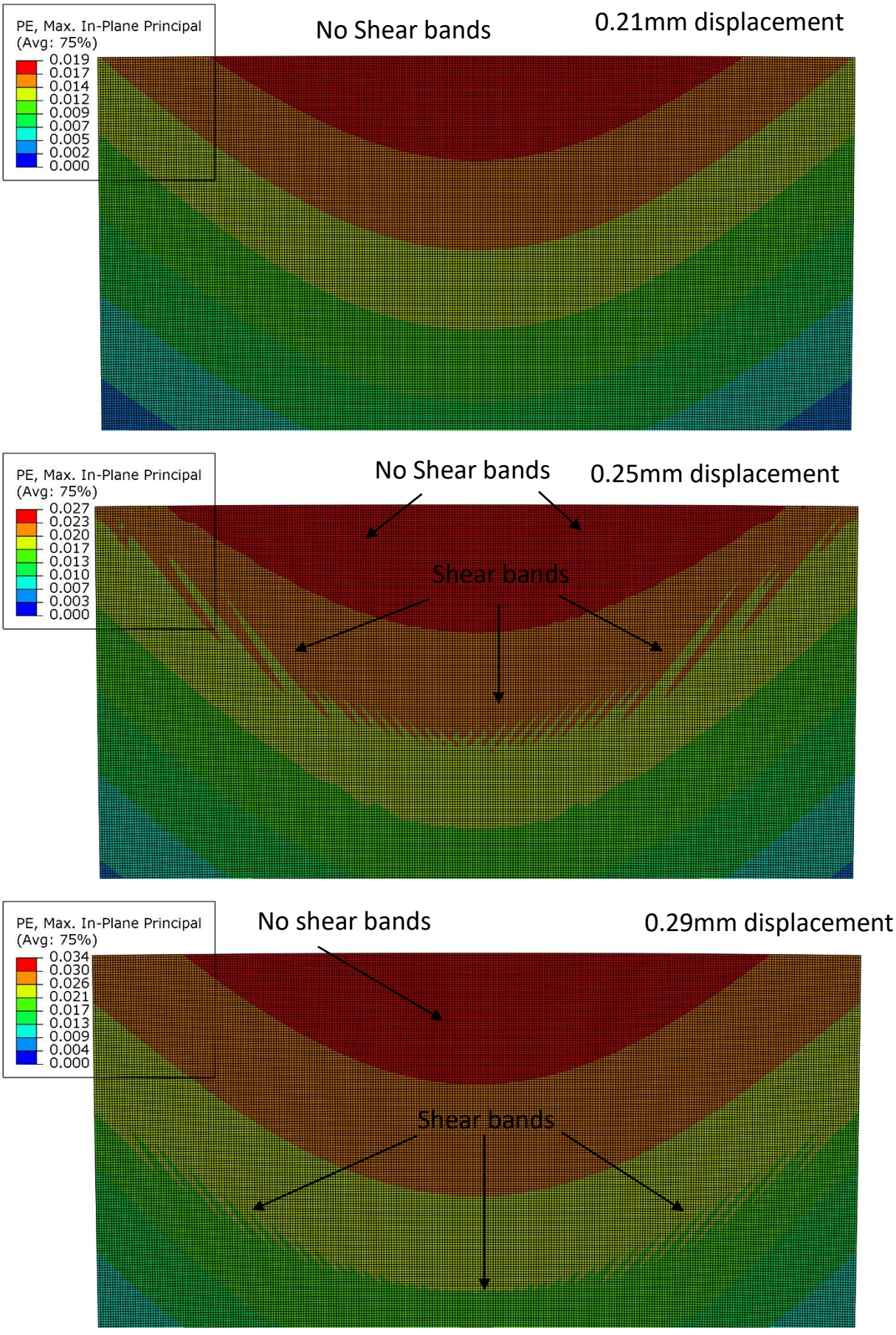


*Figure 6-14: Shear band development in the 17DF4/1 material*

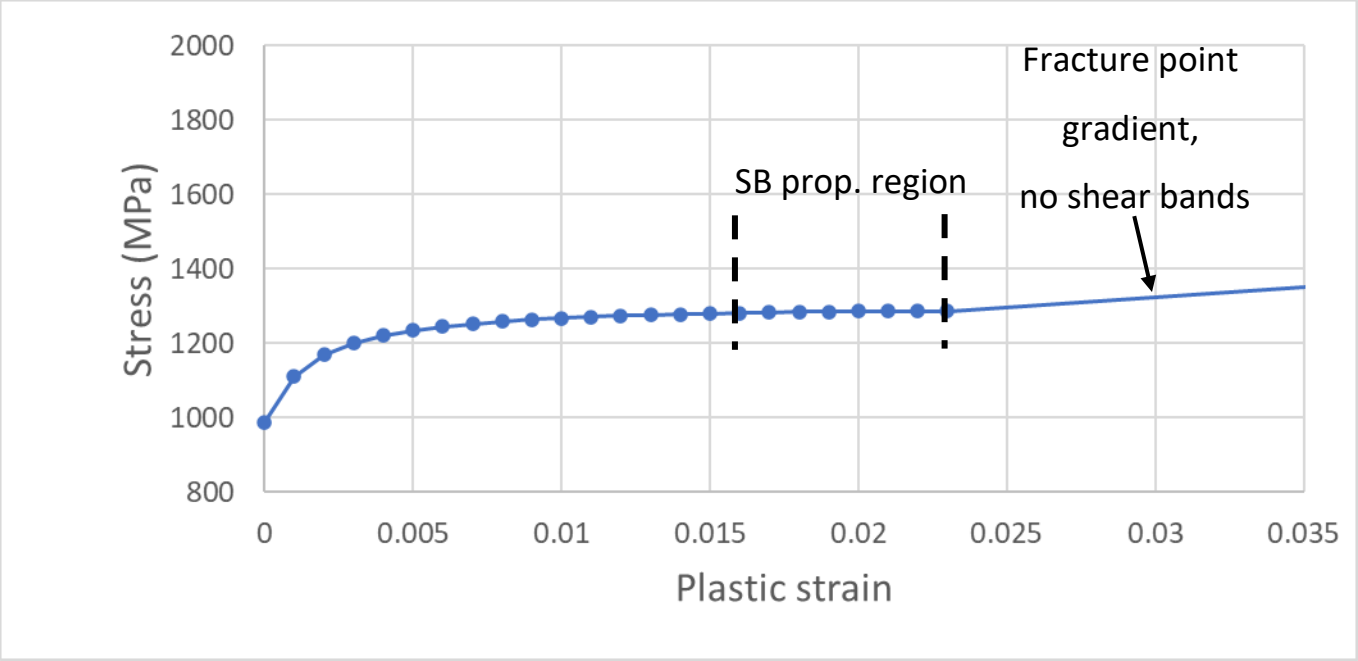


*Figure 6-15: 17DF4/1 material model with the region at which shear bands are generated is identified.*

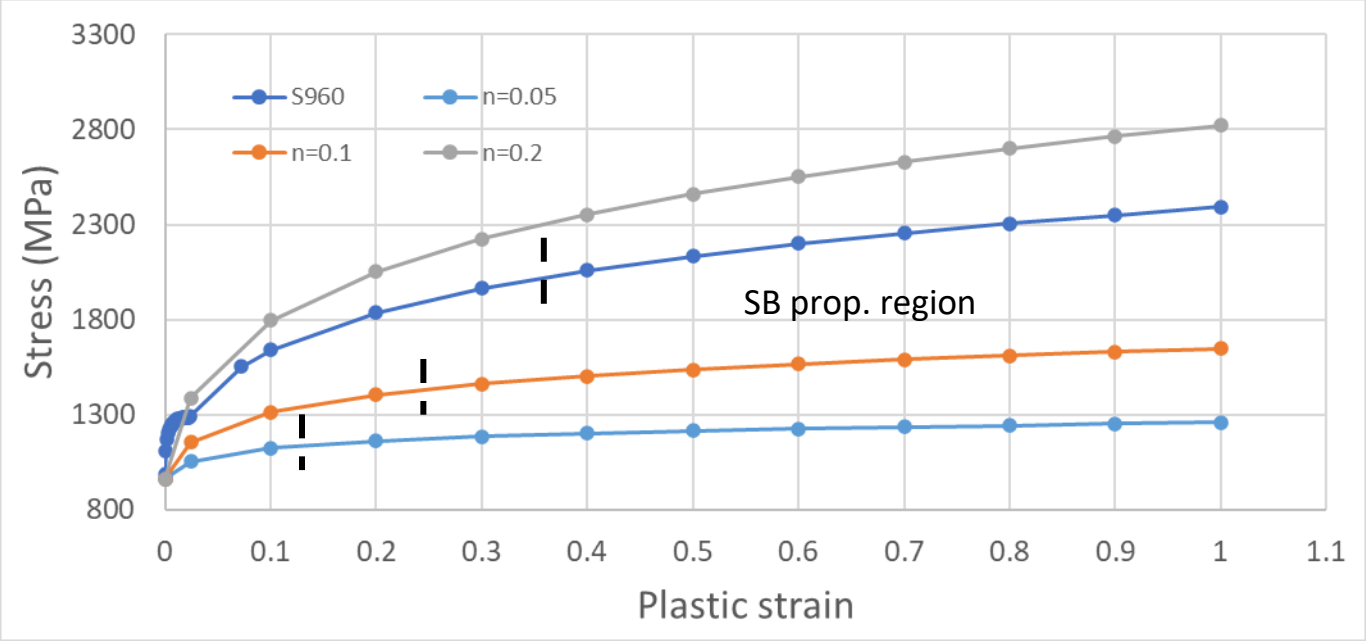


*Figure 6-16: True stress plastic strain curve with the shear band initiation locations in the material models identified.*

| | First submodel shear band strain analysis | |
|---|---|---|
| Mat. model | Displacement (mm) | The gradient at shear band initiation point (MPa/dimensionless strain) |
| n=0.05 | 0.61 | 383 |
| n=0.1 | 1.95 | 570 |
| 17DF4/1 | 0.25 | 170 |
| 17DF4/1 | 2.93 | 950 |
| n=0.2 | | |

*Table 6-4: identification of the gradient at which shear bands initialise.*

#### *6.3.5.1 FEM shear band initialisation calculation*

In section 6.3.1 a method of identifying the plastic strain was identified and using calculations were derived using the alpha value from the ECAP process [41]. Using FEM data the same method can be deployed with these material models by imputing them into Equation 11 to find the α value for the initiation of shear bands has been found in Table 6-5.

| | First submodel α value identification | | |
|---|---|---|---|
| Mat. model | displacement (mm) | strain at shear band initiation | α value |
| n=0.05 | 0.61 | 0.111 | 54.95495 |
| n=0.1 | 1.95 | 0.228 | 56.14035 |
| 17DF4/1, n=0.1642 | 2.93 | 0.364 | 54.89011 |

*Table 6-5: α value identification with FEM submodel data*

As shown in Table 6-5 the material models using the Hollomon equation have very consistent α values of 55 for the submodel. When the same analysis is performed on the sole shear bands initiated in the global model on n=0.05 the α value is found to be higher at 72.

| | Global model α value identification | | |
|---|---|---|---|
| Mat. model | Displacement (mm) | Strain at shear band initiation | α value |
| n=0.05 | 0.88 | 0.18 | 72.22222 |
| n=0.1 | 0 | | |
| 17DF4/1 | 0 | | |
| n=0.2 | 0 | | |

*Table 6-6: α value identification with FEM global model data*

Although the α values in the submodel are found to be around 55, if the stress-strain gradient is dictating the strain this changes every 0.1 strain hence the shear band initiation for n=0.05 is 0.1 strain and 0.2 for n=0.1 and 0.3 for n=0.1642 results in a slightly lower α value of 45-50.
If applying the same consideration to the gradient at the shear band initiation in the global model in Table 6-6 the strain would drop to 0.1. This results in the same α value an n=0.05 in the submodel of 50. So bending in FEM suggests higher stability than the ECAP process as found by M. H. Farshidi et al [41].
This modelling approach would be improved with a more detailed material model to identify the location of strain transition by having a better-defined stress-strain curve in the Hollomon equation by getting a stress value every 0.01 or less. The true assessment for this is from the experimental data.
If this is compared to the micro shear bands generated in the microstructure in Figure 6-4 near the polished top surface, this generates a much lower α value of -37 and 3 in Table 6-7, these were calculated with an n value of 0.1642. This is erroneous in the microstructure at this detail when using the bulk formability at the fracture point data from a tensile test. The micro shear bands observed are singular events occurring in the specimen and are not observed frequently. Further analysis of this process with a detailed nano hardness cyclic loading process could be used to obtain localised material properties and fit an accurate strain-hardening coefficient to this data.

| | Experimental shear band strain analysis | | |
|---|---|---|---|
| Mat. model | Displacement (mm) | Strain at shear band initiation | α value |
| 17DF4/1 band 1 | 1.00 | 0.120 | -36.83 |
| 17DF4/1 band 2 | 1.40 | 0.170 | 3.41 |

*Table 6-7: α value identification with experimental data from the top surface bend test in Figure 6-4*

### *6.3.5.2 Surface waviness*

The application of surface waviness and varying the period and depth in the FEM has been found to impact the strain localisation and mechanism the strain localises in bending. To explore this the period and depth have been varied to analyse the effect of surface roughness.

#### 6.3.5.2.1 Varied period

In section 5.4.1.2.1 as the period decreases in size, the strain is found to localise in bending. This reduced the model's 100% plastic strain displacement limit from 1.25mm to 0.77mm by halving the

period from 150µm to 75µm. The author believes this is due to the stress raiser effect of having a smaller effective radius to act as a notch and promote strain localisation. This causes the strain to localise in a vertical direction for the 75µm period simulations. While in both the 100µm and 150µm periods shear bands can be observed more dominantly as they increase.

This helps to demonstrate the importance of shear bands in bending. Where the strain localisation of shear bands is found to be preferable to that from a stress raiser that can be formed from surface roughness. It is shown with shear bands the strain is distributed between many elements whereas with a stress raiser it localises in only a few elements.

Within material production, the use of adding a waviness could be a viable method of localising shear bands further apart. Thus, the intersections of shear bands at the subsurface will be deeper within the material at a lower average strain, reducing the likelihood of failure. The author considers this to be a flawed concept though, as all damage observed has been initiated at the surface. These have been at points of strain localisation and as such adding any intentional waviness will act as strain localisation, instigating plastic instability.

#### 6.3.5.2.2 Varied depth

Depth is found to have a similar effect as period but as depth is reduced, as does the localised strain. As shown in Figure 5-88 with the 100µm period the change of waviness depth from 5µm to 20µm reduces the model's 100% plastic strain displacement limit from 1.29mm to 0.65mm. The author believes this is again down to the effective radius of the notch acting as a stress raiser. The reduction in period has a larger impact on this than the increase in depth. A combination of small periods with large depths would cause a significant strain localisation effect and severely hamper bendability.

## 6.4 Discussion summary

In this chapter a method for studying the localisation of shear bands and how they can remain stable or promote instability in bending. Different failure modes have been observed with the use of the interrupted insitu bend test process and DIC allows us key insight into the strains at shear band initiation and specimen fracture. That combined with a study on FEM has allowed new insight into the properties linked to bendability.

High strains have been observed in micro tensile tests and bend tests in the microstructures and both feature shear bands. The shear bands found in the tensile test realign themselves to be perpendicular to the applied strain. While the shear bands in bending were found to undergo damage due to mode 2 shearing, both for the top surface polished specimens and the subsurface. This suggests that the

failure mode in the tensile test is due to the applied directional strain while in bending this is due to the shear band.

Multiple means of shear bands evolving and developing both experimentally and in modelling are explored. The size of microstructure, the microstructure, strain-hardening and homogeneity.

The use of polished top surface and 0.6mm depth polished surface bend testing has shown that the softer top surface reduces the intensity of shear bands by increasing their quantity. A harder, martensitic top surface can promote fractures that have been observed as both sudden top surface cracking and development of shear bands in more ductile regions promoted fracture in the local less ductile martensite.

The angled bend tests were used to promote shear bands and damage propagation in plane stress. This approach can be applied to other materials testing. This promoted plastic tearing at the top surface that localised visible shear bands. As the tearing reached a lower depth within the specimen the damage mode changed to a sharp crack. the strain localisation combined with increased hardness as the damage propagated into the subsurface quickly resulting in specimen failure. This further demonstrates the effect of high hardness resulting in reduced bendability.

In UHSS a combination of high strain-hardening coefficient and softness has been demonstrated to improve bendability. It has been demonstrated in FEM that if the strain-hardening coefficient meets or exceeds 0.2, shear bands will be resisted and not generated in bending.

Using a simple strain-hardening calculation the FEM is found to strongly agree with this conclusion with the surface waviness approach showing that a greater number of shear bands is beneficial to the homogenous distribution of strain. Further work it is possible to calibrate the shear band instability parameter $\alpha$ and demonstrate its application in experimental work. This would allow a simple analysis of the bendability of UHSS as long as other properties such as inclusions and texture do not become dominant failure mechanisms.

# 7 Conclusion

Shear bands are the failure mode in bending of UHSS but their impact on bendability seems to be misunderstood. Insitu bend testing within an SEM has allowed the observation of shear bands at microscopic detail. To study shear bands in 3-point bending, a very robust, new bending tooling has been developed and is 80 times stiffer than the original tooling. This promotes very large deformation in insitu bend test specimens with an increase of strain by up to 50%. The tooling was used in conjunction with a new specimen design and production methodology. This varied the material hardness at the bend test surface in tension to promote shear bands and damage, visible to the SEM.

The strain inhomogeneity is found to promote the failure in bending. This is found to cause softening in that region and promote micro shear bands. There can be many drivers of strain localisation including surface hardness, strain-hardening, homogeneity, grain boundary orientation and texture. These have been explored with a combination of experimental work and FEM.

To test the material with a higher hardness samples with 0.6mm depth of its top surface was removed to expose a sub-surface region 21HV0.5 or greater, harder than the top surface. Both these surfaces were bend tested. Using the new tooling it was found that the softer specimen damage initiates at the top surface at 15% maximum shear strain. This did not result in the damage propagating into the subsurface as the softness allowed shear bands on average spaced every 16µm and drop to every 15µm during the bend test. While in the harder 0.6mm depth sub-surface the shear bands are spaced at 18µm and increase to 21µm during the test. This spacing promotes the strain to localise at the individual shear bands causing instability.

FEM provided further insight into the promotion of shear bands. This found that the strain-hardening resists the promotion of shear bands, and is strongly correlated with the strain-hardening-shear band instability formula [41]. The higher the strain-hardening coefficient the later the formation of shear bands. The initiation of shear bands also increases from 0.61mm to 1.95mm for n=0.05 and n=0.1 respectively. The increase in strain-hardening coefficient reduces the average spacing of shear bands in the second submodel from 25.28µm to 12.5µm for a strain-hardening coefficient of 0.05 and 0.1 respectively and no shear bands with a strain-hardening coefficient of 0.2. The strain-hardening coefficient is also found to have an inverse correlation with the displacement of the material model reaching 100% strain which was at 0.77mm and 2.33 for n=0.05 and n=0.1 respectively. This is due to the shear bands spacing being larger thus localising a larger strain. This then promotes softening that then further localises the strain.

Surface waviness was simulated to test the effect of surface roughness by varying the period and depth of the waves. It was found that decreasing period and increasing the depth resulted in a stress raiser that localised strain. This found that the 75µm period had only 0.77mm and at 150µm period this increased to 1.25mm before reaching 100% strain. Increasing the depth promotes a stress raiser by making the trough more acute and so localises strain. Shear bands are observed in all the simulations with smaller stress raisers. Reducing the period or increasing the depth resulted in a single localised vertical strain concentration due to the stress raiser effect.

This did not agree with the experimental results. Shear bands are found to appear at the onset of plastic strain, due to properties making the material inhomogeneous, unlike the FEM. This introduces instability and causes strain to localise in shear bands as soon as they deform plastically. The shear bands do not move and develop by strain localising, the damage initiates in a mode 2 loading shear strain mechanism. This was found to be a different failure mode to tensile tests that were observed to fail due to shear bands deforming and aligning with the applied strain. Therefore, the failure mode for bending is shear strain.

The use of different depth specimens was also enhanced by the use of angled bend tests. This showed the top surfaces ductility resulted in damage forming by plastic tearing. Once it reached the subsurface the strain localised in shear bands and sharp cracks formed creating stress raisers which quickly resulted in specimen failure.

The orientation of elongated grain boundaries at 45° to the top surface has been found to localise strain in shear bands as the shear strain can use the microstructural boundary interfaces to localise strain. The process of pancaking the top surface by reducing final rolling temperatures could act as a means of compressing these microstructures at 45° to the top surface. This will work to homogenise strain without needing to increase material hardenability or softness.

The texture and inclusions are both reported to have significant impacts on bendability, and both add instability. As demonstrated with this work the localised strain softens a region so homogeneity is required to resist the formation of localised strains. To do so a small spacing between shear bands at a microscopic level is required to distribute the strains as homogeneously as possible.

With these improvements in bendability the use of welding when producing structures from UHSS. This brings cost savings to manufacturers but has a much wider impact on the welder's quality of life as the fumes can be harmful and also provides environmental benefits of not burning welding gases. So improving the bendability of UHSS brings significant benefits to all parties and can help foster greater use of UHSS which also bring environmental benefits due to thinner, lighter strips having the same strength.

## 7.1 Actions for Tata Steel to improve the bendability of UHSS

- Increase the softness and work hardening capacity at the top and bottom 10% of the thickness in strip steel.
- Promote bainite in these regions for its superior work hardening properties. Ferrite will still offer benefits over martensite due to its softness.
- Add a rolling reduction to the top and bottom 10% of the thickness to control the orientation of the grain boundaries. This can help to resist the onset of MSBs.
- Look at the effect of increasing grain refinement at the top and bottom 10% regions as this might allow the shear bands to be distributed as micro shear bands. Thus resisting the development of macroscale shear bands.
- Continue to improve the cleanliness of the steel production to reduce inclusions. These are found to localise strain and promote MSBs.
- Try to have as little surface roughness as possible.

## 7.2 Further work

The new 2.5mm diameter bend test tooling has been rigorously tested and demonstrated its value with UHSS and can be used with other materials. Likewise, the angled bend test geometry can be used in other applications with any material to test bendability.

The new bend test methodology could be further improved and applied in other applications to research further novelty. Several ways the bend tests could be improved including:

1. New higher magnification SEM, would improve the imaging, DIC and the quantity of data extracted.
2. Use of new materials.
3. The implementation of EBSD during an insitu bend test.
4. The use of 3D tomography to observe bending in 3D. This would allow the study of the formation of voids in any region of the specimen.

New alloying compounds and manufacturing processes should be studied for UHSS. An analysis of the use of a softer top surface at 10% of the thickness at the top and bottom should be performed [52]. The new steels should look at using either ferrite or bainite at these softer regions. The ferrite is the softest microstructure but has very low strain-hardening, while the bainite will offer a softer microstructure and good hardenability [76]. The tests should be repeated on this UHSS.

Further development of the FEM will offer a great deal of insight into the bendability of UHSS. The addition of a crystal plasticity model would add the instability that should initiate shear bands with

any plastic strain as found in the experiments. Another area of improvement would be the development of a 3D FEM for bending. This would enable an analysis of the development of shear bands across the width of the specimen.

Experimentally use of nanoindentation hardness can be used to study the stress-strain curves at the top surface at the top and bottom 10% of the material thickness. This can be integrated with the strain-hardening shear band initiation formula to verify its application in experimental applications.

# 8 Bibliography


[1] LVD group, “LVD Press brakes,” *LVD Company nv*, 2021. .

[2] Aliko, “Aliko press brakes.” .

[3] Trumpf, “Trumpf press brakes.” .

[4] ASTM International, “Standard Test Methods for Bend Testing of Material for Ductility 1,” *Current*, vol. 14, pp. 1–10, 2014, doi: 10.1520/E0290-13.Copyright.

[5] BSI, “BS EN ISO 7438 : 2020 BSI Standards Publication Metallic materials — Bend test,” pp. 1–13, 2020.

[6] F. Boiocchi, “LVD unveils more automation choices for highly efficient sheet metalworking,” *Sheet metal, Metalworking World Magazine*, 2018. .

[7] A. More, “Ultra-High Strength Steel Market at 2.88% of CAGR, Research with Detailed Insights, Business Profiles, Global Forecast 2021-2027.” https://www.thecowboychannel.com/story/44956561/ultra-high-strength-steel-market-at-2-88-of-cagr-research-with-detailed-insights-business-profiles-global-forecast-2021-2027.

[8] Maximize Market Research, “Global Ultra-High Strength Steel Market: Industry Analysis and Forecast (2020-2026) by Type, End-Use, and Region,” 2021. https://www.maximizemarketresearch.com/market-report/global-ultra-high-strength-steel-market/97258/.

[9] Dataintelo, “Ultra High Strength Steel Market Research Report.” https://dataintelo.com/report/global-ultra-high-strength-steel-market-2/ (accessed Dec. 27, 2021).

[10] A. Weber, “Reducing Weight of Electric Vehicles,” *Assembly*, 2021. https://www.assemblymag.com/articles/96600-reducing-weight-of-electric-vehicles.

[11] Welder academy, “Welding vs. Bending: Which is Stronger?” https://welderacademy.com/welding-vs-bending-which-is-stronger/.

[12] F. Golbabaei and M. Khadem, “Air Pollution in Welding Processes — Assessment and Control Methods,” in *Current Air Quality Issues*, 2015.

[13] BSI, “BS EN ISO 21904-1:2020: Health and safety in welding and allied processes — Equipment for capture and separation of welding fume Part 1: General requirements.” 2020.

[14] D. C. Shuwen Wen, Bev Wade, “Numerical and Experimental Characterisation of Shear Band Formation during Bend Testing of Grade S960 Steel Sheet,” 2016.

[15] Tata Steel Europe, “Advanced and ultra high-strength steel (AHSS/UHSS).”

https://www.tatasteeleurope.com/automotive/products/metallic-coated/ahss-uhss (accessed Jan. 05, 2022).

[16] D. L. Anderson, “CHEMICAL COMPOSITION OF THE MANTLE.,” *J. Geophys. Res.*, 1983, doi: 10.1029/jb088is01p00b41.

[17] M. for Dummies, “Study Iron-Carbon (Fe-C) Phase Diagram.” .

[18] H. Bhadeshia and R. Honeycombe, *Steels: Microstructure and Properties*. 2006.

[19] J. W. Christian, “Military transformations: An introductory survey,” 1965.

[20] M. X. Wei, S. Q. Wang, L. Wang, X. H. Cui, and K. M. Chen, “Effect of tempering conditions on wear resistance in various wear mechanisms of H13 steel,” *Tribol. Int.*, 2011, doi: 10.1016/j.triboint.2011.03.005.

[21] S. Zajac, V. Schwinn, and K. H. Tacke, “Characterisation and Quantification of Complex Bainitic Microstructures in High and Ultra-High Strength Linepipe Steels,” *Mater. Sci. Forum*, 2005, doi: 10.4028/www.scientific.net/msf.500-501.387.

[22] B. Yan *et al.*, “A new dual phase steel for automotive body panels,” in *SAE Technical Papers*, 2003, doi: 10.4271/2003-01-0518.

[23] Y. Mazaheri, A. Kermanpur, A. Najafizadeh, and N. Saeidi, “Development of a new ultrafine/nano ferrite-carbide microstructure by thermomechanical processing,” *Acta Metall. Sin. (English Lett.*, 2015, doi: 10.1007/s40195-014-0191-7.

[24] G. Anand, P. Dey, P. J. J. Kok, D. Chakraborty, and P. P. Chattopadhyay, “Architectured microstructures in steel,” *Mater. Sci. Technol. (United Kingdom)*, vol. 30, no. 9, pp. 1086–1093, 2014, doi: 10.1179/1743284714Y.0000000535.

[25] G. H. Akbari, C. M. Sellars, and J. A. Whiteman, “Microstructural development during warm rolling of an if steel,” *Acta Mater.*, vol. 45, no. 12, pp. 5047–5058, Dec. 1997, doi: 10.1016/S1359-6454(97)00170-5.

[26] A. J. Kaijalainen, P. P. Suikkanen, L. P. Karjalainen, and D. A. Porter, “Influence of subsurface microstructure on the bendability of ultrahigh-strength strip steel,” *Mater. Sci. Eng. A*, vol. 654, pp. 151–160, 2016, doi: 10.1016/j.msea.2015.12.030.

[27] A. M. Arola, A. Kaijalainen, V. Kesti, L. Troive, J. Larkiola, and D. Porter, “The effect of mechanical behavior on bendability of ultrahigh-strength steel,” *Mater. Today Commun.*, vol. 26, no. November 2020, p. 101943, 2021, doi: 10.1016/j.mtcomm.2020.101943.

[28] P. A. Beck and P. R. Sperry, “Strain induced grain boundary migration in high purity aluminum,” *J. Appl. Phys.*, 1950, doi: 10.1063/1.1699614.

[29] C. Zhang, Z. Liu, and G. Wang, “Effects of hot rolled shear bands on formability and surface

ridging of an ultra purified 21%Cr ferritic stainless steel," *J. Mater. Process. Technol.*, vol. 211, no. 6, pp. 1051–1059, Jun. 2011, doi: 10.1016/j.jmatprotec.2011.01.005.

[30] J. J. Jonas, "Effects of shear band formation on texture development in warm-rolled IF steels," in *Journal of Materials Processing Technology*, Nov. 2001, vol. 117, no. 3, pp. 293–299, doi: 10.1016/S0924-0136(01)00786-5.

[31] A. J. Kaijalainen, P. Suikkanen, L. P. Karjalainen, and J. J. Jonas, "Effect of Austenite pancaking on the microstructure, texture, and bendability of an ultrahigh-strength strip steel," *Metall. Mater. Trans. A Phys. Metall. Mater. Sci.*, vol. 45, no. 3, pp. 1273–1283, 2014, doi: 10.1007/s11661-013-2062-7.

[32] A. J. Kaijalainen, M. Liimatainen, V. Kesti, J. Heikkala, T. Liimatainen, and D. A. Porter, "Influence of Composition and Hot Rolling on the Subsurface Microstructure and Bendability of Ultrahigh-Strength Strip," *Metall. Mater. Trans. A Phys. Metall. Mater. Sci.*, vol. 47, no. 8, pp. 4175–4188, 2016, doi: 10.1007/s11661-016-3574-8.

[33] Tata Steel Europe, "Tata Steel opens Europe's most powerful decoiler," 2015. .

[34] L. Troive, "New method for evaluation of bendability based on three-point-bending and the evolution of the cross-section moment," in *Journal of Physics: Conference Series*, 2017, vol. 896, no. 1, doi: 10.1088/1742-6596/896/1/012006.

[35] L. Lanzoni and A. M. Tarantino, "Finite Anticlastic Bending of Hyperelastic Solids and Beams," *J. Elast.*, vol. 131, no. 2, pp. 137–170, 2018, doi: 10.1007/s10659-017-9649-y.

[36] K. Alharbi *et al.*, "Damage in dual phase steel DP1000 investigated using digital image correlation and microstructure simulation," *Model. Simul. Mater. Sci. Eng.*, vol. 23, no. 8, 2015, doi: 10.1088/0965-0393/23/8/085005.

[37] S. L. Semiatin and J. J. Jonas, "Formability and workability of metals: plastic instability and flow localization," *Am. Soc. Met. 1984,* 1984.

[38] I. L. Dillamore, J. G. Roberts, and A. C. Bush, "Occurrence of shear bands in heavily rolled cubic metals," *Met. Sci.*, vol. 13, no. 2, pp. 73–77, 1979, doi: 10.1179/msc.1979.13.2.73.

[39] A. Kaijalainen *et al.*, "Effect of inclusions on the properties of ultra-high-strength low-alloy steel with a martensitic-bainitic microstructure," *Proc 8th Int Conf Clean Steel*, 2012.

[40] M. Kang, J. Park, S. S. Sohn, H. Kim, K. H. Kim, and S. Lee, "Adiabatic shear banding and cracking phenomena occurring during cold-forging simulation tests of plain carbon steel wire rods by using a split Hopkinson's pressure bar," *Met. Mater. Int.*, vol. 21, no. 6, 2015, doi: 10.1007/s12540-015-5252-6.

[41] M. H. Farshidi, H. Doryo, M. Yuasa, and H. Miyamoto, "Formation of Micro Shear Bands During

Severe Plastic Deformation of BCC Alloys," vol. 3, no. 1, pp. 47–51, 2018.

[42] S. L. Semiatin and J. J. Jonas, "Formability and Workability of Metals," *ASM, Met. Park. Ohio*, p. 299, 1984.

[43] A. J. Kaijalainen, P. P. Suikkanen, T. J. Limnell, L. P. Karjalainen, J. I. Kömi, and D. A. Porter, "Effect of austenite grain structure on the strength and toughness of direct-quenched martensite," *J. Alloys Compd.*, vol. 577, no. SUPPL. 1, pp. S642–S648, 2013, doi: 10.1016/j.jallcom.2012.03.030.

[44] R. Cicoria, B. Chehab, and H. Zurob, "Diffusion as a method for producing architectured materials," *Scr. Mater.*, vol. 68, no. 1, pp. 17–21, 2013, doi: 10.1016/j.scriptamat.2012.08.004.

[45] H. Luo *et al.*, "Plasticity without dislocations in a polycrystalline intermetallic," *Nat. Commun.*, 2019, doi: 10.1038/s41467-019-11505-1.

[46] M. Dao and M. Lit, "A micromechanics study on strain-localization-induced fracture initiation in bending using crystal plasticity models," *Philos. Mag. A Phys. Condens. Matter, Struct. Defects Mech. Prop.*, 2001, doi: 10.1080/01418610108216649.

[47] H. Kaneko, T. Morikawa, M. Tanaka, H. Inoue, and K. Higashida, "Recrystallization texture and shear band formation in bending," *Mater. Trans.*, vol. 58, no. 2, 2017, doi: 10.2320/matertrans.M2016363.

[48] R. Roumina *et al.*, "Bending properties of functionally graded 300M steels," *Mater. Sci. Eng. A*, vol. 653, pp. 63–70, 2016, doi: 10.1016/j.msea.2015.12.012.

[49] F. B. Pickering, "Some effects of non-metallic inclusions on the properties of steels," Sheffield, 1989.

[50] A. Kaijalainen, M. Liimatainen, V. Kesti, S. Anttila, P. Suikkanen, and D. A. Porter, "Effect of red scale on the bendability of ultrahigh-strength strip steel," *Mater. Sci. Forum*, vol. 879, no. November, pp. 879–884, 2017, doi: 10.4028/www.scientific.net/MSF.879.879.

[51] J. Steninger and A. Melander, "RELATION BETWEEN BENDABILITY, TENSILE PROPERTIES AND PARTICLE STRUCTURE OF LOW CARBON STEEL.," *Scand. J. Metall.*, 1982.

[52] W. Muhammad *et al.*, "Bendability enhancement of an age-hardenable aluminum alloy: Part II — multiscale numerical modeling of shear banding and fracture," *Mater. Sci. Eng. A*, vol. 754, 2019, doi: 10.1016/j.msea.2019.03.050.

[53] D. Hull, *Observing, Measuring and Interpreting Fracture Surface Topography*. Cambridge University Press, 1999.

[54] G. R. Johnson and W. H. Cook, "Fracture characteristics of three metals subjected to various strains, strain rates, temperatures and pressures," *Eng. Fract. Mech.*, vol. 21, no. 1, pp. 31–48,

Jan. 1985, doi: 10.1016/0013-7944(85)90052-9.

[55] F. J. P. Reis and F. X. C. Andrade, “Implementation and Application of a new Plasticity Model in LS-DYNA including Lode Angle Dependence,” *11th Ger. LS-Dyna Forum 2012*, 2012.

[56] W. Lode, “Versuche über den Einfluß der mittleren Hauptspannung auf das Fließen der Metalle Eisen, Kupfer und Nickel,” *Zeitschrift für Phys.*, vol. 36, no. 11–12, 1926, doi: 10.1007/BF01400222.

[57] F. Concli and L. Maccioni, “Experimental–numerical calibration of the fracture locus of weathering steel,” in *WIT Transactions on Engineering Sciences*, 2019, vol. 124, doi: 10.2495/MC190211.

[58] Y. Lou and H. Huh, “Extension of a shear-controlled ductile fracture model considering the stress triaxiality and the Lode parameter,” *Int. J. Solids Struct.*, vol. 50, no. 2, 2013, doi: 10.1016/j.ijsolstr.2012.10.007.

[59] K. Yamazaki, M. Oka, H. Yasuda, Y. Mizuyama, and H. Tsuchiya, “Recent advances in ultrahigh-strength sheet steels for automotive structural use,” *Nippon Steel Technical Report*, no. 64. pp. 37–44, 1995.

[60] J. Lämsä, A. Väisänen, J. Heikkala, and A. Järvenpää, “Correlation of tensile test parameters and bendability of high-strength Steels,” in *Key Engineering Materials*, 2013, doi: 10.4028/www.scientific.net/KEM.554-557.12.

[61] A. M. Arola, A. Kaijalainen, and V. Kesti, “The effect of surface layer properties on bendability of ultra-high strength steel,” *AIP Conf. Proc.*, vol. 1769, 2016, doi: 10.1063/1.4963642.

[62] I. Tsoupis, S. Hildering, and M. Merklein, “Bending of high-strength low-alloyed steel with respect to edge crack sensitivity caused by shearing operations,” in *Procedia Engineering*, 2014, vol. 81, doi: 10.1016/j.proeng.2014.10.065.

[63] V. Kesti *et al.*, “Bendability and microstructure of direct quenched Optim® 960QC,” *Mater. Sci. Forum*, vol. 783–786, pp. 818–824, 2014, doi: 10.4028/www.scientific.net/MSF.783-786.818.

[64] W. A. Steel, “Advanced High-Strength Steel (AHSS) Definitions.” https://www.worldautosteel.org/steel-basics/automotive-advanced-high-strength-steel-ahss-definitions/ (accessed Jan. 05, 2022).

[65] M. Kaupper and M. Merklein, “Bendability of advanced high strength steels - A new evaluation procedure,” *CIRP Ann. - Manuf. Technol.*, vol. 62, no. 1, pp. 247–250, Jan. 2013, doi: 10.1016/j.cirp.2013.03.049.

[66] A. Kaijalainen, V. Kesti, J. Heikkala, R. Ruoppa, D. Porter, and J. Kömi, “Bendability of shot blasted ultrahigh-strength steels,” *Mater. Sci. Forum*, vol. 941 MSF, pp. 510–515, 2018, doi:

10.4028/www.scientific.net/MSF.941.510.

[67] M. Kuroda and V. Tvergaard, “Effects of texture on shear band formation in plane strain tension/compression and bending,” *Int. J. Plast.*, vol. 23, no. 2, pp. 244–272, Feb. 2007, doi: 10.1016/j.ijplas.2006.03.014.

[68] S. Morito, H. Tanaka, R. Konishi, T. Furuhara, and T. Maki, “The morphology and crystallography of lath martensite in Fe-C alloys,” *Acta Mater.*, vol. 51, no. 6, pp. 1789–1799, 2003, doi: 10.1016/S1359-6454(02)00577-3.

[69] R. Roumina, J. D. Embury, O. Bouaziz, and H. S. Zurob, “Mechanical behavior of a compositionally graded 300M steel,” *Mater. Sci. Eng. A*, vol. 578, pp. 140–149, 2013, doi: 10.1016/j.msea.2013.04.006.

[70] R. Becker, “An analysis of shear localization during bending of a polycrystalline sheet,” *J. Appl. Mech. Trans. ASME*, vol. 59, no. 3, pp. 491–496, 1992, doi: 10.1115/1.2893750.

[71] N. Ramakrishnan and S. N. Atluri, “Simulation of shear band formation in plane strain tension and compression using FEM,” *Mech. Mater.*, 1994, doi: 10.1016/0167-6636(94)90068-X.

[72] C. Soyarslan, M. Malekipour Gharbi, and A. E. Tekkaya, “A combined experimental-numerical investigation of ductile fracture in bending of a class of ferritic-martensitic steel,” *Int. J. Solids Struct.*, vol. 49, no. 13, pp. 1608–1626, 2012, doi: 10.1016/j.ijsolstr.2012.03.009.

[73] H. Ghadbeigi, C. Pinna, S. Celotto, and J. R. Yates, “Local plastic strain evolution in a high strength dual-phase steel,” *Mater. Sci. Eng. A*, vol. 527, no. 18–19, pp. 5026–5032, 2010, doi: 10.1016/j.msea.2010.04.052.

[74] S. H. Choi, E. Y. Kim, W. Woo, S. H. Han, and J. H. Kwak, “The effect of crystallographic orientationonthe micromechanical deformation and failure behaviors of DP980 steel during uniaxial tension,” *Int. J. Plast.*, vol. 45, pp. 85–102, 2013, doi: 10.1016/j.ijplas.2012.11.013.

[75] W. Muhammad *et al.*, “Bendability enhancement of an age-hardenable aluminum alloy: Part I — relationship between microstructure, plastic deformation and fracture,” *Mater. Sci. Eng. A*, vol. 753, 2019, doi: 10.1016/j.msea.2019.03.053.

[76] A. Ramazani, P. T. Pinard, S. Richter, A. Schwedt, and U. Prahl, “Characterisation of microstructure and modelling of flow behaviour of bainite-aided dual-phase steel,” *Comput. Mater. Sci.*, vol. 80, pp. 134–141, 2013, doi: 10.1016/j.commatsci.2013.05.017.

[77] A. C. Bell and S. Ramalingam, “Design and application of tensile testing stage for the SEM,” *J. Eng. Mater. Technol. Trans. ASME*, vol. 96, no. 3, 1974, doi: 10.1115/1.3443204.

[78] M. Gasperini, C. Pinna, and W. A. Swiatnicki, “Microstructural evolution of an aluminium alloy during high shear deformation,” vol. 44, no. 10, pp. 4195–4208, 1996.

[79] M. F. Kiu, C. Pinna, and D. C. J. Farrugia, “New Experimental Procedure for the Analysis of Micro-Scale Surface Damage at High Temperature,” *Exp. Mech.*, vol. 56, no. 6, 2016, doi: 10.1007/s11340-016-0151-4.

[80] M. A. Haque and M. T. A. Saif, “In-situ tensile testing of nano-scale specimens in SEM and TEM,” *Exp. Mech.*, 2002, doi: 10.1177/0018512002042001797.

[81] Deben, “2kN & 5kN Tensile compression and horizontal bending stage.” .

[82] S. B. Hosseini, C. Temmel, B. Karlsson, and N. G. Ingesten, “An in-situ scanning electron microscopy study of the bonding between MnS inclusions and the matrix during tensile deformation of hot-rolled steels,” *Metall. Mater. Trans. A Phys. Metall. Mater. Sci.*, vol. 38, no. 5, pp. 982–989, 2007, doi: 10.1007/s11661-007-9122-9.

[83] A. Ramazani, A. Schwedt, A. Aretz, U. Prahl, and W. Bleck, “Characterization and modelling of failure initiation in DP steel,” *Comput. Mater. Sci.*, vol. 75, pp. 35–44, 2013, doi: 10.1016/j.commatsci.2013.04.001.

[84] ASTM Int., “Standard Test Methods for Tension Testing of Metallic Materials 1 - ASTM E8M-13a,” *Astm*, vol. i, no. C, pp. 1–28, 2014, doi: 10.1520/E0008.

[85] H. W. Schreier and M. A. Sutton, “Systematic errors in digital image correlation due to undermatched subset shape functions,” *Exp. Mech.*, vol. 42, no. 3, 2002, doi: 10.1177/001448502321548391.

[86] P. Reu, “All about speckles: Speckle size measurement,” *Exp. Tech.*, vol. 44, no. 11, pp. 4–5, 2014, doi: 10.1111/ext.12110.

[87] LaVision, “Digital Image Correlation (DIC).” .

[88] H. Ghadbeigi, C. Pinna, and S. Celotto, “Quantitative Strain Analysis of the Large Deformation at the Scale of Microstructure: Comparison between Digital Image Correlation and Microgrid Techniques,” *Exp. Mech.*, vol. 52, no. 9, pp. 1483–1492, 2012, doi: 10.1007/s11340-012-9612-6.

[89] M. A. Sutton, N. Li, D. C. Joy, A. P. Reynolds, and X. Li, “Scanning electron microscopy for quantitative small and large deformation measurements Part I: SEM imaging at magnifications from 200 to 10,000,” *Exp. Mech.*, 2007, doi: 10.1007/s11340-007-9042-z.

[90] W. Ye, P. Efthymiadis, C. Pinna, A. Ma, B. Shollock, and R. Dashwood, “Experimental and modelling study of fatigue crack initiation in an aluminium beam with a hole under 4-point bending,” *Int. J. Solids Struct.*, vol. 138, no. February, pp. 87–96, 2018, doi: 10.1016/j.ijsolstr.2018.01.001.

[91] L. L. Mishnaevsky, N. Lippmann, and S. Schmauder, “Micromechanisms and modelling of crack

initiation and growth in tool steels: Role of primary carbides," *Zeitschrift fuer Met. Res. Adv. Tech.*, vol. 94, no. 6, pp. 676–681, 2003, doi: 10.3139/146.030676.

[92] J. C. Lautridou and A. Pineau, "Crack initiation and stable crack growth resistance in A508 steels in relation to inclusion distribution," *Eng. Fract. Mech.*, vol. 15, no. 1–2, pp. 55–71, 1981, doi: 10.1016/0013-7944(81)90105-3.

[93] V. García Navas, I. Ferreres, J. A. Marañón, C. Garcia-Rosales, and J. Gil Sevillano, "Electro-discharge machining (EDM) versus hard turning and grinding-Comparison of residual stresses and surface integrity generated in AISI O1 tool steel," *J. Mater. Process. Technol.*, 2008, doi: 10.1016/j.jmatprotec.2007.04.131.

[94] B. Ekmekci, "Residual stresses and white layer in electric discharge machining (EDM)," *Appl. Surf. Sci.*, vol. 253, no. 23, pp. 9234–9240, 2007, doi: 10.1016/j.apsusc.2007.05.078.

[95] H. T. Lee, F. C. Hsu, and T. Y. Tai, "Study of surface integrity using the small area EDM process with a copper-tungsten electrode," *Mater. Sci. Eng. A*, 2004, doi: 10.1016/j.msea.2003.08.046.

[96] A. Inc., "J-Bonest, digital caliper." .

[97] Buehler Ltd, "Final Polishing Suspensions." .

[98] ASTM Standard, "Standard Test Method for Microindentation Hardness of Materials," *ASTM Int.*, 2017.

[99] Y. Lu *et al.*, "Conversion between Vickers hardness and nanohardness by correcting projected area with sink-in and pile-up effects," *Plasma Sci. Technol.*, vol. 22, no. 6, 2020, doi: 10.1088/2058-6272/ab7d47.

[100] "Instrumented Indentation Testing," in *Mechanical Testing and Evaluation*, 2018.

[101] X. Li and B. Bhushan, "A review of nanoindentation continuous stiffness measurement technique and its applications," *Mater. Charact.*, vol. 48, no. 1, 2002, doi: 10.1016/S1044-5803(02)00192-4.

[102] L. Qian, M. Li, Z. Zhou, H. Yang, and X. Shi, "Comparison of nano-indentation hardness to microhardness," *Surf. Coatings Technol.*, 2005, doi: 10.1016/j.surfcoat.2004.07.108.

[103] B. Yngve, "The Hollomon n – value , and the strain to necking in steel," *Paper8*, no. February, 2011.

[104] D. Hollis, "StrainMaster DaVis v10 Digital Image Correlation Software Experimental Mechanics," 2018, pp. 1–20.

[105] D. S. Simulia, "Abaqus 6.14," *Abaqus 6.14 Anal. User's Guid.*, 2014.

[106] H. Hollomon, "Metals Technology, 1945, Vol. XII - June 1945 - Tensile Deformation," *Am. insititute Min. Metall. Eng. insititute Min. Metall. Eng.*, vol. 879, no. I, 1945.

[107] D. S. Simulia, “Solidworks 2014.” 2014.

[108] OTAI, “M2 Tool Steel | 1.3343 | HS-6-5-2C| SKH51.” .

[109] R. G. Dowding, C. Pinna, H. Ghadbeigi, and D. Farrugia, “Localized damage analysis for high strength S960 steel using micro-tensile testing and digital image correlation,” in *Small sample test techniques*, 2018, pp. 272–276.

[110] Ssab, “Bending of High Strength Steel,” p. 8, 2016.

[111] W. Wang, Y. Ma, M. Yang, P. Jiang, F. Yuan, and X. Wu, “Strain rate effect on tensile behavior for a high specific strength steel: From quasi-static to intermediate strain rates,” *Metals (Basel).*, vol. 8, no. 1, 2018, doi: 10.3390/met8010011.

[112] E. H. Atzema *et al.*, “List of contributors,” in *Automotive Steels*, 2017.

# 9 Appendix

## 9.1.1 Macroscale results

### *9.1.1.1 17DF4/1 tensile test results*

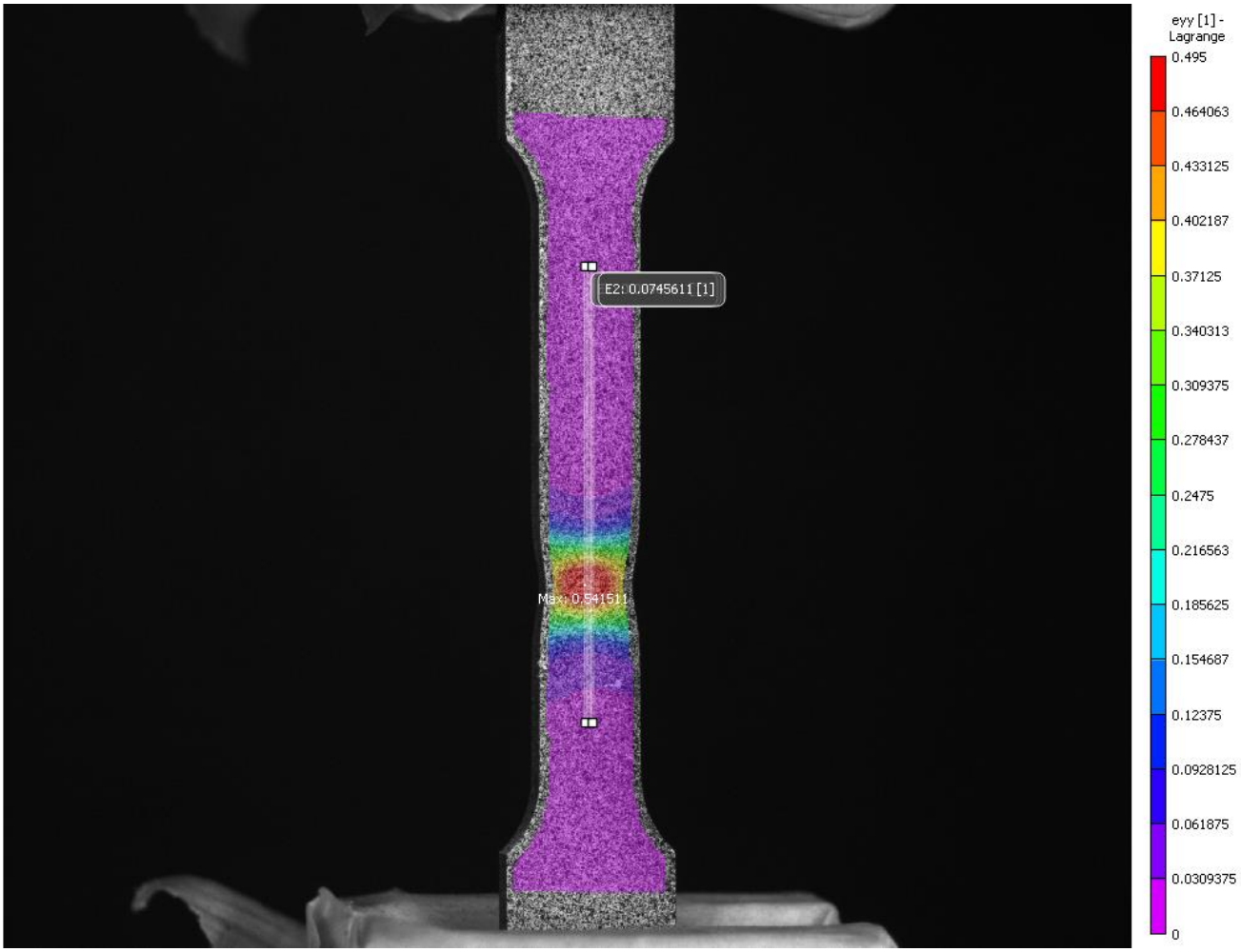

*Figure 9-1: TD1, image taken from the left camera with the Eyy strain surface profile.*

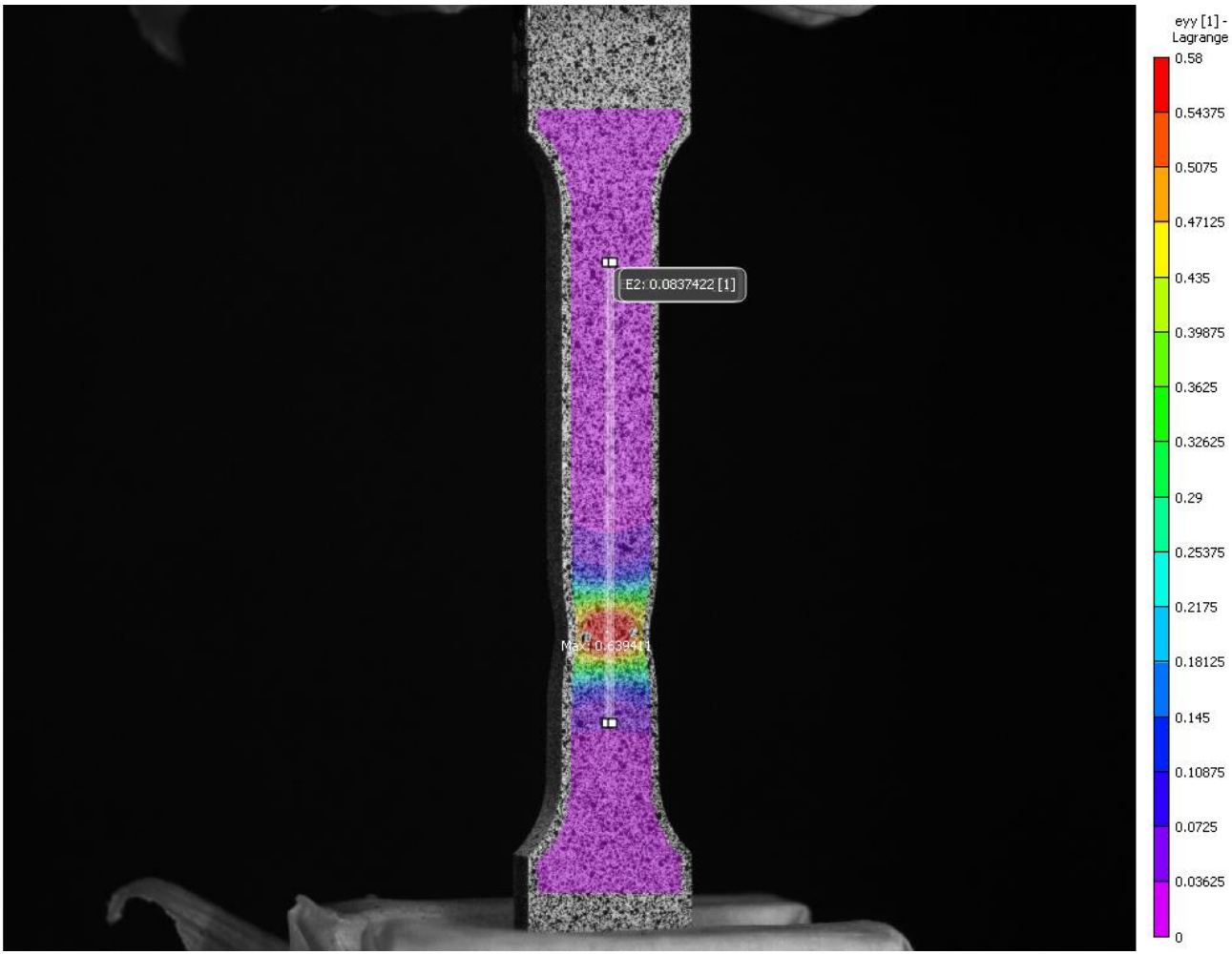


*Figure 9-2: TD2, image taken from the left camera with the Eyy strain surface profile.*

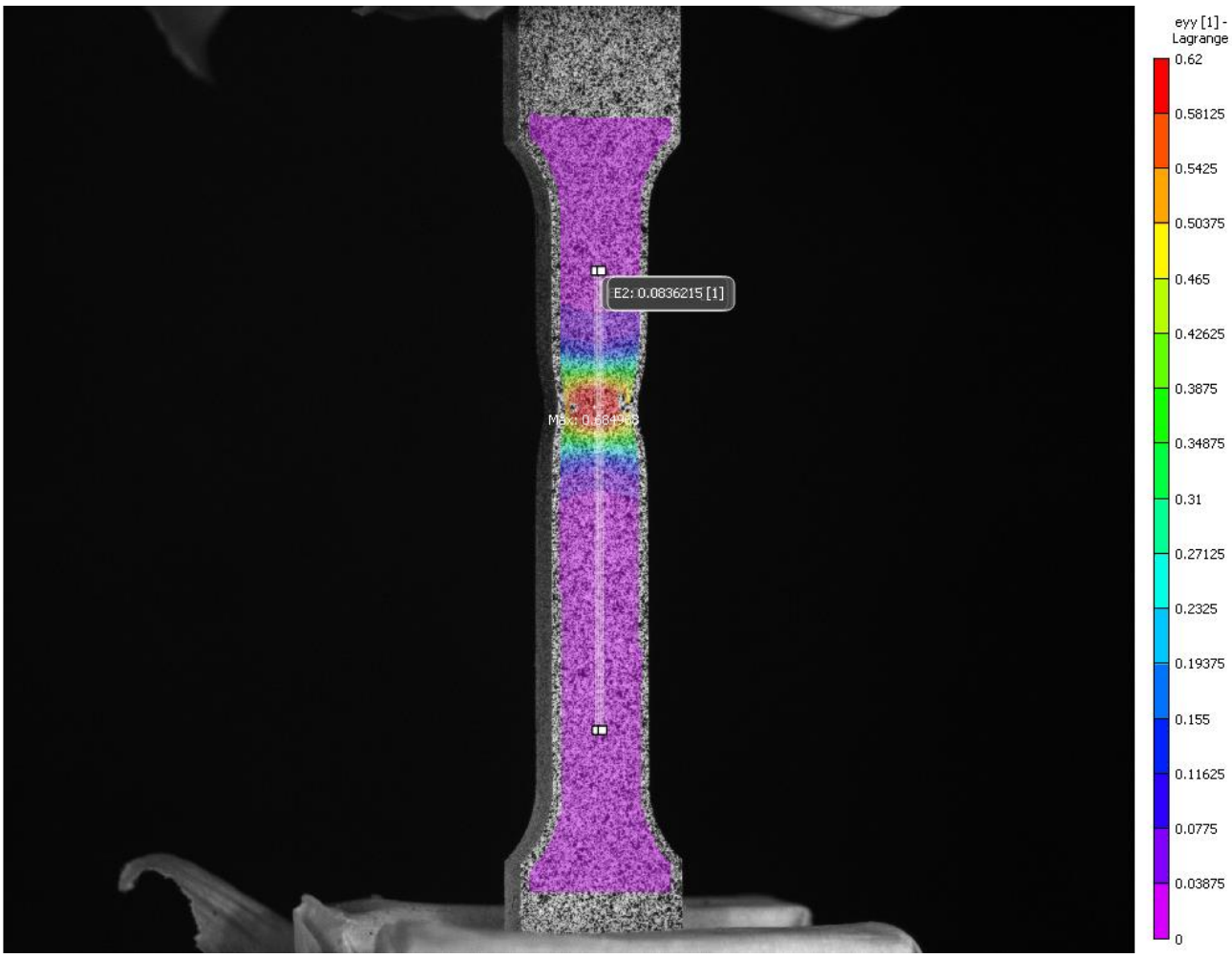


*Figure 9-3: TD3, image taken from the left camera with the Eyy strain surface profile.*

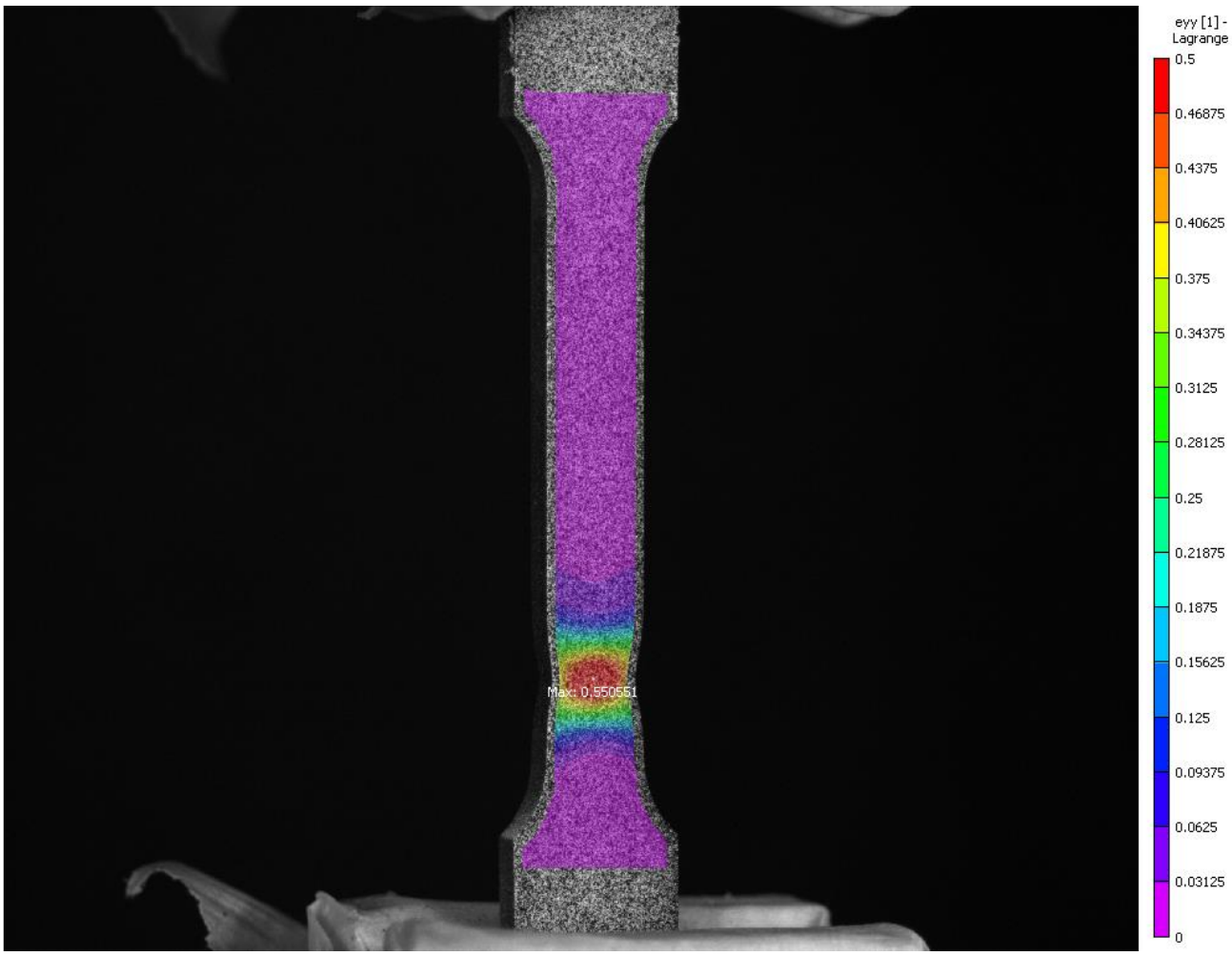


*Figure 9-4: TD4, image taken from the left camera with the Eyy strain surface profile.*

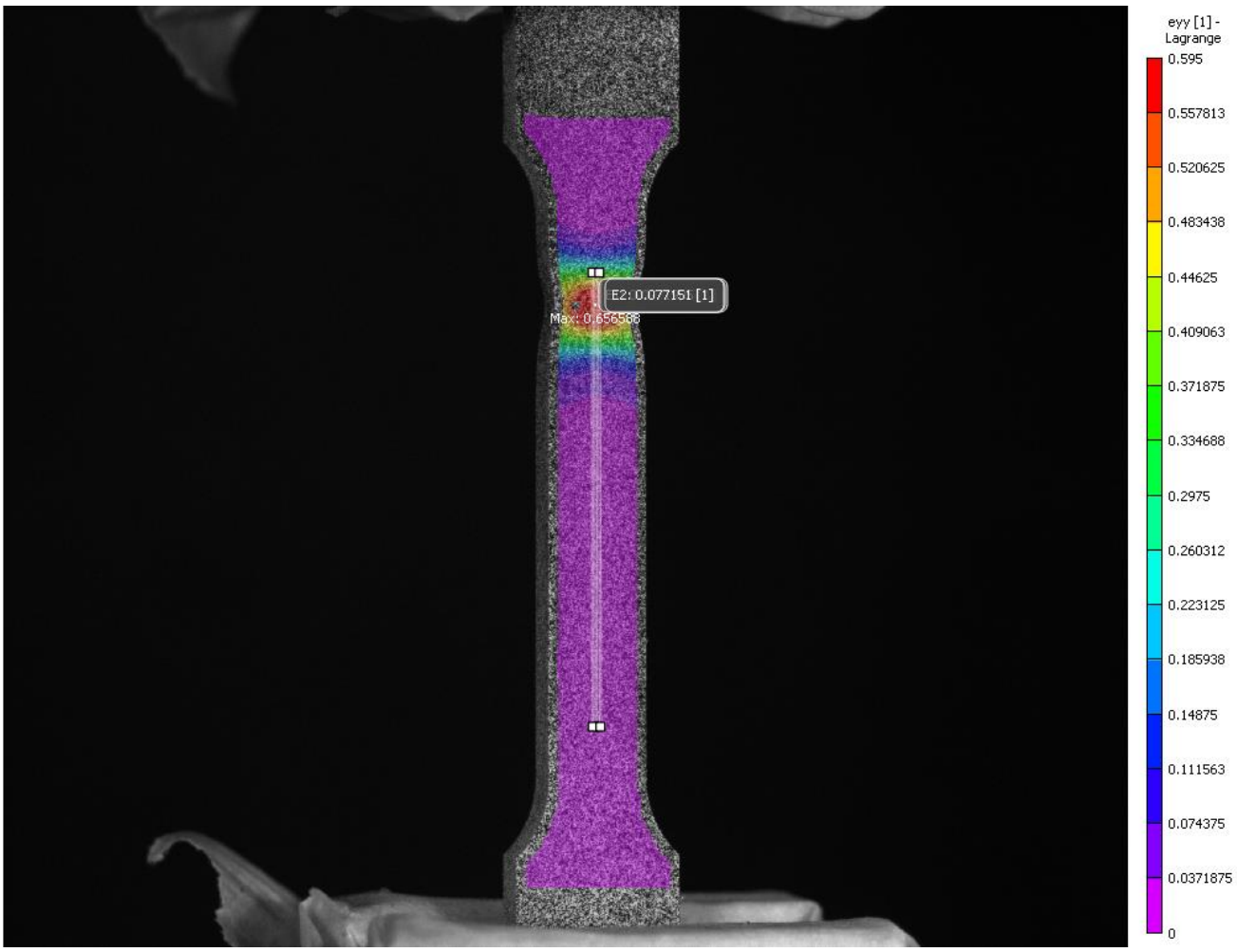


*Figure 9-5: TD5, image taken from the left camera with the Eyy strain surface profile.*

## 9.2 Appendix B: Micro hardness and nano hardness data

### 9.2.1 Micro Hardness

| Test Point | Method | Objective Lens | | | Depth (mm) | | | | | | | | | | |
|---|---|---|---|---|---|---|---|---|---|---|---|---|---|---|---|
| 1 | HV 0,5 | 40x | | Horisontal position (mm) | 0.15 | 0.3 | 0.45 | 0.6 | 0.75 | 0.9 | 1.05 | 1.2 | 1.35 | 1.5 | 1.65 |
| 2 | HV 0,5 | 40x | | 0 | 401 | 415 | 424 | 431 | 423 | 425 | 424 | 413 | 404 | 418 | 399 |
| 3 | HV 0,5 | 40x | | 0.3 | 408 | 422 | 423 | 433 | 422 | 425 | 416 | 414 | 421 | 413 | 404 |
| 4 | HV 0,5 | 40x | | 0.6 | 407 | 414 | 425 | 419 | 427 | 418 | 402 | 419 | 410 | 424 | 397 |
| 5 | HV 0,5 | 40x | | 0.9 | 397 | 416 | 428 | 428 | 418 | 423 | 409 | 415 | 410 | 430 | 404 |
| 6 | HV 0,5 | 40x | | 1.2 | 406 | 411 | 422 | 423 | 424 | 424 | 409 | 409 | 405 | 424 | 406 |
| 7 | HV 0,5 | 40x | | 1.5 | 410 | 414 | 421 | 421 | 418 | 416 | 402 | 417 | 406 | 428 | 435 |
| 8 | HV 0,5 | 40x | | 1.8 | 398 | 417 | 421 | 439 | 415 | 421 | 406 | 410 | 408 | 414 | 511 |
| 9 | HV 0,5 | 40x | | 2.1 | 410 | 416 | 428 | 419 | 424 | 427 | 406 | 409 | 404 | 422 | 439 |
| 10 | HV 0,5 | 40x | | 2.4 | 409 | 423 | 413 | 425 | 431 | 421 | 408 | 414 | 409 | 416 | 432 |
| | | | | 2.7 | 407 | 419 | 422 | 454 | 423 | 418 | 415 | 406 | 421 | 510 | 484 |

## 9.2.2 Nano Hardness

Hardness HV

| Depth (μm) | 0 | 50 | 100 | 150 | 200 |
|---|---|---|---|---|---|
| 2000 | 553.2434 | 530.6374 | 520.9708 | 530.1624 | 527.0243 |
| 1950 | 503.5492 | 540.8778 | 485.7175 | 499.8748 | 532.0628 |
| 1900 | 482.031 | 511.5842 | 567.3586 | 522.6193 | 550.3992 |
| 1850 | 511.2139 | 539.477 | 529.0162 | 529.3972 | 522.3113 |
| 1800 | 495.0468 | 479.9363 | 491.136 | 473.9881 | 499.172 |
| 1750 | 497.2298 | 526.3044 | 552.0552 | 502.0377 | 500.9276 |
| 1700 | 507.8968 | 523.8986 | 489.2024 | 537.5615 | 537.0197 |
| 1650 | 516.0258 | 492.7842 | 589.4616 | 507.7197 | 525.0359 |
| 1600 | 480.475 | 493.668 | 460.9521 | 530.7053 | 490.6839 |
| 1550 | 506.8972 | 546.8547 | 488.4994 | 477.935 | 526.4155 |
| 1500 | 536.8671 | 550.6694 | 540.3417 | 569.811 | 540.0502 |
| 1450 | 505.2778 | 531.8428 | 534.8889 | 435.1066 | 512.9332 |
| 1400 | 468.1827 | 516.6687 | 496.5943 | 543.0589 | 520.4469 |
| 1350 | 539.0848 | 546.209 | 498.4492 | 492.9173 | 562.8104 |
| 1300 | 563.2217 | 523.9234 | 533.9879 | 560.9102 | 536.5292 |
| 1250 | 530.4808 | 572.8589 | 489.1341 | 538.5808 | 520.3474 |
| 1200 | 512.122 | 531.2373 | 508.9903 | 547.8826 | 496.5045 |
| 1150 | 529.3896 | 484.7915 | 516.8784 | 533.5927 | 514.2514 |
| 1100 | 535.7468 | 534.5127 | 569.5013 | 535.8967 | 534.1007 |
| 1050 | 548.9742 | 529.7329 | 563.5889 | 465.4876 | 468.0774 |
| 1000 | 521.7244 | 503.5019 | 523.0825 | 496.4011 | 498.1759 |
| 950 | 511.2708 | 519.6976 | 538.9213 | 520.6533 | 527.5292 |
| 900 | 492.6493 | 513.8734 | 505.9056 | 490.733 | 517.9304 |
| 850 | 523.9514 | 506.1969 | 526.5869 | 536.0187 | 534.003 |
| 800 | 487.7792 | 501.6141 | 525.2879 | 491.7634 | 501.5758 |
| 750 | 541.1146 | 499.314 | 490.808 | 502.1315 | 558.54 |
| 700 | 480.132 | 485.0531 | 530.1548 | 526.9084 | 533.9406 |

| | | | | | |
|---|---|---|---|---|---|
| 650 | 557.7258 | 536.8047 | 528.3603 | 543.6121 | 526.6259 |
| 600 | 528.9108 | 456.1828 | 493.6277 | 500.9515 | 499.838 |
| 550 | 482.4877 | 533.1927 | 530.1494 | 550.4645 | 532.6285 |
| 500 | 570.5718 | 496.3498 | 514.5748 | 506.056 | 471.6437 |
| 450 | 515.2809 | 522.7325 | 521.9115 | 509.3453 | 511.0968 |
| 400 | 508.2365 | 523.5561 | 534.9783 | 552.7199 | 540.1697 |
| 350 | 479.589 | 512.7116 | 547.2618 | 503.1236 | 491.7906 |
| 300 | 454.2901 | 487.5329 | 552.6331 | 483.6207 | 490.3991 |
| 250 | 476.6789 | 549.8971 | 482.1086 | 483.9719 | 532.4612 |
| 200 | 475.6145 | 481.4533 | 479.0884 | 486.1097 | 518.8063 |
| 150 | 471.6648 | 470.9477 | 492.3809 | 492.6484 | 522.5703 |
| 100 | 482.0665 | 508.7285 | 493.5983 | 428.1633 | 527.9738 |
| 50 | 445.6286 | 484.2225 | 475.761 | 518.341 | 451.1485 |